A. Summary of Research on Inelastic Analysis Procedures

A.1 Introduction

Inelastic analysis of structures is a field with a number of active researchers. In order to gauge the current situation with respect to information and data that might be used to evaluate and improve procedures, ATC solicited information from investigators on relevant published research as well as on research in progress and unpublished insights and perspectives. The purpose was to obtain insight for the direction of the project. This section summarizes the information obtained from these investigators including limited review of literature relevant to the objectives of the project. Announcements in professional newsletters informed the engineering community of the project and directed interested persons to the ATC web site. There they found a description of the project and a form for initial researcher input. Project team members met with investigators in face-to-face meetings from March through June 2001. This effort was supplemented by interviews and e-mail discussions. In total, the project team members contacted over fifty researchers in the United States, Europe, and Japan. Over thirty in structural engineering, risk and reliability; geotechnical engineering, and engineering seismology provided input, for which ATC, FEMA and PEER are most thankful. Table A-1 contains a partial list of the researchers contacted, along with an indication of the format in which information was collected.

Table A-1   Investigator Research Data

Researchers Contacted	Researcher Input Form	Discussion Notes			
		Meeting Notes	Telephone Notes	E-mail	Other
Risk and Reliability					
Allin Cornell	✓	✓			
Y.K. Wen		✓			
Structural Engineering					
Mark Aschheim					✓
John Bonacci				✓	
Joe Bracci		✓			
Anil Chopra		✓		✓	
Michael Constantinou		✓			
Greg Deierlein		✓			
Amr Elnashai		✓			
Peter Fajfar					✓
Greg Fenves		✓			
Andre Filiatrault		✓			
Doug Foutch		✓			
Sig Freeman		✓			
Rakesh Goel			✓		

Table A-1   Investigator Research Data (continued)

Researchers Contacted	Researcher Input Form	Discussion Notes			
		Meeting Notes	Telephone Notes	E-mail	Other
Ron Hamburger				✓	
Bill Iwan	✓				
Mervyn Kowalsky		✓			
Helmut Krawinkler		✓			
Sashi Kunnath			✓		
Andres Lepage			✓		
Greg MacRae			✓		
Joe Maffei		✓			
Eduardo Miranda		✓			
Jose Pincheira		✓			
Graham Powell		✓		✓	
Nigel Priestley					✓
Andrei Reinhorn			✓		
Mete Sozen					
John Stanton		✓			
Masaomi Teshigawara	✓				
Mike Valley		✓			
Ed Wilson				✓	
Geotechnical Engineering and Site Effects					
Youssef Hashash		✓			
Engineering Seismology and Ground Motions					
Bruce Bolt			✓		
Mehmet Celebi			✓		

The summary that follows is a composite of information submitted by or obtained from interviews of researchers, and the results of literature review by project team members. Last name references are used to attribute thoughts and opinions of individual researchers contacted. In a few instances, the work of other researchers not contacted is mentioned without a formal citation. Information from published and pending articles and reports is cited by lead author and date as listed in the References section.

A.2 Classification of Analysis Methods

The research summary addresses various methods of inelastic analysis, but focuses upon the nonlinear static procedures known as the Capacity-Spectrum Method, as described in ATC-40 (ATC, 1996), and the Displacement Coefficient Method, as described in FEMA 273 (ATC/BSSC, 1997) and FEMA 356 (ASCE, 2000). Inelastic analysis methods differ based in the approximations used to model the structural system (e.g. "equivalent" single-degree-of-freedom (SDOF)

considering one or more modes, stick models, "fishbone" models, 2D planar models, 3D models) and the form of the representation of demand (e.g. elastic spectra, approximate inelastic spectra, one or more elastic or nonlinear time histories, or energy-based methods). Both the Capacity-Spectrum Method and Displacement Coefficient Method use "equivalent" SDOF systems to estimate the response of an inelastic system from the response of an elastic system to an elastic response spectrum.

MacRae and Maffei observe that methods for estimating the response of inelastic systems based on elastic response spectra may be classified further based on the assumption used for the elastic period in the estimate of peak inelastic displacement response. Lateral force reduction factors, R-μ-T relations, and the Displacement Coefficient Method are similar in their adoption of the initial elastic period in this regard. In contrast, one of the fundamental features of equivalent linearization techniques is the use of a period longer than the initial to reflect inelastic effects. The Capacity-Spectrum Method, for example, uses the secant period corresponding to the maximum inelastic displacement. Notably, there is a simple algebraic relationship relating the initial and periods if they are both known. Consequently, the graphic representation of a method can be de-coupled from the underlying relationships that are used to estimate displacements. For example the use of inelastic spectra in a Capacity-Spectrum Method format allows secant stiffnesses to be used with R-μ-T relations based on the initial, elastic stiffness for estimating displacements. A variant of the Capacity-Spectrum Method known as Yield Point Spectra (Aschheim) allows initial stiffnesses to be used with the same R-μ-T relations. In both cases, the underlying displacement estimate is based on the initial stiffness, because the initial stiffness is used in the definition of the R-μ-T relationships. The original Capacity-Spectrum Method bases the displacement estimate on the elastic response of an oscillator having the secant stiffness of the nonlinear system.

A.3 Nonlinear Static Procedures

A.3.1 Overview of Current Procedures

A.3.1.1 Capacity-Spectrum Method

Description. The peak displacement of a nonlinear system is estimated as the intersection of the capacity curve and an elastic response spectrum that is reduced to account for energy dissipated by the yielding structure. The underlying basis of the Capacity-Spectrum Method (CSM) is the concept of an "equivalent linear" system, wherein a linear system having reduced stiffness ($K_{eff} = K_{secant}$), and increased damping proportional to hysteretic energy, is used to estimate the response of the nonlinear system. The CSM is documented thoroughly in ATC-40. It is also described in further detail in Section 7 of this document.

Advantages

1. The intersection of "capacity" and "demand" curves implies a sense of dynamic equilibrium.

2. The influence of strength and stiffness on peak displacement is represented by the graphic nature of the procedure.

3. As currently presented in ATC-40, the procedure equates viscous damping to hysteretic damping providing an appealing link to the actual characteristics of the structure.

4. The interpretation of the graphic solution can provide insight for an effective retrofit strategy.

Drawbacks

1. There is a controversy over the accuracy of displacement estimates.

2. The iterative procedure is time-consuming and may sometimes lead to no solution or multiple solutions (Chopra).

3. The equating of hysteretic energy dissipation to viscous damping energy dissipation provides a somewhat specious sense that the procedure is "theoretically" based on fundamental physical properties.

Accuracy. Some investigators find the CSM overestimates displacement response while others find the CSM underestimates displacement response. Albanesi et al. (2000) find significant disparities between estimates of response made with the CSM, equal energy, and equal displacement assumptions when compared to the results from nonlinear response history analyses. Chopra and Goel (1999a, 1999b) report that the CSM procedure significantly underestimates displacement response for a wide range of periods and ductility values, relative to the Newmark Hall and other R-μ-T relations. Tsopelas et al. (1997) finds that the CSM either accurately estimates or overestimates the mean displacements obtained from nonlinear reponse history analysis. MacRae observes that the CSM both overestimates the effective damping for a given ductility and reduces the 5% damped

spectrum too much for a given level of damping. Iwan reports that the CSM is accurate in a mean sense for some cases, but the scatter in displacement estimates is large because the combination of effective stiffness and damping used in the CSM is not optimal. Iwan et al. (2000) report that the use of equivalent viscous damping to account for inelastic behavior in the CSM yields satisfactory results for the limited period ranges where a resonance type of response occurs; but the CSM is not generally valid for near-field ground motions. Akkar and Gulkan (2000) also report that the CSM underestimates response to near field earthquakes. Freeman notes the intersection point is least ambiguous when the capacity and demand curve form a sharp intersection; whereas when the curves approach each other gradually, the expected displacement may be less certain.

The range of findings on the accuracy of the CSM reflect the various strategies and assumptions used in the evaluation studies. The assessment of the accuracy of the method is likely to vary with the ground motions used to evaluate it, with clear differences emerging, for example, for near-field motions relative to far-field motions. As a part of the current work the Capacity-Spectrum Method as presented in ATC-40 was evaluated for a wide range of parametric values (see Chapter 3)

Theory . The apparent theoretical basis of the Capacity-Spectrum Method of ATC-40 is a strength and a weakness. In reality the underpinnings of the current procedure are obscure. As discussed in Section A.3.2.1, the CSM is a form of the empirically based equivalent linearization. Also the need for empirically-determined coefficients (e.g. to account for structure framing type [Valley]) adds an element of empiricism to the method. The use of spectral reduction factors to be applied to a designated spectral shape makes it unclear if the method is even applicable to site specific spectra that depart from the designated spectral shape (Iwan).

Enhancements. Improvements and modifications to the basic CSM have been suggested by some investigators. For example, Albanesi et al. (2000) suggest the use of a variable damping response spectrum, in which the damping level increases as the ductility of the system increases. Potential enhancements to the method involve using re-calibrated ductility/damping spectral reduction factor relationships or, more directly, ductility-related spectral reduction factor relationships in:

1. The so-called Direct Capacity Spectra Method (MacRae and Tagawa, 2001).

2. The use of inelastic spectra based on R-μ-T relationships.

3. Using a graphic representation in which an intersection of a "demand curve" and a "capacity curve" defines the maximum displacement similar to the Capacity-Spectrum Method (Chopra and Fajfar).

4. The use of inelastic spectra based on R-μ-T relationships, plotted with yield displacement on the abscissa, in a format known as Yield Point Spectra (Aschheim).

Further discussion may be found in Sections A.3.2.1 and A.3.2.2. Finally, Direct Displacement Based Design is a design version of the CSM (Kowalsky) and is discussed in Section A.3.1.4

A.3.1.2   Displacement Coefficient Method

Description. The peak displacement of a nonlinear system is estimated as the peak displacement of an elastic system ($K_{eff} = K_{initial}$) multiplied by a series of coefficients. Of primary interest here are the coefficients C_1, the ratio of the peak displacement of the inelastic system and the peak displacement of the elastic system having the same period of vibration; C_2, which accounts for the effect of pinching in the load-deformation relation; and C_3, which accounts for second-order (P-Delta) effects. FEMA 356 is the primary source of documentation for the Displacement Coefficient Method (DCM). It is described further in Chapter 5 of this document. The coefficients are empirical and derived primarily from statistical studies of the nonlinear response history analyses of SDOF oscillators. In particular, C_1 is conventionally characterized in terms of strength, ductility, and period (R-μ-T relationships). The coefficient C_1 usually is greater than 1.0 for relatively short periods and converges to approximately 1.0 as period increases (equal displacement approximation). In the DCM, initial stiffness has a predominant effect on peak displacement response, while strength has little effect.

Advantages. The principal advantages of the method are that it is direct and simple to apply. It is also based on empirical parameters (R-μ-T relationships) that have been studied and generally accepted in the technical community for some time, leading to relatively little controversy.

Drawbacks. The Displacement Coefficient Method has received little scrutiny in recent literature, at least relative to the Capacity-Spectrum Method. Thus, potential drawbacks of the method may not be as apparent. The product formulation for representing the effects of strength, pinching, and P-Delta effects may be questioned. Krawinkler stated that P-Delta effects in multistory structures can not be accounted for accurately using simplified procedures, and realistic spectra should be used for soft soil sites, rather than using a coefficient approach.

Accuracy. Many compromises were required to transform research results into the FEMA 273/356 nonlinear static procedure (Krawinkler). The C_1 factor as defined in FEMA 356 is smaller than research indicates, as noted in FEMA 274. Miranda (2001) points out that the C_1 term should be derived from oscillator response values and not from the R-μ-T relations that are based on these responses, to avoid statistical bias in the results. MacRae and Tagawa (2001) note that the coefficient C_2 should approach unity as the strength of the pinched system approaches the strength required for elastic response.

Song and Pincheira (2000) find that the FEMA 273 recommendations provide conservative estimates of the displacement amplification factors for degrading oscillators with periods greater than 0.3 sec on firm soils, and are unconservative at shorter periods.

Lew and Kunnath (2000) compare demands computed using the LSP, LDP, NSP, and NDP of FEMA 273 with the acceptance criteria of the document for an instrumented 7-story reinforced concrete frame building (the Holiday Inn, Van Nuys, California) subjected to ground motions having a 10% probability of exceedance in 50 years, as developed for the FEMA-funded SAC[1] project. A triangular load pattern was used in the pushover analysis, and member plastic rotations were calculated from chord rotations as suggested in FEMA 273. The beam plastic rotation demands determined in this way were similar to the mean beam plastic rotations determined by nonlinear dynamic analysis, with pushover analysis underestimating the plastic rotation demands in the columns relative to those determined by nonlinear dynamic analysis, particularly in the upper stories.

---

1. SAC: a joint venture partnership of the Structural Engineers Association of California, the Applied Technology Council, and California Universities for Research in Earthquake Engineering

As a part of the current work for the ATC-55 project, the Displacement Coefficient Method as presented in FEMA 356 was evaluated for a wide range of parametric values (see Appendix B).

Enhancements. The Displacement Coefficient Method could be improved by deriving C_1 factors directly from nonlinear response data. The expression for C_1 could be made a function of the degree of degradation of the oscillator load-deformation response and the degree of P-Δ effects present. MacRae and Tagawa (2001) suggest improved C_1 factors to account for near-field effects. See the discussion in Section A.3.3 below.

A.3.1.3 Drift-Based Approaches

Simple methods to consider drift in the design of multistory buildings have been put forward by Sozen and his coworkers. Lepage (1998) describes a method for estimating peak drift, in which an effective period and an elastic displacement spectrum determined for 2% damping are used with a linear model of the structure. Browning (2000) uses the technique to determine a target period to limit the expected roof drift and interstory drifts during a design level event.

A.3.1.4 Direct Displacement-Based Design

Kowalksy considers Direct Displacement Based Design to be a design-oriented implementation of CSM. Rather than estimating peak displacements, a limit on displacement is used to determine the required properties of the system. Lepage noted that this method has been criticized for overestimating the effective damping present, but at the same time, Fenwick finds that uncracked properties make individual components stiffer than is considered in the method. As a result, the higher damping tends to compensate for the use of a more flexible building, resulting in the apparently reasonable displacement estimates. Chopra and Goel (2001,a,b,c) report that the use of linear elastic spectra with increased damping, as recommended by Priestley, does not work well in comparison with an inelastic design spectrum derived using the Newmark-Hall relations.

Filiatrault and Folz (2001) have adapted this procedure to wood frame construction. Because wood softens gradually, a sharp yield point does not exist. This makes the use of R-μ-T relationships very difficult, while approaches that use the CSM format can handle softening more easily.

A.3.2 Fundamental Bases and Relationships

The Capacity-Spectrum Method and Displacement Coefficient Method rely on different underlying relationships to estimate the response of nonlinear systems based on an elastic response spectrum. The Capacity-Spectrum Method relies on the concept of equivalent linearization while the Displacement Coefficient Method uses R-μ-T relationships (where R = the strength required for elastic response divided by the effective yield strength of the system and μ= the displacement ductility response of the system). These fundamental relations are reviewed in the following sections. As presented and utilized currently, the graphical characteristics of the two procedures are also different. However, these differences are not fundamental and results from either approach may be readily transformed into various graphical representations.

A.3.2.1 Equivalent Linearization

The basis of the Capacity-Spectrum Method is the premise that the peak response of an inelastic system can be estimated as the peak response of a linear elastic system having reduced stiffness and increased damping. Different approaches have been used to determine the properties of the "equivalent" linear system. In some cases, relationships between the energy dissipated by material nonlinearity and the energy dissipated by viscous damping are used, while in others, empirical calibrations are used to identify the viscous damping (and, in some cases, stiffness) that result in the best estimates of peak displacement response. This section reviews various conceptual approaches that have been taken and discusses empirical observations that bear on the hypothesis that viscous damping is a suitable surrogate for the energy dissipated by hysteretic behavior in nonlinear systems. More discussion of equivalent linearization is included in Chapter 6.

Empirical Methods. Equivalent linearization requires that the stiffness and viscous damping of the equivalent linear system be established. A nonlinear system having μ=4, for example, can be represented by a linear system having stiffness equal to the secant stiffness and sufficient damping to cause the peak displacement response to equal the peak displacement of the nonlinear system. Iwan observes that the secant stiffness is a lower bound to the stiffnesses that could potentially be selected, and that for each admissible stiffness, there is an associated damping level that results in the desired peak displacement. Thus, the challenge is to identify the optimal combination of stiffness and damping that results in a least biased

estimate of the peak response and minimizes the dispersion in the estimates.

Tagawa and MacRae (2001) identify effective damping values by adjusting the damping of an elastic system, having a period based on the secant stiffness, to obtain peak displacements equal to the peak displacement of the inelastic system. MacRae reports that negative values of substitute damping are required for some combinations of oscillator characteristics and ground motion records to match the peak displacement of an inelastic oscillator, although the mean values tend to be somewhere between the ATC-40 and Japanese Building Standard Law versions of CSM.

The Building Research Institute of Japan studied the CSM for adoption into the Japanese building code. The Japanese implementation (Otani, 2000) uses a lower amount of damping, h_{eq}, than the ATC-40 implementation. The effective damping is a function of ductility, μ. For reinforced concrete and steel members in flexure,

$$h_{eq} = \frac{1}{4}\left(1 - \frac{1}{\sqrt{\mu}}\right) + 0.05 \qquad \text{(A-1)}$$

and for reinforced concrete members with pinching or slip related to shear cracking or bar slip,

$$h_{eq} = \frac{1}{5}\left(1 - \frac{1}{\sqrt{\mu}}\right) + 0.05 \qquad \text{(A-2)}$$

Energy Methods. Judi et al. (2000) summarize the concepts of equivalent damping and substitute damping. Equivalent damping comes from Jacobsen (1930) and is applicable to nonlinear systems subjected to sinusoidal displacement histories. Substitute damping was defined by Gulkan and Sozen (1974) as the viscous damping needed in an elastic structure to dissipate the same amount of energy input to a structure responding inelastically to an earthquake ground motion, where the elastic system has a fundamental period based on the secant stiffness of the inelastic structure at its peak displacement. Gulkan and Sozen worked with stiffness-degrading systems. Hudson, working with bilinear systems responding to earthquake ground motions reportedly found (in 1965) that substitute damping values were approximately a third of the counterpart equivalent damping values. This observation may reflect the smaller amount of energy dissipation associated with the relatively few cycles of

earthquake shaking oscillations at or near the peak displacements compared to a uniform sinusoidal displacement history.

The Capacity-Spectrum Method assumes that the energy dissipated by nonlinear behavior can be equated to the energy dissipated by a linear elastic system undergoing simple harmonic oscillations at the peak displacement response. The stiffness of the linear elastic system is set equal to the secant stiffness of the nonlinear system at the peak displacement.

Following the same concept employed for evaluating nonlinear site response in the SHAKE program, Powell suggests that the secant stiffness be evaluated at 70-80% of the maximum displacement, since there may be only one or two cycles at or near the peak displacement, with most cycles having peak displacements that are substantially less than the peak displacement. Powell suggests this would result in a smaller period and smaller effective damping relative to the ATC-40 Capacity-Spectrum Method, and therefore would result in larger displacement estimates. The *Perform-2D* computer program allows the equivalent linear stiffness to be set to a proportion of the peak displacement.

Several observations diminish the hypothesis that equivalent damping should be obtained by equating hysteretic energy dissipation to viscous energy dissipation:

1. Oscillators with different hysteretic properties can have the same peak displacement (Kowalsky).

2. As the post-yield stiffness changes from positive to negative, there is a disproportionate increase in displacement response amplitudes (Aschheim).

3. Nonlinear elastic systems (e.g. rocking walls) have no hysteretic energy dissipation, yet peak displacements are not much greater than systems with full energy dissipation (Miranda).

4. Initially undamaged and initially damaged oscillators were found to have nearly identical peak displacements, indicating that differences in the energy dissipated through hysteretic losses has little effect on peak displacement response (Aschheim and Black, 2000).

5. Changes in stiffness associated with nonlinear response interrupts the build up of resonance that drives the elastic spectral ordinates to their peaks (Paret, 2002).

Accuracy of Effective Damping Relationships. Iwan notes there may be some sensitivity of the optimal effective stiffness and damping values to the suite of ground motions used. Miranda reports that he is finding that Iwan and Gates (1979) relationships are very good, and the Gulkan and Sozen damping is not very accurate. Fenves, however, reports that the Gulkan and Sozen damping is good for reinforced concrete structures. Kowalsky indicates that effective damping may differ for near-field motions containing significant velocity pulses. R. Goel reports that the Japanese Building Standard Law underestimates damping and leads to overestimates of displacements. Stanton expressed concern that the baseline value of damping, to which the equivalent or substitute damping is added, is not necessarily 5% and might be lower. MacRae has recalibrated the Capacity-Spectrum Method and finds the scatter is similar to a recalibrated version of the Displacement Coefficient Method, except for periods above 1.5 sec, where the recalibrated CSM has greater scatter.

Spectral Reduction Factors. Reduction factors to be applied to smoothed elastic design spectra to establish spectral amplitudes for larger amounts of effective damping are tabulated for the Capacity-Spectrum Method. Tagawa and MacRae (2001) find the actual reduction associated with elastic response for a given damping level is not as large as is determined in ATC-40. While the Capacity-Spectrum Method specifies (a) a ductility-effective damping relationship and (b) an effective damping-spectral reduction factor relationship, it is possible to establish a direct relationship between ductility and the spectral reduction factor (MacRae and Tagawa, 2001). MacRae reports that less scatter results when this single relationship is used, in the so-called Direct Capacity Spectra Method.

A.3.2.2 Displacement Modification

The coefficient C_1 of the Displacement Coefficient Method as currently is derived from R-μ-T relationships. Such relationships are usually determined by statistical analysis of the computed response of a large number of SDOF oscillators having prescribed load-deformation relationships to actual ground motion records. There is general agreement on the form of the R-μ-T relationship (e.g. Miranda and Bertero, 1994), although there are some differences in the relationships determined by various investigators. There is significant variability in the R-factors determined for individual records. Larger R-factors generally can be expected for long-duration motions that allow resonance to build up the elastic response, and smaller

R-factors can generally be expected for systems subjected to predominantly pulse-type motions.

Most investigators have determined R-μ-T relationships based on statistics computed on R, and have further determined displacement ratios such as C_1 by algebraic manipulation of R-μ-T relationships. Miranda observes that when required strengths are determined by applying R factors to elastic spectral amplitudes, the parameter of interest is R^{-1}. Furthermore if one assumes a given ductility for an oscillator, then the "required" R can be determined statistically from the analysis of the oscillator response to a suite of ground motions. If one then assumes the "required" R and calculates the ductility demand, it is not necessarily equivalent to that assumed in the first instance. Since the expected R factor for a given ductility level is not precisely correlated to the expected ductility that results from a given R factor, coefficients such as C_1 should be determined from the oscillator response data and not by algebraic manipulation of the R-μ-T relationship. This is further complicated by the non-monotonic nature of the strength-ductility relationship, in which different strengths may result in the same ductility response. Recommended R factors are usually based on the largest strength associated with a desired ductility level. Cuesta et al. (2001) minimize the error in estimated strengths, and find that R-factors should be expressed in relation to a characteristic period of the ground motion (i.e. R-μ-T/T_g relationships). This is an observation also made by Vidic et al. (1994). Even so, there is some ambiguity in the identification of the characteristic period of a site, because ground motions recorded in different horizontal directions or in different earthquakes may display different characteristic periods.

A.3.2.3 Choosing Between Equivalent Linearization and Displacement Modification

While some investigators find the computation of R-factors to be more direct than the use of equivalent linearization, Fenves observed that the averaging of R-factors over many ground motions to obtain R-μ-T relationships separates the relationships from the actual dynamics, and effective damping relationships may be as good. Fajfar noted that both approaches involve approximations, but R-μ-T relationships are easier to use, in part because no iteration is required, and most people accept the equal displacement approximation that is expressed in many R-μ-T relationships for

periods greater than T_g. Fajfar (1999) and Chopra and Goel (1999a, 1999b) have recommended R-μ-T relationships be used for reducing the elastic response spectra in the CSM. Aschheim and Black (2000) have also recommended the use of these relationships with smoothed elastic design spectra or the display of the actual, jagged, constant ductility spectra of a suite a ground motions, in the Yield Point Spectra format.

The choice between the two procedures is largely a matter of personal preference as opposed to relative accuracy. The comparisons of relative accuracy prior to the ATC 55 project are very limited. There have been no comprehensive studies that simultaneously incorporate the relevant scope (strength, period, hysteretic characteristics, site conditions, etc.) and range of parameters required to make conclusive judgements or recommendations for improvement. This fact is the motivation for the comparisons made in ATC 55 as summarized in Section 5.

A.3.3 Near-Field Effects on SDOF Systems

Near field motions are those that contain one or more large velocity pulses, usually originating from the superposition of waves emanating from the fault as the rupture progresses towards a site (i.e. directivity effect). Short-period systems experience the near-field effects as impulses. The large velocity pulses can cause the elastic spectra to be larger. The R factors associated with such pulses are smaller, in general, than those associated with motions in which resonance contributes to the elastic spectral amplitudes. It is now appreciated that structures with periods less than the characteristic period of the pulse may be severely affected (Krawinkler). Long-period structures may experience large interstory drifts associated with the large amplitude ground motion reversals

Iwan et al. (2000) observe that larger displacement amplification factors and smaller strength reduction factors are indicated for structures having fundamental periods less than the predominant period of the near field ground motion, relative to far-field cases. Baez and Miranda (2000) find that displacement amplification factors (the peak displacement of an inelastic system having a specified ductility divided by the peak displacement of an elastic system having the same initial stiffness) are up to about 20% larger for near field sites, with fault normal amplifications being larger than fault parallel amplifications. MacRae and Tagawa (2001) recommend an R-μ-T relation for near field motions that changes with directivity.

A.3.4   Equivalent SDOF Systems

Both the Capacity-Spectrum Method and the Displacement Coefficient Method use an "equivalent" SDOF model to represent the resistance of the structure to deformation as it responds in its predominant "mode." Various techniques have been recommended for determining the properties of the "equivalent" SDOF system. Specifically, the relationships used in FEMA 356 and ATC-40 result in different SDOF systems. In many cases the period of the SDOF analogue differs from the natural period of vibration of the structure (Aschheim). For structures in which the predominant mode of response involves a change in the shape vector (e.g. once a plastic hinge develops at the base of a slender structural wall), further adjustments in the post-yield capacity curve of the SDOF analogue may be warranted, although such refinements may be overly precise given the approximate nature of the displacement estimate. Several alternative "equivalent" SDOF techniques have been proposed including those by Rothe and Sozen (1983), Miranda and Bertero, Qi and Moehle (1991), Fajfar and Gaspersic, (1996), Villaverde (1996), Han and Wen (1997), and Chopra and Goel (2001b).

A.3.5   Behavior Mode Effects

Many structures will not exhibit the full hysteretic loops that are often used in analytical research studies. The presence of stiffness degradation, pinching, strength deterioration, and foundation rocking may influence peak displacement estimates. The general consensus appears to be that moderate levels of stiffness degradation and pinching will cause peak displacements of short period systems (below 0.3 to 0.5 sec) to increase slightly above those determined for bilinear systems. Negative values of post-yield stiffness, arising either due to the load-deformation behavior of the component or the presence of P-Delta effects, can cause increases in peak displacement, as can rapid strength deterioration.

Gupta and Kunnath (1998) investigated stiffness degradation and pinching, and found that "severe" degradation causes only structures with periods less than about 0.5 sec to have mean displacements substantially greater than elastic values. Gupta and Krawinkler (1998) find that peak displacements increase with the introduction of pinching, with the increase becoming larger with decreasing initial period. The ratio of peak displacement for a pinching model to the peak displacement without pinching seems to be nearly independent of the ductility of the system. This study finds that peak displacements increase

substantially as the post-yield stiffness becomes increasingly negative, and the increase is larger for weaker systems. However, the effect of negative post-yield stiffness on increasing peak displacement is reduced in the presence of pinching.

Song and Pincheira (2000) discuss effects of pinching, stiffness degradation, and negative post-yield stiffness on displacement response. They find that the equal displacement approximation is generally applicable to degrading systems for periods greater than a characteristic period (T_g) of the ground motion. Peak displacements were generally larger than those of non-degrading systems for periods less than T_g. For systems on rock or firm soil, displacement amplification factors of 2 were found at T=0.3 sec, with even larger values possible at shorter periods or on soft soils. Fischinger reports that the shape of the hysteretic loop is important for short-period systems and for cases with negative post-yield stiffness or strength deterioration. Otani agreed that loop shape will not affect peak response amplitudes in the displacement-controlled portion of the spectrum.

Miranda reports that the period T_c that represents a breakpoint in the R-μ-T relationship depends on μ, as provided for in the Vidic et al. (1994). R factor relationship. Miranda reports that the shifting of the period at which the R factors change is moderate for cases of pinching and stiffness degradation, but is large for strength deterioration. Miranda (2000) has developed C_1 values for oscillators having bilinear load-deformation relations located on firm sites, and has developed C_1 values for stiffness degrading systems. Sause reportedly is determining similar parameters for nonlinear elastic systems.

A.3.6   MDOF and Inelastic Mechanism Effects

The use of "equivalent" SDOF systems to characterize the nonlinear response of multistory structures potentially may be misleading if higher modes play a significant role in the response or if inelastic mechanisms develop that were not identified in the nonlinear static (pushover) analysis. Higher modes may influence the mechanisms that develop, and different excitations potentially may cause different mechanisms to develop. This may be more pronounced in buildings in which mechanism strengths or modes of failure are not well separated in a dynamic sense. An example of the latter case would be the development of shear failures in beams or columns due to higher mode forces, in a structure that developed a ductile

mechanism in a pushover analysis. Analytical studies have focused on only a limited number of case study buildings. Sufficient research to address these mechanism issues conclusively is not presently available.

Gupta and Krawinkler (2000a) relate the peak inelastic drifts observed in steel frame buildings to the elastic response of a SDOF oscillator through a series of factors that account separately for roof drift relative to SDOF response, the development of inelasticity, the presence of P-delta effects, the ratio of interstory to average roof drift, and the relation between element deformations and interstory drift. Three-, nine-, and twenty story steel moment frame buildings were subjected to the components of the SAC ground motions having a 2% probability of exceedance (PE) in 50 years, a 10% PE in 50 years and a 50% PE in 50 years, oriented at 45 degrees to the fault-normal and fault-parallel directions. They report that a good estimate of the ratio of elastic roof drift to the first mode spectral displacement is given by the first mode participation factor, but for structures with periods greater than 2 sec they advise use of 1.1 times the first mode participation factor. The effects of inelasticity on roof drift for the MDOF structures are consistent with and similar to the effects observed for SDOF systems. For the period range considered, inelasticity tended to cause peak drifts to be about 70 to 80% of the elastic values, at the median level. The MDOF inelasticity factor tended to become smaller with an increase in roof drift. This was explained as possibly being the result of a concentration of interstory drift demand in a few stories leading to a reduction in roof drift. Gupta and Krawinkler (2000b) find that P-Delta is a relatively benign phenomenon except in the instance when the ground motion drives the structure into the range of global negative post-yield stiffness, at which point large increases in displacement may occur. The ratio of peak story drift to peak roof drift is strongly dependent on the ground motion and structure characteristics. Median values of this ratio increase from about 1.2 for low-rise structures to 2.0 for mid-rise structures to about 2.5 to 3.0 for tall structures, for the structures and motions considered. The drift patterns observed for these structures suggest that a common drift distribution that can be generalized does not exist.

Foutch and Shi (1998) report the results of nonlinear dynamic analyses of steel frame buildings for the SAC steel program in which the beam plastic hinges were modeled with different load-deformation models. Steel moment frame buildings were analyzed that ranged from 3 to 9 stories in height. Eight hysteretic models

were considered for the beam plastic hinges: bilinear (with and without strength degradation), stiffness degrading (with and without strength degradation), pinched stiffness degrading (with and without strength degradation), fracturing, and bilinear elastic. The plastic hinge model did affect response histories at the connections. The effect on the maximum story ductility demand relative to the maximum story ductility demand for the non-degrading bilinear model is as follows: a maximum increase of 10-20% for the non-pinching hysteretic models, a maximum increase of 20-30% for the pinching hysteretic models, and a maximum increase of 30-50% for the bilinear elastic model (which has no hysteretic energy dissipation). The Foutch and Shi results may be applicable to buildings that develop desirable mechanisms. Aschheim expects that a weak-story system having degrading column hinges would have much worse performance than the buildings described above.

Naeim et al (2000) also investigated the response of steel moment frame buildings for the SAC steel project. Three-, nine-, and twenty-story steel moment frame structures were investigated using a variety of hysteretic models. Stiffness degradation with slip or pinching was modeled in addition to bilinear response. Strength deterioration was modeled but results were not described. Severe stiffness deterioration increased interstory drifts and residual interstory drifts, with interstory drifts often increasing in the upper stories, and sometimes reducing in the lower stories. The authors suggest this may be attributed to higher modes causing the upper stories to go through many more cycles of sufficient amplitude to be affected by deterioration of the load-deformation response. The observed increases tended to be larger than those observed by Foutch and Shi. Stiffness degradation generally reduced force demands. Slip often reduced lower- and upper-story interstory drift demands, although increases were observed for some combinations of building height, city, and ground motion intensity level. Slip tended to decrease story shears and overturning moments.

Iwan et al. (2000) used a shear beam building model to compare the Capacity-Spectrum Method with nonlinear dynamic analysis for near-field motions. They find that for structural periods shorter than the ground pulse duration, the MDOF model exhibits a fundamental mode type of response, and higher mode contributions to drift and shear demands are negligible. For long period structures, the large displacement and velocity pulses of near field records cause greater participation of the higher modes, resulting in the potential for very

misleading results if a single mode analysis is used. Large interstory drifts were observed at the base, during the forward movement of the ground motion, and were again observed at the upper stories during a large reversal of the ground motion, associated with wave propagation through the structure. This latter case is not associated with the development of the maximum roof drift and does not correspond to a first mode shape. Thus, a fundamental mode analysis would not detect these effects. The investigators conclude that the use of a single-mode "equivalent" system provided a reasonable estimate of the maximum roof displacement regardless of building period, degree of nonlinearity, or distribution of stiffness, even for pulse type motions; but estimates of interstory drift for tall buildings (fundamental period significantly greater than the ground pulse duration) were poor, particularly in the upper stories.

A.3.7   *Pushover Analysis*

Nonlinear static (pushover) analysis is used to quantify the resistance of the structure to lateral deformation and to gauge the mode of deformation and intensity of local demands. Various techniques have been recommended, including the use of constant lateral force profiles and the use of adaptive and multimodal approaches. Pushover techniques provide useful information on the overall characteristics of the structural system and can be used to identify some (but not necessarily all) of the likely mechanisms. Because the prescribed loading used in pushover analyses can not represent the potential range of loading experienced in dynamic response, the results obtained by pushover analyses at best represent an approximation of the nonlinear behavior expected to develop in the response to earthquake ground motions. The applicability of pushover analyses is less clear for systems having discontinuities in strength and stiffness. Results may be misleading where multiple collapse mechanisms potentially may develop because mechanism strengths are not well separated, or where different modes of behavior potentially may develop (higher modes cause demands to approach or exceed the capacities of strength-controlled components).

Pushover techniques are useful to estimate peak displacement response in conjunction with the use of "equivalent" SDOF systems. While higher modes typically have a small or negligible contribution to displacements, higher modes can significantly affect interstory drifts, plastic hinge rotations, story shears, and overturning forces. The contribution to interstory drifts stems directly from the higher mode shapes being

more tortuous and therefore having a greater contribution to interstory drift. Consequently, estimates of interstory drift based on a first mode pushover analysis is prone to be inaccurate as the number of stories and period increases. Pushing to a target displacement will not necessarily develop the maximum interstory drifts in each story because the maximum values in each story do not occur simultaneously, and the sum of the individual maximum interstory drifts may be twice the peak roof displacement, depending on the mechanism that develops (Krawinkler). Some evidence suggests that pushovers tend to overestimate weak story drifts.

The application of lateral forces in a pushover analysis is preferred to applying a prescribed displacement pattern because the former allows softening of the structure to develop and allows story collapse mechanisms to develop. Many techniques involving application of lateral forces have been used. The simplest technique uses a fixed lateral force profile, with lateral forces being proportional to the mass and mode shape amplitude at each floor. An updated load vector would be more likely to identify concentrations of damage, although this presumes that first mode response is dominant. These techniques update the lateral force profile to adapt to the softening structure by using a step-wise lateral force profile that is modified from the first mode pattern to account for higher modes or by combining the results obtained from independent pushover analyses in each of several modes. Adaptive techniques that update the lateral load vector can make the updated load vector be proportional to the current displaced shape or to the current first mode (based on the current stiffness properties of the structure) or may make the increment in lateral loads proportional to the current displaced shape or mode shape. The displaced shape changes more quickly than does the mode shape (Valley). Inconsistencies can be introduced if the load vector is updated without updating the mode participation and mass participation factors used for determining the properties of the "equivalent" SDOF system. Methods that consider higher modes must contend with uncertainty in the amplitudes and algebraic signs of the higher modes, along with their timing relative to the first mode peaks. The question of how simple or complex a pushover technique to use depends on one's analysis objectives. Simple techniques can provide very valuable but incomplete information, while techniques that are more complex are still unable to represent the full range of response that potentially may develop.

Valley and Harris (1998) describe the development of a static pushover curve by repeated elastic analyses, with members removed sequentially as deformations exceed the member yield or ultimate capacities, and with loads reapplied in accordance with updated Ritz vectors. Reinhorn describes multimodal procedures (1997) that rely on updated modal properties. Bracci et al. (1997) also determined demand estimates based on the instantaneous dynamic properties of the structure. Gupta and Kunnath (2000) coupled the use of the instantaneous dynamic properties and the elastic spectral ordinates of the ground motion to determine incremental lateral forces to be applied in the pushover analysis. More recently, Kunnath has looked at sums and differences of modes. Elnashai (2000) also has applied adaptive techniques that make use of the instantaneous modal properties, and is able to follow the S_a vs S_d plot obtained in Incremental Dynamic Analysis reasonably well. Reinhorn suggests that the multi-mode pushover force distribution can be simplified to a linear distribution that is unique for each structure. Kunnath reports that even adaptive pushover techniques fail to capture the response of some stories in some buildings.

Sasaki et al. (1998) perform pushover analyses independently in each of several modes using invariant lateral force distributions, to identify the potential for higher modes to cause mechanisms to develop. Black and Aschheim (2000) combined the peak displacements and interstory drifts determined independently for the first two modes using square-root-of-the-sum-of-the-squares (SRSS) combinations, and observed significant disparities between the peak interstory drifts and the SRSS estimates. This procedure is termed a Modal Pushover Analysis (MPA) by Chopra and Goel (2001b), who consider up to three or five modes. Chopra suggests that SRSS combination rules may be used for all computed quantities (e.g. member forces and moments), not just displacements and interstory drifts. Chopra and Goel (2001c) demonstrate that median estimates of interstory drift of the SAC buildings are improved by the use of three modes for the 9-story buildings and five modes for the 20-story buildings, with baseline values established by nonlinear dynamic analysis. Errors in the interstory drift estimates were larger, in general, than the errors associated with response spectrum analysis of linear elastic buildings and were largest for the "Los Angeles" buildings, which generally had larger interstory drift responses than the "Seattle" and "Boston" buildings. Patterns of the distribution of median interstory drifts of the "Los Angeles" and "Seattle" 9- and 20- story buildings

differed. Chopra and Goel (2001b) also put forward an Uncoupled Modal Response History Analysis (UMRHA), in which dynamic response histories determined for each "equivalent" SDOF system are summed algebraically in time, and maximum values are determined from the summed response history. If nonlinearities are absent, the MPA and UMRHA approaches are equivalent to the traditional response spectrum and linear dynamic analysis methods, respectively.

Iwan is working on load profiles to better predict spatial distribution of damage. Carr also is reported to be working on improved pushover techniques. Bracci recently has been doing pushovers on frames one story at a time. Deierlein suggested that one could apply a perturbation to a first mode load pattern, consisting of an additional force that is allowed to change its location over the height of the structure, to identify sensitivity in the development of the mechanism.

A.4 Nonlinear Dynamic Procedures

A.4.1   Simplified Models

Nakashima has described the use of simplified models for nonlinear dynamic analysis. Much like the "notional frames" used by Sozen and Lepage, the generic frame or "fishbone" model consists of a single column with beams at every floor level extending halfway towards an adjacent column, with a roller supporting each beam at midspan. The model allows beam plastic hinges and story mechanisms to develop, much as they can in complete frames. The generic frame model, however, does not determine actions on individual members of the frame (Otani).

A.4.2   Incremental Dynamic Analysis

Incremental Dynamic Analysis (IDA) determines peak response quantities (e.g. roof drift) by a series of independent nonlinear dynamic analyses of a structure subjected to one or more scaled ground motions. The scale factor is increased successively from a small initial value, and peak response quantities are plotted against a measure of the ground motion intensity. Data from such analyses has been represented in two ways. Cornell and Krawinkler plot peak interstory drift as a function of the scaled S_a at the fundamental period of the building ($S_a(T_1)$). Elnashai plots the peak roof displacement versus $S_a(T_1)$. Both investigators plot S_a on the vertical axis and the response measure on the horizontal axis, to be consistent with the conventional plotting of deformations and displacements on the

abscissa and forces on the ordinate. Cornell has developed relationships between the nonlinear static pushover capacity curve and the IDA curve that are implemented in a spreadsheet, allowing an engineer to observe the influence of changes in the capacity curve on response parameters, based on relationships embedded in the spreadsheet. Because these relationships reflect the behavior of the structure, it seems they must change as the relative distributions of strength, stiffness, and mass of the structure vary.

The strength of the IDA is that it captures aspects of the dynamic behavior of the system, and when done for a sufficient number of ground motions, reflects a range of response that may result. Although investigators apparently have not used the technique to characterize the range of mechanisms that may potentially occur under different excitations, the ability to recover this information seems to be another benefit of this form of analysis. Interstory drifts are observed to increase dramatically when the intensity measure is large enough. Such an increase suggests the structure has reached its "capacity". This capacity might be viewed as the collapse limit as defined essentially by loss of dynamic stability as the intensity measure reaches higher levels. This is analogous to the capacity of a steel bar being measured by its ultimate strength, except that the capacity is expressed in terms of the spectral acceleration of a specific excitation waveform. Typically, there is substantial scatter in the capacities determined in this way, reflecting variability in the response of the structure to different excitations.

Concern has been expressed regarding (1) the validity of scaling the ground motion amplitude uniformly (because high frequencies attenuate more rapidly as distance from the fault increases), (2) the uncertainty in establishing an accurate structural model, (3) ambiguity in the definition of "capacity," with Cornell focusing on the interstory drifts and Krawinkler now focusing on the value of the intensity measure ($S_a(T_1)$) at which the response parameter seems to increase without limit, and (4) whether interstory drift is an appropriate parameter to monitor collapse, when collapse may be due to gravity loads acting, for example, after columns have failed in shear.

The IDA curves are interesting because of the peculiar dynamic response characteristics that are apparent in this representation, and may be useful for identifying variability in demands, the "capacity" of the structure, as well as the onset of collapse, subject to limitations on

modeling. The usefulness of IDA for design verification has not been investigated as yet.

A.5 Modeling Limitations

Accuracy in the estimate of response of a given structural model is of little value if the structural model itself is inaccurate. Issues relating to the accuracy of mathematical models used for estimating response include:

1. Evaluation of initial stiffness and strength.

2. Uncertainty and variation in the actual material properties and dimensions of the as-built structure.

3. Variation of the actual component strengths from calculated estimates.

4. The complexity of behaviors to be represented.

5. Limitations in the understanding and modeling of response to complex, inelastic loading histories.

Uncertainty in the initial stiffness and strength of a structure leads to further dispersion in the accuracy of the displacements estimated using the Capacity Spectrum and Displacement Coefficient Methods (Miranda). For reinforced concrete structures, there is ambiguity in how the period of vibration of the structure should be computed (Otani). An additional difficulty relates to actual compressive strengths exceeding the specified strength, leading to likely increases in the modulus of elasticity (Otani). Valley noted that of three tuned-mass-damper buildings that his firm designed, the estimate of period for one was sufficiently off that they had to redesign the tuned mass damper after construction. The Mexico City Building Code of 1976 reportedly considered a range of possible periods, in response to concerns raised by Rosenblueth (Chopra).

Choices made by structural engineers in modeling of a structure can affect computed response. Krawinkler recalled that in the SAC project, a centerline model of a 20-story building was found to collapse in the presence of P-Delta, but had drifts of no more than about 5% when panel zones and gravity columns were modeled. Krawinkler noted that different investigators using different computer codes obtained very different results when first modeling buildings for the SAC project. Only when assumptions were made consistent were the results more or less identical. Diaphragm flexibility generally has not been incorporated into simplified inelastic procedures; an approximate method is described by Nakaki (2000).

There are relatively few instances in which models have been developed of instrumented buildings that were heavily damaged by ground shaking. Kunnath et al. (2000) considered four instrumented buildings, of which two were moderately damaged. He finds that calibrating structural models to observed response is sensitive to mass and stiffness modeling assumptions. Kunnath reports that linear and nonlinear static procedures did not adequately predict interstory drift estimates, and no one procedure consistently gave good results. Islam et al. (1998) modeled the 7-story instrumented reinforced concrete building in Van Nuys, and found that extensive flexural cracking in the beams observed in the pushover analysis at the measured roof drift did not occur; the actual building had only minor flexural cracking at the lower level beams. Browning et al. (2000) report on the ability of various analysis procedures to estimate peak drifts and interstory drifts of this building, and the difficulty in matching locations of column shear failure.

Multiple actions (e.g. axial, shear, and flexural) result in inelastic behaviors that are not well-understood and represented poorly in analysis software. Modeling of collapse requires careful attention to component degradation and may require that the assumptions of small displacement theory be supplanted by large displacement theory. The accuracy of computed predictions of collapse has not been established; even the definition of a collapse limit state is ambiguous.

A.6 Demand Characterization

The lack of an accepted and clearly-defined relationship between smoothed design spectra and the actual motions they ostensibly represent creates difficulties in (1) evaluating the accuracy of inelastic procedures, (2) assessing variability in response estimates, and (3) establishing design ground motions for use in performance-based earthquake engineering. Traditionally, smoothed design spectra were fit by judgment to the jagged elastic response spectra computed for real ground motions. Current approaches fit a smoothed design spectrum at $T = 1$ sec and at "short" periods, using values determined from a seismic hazard curve. The degree to which actual spectra may, and should, depart from a smoothed spectrum is not defined, yet the degree of variability surely affects the statistical distribution of peak displacements relative to estimates based on smoothed elastic response spectra. Scaling ground motions to precisely match a target design spectrum has been found to result in a systematic underestimate of inelastic response, because response amplitudes to the stronger ground motions are often

disproportionately higher than those to weaker ground motions (Wen).

Cornell notes that demand is not a design spectrum but a set of earthquake events that cannot be collapsed into a single spectrum. Particularly for uniform hazard spectra, there does not seem to be a clear answer on how to choose records (Cornell). However, to represent record-to-record variability, it appears to be necessary to use recorded ground motions rather than synthetic motions. For design applications, Wen and Wu (2001) suggests using records based on regional seismicity—perhaps a Magnitude (M) 8 earthquake at 40 km, a few M7.5 earthquakes at 20 km, a few M6 earthquakes at closer distances, etc.

A.7 Applicability for Performance-Based Earthquake Engineering and Design

A.7.1   Role for Inelastic Procedures

Many researchers have focused on improving simplified analysis procedures with the goal of accurately representing response quantities determined in nonlinear dynamic analyses, with some operating under the notion that analysis and design are so intertwined that they cannot be separated. Other researchers view the role of analysis is to enable good design, acknowledging that even the best analyses are approximate and that approximate analyses are sufficient. Given uncertainty in the accuracy of the mathematical model of a structure and uncertainties in future ground motions, engineers often must rely on their judgment to interpret analytical results. There is a fundamental uncertainty in response amplitudes that applies to all analysis techniques because of variability in the R-μ-T relationship from one motion to another, and variability in the elastic spectral ordinates, timing, and algebraic signs of the higher modes. Because even the best analysis techniques are prone to uncertainty with regard to performance under future earthquakes, there may be a role to be played by simplified analysis techniques.

Simplified inelastic procedures can be used for preliminary proportioning and may also be useful for characterizing performance. Simple inelastic procedures can give good estimates of peak roof displacement, at least for regular structures in which response is dominated by the first mode under conditions where P-Delta effects are negligible. Estimates of interstory drift indices, story shears, and plastic rotations in relatively flexible buildings are prone to be inaccurate, due to higher mode

contributions. Therefore, inelastic analysis procedures may be useful as a first approximation and to indicate when analyses of higher precision are needed. Elastic analysis procedures also can serve this purpose, although one would expect inelastic procedures to provide higher fidelity. Inelastic analysis procedures could be used to encourage capacity design approaches in new design.

The profession is in the midst of a transition from force-based design approaches to displacement-based design approaches. A complete implementation of a displacement-based approach involves (1) determining displacement demand, (2) breaking down overall demand into local components, and (3) comparing local capacity to demand (Bonacci). Simplified inelastic procedures can be used to move from force-based approaches (which are very imprecise but were useful for proportioning structures) to displacement-based approaches. Bonacci urges caution in rushing too rapidly to compare local demands and capacities, and cites as an example the difficulty in evaluating whether a stiffener will buckle when we may be 50% off on T_g and PGA (peak ground acceleration). The desire for accurate analytical results must be balanced against the significant uncertainties in deformation capacities (Krawinkler). Furthermore, complicated techniques may be misused by engineers that are unfamiliar with them (Krawinkler).

Foutch suggested that if inelastic analysis techniques are used, they should be simple enough to be useful for conceptual design. Reinhorn suggested that one might use a simple technique to proportion the structure, then iteratively adjust the relative distributions of strength to ensure undesirable mechanisms will not form, and then follow with a more complex procedure to develop statistics on response. Miranda suggested that a simplified static procedure would be useful with estimates of dispersion, followed by nonlinear dynamic analyses to assess simulated response statistics. Aschheim suggests a simple inelastic analysis technique could be used for preliminary design, with nonlinear dynamic analysis being used to develop response statistics only for those structures where this comparison is deemed necessary (e.g. substantial irregularities, high importance, or to satisfy client requirements).

Because of uncertainties in the effects of higher modes, any simple procedure will require that prescriptive provisions are used to ensure that (1) desirable mechanisms form, with plastic hinges having sufficient ductility capacity to absorb uncertainties in plastic rotation demands arising from the presence of higher modes, (2) undesirable mechanisms (e.g. weak story mechanisms) will not form, even under the influence of higher modes, and (3) force-controlled components or modes of behavior have sufficient strength that forces associated with higher modes do not cause brittle failures to result. Variability due to higher modes can be expected to be a function of the number of stories as well as the spectral amplitudes at the higher mode periods. The separation of strengths required to prevent brittle modes of failure and undesirable mechanisms depends in part on the variability of material strengths in the as-built structure and the variability of actual strengths relative to calculated estimates.

Otani expressed concern about safety in view of the scatter in displacement estimates. The Japanese are using a modified form of the Capacity-Spectrum Method for checking the performance of designs that satisfy other criteria. Wilson expressed concern that nonlinear response spectra are 1not applicable to multi-degree-of-freedom (MDOF) systems; response of 2D and 3D structures can and should be determined by nonlinear dynamic analysis, in part because only nonlinear dynamic analysis can really inform the engineer about the behavior of the systems being designed.

Lepage suggested that an iterative procedure could be used, wherein a variety of load patterns are used to determine a variety of deflected shapes and possibly a number of different mechanisms. If similar deflected shapes result, then the deflected shape would be used to determine the "equivalent" SDOF system for each of a suite of ground motions, recognizing that iteration will be required to identify the right shape to be used for different drift levels. Lepage also suggested an alternate approach in which linear estimates of roof displacement are coupled with a collapse mechanism analysis—if drifts concentrate in just a few stories, then all of the estimated drift would be assigned to those stories.

Otani notes that one could use a nonlinear static procedure to get design moments for beam hinge regions, and then apply a factor of safety to design the columns to prevent or limit the development of plastic hinges in the columns.

A.7.2   Design Formats

Design procedures have been formulated for use with three different types of spectral representations. Direct

Displacement Based Design uses the concept of effective damping to establish response spectra that are plotted on the same axes (ADRS) used in the Capacity-Spectrum Method. The period of vibration (or stiffness) required to satisfy a performance objective is determined, along with a required strength. The use of effective damping is supplanted in design procedures recommended by Fajfar and by Chopra and Goel, who use inelastic spectra (based on R-μ-T relations) plotted on the same axes used in the Capacity-Spectrum Method to estimate peak displacements and to determine required strengths. Black and Aschheim (2000) used Yield Point Spectra (based on R-μ-T relations or the actual jagged spectra associated with design ground motions) to determine the strength required to satisfy multiple performance objectives using admissible design regions. An iterative approach was suggested in which nonlinear static analyses are avoided entirely by relying only on design strengths and elastic properties.

A.7.3 Quantities to be Determined and Measures of Performance

There is uncertainty in estimates of both demands and capacities. Rather than compare very approximate values of local demands and capacities, some suggest that it may be preferable to focus on quantities that are of a more global nature, such as interstory drift (Goel). Estimates of deformation capacity are fairly crude. Krawinkler observed that the best measure of inelastic deformation capacity (e.g., total or plastic rotation, curvature ductility) has not even been identified yet.

One approach is to estimate peak interstory drifts as a factor times the average global roof drift. For regular buildings, the factor varies with the number of stories and may not follow a consistent pattern over the height of the building (Gupta and Krawinkler, 2000a), and may depend on the ground motion (MacRae). Uetani and Tagawa (1998) reportedly find that interstory drifts concentrate less in structures in which the eigenvalues obtained during the nonlinear response are more positive. Fenwick reportedly has introduced into the New Zealand Code an estimate of interstory drift equal to twice the drifts determined by elastic analysis. Interstory drifts for near-field motions appear to be related to ground motion reversals (Iwan), and might be better estimated using concepts of wave propagation theory rather than conventional modal response approaches.

The actual shears in a building can be significantly higher that those associated with development of capacity in the predominant mode. Dynamic shears, therefore, may be significantly higher than estimated by pushover analysis. Rodriguez, Restrepo, and Carr (2002) reportedly found the second and higher modes respond essentially elastically, contributing to the shears associated with inelastic first mode response. Forces in reinforced concrete collectors may be poorly estimated by typical procedures because their larger stiffness in compression causes greater force to be carried in compression than in tension.

Kunnath notes that plastic hinge rotation demands are calculated differently in different software programs. The post-yield stiffness, hinge lengths, and use of distributed or concentrated plasticity affects the values, as do the different solution strategies used by the programs. Estimates of yield and plastic rotation are often based on assuming points of inflection occur at midspan, leading to errors of 50 to 100%. The approximate nature of the demands estimated by any procedure makes comparison with estimated capacities less certain; significant improvements are needed to improve the reliability of estimates of local demands and capacities, to make their comparison more meaningful.

A.7.4 Statistical Measures and Treatment of Uncertainty

Performance may be evaluated in different ways and may include or exclude various types of uncertainties. For example, Wen determines the annual probability of exceeding drifts of various levels. Cornell's work for SAC focuses on the level of confidence in the hypothesis that the structure will satisfy a given performance objective, for ground motions that have a stated probability of exceedance. Uncertainty in the hazard is neglected in the SAC work, although Cornell et al. (2000) presents a theoretical formulation that accounts for uncertainty in the hazard. While it stands to reason that variations in capacities (strengths, deformation capacities) should have an influence on demands, current formulations neglect such interaction.

A.8 References and Bibliography

Akkar, S., and Gulkan, P., 2000, "Comparative performance evaluation of displacement based design procedures for near field earthquakes," *Proceedings of the 12th World Conference on Earthquake Engineering*, New Zealand Society for Earthquake Engineering, Upper Hutt, New Zealand.

Albanesi, T., Nuti, C., and Vanzi, I., 2000, "A simplified procedure to assess the seismic response of nonlinear structures," *Earthquake Spectra*, Vol. 16, No. 4, Earthquake Engineering Research Institute, Oakland, California, pp. 715-734.

ASCE, 2000, *Prestandard and Commentary for the Seismic Rehabilitation of Buildings*, FEMA 356 Report, prepared by the American Society of Civil Engineers for the Federal Emergency Management Agency, Washington, D.C.

Aschheim, M., and Black, E.F., 2000, "Yield Point Spectra for seismic design and rehabilitation," *Earthquake Spectra*, Vol. 16, No. 2, Earthquake Engineering Research Institute, Oakland, California, pp. 317-335.

Aschheim, M.A., Maffei, J., and Black, E.F., 1998, "Nonlinear static procedures and earthquake displacement demands," *6th US National Conference on Earthquake Engineering, Seattle, Washington*, Earthquake Engineering Research Institute.

ATC, 1996, *Seismic Evaluation and Retrofit of Concrete Buildings,* ATC-40 Report, Volumes 1 and 2, Applied Technology Council, Redwood City, California.

ATC/BSSC, 1997, *NEHRP Guidelines for the Seismic Rehabilitation of Buildings*, FEMA 273 Report *(Guidelines)* and FEMA 274 Report *(Commentary)*, prepared by the Applied Technology Council for the Building Seismic Safety Council, published by the Federal Emergency Management Agency, Washington, D.C.

Baez, J.I., and Miranda, E., 2000, "Amplification factors to estimate inelastic displacement demands for the design of structures in the near field," *Proceedings of the 12th World Conference on Earthquake Engineering*, New Zealand Society for Earthquake Engineering, Upper Hutt, New Zealand.

Black, E.F., and Aschheim, M., 2000, *Seismic Design and Evaluation of Multistory Buildings using Yield Point Spectra*, CD Release 00-04, Mid-America Earthquake Center, University of Illinois, Urbana.

Blume, J.A., Newmark, N.M., and Corning, L.H., 1961, *Design of Multistory Reinforced Concrete Buildings for Earthquake Motions*, Portland Cement Association, Skokie, Illinois.

Bracci, J.B., Kunnath, S.K., and Reinhorn, A.M., 1997, "Seismic performance and retrofit evaluation of reinforced concrete structures," *Journal of Structural Engineering*, Vol. 123, American Society of Civil Engineers, pp. 3-10.

Browning, J., 2000, "Implications of a proportioning method for earthquake-resistant RC frames subjected to strong ground motion," *Proceedings of the 12th World Conference on Earthquake Engineering*, New Zealand Society for Earthquake Engineering, Upper Hutt, New Zealand.

Browning, J., Li, R., Lynn, A., and Moehle, J.P., 2000, "Performance assessment for a reinforced concrete frame building," *Earthquake Spectra*, Vol. 16, No. 3, Earthquake Engineering Research Institute, Oakland, California, pp. 541-555.

Chopra, A.K., and Goel, R.K., 1999a, *Capacity-Demand Diagram Methods for Estimating Seismic Deformation of Inelastic Structure: SDF Systems*, Report No. PEER-1999/02, Pacific Earthquake Engineering Center, University of California, Berkeley.

Chopra, A.K., and Goel, R.K., 1999b, "Capacity-demand diagram methods based on inelastic design spectrum," *Earthquake Spectra*, Vol. 15, No. 4, Earthquake Engineering Research Institute, Oakland, California, pp. 637-656.

Chopra, A.K., and Goel, R.K., 2001a, "Direct displacement based design: use of inelastic vs. elastic design spectra," *Earthquake Spectra*, Vol. 17, No. 1, Earthquake Engineering Research Institute, Oakland, California, pp. 47-64.

Chopra, A.K., and Goel, R.K., 2001b, *A Modal Pushover Analysis Procedure to Estimate Seismic Demands for Buildings: Theory and Preliminary Evaluation*, Report No. PEER 2001/03, Pacific Earthquake Engineering Research Center, University of California, Berkeley.

Chopra, A.K., and Goel, R.K., 2001c, "Modal pushover analysis of SAC buildings," *Third U.S.-Japan Workshop on Performance-Based Earthquake Engineering Methodology for Reinforced Concrete Building Structures,* August 16-18, Seattle, Washington.

Cornell, C.A., Vamvatsikos, D., Jalayer, F., and Luco, N., 2000, "Seismic reliability of steel frames," *Proceedings of the 9th IFIP WG 7.5 Working Conference on Reliability and Optimization of Structural Systems*, Ann Arbor, Michigan.

Cuesta, I., and Aschheim, M., 2001, *Using Pulse R-Factors to Estimate Structural Response to Earthquake Ground Motions*, CD Release 01-03, Mid-

America Earthquake Center, University of Illinois, Urbana.

Cuesta, I., Aschheim, M., and Fajfar, P., 2003, "Simplified R-factor relationships for strong ground motions," *Earthquake Spectra*, Vol. 19, No. 1, Earthquake Engineering Research, pp. 22-45

Elnashai, A.S., 2000, "Advanced inelastic static (pushover) analysis for seismic design and assessment," *G. Penelis International Symposium on Concrete and Masonry Structures*, Aristotle University of Thessaloniki, Thessaloniki, Greece, pp. 23-34.

Fajfar, P., 1999, "Capacity-Spectrum Method based on inelastic demand spectra," *Earthquake Engineering and Structural Dynamics*, Vol. 28, pp. 979-993.

Fajfar, P., and Gaspersic, P., 1996, "The N2 method for the seismic damage analysis of RC buildings," *Earthquake Engineering and Structural Dynamics*, Vol. 25, No. 1, pp. 31-46.

Filiatrault, A., and Folz, B., 2001, "Performance-based seismic design of wood framed buildings," accepted for publication in *Journal of Structural Engineering,* American Society of Civil Engineers.

Foutch, D.A, and Shi, S., 1998, "Effects of hysteresis type on the seismic response of buildings," *Proceedings of 6th U.S. National Conference on Earthquake Engineering,* Seattle, Washington, Earthquake Engineering Research Institute, Oakland, California.

Gulkan P., and Sozen, M.A., 1974, "In-elastic responses of reinforced concrete structures to earthquake motions," *Proceedings of the American Concrete Institute*, Vol. 71, No. 12, pp. 605-610.

Gupta, A., and Krawinkler, K., 1998, "Effect of stiffness degradation on deformation demands for SDOF and MDOF structures," *6th US National Conference on Earthquake Engineering*, Seattle, Washington, Earthquake Engineering Research Institute, Oakland, California.

Gupta, A., and Krawinkler, K., 2000a, "Estimation of seismic drift demands for frame structures," *Earthquake Engineering and Structural Dynamics*, Vol 29, pp. 1287-1305.

Gupta, A., and Krawinkler, K., 2000b, "Dynamic p-delta effects for flexible inelastic structures," *Journal of Structural Engineering*, Vol. 126, No. 1, American Society of Civil Engineers.

Gupta, B., and Kunnath, S.K., 1998, "Effect of hysteretic model parameters on inelastic seismic demands," *6th US National Conference on Earthquake Engineering, Seattle, Washington*, Earthquake Engineering Research Institute.

Gupta, B., and Kunnath, S.K., 2000, "Adaptive spectra-based pushover procedure for seismic evaluation of structures," *Earthquake Spectra*, Vol. 16, No. 2, Earthquake Engineering Research Institute, Oakland, California, pp. 367-391.

Han, S.W., and Wen, Y.K., 1997, "Method of reliability-based seismic design. I: Equivalent nonlinear system," *Journal of Structural Engineering*, Vol. 123, American Society of Civil Engineers, pp. 256-265.

Hudson, D.E., 1965, "Equivalent viscous friction for hysteretic systems with earthquake-like excitations," *3rd World Conference on Earthquake Engineering, New Zealand*, pp. II:185-201.

Islam, M.S., Gupta, B., and Kunnath, S., 1998, "A critical review of state-of-the-art analytical tools and acceptance criterion in light of observed response of an instrumented nonductile concrete frame building," *Proceedings of 6th U.S. National Conference on Earthquake Engineering*, Seattle, Washington, Earthquake Engineering Research Institute, Oakland, California.

Iwan, W.D., and Gates, N.C., 1979, "Estimating earthquake response of simple hysteretic structures," *Journal of the Engineering Mechanics Division*, Vol. 105, EM3, American Society of Civil Engineers, pp. 391-405.

Iwan, W.D., Huang, C.T., and Guyader, A.C., 2000, "Important features of the response of inelastic structures to near-field ground motion," *Proceedings of the 12th World Conference on Earthquake Engineering*, New Zealand Society for Earthquake Engineering, Upper Hutt, New Zealand.

Jacobsen, L.S., 1930, "Steady forced vibrations as influenced by damping," *Transactions ASME*, Vol. 52 (APM), pp. 169-181.

Judi, H.J., Davidson, B.J., and Fenwick, R.C., 2000, "The direct displacement based design method: a damping perspective," *Proceedings of the 12th World Conference on Earthquake Engineering,* Auckland, New Zealand Society for Earthquake Engineering, Upper Hutt, New Zealand.

Krawinkler, H., and Alavi, B, 1998, "Development of improved design procedures for near fault ground motions," *Proceedings, SMIP98 Seminar on Utilization of Strong-Motion Data*, Oakland, California.

Kunnath, S. K., and Gupta, B., 2000, "Validity of deformation demand estimates using nonlinear static procedures," *Proceedings of the U.S.-Japan Workshop on Performance-Based Engineering of Reinforced Concrete Building Structures,* Sapporo, Hokkaido, Japan.

Kunnath, S.K., Nghiem, Q., John Jr., A., and El-Tawil, S., 2000, "Validation of evaluation methods and acceptance criteria in evolving performance-based seismic codes," *Proceedings, SMIP2000 Seminar on Utilization of Strong-Motion Data:* Sacramento, California, September 14, 2000, California Division of Mines and Geology, Sacramento, pp. 39-63.

Lepage, A., 1998, "Nonlinear drift of multistory RC structures during earthquakes," *Proceedings, 6th U.S. National Conference on Earthquake Engineering*, Earthquake Engineering Research Institute, Oakland, California.

Lew, H.S., and Kunnath, S.K., 2000, "Evaluation of analysis procedures for performance-based seismic design of buildings," *Proceedings of the 12th World Conference on Earthquake Engineering,* Auckland, New Zealand Society for Earthquake Engineering, Upper Hutt, New Zealand.

MacRae, G., and Tagawa, H., 2001, *Methods to Estimate Displacements of PG&E Structures*, draft report on research conducted under PGE/PEER Task No. 505, University of Washington.

Miranda, E., 2000, "Inelastic displacement ratios for structures on firm sites," *Journal of Structural Engineering*, Vol. 126, No. 10, American Society of Civil Engineers, pp. 1150-1159.

Miranda, E., 2001, "Estimation of Inelastic Deformation Demands of SDOF Systems," *Journal of Structural Engineering*, Vol. 127, No. 9, American Society of Civil Engineers, pp, 1005-1012.

Miranda, E., and Bertero, V., 1994, "Evaluation of strength reduction factors for earthquake-resistant design", *Earthquake Spectra,* Vol. 10, No. 2, Earthquake Engineering Research Institute, Oakland, California, pp. 357-379.

Mwafy, A.M., and Elnashai, A.S., 2001, "Static pushover versus dynamic collapse analysis of RC buildings," *Engineering Structures*, Vol 23, pp. 407-424.

Naeim, F., Skliros, K., and Reinhorn, A.M., 2000, "Influence of hysteretic deteriorations in seismic response of multistory steel frame buildings," *Proceedings of the 12th World Conference on Earthquake Engineering, Auckland*, New Zealand

Society for Earthquake Engineering, Upper Hutt, New Zealand.

Nakaki, S., 2000, *Developing Design Guidelines for Precast Concrete Diaphragms*, Earthquake Engineering Research Institute, Oakland, California.

Nakashima, M., Ogawa, K., and Inoue, K., 2002, "Generic frame model for simulation of earthquake responses of steel moment frames," *Earthquake Engineering and Structural Dynamics*.

Otani, S., 2000, "New seismic design provisions in Japan," *Proceedings of the U.S.-Japan Workshop on Performance-Based Earthquake Engineering for Reinforced Concrete Building Structures,* Sapporo, Japan.

Paret, T.F., Freeman, S.A., and Dameron, R.A, 2002, "Rethinking the earthquake engineering paradigm: from response reduction to response suppression," *Proceedings, Seventh U.S. National Conference on Earthquake Engineering,* Earthquake Engineering Research Institute, Oakland, California.

Qi, X., and Moehle, J.P., 1991, *Displacement Design Approach for Reinforced Concrete Structures Subjected to Earthquakes*, Report No. UCB/EERC-91/02, Earthquake Engineering Research Center, University of California, Berkeley.

Reinhorn, A., 1997, "Inelastic techniques in seismic evaluations," in *Seismic Design Methodologies for the Next Generation of Codes*, Fajfar, P., and Krawinkler, H., eds., Bled, Slovenia.

Rodriguez, M.E., Restrepo, J.I., and Carr, A.J., 2002, "Earthquake-induced acceleration in buildings," *Earthquake Engineering and Structural Dynamics*, Vol. 31, pp. 693-718.

Rothe, D., and Sozen, M.A., 1983, *A SDOF Model to Study Nonlinear Dynamic Response of Large- and Small-Scale R/C Test Structures*, Structural Research Series No. 512, Department of Civil Engineering, University of Illinois at Urbana-Champaign, Urbana, Illinois.

Sasaki, K.K. Freeman, S.A., and Paret, T.F., 1998, "Multi-Mode pushover procedure (MMP) -- a method to identify the effects of higher modes in a pushover analysis," *Proceedings, Sixth U.S. National Conference on Earthquake Engineering,* Seattle, Washington, Earthquake Engineering Research Institute, Oakland, California.

Song, J.K., and Pincheira, J.A., 2000, "Spectral displacement demands of stiffness and strength degrading systems," *Earthquake Spectra*, Vol. 16,

No. 4, Earthquake Engineering Research Institute, Oakland, California, pp. 817-851.

Tagawa, H., and MacRae, G., 2001, "Capacity spectra method for estimating SDOF oscillator demands," *Proceedings of the 2001 Structures Congress & Exposition*, American Society of Civil Engineers, Washington, D.C.

Tsopelas, P., Constantinou, M.C., Kircher, C.A., and Whittaker, A.S., 1997, *Evaluation of Simplified Methods of Analysis of Yielding Structures*, Technical Report NCEER-97-0012, National Center for Earthquake Engineering Research, State University of New York, Buffalo, New York.

Uetani, K., Tagawa, H., 1998, "Criteria for suppression of deformation concentration of building frames under severe earthquakes," *Engineering Structures*, Vol. 20, No. 4-6, pp. 372-383.

Vidic, T., Fajfar, P., and Fischinger, M., 1994, "Consistent inelastic design spectra: strength and displacement," *Earthquake Engineering and Structural Dynamics*, Vol. 23, pp. 507-521.

Villaverde, R., 1996, "Simplified response spectrum analysis of nonlinear structures," *Journal of Engineering Mechanics*, Vol. 122, American Society of Civil Engineers, pp. 282-285.

Valley, M.T., and Harris, J.R., 1998, "Application of modal techniques in a pushover analyses," *Proceedings, Sixth U.S. National Conference on Earthquake Engineering,* Seattle, Washington, Earthquake Engineering Research Institute, Oakland, California.

Vamvatsikos, D., and Cornell, C.A., 2001, "Incremental dynamic analysis," submitted to *Earthquake Engineering and Structural Dynamics*.

Wen, Y. K., and Wu, C.L., 2001, "Uniform Hazard Ground Motions for Mid-America Cities," *Earthquake Spectra*, Vol. 17, No. 2, Earthquake Engineering Research Institute, Oakland, California, pp. 359-384.

B. Summary of Practice using Inelastic Analysis Procedures

B.1 Introduction

The state of practice inquiry conducted under Phase I of the ATC-55 Project sought information about the use of inelastic analysis procedures for a broad sample of building applications from different practicing structural engineering firms. Respondees were asked to provide information on the following:

- types of buildings and structural systems for which the procedures are used;
- procedures used;
- software used for analysis, if any; and
- Engineers' thoughts about the implementation of procedures, including problems encountered.

This appendix summarizes the information obtained from practicing engineers who responded to the state of practice inquiry, and the relation of their responses to the issues identified by the ATC-55 project team. The information was solicited through three primary means. First, a project web page was established and advertised to practitioners through e-mail and notices in professional newsletters. The website contained a "Summary of Practice Building Data" questionnaire form for completion by each respondent for each building example to be submitted. Second, the ATC-55 project team appealed directly by e-mail to a number of engineering firms, some of whom were known to have experience with inelastic analysis procedures. Finally, the e-mail requests were followed with personal telephone calls. The solicitations took place during the spring and summer of 2001. Information on over 60 examples was obtained from 23 respondents in 12 different structural engineering offices.

B.2 Typical Buildings and Structural Systems

The example buildings submitted by engineers who responded to the ATC solicitation encompassed a broad range of building types, structural systems, and foundation systems. Following are the percentages of the total example building population by ownership type, purpose of analysis, year of construction, height, and floor area. The percentages of example buildings by seismic (lateral-force resisting) system, by gravity force resist-ing system, and by foundation type are provided in Table B-1, Table B-2, and Table B-3, respectively.

Ownership Type

Private:	42%
Institutional	52%
Unspecified	6%

Purpose of Analysis

Evaluation only	32%
Upgrade or Evaluation/Upgrade	41%
New	27%

Year of Construction

Earliest	1916
Latest	2001
Mean	1935

Height (stories)

1-2	15%
3-6	36%
7-11	28%
12+	21%

Floor Area (sf)

< 10,000	3%
10,000 – 50,000	14%
50,000 – 100,000	19%
100,000 – 200,000	60%
200,000 – 500,000	2%
> 500,000	2%

B.3 Inelastic Analysis Procedures

The procedures used by the respondents included the following:

- FEMA 273/356 (Coefficient Method)
- Nonlinear response history analysis

Table B-1   **Seismic Systems of Example Buildings Submitted by Respondees**

Seismic System(s)	Number	Percentage of Total
Concrete shear walls	17	29%
Concrete moment frame	9	15%
Concrete frame/brick infill	6	10%
Steel CBF (concrete braced frame)	3	5%
Steel EBF (eccentric braced frame)	4	7%
Steel BRBF (unbonded braced frame)	2	3%
Steel moment frame	6	10%
Steel frame/brick infill	3	5%
Steel truss moment frame	1	2%
Plywood or OSB shear walls	3	5%
Reinforced masonry walls	1	2%
Passive damped frame	1	2%
Other	3	5%

Table B-2   **Gravity Systems of Example Buildings Submitted by Respondees**

Gravity System(s)	Number	Percentage of Total
Concrete columns/ beams and/or slab	22	37%
Concrete bearing walls	2	3%
Wood frame	5	8%
Steel frame /wood infill	2	3%
Steel frame/concrete slab	24	41%
Other	4	7%

- FEMA 351/SAC method
- ATC-40 (Capacity-Spectrum Method)
- Unspecified nonlinear static

A number of the respondents used two or more procedures for the same building example. The number of primary uses of each procedure (i.e., not accounting for secondary procedures), and the respective percentage of the total number of buildings are listed in Table B-4.

Table B-3   **Foundation Systems of Example Buildings Submitted by Respondees**

Foundation System(s)	Number	Percentage of Total
Spread Footings	32	55%
Mat	9	15%
Piles	13	22%
Drilled Piers	3	5%
Unknown/Other	2	3%

Table B-4   **Inelastic Analysis Procedures**

Primary Procedure	Number	Percentage of Total
FEMA 273/356 (Coefficient Method)	21	36%
Nonlinear response history analysis	12	20%
FEMA 351/SAC method	3	5%
ATC-40 (Capacity-Spectrum Method)	8	14%
Unspecified nonlinear static[1]	15	25%
Multiple of above procedures	8	14%

1. The heading "Unspecified nonlinear static" indicates entries such as "NSP," "CSM," and "Equal Displacement." It was noted that most such entries were associated with analyses that were implemented prior to the publication of ATC-40 and FEMA 273. Several examples cited the use of the Miranda-Bertero procedure, and one example cited the Army TM-5-809-10-1 document.

B.4   Software

With one exception, the inelastic procedures were implemented with the aid of computer analysis software. Table B-5 lists the programs used, the number of listings of each program name, and the percentage of listings of the total number of program usage listings.

Several examples utilized multiple linear elastic analyses with sequential stiffness modification to represent progressive yielding and degradation. These applications utilized extensive spreadsheet bookkeeping to sum member forces and check member demands against capacities from one analysis to the next.

Table B-5   Computer Program Usage

Program Name	Number of Listings	Percentage of Listings
ABAQUS	1	1%
ANSYS	3	5%
CASHEW / RUAUMOKO	3	5%
(Custom software)	6	9%
DRAIN 2D	9	14%
DRAIN 2DX	8	12%
ETABS	3	5%
FEM-I	2	3%
FEM-II	1	1%
SAP 90	6	9%
SAP 2000	24	35%
Other	1	1%
Total Listings	**66**	

B.5   Implementation Issues

A total of 65 comments were submitted relating to the implementation of the inelastic procedures. A synopsis of the respondents' comments on major issues follows:

The majority of the comments submitted were related to the relative accuracy of procedures. Engineers' preoccupation with the topic of relative accuracy was indicated by the techniques used, such as variation of parameters (or "bounding"), by comments about the sensitivity of procedures to various assumptions, and by the implementation of comparative analyses using multiple procedures for the same building. Significantly, the large variation in ground motion parameters was not mentioned in any of the practitioners' comments, although one respondent expressed doubt in the validity of using a static procedure to represent the effect of ground motion at a near-field location. Three of the example buildings were full-scale test specimens of wood buildings that were shaken on a simulator and evaluated using a nonlinear response history analysis procedure, for the purpose of research and comparison. Several of the respondents commented on the difficulty of reasonably accounting for cyclic degradation and P-delta effects with existing procedures and/or software. Also, difficulty in establishing a suitable target displacement or ultimate drift was mentioned in two examples.

It is evident that some respondents question the appropriateness of procedures to determine the target displacement. One respondent wrote "FEMA 273 shear strain ratios [were] exceeded in local areas – deemed not to be hazardous." Another wrote "Immediate Occupancy provisions [of FEMA 273] are too conservative." A third wrote "Analysis was straightforward. Determination of target displacement was problematic."

There were several comments regarding the complexity of the procedures. For example, one respondent wrote "The most troublesome problem in implementing the FEMA [273] procedures was developing nonlinear hinge properties (strength and ductility)." Another wrote: "The shear capacity of the concrete columns was difficult to evaluate by the FEMA 273 methods (Eq. 6-4) due to constantly changing parameters." A third wrote: "Convergence was difficult to achieve even for a relatively simple model and depended greatly on the method of solution used."

Several respondents commented during verbal discussions that the established analysis procedures did not allow the evaluation of behavior in the range of severe damage prior to collapse, such as damage to many structures observed in postearthquake reconnaissance.

Several respondents indicated that the results of inelastic procedures are very sensitive to assumptions regarding such parameters as initial stiffness, and pushover loading profile. There is also recognition among respondents that the dynamic and multi-degree-of-freedom (MDOF) effects that would be captured in a nonlinear response history analysis procedure could be quite different from the results of a nonlinear static procedure. Several respondents attempted to account for dynamic behavior, yielding, and MDOF effects by such techniques as adapting pushover loading profiles and use of simplified dynamic analysis.

One respondent discussed the inability of static procedures to represent the response of structures to near-field earthquake pulse-type motions.

Two other respondents collaborated in a comparison of the Capacity Spectrum approach for a single-degree-of-freedom system with nonlinear response history analysis. They identified that the differences in results between the two methods could be largely explained by the dynamic response of the structure to the predominant velocity pulses in the time-history records. They developed a simplified technique to calculate the single-

degree-of-freedom (SDOF) dynamic displacement response for a single velocity pulse, and applied this technique to several structures, evaluating the response of each structure to various pulses for site-specific ground motion records.

One respondent questioned the validity of static proce- dures for high-rise buildings that would experience sig- nificant higher mode components in their response.

There seems to be a lack of understanding among prac- titioners about how to represent MDOF effects for static procedures. Only one respondent commented about the sensitivity of the static solution to such parameters as initial period and pushover profile. Another used an adaptive load pattern based on modal response at each significant step in the analysis process. A third simply assumed that all stories experienced equal drift.

B.6 Use of Limitations on Coefficient C_1 in FEMA 356

FEMA 356 currently contains arbitrary limitations (caps) on the maximum value of the coefficient C_1. This cap tends to reduce the predicted inelastic displacement of relatively short period structures. At an early stage of the second phase of the ATC-55 project, it became apparent that the cap might influence the accuracy of the Coefficient Method. While there may be valid rea- sons that the response of short-period structures varies from that predicted by current analysis procedures, it seemed that the arbitrary nature of the cap conflicted with the goals of the project. In an effort to gauge qual- itatively how this issue affected current practice, the project team contacted twelve practicing engineers from seven different firms from the respondents to the Phase I Practice Study. These individuals and firms are repre- sentative of a relatively high level of seismic expertise among practitioners. Three basic questions were posed:

a. Do you use the cap?

b. Why, or why not?

c. What are your thoughts and understanding on this choice?

All but a few engineers follow the same procedure. First they calculate C_1 using the empirical equation. If this value is less than 1.5, they use it. If it is higher, they use 1.5. Thus the practice is to neglect the interpo- lation allowed between 0.10 sec and T_s. The pervasive attitude was that they use the cap because it is allowed.

Very few were aware of the discussion on this issue in FEMA 273/274/356/357. These were the same few who tended not to use the cap.

B.7 Practical Guidance and Education

Respondents provided feedback (either in writing, ver- bally, or implicitly) about the following topics or ques- tions related to the issue of practical guidance and education:

- *The various methods lead to different results. Why?*

It is evident that practicing engineers do not necessarily know why the various NSP methods result in different answers, or why the answers may differ significantly from those resulting from the use of nonlinear response history analysis. Consequently, engineers may lack a way to answer the next item:

- *Which method is the most effective for a given project?*

Respondents indicated that there is a general lack of understanding about how to select a method. In numer- ous cases, the methods had been dictated by the owner/ client. For instance, FEMA 273 is quickly being adopted as the governing guideline by government agencies and is therefore required for evaluations and design of government-funded retrofits.

- *Certain guidelines or evaluation techniques require an impractical amount of effort.*

Some engineers indicated that they chose to adopt an approach using sequential elastic analyses to develop- ing a "backbone" resistance curve for their pushover analysis. In some cases a cumbersome amount of "bookkeeping" was required to keep track of individual member stresses, and to compare these stresses with estimated stress or strain capacities as they changed the model to simulate yielding or degradation.

- *What is the most efficient way to compute results for a given method?*

Based on responses received, it is evident that practic- ing engineers have searched for efficient ways to handle the large amount of computational effort required for nonlinear analysis.

- *More effective software tools are needed.*

Some respondents indicated that the software programs they currently use for inelastic analysis are sometimes

difficult to use, or do not allow the user to model important aspects of the structure, such as degradation.

Other issues identified related to practical guidance and education, including the following:

• Clients who require these evaluations need to be educated about effort and fees required. Normally, this information comes from the engineer. However, without sufficient experience, the engineer would not be able to accurately estimate the required effort. This relates to the next issue:

• Some practicing engineers have embraced these methods as an improvement. Others have avoided them as requiring a steep learning curve and more effort, with an uncertain outcome. The methods are therefore more risky for the owner as well as the engineer.

C. Supplemental Data on the Evaluation of Current Procedures

This appendix supplements Chapter 3 on the evaluation of current nonlinear static procedures. The contents are summarized as follows: Section C.1 tabulates the ground-motion data used for the evaluation; Section C.2 presents the results of the response history analyses of the oscillators; Section C.3 presents data on the results of the evaluation of the ATC-40 version of the Capacity Spectrum Method; and Section C.4 presents data on the results of the evaluation of the Coefficient Method of FEMA 356.

C.1   Ground Motions

Table C-1   Ground Motions Recorded on Site Class B

Date	Earthquake Name	Magnitude (Ms)	Station Name	Station Number	Component (deg)	PGA (cm/s^2)
06/28/92	Landers	7.5	Silent Valley, Poppet Flat	12206	0	48.9
06/28/92	Landers	7.5	Twentynine Palms Park Maintenance Bldg	22161	0	78.7
06/28/92	Landers	7.5	Amboy	21081	90	146.0
10/17/89	Loma Prieta	7.1	Point Bonita	58043	297	71.4
10/17/89	Loma Prieta	7.1	Piedmont, Piedmont Jr. High Grounds	58338	45	81.2
10/17/89	Loma Prieta	7.1	San Francisco, Pacific Heights	58131	270	60.2
10/17/89	Loma Prieta	7.1	San Francisco, Rincon Hill	58151	90	88.5
10/17/89	Loma Prieta	7.1	San Francisco, Golden Gate Bridge	1678	360	228.6
10/17/89	Loma Prieta	7.1	Hollister-SAGO vault	1032	360	60.1
10/17/89	Loma Prieta	7.1	South San Francisco, Sierra Point	58539	205	102.7
10/17/89	Loma Prieta	7.1	Berkeley, Lawrence Berkeley Lab.	58471	90	114.8
10/17/89	Loma Prieta	7.1	Coyote Lake Dam, Downstream	57504	285	175.6
01/17/94	Northridge	6.8	Mt Wilson, CIT Seismic Station	24399	90	228.5
01/17/94	Northridge	6.8	Antelope Buttes	24310	90	99.7
01/17/94	Northridge	6.8	Los Angeles, Wonderland	90017	185	168.7
01/17/94	Northridge	6.8	Wrightwood, Jackson Flat	23590	90	54.5
01/17/94	Northridge	6.8	Littlerock-Brainard Can	23595	90	7.2
01/17/94	Northridge	6.8	San Gabriel, E. Grand Ave.	90019	180	256.0
10/01/87	Whittier Narrows	6.1	Los Angeles, Gritfith Park Observatory	141	0	133.8
10/15/79	Imperial Valley	6.8	Superstition Mountain	286	135	189.2

Table C-2   **Ground Motions Recorded on Site Class C**

Date	Earthquake Name	Magnitude (Ms)	Station Name	Station Number	Component (deg)	PGA (cm/s^2)
10/15/79	Imperial Valley	6.8	El Centro, Parachute Test Facility	5051	315	200.2
02/09/71	San Fernando	6.5	Pasadena, CIT Athenaeum	80053	90	107.9
02/09/71	San Fernando	6.5	Pearblossom Pump	269	21	133.4
06/28/92	Landers	7.5	Yermo, Fire Station	12149	0	167.8
10/17/89	Loma Prieta	7.1	APEEL 7, Pulgas	58378	0	153.0
10/17/89	Loma Prieta	7.1	Gilroy #6, San Ysidro Microwave site	57383	90	166.9
10/17/89	Loma Prieta	7.1	Saratoga, Aloha Ave.	58065	0	494.5
10/17/89	Loma Prieta	7.1	Gilroy, Gavilon College Phys Sch Bldg	47006	67	349.1
10/17/89	Loma Prieta	7.1	Santa Cruz, University of California	58135	360	433.1
10/17/89	Loma Prieta	7.1	San Francisco, Diamond Heights	58130	90	110.8
10/17/89	Loma Prieta	7.1	Fremont, Mission San Jose	57064	0	121.6
10/17/89	Loma Prieta	7.1	Monterey, City Hall	47377	0	71.60
10/17/89	Loma Prieta	7.1	Yerba Buena Island	58163	90	66.70
10/17/89	Loma Prieta	7.1	Anderson Dam, Downstream	1652	270	239.40
04/24/84	Morgan Hill	6.1	Gilroy, Gavilon College Phys Sci Bldg	47006	67	95.0
04/24/84	Morgan Hill	6.1	Gilroy #6, San Ysidro Microwave Site	57383	90	280.4
07/08/86	Palmsprings	6.0	Fun Valley	5069	45	129.0
01/17/94	Northridge	6.8?	Littlerock, Brainard Canyon	23595	90	70.60
01/17/94	Northridge	6.8	Castaic, Old Ridge Route	24278	360	504.2
01/17/94	Northridge	6.8	Lake Hughes #1, Fire station #78	24271	0	84.9

Table C-3   Ground Motions Recorded on Site Class D

Date	Earthquake Name	Magnitude (Ms)	Station Name	Station Number	Component (deg)	PGA (cm/s^2)
6/28/92	Landers	7.5	Yermo, Fire Station	22074	270	240.0
6/28/92	Landers	7.5	Palm Springs, Airport	12025	90	87.2
6/28/92	Landers	7.5	Pomona, 4th and Locust, Free Field	23525	0	65.5
01/17/94	Northridge	6.8	Los Angeles, Hollywood Storage Bldg.	24303	360	381.4
01/17/94	Northridge	6.8	Santa Monica City Hall	24538	90	866.2
01/17/94	Northridge	6.8	Los Angeles, N. Westmoreland	90021	0	393.3
10/17/89	Loma Prieta	7.1	Gilroy 2, Hwy 101 Bolsa Road Motel	47380	0	394.2
10/17/89	Loma Prieta	7.1	Gilroy 3, Sewage Treatment Plant	47381	0	531.7
10/17/89	Loma Prieta	7.1	Hayward, John Muir School	58393	0	166.5
10/17/89	Loma Prieta	7.1	Agnews, Agnews State Hospital	57066	0	163.1
10/01/87	Whittier Narrows	6.1	Los Angeles, 116th St School	14403	270	288.4
10/01/87	Whittier Narrows	6.1	Downey, County Maintenance Bldg	14368	180	193.2
10/15/79	Imperial Valley	6.8	El Centro #13, Strobel Residence	5059	230	136.2
10/15/79	Imperial Valley	6.8	Calexico, Fire Station	5053	225	269.6
04/24/84	Morgan Hill	6.1	Gilroy #4, 2905 Anderson Rd	57382	360	341.4
04/24/84	Morgan Hill	6.1	Gilroy #7, Mantnilli Ranch, Jamison Rd	57425	0	183.0
04/24/84	Morgan Hill	6.1	Gilroy #2, Keystone Rd.	47380	90	207.9
04/24/84	Morgan Hill	6.1	Gilroy #3 Sewage Treatment Plant	47381	90	189.8
02/09/71	San Fernando	6.5	Los Angeles, Hollywood Storage Bldg.	135	90	207.0
02/09/71	San Fernando	6.5	Vernon, Cmd Terminal Building 4814 Loma Vista	288	277	104.6

Table C-4   **Ground Motions Recorded on Very Soft Soil Sites Used in This Study**

Date	Earthquake Name	Magnitude (Ms)	Station Name	Station Number	Component (deg)	PGA (cm/s^2)
10/17/89	Loma Prieta	7.1	Foster City (APEEL 1; Redwood Shores)	58375	90	277.6
10/17/89	Loma Prieta	7.1	Foster City (APEEL 1; Redwood Shores)	58375	360	63.0
10/17/89	Loma Prieta	7.1	Larkspur Ferry Terminal	1590 (USGS)	270	134.7
10/17/89	Loma Prieta	7.1	Larkspur Ferry Terminal	1590 (USGS)	360	94.6
10/17/89	Loma Prieta	7.1	Redwood City (APEEL Array Stn. 2)	1002 (USGS)	43	270.0
10/17/89	Loma Prieta	7.1	Redwood City (APEEL Array Stn. 2)	1002 (USGS)	133	222.0
10/17/89	Loma Prieta	7.1	Treasure Island (Naval Base Fire Station)	58117	0	112.0
10/17/89	Loma Prieta	7.1	Treasure Island (Naval Base Fire Station)	58117	90	97.9
10/17/89	Loma Prieta	7.1	Emeryville, 6363 Christie Ave.	1662 (USGS)	260	254.7
10/17/89	Loma Prieta	7.1	Emeryville, 6363 Christie Ave.	1662 (USGS)	350	210.3
10/17/89	Loma Prieta	7.1	San Francisco, International Airport	58223	0	231.5
10/17/89	Loma Prieta	7.1	San Francisco, International Airport	58223	90	322.7
10/17/89	Loma Prieta	7.1	Oakland, Outer Harbor Wharf	58472	35	281.4
10/17/89	Loma Prieta	7.1	Oakland, Outer Harbor Wharf	58472	305	265.5
10/17/89	Loma Prieta	7.1	Oakland, Title & Trust Bldg. (2-story)	58224	180	191.3
10/17/89	Loma Prieta	7.1	Oakland, Title & Trust Bldg. (2-story)	58224	270	239.4
10/15/79	Imperial Valley	6.8	El Centro Array 3, Pine Union School	5057	140	260.9
10/15/79	Imperial Valley	6.8	El Centro Array 3, Pine Union School	5057	230	216.8
04/24/84	Morgan Hill	6.1	Foster City (APEEL 1; Redwood Shores)	58375	40	45.1
04/24/84	Morgan Hill	6.1	Foster City (APEEL 1; Redwood Shores)	58375	310	66.7

Table C-5 **Near-Fault Records with Forward Directivity Used in this Study**

Date	Earthquake Name	Magnitude (Ms)	Station Name	NEHRP Site Class	PGA (cm/s^2)
10/17/89	Loma Prieta	7.1	Los Gatos	D	704.0
10/17/89	Loma Prieta	7.1	Lexington Dam	D	673.0
01/16/95	Hyogo-Ken-Nanbu, Kobe	6.9	Takatori Station	D	771.0
01/16/95	Hyogo-Ken-Nanbu, Kobe	6.9	Kobe Station	D	1067.0
01/16/95	Hyogo-Ken-Nanbu, Kobe	6.9	Port Island	D	426.0
03/13/92	Erzican, Turkey	6.9	Erzican Station	D	424.0
01/17/94	Northridge	6.8	Rinaldi Receiving Station	D	873.0
01/17/94	Northridge	6.8	Sepulveda	D	715.0
01/17/94	Northridge	6.8	Sylmar County Hospital	D	718.0
01/17/94	Northridge	6.8	Newhall, LA County Fire Station	D	709.0
10/15/79	Imperial Valley	6.8	Meloland	D	372.0
10/15/79	Imperial Valley	6.8	El Centro Array 6	D	424.0
04/24/84	Morgan Hill	6.1	Coyote Dam	D	712.0
04/24/84	Morgan Hill	6.1	Anderson Dam	D	436.0
08/17/99	Kocaeli, Turkey	7.8	YPT	D	311.5
08/17/99	Kocaeli, Turkey	7.8	DZC1	D	390.1
11/12/99	Duzce, Turkey	7.8	DZC2	D	404.2
08/17/99	Kocaeli, Turkey	7.8	IZT1	AB	164.3
11/12/99	Duzce, Turkey	7.8	BOL2	D	755.9
08/17/99	Kocaeli, Turkey	7.8	GBZ1	AB	240.2

C.2 Response History Results

C.2.1 *Effect of Site Class on C_1 of SDOF Systems with Elastoplastic Perfectly Plastic (EPP) Hysteretic Behavior*
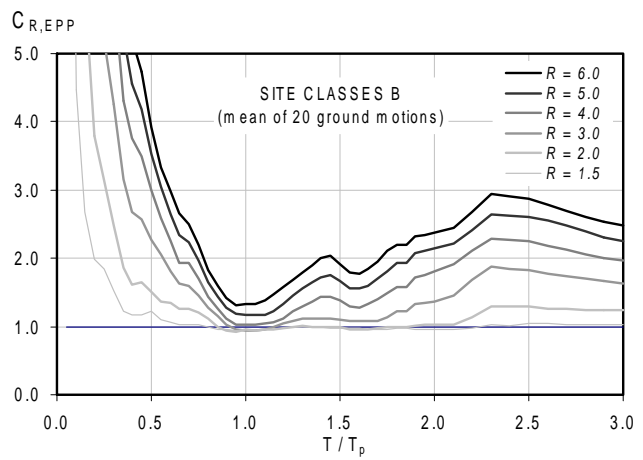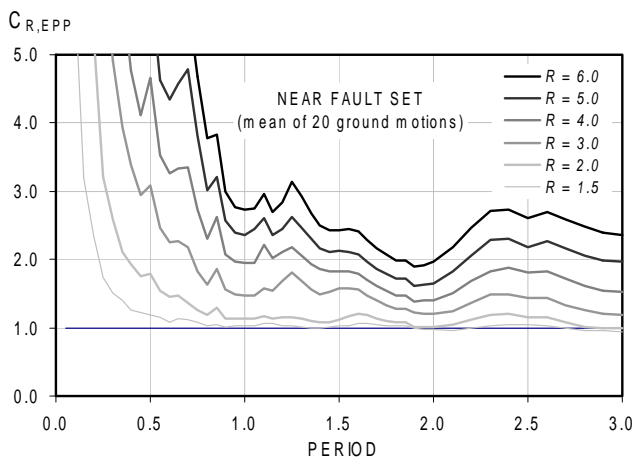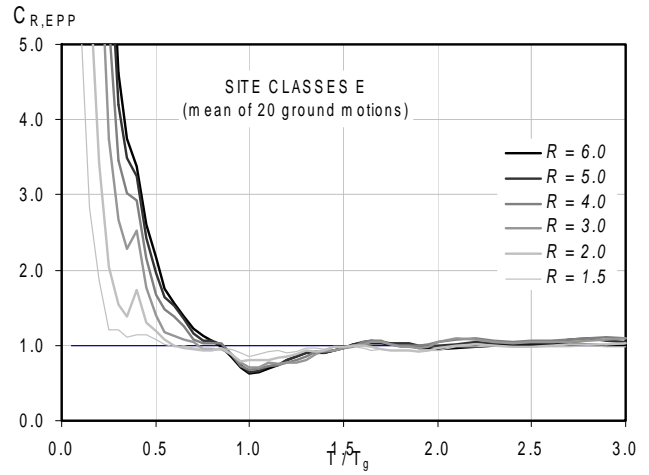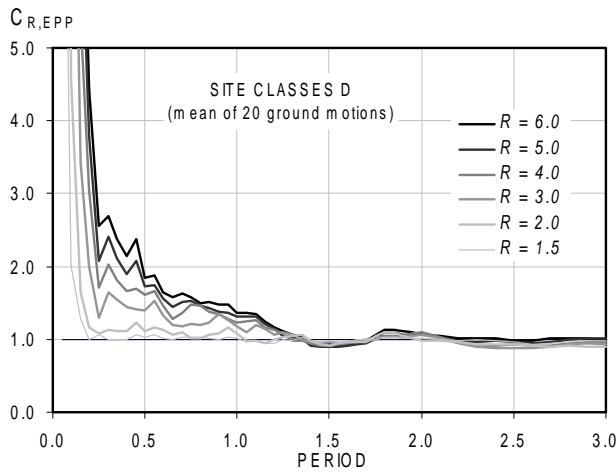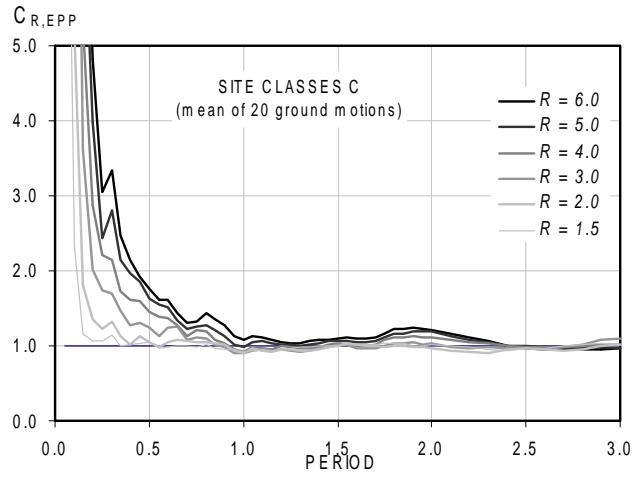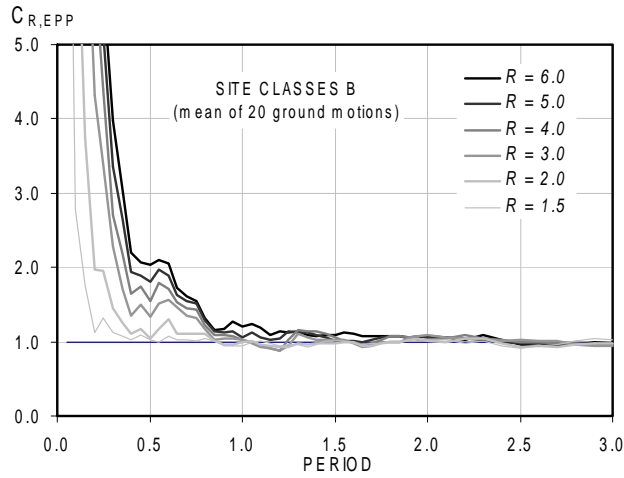
C.2.2 Effect of Site Class on C_1 of SDOF Systems with Stiffness Degrading (SD) Hysteretic Behavior
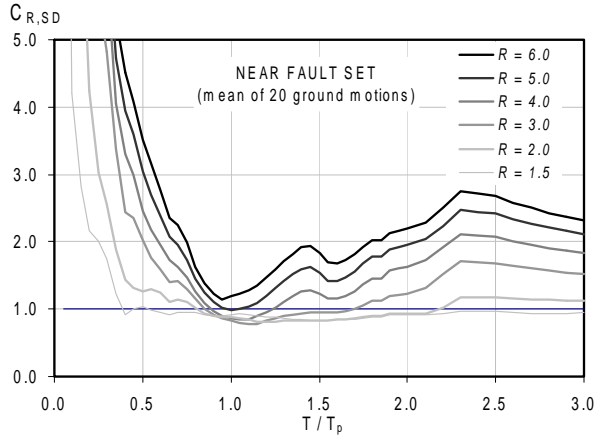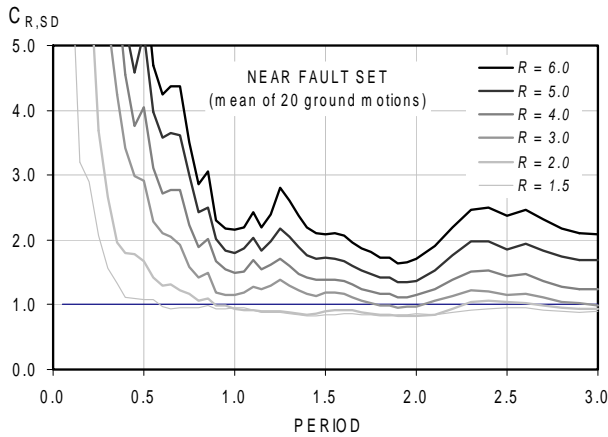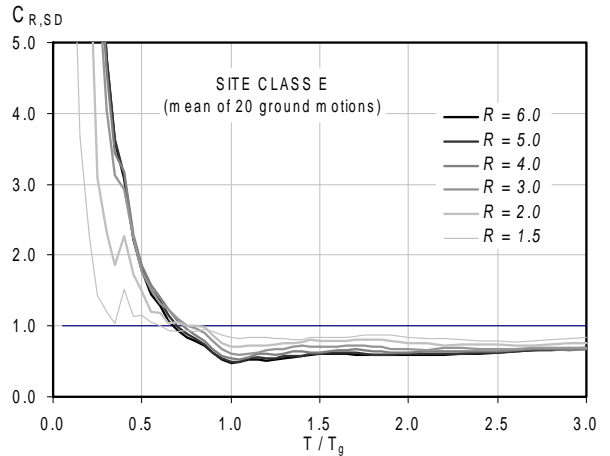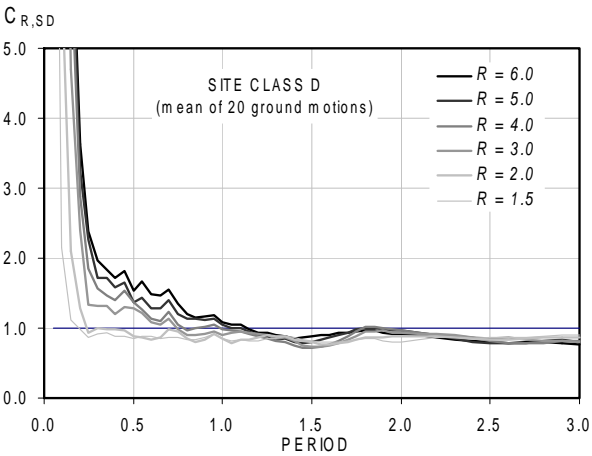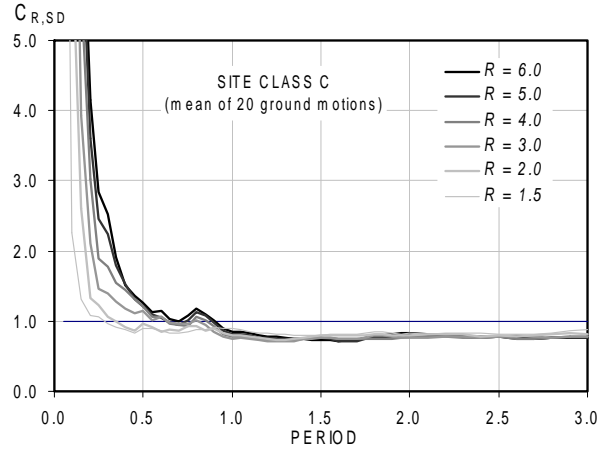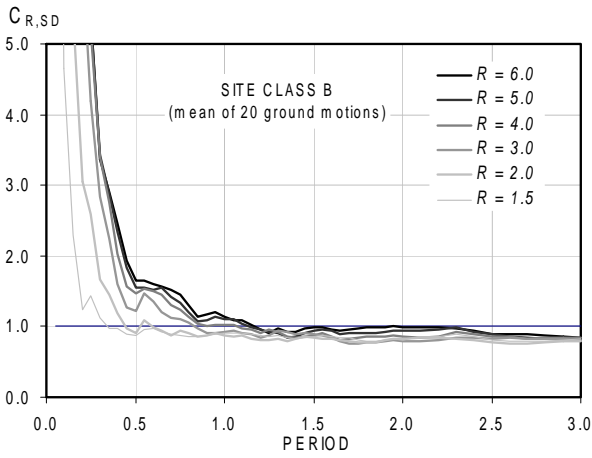
C.2.3 Effect of Site Class on C_1 of SDOF Systems with Strength and Stiffness Degrading (SSD) Hysteretic Behavior
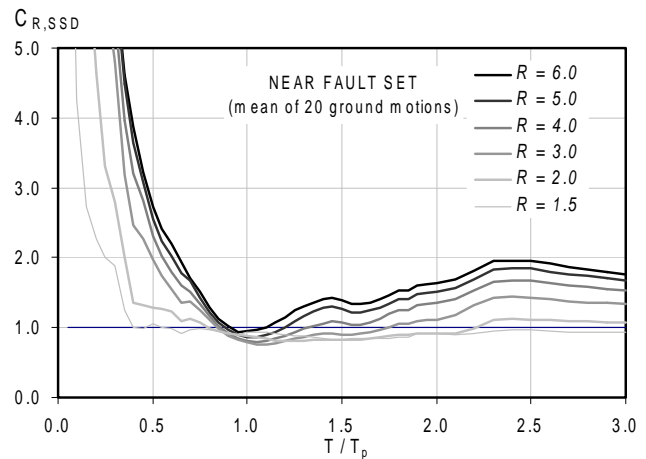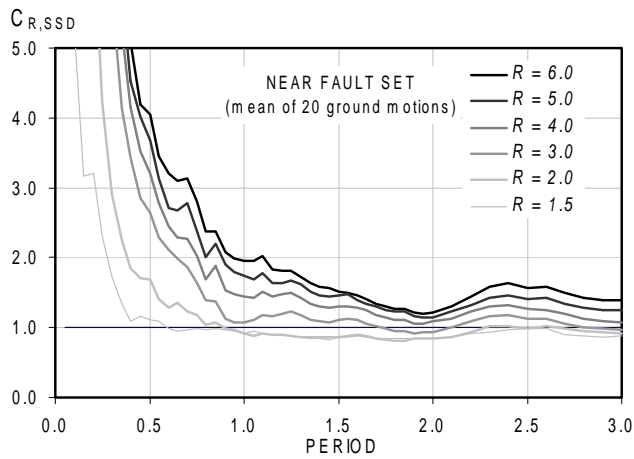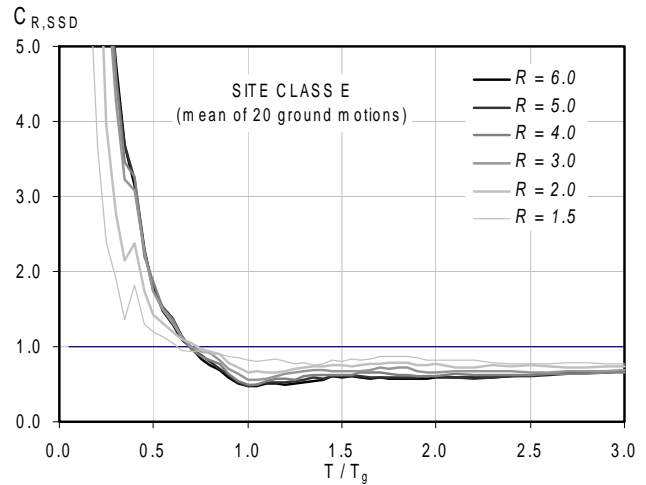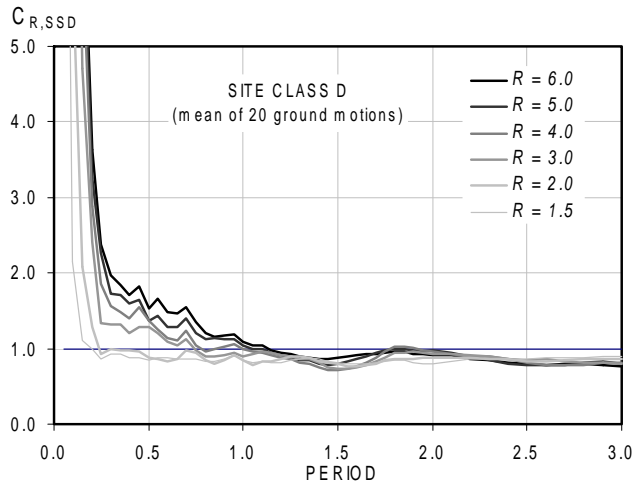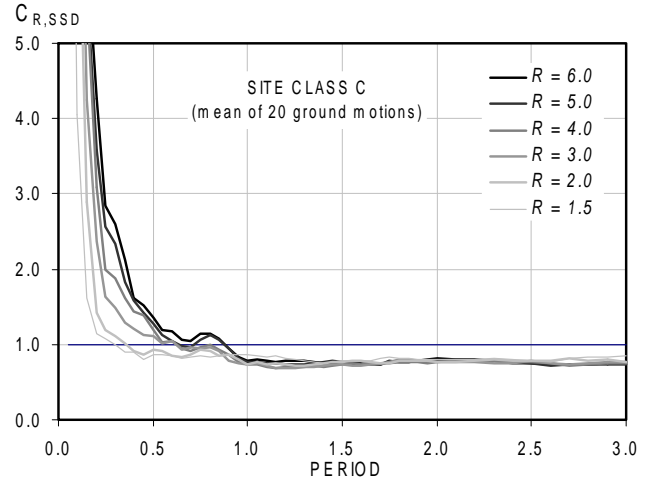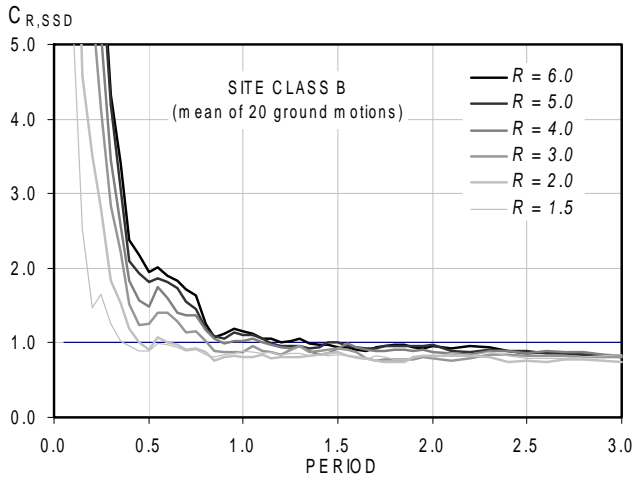
C.2.4 Effect of Site Class on C_1 of SDOF Systems with Nonlinear Elastic Hysteretic Behavior
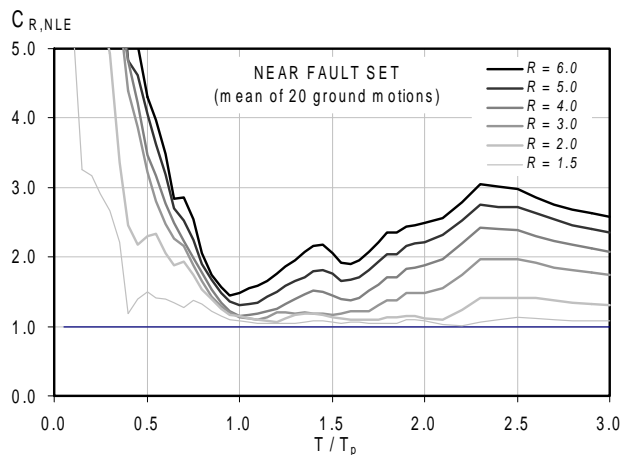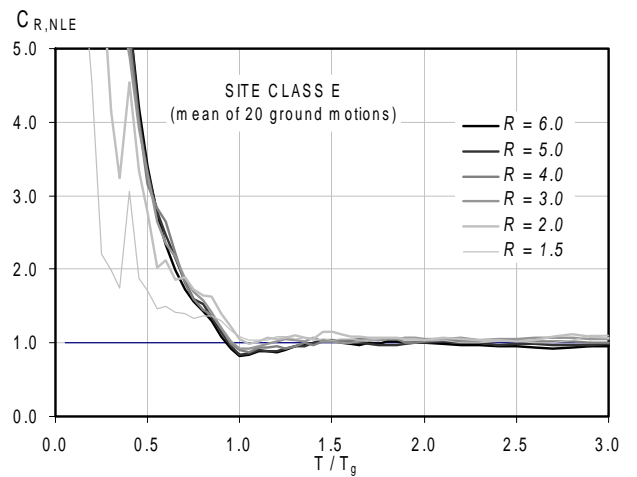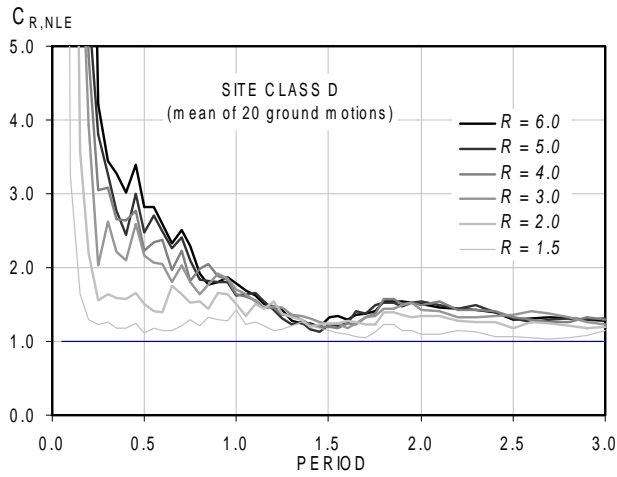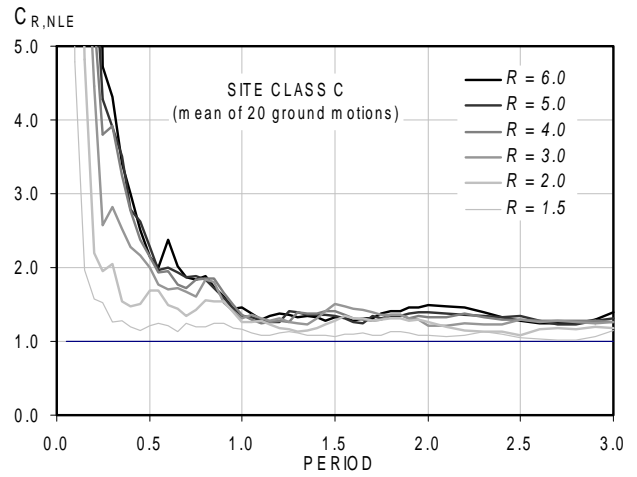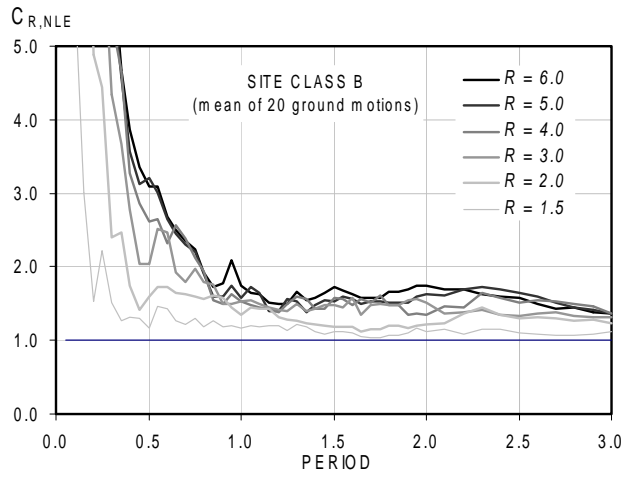
C.2.5 Evaluation of Coefficient C_2 for Site Class B
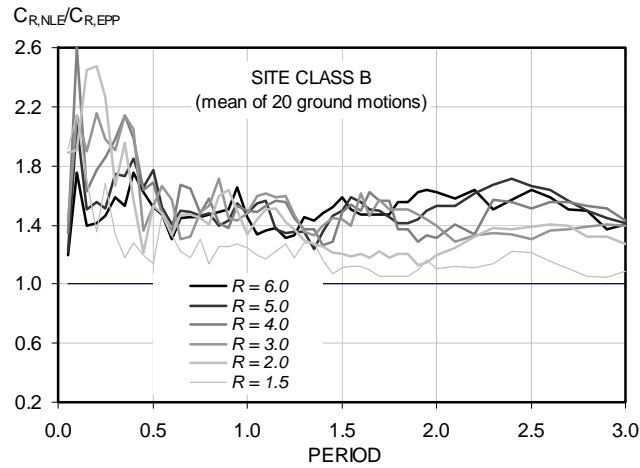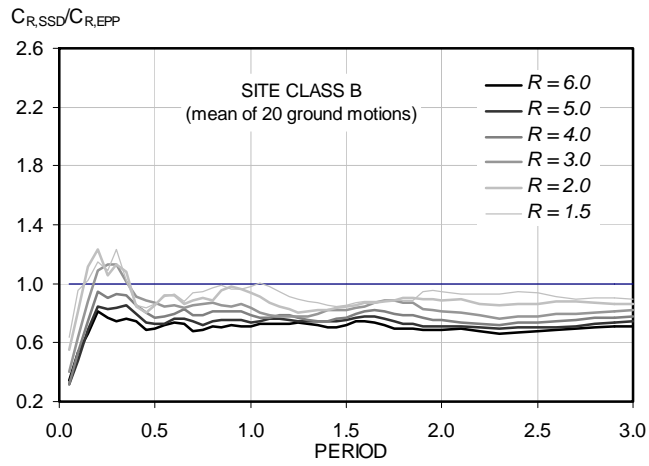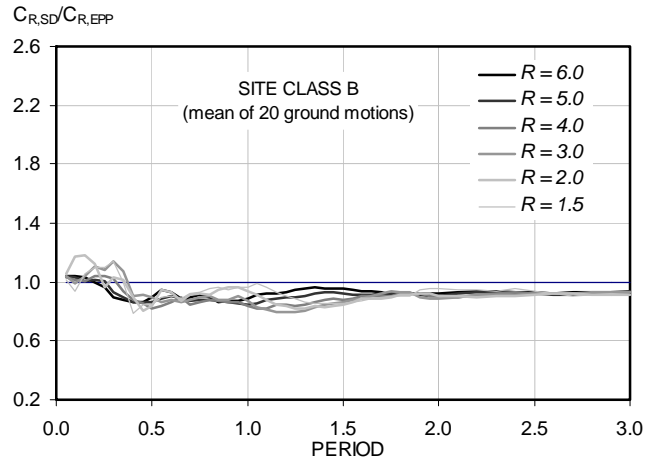
C.2.6   Evaluation of Coefficient C_2 for Site Class C
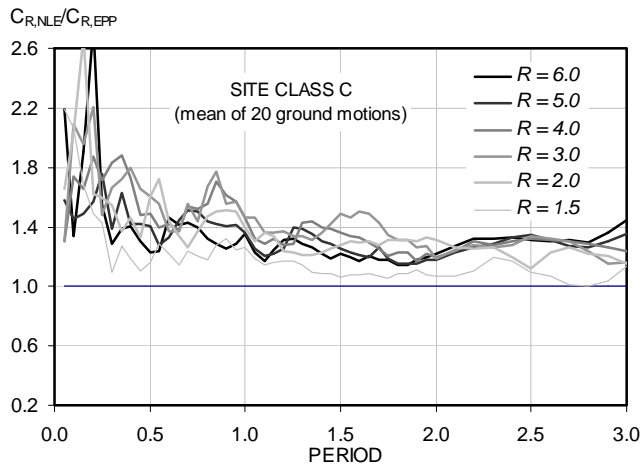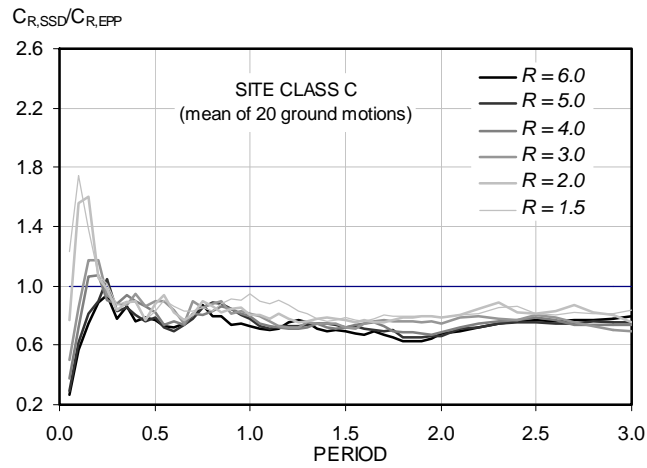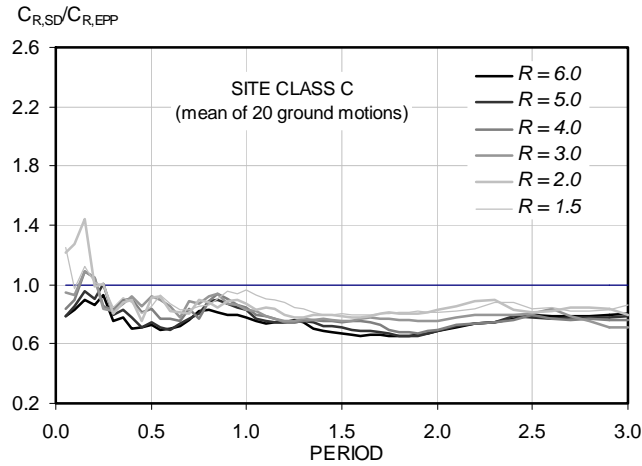
C.2.7 Evaluation of Coefficient C_2 for Site Class D

C.2.8 Evaluation of Coefficient C_2 for Site Class E

$C_{R,SD}/C_{R,EPP}$

SITE CLASS E
(mean of 20 ground motions)

R = 6.0
R = 5.0
R = 4.0
R = 3.0
R = 2.0
R = 1.5

T/T_g

$C_{R,SSD}/C_{R,EPP}$

SITE CLASS E
(mean of 20 ground motions)

R = 6.0
R = 5.0
R = 4.0
R = 3.0
R = 2.0
R = 1.5

T/T_g

$C_{R,NLE}/C_{R,EPP}$

SITE CLASS E
(mean of 20 ground motions)

R = 6.0
R = 5.0
R = 4.0
R = 3.0
R = 2.0
R = 1.5

T/T_g
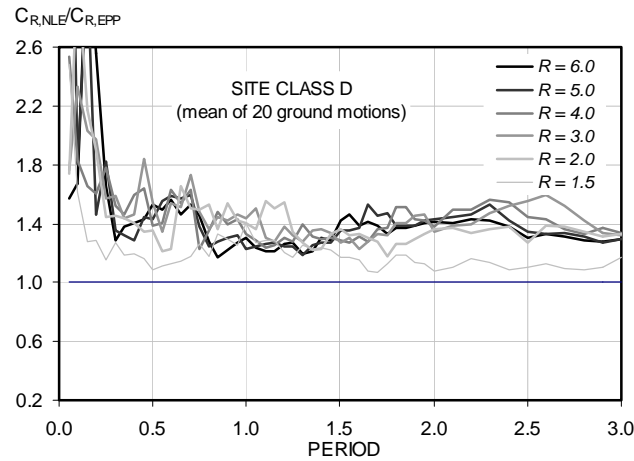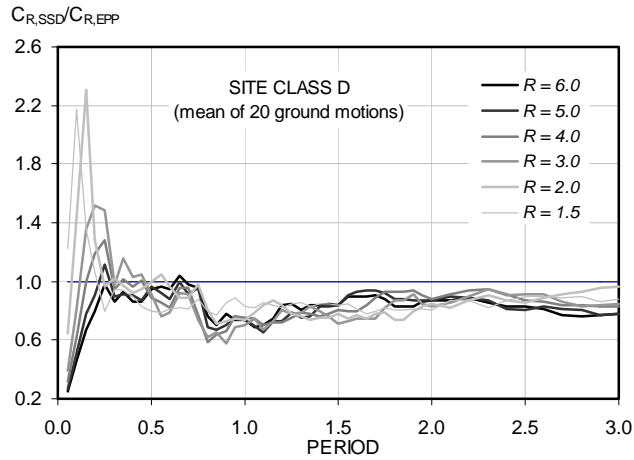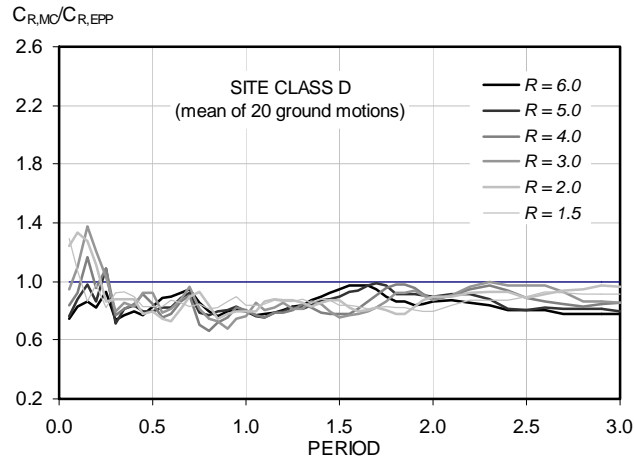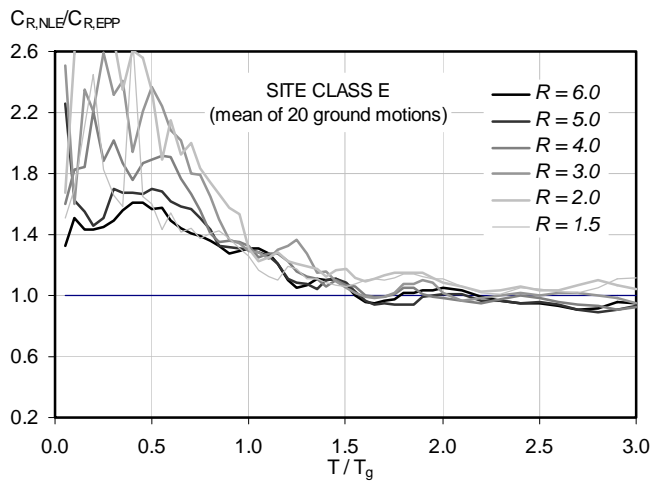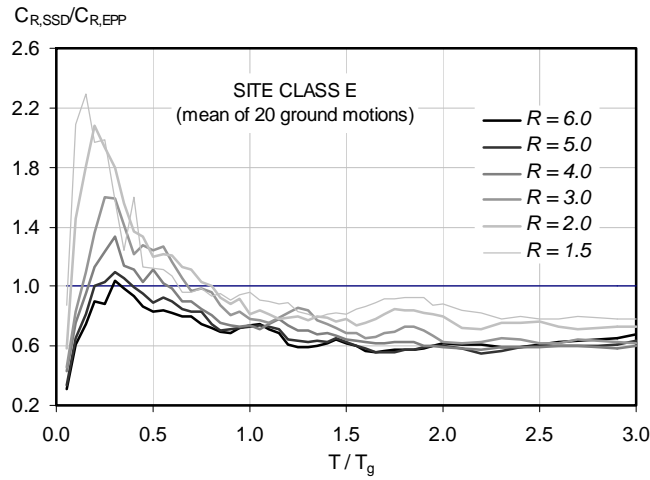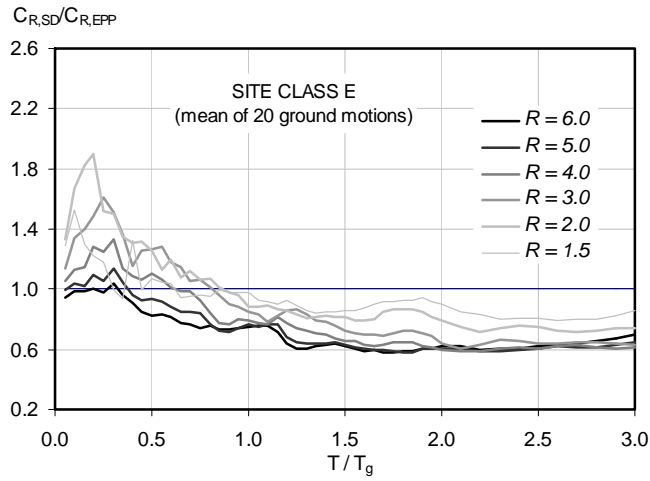
C.2.9 Evaluation of Coefficient C_2 for Near Fault Set

$C_{R,SD}/C_{R,EPP}$

$C_{R,SSD}/C_{R,EPP}$

$C_{R,NLE}/C_{R,EPP}$
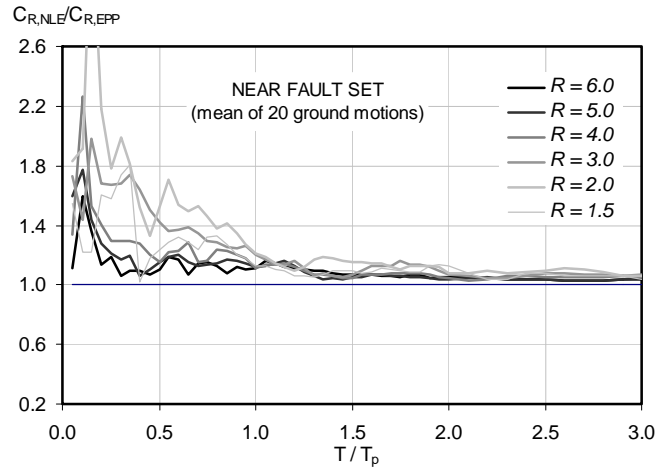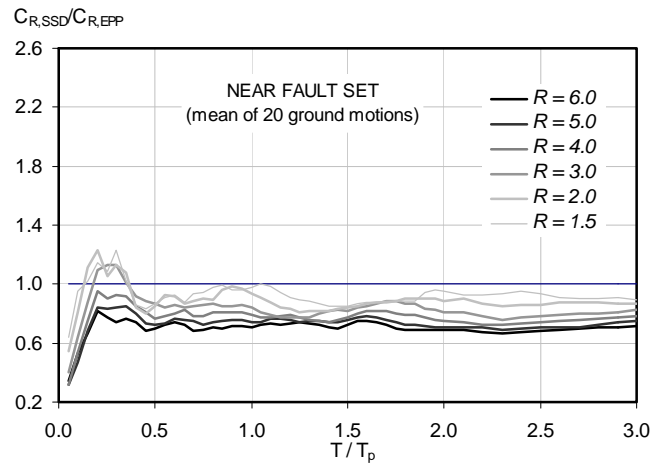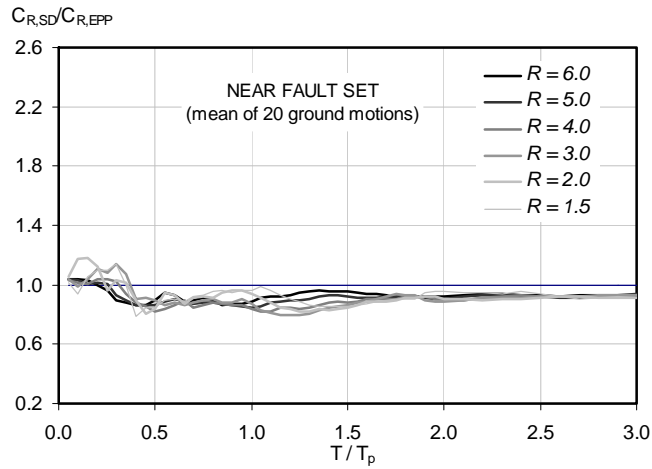
C.2.10   *Effect of Site Class on Coefficient C$_2$ (Stiffness Degrading Hysteretic Behavior)*
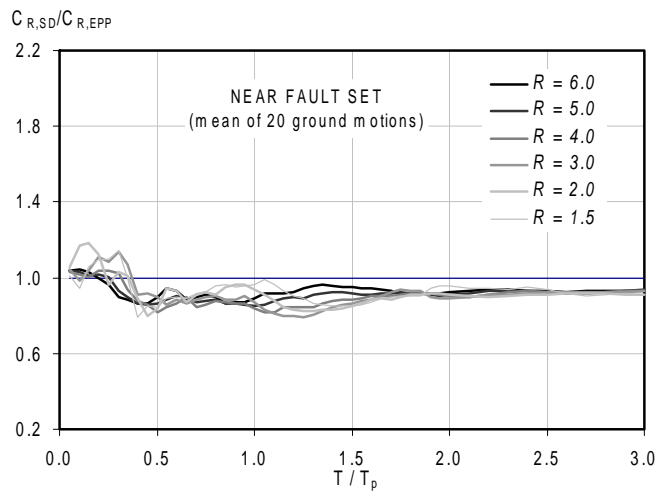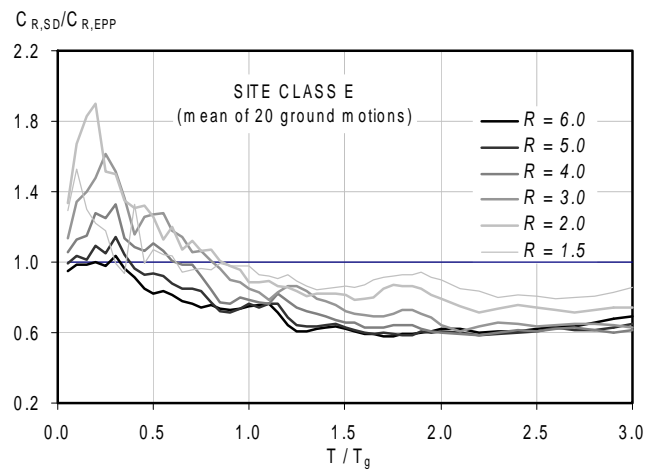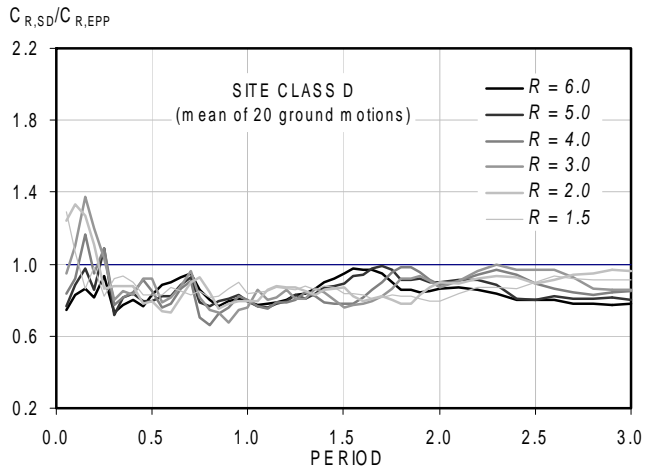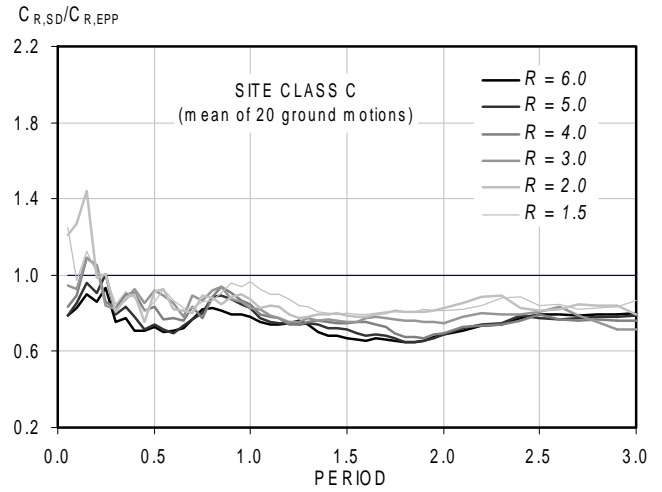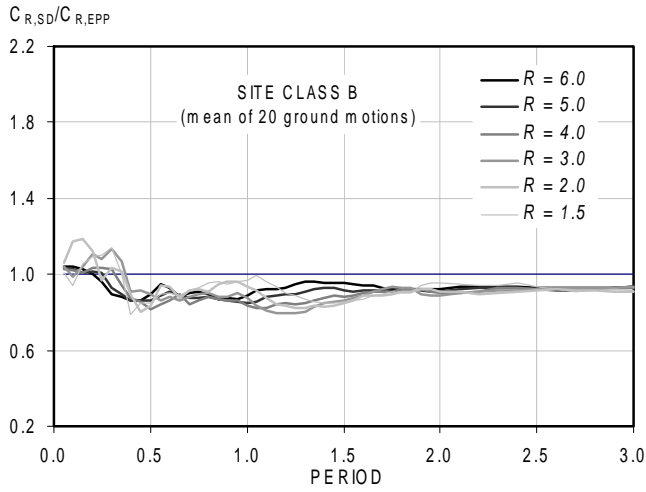
C.2.11   *Effect of Site Class on Coefficient C_2 (Strength-Stiffness Degrading Hysteretic Behavior)*
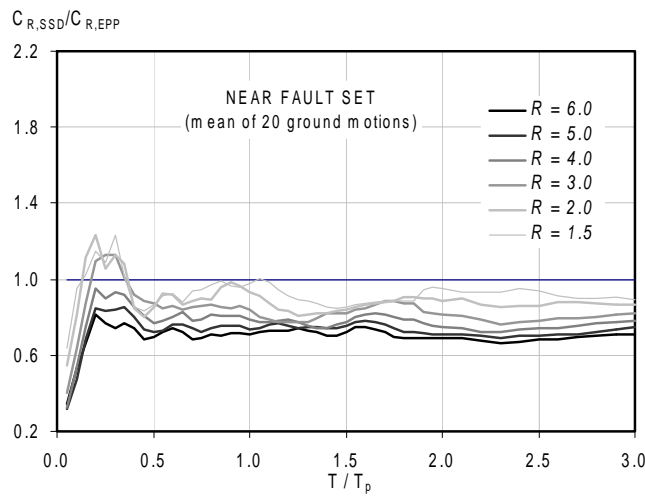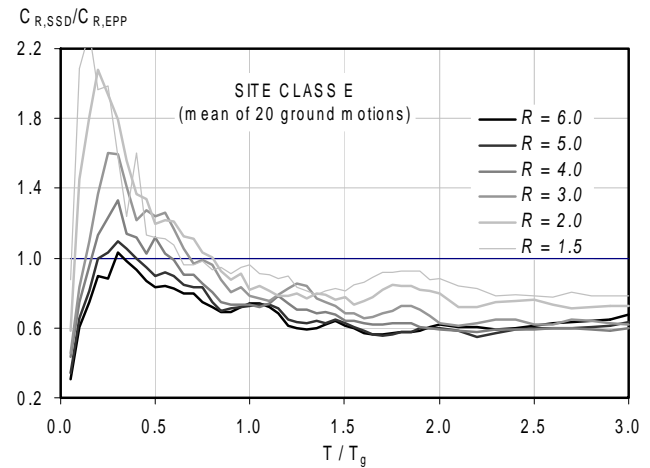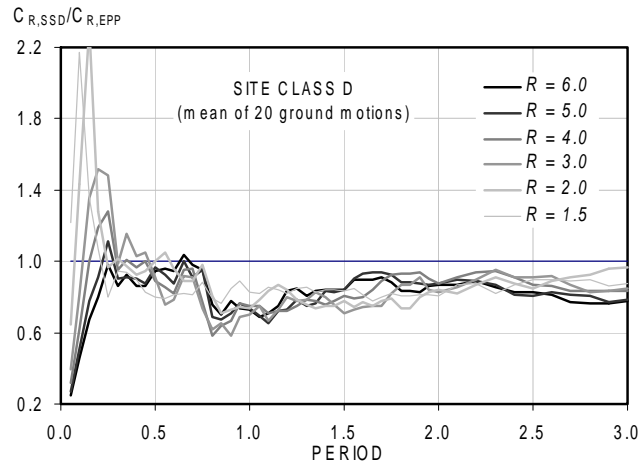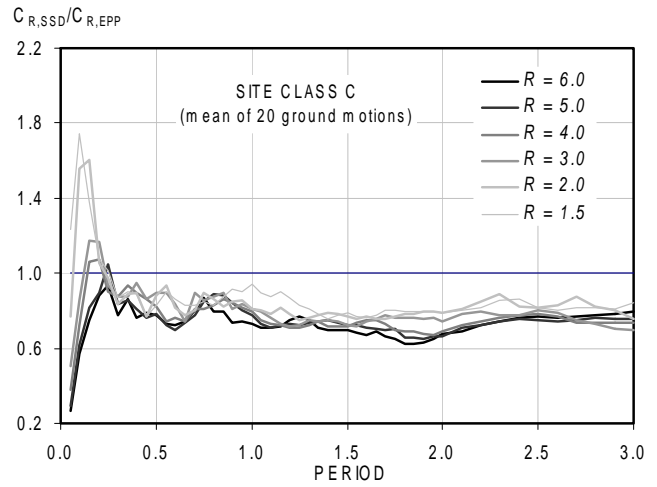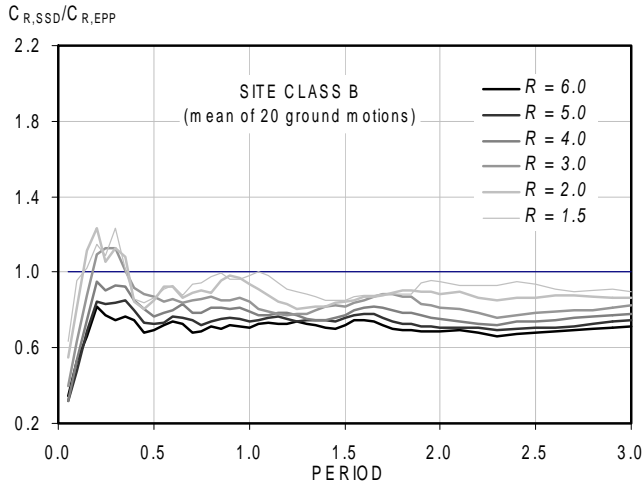
C.2.12 Effect of Site Class on Coefficient C_2 (Nonlinear Elastic Hysteretic Behavior)
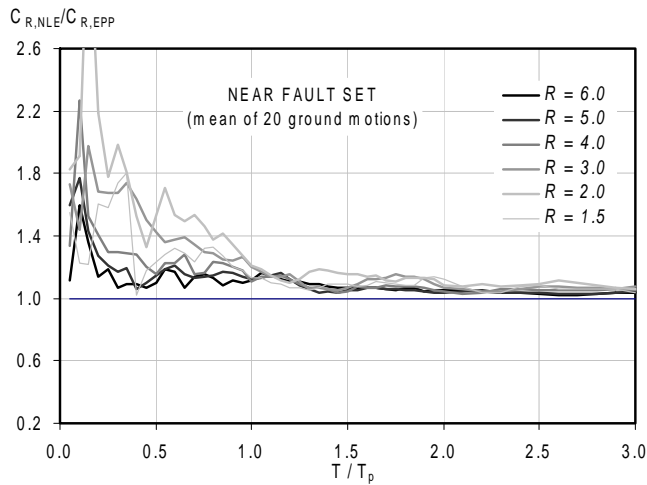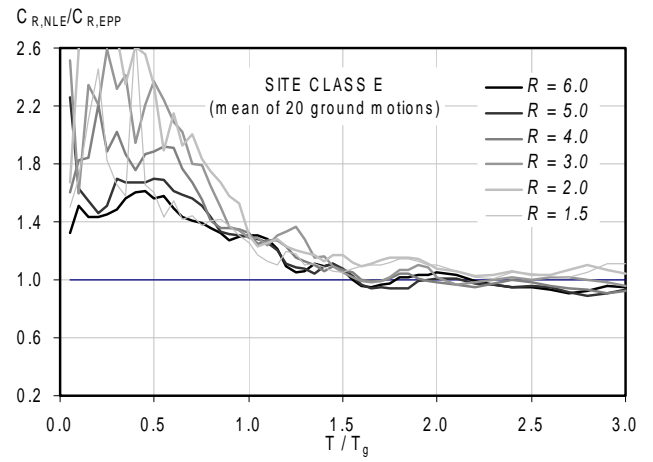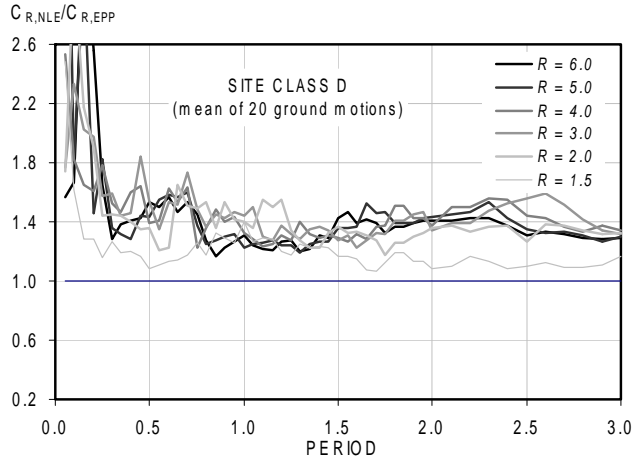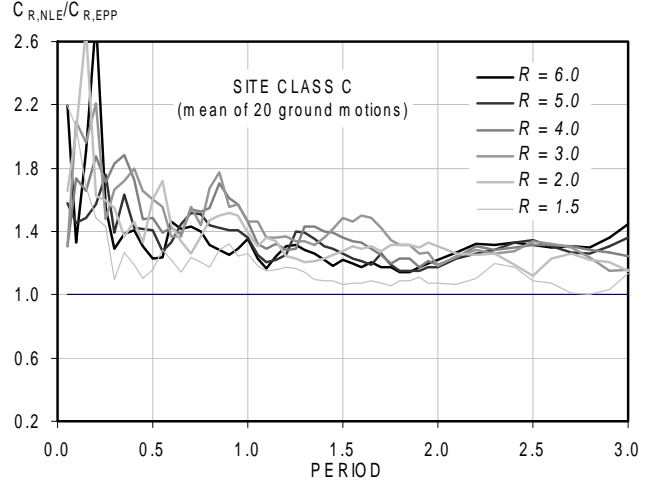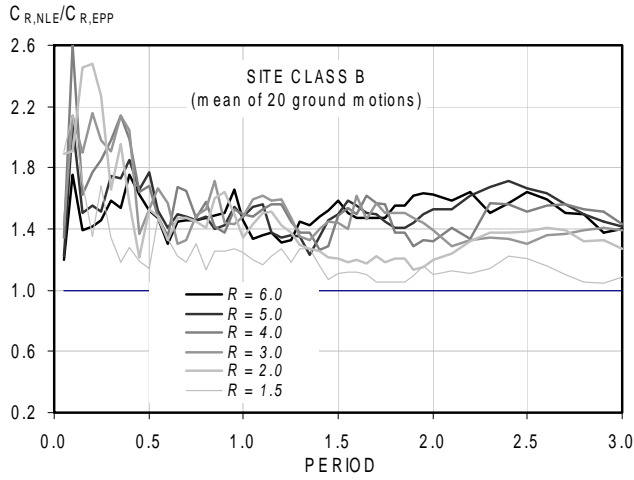
C.2.13 Effect of Hysteretic Behavior on C_1 of SDOF Systems (Site Class B)
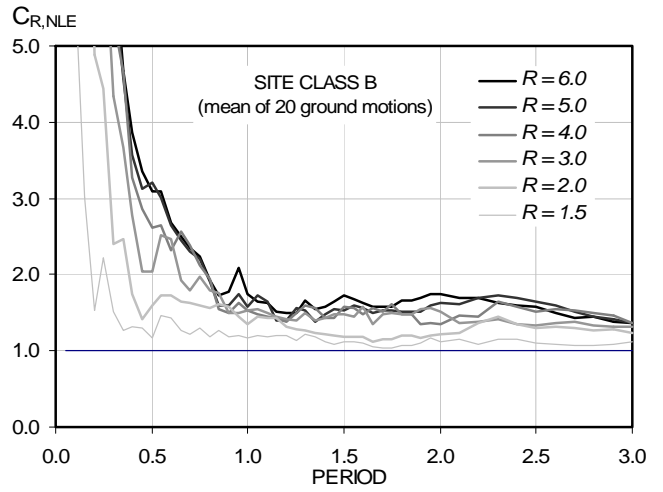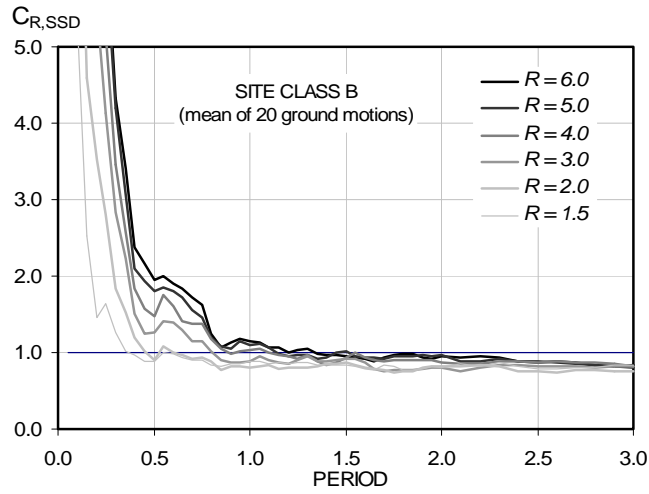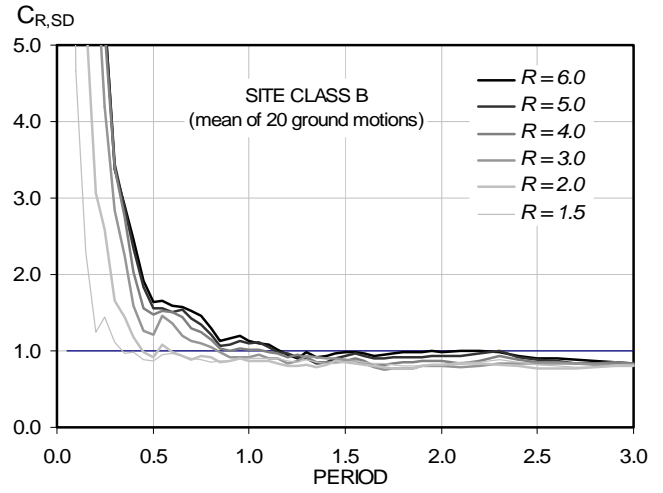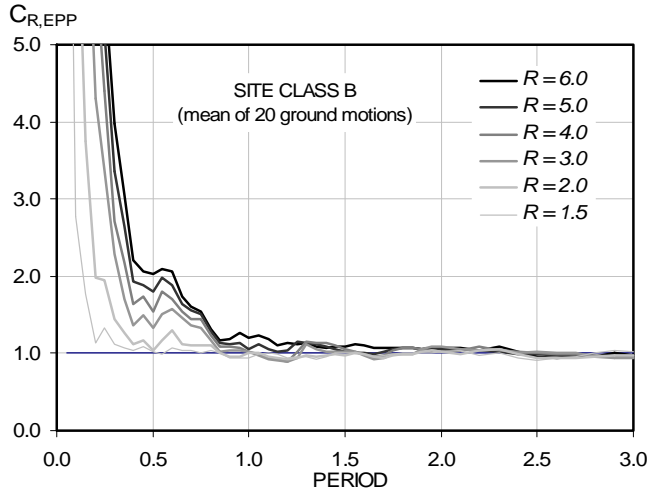
C.2.14 Effect of Hysteretic Behavior on C_1 of SDOF Systems (Site Class C)
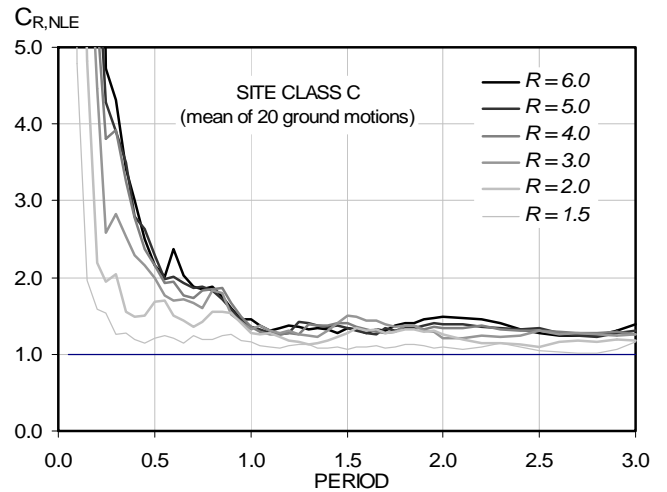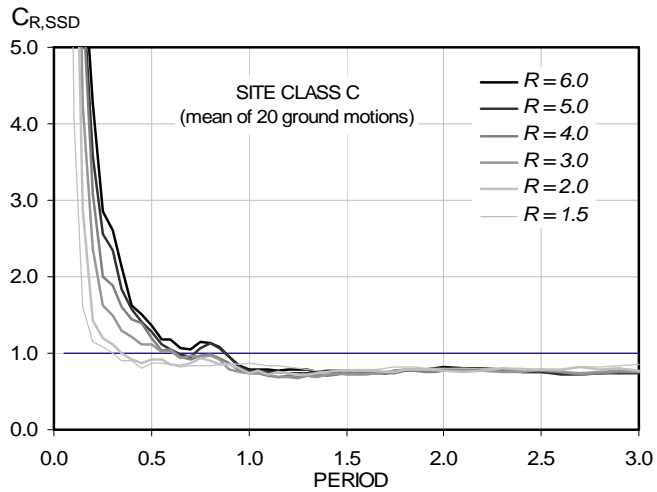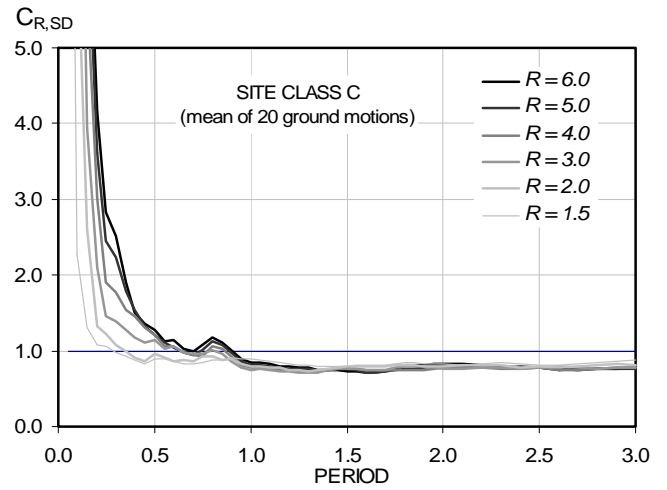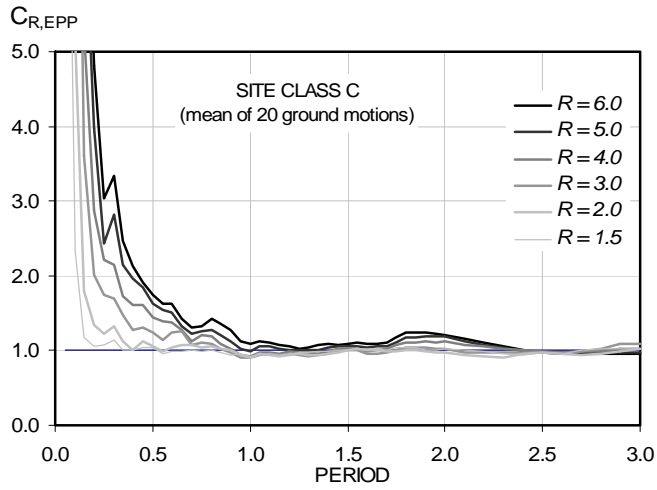
C.2.15 Effect of Hysteretic Behavior on C_1 of SDOF Systems (Site Class D)
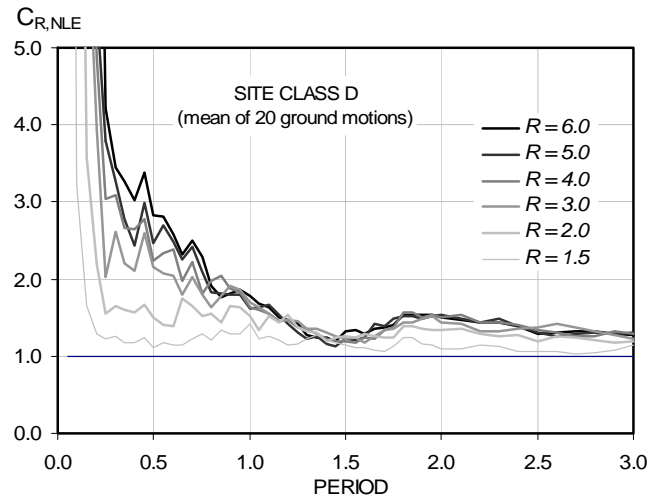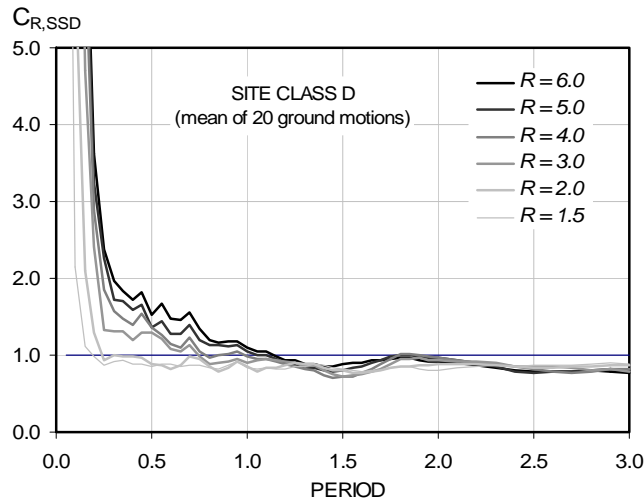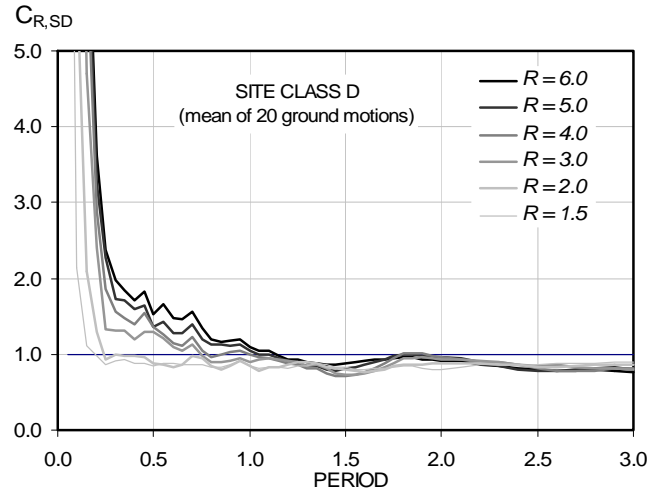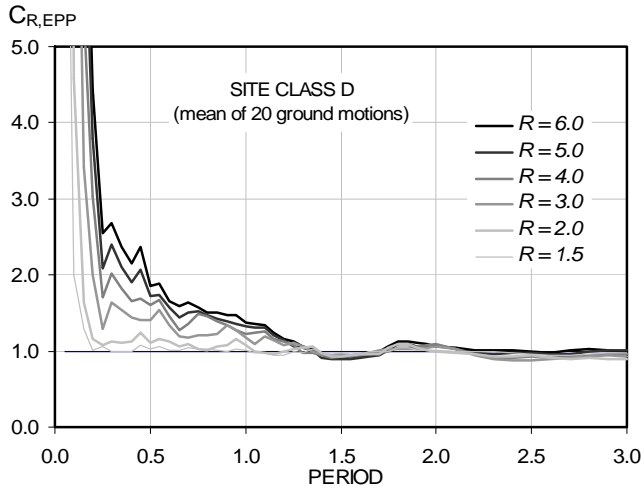
C.2.16 Effect of Hysteretic Behavior on C_1 of SDOF Systems (Site Class E)
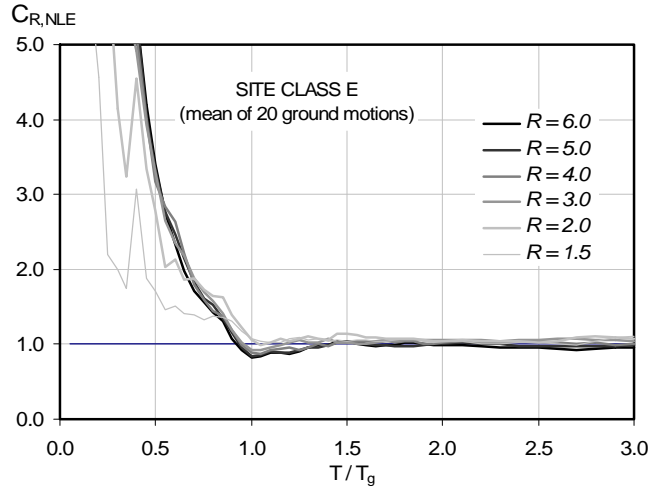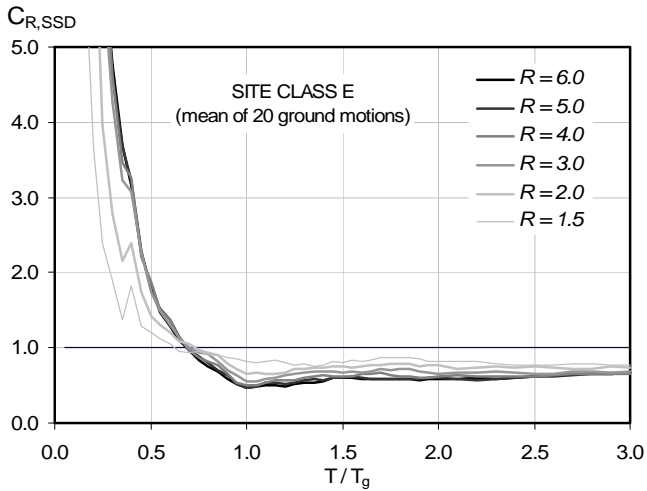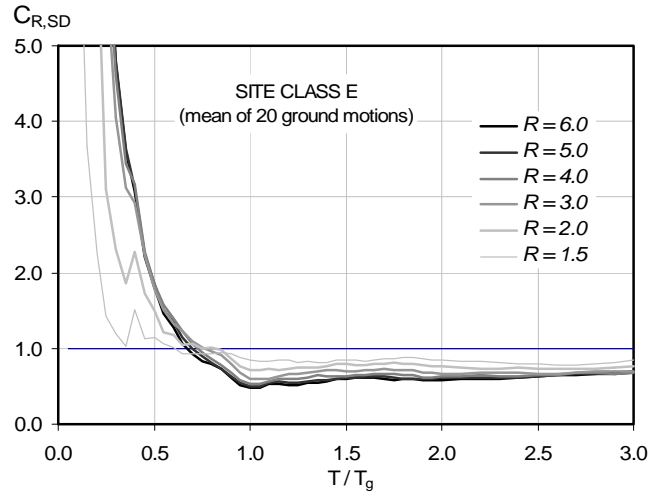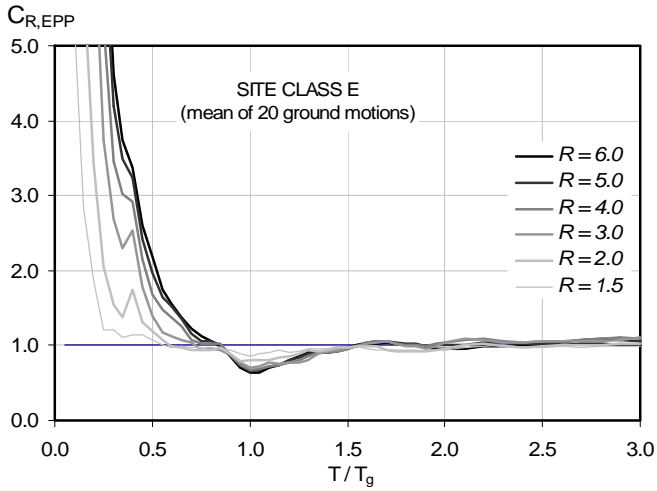
C.2.17 Effect of Hysteretic Behavior on C_1 of SDOF Systems (Near Fault Set)

Improvement of Nonlinear Static Seismic Analysis Procedures
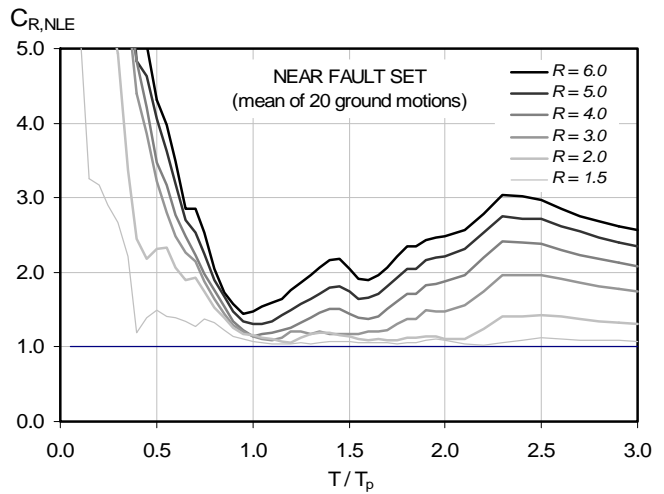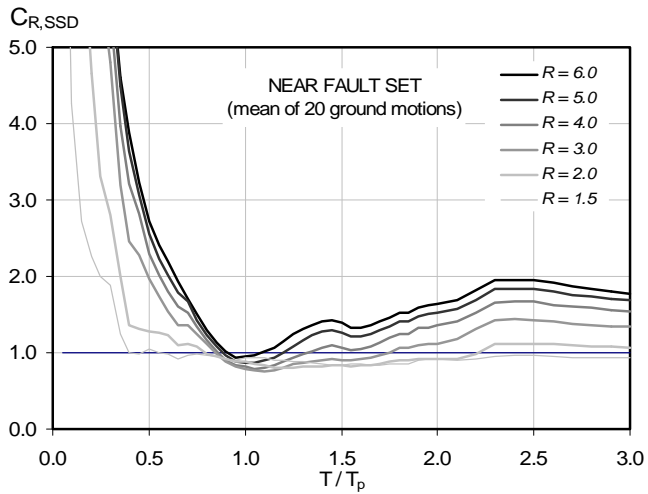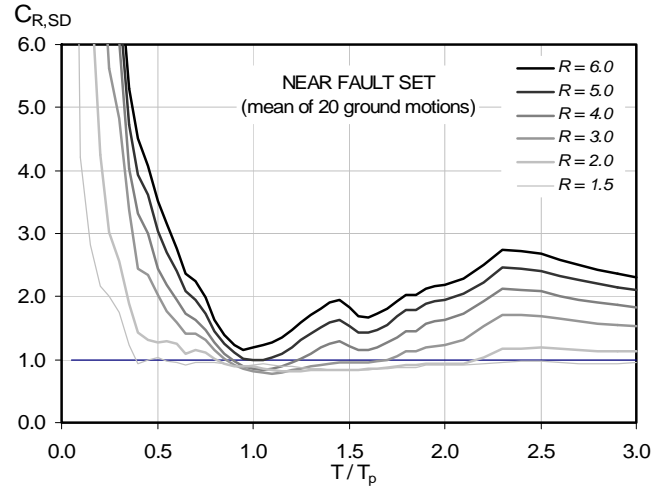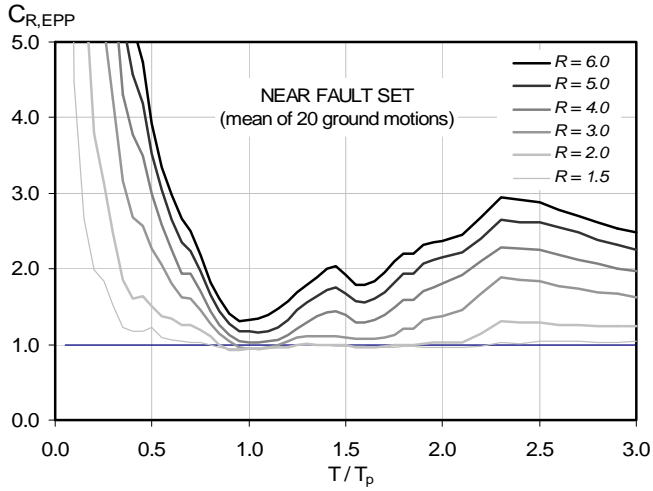
C.3   Evaluation of ATC-40 Version of Capacity Spectrum Method: Summary Results
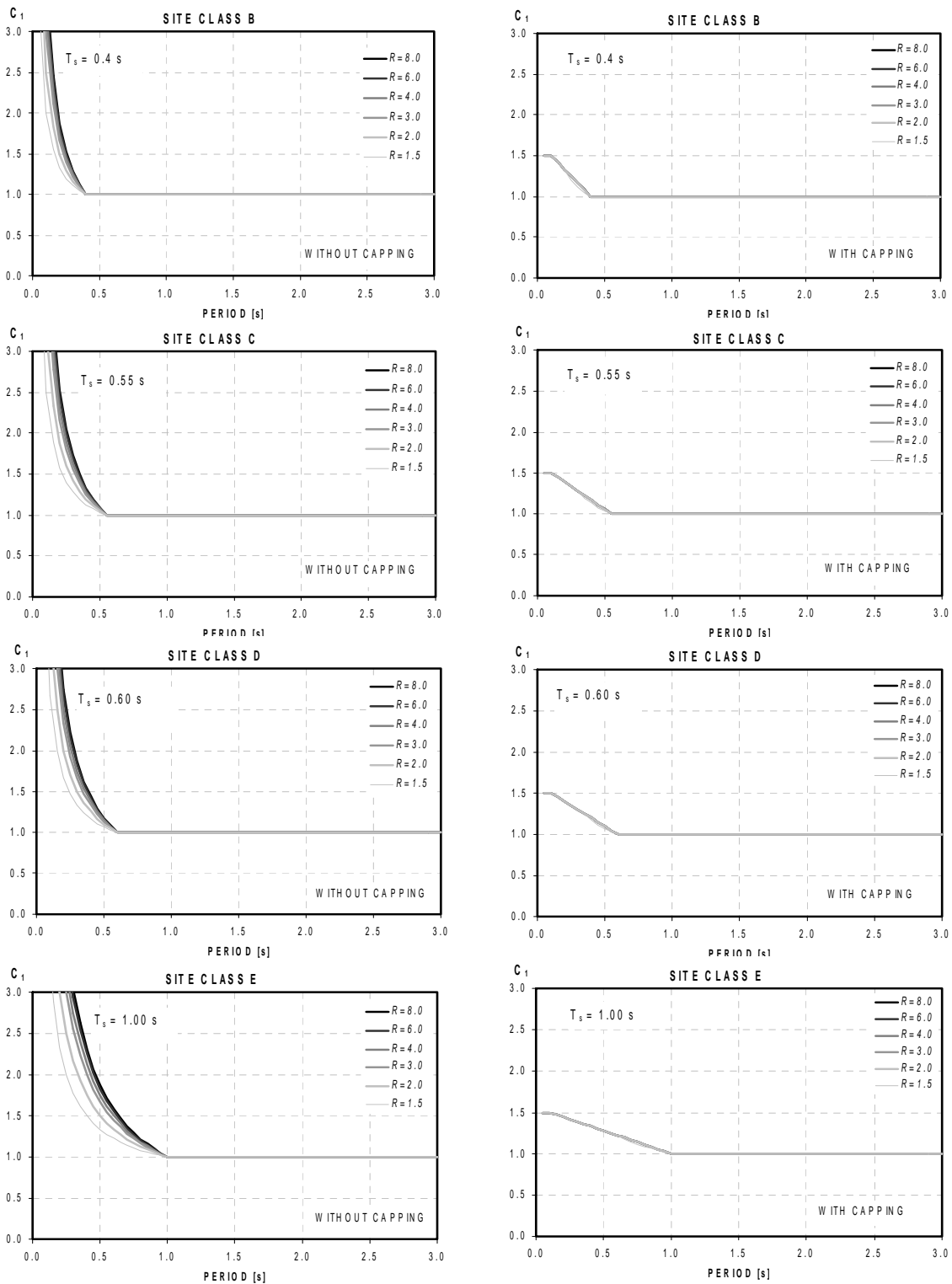
C.3.1   Comparisons for Site Class B:

<table>
<tr><td><h1>MEAN ERROR</h1></td><td><h1>ERROR DISPERSION</h1></td></tr>
</table>
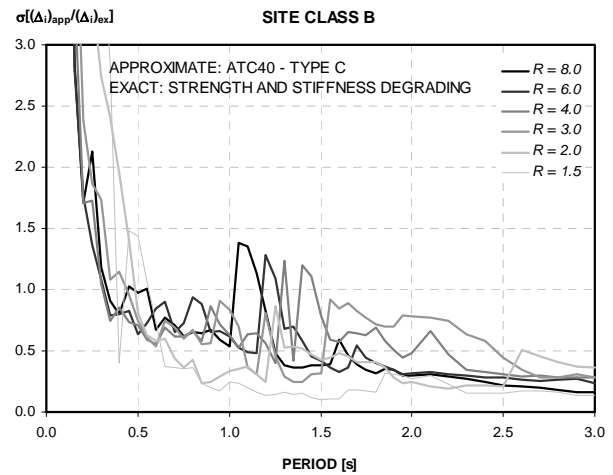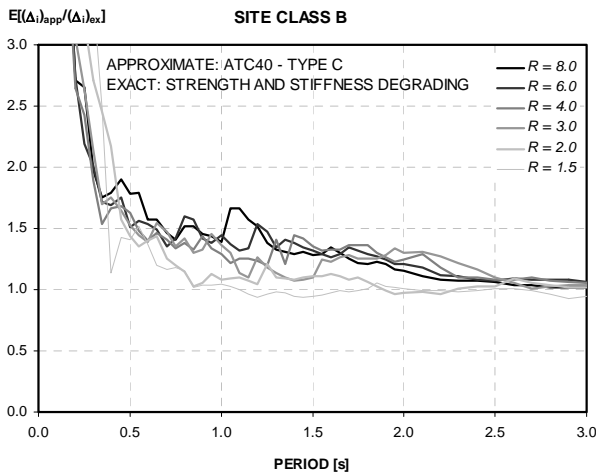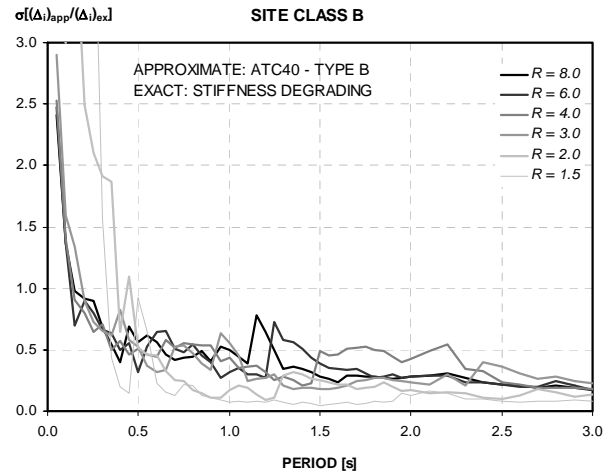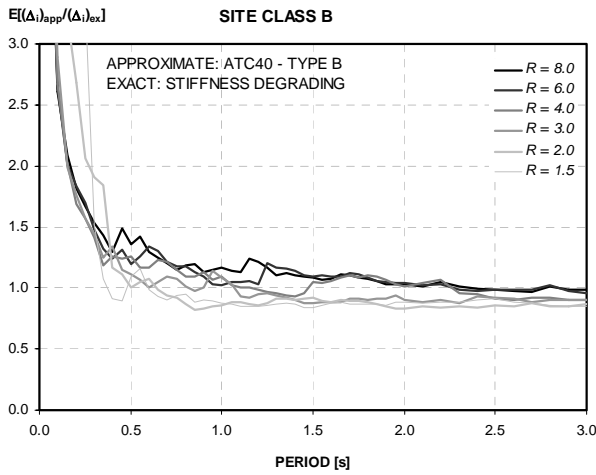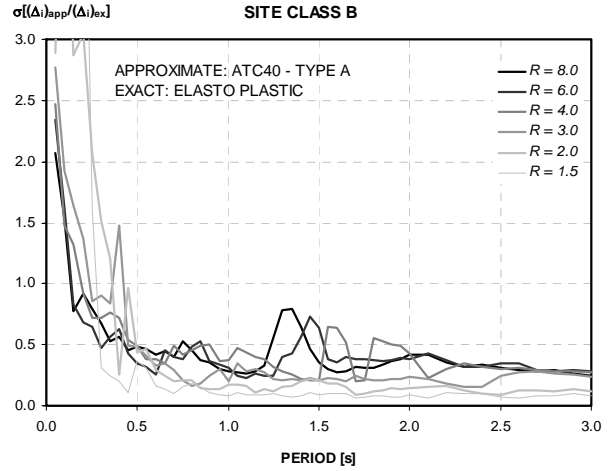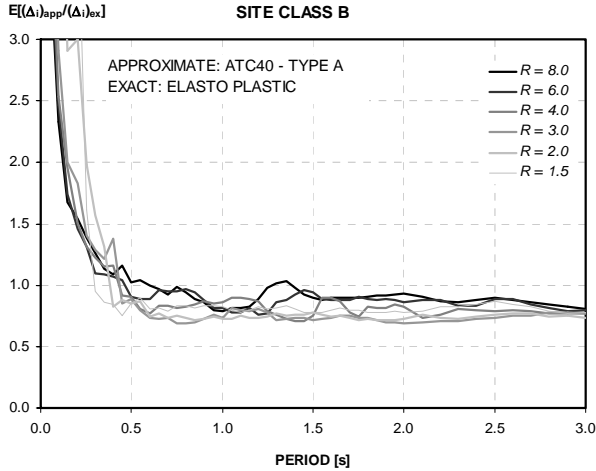
C.3.2   Comparisons for Site Class C:

<table>
<tr><th>MEAN ERROR</th><th>ERROR DISPERSION</th></tr>
</table>
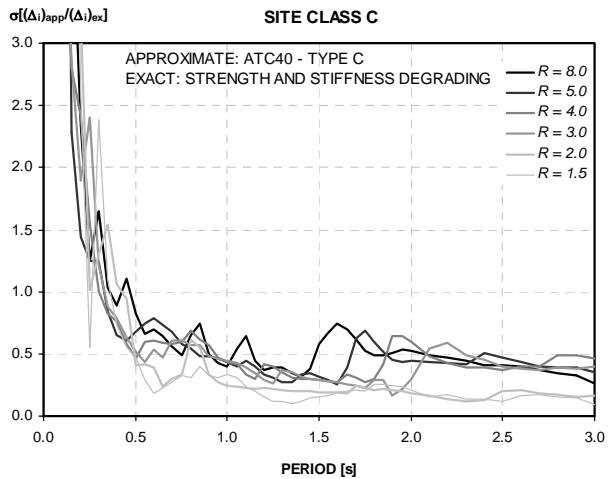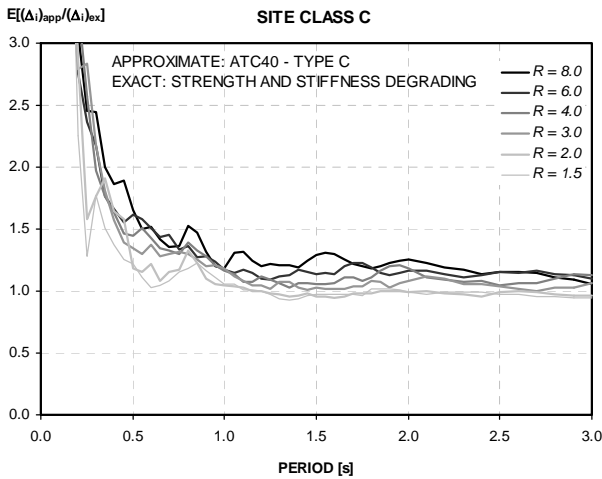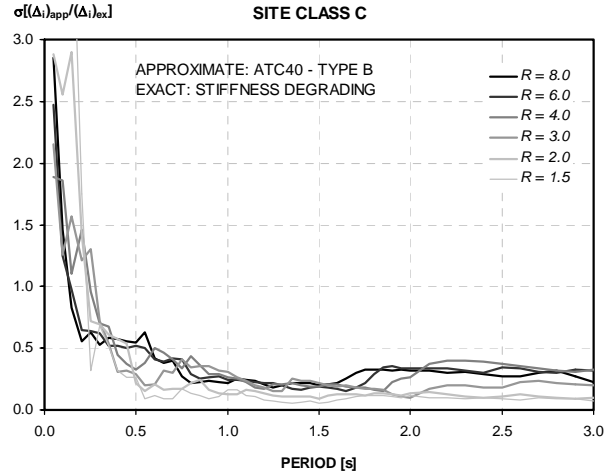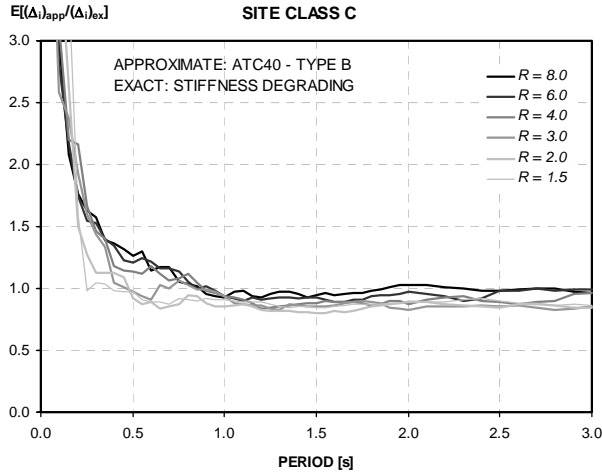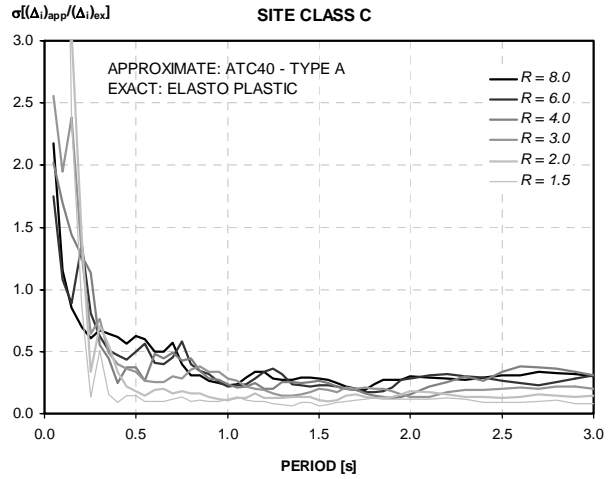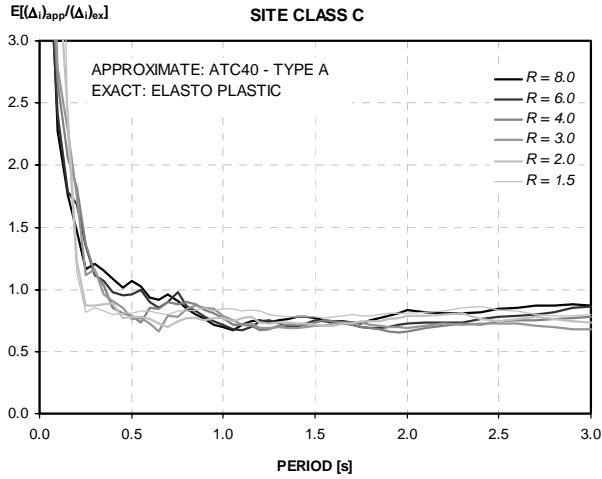
C.3.3 Comparisons for Site Class D:

MEAN ERROR

ERROR DISPERSION
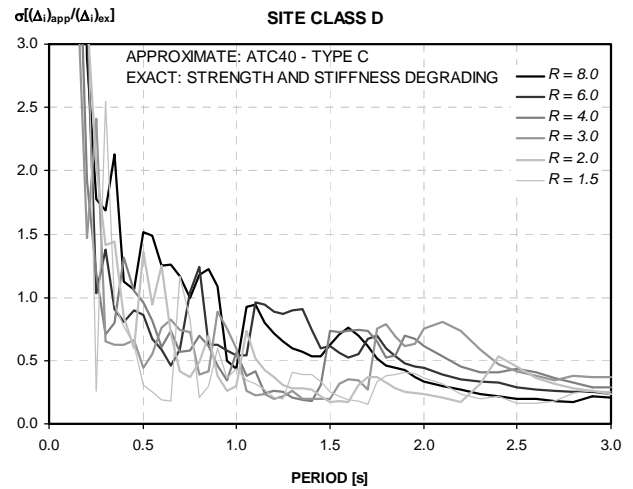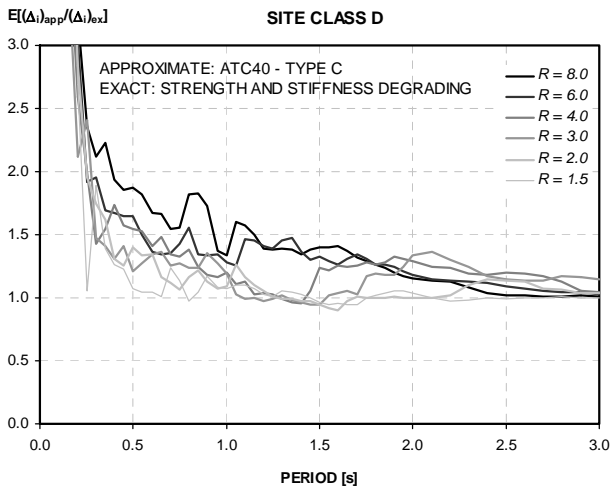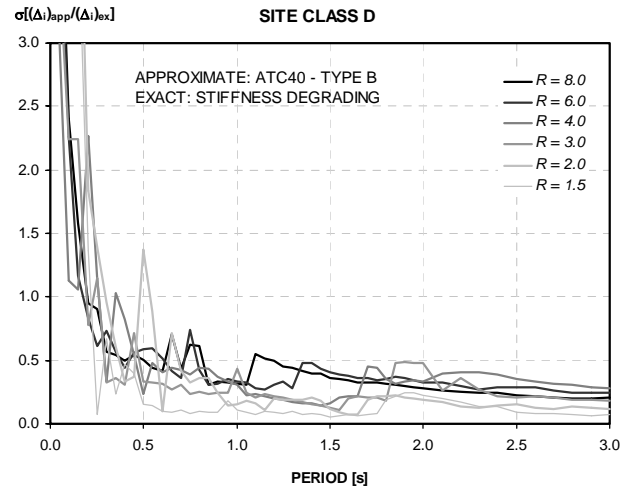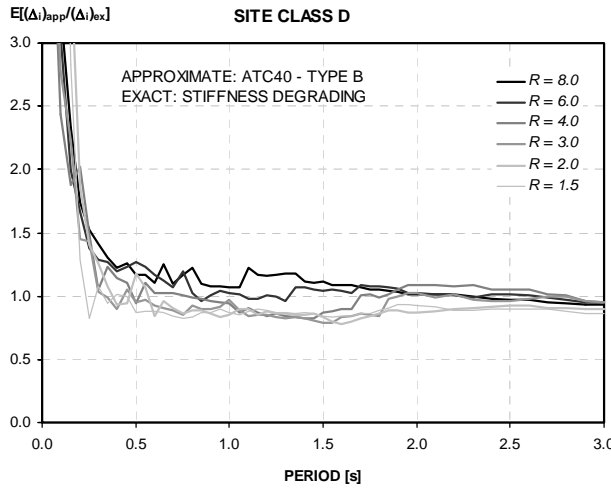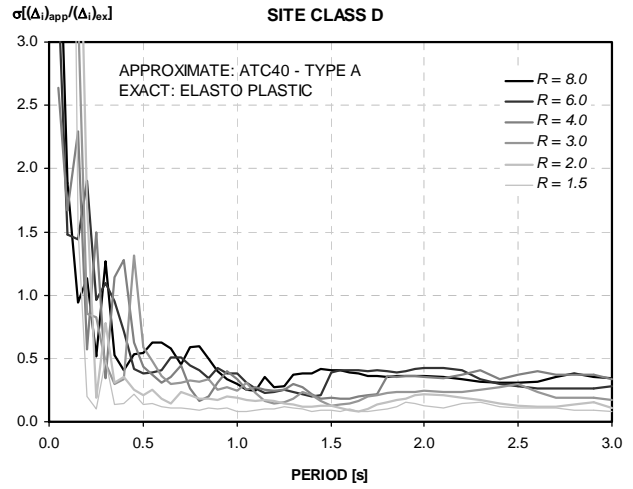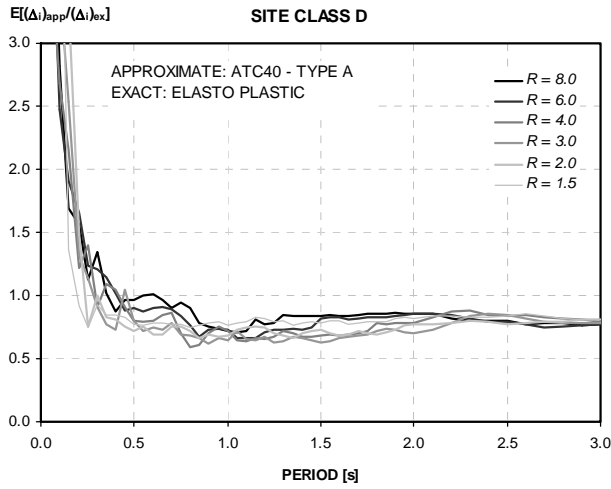
C.3.4 Comparisons for Site Class E:

MEAN ERROR

$E[(\Delta_i)_{app}/(\Delta_i)_{ex}]$ SITE CLASS E (T_s=1.0 s)

APPROXIMATE: ATC40 - TYPE A
EXACT: ELASTO PLASTIC

R = 8.0
R = 6.0
R = 4.0
R = 3.0
R = 2.0
R = 1.5

T/T_s

$E[(\Delta_i)_{app}/(\Delta_i)_{ex}]$ SITE CLASS E (T_s = 1.0 s)

R = 8.0
R = 6.0
R = 4.0
R = 3.0
R = 2.0
R = 1.5

APPROXIMATE: ATC40 - TYPE B
EXACT: STIFFNESS DEGRADING

T/T_s

$E[(\Delta_i)_{app}/(\Delta_i)_{ex}]$ SITE CLASS E (T_s=1.0 s)

R = 8.0
R = 6.0
R = 4.0
R = 3.0
R = 2.0
R = 1.5

APPROXIMATE: ATC40 - TYPE C
EXACT: STRENGTH AND STIFFNESS DEGRADING

T/T_s

ERROR DISPERSION

$\sigma[(\Delta_i)_{app}/(\Delta_i)_{ex}]$ SITE CLASS E (T_s=1.0 s)

R = 8.0
R = 6.0
R = 4.0
R = 3.0
R = 2.0
R = 1.5

T/T_s

$\sigma[(\Delta_i)_{app}/(\Delta_i)_{ex}]$ SITE CLASS E (T_s = 1.0 s)

APPROXIMATE: ATC40 - TYPE B
EXACT: STIFFNESS DEGRADING

R = 8.0
R = 6.0
R = 4.0
R = 3.0
R = 2.0
R = 1.5

T/T_s

$\sigma[(\Delta_i)_{app}/(\Delta_i)_{ex}]$ SITE CLASS E (T_s=1.0 s)

APPROXIMATE: ATC40 - TYPE C
EXACT: STRENGTH AND STIFFNESS DEGRADING

R = 8.0
R = 6.0
R = 4.0
R = 3.0
R = 2.0
R = 1.5

T/T_s

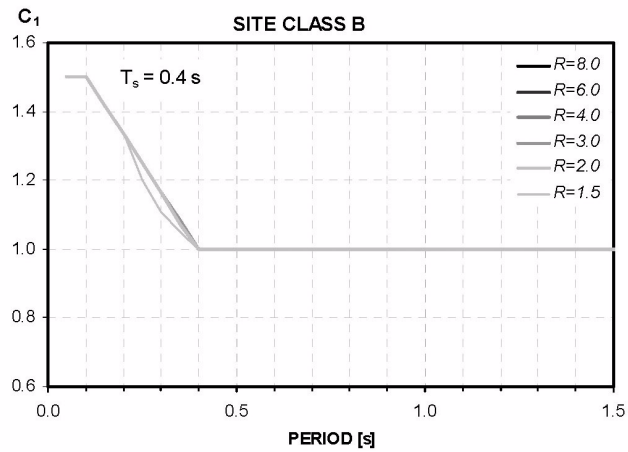### C.3.5 Comparisons for Near-Fault Ground Motions:

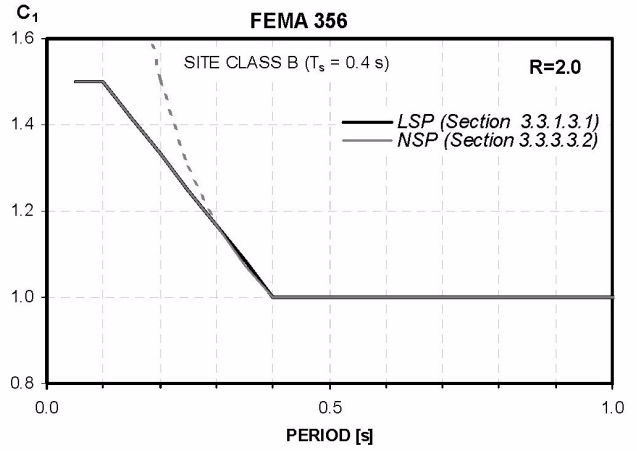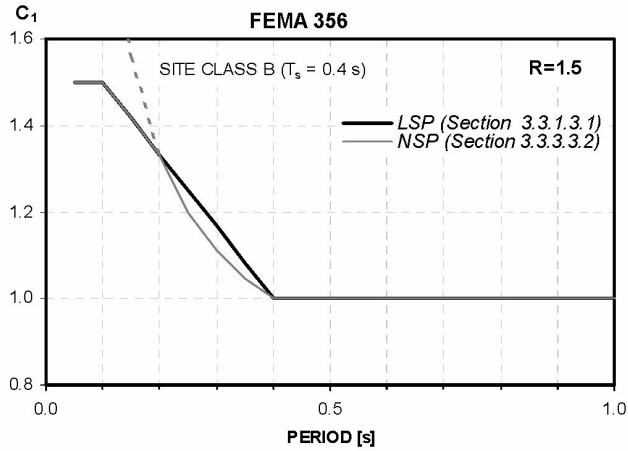## MEAN ERROR

ERROR DISPERSION
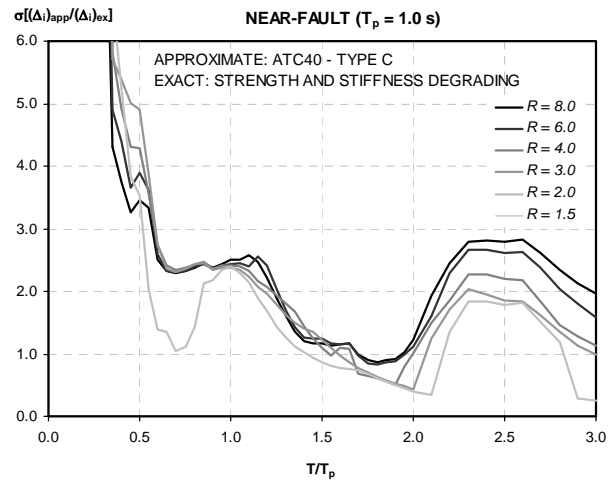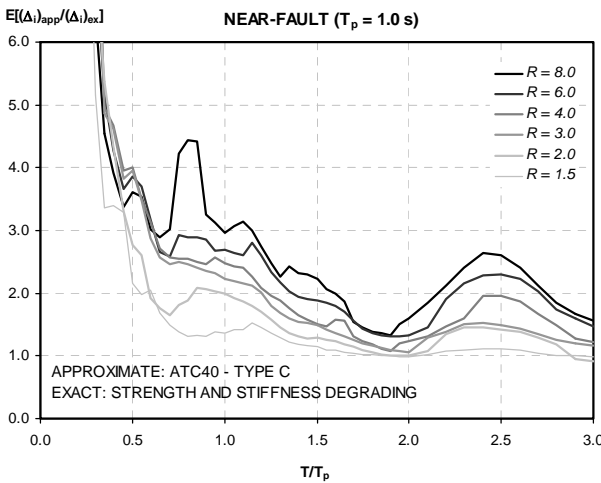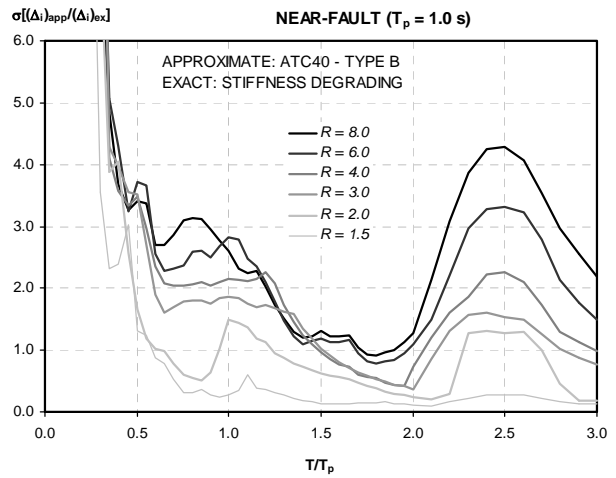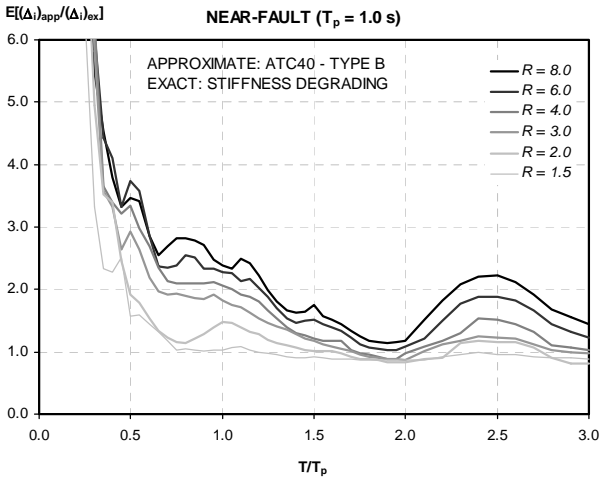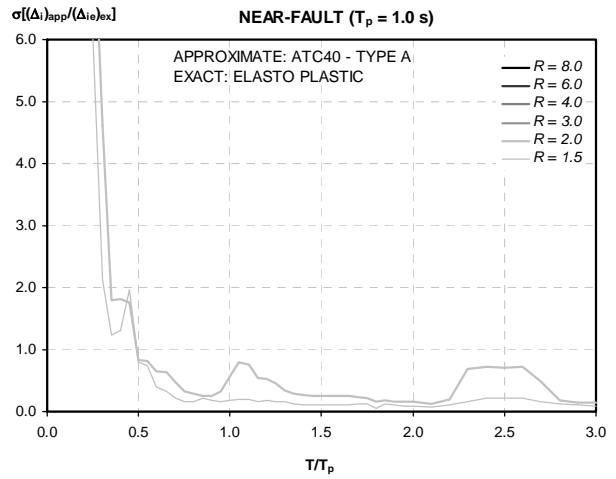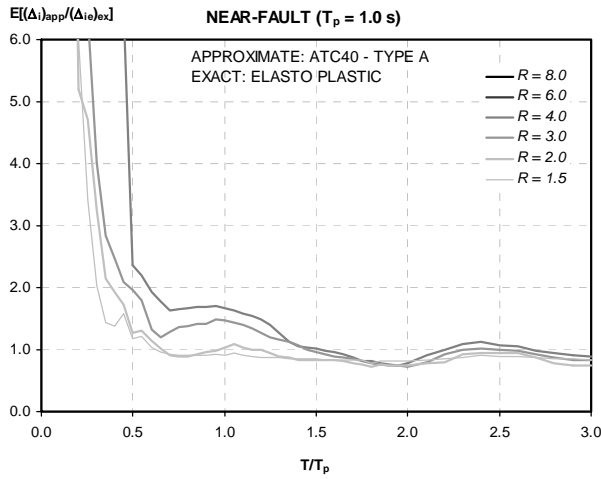
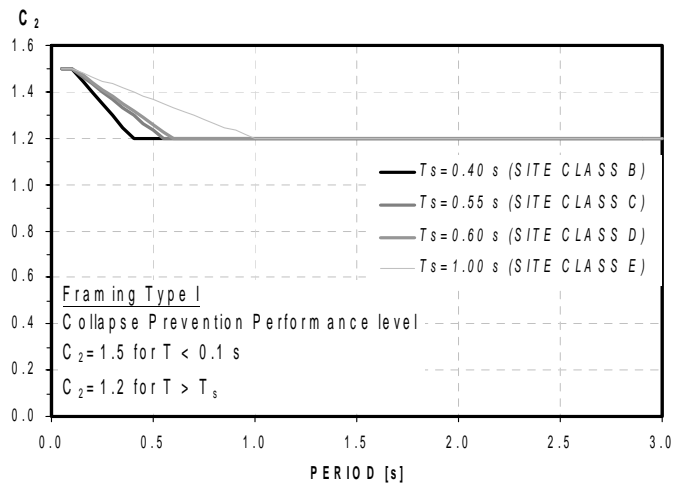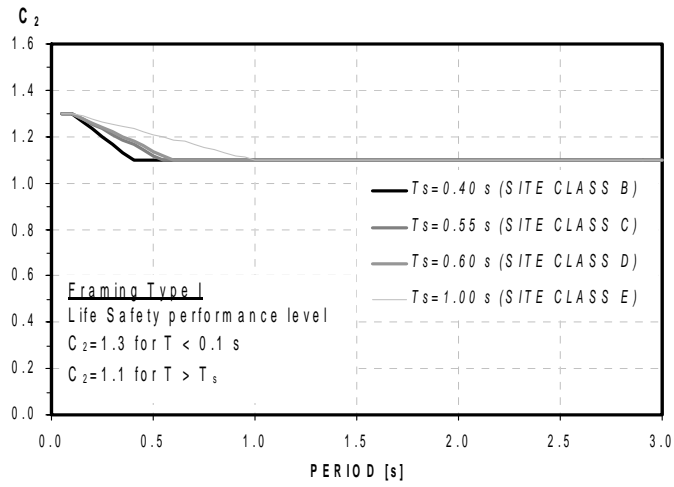## C.4 Evaluation of the Coefficient Method of FEMA 356: Summary Results

C.4.1 FEMA 356 Nonlinear Static Procedure (NSP) C_1 Values for Different T_S Values:
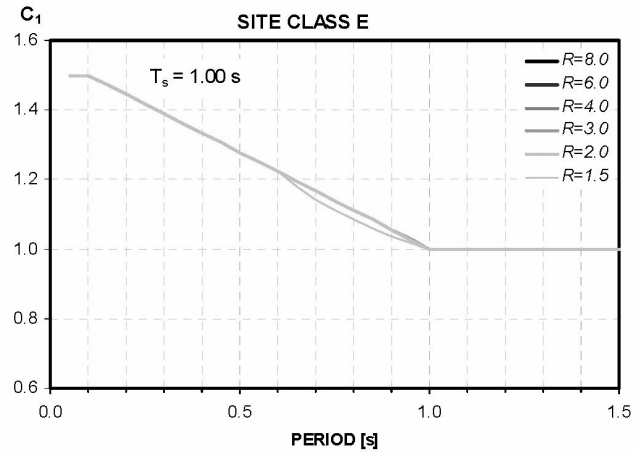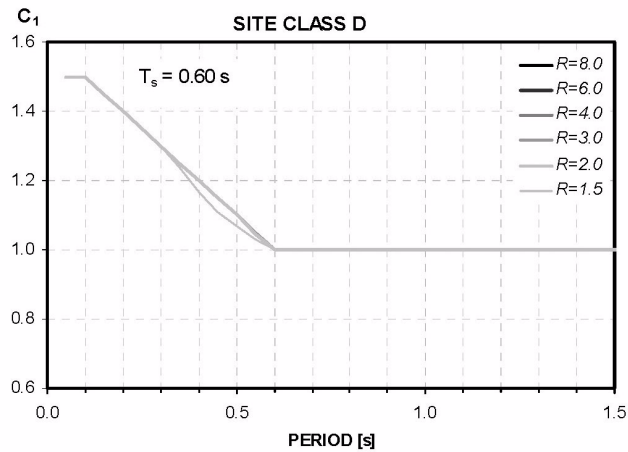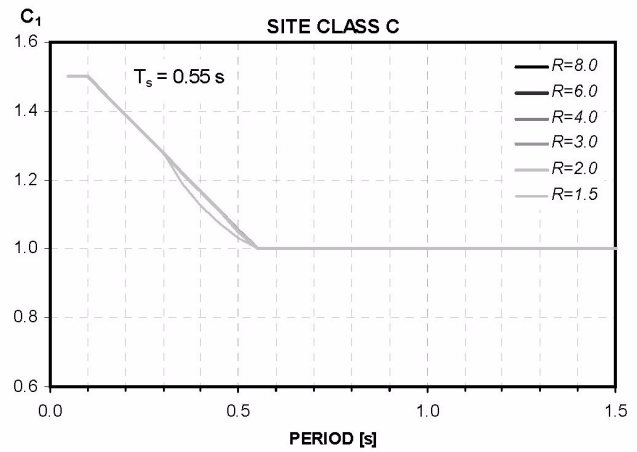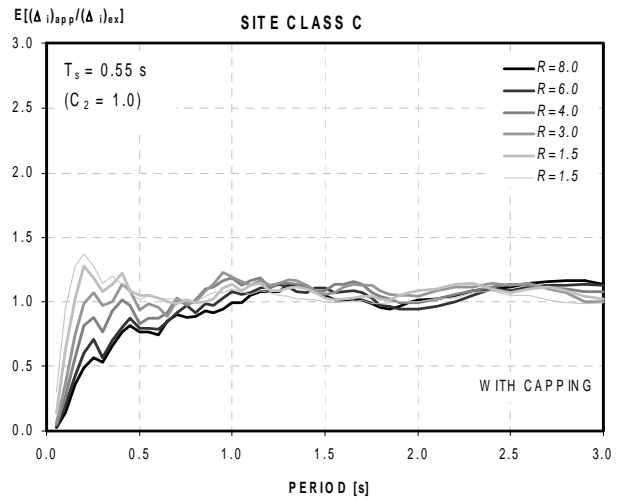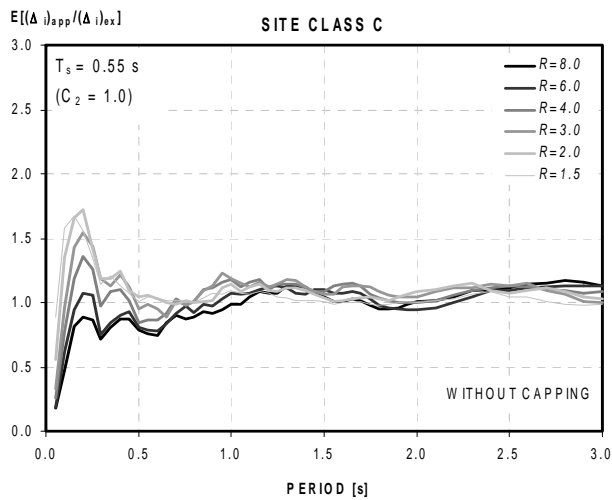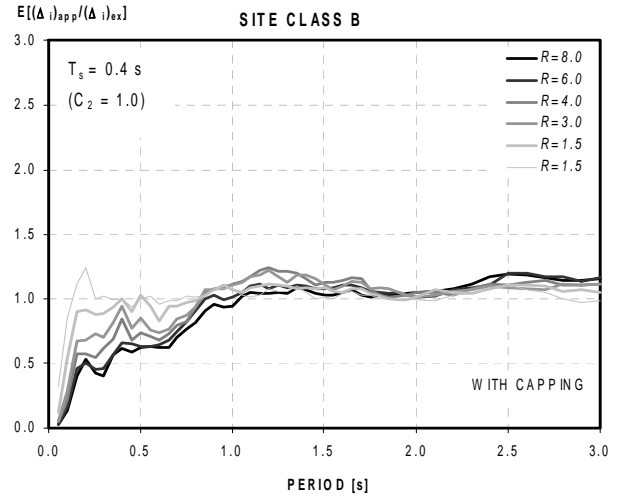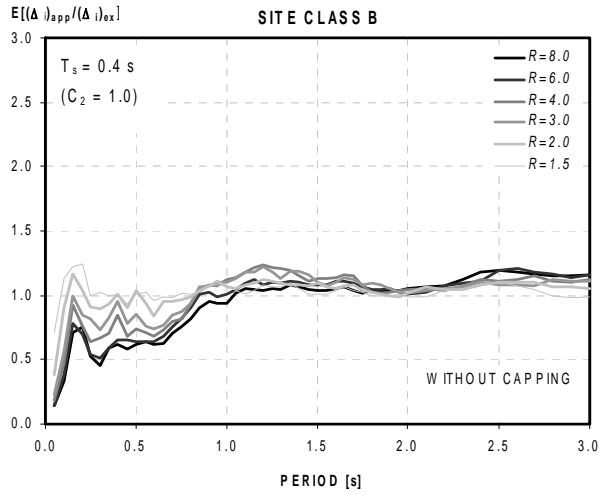
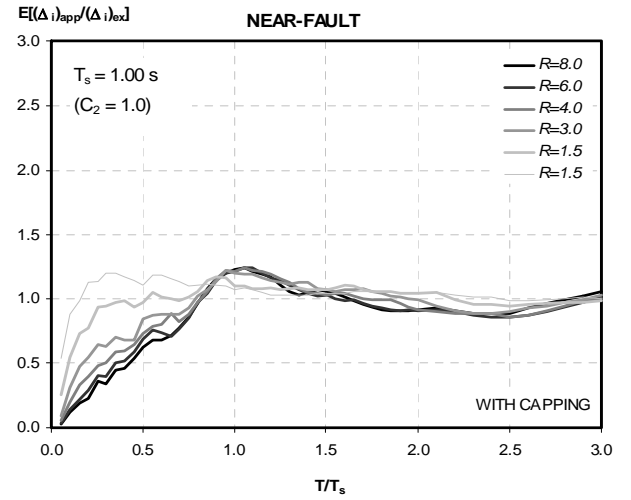### C.4.2 FEMA 356 NSP C_2 Values for Different T_s Values:

C.4.3 Mean Error of FEMA 356 NSP (Mean of Approximate to Exact Maximum Inelastic Displacements):

C.4.3.1 Comparison with Elastic Perfectly Plastic Hysteretic Behavior:
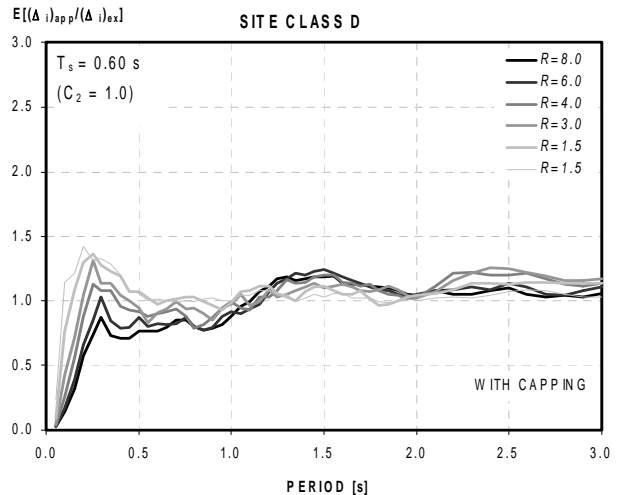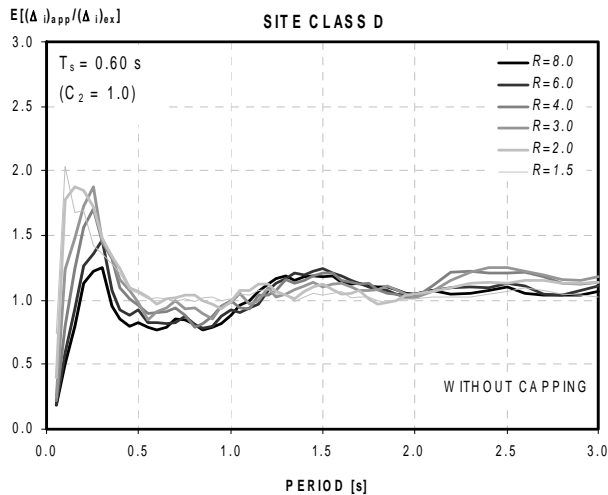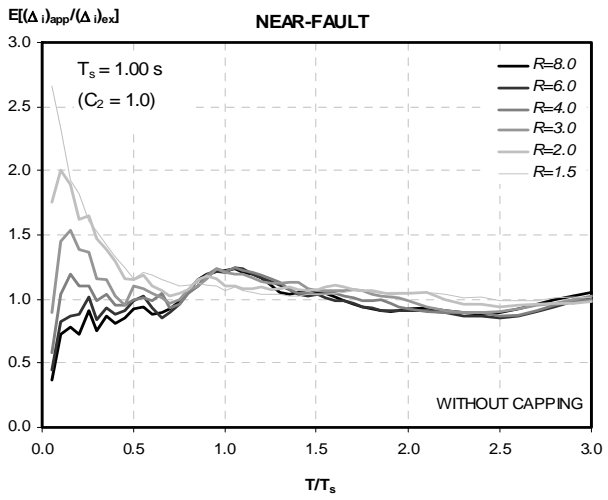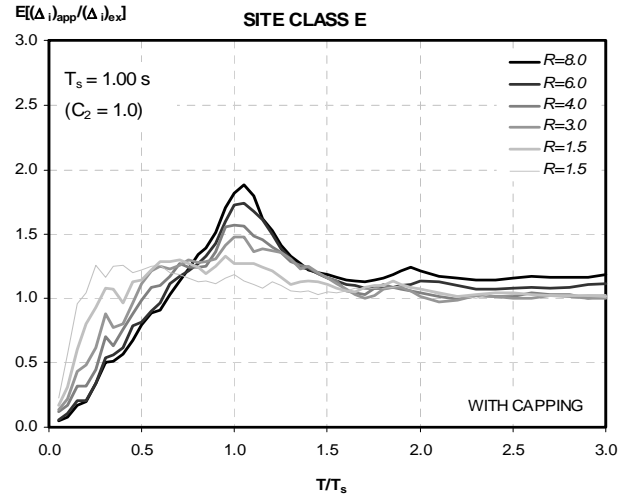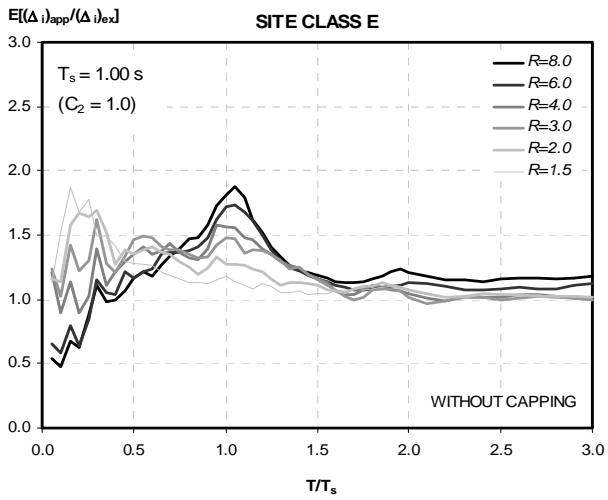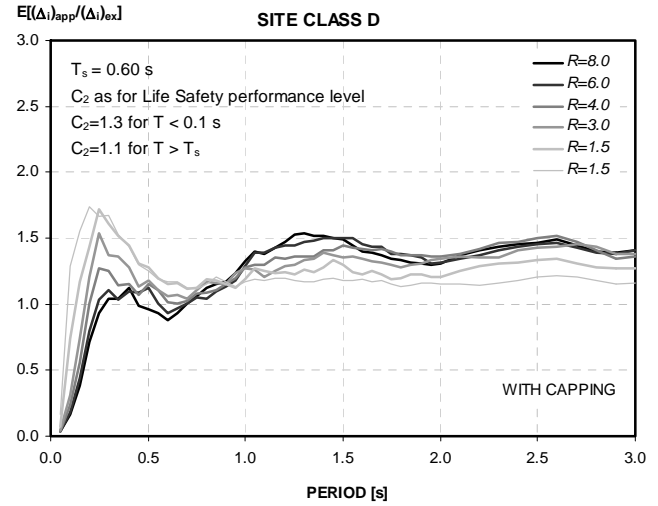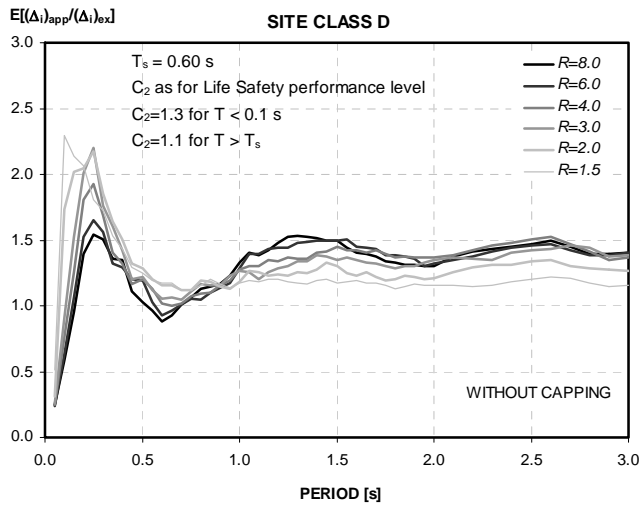
C.4.3.2   Comparison with Stiffness Degrading Hysteretic Behavior:

C.4.3.3 Comparison with Stiffness and Strength Degrading Hysteretic Behavior:
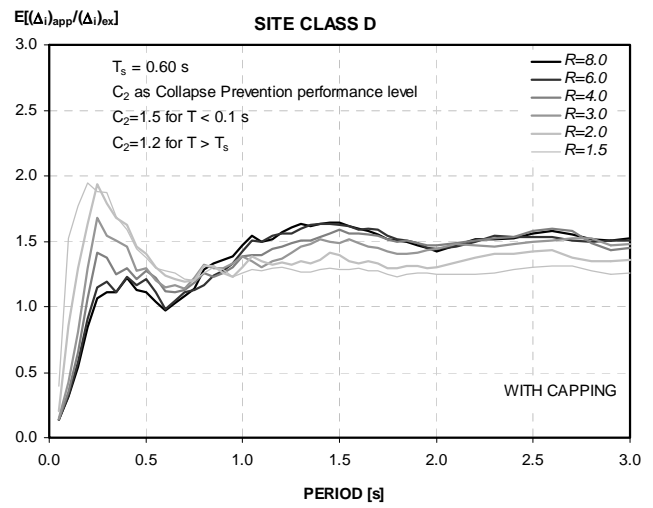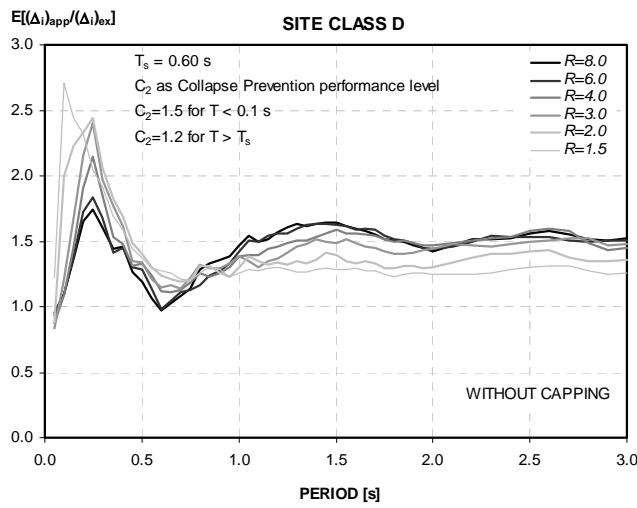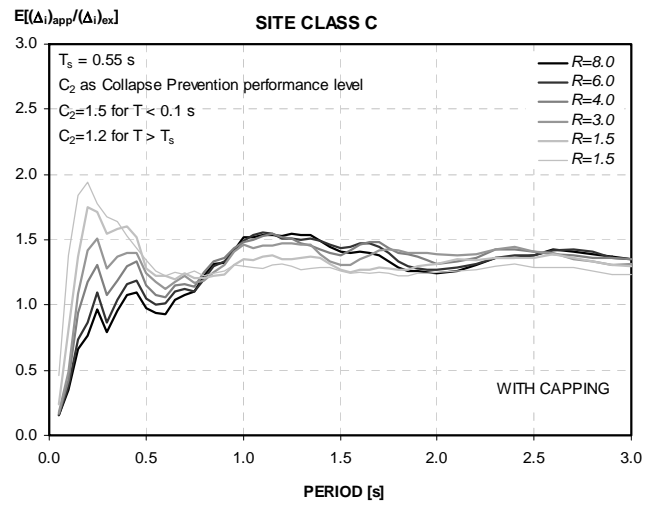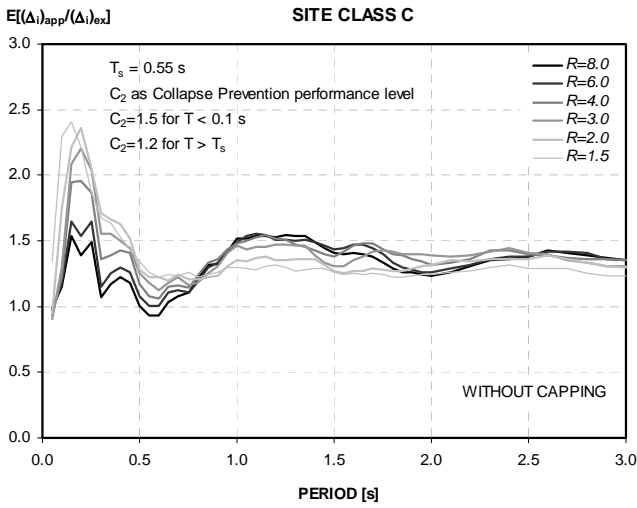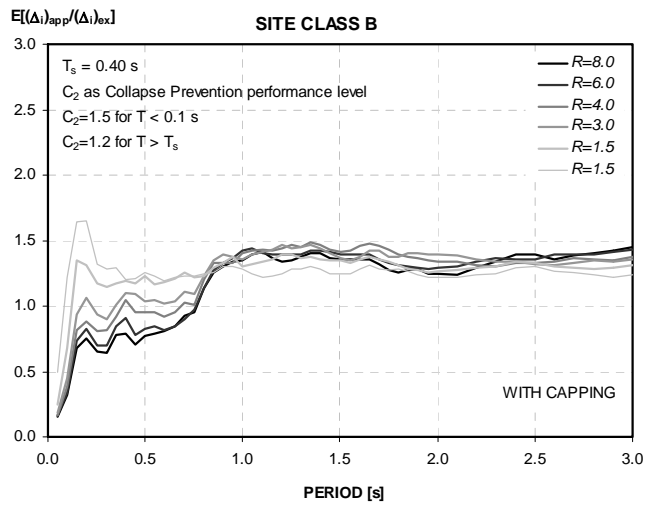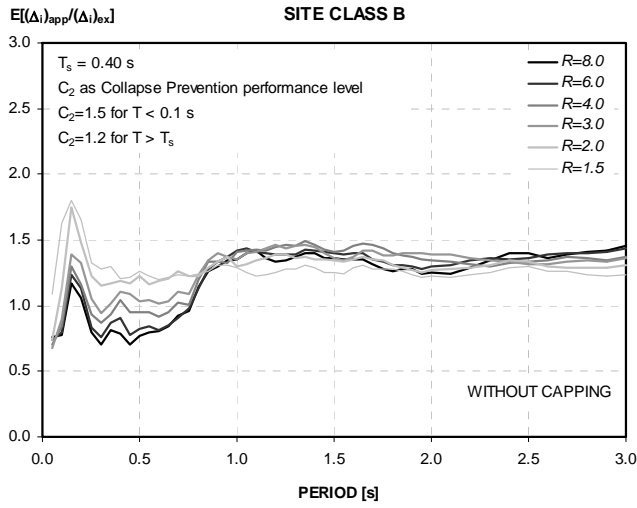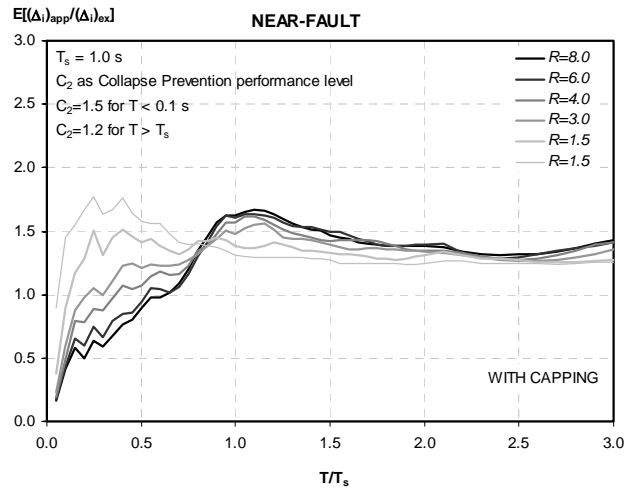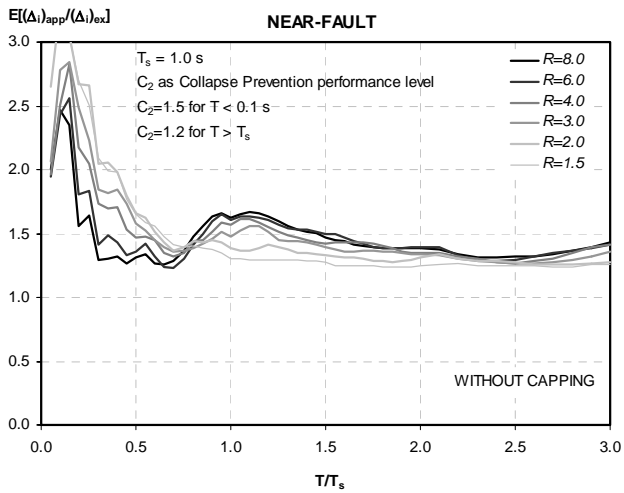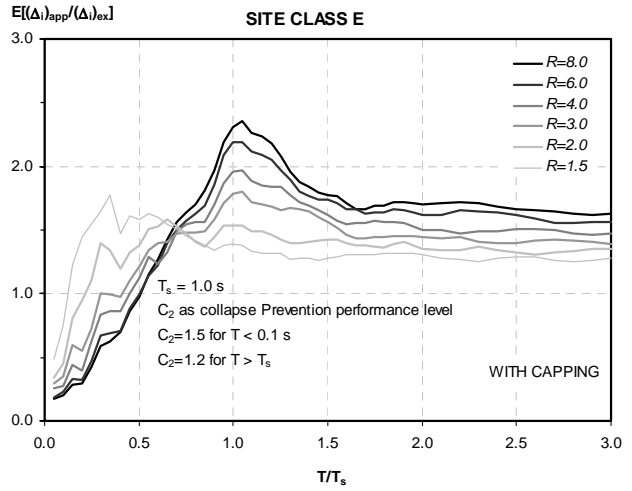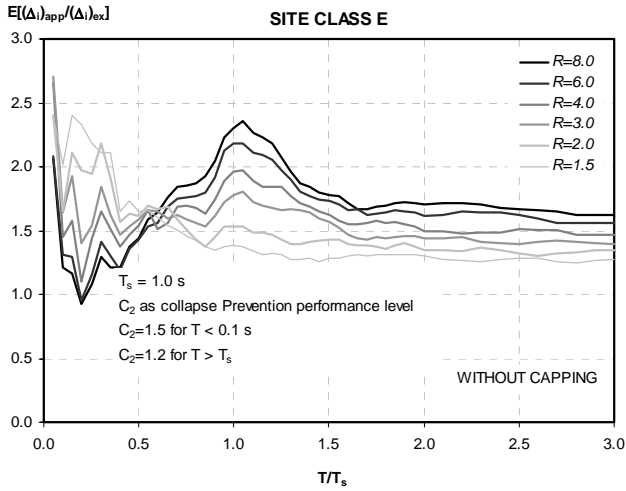
C.4.4 *Dispersion of the Error in FEMA 356 NSP (Standard Deviation of Approximate to Exact Maximum Inelastic Displacements):*
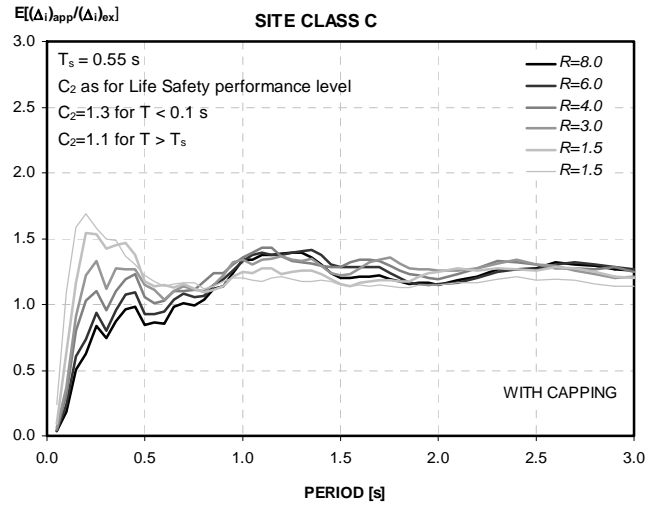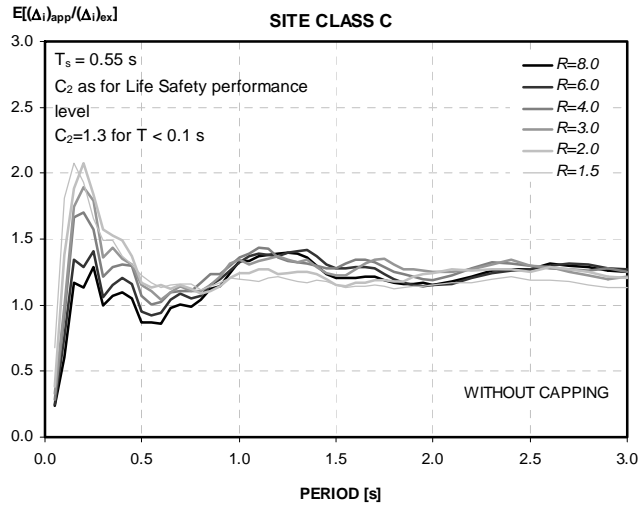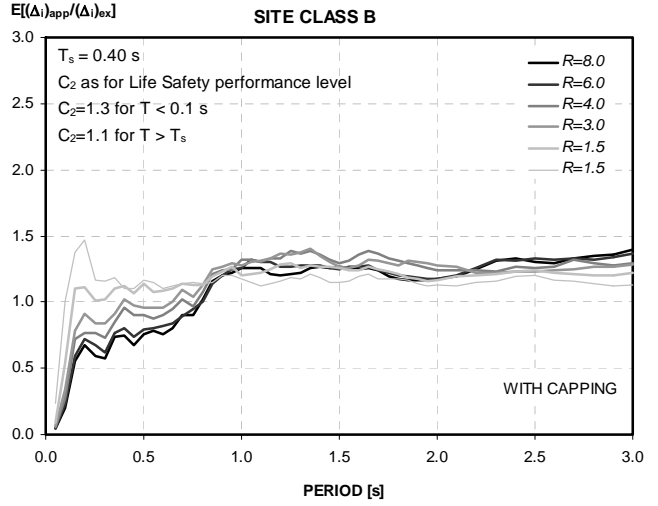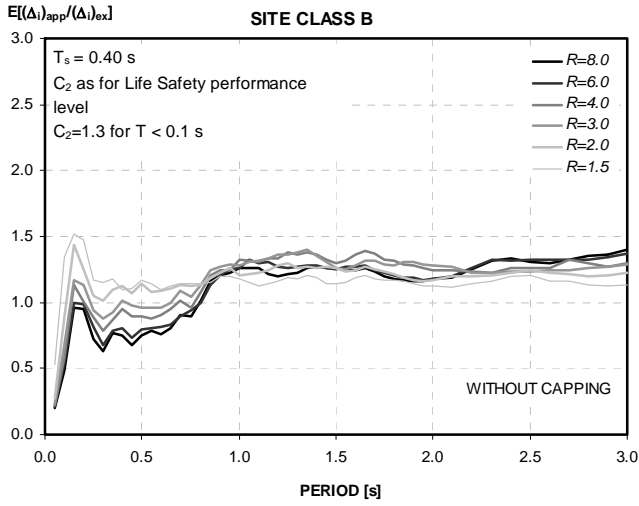
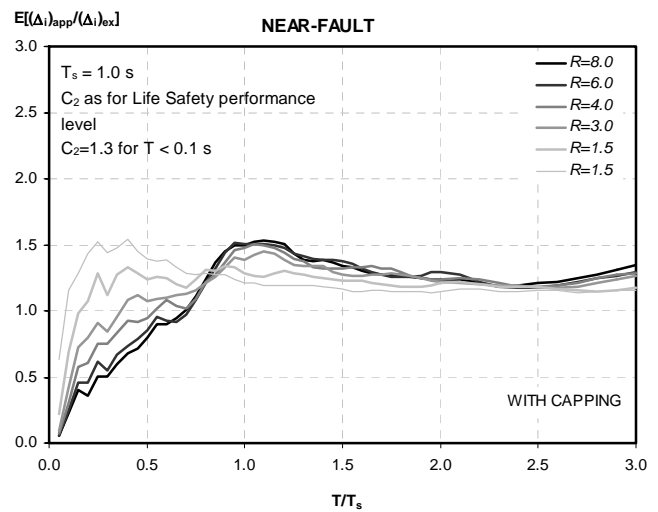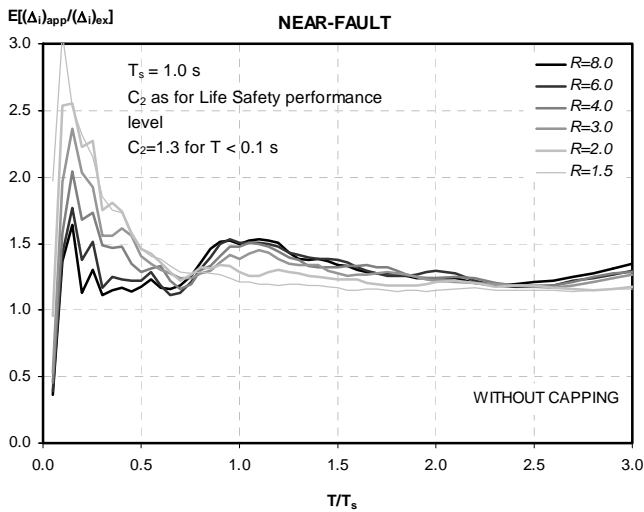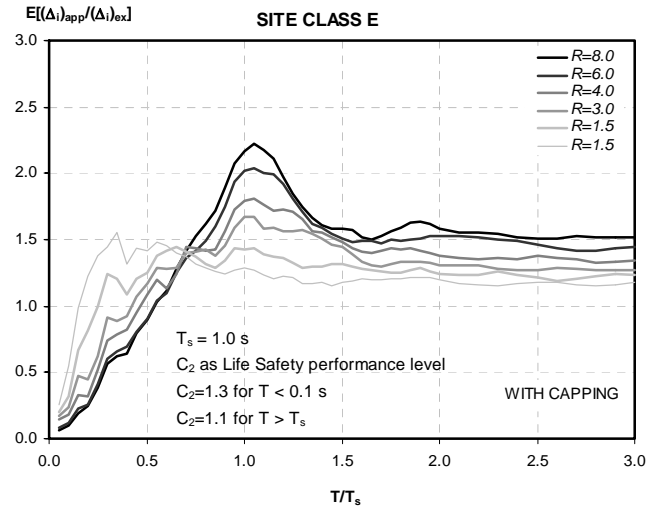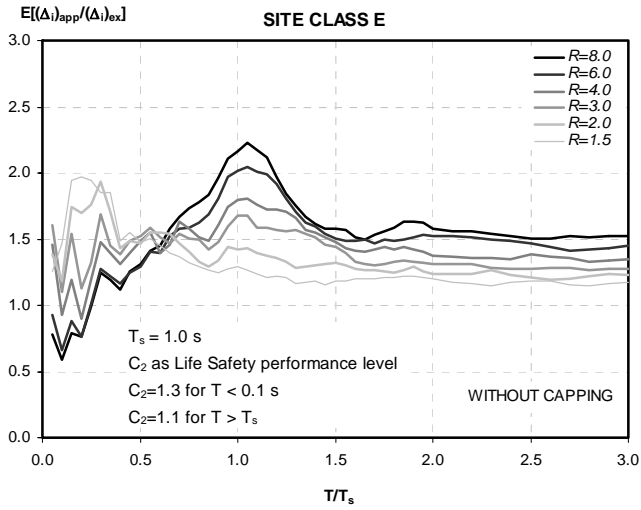### C.4.4.1 Comparison with Elastic Perfectly Plastic Hysteretic Behavior:
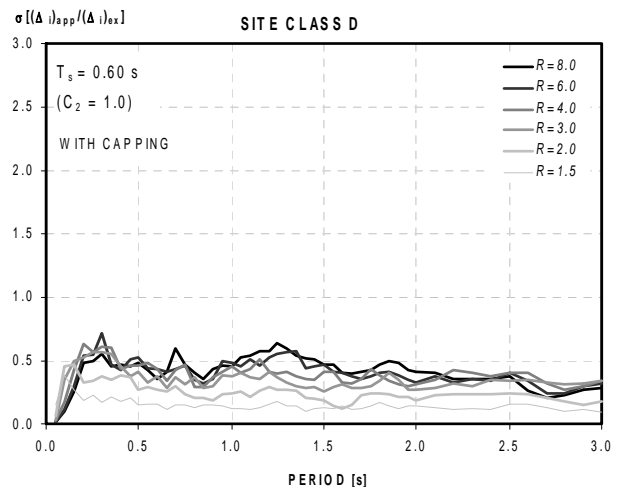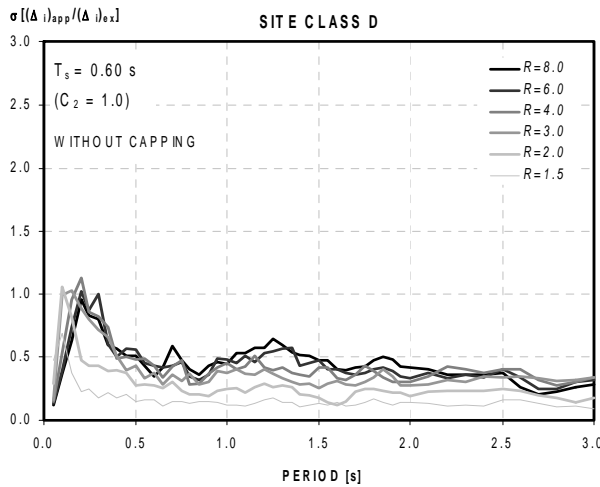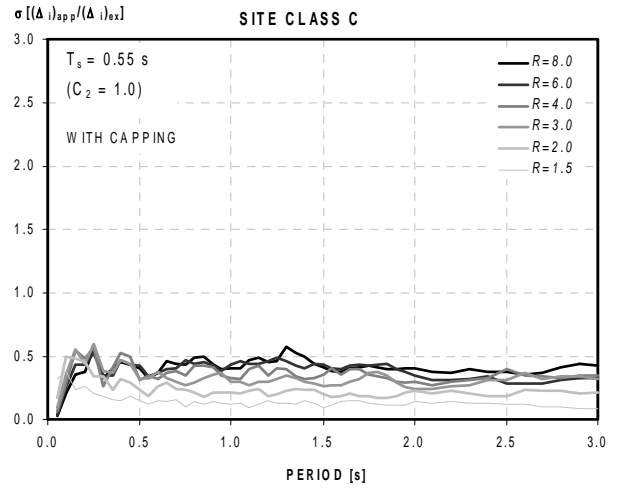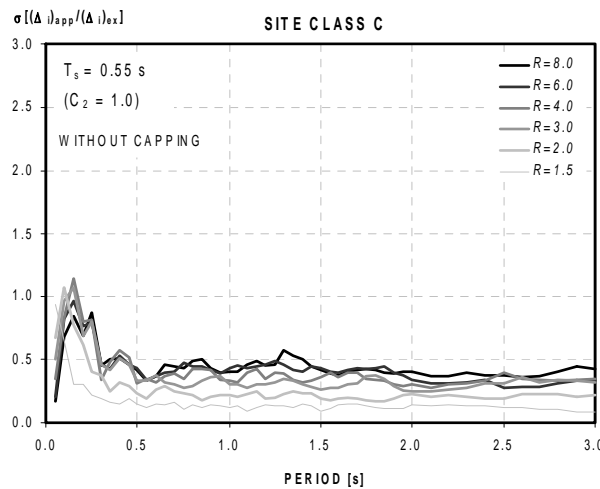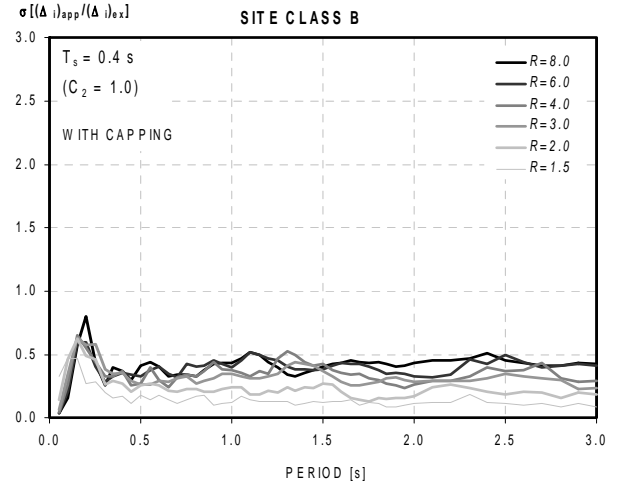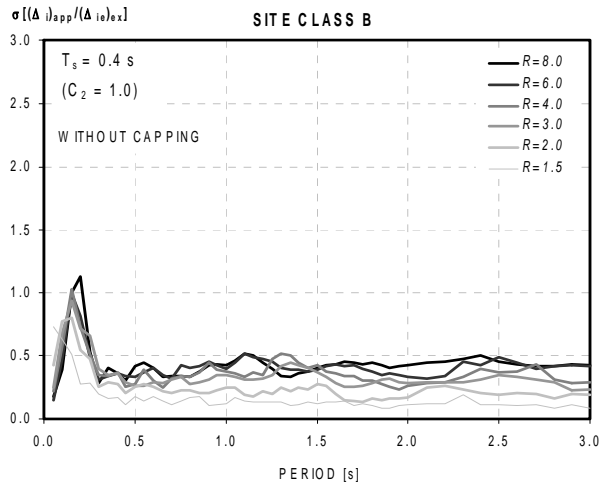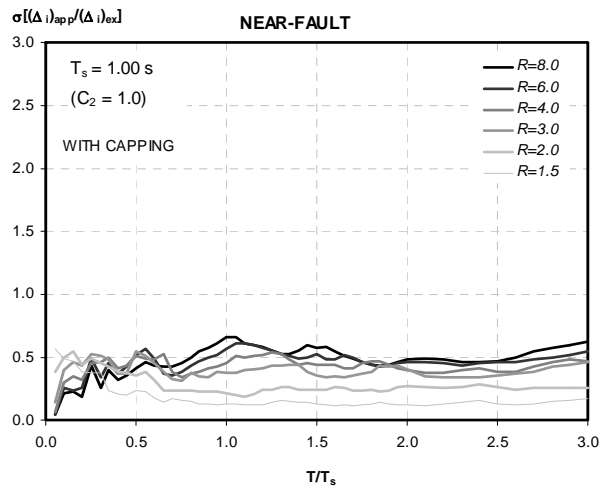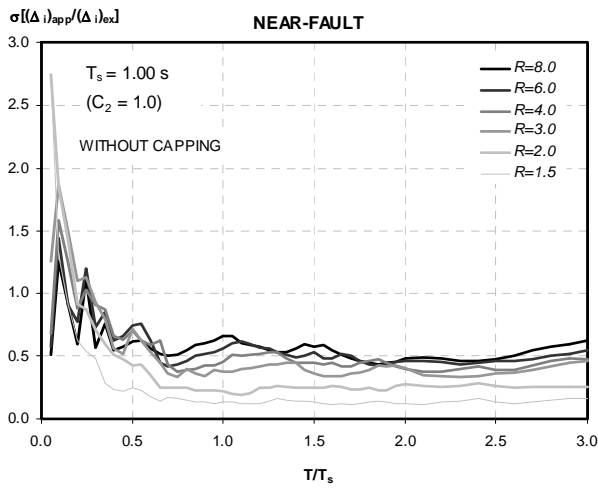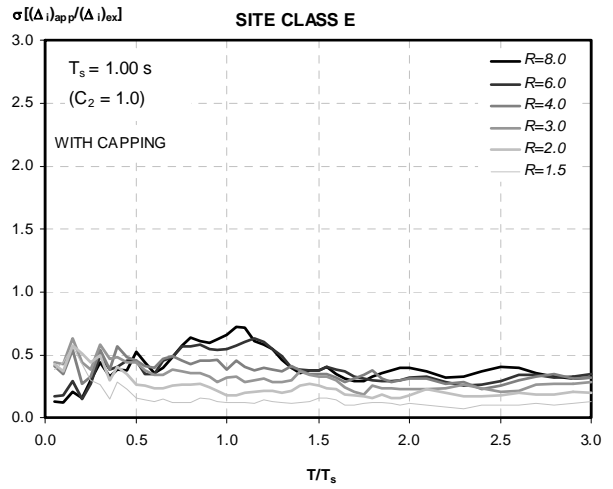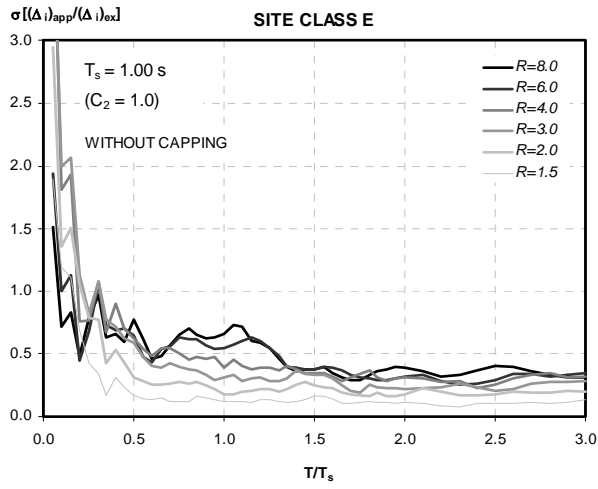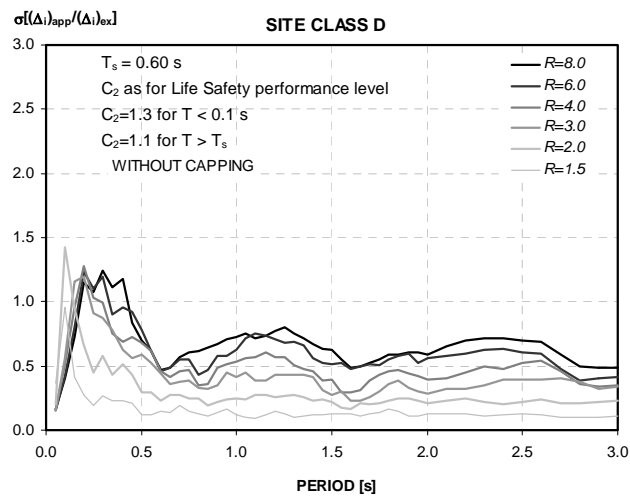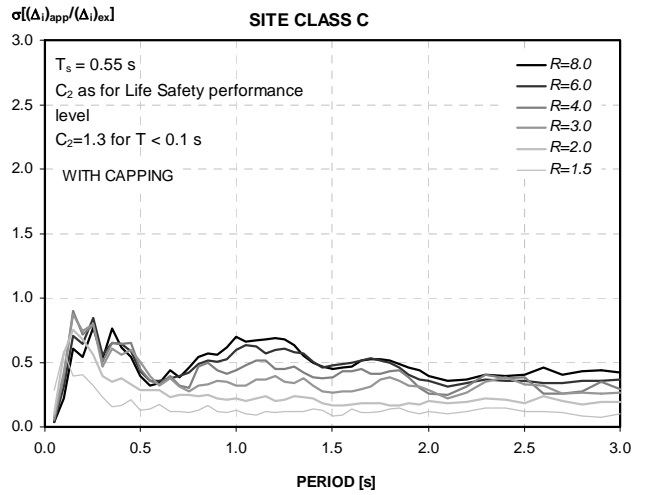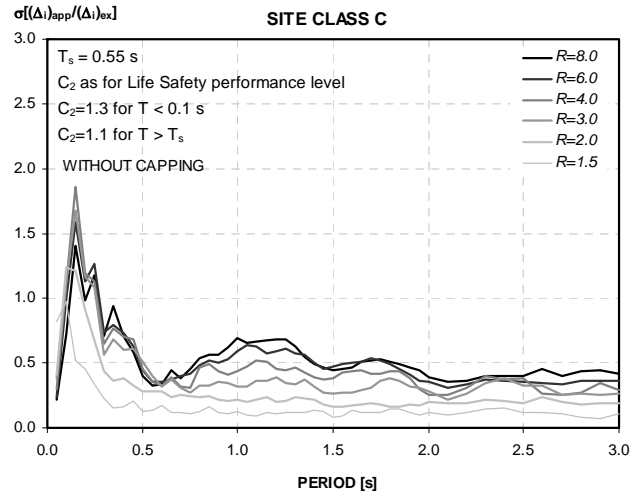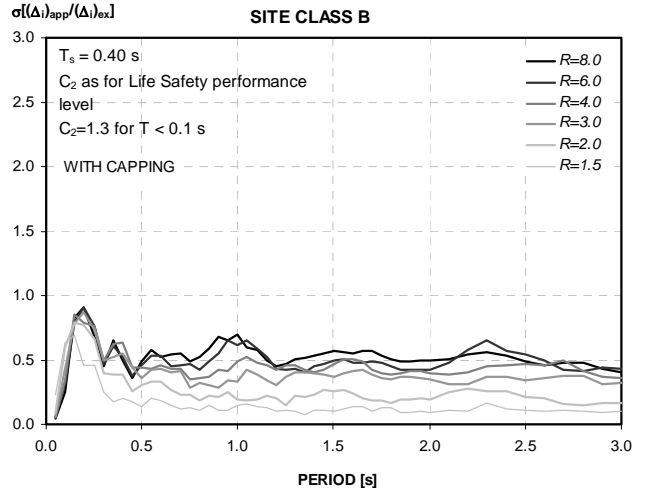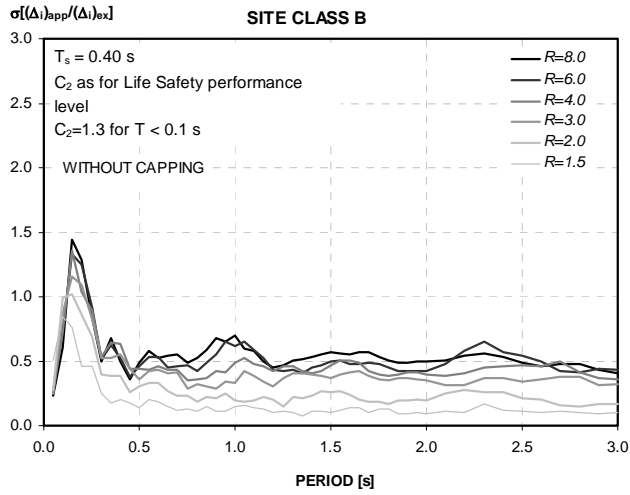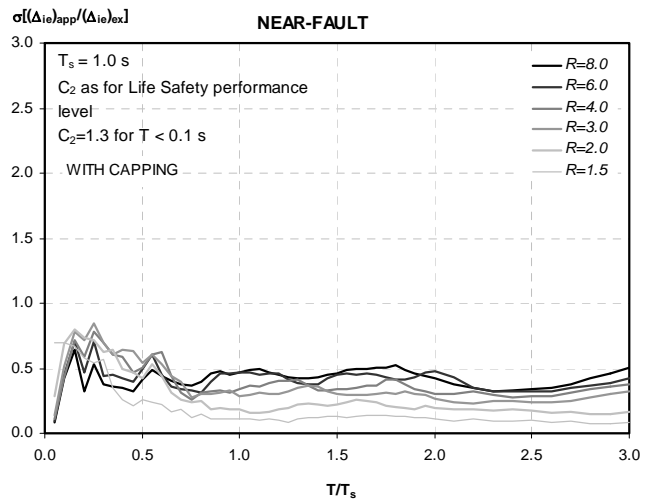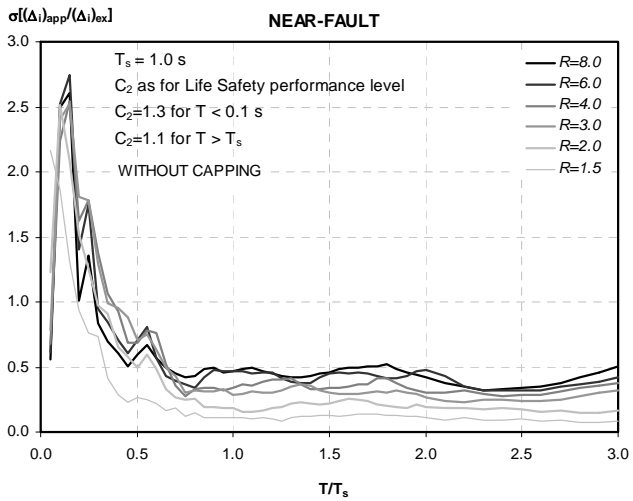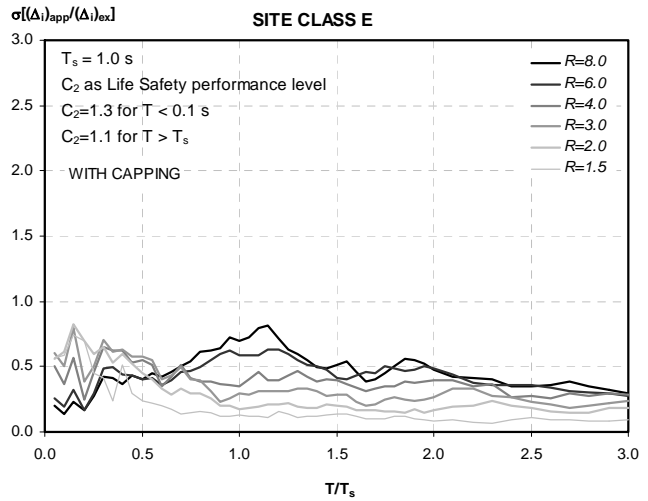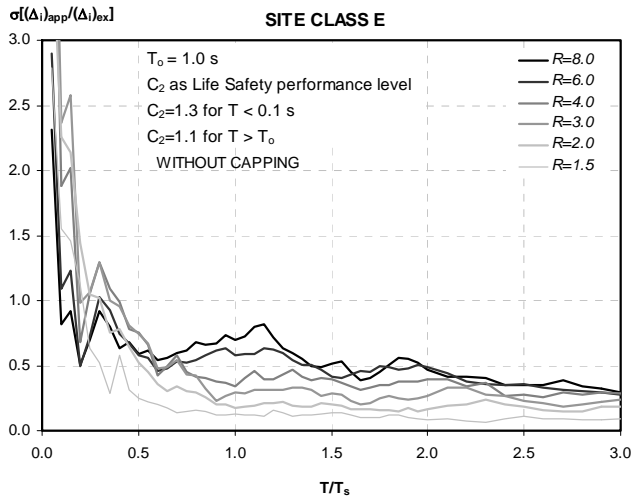
C.4.4.2   Comparison with Stiffness Degrading Hysteretic Behavior:

C.4.4.3 Comparison with Stiffness and Strength Degrading Hysteretic Behavior:
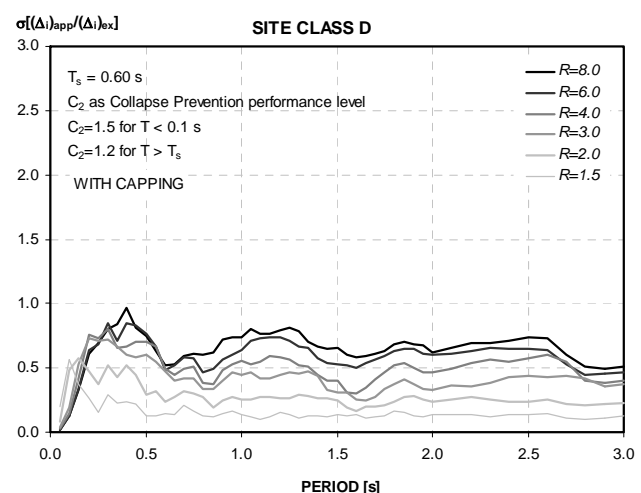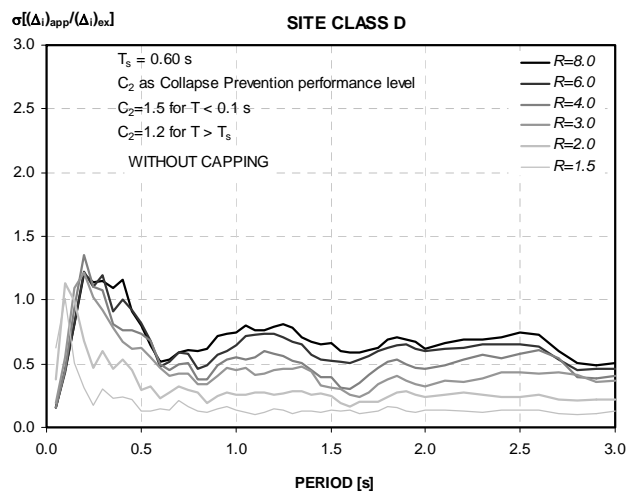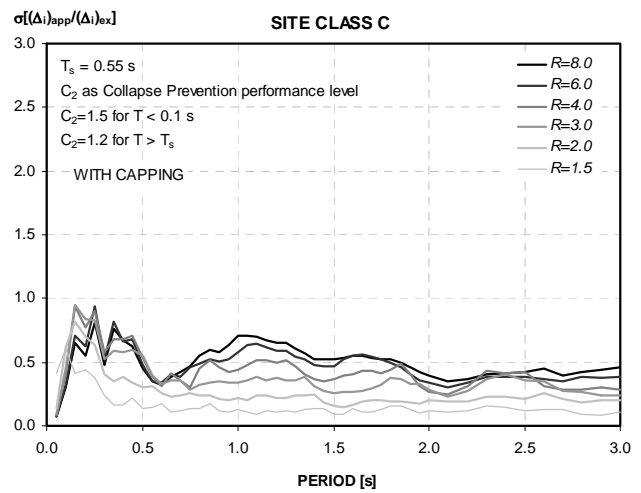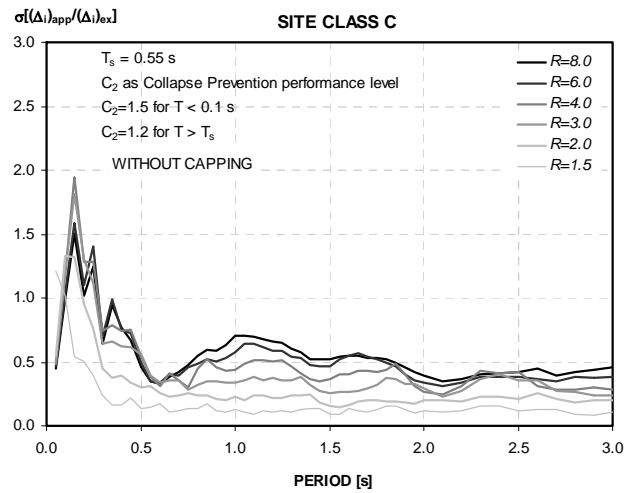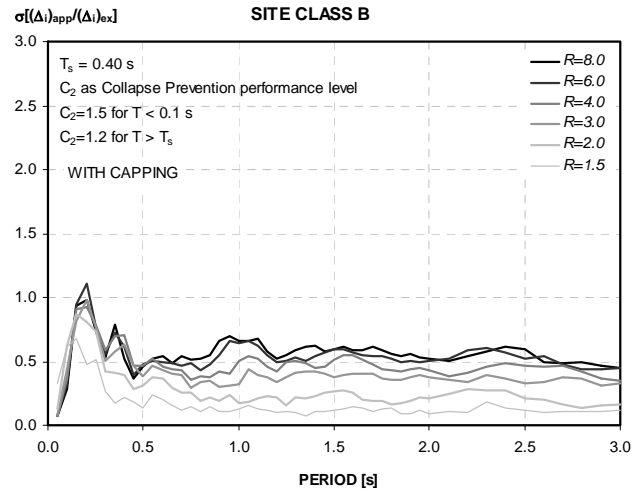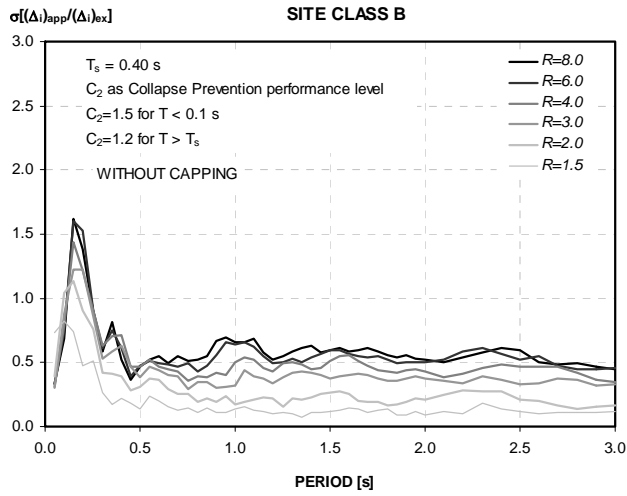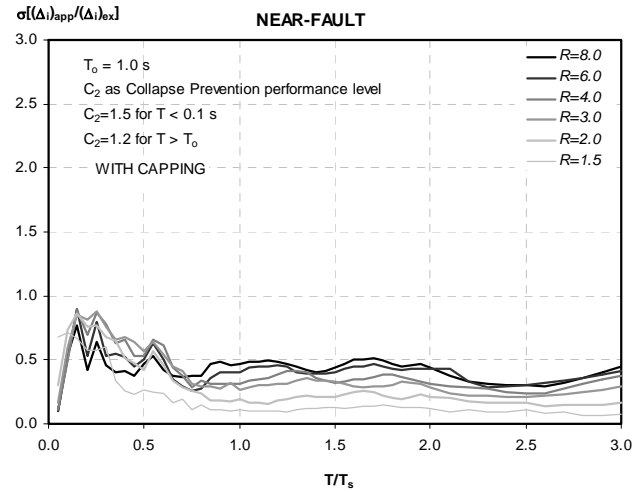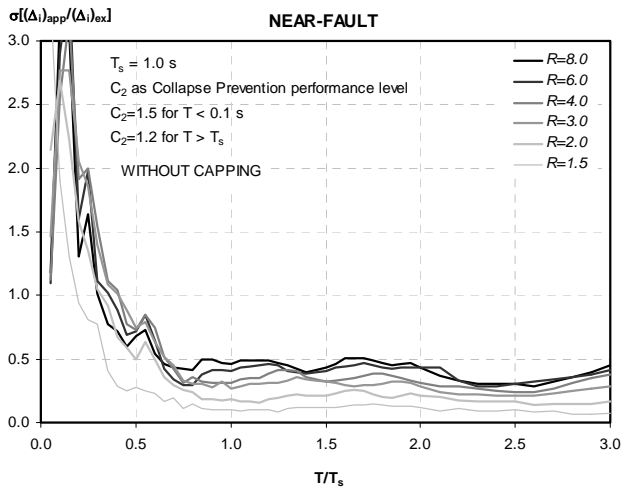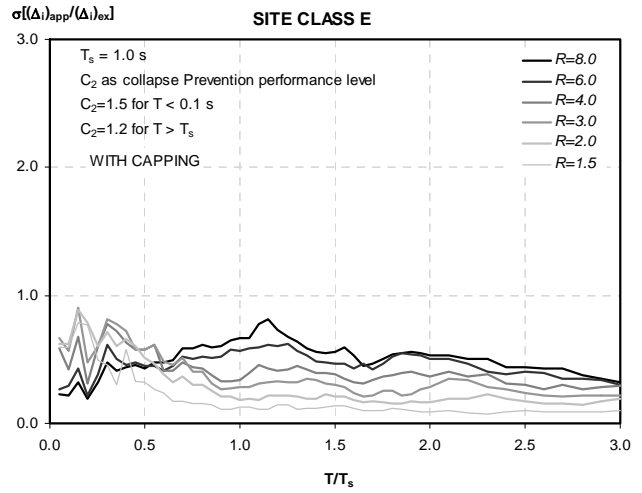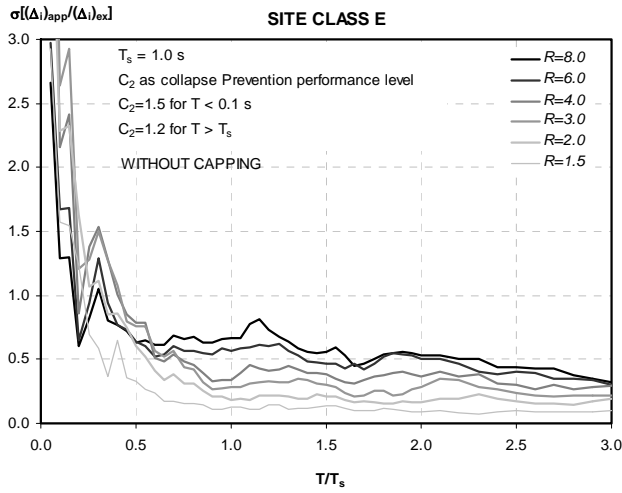
D. Supplementary Information and Data on Equivalent Linearization

D.1 Introduction

This appendix provides material supporting the improved procedures contained in Chapter 6. It provides a basic discussion of structural capacity and seismic demand for use with equivalent linearization procedures. It then reviews the theoretical underpinnings and past development of equivalent linearization procedures. It describes the new methodology for developing the improved effective period and damping equations found in Sections 6.2.1 and 6.2.2.

D.2 Capacity-Spectrum Method

The Capacity-Spectrum Method (CSM) has rapidly grown in acceptance as a tool for determining the displacement response of structures in the inelastic response range. One of the attributes that makes the CSM appealing is its intuitive nature. It is relatively straightforward to think of an earthquake as presenting a demand on a structure and the structure as possessing a certain capacity to resist this demand. When the capacity and maximum demand are equal, the system can be considered to be in a state of "Equilibrium" that defines the expected performance of the structure.

The use of effective or equivalent linear parameters in the CSM is also appealing from an intuitive point of view. First, it seems reasonable that the period of a structure lengthens as it loses stiffness. Second, it seems logical that inelastic behavior and damage produce increased damping. The use of equivalent linear parameters also allows the CSM procedure to be applied with equal ease to cases where the earthquake demand is specified by a smooth design spectrum, a uniform hazard spectrum, some other form of site-specific design spectrum. Additionally, an extension of the conventional CSM solution procedure can provide the designer and researcher with useful information about the nature of the response beyond just the projected maximum amplitude of response.

The CSM approach was initially conceived using the secant stiffness as the effective linear stiffness along with various formulas or rules for effective viscous damping. However, from nonlinear vibration theory it is know that the secant stiffness is not an optimal equivalent linear stiffness parameter for defining the response of inelastic systems subjected to random-like excitations. Therefore, this and related elements of the CSM approach deserve re-examination with the goal of developing improved linearization procedures.

Herein, optimal equivalent linear stiffness and damping parameters are determined through a statistical analysis that minimizes the extreme occurrences of the difference (i.e., error) between the response of an actual inelastic system and its equivalent linear counterpart. The linear parameters are determined as functions of response ductility. Ductility is defined as the maximum inelastic response displacement divided by the yield displacement. A variety of different inelastic systems have been studied including bilinear hysteretic, stiffness degrading, and strength degrading behavior. It is found that the proposed linearization parameters provide a significant improvement over those employed in ATC-40, as judged by either response amplitude or performance point error measures.

D.2.1 Structural Capacity: Inelastic Pushover

Nonlinear static procedures generally employ a "pushover" analysis to develop a representation of structural capacity. The ability to perform a nonlinear static analysis is based on the fundamental requirement that accurate information is obtainable about the structure, components, connections and material properties. These techniques are summarized in Section 2.4 and covered in detail in ATC-40 and FEMA 356.

The pushover curve is a structural surrogate for the actual multi-degree-of-freedom building model. The pushover curve characterizes the load versus deformation of cyclic structural response. It is generally taken to represent the backbone curve of the load-deformation hysteresis loops. From a pushover curve, the value of the initial elastic stiffness (elastic period) can be determined, as well as an estimate of the post- elastic stiffness.

The structural response behavior may also be categorized by hysteresis loop category. The backbone curve of response (from the push-over curve) does not fully specify how the building will respond to earthquake excitation. The hysteresis loop shape may be roughly bilinear and stable for subsequent cycles of response, or there may exhibit stiffness only or stiffness
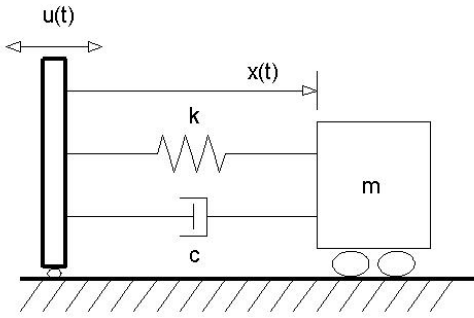
Figure D-1   SDOF oscillator model subjected to ground motion, u(t).

and strength degradation. Another type of hysteretic behavior is the "pinching" of the hysteresis loops that is associated with many concrete structures. However, this latter type of behavior has not been addressed in this document. Categorizing the hysteretic behavior as being of a certain type is left to the discretion of the engineer and usually requires considerable engineering judgment.

D.2.2   Seismic Demand: Response Spectra

Traditional linear analysis methods use lateral forces to represent a design condition. For nonlinear methods it is easier and more direct to use a set of lateral displacements as a design condition. For a given structure and ground motion, the displacement demand is the maximum expected response of the building during the ground motion.

The differential equation of motion for the system in Figure D-1 is expressed as:

$$m\ddot{x}(t) + c\dot{x}(t) + kx(t) = -m\ddot{u}(t) \qquad \text{(D-1)}$$

Rearranging the equation and dividing through by the mass, m, results in:

$$(\ddot{x}(t) + \ddot{u}(t)) + 2\beta\omega\dot{x}(t) + \omega^2 x(t) = 0 \qquad \text{(D-2)}$$

where β is the fraction of critical damping and ω is the natural frequency which is related to the natural period by $T = 2\pi/\omega$. Equation D-2 can be rearranged as:

$$\ddot{x}(t) + \ddot{u}(t) = -2\beta\omega\dot{x}(t) - \omega^2 x(t) \qquad \text{(D-3)}$$

Define Spectral Displacement (*SD*) and Pseudo-Spectral Acceleration (*PSA*) as follows:

$$SD = \max \forall t \, |x(t)| \qquad \text{(D-4)}$$

$$PSA = \max \forall t \, |\omega_n^2 x(t)| \qquad \text{(D-5)}$$

where $\forall t$ has the mathematical meaning, "for all time." Although Spectral Acceleration (*SA*) may also be defined from Equation D-3 it is assumed in this document that *SA* is interchangeable with *PSA*. Therefore, no distinction will be made between *SA* and *PSA* and for consistency, only *SA* will be used in the remainder of this appendix.

In the ADRS format, a radial line represents a constant structural period, *T*, independent of the amount of damping present in the system. The relationship between *SA, SD* and *T* may be determined using Equations D-4 and D-5 which results in:

$$T = 2\pi \sqrt{SD \Big/ SA} \qquad \text{(D-6)}$$

An example of this is shown in Figure D-2 for 5% damping.

D.3   Theoretical Basis for Equivalent Linearization

The general form of a SDOF oscillator equation of motion for the system shown in Figure D-3 can be expressed as

$$m\ddot{x}(t) + f(x(t), \dot{x}(t)) = -m\ddot{u}(t) \qquad \text{(D-7)}$$

where m is the mass of the system and $\ddot{u}(t)$ is the acceleration time history imparted to the oscillator. The term $f(x(t), \dot{x}(t))$ can have many forms. For this formulation, a linear system will be expressed as $f(x(t), \dot{x}(t)) = k_{eff} x(t) + c_{eff} \dot{x}(t)$ where k_{eff} is the effective linear stiffness and c_{eff} is the constant of proportionality for the effective viscous damping force,
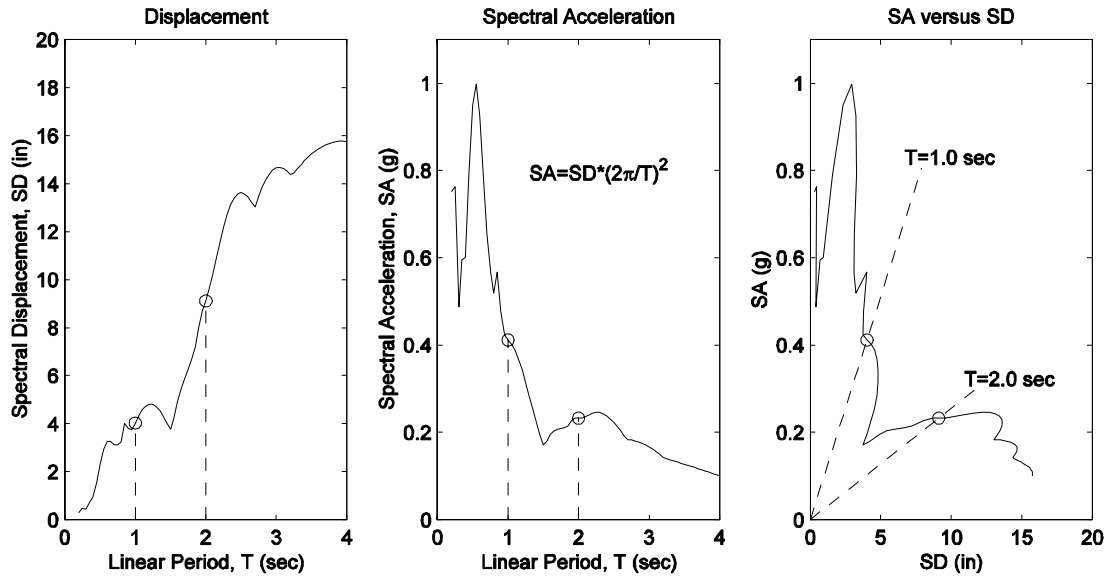
Figure D-2   Components of the ADRS format for representing Seismic Demand - *PSA* versus *SD*; left plot shows *SD* as a function of period, *T*; middle plot shows *PSA* as a function of period, *T*; right plot (ADRS format) is a compilation of the left and middle plots showing *PSA* versus *SD*, with period *T* defined by radial lines stemming from the origin.

Figure D-3   SDOF oscillator model represented by Equation D-7.

$c_{eff} \dot{x}(t)$. Hysteretic systems, possess history dependent restoring forces that are non-separable functions of both displacement and velocity.

Equivalent linearization is an approximate technique for solving nonlinear differential equations. Equation D-7 may be rewritten as

$$m\ddot{x}(t) + c_{eff} \dot{x}(t) + k_{eff} x(t) + \varepsilon(x(t), \dot{x}(t)) = -m\ddot{u}(t) \quad \text{(D-8)}$$

where

$$\varepsilon(x(t), \dot{x}(t)) = f(x(t), \dot{x}(t)) - c_{eff} \dot{x}(t) - k_{eff} x(t) \quad \text{(D-9)}$$

The objective of equivalent linearization is to somehow select optimal values for the linear coefficients c_{eff} and k_{eff} such that the quantity $\varepsilon(x(t), \dot{x}(t))$ is in some sense minimized. Then, $\varepsilon(x(t), \dot{x}(t))$ is ignored and Equation D-8 is solved as an ordinary linear differential equation. The approximate linear system is shown in Figure D-4.

One possible approach is to minimize the mean square value of ε. The minimization criteria can be written as

$$\frac{\partial \overline{\varepsilon^2}}{\partial K} = 0 \quad \text{(D-10)}$$

$$\frac{\partial \overline{\varepsilon^2}}{\partial \gamma} = 0 \quad \text{(D-11)}$$

where the over bar represents an averaging operation.
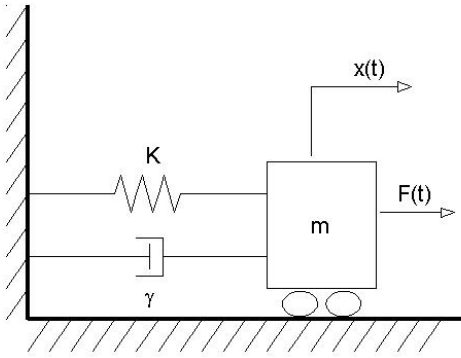
Figure D-4   Linear SDOF oscillator model with effective linear parameters as represented by Equation D-8.

If the excitation, $\ddot{u}(t)$, is a harmonic function of time, the steady-state solution can be assumed to be of the form

$$x(t) = x_{\max} \cos(\theta) \text{ where } \theta = \omega t - \phi \qquad \text{(D-12)}$$

Analyzing a single cycle of the steady state response leads to the following equation

$$\overline{\varepsilon}^2 = \frac{1}{2\pi} \int_0^{2\pi} (f(x_{\max}, \theta) - c_{eff} \omega x_{\max} \sin\theta - k_{eff} x_{\max} \cos\theta)^2 d\theta$$

(D-13)

Applying the minimization criteria in Equations D-10 and D-11 to Equation D-13 results in

$$c_{eff} = -\frac{1}{x_{\max} \omega \pi} \int_0^{2\pi} f(x_{\max}, \theta) \sin\theta d\theta \qquad \text{(D-14)}$$

and

$$k_{eff} = \frac{1}{x_{\max} \pi} \int_0^{2\pi} f(x_{\max}, \theta) \cos\theta d\theta \qquad \text{(D-15)}$$

This approach leads to an effective stiffness similar to what is seen in Figure D-5 where the effective stiffness is less than the secant stiffness, K_{sec}.

Another way to determine equivalent linear damping parameter is through energy balance. The energy dissipated by the hysteretic system may be equated to the energy dissipated by an equivalent viscous damper. Assume the response to be of a harmonic form over one full cycle of response expressed as

$$x(t) = x_{\max} \cos(\theta) \text{ where } \theta = \omega t - \phi \qquad \text{(D-16)}$$

Then, energy dissipated by a viscous damper over one cycle of response, E, can be expressed as

$$E = 2\pi^2 c_{eff} x_{\max}^2 / T \qquad \text{(D-17)}$$

where T is the period of cyclic motion.

For the bilinear hysteretic model seen in Figure D-5, the energy dissipated over one cycle of response, E, can be expressed as

$$E = 4x_y (k_o - \alpha k_o)(x_{\max} - x_y) \qquad \text{(D-18)}$$
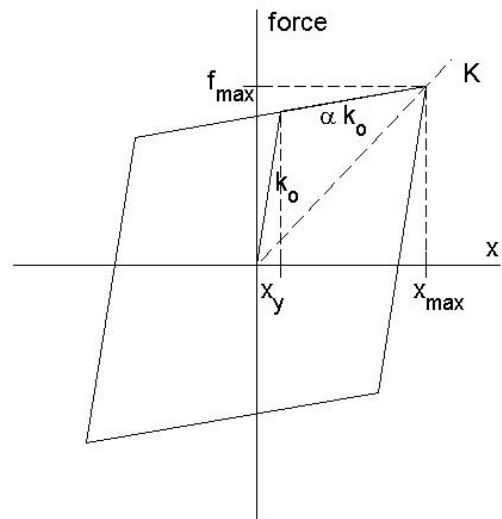
Figure D-5   Bilinear hysteretic system.

Equating energies from Equations D-17 and D-18 leads to

$$c_{eff} = 4(k_o - \alpha k_o)x_y(x_{max} - x_y)T/(2\pi^2 x_{max}^2) \quad \text{(D-19)}$$

In Figure D-5, the secant stiffness is labeled K_{sec} and can be expressed as

$$K_{sec} = k_o(x_y + \alpha(x_{max} - x_y))/x_{max} \quad \text{(D-20)}$$

If the secant period, T_{sec}, is assumed to be the period of structural response, then

$$k_{eff} = K_{sec} \quad \text{(D-21)}$$

The secant stiffness can be related to the secant period and substituting Equation D-20 into Equation D-19 leads to the following expression for c_{eff}.

$$c_{eff} = 4(k_o - \alpha k_o)x_y(x_{max} - x_y)\sqrt{\frac{m}{K_{sec}}}/(\pi x_{max}^2) \quad \text{(D-22)}$$

Equation D-22 corresponds to the equivalent viscous damping equation found in ATC-40 (Section 8.2.2.1). However, the response of inelastic systems to earthquake ground motions is not the same as the steady-state response to a constant amplitude sinusoidal forcing function as assumed in the above equivalent linearization formulation. Repeated full hysteresis loops with constant amplitude occur infrequently for inelastic systems subjected to earthquake time histories. Furthermore, partial and one-sided loops are likely to occur.

D.4   Starting Point For Optimization

The ductility demand, μ, is defined as the maximum displacement of the inelastic system divided by its yield displacement. For the bilinear hysteretic system shown in Figure D-5, the ductility demand is x_{max}/x_y. In 1980, an optimal set of equivalent linear parameters for earthquake excitation was defined based on making an adjustment to the linear response spectrum. In that study (Iwan, 1980) ductility dependent inelastic response spectra were compared with elastic response spectra, and displacement preserving shifts of the inelastic spectra were determined which minimized the average absolute value difference between the inelastic and equivalent linear spectra over a range of periods. A family of hysteresis behavior was considered including
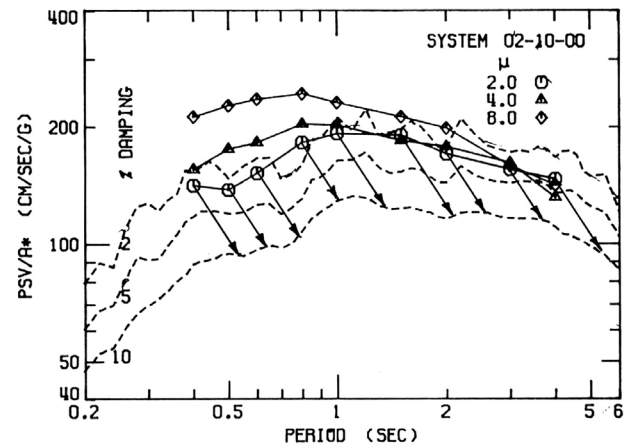
Figure D-6   Early effort to define optimal equivalent linear parameters (Iwan, 1980).

bilinear hysteretic as well as pinching hysteretic models. Figure D-6 shows a typical set of inelastic and elastic response spectra and indicates the manner in which the spectra were adjusted.

Using the stated procedure, the following relationships were obtained for the optimal effective linear parameters:

$$T_{eff}/T_0 - 1 = 0.121(\mu - 1)^{0.939} \quad \text{(D-23)}$$

$$\beta_{eff} - \beta_0 = 5.87(\mu - 1)^{0.371} \quad \text{(D-24)}$$

It is easily shown that the optimal effective period defined by the above relationship is significantly *less* than the period associated with the secant stiffness that is employed in the conventional CSM approach found in ATC-40 (or, the optimal stiffness is significantly *greater* than the secant stiffness). Indeed, the secant stiffness may overestimate the optimal effective period by more than 50% for larger values of ductility. It is also observed that the damping value used in the conventional CSM approach is significantly greater than the optimal damping parameter in Equation D-24. Thus, the conventional CSM approach significantly overestimates both the effective period and damping of inelastic systems. In some regions of response, these two overestimates combine in such a manner that the resultant response prediction is not much different from the prediction obtained from the optimal parameters. However, these two overestimates do not always counteract each other to produce reliable estimates of displacement.

Even though the conventional and some more optimal set of equivalent linear parameters may predict about the same average response for some range of cases, that does not mean they are equally effective. This may be illustrated by considering the distribution of the error for the two different approaches. Figure D-7 shows the distribution of the Performance Point displacement error that is obtained using the early optimal parameters and the conventional CSM parameters for an elastoplastic system. It is evident from the figure that there is only a modest difference between the mean values of the error for the two approaches. The optimal parameters give a mean Performance Point error of -4.4% while the conventional CSM approach gives a mean error of -9.5%. However, there is a very substantial difference in the standard deviation of the error for the two approaches. The optimal approach error has a standard deviation of 21.2% while that of the conventional CSM approach is 68.7%. As seen from the figure, the conventional CSM approach has a much greater probability of exhibiting extreme over prediction errors than does the optimal approach, even though the mean error of the conventional approach is less conservative than the optimal approach. Hence, it is clear that it is inadequate to merely minimize the mean value of the displacement error when defining an optimal set of effective linear parameters. It is necessary to simultaneously minimize *both* the mean and standard deviation in some sense.

D.5   Alternative Statistical Analysis

The results of the early optimization study described above provide the motivation for a more comprehensive study of equivalent linearization for earthquake response prediction. In the earlier study, the error measure used for optimization was the mean of the absolute value of the displacement error. This is an intuitive error measure which leads to reasonable results. However, this error measure may not be as directly meaningful as other possible measures. In practice, it would seem to be more appropriate to have the measure of goodness of the optimal effective linear parameters based on some measure of engineering acceptability. This is the approach used in this study.

Recall the equation of motion for the single-degree-of-freedom system in Figure D-3. When $f(x,\dot{x})$ represents a linear viscous damped system, the equation of motion may be expressed as

$$m\ddot{x}_{lin} + c_{eff}\dot{x}_{lin} + k_{eff}x_{lin} = -m\ddot{u}(t) \qquad \text{(D-25)}$$
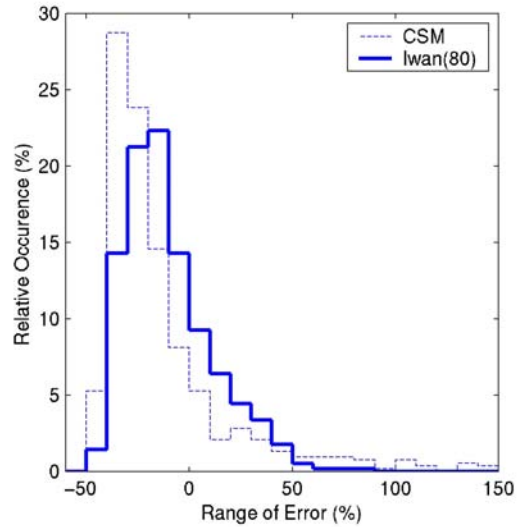
Figure D-7   Distribution of percent error in Performance Point displacement. Bilinear system with alpha=0, T_0 = 0.1-2.0 sec (0.1 sec increments), μ=2, 28 far-field earthquakes.

where c_{eff} and k_{eff} are the viscous damping coefficient and spring stiffness, respectively. For a given ground excitation, $\ddot{u}(t)$, the solution, $x_{lin}(t)$, may be computed using any numerical solution procedure. For an inelastic system, the restoring force, $f(x,\dot{x})$, may take a variety of forms. The solution for the inelastic system will be designated as $x_{inel}(t)$.

Many different approaches are available for making a comparison between the displacement time histories $x_{inel}(t)$ and $x_{lin}(t)$. These include, but are not limited to, a point by point comparison of the displacement, velocity or acceleration time histories, comparing the number of zero displacement crossing or comparison of the amplitude spectra from a Fourier Transform. However, to quantify a comparison, there must be a value assigned to the amount of similarity or difference. Within the framework of performance-based engineering, the key performance variable is the maximum relative displacement amplitude that a structure experiences from the demand earthquake. The relative displacements for the inelastic and linear single-degree-of-freedom systems are $x_{inel}(t)$ and $x_{lin}(t)$, respectively.

The effective linear parameters obtained based on a comparison of displacement values would not be appropriate to be used in a velocity or force-based

design procedure. For example, the maximum velocities or accelerations from the linear solution should not be used as estimates for the maximum values of $\dot{x}_{inel}(t)$ or $\ddot{x}_{inel}(t)$. The maximum acceleration or maximum pseudo-acceleration would be a much better comparison parameter for effective linear parameters intended for use in a force-based approach.

The maximum displacement amplitude of the nonlinear time history x_{inel} (t) will be designated as D_{inel} and the maximum displacement amplitude of the linear time history x_{lin}(t) will be designated as D_{lin}. The effective linear parameters developed in this study will be used for estimating the response of structures subjected to earthquake excitations. Therefore, using real earthquake time histories as the model inputs is most logical.

The methodology developed in this study employs a search over a two-dimensional parameter space related to the linear system coefficients c_{eff} and k_{eff} in Equation D-25. One can expect to find a combination or combinations of c_{eff} and k_{eff} that give the best "match" with an inelastic system, in some sense. The terms c_{eff} and k_{eff} will be replaced by the fraction of critical damping, β_{eff}, and the natural period of oscillation, T_{eff}. Equation D-25 can be expressed as

$$\ddot{x} + \frac{4\pi\beta_{eff}}{T_{eff}}\dot{x} + \left(\frac{2\pi}{T_{eff}}\right)^2 x = -\ddot{u}(t) \qquad \text{(D-26)}$$

The system parameters β_{eff} and T_{eff} completely describe the linear single-degree-of-freedom system.

D.5.1   Error Measure

In order to compare the maximum displacements, D_{inel} and D_{lin}, an error measure must be defined. In engineering design, unconservative displacement predictions are generally less desirable than conservative predictions. Therefore, a fundamental requirement of any error measure is that it distinguish between a conservative displacement prediction and a non-conservative displacement prediction. An error measure that uses an absolute value of the difference between D_{inel} and D_{lin} would not satisfy this requirement.

A simple error measure satisfying the above requirement is the ratio of the difference between the linear system maximum displacement, D_{lin}, and the inelastic system maximum displacement, D_{inel}, to the inelastic system maximum displacement.
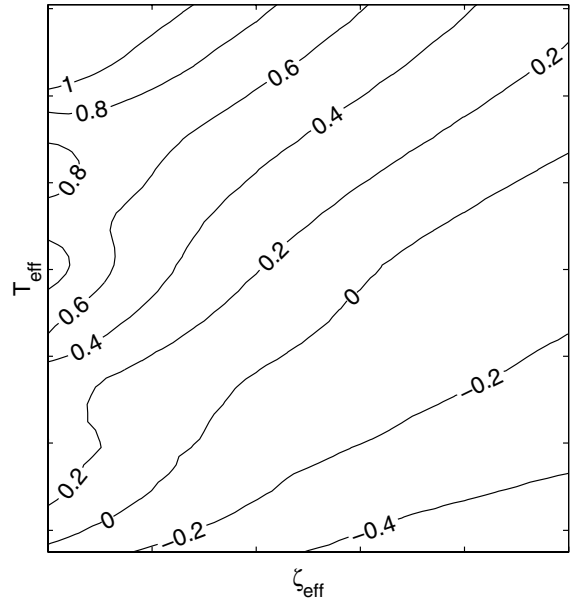
Figure D-8   Contour values of ε_D over the two-dimensional parameter space of T_{eff} and β_{eff} for a single combination of inelastic system and ground excitation.

$$\varepsilon_D = \frac{D_{lin} - D_{inel}}{D_{inel}} \qquad \text{(D-27)}$$

Using this definition, a negative value of ε_D reflects an unconservative displacement prediction while a positive value reflects a conservative displacement prediction. ε_D might be considered to have a positive bias as it ranges from -1 to ∞. However, for the range of systems and excitations considered in this study, the slight positive bias in the statistical distribution of ε_D is inconsequential.

For a given inelastic system and ground excitation, there will be a certain topology associated with the error, ε_D, as a function of linear system parameters T_{eff} and β_{eff} as shown in Figure D-8. Note that there exists a nearly diagonal contour of zero error. For any combination of T_{eff} and β_{eff} lying along this contour there will be a perfect match between D_{lin} and D_{inel}.

For any specified ensemble of inelastic systems and ground excitations, distributions of ε_D can be obtained for every combination of T_{eff} and β_{eff}. This is illustrated in Figure D-9.

Distributions of ε_D

T_{eff} ζ_{eff}
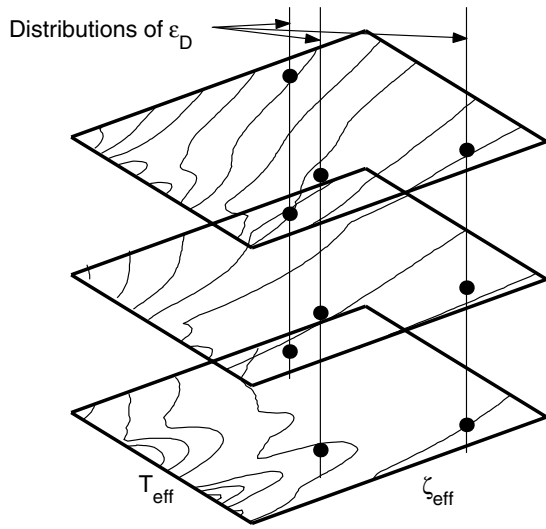
Figure D-9   Illustration of assembling ε_D error distributions at every combination of T_{eff} and β_{eff} over an ensemble.

The importance of using the standard deviation as well as the mean of the error distribution is illustrated in the following example. Two hypothetical probability density functions are shown in Figure D-10. For the more widely spread error distribution, the mean error value is zero, while for the tighter distribution, the mean error value is -5%. Solely in terms of the mean value, the widely spread distribution is more accurate than the tighter distribution. However, a more insightful way to analyze the distributions would be in terms of an acceptable range of error values. In this example, an acceptable range of error values might be chosen to be from -20% to 20%. In this case, the distribution with the mean value of -5% would be both more "acceptable" compared to the distribution with a mean value of 0%.

Let $\Re$ be the probability that the error ε_D lies outside the range from a to b. Then, $\Re$ may be expressed as

$$\Re = 1 - \Pr(a < \varepsilon_D < b) \qquad \text{(D-28)}$$

If the distribution of ε_D is assumed to be Normal, $\Re$ can be expressed as
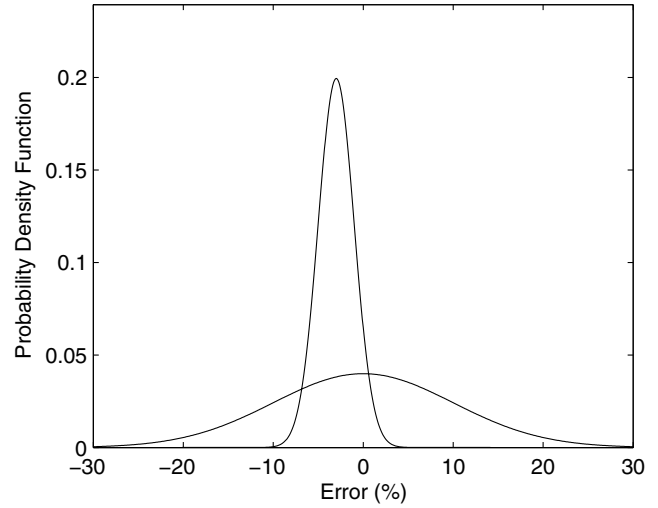
Figure D-10   Illustration of probability density functions of displacement error for a Normal distribution.

$$\Re = 1 - \int_a^b \frac{1}{\sigma\sqrt{2\pi}} e^{\frac{-(x-m)^2}{2\sigma^2}} dx \qquad \text{(D-29)}$$

where m is the mean value and σ is the standard deviation of the distributions of ε_D values. It will be assumed that the desirable range of error values, ε_D, from an engineering design point of view is between -10% and +20%. This assumption has been adopted after consultation with several members of the practicing structural engineering community. This range of error values will be referred to as the Engineering Acceptability Range (EAR). This range takes into account the general desire for a more conservative design rather than an unconservative design. That is, a 20% error is more acceptable than a -20% error.

D.5.2   Optimization Criterion

The *optimum* point in the T_{eff}, β_{eff} parameter space is chosen to be the point that minimizes the probability that the error, ε_D, will be outside the Engineering Acceptability Range. The *Engineering Acceptability Criterion* may therefore be defined as σ.

$$\Re_{EAR} \equiv 1 - \Pr(-0.1 < \varepsilon_D < 0.2) = \min \qquad \text{(D-30)}$$

Figure D-11 shows contours of $\Re_{EAR}$ as a function of T_{eff} and β_{eff}. Also shown is the optimal point over the
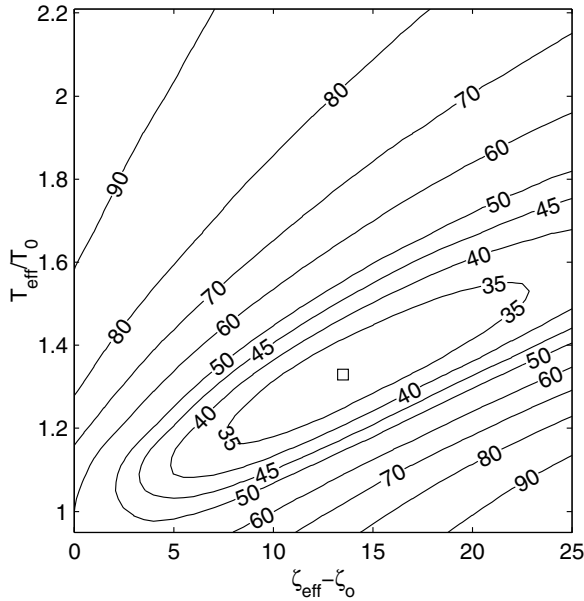
Figure D-11   Contours of $\mathfrak{R}_{EAR}$ over the T_{eff}, β_{eff} parameter space. The optimum point is marked by a square.

two-dimensional parameter space which is denoted by a square.

The diagonal trend to the contours in Figure D-11 can be explained by the following physical reasoning. Consider the displacement response of a linear oscillator subjected to an earthquake excitation. Decreasing the system damping will always increase the displacement response. Generally speaking, decreasing the natural period will also decrease the displacement response. Although this is not true in all cases, especially for near-field ground motions, it is a general trend that by increasing period and damping in the correct proportion, a nearly constant maximum displacement can be achieved.

The size and shape of the contours in Figure D-11 give insight into the ramifications of using effective linear parameters that are different from the values at the optimal point. In Figure D-11, the contour closest to the optimum point has a value of 0.35 while the minimum value of $\mathfrak{R}_{EAR}$ ($\mathfrak{R}_{EAR_{min}}$) is 0.31. The gradient of the contours is more gradual along a line roughly from lower left to upper right. Therefore, if the effective period is under predicted, it is best to also have an under-predicted damping. If the effective period is over

predicted, it is best to also have an over-predicted damping. In the general direction from lower right to upper left, the gradient of the contours is very large and the value of $\mathfrak{R}$ quickly increases for relatively small changes in the effective parameters. Over predicting one parameter and under predicting the other can have serious repercussions on the reliability of the displacement prediction.

D.6   Effective Linear Parameters

The full explicit functional dependence of ε_D may be indicated as follows

$$\varepsilon_D(\frac{T_{eff}}{T_o}, \beta_{eff} - \beta_o, \alpha, \mu, HYST)$$

$$= \frac{D_{lin}(T_{eff}, \beta_{eff}) - D_{inel}(T_o, \beta_o, \alpha, \mu, HYST)}{D_{inel}(T_o, \beta_o, \alpha, \mu, HYST)} \quad (D\text{-}31)$$

The maximum displacement of the nonlinear system, D_{inel}, is a function of initial period, T_0, linear viscous damping, β_0, second slope ratio, α, response ductility, μ, and hysteretic model, denoted ``HYST''. The linear system response, D_{lin}, is a function of the two linear system parameters: period, T_{eff}, and damping, β_{eff}. It is desired to find effective linear parameters that are applicable over a range of T_0 and β_0 values. Therefore, multiple values of T_0 and β_0 will be included in the same ensemble. The two-dimensional T_{eff}, β_{eff} parameter space is transformed into the T_{eff} - T_0, β_{eff} - β_0 parameter space.

The Engineering Acceptability Criterion is applied to the error distributions over the entire T_{eff} / T_0, $\beta_{eff} - \beta_0$ parameter space and the optimum combination of T_{eff} / T_0 and $\beta_{eff} - \beta_0$, is determined. Next, the ductility value is changed, and the entire process is repeated. The ductility values used in this study range from 1.25 to 6.5 in increments of 0.25. Additionally, ductilities of 8 and 10 are included.

The optimum values of T_{eff} / T_0 and $\beta_{eff} - \beta_0$ may be graphed as functions of ductility. Then, these results can be fitted with an analytical expression. Figure D-12 shows a typical example of the discrete optimum values of T_{eff} / T_0 and $\beta_{eff} - \beta_0$ graphed as a function of ductility along with a curve fit of the data. Information pertaining to the details of the curve fitting process may be found in Guyader, 2004.
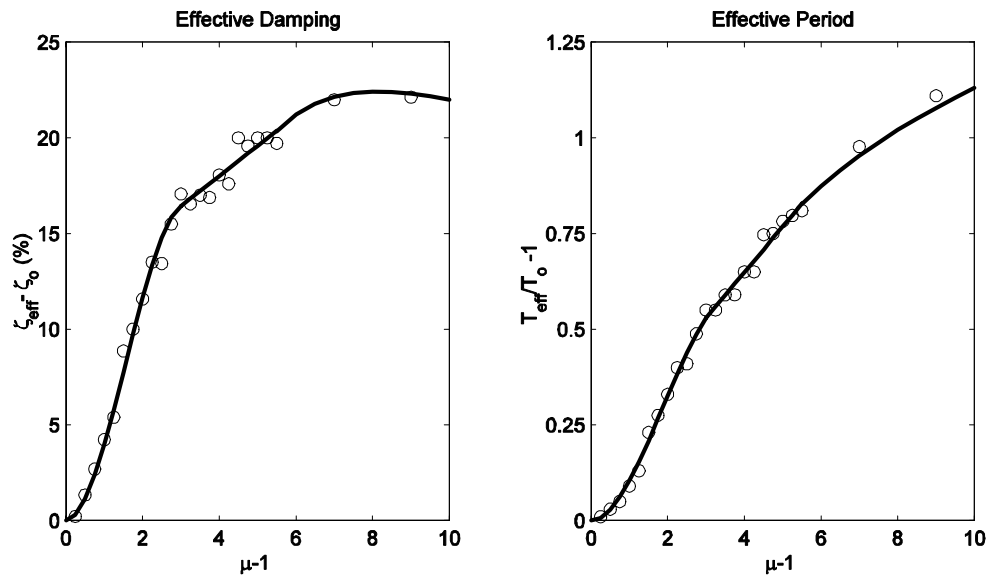
Figure D-12   Example of optimal effective linear parameters - discrete points and the curve fitted to the data
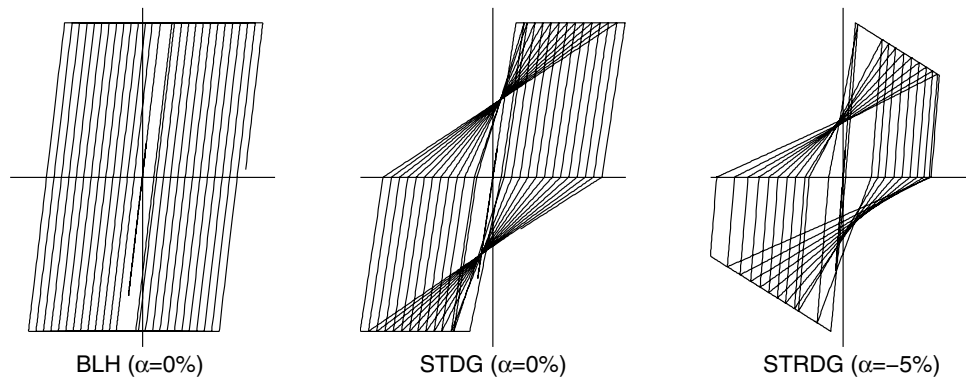
Figure D-13   Types of inelastic behavior considered. BLH=Bilinear hysteretic, STDG=Stiffness Degrading, and STRDG=Strength Degrading.

The new optimization criterion has been applied to the basic hysteretic models shown in Figure D-13. In each case, the basic model has been augmented by the addition of a linear spring element to create a non-zero second slope. α is the ratio of the post-yield stiffness to the elastic stiffness as seen in Figure D-6. The BLH and STDG models have been analyzed for alpha values of 0,2,5 and 10% while the STRDG model has been computed for alpha values of -3 and -5%. Results for all models and certain combinations of models are presented and discussed in Chapter 6. The elastoplastic system represents the greatest challenge in application of equivalent linearization due to the existence of long-period drifting displacement response in addition to the more quasi-harmonic motion (Paparizos and Iwan, 1988). It is noted that in general the results for the systems with alpha greater than zero are more favorable than for the systems with alpha equal to or less than zero.

D.7 Performance Point Errors

The Capacity-Spectrum Method incorporates both structural capacity and seismic demand to determine a point where the demand and capacity are equal, referred to as the *Performance Point*. This point gives the expected displacement in the structure. The accuracy of the Capacity-Spectrum Method will be evaluated using a new error measure. For a given ground motion, the Performance Point Error, $\varepsilon_{D_{pp}}$, is defined as the difference between the displacement at the Performance Point, as determined using equivalent linear parameters, and the actual maximum inelastic displacement response divided by the maximum inelastic displacement. This can be expressed as

$$
\begin{aligned}
&\varepsilon_{D_{PP}}(\alpha, \mu, HYST) \\
&= \frac{D_{lin}(T_{eff}(T_o, \alpha, \mu_{PP}), \beta_{eff}(T_o, \alpha, \mu_{PP}))}{D_{inel}(T_o, \beta_o, \alpha, \mu, HYST)} \\
&\quad - \frac{D_{inel}(T_o, \beta_o, \alpha, \mu, HYST)}{D_{inel}(T_o, \beta_o, \alpha, \mu, HYST)}
\end{aligned}
\qquad (D\text{-}32)
$$

Error statistics are created by combining all T_0 and β_0 values for a given hysteretic model, second slope ratio and ductility.

Several sources of error are introduced by the Capacity-Spectrum Method. Errors may arise in both the determination of structural capacity and seismic demand. To evaluate the error from the equivalent linear parameters alone, all other sources of error must either be eliminated or shown to be negligible.

In determining structural capacity, two sources of error exist: the capacity spectrum calculation and the hysteretic classification. A large source of error may come from representing a multi-degree-of-freedom building model by a single-degree-of-freedom system. This source of error is eliminated herein by considering only single-degree-of-freedom structures.

The second source of error in determining the structural capacity is the hysteretic classification. In what follows, errors associated with determination of the hysteretic model are eliminated since the actual hysteretic model is assumed apriori. In this way, both sources of error associated with the structural capacity have been removed.

In determining seismic demand, errors may be introduced through smoothing of the demand spectrum. A design spectrum that represents the effects of many possible earthquake sources is generally smooth and conservative. However, the spectrum of any actual earthquake ground motion is generally quite irregular. The potential errors associated with using a design spectrum instead of an actual earthquake response spectrum are eliminated in what follows by using actual earthquake response spectra. Demand spectra are calculated using the appropriate effective linear parameters. The only remaining source of error in the Capacity-Spectrum Method are errors associated with the effective linear parameters.

Performance Point Error results are presented for the bilinear hysteretic (BLH) and strength degrading (STDG) models with second slope ratios of 0% and 5% in Figures D-14 and D-15. The results clearly show an improvement using the new effective parameters as compared to the effective parameters used in ATC-40. For all cases, the probability of the Performance Point Error lying within the range of Engineering Acceptability is much higher for the new approach than for the current Capacity-Spectrum Method, especially for lower ductilities. This would appear to validate the use of higher order curve fitting for lower ductilities to help capture important local variations in the effective parameters.

At low values of ductility, the conventional Capacity-Spectrum Method approach is noticeably unconservative. Therefore, a building needing rehabilitated could be judged to not need an upgrade using the conventional Capacity-Spectrum Method approach. Within the framework of performance-based engineering, where Performance Objectives are very precise, accurate prediction at the lower ductility values can be quite important in terms of Immediate Occupancy and Operational building performance levels.

D.8 References

Iwan, W.D., 1980, "Estimating inelastic response spectra from elastic spectra," *Earthquake Engineering and Structural Dynamics*, Vol. 8, pp. 375-388.

Guyader, A, 2004, *A Statistical Approach to Equivalent Linearization with Application to Performance-Based Engineering*, EERL 2004-04 Report, Pasadena, California.

Paparizos, L.G., and W.D., Iwan, 1988, "Some observations on the random response of an elasto-plastic system," *Journal of Applied Mechanics*, Paper No. 88-WA/APM-64, American Society of Civil Engineers.
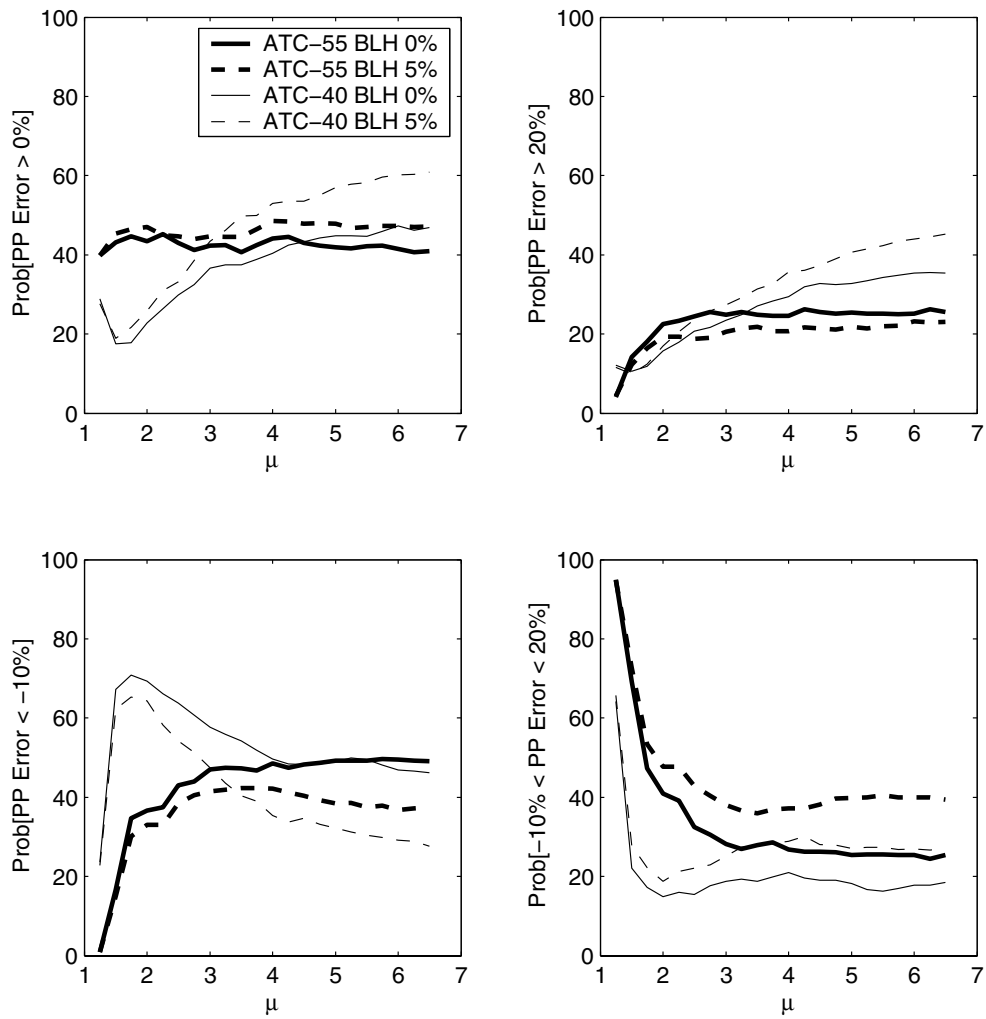
Figure D-14   Summary of Performance Point errors for bilinear hysteretic (BLH) model
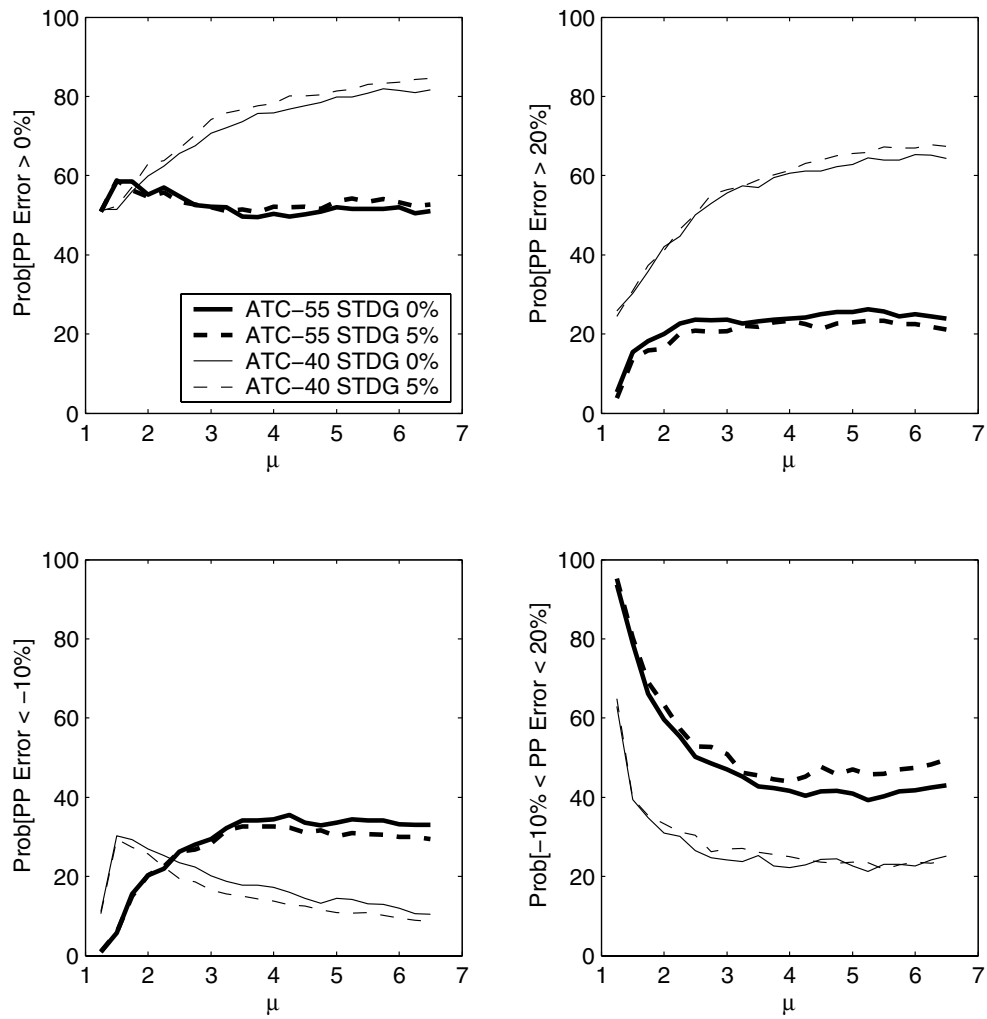
Figure D-15   Summary of Performance Point Errors for Strength Degrading (STDG) model

E. Supplementary Information and Data on Soil-Structure Interaction Effects

E.1   Introduction

This appendix provides detailed information on soil-structure (SSI) effects. The intent is to provide background information supporting the simplied design procedures presented in Chapter 8. Section E.2 describes kinematic interaction effects and engineering models used to describe these effects. Section E.3 describes foundation damping effects and how these effects contribute to the system damping ratio, which is the damping ratio for which the initial seismic demand spectrum should be computed. Reference citations are provided in Section E.4.

The soil-structure interaction effects described in this appendix are relevant at the stage of defining the elastic response spectrum, to be used during application of the Capacity-Spectrum Method of ATC-40, or the Coefficient Method of FEMA 356 (ASCE, 2000). The elastic spectra used during these procedures pertain to a free-field condition and for 5% damping. The spectral ordinates of the elastic spectra can be modified for kinematic interaction and foundation damping using the procedures presented in Sections E.2.4 and E.3.3, respectively (and summarized in Sections 8.2 and 8.3 of the main body of the report). The modified spectral ordinates can then be used in nonlinear static analyses of structural response and performance.

E.2   Kinematic interaction

Kinematic interaction results from the presence of stiff foundation elements on or in soil, which causes foundation motions to deviate from free-field motions as a result of base slab averaging and embedment effects. The base slab averaging effect can be visualized by recognizing that the motion that would have occurred in the absence of the structure within and below the footprint of the building is spatially variable. Placement of a foundation slab across these variable motions produces an averaging effect in which the foundation motion is less than the localized maxima that would have occurred in the free-field. The embedment effect is simply associated with the reduction of ground motion that tends to occur with depth in a soil deposit.

The information provided in this section on kinematic interaction covers simple models for the analysis of ground motion variations between the free-field and

shallow foundations at the ground surface (in which case kinematic interaction is dominated by base slab averaging) and embedded shallow foundations (in which case kinematic interaction can result from both base slab averaging and embedment effects). Kinematic interaction for pile-supported foundations is not covered. Theoretical models for kinematic interaction effects are expressed as frequency-dependent ratios of the Fourier amplitudes (i.e., transfer functions) of foundation input motion (FIM) to free-field motion. The FIM is the theoretical motion of the base slab if the foundation and structure had no mass, and is a more appropriate motion for structural response analysis than is the free-field motion.

In the following subsections, formulations for transfer functions that account for base slab averaging and embedment effects are presented. Recommendations are then provided regarding how transfer functions can be used to modify a free-field response spectrum or time history suite to estimate foundation input motions (FIMs) for use in nonlinear static procedures.

E.2.1   Shallow Foundations at the Ground Surface

Base-slab averaging results from inclined or incoherent incident wave fields. Motions of surface foundations are modified relative to the free-field when incident waves impinge upon the foundation with an angle to the vertical axis, α_v, or when the incident wave is incoherent. The first case is referred to as the wave passage effect and the second case as the ground motion incoherence effect. In the presence of these wave fields, translational base-slab motions are reduced relative to the free-field, and rotational motions are introduced. The reductions of base-slab translation, and the introduction of torsion and rotation in the vertical plane, are all effects that tend to become more significant with decreasing period. The period-dependence of these effects is primarily associated with the increased effective size of the foundation relative to the seismic wavelengths at low periods. In addition, ground motions are more incoherent at low periods.

Veletsos and Prasad (1989) and Veletsos et al. (1997) developed useful models for base slab averaging that combine an analytical representation of the spatial variation of ground motion with rigorous treatment of

foundation-soil contact. The models evaluate the response of rigid, massless circular and rectangular foundations on the surface of an elastic halfspace to incoherent SH waves propagating either vertically or at an angle α_v to the vertical. A result of the model is a transfer function between free-field motions and translational foundation motions (denoted with subscript 'u').

The transfer function amplitudes computed by Veletsos and his co-workers are presented in Figure E-1 for circular and rectangular foundations subject to vertically incident incoherent SH waves. Similar curves are available for nonvertically incident coherent waves in the references. The transfer functions in Figure E-1 are plotted against the dimensionless frequency parameter $\tilde{a}_o$, defined as follows for circular and rectangular foundations, respectively,

$$\tilde{a}_0 = a_0 \sqrt{\kappa^2 + \sin^2 \alpha_v} \qquad \textbf{Circular}$$

$$\tilde{a}_o = \frac{\omega b_e}{2 v_{s,r}} \sqrt{\kappa^2 + \sin^2 \alpha_v \left(\frac{b}{b_e}\right)^2} \quad \textbf{Rectangular} \qquad \text{(E-1)}$$
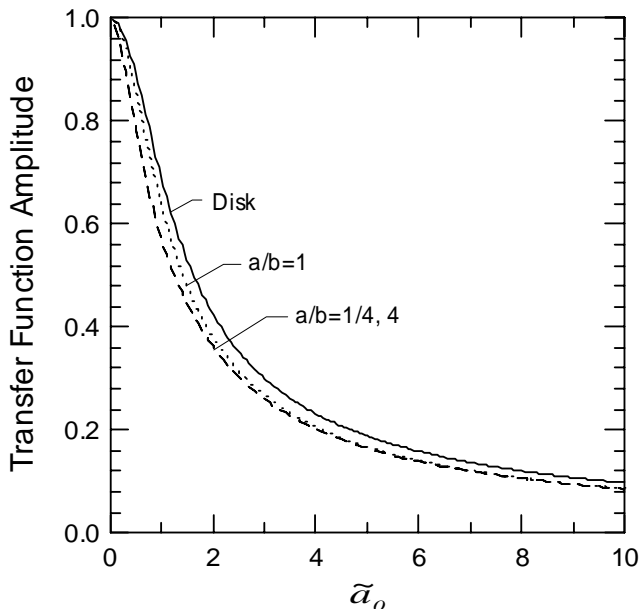
Figure E-1   Amplitude of transfer function between free-field motion and foundation input motion for vertically incident incoherent waves (Veletsos and Prasad, 1989; Veletsos et al., 1997).

where $a_0 = \omega r / V_{s,r}$, $V_{s,r}$ denotes a strain-reduced shear wave velocity, r = radius of circular foundation, $a \times b$ = full footprint dimensions of rectangular foundation (b being measured perpendicular to the direction of SH wave polarization), $b_e = \sqrt{ab}$, and κ = a ground motion incoherence parameter (information on the selection of κ values are presented below).

Figure E-1 indicates that the transfer functions for circular and various rectangular geometries are similar to each other for small $\tilde{a}_o$. As noted by Veletsos et al. (1997), the near equivalence of the results for different aspect ratios (a/b=1/4 - 4) of rectangular foundations suggests that translational transfer functions primarily depend on foundation area. Given this near equivalence, the transfer function is principally a function of dimensionless frequency $\tilde{a}_o$. As shown in Equation E-1, $\tilde{a}_o$ is essentially the foundation dimension normalized by the wavelength (since wavelength is wave velocity divided by frequency), and then scaled by an incoherence/wave inclination term. When the foundation dimension is large relative to the wave length, $\tilde{a}_o$ is large and the transfer function ordinate is low. Conversely, small foundation dimensions relative to the wavelength produce transfer function ordinates near unity.

Kim and Stewart (2003) calibrated the above analysis procedure against observed foundation / free-field ground motion variations as quantified by frequency-dependent transmissibility function amplitudes, |H|. The above analytical models were fit to |H| for the assumed condition of a rigid base slab and a vertically propagating, incoherent incident wave field. Calibrated from the fitting process was a ground motion incoherence parameter, κ. Since the limiting assumptions of the model were not strictly satisfied for actual structures, the results of the identification were denoted apparent κ values (κ_a) that reflect not only incoherence effects, but also average foundation flexibility and wave inclination effects within the calibration data set. The foundation flexibility effects within the calibration data set generally correspond to shallow foundation conditions in which foundation components are inter-connected (i.e., continuous mats or footings inter-connected with grade beams). Parameter κ_a was found to be correlated to average soil shear wave velocity as shown in Figure E-2. These values of κ_a can be used with Figure E-1 (assuming α_v = 0) to define site-specific transfer functions given the foundation radius (r) and effective small-strain shear wave velocity (v_s). In these procedures, effective foundation radius is defined as $r = \sqrt{A_f / \pi}$ (where
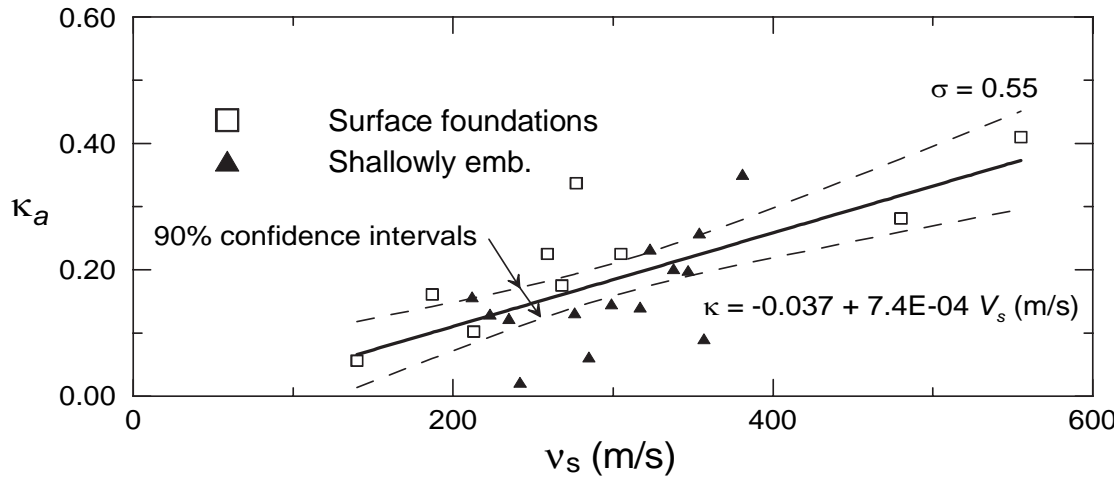
Figure E-2   Relationship between effective incoherence parameter k_a and small-strain shear wave velocity v_s from case histories (from Kim and Stewart, 2003).

A_f = foundation area) and the effective v_s for the site is defined as r / (travel time for shear wave to travel from depth r to ground surface). Depth is measured down from the base of the foundation.

The model has not been validated for foundations with low in-plane stiffness, buildings with large footprint dimensions (> 200 ft), and pile-supported foundations in which the cap and soil are not in contact. However, the judgment of the project technical team that developed this report is that the model can provide a reasonable first order estimate of the kinematic interaction effect for those conditions.

E.2.2   Embedded Shallow Foundations

Foundation "embedment" refers to a foundation base slab that is positioned at a lower elevation than the surrounding ground, which will usually occur when buildings have a basement. When subjected to vertically propagating coherent SH waves, embedded foundations experience a reduction in base-slab translational motions relative to the free-field, and rotations in the vertical plane are introduced. The rotations are caused by incompatible shear strains along the sides of the excavation and the free-field.

Elsabee and Morray (1977) and Day (1978) have developed analytical transfer functions relating base-slab translational and rotational motions to free-field translations for an incident wave field consisting of vertically propagating, coherent SH waves. Base-slab averaging does not occur within this wave field, but foundation translations are reduced relative to the free-field due to ground motion reductions with depth and wave scattering effects. Day (1978) used finite element analyses to evaluate the base motions of a rigid cylindrical foundation embedded in a uniform elastic half space ($\beta = 0$, $v = 0.25$) and subjected to vertically incident, coherent SH waves. Elsabee and Morray (1977) performed similar studies but for the case of a visco-elastic soil layer of finite depth over a rigid base ($\beta = 0.05$ and $v = 0.33$). The amplitude of the halfspace and finite soil layer transfer functions are shown together in Figure E-3 for foundation embedment / radius ratio $e/r = 1.0$. The primary difference between the two solutions is oscillations in the finite soil layer case at high frequencies. Also shown in Figure E-3a is the following approximate transfer function amplitude model developed by Elsabee and Morray (1977):

$$\left| H_u\left(\omega\right) \right| = \cos\left(\frac{e}{r}a_0\right) = \cos\left(\frac{e\omega}{v_s}\right)$$

$$[H_u \text{ must be} \geq 0.454] \qquad \text{(E-2)}$$

where $a_0 = \omega r/v_s$ and e = foundation embedment. Figure E-3b shows the transfer function amplitude model is a somewhat more convenient form in which it is plotted as a unique function of $\omega e/v_s$.
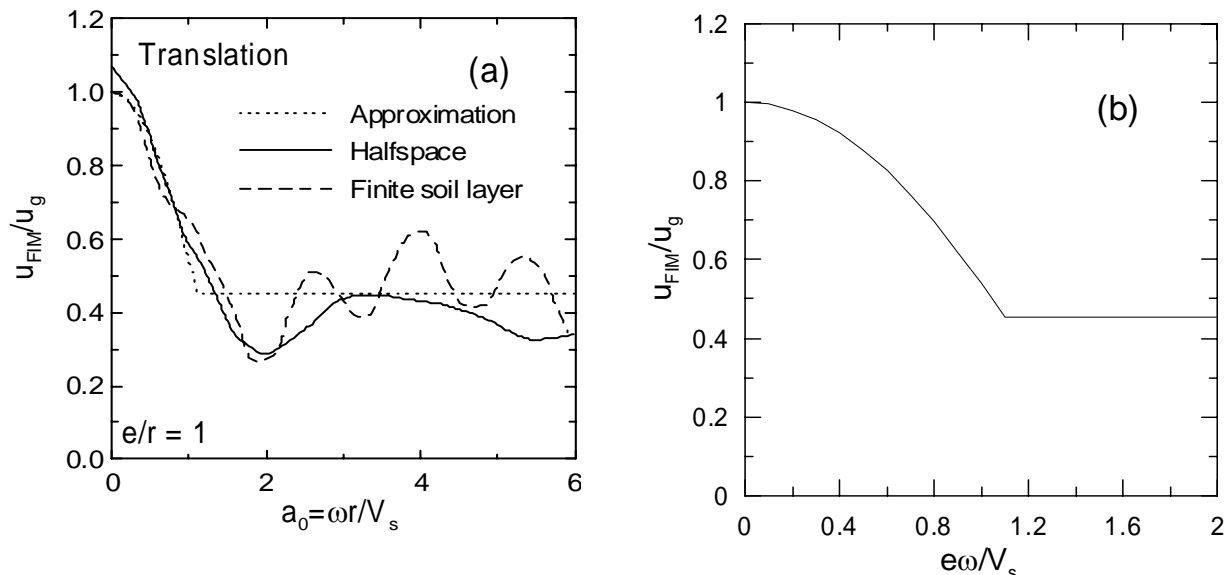
Figure E-3　　(a) Transfer function amplitudes for embedded cylinders from Day (1978) and Elsabee and Morray (1977) along with approximate solution by Elsabee and Morray; (b) Transfer function amplitude model by Elsabee and Morray (1977).

The results in Figure E-3 can be contrasted with the behavior of a surface foundation, which would have no reduction of translational motions and no rotational motions when subjected to vertically incident coherent shear waves. Transfer function amplitudes in the presence of more realistic incident wave fields can be estimated at each frequency by the product of the transfer function ordinates from the previous section (for base slab averaging) and those from this section at the corresponding frequency.

Elsabee and Morray (1977) found these transfer functions to also be applicable to nonhomogeneous soil profiles, provided $v_{s,r}$ is averaged across the embedment depth. Mita and Luco (1989) found that solutions for circular foundations can be extended to square foundations, provided the radius of the equivalent cylinder is the average of the radii necessary to match the area and moment of inertia of the square base.

The analysis procedure described herein has been verified against recorded motions from two relatively deeply embedded structures with circular foundations having e/r = 0.9 and 2.9 (Kim, 2001). Embedment effects dominated the kinematic interaction for these deeply embedded foundations; for foundations with e/r

< 0.5 Kim (2001) found that the embedment and base slab averaging models should be coupled by multiplying the respective transfer function ordinates from the two models to accurately simulate observed transfer functions.

E.2.3　Application of Transfer Functions to Calculation of Foundation Motions

The analysis of free-field motions generally results in the specification of a design-basis acceleration response spectrum. Sometimes suites of time histories are specified that are compatible with this spectrum. The question addressed in this section is how this spectrum or time history suite should be modified once the transfer function amplitude for the site has been evaluated using the analysis procedures described above.

When free-field motions are specified only as response spectral ordinates, the evaluation of a modified response spectrum consistent with the FIM is needed. Veletsos and Prasad (1989) evaluated ratios of foundation / free-field response spectral ordinates (at 2% damping) for conditions where the corresponding transfer function ordinates could be readily determined. The transfer function ordinates and ratios of response spectra (RRS) were compared for an input motion with

specified power spectral densities and random phase. The results indicated that transfer function ordinates provide a reasonable estimate of response spectral ratios for low frequencies (e.g., < 5 Hz), but that at high frequencies ($\geq$ 10 Hz) transfer function ordinates are significantly smaller than response spectrum ratios. The inconsistency at high frequencies is attributed to the low energy content of free-field excitation at high frequencies and the saturation of spectral ordinates at these frequencies.

The analytical results of Veletsos and Prasad were checked by (1) calculating the transfer function for a fixed set of conditions (surface foundation, $r = 50$ m, $V_s = 250$ m/s), (2) using this transfer function to modify a set of recorded free-field time histories to corresponding foundation-level time histories, and (3) evaluating the RRS using the two time histories. Representative results of these analyses are presented in Figure E-4. The left frame shows results for a time
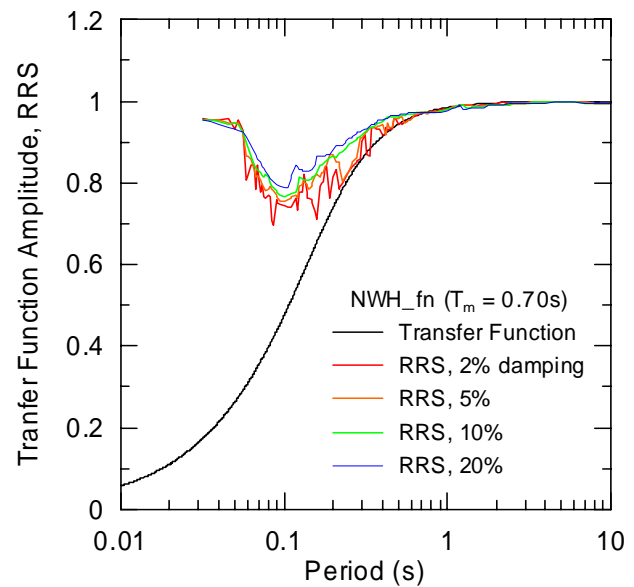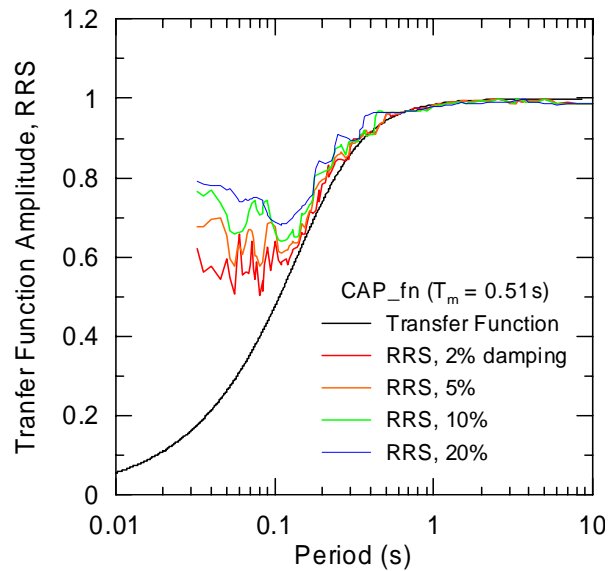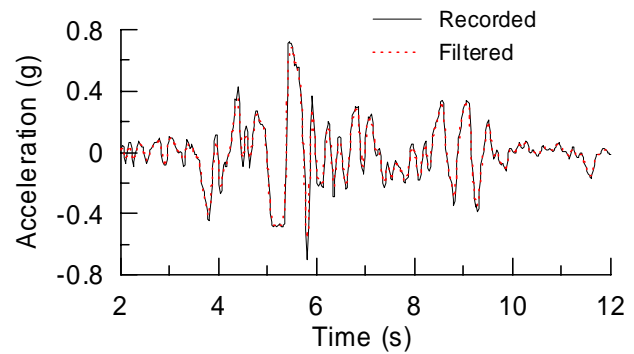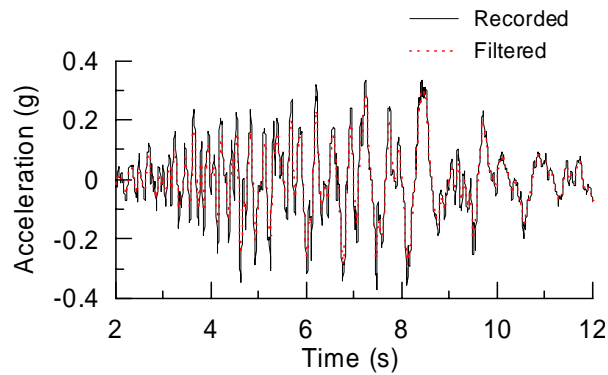

Figure E-4   Comparison of transfer function amplitude to ratios of response spectra (RRS) at different damping ratios. Left figure applies for time histories in which the spectral response is dominated by high-frequency spikes in the accelerogram, whereas in the right figure the response is dictated by lower frequency spikes.

history in which the spectral response is largely controlled by relatively high-frequency components of the waveform. The right frame shows results for a time history in which the peak response is associated with relatively low-frequency pulses. These types of low-frequency pulses are common for sites located on soft soils, but are also found in some sites subjected to significant near-fault, forward rupture directivity effects. The results suggest that for ordinary ground motions, RRS over a wide range of damping ratios can be reasonably estimated by transfer function ordinates for $T > 0.2$ s, but that some caution should be exercised for soft soil sites and perhaps for near-fault ground motions. It should be noted that only a few ground motion time histories were used in these analyses, and additional research is needed to evaluate the relationship between RRS and transfer function ordinates as a function of ground motion characteristics and damping ratio.

Based on the above, the following procedure is recommended for estimation of RRS from transfer function ordinates:

1. For periods > 0.2 s, estimate foundation response spectral ordinates as the product of free-field response spectral ordinates and the transfer function amplitude at the corresponding frequency.

2. For periods < 0.2 s, estimate foundation response spectral ordinates as the product of free-field response spectral ordinates and the transfer function amplitude at 0.2 s.

For structures on very soft soils (i.e., NEHRP Site Category E), no reductions of response spectra for kinematic interaction should be taken.

When free-field motions are specified as time histories for use in nonlinear time history analyses of structures, modified time histories representing the FIM can be evaluated as follows:

1. Calculate the Fourier transforms of the free-field time histories.

2. Multiply the amplitude of the free-field motions by the transfer function amplitude.

3. Use the amplitudes from (2) along with the phase angles of the free-field motions, and perform reverse Fourier transforms to estimate FIM time histories.

4. If needed, a revised response spectrum that accounts for kinematic interaction effects could be calculated from the FIM time histories.

It should be noted that maintaining the free-field phase angles in Step 3 is not strictly correct, especially for embedded foundations. If desired, phase shifts of $\omega e / V_s$ (in radians) could be introduced for motions of embedded foundations relative to ground surface motions. Models for phase adjustment are not available for kinematic interaction effects involving surface foundations, but the assumption of consistent phase should not significantly bias response spectral ordinates for estimated FIMs.

E.2.4 Simplified Procedure for Design

The Kim and Stewart (2003) model for incoherence parameter κ_a (presented in Section E.2.1), along with the procedure for converting transfer function ordinates to RRS (presented in Section E.2.3), enables the development of simplified design charts for kinematic interaction effects for non-embedded base slabs founded on alluvial soils. A significant simplification results from the fact that κ_a is nearly proportional to v_s (as seen in Figure E-2), which per Equation E-1 causes dimensionless frequency term $\tilde{a}_o$ to effectively reduce to a function of frequency and foundation size (b_e). This is shown below, written for vertically propagating waves ($\alpha_v = 0$):

$$
\tilde{a}_0 = \frac{\omega b_e}{2 V_{s,r}} \sqrt{\kappa^2 + \sin^2 \alpha_v \left(\frac{b}{b_e}\right)^2}
$$
$$
\approx \frac{\omega b_e \kappa}{2 V_{s,r}} \approx \frac{\omega b_e n_1 V_s}{2 n_2 V_s} = \frac{\omega b_e n_1}{2 n_2}
$$

(E-3)

where $n_1 \approx 6.5 \times 10^{-4}$ s/m and n_2 is the square root of the soil modulus reduction factor, which can be estimated as shown in Table E-1.

Figure E-5 shows the degree of approximation associated with taking κ_a as proportional to v_s (using

Table E-1   *Approximate values of n*

	Peak Ground Acceleration (PGA)			
	0.10	0.15	0.20	0.30
n	0.90	0.80	0.70	0.65
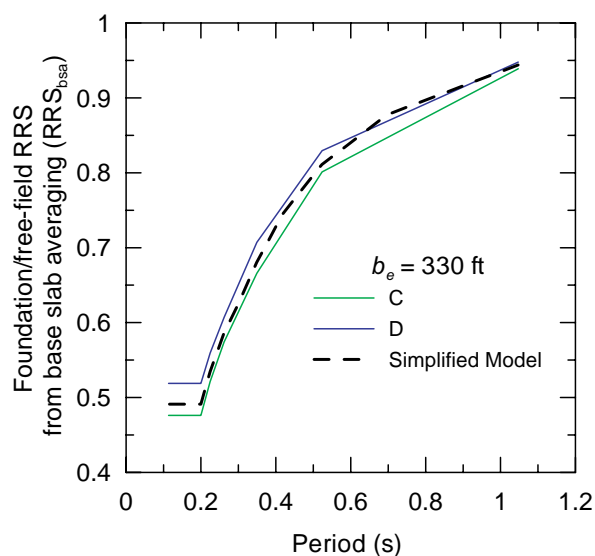
Figure E-5   RRS for foundation with $b_e = 330$ ft. Simplified model ($\kappa_a / v_s = n_1$) vs. exact solution for κ_a
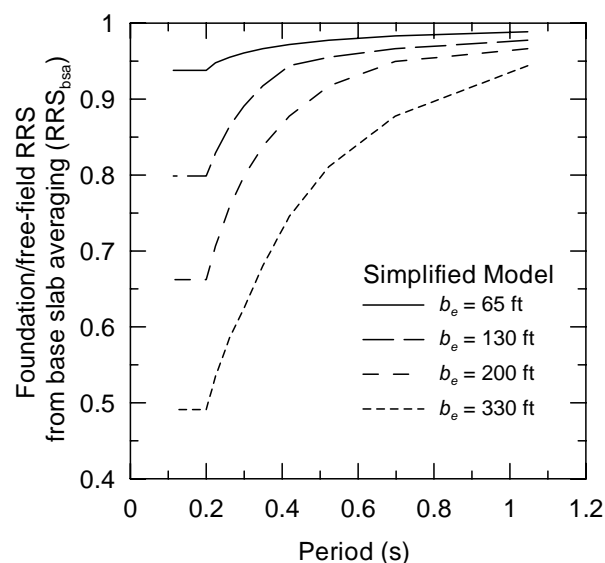
Figure E-6   RRS from simplified model as function of foundation size, b_e

proportionality term n_1). In this and subsequent figures, parameter $n_2 = 0.65$, which is the appropriate value for regions of high seismicity. The results for site classes C-D are shown for typical shear wave velocities within the categories based on borehole compilations. The difference between the simplified model and the result for individual site classes is small. Figure E-6 shows the resulting curves of RRS per Equation E-3 for foundations of various sizes. As expected, the kinematic interaction effect increases as the foundation size increases and as period decreases.

As with the base slab averaging model for surface foundations, simplified design charts for the RRS of embedded foundations can also be developed. These charts are based on the simplified model of Elsabee and Morray (1977) shown in Figure E-3b, but with the RRS interpreted from the transfer function amplitude as described in Section E.2.3. Figure E-7a presents RRS as a function of period in site categories A-D for a relatively large embedment depth of 30 ft. As can be seen in the figure, embedment effects are negligible at practical levels of embedment for firm rock site conditions (Site Categories A and B). Accordingly, Figure E-7b presents RRS values at three levels of embedment (e = 10, 20, and 30 ft) only for Site Classes C and D.

Based on the above, the following simplified procedure is recommended for analysis of kinematic interaction effects:

1. Evaluate effective foundation size $b_e = \sqrt{ab}$, where a and b are the foundation dimensions in plan view.

2. Evaluate period-dependant RRS from base slab averaging (RRS_{bsa}) using Figure E-6. An approximate equation to the curves in Figure E-6 is presented below:

$$RRS_{bsa} = 1 - \frac{1}{14100}\left(\frac{b_e}{\tilde{T}_{eq}}\right)^{1.2} \qquad \text{(E-4)}$$

where b_e = effective foundation size (from Step 1) in feet, and T = period in sec.

3. If the foundation is embedded a depth e from the ground surface, evaluate an additional RRS from embedment (RRS_e) as a function of period due to embedment effects using Figure E-7. The equation of the curves in Figure E-7 is,
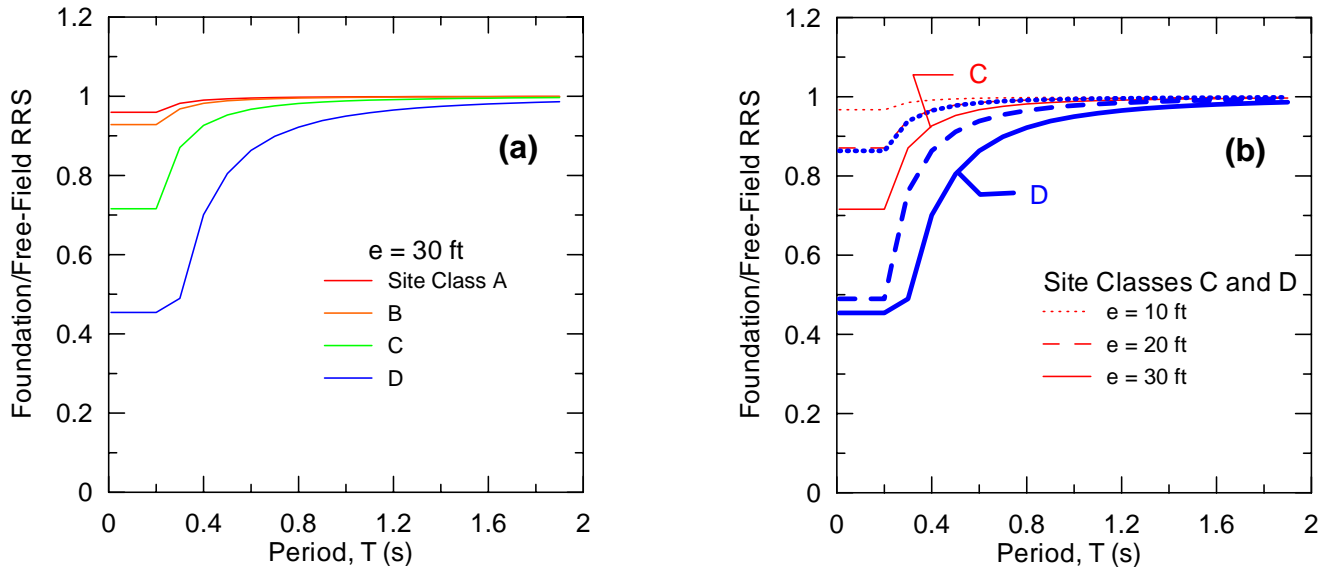
Figure E-7   (a) RRS for foundation embedded to depth e = 30 ft in different site categories; (b) RRS for foundations with variable depths in Site Classes C and D.

$$RRS_e = \cos\left(\frac{2\pi\, e}{\tilde{T}_{eq} v_{s,r}}\right) \geq \text{ larger of 0.453 or}$$

the value of RRS_e at $T = 0.2$ sec   (E-5)

where $e =$ foundation embedment (in feet) and $v_{s,r}$ = effective strain-degraded shear wave velocity in the soil (in ft/s). Factors that can be used to estimate $v_{s,r}$ from small-strain shear wave velocity v_s are given in Table E-1.

4. Evaluate the product RRS_{bsa} times RRS_e to obtain the total RRS. The spectral ordinates of the foundation input motion is the product of the free-field spectral ordinates and the total RRS.

Limitations associated with application of this approach include the following:

- Kinematic interaction effects should be neglected for soft clay sites, such as Site Class E.

- Embedment effects can be neglected for foundations embedded in firm rock (Site Classes A and B).

- The base slab averaging model has the following limitations:

   a) Underestimates ground motion reduction for sites on rock (i.e., use of the above formulation is conservative).

   b) The model has not been validated for foundations with low in-plane stiffness, buildings with large footprint dimensions (> 200 ft), and pile-supported foundations in which the cap and soil are not in contact. However, the judgment of the project technical team that developed this report is that the model can provide a reasonable first order estimate of the kinematic interaction effect for those conditions.

   c) The model should not be used for structures that have both foundations without significant connectivity of lateral elements and flexible floor and roof diaphragms.

E.3   Foundation Damping

Inertia developed in a vibrating structure gives rise to base shear, moment, and torsion at the foundation soil interface, and these loads in turn cause displacements and rotations of the structure relative to the free field. These relative displacements and rotations are only possible because of compliance in the soil, which can significantly contribute to the overall structural flexibility in some cases. Moreover, the difference between the foundation input motion and free-field motion gives rise to energy dissipation via radiation damping and hysteretic soil damping, and this energy dissipation affects the overall system damping. Since these effects are rooted in the structural inertia, they are

referred to as *inertial interaction* effects, in contrast to the *kinematic interaction* effects discussed in the prior section.

The ATC-40 and FEMA 356 documents contain provisions for evaluating the properties of foundation springs (e.g., Sections 10.3 and 10.4 of ATC-40), and hence this aspect of inertial interaction is not emphasized here. Rather, the focus of this section is on the damping component of inertial interaction and the contribution of this damping to the overall system damping.

In the SSI literature, foundation stiffness and damping effects are often described in terms of an *impedance function*. The impedance function should account for the soil stratigraphy and foundation stiffness and geometry, and is typically computed using equivalent-linear soil properties appropriate for the in situ dynamic shear strains. Impedance functions can be evaluated for multiple independent foundation elements, or (more commonly) a single 6×6 matrix of impedance functions is used to represent the complete foundation (which assumes foundation rigidity).

In the following sub-sections, factors affecting foundation impedance functions are described, with an emphasis on those factors significantly affecting the damping component. The section is concluded with a discussion of how system damping ratios can be evaluated once factors affecting impedance functions and the fixed-based structural damping ratio are known.

E.3.1   Analysis of Impedance Functions

E.3.1.1   Basic Case

Simplified impedance function solutions are available for rigid circular or rectangular foundations located on the ground surface and underlain by a uniform, visco-elastic halfspace. A thorough listing of impedance functions for these and other foundation shapes is provided in Gazetas (1991a, 1991b). A circular foundation shape with the above assumptions of foundation rigidity and soil uniformity comprise the "basic case" for foundation impedance considered here.

Terms in the complex valued impedance function are expressed in the form

$$\bar{k}_j = k_j(a_0, \upsilon) + i\omega c_j(a_0, \upsilon) \qquad (E-6)$$

where j denotes either deformation mode x (for translation) or θ (for rotation in the vertical plane), ω is angular frequency (radians/sec.), a_0 is a dimensionless frequency defined by $a_0 = \omega r/v_s$, r = foundation radius, v_s = soil shear wave velocity, and υ = soil Poisson ratio. Foundation radii can be computed separately for translational and rotational deformation modes to match the area (A_f) and moment of inertia (I_f) of the actual foundation (i.e. $r_x = \sqrt{A_f/\pi}$, $r_\theta = \sqrt[4]{4I_f/\pi}$). There are corresponding $(a_0)_x$ and $(a_0)_\theta$ values as well.

The real stiffness and damping of the translational and rotational springs and dashpots are expressed, respectively, by

$$k_x = \alpha_x K_x \qquad c_x = \beta_x \frac{K_x r_x}{v_S} \qquad (a)$$

$$k_\theta = \alpha_\theta K_\theta \qquad c_\theta = \beta_\theta \frac{K_\theta r_\theta}{v_S} \qquad (b) \qquad (E-7)$$

where α_x, β_x, α_θ, and β_θ express the frequency dependence of the impedance terms, and K_x and K_θ are the static stiffness of a disk on a halfspace,

$$K_x = \frac{8}{2-\upsilon}Gr_x \qquad K_\theta = \frac{8}{3(1-\upsilon)}Gr_\theta^3 \qquad (E-8)$$

where G = soil dynamic shear modulus. Additional solutions for K_x and K_θ that take into account the foundation geometry in plan are presented in Table 10-2 of ATC (1996). Presented in Figure E-8 are the frequency-dependent values of α_x, β_x, α_θ, and β_θ for a rigid circular foundation on the surface of a visco-elastic halfspace with soil hysteretic damping ratio β_s (Veletsos and Wei, 1971; Veletsos and Verbic, 1973).

Validation studies for the above and similar impedance function formulations have been conducted by Lin and Jennings (1984) and Crouse et al. (1990) for small foundations (< 10 ft plan dimension), and by Luco et al. (1988), Wong et al. (1988), and DeBarros and Luco (1995) for larger scale building foundations (up to 80 ft plan dimension). These studies have generally found reasonably good agreement between experimental observations and analytical predictions, although the fit is usually markedly better for rotation vibration modes than for translation. The improved fit for rotation likely results from the relative ease of identifying impedance functions from rotation data as compared to relative
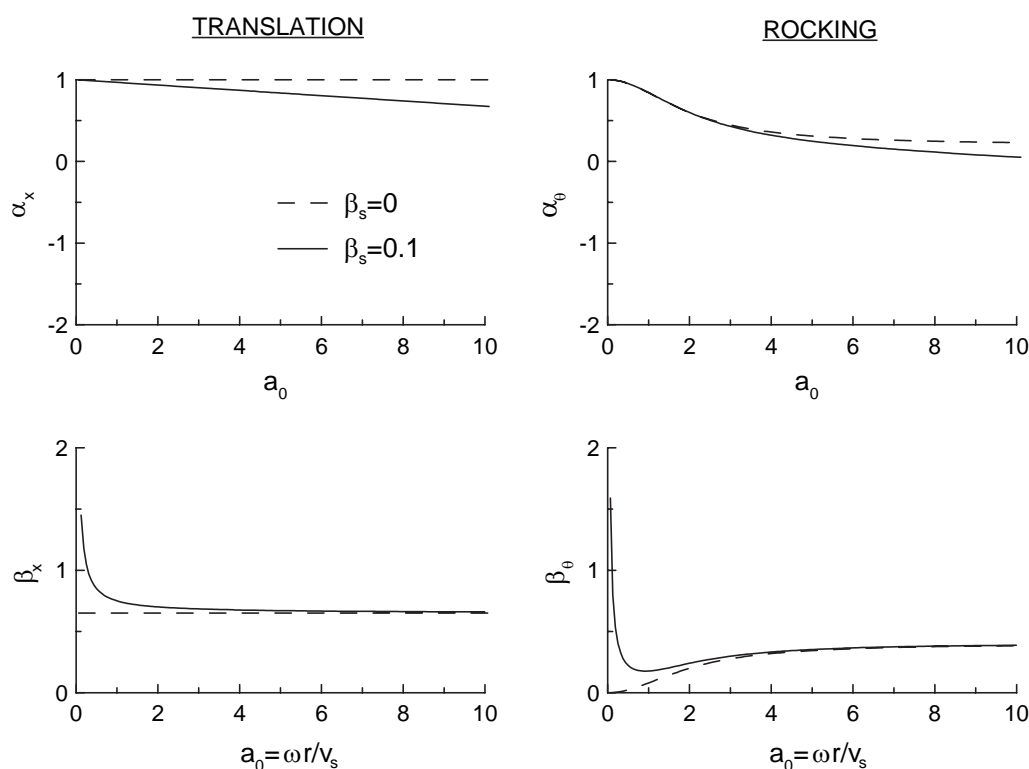
Figure E-8   Foundation stiffness and damping factors for elastic and viscoelastic halfspaces ($\upsilon = 0.4$). After Veletsos and Verbic, 1973.

foundation/free-field translations, which have weaker signals.

The above solutions for rigid, circular foundations on a halfspace can provide reasonable estimates of foundation impedance in many cases. However, the potentially significant effects of non-uniform soil profiles, embedded foundations, non-circular foundation shapes, and flexible foundations should be accounted for in some cases. The following sections discuss the effects of these factors on the damping component of impedance functions.

E.3.1.2   Nonuniform Soil Profiles

Gazetas (1991b) provides solutions for the impedance of rigid foundations overlying soil for which the shear stiffness increases with depth according to prescribed functions. The damping components of these solutions are plotted in Figure E-9 in terms of the frequency-dependent and dimensionless β_x and β_θ terms; actual dashpot coefficients can be computed using these terms in Equations E-7a and b. Also plotted for comparative

purposes are the solutions for a halfspace presented previously in Figure E-8. Note that the damping values for non-uniform profiles are plotted for a zero hysteretic damping condition (radiation damping only) and that the normalizing shear modulus and shear wave velocity are the values at the ground surface (G_0 and v_{s0}, respectively).

From Figure E-9, radiation damping in translation for a nonuniform profile is seen to be less than that for a halfspace at low frequencies. For rotation, a small reduction can occur at low frequencies, but the effect is less significant than for translation. At large frequencies, the radiation damping for nonuniform profiles exceeds that for the halfspace.

The low-frequency reduction in damping is due to reflections of body waves emanating from the foundation; the frequency dependence of the reduction is related to the depth over which the shear modulus increases relative to wavelength. For short-period (and short-wavelength) body waves, the nonuniform soil medium is "seen" as being effectively uniform, whereas
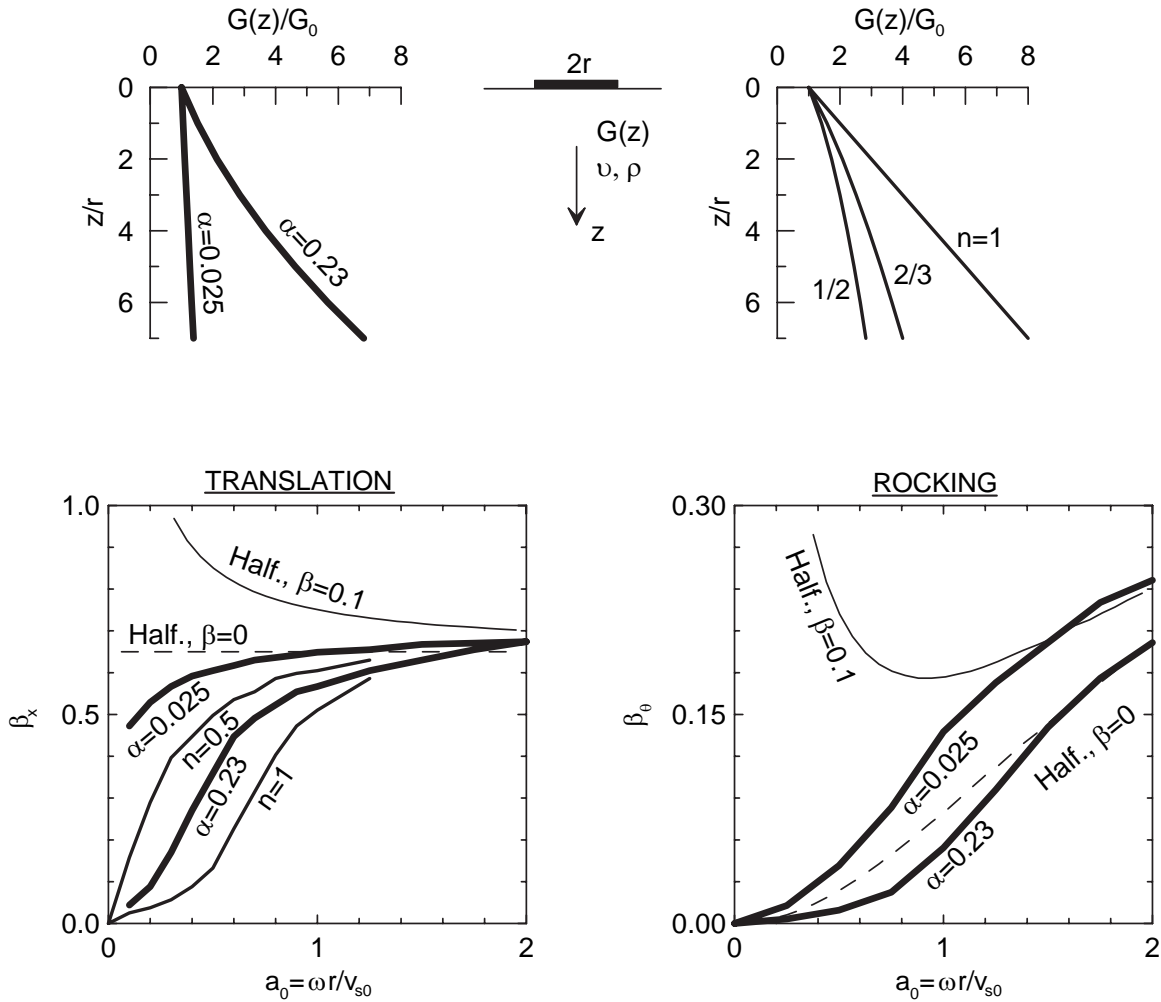
Figure E-9   Foundation damping factors for halfspace with and without hysteretic damping (Veletsos and Verbic, 1973) and for soil profiles with indicated shear modulus profiles and no hysteretic damping (Gazetas, 1991b).

long-period waves (with long wavelengths) "see" a much more nonuniform medium and wave transmission into the medium is impeded. The increase of radiation damping at high frequencies is due to the higher v_s of the nonuniform profiles at depth as compared to the velocity of the halfspace model (for which v_s was taken as v_{s0}).

The above effects on low-frequency damping can be contrasted with the effect of soil nonuniformity on foundation stiffness. A number of researchers (e.g., Roesset, 1980; Gazetas, 1991b; Stewart et al., 2003)

have suggested that effective foundation stiffnesses can be computed from an average v_s value over a specified depth range. For the common case in which soil stiffness increases with depth, this averaging will result in an effective v_s value that is larger than v_{s0}. The use of this averaged v_s would be unconservative in the case of damping, as the low-frequency damping is overpredicted by a halfspace model even when the halfspace velocity is taken as v_{s0}. Thus, different effective velocities of nonuniform soil profiles should be used for calculations of foundation stiffness and damping.

For the case of a finite soil layer overlying a much stiffer material, the key issue is a lack of radiation damping at periods greater than the fundamental period of the finite soil layer, $T_s = 4H/v_s$. Halfspace damping ratios can be used for periods less than the soil layer period. Above this period in materials with hysteretic damping, Elsabee and Morray (1977) developed the following damping recommendations:

$$\beta_x \approx 0.65\beta \frac{a_0/a_{01}}{1-(1-2\beta)(a_0/a_{01})^2} \text{ for } a_0/a_{01} \leq 1 \text{ (E-9)}$$

$$\beta_\theta \approx 0.50\beta \frac{a_0/a_{01}}{1-(1-2\beta)(a_0/a_{01})^2} \leq \frac{0.35a_0}{1+a_0^2}$$
$$\text{for } a_0/a_{01} \leq v_p/v_s \qquad \text{(E-10)}$$

where $a_{01} = 0.5\pi r/H$, r = foundation radius, and H = finite soil layer thickness.

In terms of practical application of the above results, the following observations are noted:

- For translational damping, profile non-uniformity is not significant for $a_0=\omega r/v_s > 1$. Case history studies suggest that inertial soil-structure interaction is generally not important for $h/(v_sT) < 0.1$ (Stewart et al., 1999). Hence, for sites where SSI is important, profile non-uniformity need not be considered if $h/r < 2\pi h/(v_sT)$. The value on the right hand side of the inequality will generally be more than 2/3 for cases where inertial SSI is important, which is larger than the aspect ratios for many short-period buildings. Accordingly, it is often justified to treat the nonuniform soil as a halfspace, taking the halfspace velocity as the in situ value immediately below the foundation. Note that the above inequality to allow profile non-uniformity effects to be neglected can be re-written as $v_sT/r < 2\pi$.

- Rotational damping for a non-uniform profile can generally be reasonably well estimated by a halfspace model, with the halfspace velocity taken as the in situ value immediately below the foundation.

- The use of halfspace models is unconservative for sites with a finite soil layer overlying a very stiff layer, if the structural system period is greater than the soil layer period. Alternative dashpot

coefficients for such cases can be developed using Equation E-10.

E.3.1.3 Embedded Foundations

Foundation "embedment" refers to a foundation base slab that is positioned at a lower elevation than the surrounding ground, which will usually occur when buildings have a basement. The impedance of embedded foundations differs from that of shallow foundations in several important ways. First, the static stiffness of embedded foundations is increased, which is accounted for with the embedment factors given in Table 10.3 of ATC-40 (ATC, 1996). For circular foundations, these embedment terms are as follows:

$$(K_x)_E = K_x\left(1+\frac{2}{3}\frac{e}{r_u}\right)$$
$$\qquad \text{(E-11)}$$
$$(K_\theta)_E = K_\theta\left(1+2\frac{e}{r_\theta}\right)$$

where e = embedment depth. The second important difference between embedded and surface foundations is that embedded foundations can produce much larger damping due to the greater foundation-soil contact area.

An approximate and generally conservative approach for estimating the damping of embedded foundations consists of using the modified static stiffness terms from Equation E-11 coupled with the dynamic modifiers for a surface foundation in Figure E-8. This approach has been found to provide reasonable estimates of observed foundation damping in actual structures for embedment ratios $e/r_u < 0.5$ (Stewart et al., 1999). As short-period structures are seldom deeply embedded, this approximate approach will often suffice for practical applications. For more deeply embedded foundations, alternative formulations can be used such as Bielak (1975) or Apsel and Luco (1987). However, caution should also be exercised in the application of these approaches for embedded foundations with poor quality backfill against basement walls. For such foundations, gapping is likely and impedance functions should probably be formulated using the shallow foundation approach noted previously.

E.3.1.4 Foundation Shape

Impedance functions for foundations of arbitrary shape are commonly analyzed as equivalent circular mats (BSSC, 2001). As described previously, an equivalent

radius for translational stiffness is derived by equating the areas of the mats, while an equivalent radius for rotational stiffness is derived by equating the moments of inertia of the mats. The issue addressed in this section is the adequacy of this assumption for oblong foundations.

Combining a number of analytical impedance function solutions from the literature for foundations of arbitrary shape, Dobry and Gazetas (1986) found that the use of equivalent circular mats is acceptable for aspect ratios less than 4:1, with the notable exception of dashpot coefficients in the rotation mode. As shown in Figure E-10, dimensionless radiation damping coefficients c_{rx} and c_{ry} (for longitudinal and transverse rotations, respectively) are seen to be underestimated by the equivalent disk assumption at low frequencies. This is a consequence of the tendency for rotational vibrations to be dissipated into the soil primarily via the ends of the foundation. Hence, as aspect ratio increases, the two ends act increasingly as independent wave sources with reduced destructive interference between waves emanating from the foundation. For the case of longitudinal rotations, damping can be underpredicted by a factor of two or more for aspect ratios of L/B ≈ 4. For higher frequencies ($a_0 > 3$-4, not shown in figure), the results for the various aspect ratios converge to c_{rx}, $c_{ry} = \sim 1$. This occurs because these high frequency waves have short wavelengths relative to the foundation dimension regardless of L/B, so destructive interference between the waves is small in all cases.

The use of dashpot coefficients for disk-shaped foundations can be used to provide conservative (lower-bound) estimates of the damping of oblong foundations. This approximation may be sufficient for many practical applications, especially given the relatively small influence of damping from rotations on system damping (damping from horizontal vibrations often contribute more significantly, see Section E.3.2). If more refined analysis of rotational damping is needed, rotational radiation dashpot coefficients for oblong, non-circular foundations can be calculated using procedures given in Gazetas (1991a, b).

E.3.1.5   Foundation Flexibility

This section addresses flexibility in the foundation structural system (i.e., the base mat, or assemblage of a base mat and grade beams/footings). The foundation flexibility referred to here is not associated with the soil.

Impedance functions for flexible circular foundation slabs supporting shear walls have been evaluated for a number of wall configurations, including: (1) rigid core walls (Iguchi and Luco, 1982), (2) thin perimeter walls (Liou and Huang, 1994), and (3) rigid concentric interior and perimeter walls (Riggs and Waas, 1985). These studies focused on the effects of foundation flexibility on rotation impedance; the horizontal impedance of flexible and rigid foundations are similar (Liou and Huang, 1994). Foundation flexibility effects on rotation impedance were found to be most significant for a rigid central core with no perimeter walls. For this case, the flexible foundation has significantly less stiffness and damping than the rigid foundation. The reductions are most significant for narrow central cores and large deviations between soil and foundation slab rigidity.

Significant additional work remains to be done on foundation flexibility effects on impedance functions because the existing research generally has investigated wall/slab configurations that are seldom encountered in practice for building structures. Nonetheless, based on the available studies and engineering judgment, the following preliminary recommendations are provided:

1. The rigid foundation assumption is probably generally acceptable for the analysis of damping associated with horizontal vibrations of reasonably stiff, inter-connected foundation systems.

2. For buildings with continuous shear walls or braced frames around the building perimeter, and continuous footing or mat foundations beneath these walls, the rigid foundation approximation can likely be used to provide a reasonable estimate of damping from rotation vibrations. In this case, the effective foundation radius (r_θ) would be calculated using the full building dimensions. This recommendation also applies if continuous basement walls are present around the building perimeter. This case is referred to as stiff rotational coupling.

3. For buildings with a core of shear walls within the building, but no shear walls outside of this core, a conservative estimate of foundation damping can be obtained by calculating the effective foundation radius (r_θ) using the dimensions of the wall foundations (which, in this case, would be smaller than the overall building plan dimensions). This is an example of soft rotational coupling between the shear walls and other load bearing elements.
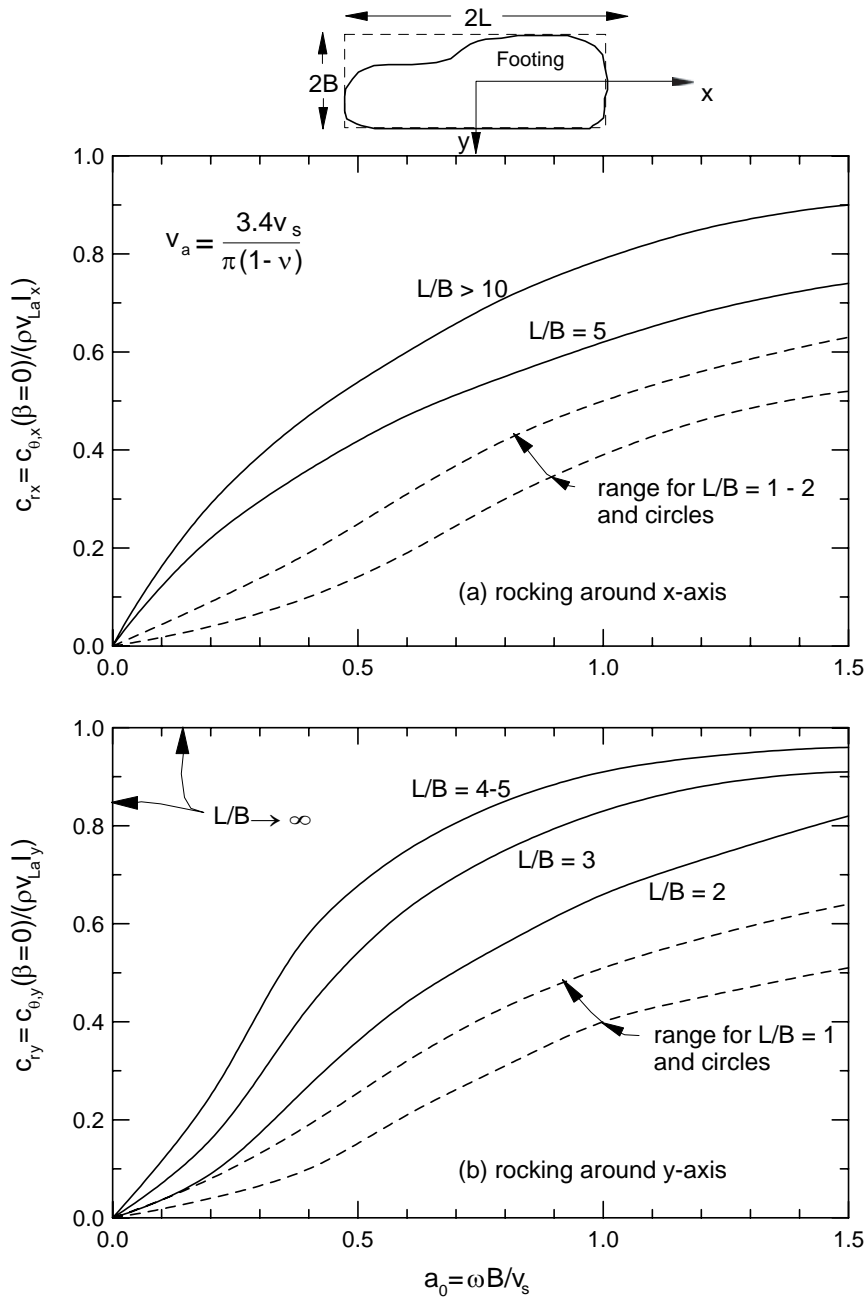
Figure E-10   Dashpot coefficients for radiation damping vs. normalized frequency for different foundation shapes (after Dobry and Gazetas, 1986).

4. For buildings with distributed shear walls at various locations around the building plan, the key issues are (1) the rotational stiffness of the building system as a whole (i.e., does the building tend to rotate as a single rigid block due to significant rotational stiffness coupling between adjacent elements, or do individual vertical components such as shear walls rotate independently of each other?), and (2) the degree to which destructive interference occurs between waves emanating from rotation of distinct foundation components.

In practice, it may sometimes be difficult to decide on the degree of rotational coupling between foundation elements. However, pushover analyses of the building with foundation springs utilized below foundation elements incorporate rotational coupling between foundation elements in a natural way. Hence, the results of such analyses can be used to infer the effective foundation size associated with the building's rotational impedance. This process is described in the following.

The derivation begins with the relationship between period lengthening and foundation spring stiffness values by Veletsos and Meek (1974):

$$\frac{\tilde{T}}{T} = \sqrt{1 + \frac{K^*_{fixed}}{k_x} + \frac{K^*_{fixed}h^2}{k_\theta}} \qquad \text{(E-12)}$$

In Equation E-12, the following quantities are known or can be estimated reliably:

- T is the fixed base first mode period, and can be evaluated from the model of the structure utilized in pushover analyses, but with foundation spring stiffnesses set to infinity.

- $\tilde{T}$ is the flexible base first mode period, and can be evaluated from the model of the structure utilized in pushover analyses including foundation springs. The foundation spring stiffness should reflect strain-degraded soil properties.

- Stiffness parameter K^*_{fixed} is the stiffness of the fixed-base structure, and can be evaluated as

$$K^*_{fixed} = M^* \left(\frac{2\pi}{T} \right)^2 \qquad \text{(E-13)}$$

   where M^* is the effective mass for the first mode calculated as the total mass times the effective mass coefficient (see ATC-40, Equation 8-21).

- Foundation stiffness parameter k_x represents the horizontal stiffness of the foundation system, and can be evaluated as described previously (Sections Sections E.3.1.1 – E.3.1.3). For the present application, a good approximation of k_x is K_x.

- Height h is the effective structure height taken as the full height of the building for one-story structures, and as the vertical distance from the foundation to the centroid of the first mode shape for multi-story

structures. In the latter case, h can often be well approximated as 70% of the total structure height.

Equation E-12 can then be re-arranged to estimate K_θ as follows:

$$K_\theta = \frac{K^*_{fixed}h^2}{\left(\dfrac{\tilde{T}}{T} \right)^2 - 1 - \dfrac{K^*_{fixed}}{K_x}} \qquad \text{(E-14)}$$

In the above, it has been assumed that $k_u \approx K_u$ and $k_\theta \approx K_\theta$, which is generally a reasonable approximation. The evaluation of an effective foundation radius from K_θ can be accomplished using Equation E-8, with the following result:

$$r_\theta = \left(\frac{3(1-\upsilon)K_\theta}{8G} \right)^{\frac{1}{3}} \qquad \text{(E-15)}$$

The value r_θ will decrease as the degree of rotational coupling decreases. For very stiff rotational coupling r_θ will approach the value that would be calculated from the moment of inertia derived from the full foundation dimension ($r_\theta = \sqrt[4]{4I_f/\pi}$).

A potential complication to the above may occur when foundations are closely spaced, and destructive interference occurs between waves emanating from adjacent foundation elements. If this occurred, the above formulation would be unconservative. Unfortunately, this topic has not been researched, and thus what footing separation distances constitute "close" and "widely spaced" is unknown, which in turn precludes the development of recommendations for the analysis of rotation damping for distributed walls.

Finally, it should be noted that for buildings with only moment resisting frames (no walls or braced frames), foundation rotation is not likely to be significant, and hence foundation flexibility effects on rotation damping are also likely insignificant.

E.3.2   Analysis of System Damping Ratios

The effect of foundation flexibility on the response of a structure can be visualized using the single-degree-of-freedom oscillator depicted in Figure E-11. In the figure, displacement u_g denotes the free-field ground motion, u_f denotes foundation translation relative to the
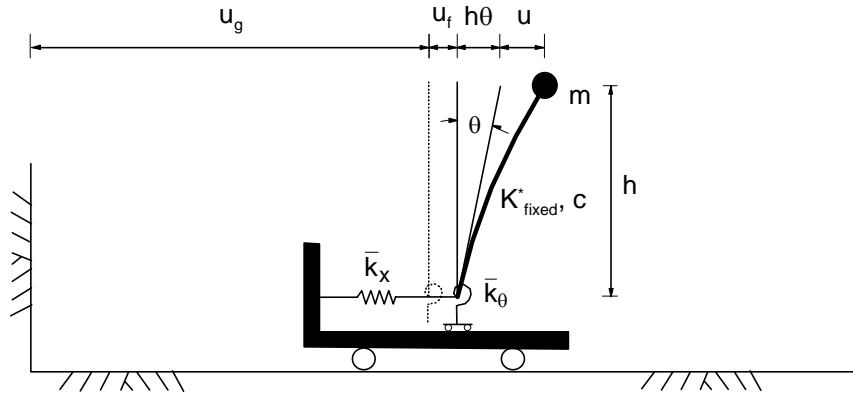
Figure E-11   Oscillator model for analysis of inertial interaction under lateral excitation.

free-field, θ denotes foundation rotation, and u denotes displacement resulting from deformation within the structure with stiffness K^*_{fixed} and dashpot coefficient c. SSI effects are manifested by a lengthening of the building period from the fixed-base case (T) to the flexible-base case ($\tilde{T}$), and by a change in the damping ratio (from β_i to β_o). These effects have been evaluated as closed-form expressions for the simple oscillator configuration shown in Figure E-11. In this case, the impedance function is represented by complex-valued terms for the translation ($\bar{k}_x$) and vertical plane rotation ($\bar{k}_\theta$) foundation vibration modes. A vertical foundation degree-of-freedom also exists (impedance term $\bar{k}_v$), but does not affect $\tilde{T}$ or β_o.

The flexible-base damping ratio of the oscillator has contributions from the viscous damping in the structure as well as radiation and hysteretic damping in the foundation. Jennings and Bielak (1973), Bielak (1975, 1976) and Veletsos and Nair (1975) expressed the flexible-base damping β_o as

$$\beta_0 = \beta_f + \frac{\beta_i}{\left(\tilde{T}_{eq}/T_{eq}\right)^3} \qquad \text{(E-16)}$$

where β_f is referred to as the foundation damping and represents the damping contributions from foundation-soil interaction (with hysteretic and radiation components), and $\tilde{T}_{eq}$ and T_{eq} represent the flexible- and fixed-base period of the structure accounting for the effects of yielding in the superstructure. From Equation E-16, it can be readily seen that the flexible-base damping, which is the damping ratio for which

response spectra should be evaluated, is a function of fixed-base damping (β_i), the period lengthening ratio ($\tilde{T}_{eq}/T_{eq}$), and β_f. Parameter β_i is generally assumed to be 5%. The period lengthening can be evaluated using the structural model used in pushover analyses as follows:

1. Evaluate the first-mode vibration period of the model, including foundation springs. This period is $\tilde{T}$. The period can be calculated using initial stiffness values for the structure and strain-degraded soil stiffness values.

2. Evaluate the first-mode vibration period of the model with the foundation springs removed (or their stiffness and capacity set to infinity). This period is T. As before, this period should correspond to pre-yield conditions.

3. Calculate the ratio $\tilde{T}/T$, which is the period lengthening under small-deformation (elastic) conditions.

4. Calculate $\tilde{T}_{eq}/T_{eq}$ using the following equation:

$$\frac{\tilde{T}_{eq}}{T_{eq}} = \left\{1 + \frac{1}{\mu_{sys}}\left[\left(\frac{\tilde{T}}{T}\right)^2 - 1\right]\right\}^{0.5} \qquad \text{(E-17)}$$

where μ_{sys} is the peak system ductility (including structure and soil effects).

With β_i and $\tilde{T}_{eq}/T_{eq}$ known, the estimation of β_o reduces to an analysis of foundation damping β_f. Graphical solutions and closed-form expressions for β_f

are available for the simple case of a circular foundation with radius r on a uniform halfspace with velocity v_s and hysteretic damping ratio β_s (Veletsos and Nair, 1975). The expression for β_f given by Veletsos and Nair is reproduced below,

$$\beta_f = \frac{\pi^4}{2}\frac{\gamma}{\sigma^3}\left(\frac{T_{eq}}{\tilde{T}_{eq}}\right)^3 \times$$

$$\left[\left[\frac{(2-\upsilon)\beta_x}{\alpha(\alpha_x + ia_0\beta_x)}\frac{r^2}{h^2} + \frac{3(1-\upsilon)\beta\beta_\theta}{\alpha_\theta(\alpha_\theta + ia_0\beta_\theta)}\right]\right] \qquad (E\text{-}18)$$

where $\sigma = v_S T/h$, $\gamma = m/(\rho\pi r^2 h)$,

$\alpha = \alpha_x - (1/(\tilde{T}f_0))^2$, $f_0 = \sqrt{K_x/m_f}/(2\pi)$, and

$$\beta = 1 - \frac{(1/(\tilde{T}_{eq}f_0))^2}{\alpha_x - ia_o\beta_x}$$

The first term within the brackets in Equation E-18 is related to damping from foundation vibration in translation whereas the second term is related to foundation rotation. To develop approximate solutions for β_f for non-circular foundations, Equation E-18 can be implemented with the radius and a_0 values in the first term taken as r_x and $(a_0)_x$, respectively, and in the second term as r_θ and $(a_0)_\theta$.

Parameters σ and γ in Equation E-18 represent the ratio of the soil-to-structure stiffness and structure-to-soil mass, respectively. Most conventional short-period building structures have $\sigma < 10$ and $\gamma \approx 0.1$ to 0.2 [a representative value of $\gamma = 0.15$ is recommended by Veletsos and Meek (1974)].

Due to the availability of these β_f formulations for rigid circular foundations on a halfspace, it is convenient to idealize actual foundation and site conditions in terms of representative values of velocity and foundation radius. As described in Section E.3.1, this can generally be accomplished by taking the representative site shear wave velocity as the soil velocity immediately beneath the foundation (v_{s0}), and by calculating effective foundation radii for translational and vertical plane rotation vibration modes (i.e. $r_x = \sqrt{A_f/\pi}$, $r_\theta = \sqrt[4]{4I_f/\pi}$). As noted in Section E.3.1.5, special consideration may be required for oblong foundations

and for the analysis of r_θ when shear walls or braced frames are distributed across the foundation plan.

Figure E-12 presents a customization of the Veletsos and Nair (1975) solution for β_f in which different ratios of r_θ/r_x are used (the original solution applied for true circular foundations in which $r_\theta/r_x = 1.0$) for three fixed values of h/r_θ. Note that terms $v_{s,r}$ and T_{eq} are used in the labeling of the horizontal axis to emphasize that strain-reduced shear wave velocities (evaluated from small-strain shear wave velocities using Table E-1) and ductility-reduced periods should be used in the analysis of β_f. Figure E-13 presents an identical set of plot to Figure E-12, but for a shallowly embedded foundation using the simplified approach for estimating embedment effects discussed in Section E.3.1.3.

In Figure E-12, β_f is seen to increase with $h/(v_{s,r}T_{eq})$ and to decrease with h/r_θ. The decrease of β_f with h/r_θ indicates that lateral movements of the foundation (which dominate at low h/r_θ) dissipate energy into soil more efficiently than foundation rotation (which dominates at high h/r_θ). For a given h/r_θ, the suites of curves within each frame indicate that β_f increases with decreasing r_θ/r_x for $h/(v_{s,r}T_{eq}) < \sim 0.2$. This occurs because decreasing r_θ/r_x implies increasing foundation area (r_x), which provides additional damping from translational vibration. Note also the significantly higher damping when hysteretic damping is included ($\beta_s = 0.1$) as opposed to radiation damping only ($\beta_s = 0$). Finally, a comparison of β_f in Figures E-12 and E-13 indicates that additional foundation damping occurs for embedded foundations, as expected.

The above analysis procedure for β_f has been found to reproduce reasonably accurately SSI effects on first-mode vibration properties of actual structures, as inferred from system identification analyses of recorded motions (Stewart et al., 1999). These case history studies revealed that the single most important parameter controlling the significance of inertial interaction is $h/(v_{s,r}T_{eq})$, and that inertial SSI effects are generally small for $h/(v_{s,r}T_{eq}) < 0.1$. This condition occurs for flexible structures such as moment frame buildings located on competent soil or rock. Conversely, SSI effects tend to be significant for stiff structures such as shear wall or braced frame buildings, particularly when located on soft soil.

To simplify the evaluation of foundation damping ratios in engineering practice, the fact that both β_f and $\tilde{T}_{eq}/T_{eq}$ are strongly dependent on $h/(v_{s,r}\tilde{T}_{eq})$ is
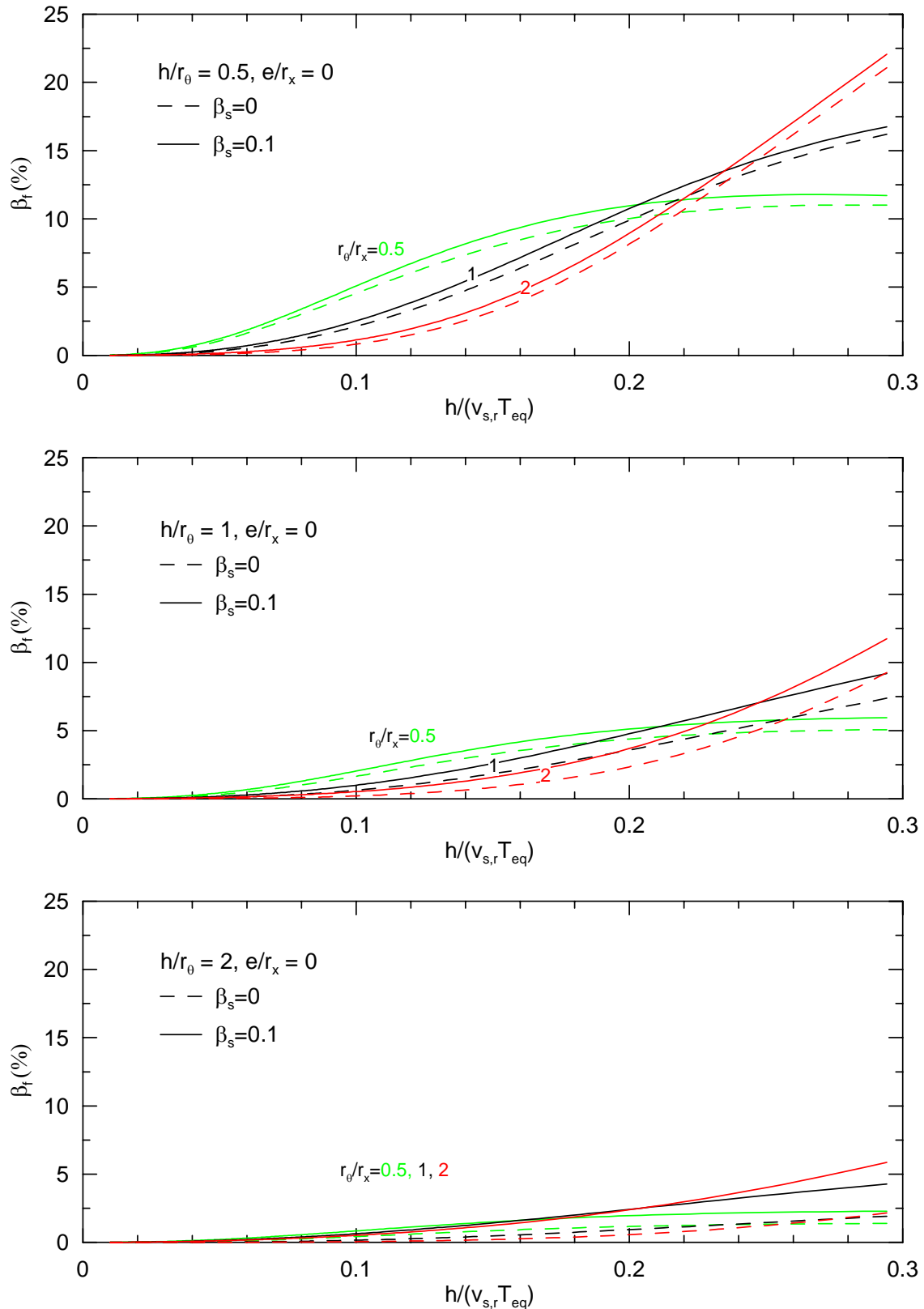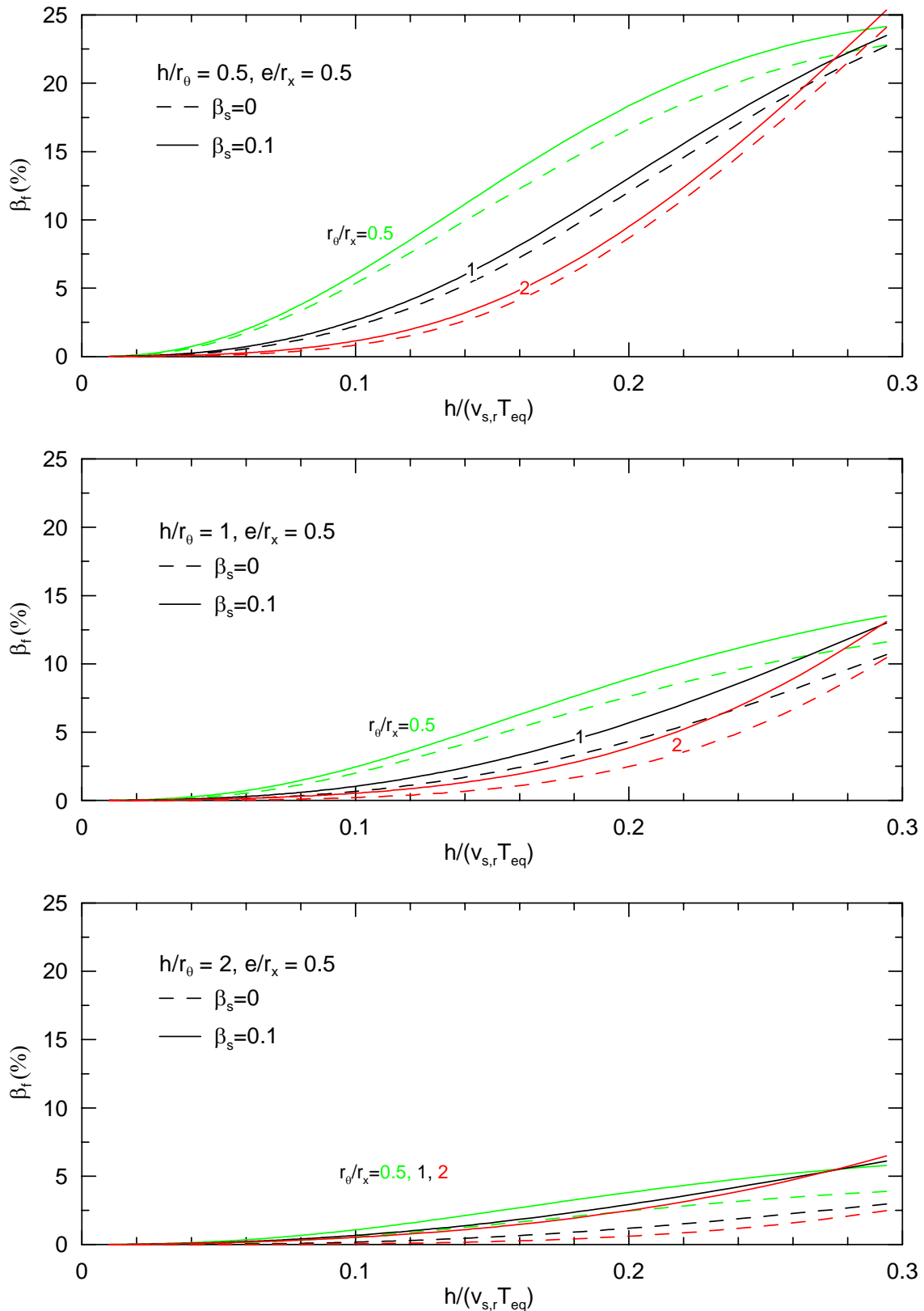
Figure E-12   Foundation damping for single degree-of-freedom structures on elastic halfspace with various aspect ratios (h/r_θ) and foundation shapes (r_θ/r_x), non-embedded foundation case $(e/r_x = 0)$.

Figure E-13   Foundation damping for single degree-of-freedom structures on elastic halfspace with various aspect ratios (h/r_θ) and foundation shapes (r_θ/r_x), small foundation embedment case $(e/r_x = 0.5)$.
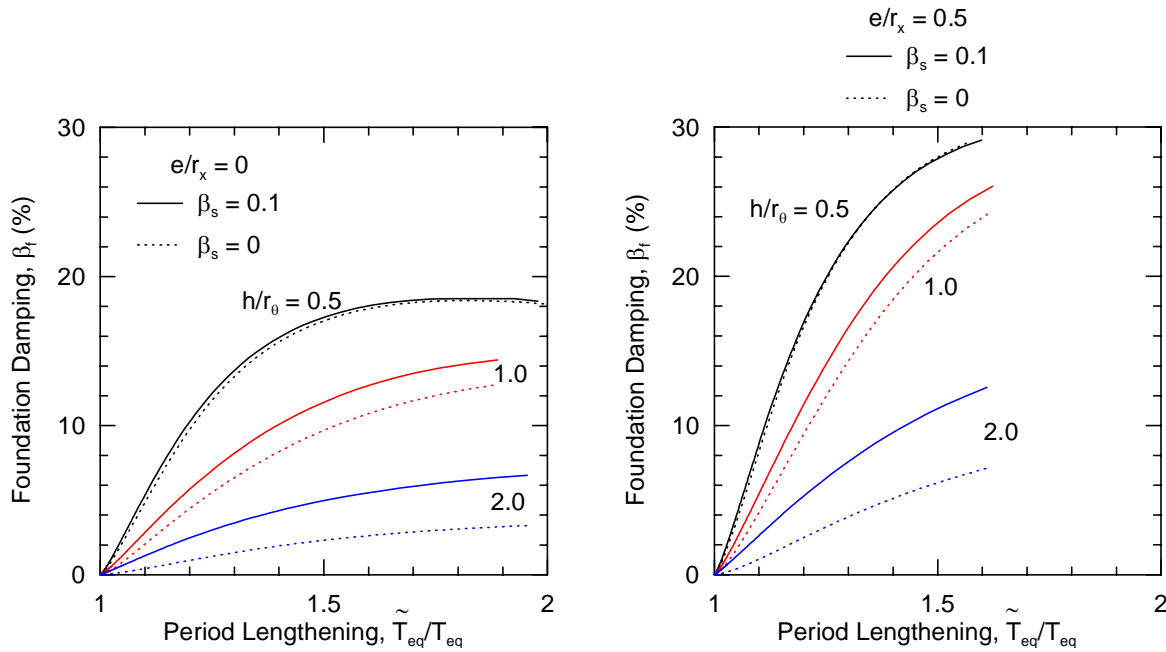
Figure E-14   Foundation damping factor β_f expressed as a function of period lengthening $\tilde{T}_{eq}/T_{eq}$ for different building aspect ratios (h/r_θ) and embedment ratios (e/r_x).

leveraged to generate curves relating β_f to $\tilde{T}_{eq}/T_{eq}$ without the use of $h/(v_{s,r}T_{eq})$. The relationship was developed by also assuming equi-dimensional foundations ($r_\theta/r_x = 1.0$). Although results are shown for significant hysteretic soil damping (β_s=0.1) and zero hysteretic damping (β_s=0), use of the β_s=0 results is recommended because ductility in soil springs is already included as part of structural pushover analysis. The result is shown in Figure E-14, and requires the user only to know $\tilde{T}_{eq}/T_{eq}$ (easily obtained from a structural model, as described above) as well as h/r_θ, and e/r_x. The damping ratios in Figure E-14 are conservative for $r_\theta/r_x < 1.0$, which is generally the case for buildings.

Another point that should be made in connection with the use of Figure E-14 is that the foundation spring stiffnesses used in the analysis of $\tilde{T}_{eq}/T_{eq}$ are based on average shear wave velocities to a depth of approximately r_x, whereas the velocity that should be used for the analysis of foundation damping at a non-uniform site is v_{s0} (the velocity immediately below the foundation, which is typically smaller than the average v_s over a depth range). The fact that β_f is evaluated in terms of $\tilde{T}_{eq}/T_{eq}$ therefore introduces a bias, although the bias will generally result in underprediction of β_f,

which is conservative and thus acceptable for a simplified design procedure.

Flexible base damping β_o can actually increase or decrease relative to β_i depending on $\tilde{T}_{eq}/T_{eq}$ and foundation damping β_f. The effect of the change in damping from β_i to β_o on spectral acceleration can be estimated using the procedures in Section 6.3.

E.3.3   Simplified Procedure for Design

1. Evaluate the linear periods for the structural model assuming a fixed base, T, and a flexible-base using appropriate foundation modeling assumptions, $\tilde{T}$. Guidelines for the evaluation of soil spring stiffnesses are provided in FEMA 356 and ATC-40.

2. Calculate the effective structural stiffness for fixed base conditions, K^*_{max} using Equation E-13.

3. Determine the equivalent foundation radius for translation, $r_x = \sqrt{A_f/\pi}$, where A_f is the area of the foundation footprint if the foundation components are inter-connected laterally.

4. Calculate the translational stiffness of the foundation, K_x. This can be evaluated using the proce-

dures in FEMA 356 (Chap. 4) or ATC-40 (Chap. 10). For many applications, K_x can be estimated using Equations E-8 and E-11.

5. Calculate the equivalent foundation radius for rotation, r_θ, using Equations E-14 and E-15.

6. Determine the foundation embedment, e, if applicable.

7. Estimate the effective period lengthening ratio, $\tilde{T}_{eff} / T_{eff}$, for the nonlinear structure using Equation E-17.

8. Evaluate the initial fixed base damping ratio for the structure (β_i), which is often taken as 5%.

9. Using Figure E-14, determine foundation damping (β_f) based on $\tilde{T}_{eq} / T_{eq}$, e/r_x, and h/r_θ. Intermediate values may be interpolated from these figures. An approximation to those curves is given by the following for the case without hysteretic soil damping (denoted $\beta_s = 0$):

$$\beta_f = a_1\left(\frac{\tilde{T}_{eq}}{T_{eq}} - 1\right) + a_2\left(\frac{\tilde{T}_{eq}}{T_{eq}} - 1\right)^2 \qquad \text{(E-19)}$$

where β_f is in percent and

$$a_1 = c_e \exp\left(4.7 - 1.6 h/r_\theta\right) \qquad \text{(E-20)}$$

$$a_2 = c_e\left[25\ln\left(h/r_\theta\right) - 16\right] \qquad \text{(E-21)}$$

$$c_e = 1.5\left(e/r_x\right) + 1 \qquad \text{(E-22)}$$

The above equations are most applicable for $\tilde{T}_{eff} / T_{eff} < 1.5$, and generally provide conservative (low) damping estimates for higher $\tilde{T}_{eff} / T_{eff}$.

10. Evaluate the flexible base damping ratio (β_0) from β_i, β_f, and $\tilde{T}_{eff} / T_{eff}$ using Equation E-16.

11. Evaluate the effect on spectral ordinates of the change in damping ratio from β_i to β_0 in accordance with Section 6.3 then modify the spectrum for free-field motion or that for the foundation input motion if kinematic effects are being included.

The change in spectral ordinate computed above can be combined with the change in spectral ordinate from kinematic interaction.

Limitations on the damping analysis described above include the following:

- The analysis approach should not be used when shear walls or braced frames are spaced sufficiently closely that waves emanating from distinct foundation elements will destructively interfere with each other across the period range of interest. Further discussion is presented in Section E.3.1.5.

- The analysis can be conservative (under-predicting the damping) when foundation aspect ratios exceed about 2:1. Further discussion is presented in Section E.3.1.4.

- The analysis is conservative when foundations are deeply embedded, $e/r_x > 0.5$. Further discussion is presented in Section E.3.1.3.

- The analysis is unconservative (over-predicting the damping) if $v_s T/r_x > 2\pi$ (where v_s = average shear wave velocity to a depth of about r_x) and the foundation soils have significant increases of shear stiffness with depth. Further discussion is presented in Section E.3.1.2.

- The analysis is unconservative if the foundation soil profile consists of a soil layer overlying a very stiff material (i.e., there is a pronounced impedance contrast within the soil profile), and if the system period is greater than the first-mode period of the layer. Further discussion is presented in Section E.3.1.2.

E.4   References

ASCE, 2000, *Prestandard and Commentary for the Seismic Rehabilitation of Buildings*, FEMA 356 Report, prepared by the American Society of Civil Engineers for the Federal Emergency Management Agency, Washington, D.C.

ATC, 1996, *Seismic Evaluation and Retrofit of Concrete Buildings*, ATC-40 Report, funded by the Seismic Safety Commission, published by the Applied Technology Council, Redwood City, California.

Apsel, R.J. and Luco, J.E., 1987, "Impedance functions for foundations embedded in a layered medium: an integral equation approach," *J. Earthquake Engrg. Struct. Dynamics*, Vol. 15, No. 2, pp. 213-231.

Bielak, J., 1975, "Dynamic behavior of structures with embedded foundations," *J. Earthquake Engrg. Struct. Dynamics*, Vol. 3, pp. 259-274.

Bielak, J., 1976, "Modal analysis for building-soil inter-action," *J. Engrg. Mech.*, Vol. 102, American Society of Civil Engineers, pp. 771-786.

BSSC, 2001, *NEHRP Recommended Provisions for Seismic Regulations for New Buildings and Other Structures,* FEMA 368 Report, prepared by the Building Seismic Safety Council for the Federal Emergency Management Agency, Washington, D.C.

Crouse, C.B., Hushmand, B., Luco, J.E., and Wong, H.L., 1990, "Foundation impedance functions: Theory versus Experiment," *J. Geotech. Engrg.*, Vol. 116, No. 3, American Society of Civil Engineers, pp. 432-449.

Day, S.M.,1978, "Seismic response of embedded foundations," *Proc. ASCE Convention,* Chicago, Illinois, October, Preprint No. 3450.

de Barros, F.C.P. and Luco, J.E., 1995, "Identification of foundation impedance functions and soil properties from vibration tests of the Hualien containment model," *J. Soil Dyn. Earthquake Eng.*, Vol. 14, pp. 229-248.

Dobry, R. and Gazetas, G., 1986, "Dynamic response of arbitrarily shaped foundations," *J. Geotech. Engrg.*, Vol. 112, No. 2, American Society of Civil Engineers, pp. 109-135.

Elsabee, F. and Morray, J.P., 1977, *Dynamic Behavior of Embedded Foundations*, Rpt. No. R77-33, Dept. of Civil Engrg., MIT, Cambridge, Massachusetts.

Gazetas, G., 1991a, "Formulas and charts for impedances of surface and embedded foundations," *J. Geotech. Engrg.*, Vol. 117, No. 9, pp. 1363-1381.

Gazetas, G., 1991b, *Foundation Vibrations, Foundation Engineering Handbook*, Chapter 15, H.-Y. Fang, ed., 2nd Edition, Chapman and Hall, New York, New York.

Iguchi, M. and Luco, J.E., 1982, "Vibration of flexible plate on viscoelastic medium," *J. Engrg. Mech.*, Vol. 108, No. 6, American Society of Civil Engineers, pp. 1103-1120.

Jennings, P.C. and Bielak, J., 1973, "Dynamics of building-soil interaction*,*" *Bull. Seism. Soc. Am.*, Vol. 63, pp. 9-48.

Kim, S., 2001, *Calibration of Simple Models for Seismic Soil Structure Interaction from Field Perfor-mance Data*, Ph.D. Dissertation, University of California, Los Angeles.

Kim, S. and Stewart, J.P., 2003, "Kinematic soil-structure interaction from strong motion recordings," *J. Geotech. & Geoenv. Engrg.*, Vol. 129, No. 4, American Society of Civil Engineers, pp. 323-335.

Lin, A.N. and Jennings, P.C., 1984, "Effect of embedment on foundation-soil impedances," *J. Engrg. Mech.*, Vol. 110, No. 7, American Society of Civil Engineers, pp. 1060-1075.

Liou, G.-S. and Huang, P.-H., 1994, "Effect of flexibility on impedance functions for circular foundations," *J. Engrg. Mech.*, Vol. 120, No. 7, American Society of Civil Engineers, pp. 1429-1446.

Luco, J.E., Trifunac, M.D., and Wong, H.L., 1988, "Isolation of soil-structure interaction effects by full-scale forced vibration tests," *J. Earthquake Engrg. Struct. Dynamics*, Vol. 16, No. 1, pp. 1-21.

Mita, A. and Luco, J.E., 1989, "Dynamic response of a square foundation embedded in an elastic halfspace," *J. Soil Dynamics and Earthquake Engrg.*, Vol. 8, No. 2, pp. 54-67.

Riggs, H.R. and Waas, G., 1985, "Influence of foundation flexibility on soil-structure interaction," *J. Earthquake Engrg. Struct. Dynamics*, Vol. 13, No. 5, pp. 597-615.

Roesset, J.M., 1980, "A review of soil-structure interaction," in *Soil-Structure Interaction: The Status of Current Analysis Methods and Research*, J.J. Johnson, ed., NUREG/CR-1780 Report and UCRL-53011 Report, U.S. Nuclear Regulatory Com., Washington D.C., and Lawrence Livermore Lab., Livermore, California.

Stewart, J.P., Seed, R.B., and Fenves, G.L., 1999, "Seismic soil-structure interaction in buildings. II: Empirical findings," *J. Geotech. & Geoenv. Engrg.*, Vol. 125, No. 1, American Society of Civil Engineers, pp. 38-48.

Stewart, J.P., Kim, S., Bielak, J., Dobry, R., and Power, M., 2003, "Revisions to soil structure interaction procedures in NEHRP design provisions," *Earthquake Spectra*, Vol. 19, No. 3, pp. 677-696.

Veletsos, A.S. and Meek, J.W., 1974, "Dynamic behavior of building-foundation systems," *J. Earthquake Engrg. Struct. Dynamics*, Vol. 3, No. 2, pp. 121-138.

Veletsos, A.S. and Nair V.V., 1975, "Seismic interaction of structures on hysteretic foundations," *J. Struct. Engrg.*, Vol. 101, No. 1, American Society of Civil Engineers, pp. 109-129.

Veletsos, A.S. and Prasad, A.M., 1989, "Seismic interaction of structures and soils: stochastic approach," *J. Struct. Engrg.*, Vol. 115, No. 4, American Society of Civil Engineers, pp. 935-956.

Veletsos, A.S. and Verbic, B., 1973, "Vibration of viscoelastic foundations," *J. Earthquake Engrg. Struct. Dynamics*, Vol. 2, No. 1, pp. 87-102.

Veletsos, A.S. and Wei, Y.T., 1971, "Lateral and rocking vibrations of footings," *J. Soil Mech. and Foundations Div.*, Vol. 97, No. 9, American Society of Civil Engineers, pp. 1227-1248.

Veletsos, A.S., Prasad, A.M., and Wu, W.H., 1997, "Transfer functions for rigid rectangular foundations," *J. Earthquake Engrg. Struct. Dynamics*, Vol. 26, No. 1, pp. 5-17.

Wong, H.L., Trifunac, M.D., and Luco, J.E., 1988, "A comparison of soil-structure interaction calculations with results of full-scale forced vibration tests," *Soil Dyn. & Earthquake Engrg.*, Vol. 7, pp. 22-31.

F. Supplementary Information and Data on Multi-Degree-of-Freedom Effects

F.1 Introduction

F.1.1 Objectives

The primary objective of the multi-degree-of-freedom (MDOF) studies is to illustrate the application of current nonlinear static procedures (proposed within ATC-40 and FEMA 356 and elsewhere) for estimating peak response quantities (floor and roof displacements, interstory drifts, story shears, and overturning moments) for a range of structural models/behaviors and for both ordinary and near-fault ground motions. The intention is to illustrate the range of results obtained with these procedures and their relationship to the results of nonlinear dynamic analysis. Secondary objectives include the identification of potential limitations of these procedures and the identification of possible improvements. The examples provide a uniform basis for evaluating the strengths and weaknesses of the various procedures in a single study, in which comparisons are made using a consistent framework and methodology. The study has a limited scope, and must be considered together with other, more detailed studies on the specific procedures.

F.1.2 Scope

The evaluation of MDOF effects is divided into two portions. The first compares the response quantities determined in dynamic analyses with those estimated using various pushover procedures, for five building models subjected to both ordinary and near-fault ground motions. These comparisons are made assuming that the peak roof drift (or target displacement) is determined accurately by the pushover procedures. The second portion assesses the accuracy of the estimates of peak roof drift determined using "equivalent" single-degree-of-freedom (SDOF) systems.

Section F.2 describes the example buildings, analytical models and properties, and ground motions. Section F.3 describes the simplified inelastic analysis procedures. Section F.4 addresses the accuracy of the estimates of response quantities made using the simplified procedures for both regular and near-field ground motions. Section F.5 addresses the accuracy of "equivalent" SDOF estimates of peak roof displacement using relationships provided in ATC-40 and FEMA 356. Section F.6 provides information relating to a new approach for using scaled ground motion records in

nonlinear response history analysis. Section F.7 reports some results obtained using an energy-based pushover procedure. Section F.8 contains (1) detailed descriptions of the ground motions used in the study, (2) detailed plots comparing the distributions of response quantities observed in the dynamic analyses with the deterministic values determined in the pushover analyses, (3) summary error statistics, and (4) plots of the observed coefficients of variation of the peak dynamic response quantities.

The ordinary ground motions were scaled to achieve predetermined values of peak roof drift. The peak roof drifts were selected to represent elastic response and two levels of nonlinear response. Thus, while the roof displacements achieved in the dynamic and static analyses were equal to the predetermined target values, the frequency content and timing of the ground motion records differed and introduced variability to the other peak response quantities. Of primary interest is the comparison of the deterministic estimates of the response quantities obtained using the simplified inelastic procedures to the statistical distributions of the peaks of these quantities determined by dynamic analyses.

The near-fault ground motions were applied at their natural (unscaled) intensities because of a concern that scaled near-fault records may be unrealistic. Thus, the target displacement used for each simplified inelastic procedure was set equal to the peak roof displacement observed for each near-fault ground motion. These results allow for comparisons of estimated and actual response quantities for individual records, as well as the determination of normalized errors. The small number of near-fault ground motions used and the lack of consistency in target displacements make the data less statistically meaningful than in the case of the ordinary ground motions. Consequently, the evaluation of the inelastic procedures for the near-fault motions is more qualitative, while the evaluation for the ordinary motions has a stronger quantitative basis.

F.2 Example Buildings and Demand Parameters

Five example buildings were selected for study. These consist of two steel moment-resistant frame buildings designed as part of the FEMA-funded SAC joint
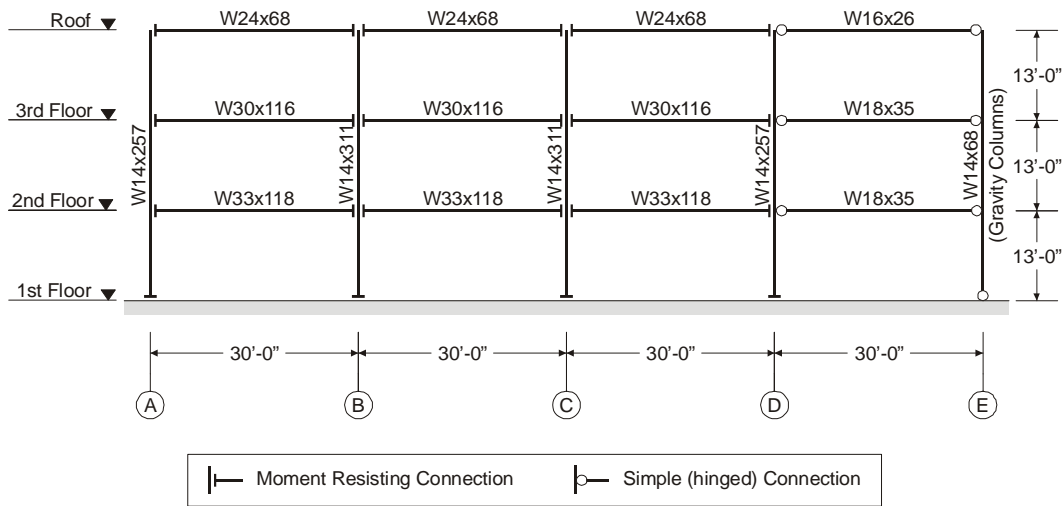

Figure F-1   Elevation view of the 3-story (regular and weak-story) steel frames used in the study.

venture project, modifications to each of these frames to induce weak story behavior, and a reinforced concrete shear wall building described in ATC-40.

The 3- and 9-story steel frames were designed and modeled in Drain-2DX as part of the SAC joint venture effort. The frames adopted in this study had been designed for Los Angeles using the 1994 *Uniform Building Code*, and employed "pre-Northridge" special moment-resistant frame connections along the building perimeter. The weak stories were introduced into the lowest story of the 3- and 9-story frames by reducing the flexural strengths of the columns, without changing their stiffnesses. This was done in order to affect the mechanism while keeping the elastic properties (e.g. periods of vibration) the same as for the regular frames. The lowest story column strengths were determined by trial and error to ensure that a weak story mechanism developed in dynamic analyses using records scaled to cause peak roof drifts equal to 4% of the building height.

The 8-story reinforced concrete wall building was based on the Escondido Village building that is described in ATC-40.

Detailed descriptions of these buildings follow.

F.2.1   Prototype Buildings

F.2.1.1   Regular 3-Story Frame

The 3-story steel frame, as shown in Figure F-1, is the north-south lateral force-resisting system of a

benchmark building for the SAC project. The building is 120 ft by 180 ft in plan and 39 ft in elevation, with a 2-ft extension from the perimeter column lines to the building edge. Typical floor-to-floor height is 13 ft. The building consists of four bays in the north-south direction and six bays in the east-west direction. As shown in Figure F-1, all connections are moment-resistant for the three left-most bays of the frame under consideration. The "gravity columns" on the right, labeled as such in the figure, are used to model *P*-delta effects, as described in Section F.2.2. The assumed gravity loading for the building is shown in Table F-1.

Table F-1   Assumed Loading for the 3- and 9-Story Buildings

Type	Intensity (psf)
Floor dead load for weight calculations	96
Floor dead load for mass calculations	86
Roof dead load excluding penthouse	83
Penthouse dead load	116
Reduced live load per floor and for roof	20

F.2.1.2   Regular 9-Story Frame

The 9-story steel frame is part of the lateral force-resisting system of another SAC model building. The building is 150 ft by 150 ft in plan and 122 ft in elevation with a 2 ft extension from the perimeter column lines to the building edge. As shown in
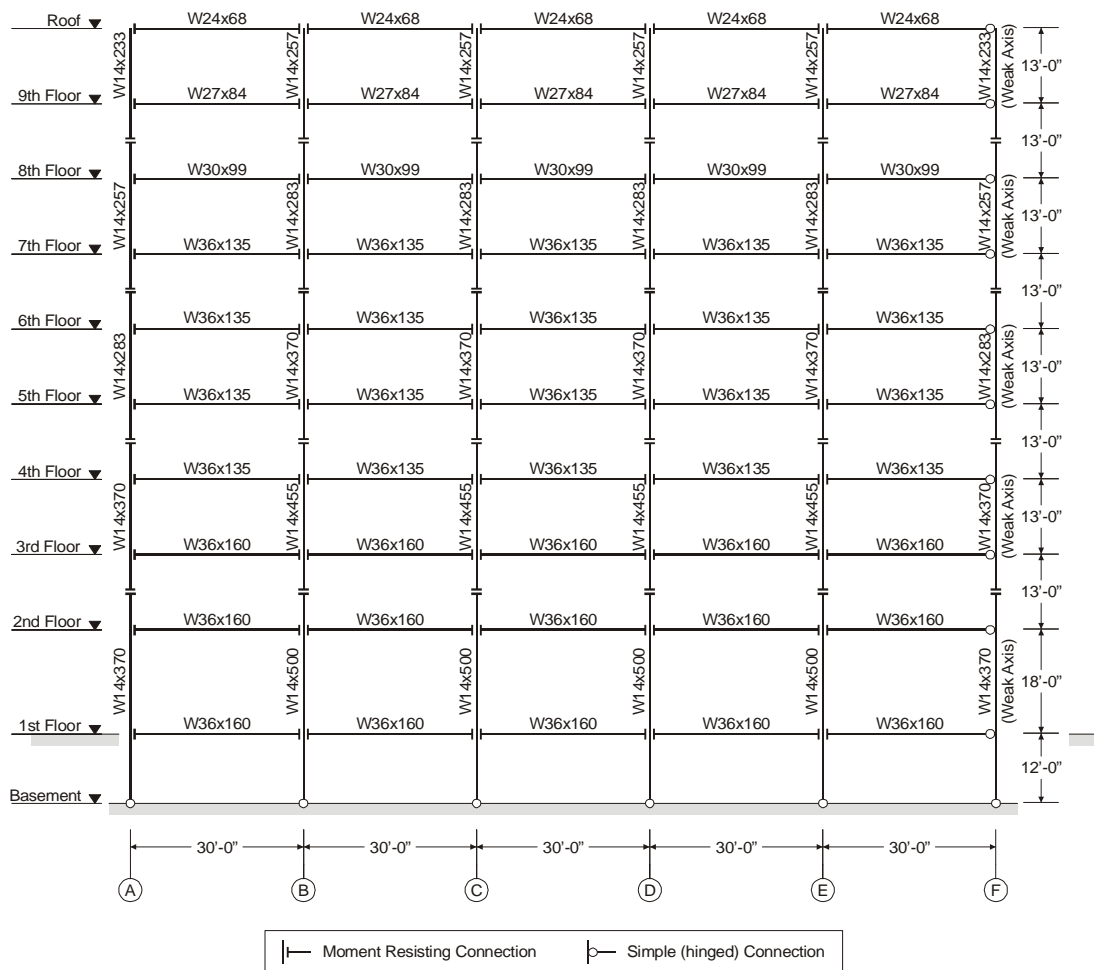
Figure F-2   Elevation view of the 9-story (regular and weak-story) steel frames used in the study.

Figure F-2, the frame considered in this study consists of five 30-ft long bays. The typical floor-to-floor height is 13 ft. The 1st story and basement floor-to-floor heights are 18 ft and 12 ft, respectively. The assumed gravity loading for this building is the same as that for the 3-story building.

F.2.1.3   3-Story Weak Story Frame

The strengths of the lowest story columns of the regular 3-story frame (Section F.2.1.1) were reduced to create the 3-story weak story frame. Based on the response observed in dynamic analyses, the lowest story column strength were reduced to 50% of their original values in order to develop weak-story behavior at a roof drift of 4% of the building height. No other changes were made.

F.2.1.4   9-Story Weak Story Frame

The strengths of the lowest story columns of the regular 9-story frame (Section F.2.1.2) were reduced to create the 9-story weak story frame. Based on dynamic response, the lowest story column strengths were reduced to 60% of their original values in order to develop weak-story behavior at a roof drift of 4% of the building height. No other changes were made.

F.2.1.5   8-Story Shear Wall

The 8-story shear wall represented in this study is one of the two longitudinal walls of the midrise building at Escondido Village, located at line A and between lines 4 and 6 of the as-built drawings of June 10, 1964. The wall is 8 stories in height, with a basement below. This structural wall was selected because it plays a substantial role in the lateral force resisting system for

Table F-2   **Properties of the 8-Story Reinforced Concrete Structural Wall**

Item	Gathered Information from ATC-40 Vol. 2 (ATC) and As-Built Drawings (DWG)		Wall Used in this Study
Typical floor height	9 ' – 1" (Source: ATC and DWG)		9 ' – 1"
Basement height	12' – 7" (Source: ATC and DWG)		12' – 7"
Wall length	25' – 5" (Source: ATC and DWG)		25'
Wall thickness	Typical floor:	10" (Source: ATC) 9 3/4" (Source: DWG)	10"
	Basement	12" (Source: ATC and DWG)	12"
Boundary reinforcement	7th floor to roof 5th floor to 7th floor 3rd floor to 5th floor Foundation to 3rd floor	3 #6 (Source: DWG) 3 #11 (Source: DWG) 6 #11 (Source: DWG) 9 #11 (Source: DWG)	3 #6 3 #11 6 #11 9 #11
Confinement reinforcement at boundary	#3 @ 12" with 135° hook (Source: ATC)		#3 @ 12" with 135° hook
Distributed vertical reinforcement	Typical floor	$\rho = 0.0023$ (Source: ATC) 2 #4 @ 18" (Source: DWG, $\rho = 0.0023$)	2 #4 @ 18" ($\rho = 0.0023$)
	Basement	2 #5 @ 18" (Source: DWG, $\rho=0.00287$)	2 #5 @ 18" ($\rho=0.00287$)
Horizontal reinforcement	Typical floor	$\rho = 0.0023$ (Source: ATC) 2 #4 @ 18" (Source: DWG, $\rho = 0.0023$)	2 #4 @ 18" ($\rho = 0.0023$)
	Basement	2 #4 @ 12" (Source: DWG, $\rho = 0.00278$)	2 #4 @ 12" ($\rho=0.00278$)
Concrete strength	3000 psi (Source: DWG) 3000 psi (Design) and 2470 psi (Test) (Source: ATC)		3000 psi
Reinforcing steel yield strength	40 ksi (Source: ATC and DWG)		40 ksi

the building and its location suggests that the degree of coupling is negligible. The information for this wall was gathered from ATC-40 Vol. 2 and the as-built drawings. Table F-2 summarizes the properties of the wall used in this study. Figure F-3 shows the elevation and cross sections of the wall. The assumed gravity loading is shown inTable F-3.

F.2.2   Modeling

Two-dimensional models of the frame and wall buildings were prepared using standard elements that are available in Drain-2DX version 1.10. The models.. were subjected to horizontal excitation or lateral forces after the application of gravity loads. Inertial mass resisted horizontal excitations only. *P*-Delta effects were considered for all building models, using dead

loads in combination with 40% of the design live loads. For the frame models, these loads were applied to a separate gravity column that was connected to the lateral force resisting system. The gravity column was pinned at each story, providing a "truss-bar" approximation of the effect of *P*-Delta on the global stiffness matrix. For the wall model, gravity loads attributary to the walls were applied. This induced compression in the concrete and steel fibers of the model, causing the wall to have an initial stiffness approximately equal to the gross section stiffness.

Fixed and variable time step solution schemes were employed, in all cases with events monitored. The default overshoot tolerances were used for members modeled with a plastic hinge beam-column element (Type 02). The overshoot tolerances for the members

(a) Wall elevation

(b) Plan view of wall cross section: basement to 1st floor
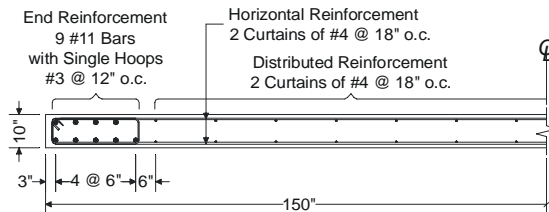
(c) Plan view of wall cross section: 1st floor to 3rd floor
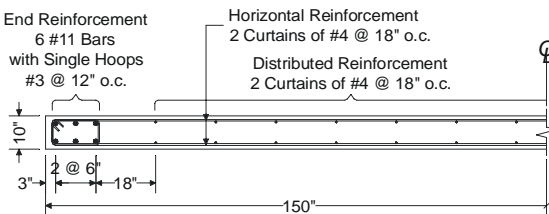
(d) Plan view of wall cross section: 3rd floor to 5th floor

Figure F-3   Elevation and plan views of the 8-story reinforced concrete shear wall used in the study

(e) Plan view of wall cross section: 5th floor to 7th floor

(f) Plan view of wall cross section: 7th floor to roof

Figure F-3   Elevation and plan views of the 8-story reinforced concrete shear wall used in the study (continued)

Table F-3   **Assumed Loading for the 8-Story Building**

Type	Intensity (psf)
Floor dead load for weight calculations	165
Floor dead load for mass calculations	165
Roof dead load	145
Reduced live load per floor and for roof	20

modeled with a fiber beam-column element (Type 15) were set to be 0.01% of the yield strengths of the fibers.

The steel frames were modeled using beam-column elements (Type 02), as illustrated in Figures F-4 and F-5. The SAC M1 model was used in this study, in which beams and columns span between nodes located at the intersections of the beam and column centerlines; rigid end offsets were set to zero and beam column joints were not modeled. Material yield strengths were 49.2 and 57.6 ksi, for the beams and columns respectively, and the post-yield stiffness of the moment-curvature relationship was set to 3% of the initial stiffness, as assumed in the SAC models. Gravity loads were applied along the frame elements as well as at the ends of these elements, at the nodes located where the
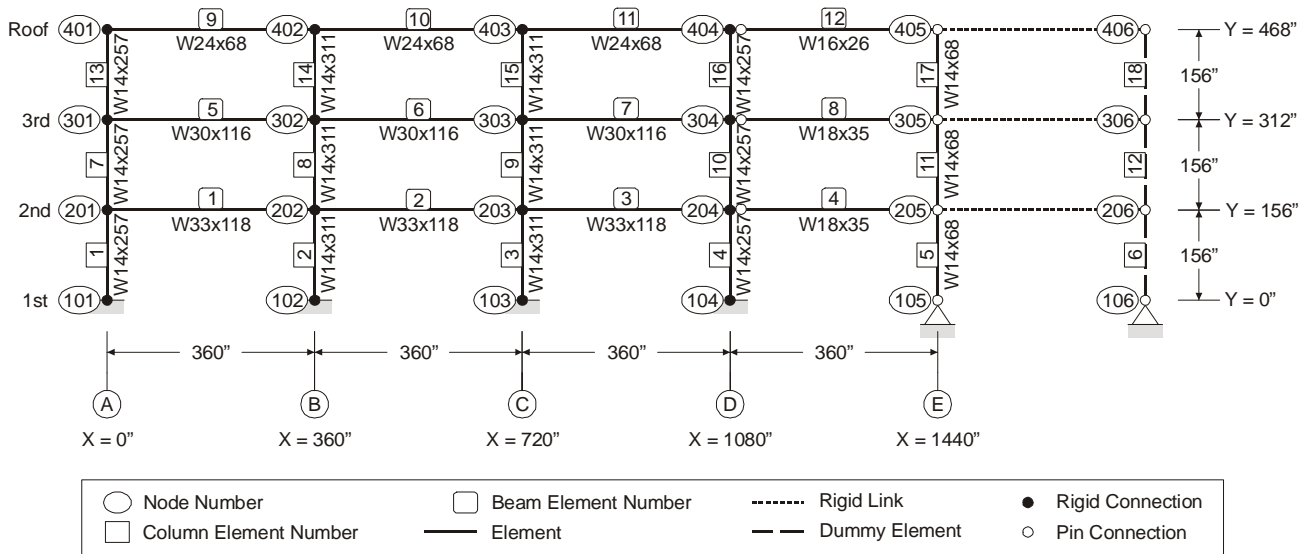
Figure F-4   Drain model of the 3-story (regular and weak story) steel frames.

beams and columns intersect. To avoid the possibility that overturning effects might influence the formation of column hinges, an effect that would be highly specific to the geometry and specific details of these particular frames, the flexural strengths of both beam and column elements were modeled to be independent of axial force. The strength and stiffness of the gravity column framing is neglected in the M1 model.

The reinforced concrete shear wall was modeled using a fiber element (Type 15), as illustrated in Figure F-6. The wall consists of nine elements, one element per story. Each element is divided into four segments along the element axis. The cross section of each segment is divided into 12 fibers. The base of the wall is assumed to be fixed, and a horizontal restraint is provided at the 1st floor. Inelasticity in flexure was modeled; it was assumed that the wall would have sufficient shear strength and that only elastic shear deformations needed to be represented. While the fibers had zero tensile strength, preloading by gravity ensured that all fibers contributed to the initial stiffness of the wall.

Because the degree of confinement at the wall boundaries is considered low, an unconfined concrete stress-strain relationship shown in Figure F-7(a) was used. For the longitudinal steel, a bilinear stress-strain relationship was employed [Figure F-7(b)].

The mass is lumped at the ends of the element. The mass contribution (assumed uniform) for the wall is

calculated in such a way that the resulting fundamental period, based on effective stiffness, matches the elastic period reported in ATC-40, resulting in a mass contribution of 19.2% of the total floor mass. The resulting base shear coefficient at yield, obtained from a pushover analysis, is 0.129.

For the frame models, a Rayleigh damping ratio of 2% was applied to the first mode period and a period of 0.2 s, as assumed in the SAC models. For the wall model, 5% Rayleigh damping was set for the first and fourth mode periods corresponding to gross-section stiffness. In all models, the modal periods used to determine the damping ratios were those computed before gravity loading was applied.

F.2.2.1   Dynamic Characteristics of Models

The first three periods and mode shapes for the frame and wall buildings are provided in Table F-4. Because flexural cracking of the reinforced concrete wall was modeled, modal properties reported for the 8-story reinforced concrete shear wall (part b of Table F-4) are the properties determined based on the tangent stiffness of the cracked wall, determined in a first mode pushover analysis at a base shear equal to 60% of the base shear corresponding to yield of a bilinear curve that was fitted to the capacity curve.

To illustrate basic characteristics of each building model, capacity curves are presented for the five
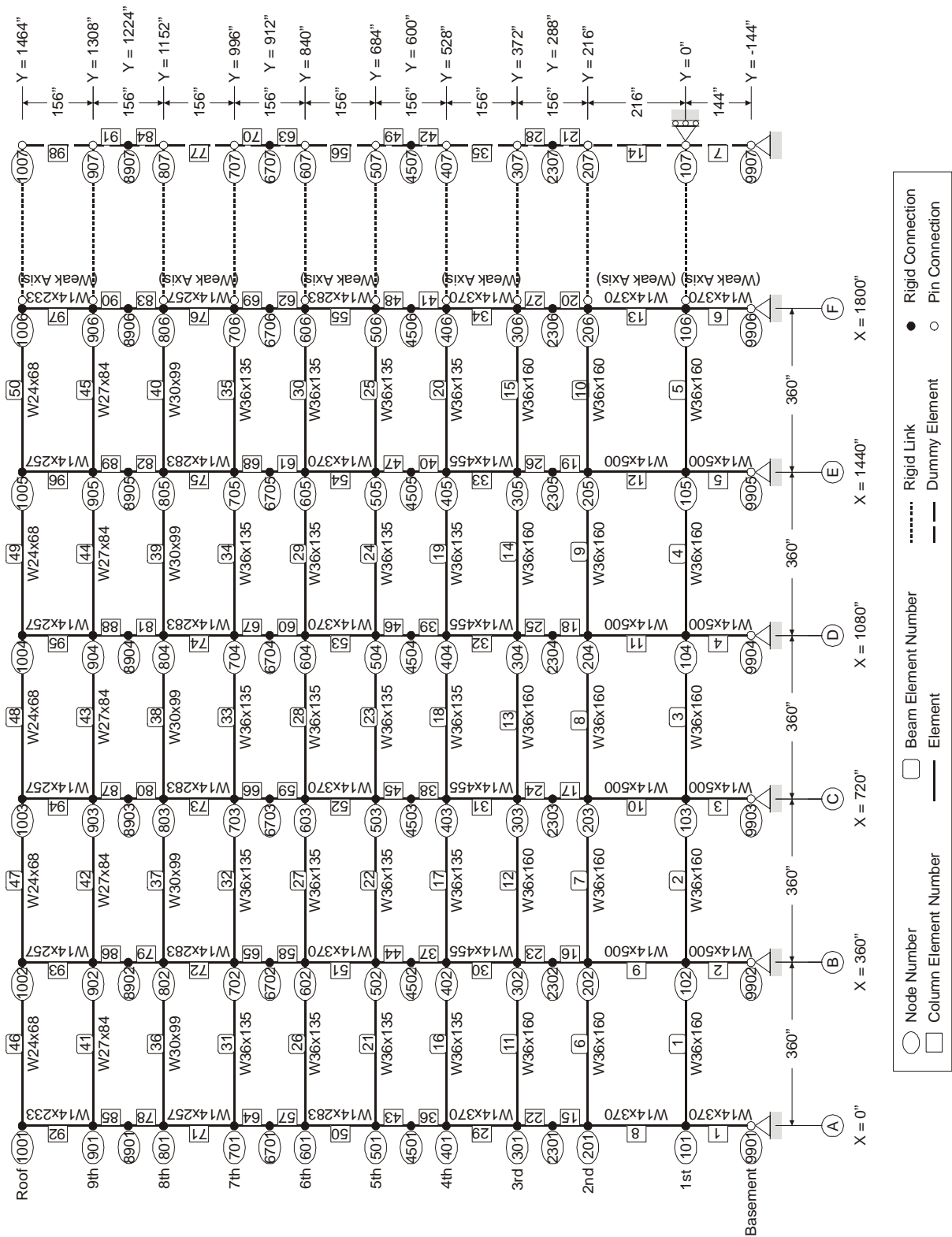
Figure F-5   Drain model of the 9-story (regular and weak-story) steel frames.
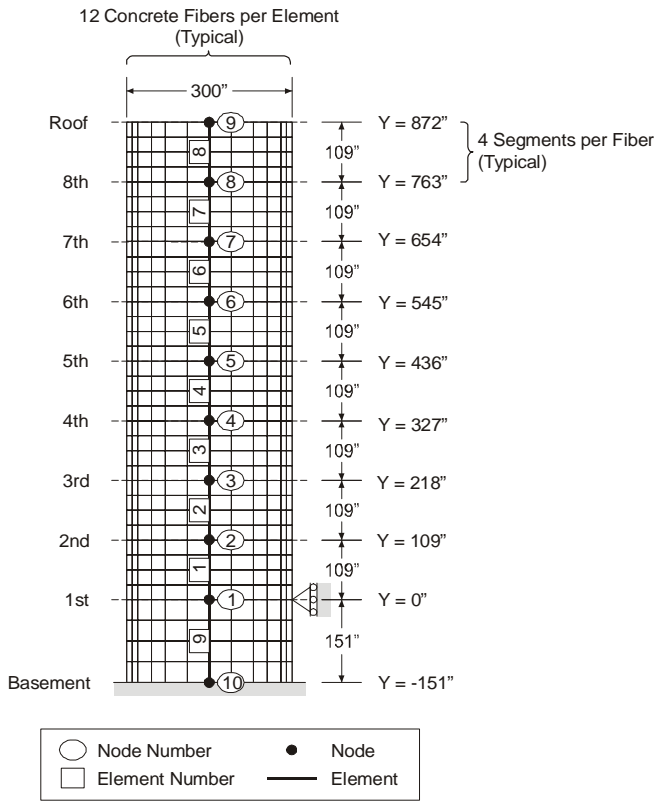
Figure F-6   Drain model of the 8-story reinforced concrete shear wall.

models in Figure F-8. The capacity curve represents the sum of the applied lateral forces at a given displacement,[1] as determined in a nonlinear static (pushover) analysis. In this case, the lateral forces were proportional to the amplitude of the first mode and mass at each floor level, where the modal amplitudes were determined with *P*-Delta effects considered. Based on a bilinear fit to the capacity curves, the base shear coefficient at yield and the drift at yield are as given in Table F-5.

F.2.2.2   Model Verification

Because the SAC frames have been the subject of prior research, the models could be validated by comparison to published research. The periods of the regular frames, reported in Table F-4, match those reported in FEMA 355C (SAC, 2000). The 9-story frame capacity curves (computed without *P*-Delta considered) are nearly the same as those published by Chopra and Goel (2002).

F.2.3   *Ground Motions and Demand Intensities*

It was desired to assess the accuracy of the pushover procedures with respect to the results obtained from

1. When *P*-Delta is modeled, the element shear forces and base shear are increased by the *P*-Delta shears. The applied lateral force may be obtained equivalently as (1) the load factor times the sum of the components of the load vector or (2) the sum of the lowest story shears minus $P\Delta/h$, where P = the gravity load on the lowest story, Δ = the displacement of the lowest story, and h = the height of the lowest story.
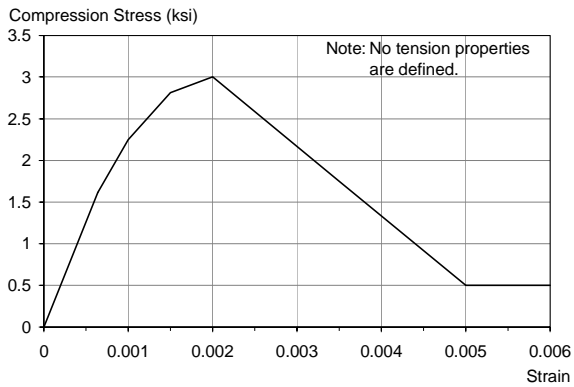
(a) Concrete
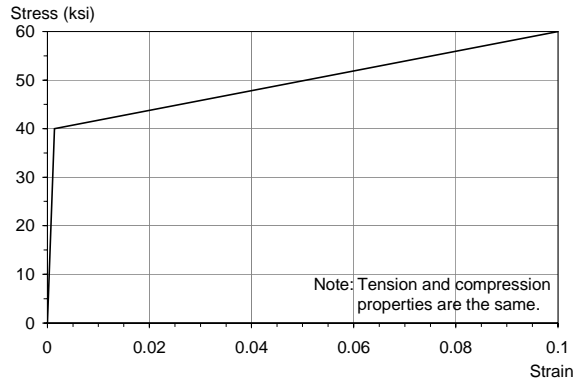
(b) Reinforcing Steel

Figure F-7   Idealized material stress-strain relationships used in drain model of the 8-story reinforced concrete shear wall

Table F-4   Periods and Mode Shapes for the Frame and Wall Buildings

Modal Properties		*Mode*					
		1		*2*		*3*	
		without P-Δ	*with P-Δ*	*without P-Δ*	*with P-Δ*	*without P-Δ*	*with P-Δ*
Part a: 3-Story (Regular and Weak-Story) Frames							
Period (sec)		1.01	1.03	0.33	0.33	0.17	0.17
Participation factor		1.27	1.27	0.33	0.33	0.06	0.06
Modal mass coefficient		0.83	0.83	0.14	0.13	0.04	0.04
Mode shape amplitude	2nd floor	0.27	0.28	1.20	1.21	4.07	4.04
	3rd floor	0.66	0.66	1.14	1.14	-3.34	-3.33
	Roof	1.00	1.00	-1.00	-1.00	1.00	1.00
Part b: 8-Story Reinforced Concrete Shear Wall							
Period (sec)		0.71	0.71	0.13	0.13	0.05	0.05
Participation factor		1.49	1.49	0.71	0.71	0.34	0.34
Modal mass coefficient		0.64	0.64	0.20	0.20	0.08	0.08
Mode shape amplitude	2nd floor	0.03	0.03	0.15	0.15	0.44	0.44
	3rd floor	0.09	0.09	0.42	0.42	0.98	0.98
	4th floor	0.19	0.19	0.68	0.68	1.06	1.06
	5th floor	0.31	0.31	0.84	0.84	0.47	0.47
	6th floor	0.46	0.46	0.77	0.77	-0.48	-0.48
	7th floor	0.63	0.63	0.42	0.42	-1.09	-1.09
	8th floor	0.81	0.81	-0.21	-0.21	-0.52	-0.52
	Roof	1.00	1.00	-1.00	-1.00	1.00	1.00
Part c: 9-Story (Regular and Weak-Story) Frames							
Period (sec)		2.27	2.34	0.85	0.87	0.49	0.50
Participation factor		1.37	1.36	0.53	0.52	0.24	0.24
Modal mass coefficient		0.83	0.84	0.11	0.11	0.04	0.04
Mode shape amplitude	2nd floor	0.17	0.17	0.38	0.39	0.80	0.81
	3rd floor	0.28	0.29	0.59	0.60	1.04	1.04
	4th floor	0.39	0.40	0.72	0.72	0.84	0.83
	5th floor	0.51	0.52	0.74	0.75	0.26	0.23
	6th floor	0.62	0.63	0.64	0.63	-0.49	-0.51
	7th floor	0.72	0.73	0.40	0.39	-1.04	-1.04
	8th floor	0.83	0.83	-0.01	-0.02	-0.96	-0.94
	9th floor	0.93	0.93	-0.54	-0.54	-0.14	-0.12
	Roof	1.00	1.00	-1.00	-1.00	1.00	1.00

Table F-5   **Base Shear Coefficient and Drift At Yield for Each Building Model**

Idealized Capacity Curve Properties	3-Story	3-Story Weak-Story	8-Story	9-Story	9-Story Weak-Story
			Building		
Yield drift (%)	1.11	0.833	0.250	1.06	0.936
Base shear coefficient	0.329	0.247	0.129	0.177	0.156

Table F-6   **Ground Motions**

#	Identifier	Earthquake	Date	Magnitude	Station Location (Number	Component	PGA (g)	PGV (cm/sec)	Char. Period (sec)	Source
					Ordinary					
1	ICC000	Superstitn	11-24-87	$M_s = 6.6$	El Centro Imp. Co. Cent (01335)	000	0.358	46.4	0.60	CDMG
2	LOS000	Northridge	1-17-94	$M_s = 6.7$	Canyon Country – W Lost Cany (90057)	000	0.41	43	0.59	USC
3	G02090	Loma Prieta	10-18-89	$M_s = 7.1$	Gilroy Array #2 (47380)	090	0.322	39.1	0.69	CDMG
4	TCU122N	Chi-Chi, Taiwan	9-20-99	$M_s = 7.6$	(TCU122)	N	0.261	34	0.85	CWB
5	G03090	Loma Prieta	10-18-89	$M_s = 7.1$	Gilroy Array #3 (47381)	090	0.367	44.7	0.40	CDMG
6	CNP196	Northridge	1-17-94	$M_s = 6.7$	Canoga Park – Topanga Can (90053)	196	0.42	60.8	0.61	USC
7	CHY101W	Chi-Chi, Taiwan	9-20-99	$M_s = 7.6$	(CHY101)	W	0.353	70.6	1.27	CWB
8	ICC090	Superstitn	11-24-87	$M_s = 6.6$	El Centro Imp. Co. Cent (01335)	090	0.258	40.9	1.03	CDMG
9	CNP106	Northridge	1-17-94	$M_s = 6.7$	Canoga Park – Topanga Can (90053)	106	0.356	32.1	0.45	USC
10	E02140	Imperial Valley	10-15-79	$M_s = 6.9$	El Centro Array #2 (5115)	140	0.315	31.5	0.29	USGS
11	E11230	Imperial Valley	10-15-79	$M_s = 6.9$	El Centro Array #11 (5058)	230	0.38	42.1	0.27	USGS
					Near-Field (Maximum Velocity Direction)					
1	ERZMV1	Erzincan	3-13-92	$M_s = 6.9$	Erzincan Station	NA	0.442	126	1.13	EERL Caltech
2	RRSMV1	Northridge	1-17-94	$M_s = 6.7$	Rinaldi Receiving Station	213	0.891	186	0.92	EERL Caltech
3	LUCMV1	Landers	6-28-92	$M_s = 7.3$	Lucerne Valley Station	280	0.732	147	0.52	EERL Caltech
4	SCHMV1	Northridge	1-17-94	$M_s = 6.7$	Sylmar County Hospital Parking Lot	190	0.865	138	0.51	EERL Caltech

CDMG: California Division of Mines and Geology
CWB: Central Weather Bureau, Taiwan
EERL Caltech: Earthquake Engineering Research Laboratory, California Institute of Technology
USC: University of Southern California
USGS: U.S. Geological Survey

nonlinear dynamic analyses and whether these procedures are suitable for the special case of near-fault ground motions. Accordingly, two sets of ground motions were used. The first set of motions was selected to represent the range of motion that may be expected at a specific building site. This range was established by selecting strong-motion records having a limited range of source distance for a specified site soil type. Site Class B motions had been proposed originally, but Site Class C motions were used because these soil conditions are more typical. The 11 motions in this set are referred to as "ordinary" motions in this

report. The second set of motions consists of motions recorded close to the epicenter that contain very strong velocity pulses. The four motions in this set are referred to as "near-fault" motions in this report. The records are summarized in Table F-6; their acceleration, velocity, and displacement time histories are plotted in Section F.8.1. The characteristic periods identified in Table F-6 correspond approximately to the corner period at the intersection of the "constant acceleration" and "constant velocity" portions of the spectrum for the ordinary motions, and were computed as

(a) 3-Story Steel Frame

(b) 3-Story Weak-Story Steel Frame

(c) 8-Story Reinforced Concrete Shear Wall

(d) 9-Story Regular Steel Frame

(e) 9-Story Weak-Story Steel Frame
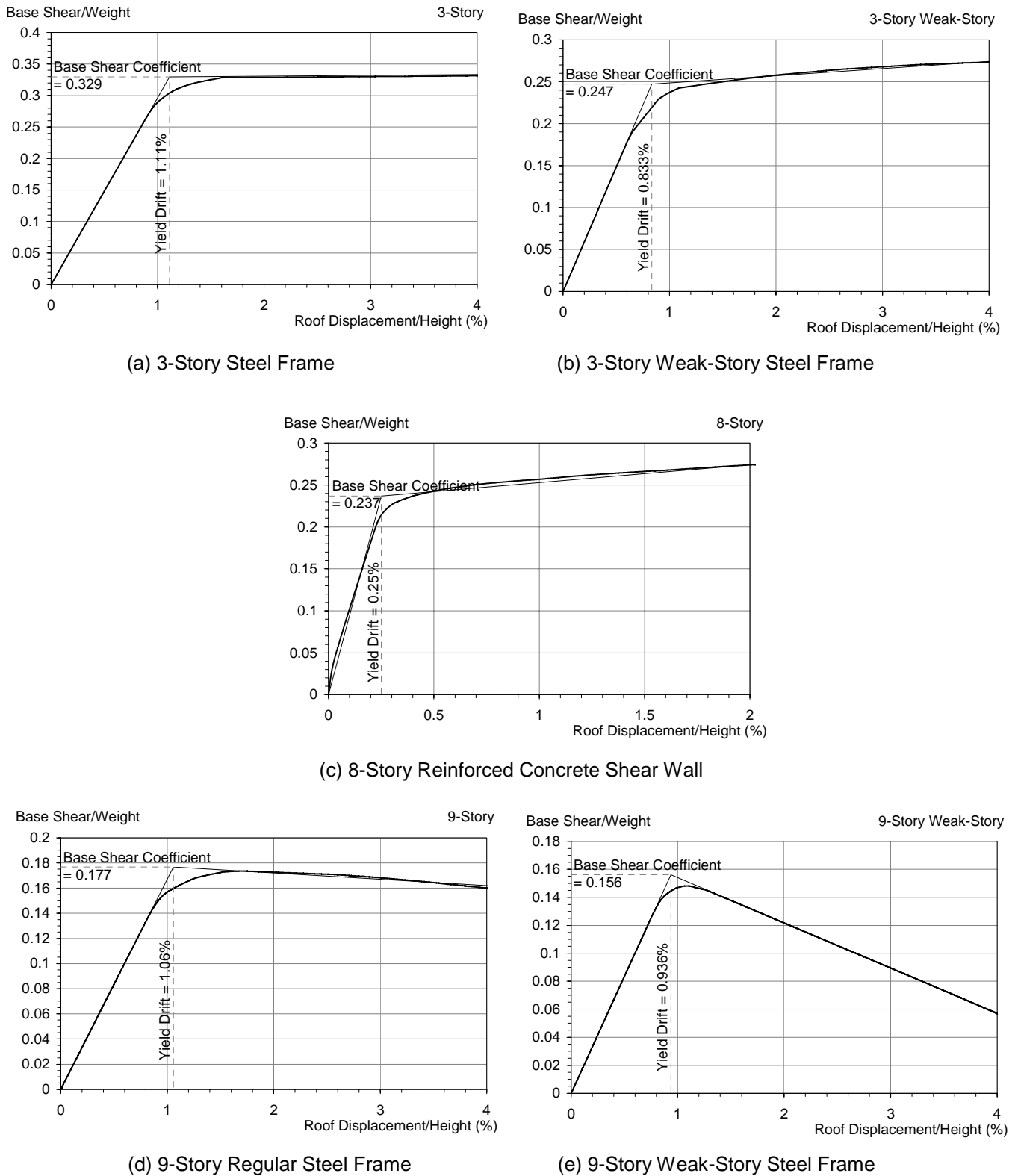
Figure F-8   Capacity curves for the five model building examples.

$$T_g = 2\pi \frac{(S_v)_{max}}{(S_a)_{max}} \qquad \text{(F-1)}$$

where S_v and S_a are the elastic pseudo-velocity and pseudo-acceleration spectra, respectively, for linear elastic systems having $\beta = 5\%$, as described by Cuesta and Aschheim (2001).

F.2.3.1   Ordinary (Site Class C) Motions

The Pacific Earthquake Engineering Research (PEER) Center strong-motion database[1] produced a set of over 50 strong ground motions in response to multiple queries in which magnitudes were restricted to the range $5.5 < M_s < 8.0$, the closest distance to fault rupture was restricted to 8 to 20 km, and site classification was restricted to Site Class C. Of these records, those with the largest elastic spectral displacements at a period of 1 second were retained, producing a set of 17 motions. Six of these were excluded based on (a) the presence of an identifiable strong velocity pulse early in the record, (b) the identification of the record as being "near-fault" or "near-field" in some research reports, and (c) a preliminary elimination of those records that would require the largest amplitude scale factors in order to achieve the drift levels described in Section 9.3. The 11 records that remain, listed in Table F-6, were generated from a number of events, with no event contributing more than 3 records.

F.2.3.2   Near-Field Motions

A variety of near-field motions was considered important for the example analyses. Recognizing that special processing is often necessary to accurately recover the record (Iwan and Chen, 1994), records were obtained from the Earthquake Engineering Research Laboratory at the California Institute of Technology (A. Guyader, personal communication). The component of near field motion used is oriented in the horizontal plane in the direction in which the maximum ground velocity occurs. These records are identified in Table F-6, and are not always aligned in the fault normal direction. The ground motion velocity histories (Section F.8.1) do show large velocity pulses. The near-field records were used without any further processing, and were applied at their natural intensities, that is, without scaling.

---

1. Available at http://peer.berkeley.edu/smcat/.

F.2.3.3   Drift Levels

The drift levels used for the ordinary ground motions were set to 0.5%, 2.0%, and 4.0% of the height of the building for the steel frames, and 0.2%, 1.0%, and 2.0% of the height of the building for the reinforced concrete structural wall building. These drift levels are referred to as "low," "moderate," and "high" in subsequent sections of this report. The low drift level results in elastic response. Because the regular 3- and 9-story steel frames have an effective yield drift of 0.83% and 1.1% of the height of the frame, the high drift levels cause system ductility demands of about 4.8 and 3.6, respectively, if response is predominantly in the first mode. The reinforced concrete wall building has a yield drift of approximately 0.25% and thus has system ductility demands of about 4 and 8 at the moderate and high drift levels, respectively.

These drift levels were used to illustrate the influence of yielding on the accuracy of the estimates obtained from the inelastic procedures for a range of response that is relevant for many buildings. For example, roof drifts of 2.5% and 5% of the height of the frame buildings and 1% and 2% of the height of the wall building correspond to the nominal Life Safety and Collapse Prevention performance limits, respectively, given in FEMA 356.

F.2.3.4   Ground Motion Scaling

The scale factors required to cause the peak roof drifts to be equal to the predetermined target values are reported for each building, drift level, and ground motion in Table F-7. These scale factors were used to determine mean elastic spectra for each building and drift level in order to determine relative contributions for the 2nd and 3rd modes as required for the square-root-of-the-sum-of-the-squares (SRSS) load vector and multimode pushover analysis (MPA) methods. This implementation detail is described more fully in Section F.3.1.6 and Section F.3.2.

F.2.4   Extensions to Address P-Delta

Nearly all the pushover procedures have been presented in the literature without explicit treatment of *P*-Delta effects. Only in the Displacement Coefficient Method are *P*-Detla effects addressed, by modification of the SDOF displacement response using the term C_3.

P-Delta affects elastic and inelastic response. Elastic response is affected because the geometric stiffness causes an increase in the period of vibration and a change in the elastic mode shape. For inelastic systems,

Table F-7   Scale Factors Applied to Each of the Ordinary Ground Motions for the Dynamic Analyses

		Ground Motion										
Building	Drift	1 ICC000	2 LOS000	3 G02090	4 TCU122n	5 G03090	6 CNP196	7 CHY101w	8 ICC090	9 CNP106	10 E02140	11 E11230
3-story	0.5%	0.5281	0.4499	0.3675	0.4416	0.3934	0.2739	0.2827	0.6529	0.5243	0.5551	0.6335
	2%	1.8493	1.6607	1.2930	1.5955	1.4885	1.4912	1.4255	2.9310	2.6645	2.8917	2.3071
	4%	2.4626	2.6943	2.3852	2.2346	2.4672	2.0994	2.9252	3.6492	4.9953	6.2765	3.0257
3-story weak-story	0.5%	0.5281	0.4499	0.3690	0.4416	0.3934	0.2739	0.2827	0.6529	0.5243	0.5551	0.6335
	2%	1.6962	1.4968	1.5223	1.4177	1.3330	1.3269	1.4034	2.3378	2.7180	2.7006	2.0535
	4%	4.0050	2.4302	2.2434	2.1137	2.6378	2.6051	2.1937	3.4655	4.6072	5.3996	4.4179
8-story	0.5%	0.476	0.323	0.690	0.811	0.750	0.267	0.542	0.936	0.421	0.606	0.581
	1%	1.957	1.858	2.246	2.480	2.396	2.162	2.530	3.889	2.084	3.069	3.412
	2%	3.213	3.947	3.329	3.349	3.401	3.318	4.172	4.641	3.586	6.220	6.540
9-story	0.5%	0.4871	0.3133	0.5683	0.4237	0.3736	0.2348	0.2372	0.3243	0.4369	0.4844	0.8223
	2%	3.0281	2.5204	4.0783	3.0244	3.2888	1.5376	1.4722	2.7696	3.9072	4.4352	2.9019
	4%	5.4384	4.6774	6.3237	4.2556	5.6177	3.2536	3.2282	5.3885	9.4438	6.8838	7.6710
9-story weak-story	0.5%	0.4871	0.3133	0.5683	0.4237	0.3736	0.2348	0.2372	0.3243	0.4369	0.4844	0.8223
	2%	2.8924	2.5527	4.0639	2.2949	3.2723	1.4242	1.8111	1.7457	2.7755	2.9933	4.5670
	4%	3.6906	4.4874	6.3830	2.7551	4.9506	1.9801	1.9313	4.2350	3.4149	5.8639	5.0538

the geometric stiffness reduces the post-yield stiffness and may result in large increases in peak displacement or collapse. The predominant mechanism may change as well.

Chopra and Goel (2001) show for elastic response that independent pushovers in each mode are equivalent to conventional modal analysis, and that superposition in time, or by combination of individual peaks, is equivalent to modal superposition and response spectral analysis, respectively. A structure responding elastically in the presence of *P*-Delta responds with altered periods of vibration and mode shapes relative to those determined without *P*-Delta. Thus, theory indicates that the elastic portions of response should be determined using the modal properties considering *P*-Delta. Thus, for the pushover techniques that use elastic mode shapes (first mode, SRSS, and MPA), the mode shapes employed were those determined with *P*-Delta effects present.

The slope of the post-yield portion of the capacity curve determined by pushover analysis is reduced in the presence of *P*-Delta. This reduced slope, particularly when negative, can be expected to cause an increase in peak displacement response. Because ground-motion scale factors were adjusted to achieve predetermined target roof drifts, as described in Section F.2.3, this

effect is subdued for the dynamic analyses using the ordinary ground motions.

F.3   Simplified Techniques

Seven pushover methods were applied. In all methods, lateral forces are applied incrementally in a nonlinear static analysis to determine a capacity curve. The capacity curve represents the relationship between the applied lateral force and the displacement at the roof. The applied lateral force at any floor is proportional to the mass and displacement associated with a shape vector at the floor under consideration. The pushover methods differ in whether the shape vector remains proportional to an initial shape (which may be the first mode or another displacement pattern) or evolves as the onset of material nonlinearity causes softening of the structure, and in whether one or multiple modes are considered. These methods used in this study are summarized in the following sections. In addition, where specific assumptions or adaptations were required to implement these methods in this study, these implementation-specific details are also described.

F.3.1   Single Load Vectors

F.3.1.1   First Mode

The first mode technique applies forces in proportion to the amplitude of the elastic first mode and mass at each

(a) 3-story (Regular and Weak-Story) Steel Frames

(b) 8-Story Reinforced Concrete Wall

(c) 9-Story (Regular and Weak-Story) Steel Frames
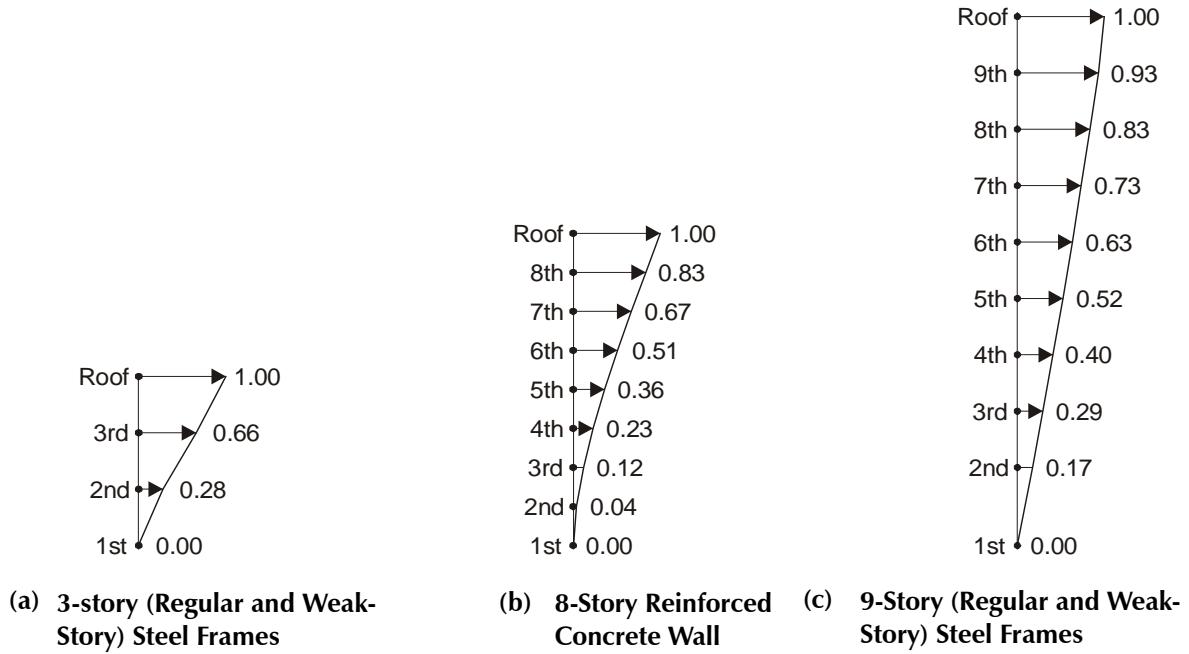
Figure F-9   Shape vectors of the 1st mode shape load pattern.

floor. The mode shapes of the five building models (Table F-4) are illustrated in Figure F-9, and the corresponding capacity curves, determined using this pushover technique, are illustrated in Figure F-8.

The capacity curve for the 8-story shear wall model (Figure F-8(c)) shows softening as cracks develop at the base of the wall. The shape vector used for this model was the elastic mode shape determined using the initial properties of the structure, after loading by gravity loads.

F.3.1.2   Inverted Triangular

The inverted triangular pattern uses a shape vector that increases linearly with height. This shape vector is also shown in Figure F-10 for the three building configurations.

F.3.1.3   Rectangular

The rectangular (or uniform) pattern uses a shape vector that is uniform with height. This shape vector is shown in Figure F-11 for the three building configurations.

F.3.1.4   Code Force Distribution

The "code" load pattern appears in many documents, including FEMA 368. The pattern varies from an inverted triangular shape for periods less than 0.5 s to a parabolic shape for periods greater than 2.5 s as a means to account for higher mode effects. The lateral force coefficient for floor x, C_{vx}, is given by

$$C_{vx} = \frac{w_x h_x^k}{\sum_{i=1}^{n} w_i h_i^k} \tag{F-2}$$

where w_x and w_i are the weights of floor i or x, h_i and h_x are the height of floor i or x above the base, and k is an exponent that varies linearly with period from 1 for $T_1 < 0.5$ s to 2 for $T_1 \geq 2.5$ s. Since these forces are equal to the product of floor mass and the amplitude of a shape vector at each floor, the corresponding shape vectors are proportional to h^k. These shape vectors are illustrated in Figure F-12 for the three building configurations.[1] For the 8-story shear wall building, k was determined based on the initial stiffness of the building, after gravity loading was applied.

(a) **3-story (Regular and Weak-Story) Steel Frames**

(b) **8-Story Reinforced Concrete Wall**

(c) **9-Story (Regular and Weak-Story) Steel Frames**
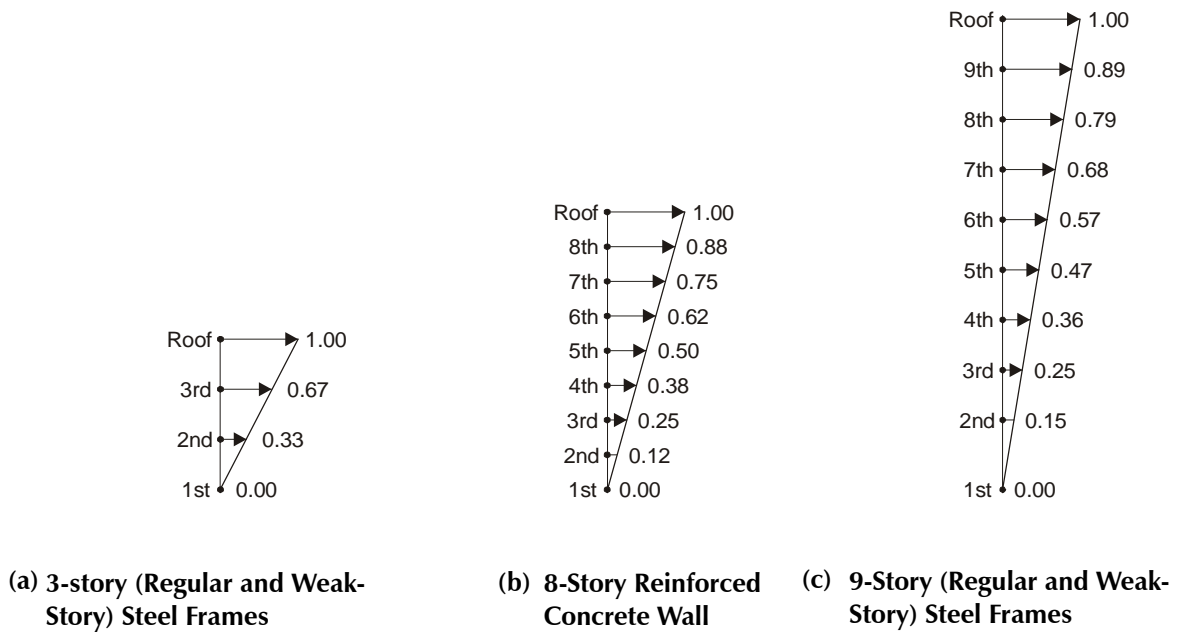
Figure F-10   Shape vectors of the triangular load pattern.

(a) **3-story (Regular and Weak-Story) Steel Frames**

(b) **8-Story Reinforced Concrete Wall**

(c) **9-Story (Regular and Weak-Story) Steel Frames**
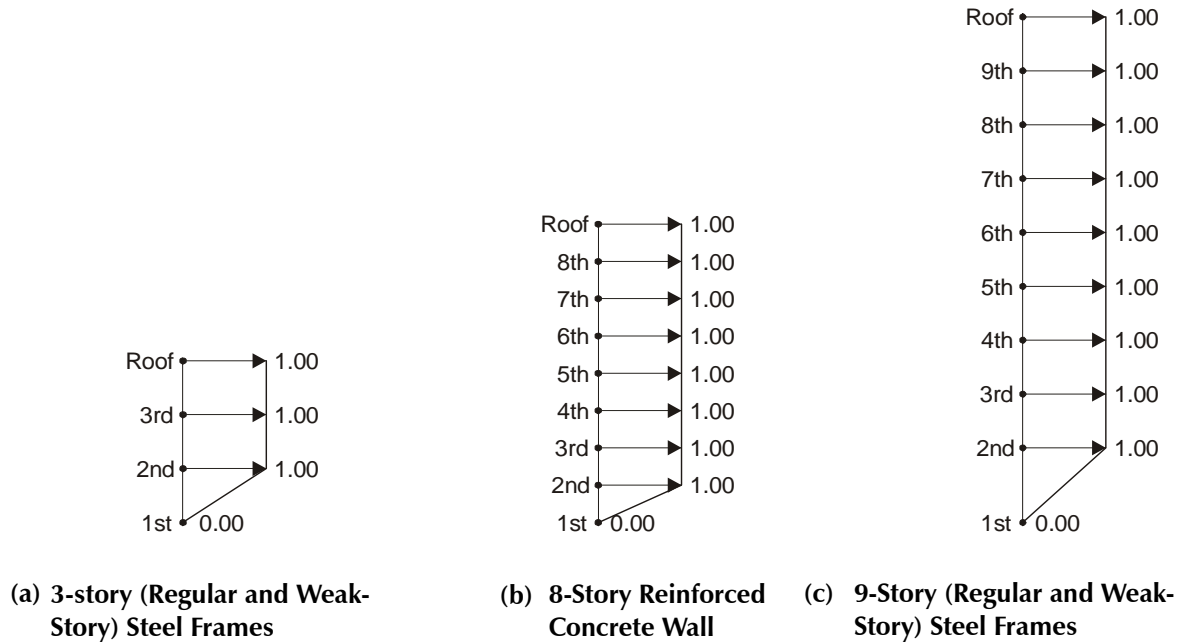
Figure F-11   Shape vectors of the rectangular load pattern.

Roof ► 1.00
9th ► 0.81
8th ► 0.63
7th ► 0.48
6th ► 0.34
5th ► 0.23
4th ► 0.14
3rd ► 0.07
2nd ► 0.03
1st ► 0.00

Roof ► 1.00
8th ► 0.88
7th ► 0.75
6th ► 0.63
5th ► 0.50
4th ► 0.38
3rd ► 0.25
2nd ► 0.13
1st ► 0.00

Roof ► 1.00
3rd ► 0.60
2nd ► 0.25
1st ► 0.00

$k = 1.27$

$k = 1$

$k = 1.92$

(a) 3-story (Regular and Weak-Story) Steel Frames

(b) 8-Story Reinforced Concrete Wall

(c) 9-Story (Regular and Weak-Story) Steel Frames
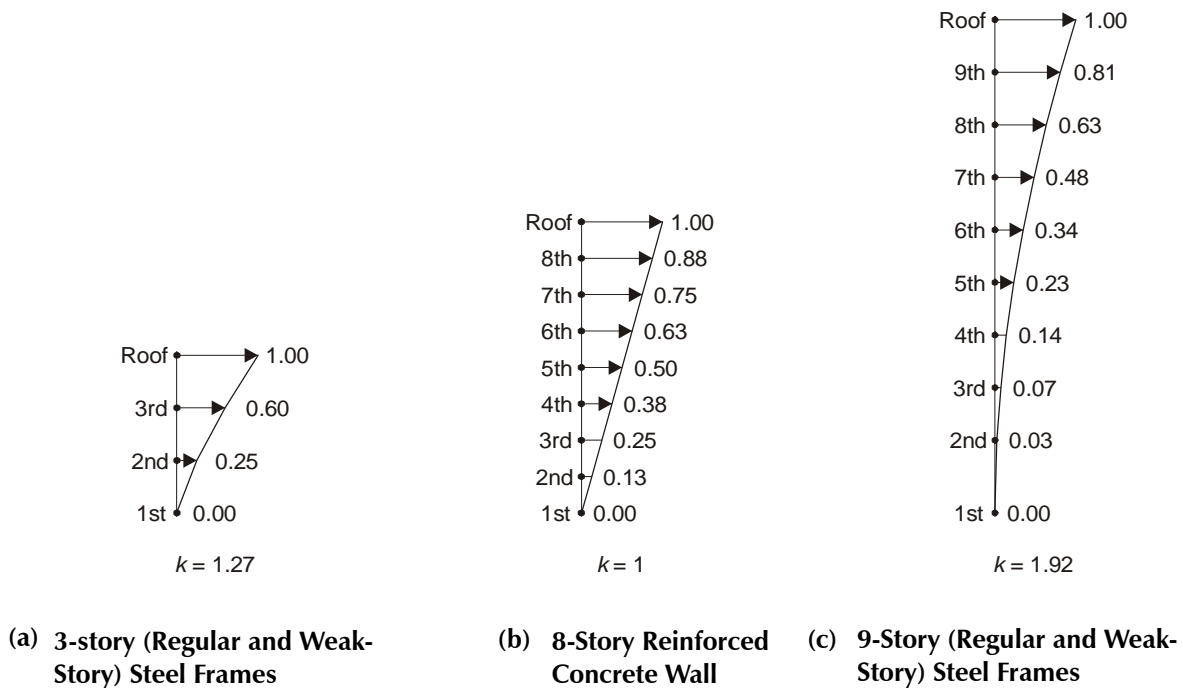
Figure F-12   Shape vectors of the code load pattern.

F.3.1.5   Adaptive First Mode

The adaptive first mode procedure recognizes that softening of the capacity curve reflects a reduction in stiffness, which, in turn, causes a change in the mode shape. Thus, lateral forces are applied proportional to the amplitude of an evolving first-mode-shape amplitude and mass at each floor.

The procedure was implemented as follows: the lateral load vector was adjusted at drift increments of 0.5% of the height of the building. The increment in lateral load for each interval (0% to 0.5%, 0.5% to 1.0%, 1.0% to 1.5% and so on) was based on the mode shape computed at the end of the preceding interval. The initial mode shape was used for the first interval.

The capacity curve of the 9-story weak story building develops a negative tangent stiffness as the roof displacement increases. Drain-2DX is not able to

provide solutions to determine the free-vibration mode shapes when this occurs. Thus, the last computed mode shape was used for the subsequent steps

F.3.1.6   SRSS

The SRSS technique is based on a consideration of elastic modal responses. Associated with the response in each mode is a lateral force pattern, which can be summed to obtain story shears associated with each mode. An SRSS combination of the modal story shears results in a particular shear profile. The lateral forces required to generate the SRSS story-shear profile are applied in this pushover technique. The elastic spectral amplitudes are used to determine the modal story shears, even when nonlinear response is anticipated. A sufficient number of modes to represent at least 90% of the mass is included.

The first three modes were used for each building model. Because a single spectrum typically would be used for design, the SRSS procedure was applied to the mean of the scaled spectra used to achieve each predetermined drift level for each building. The mean elastic spectrum differed for each building and each drift level, because the scale factors used with each

---

1. Because the weak story frames have the same elastic properties as their SAC counterparts, the load vectors that are based on elastic properties are identical for the 3-story and 9-story frames.

record were specific to each building and drift level. Thus, a different SRSS load vector was determined for each structure and drift level. Because the load vectors are proportional to the product of the amplitude of a shape vector and mass at each floor level, the shape vectors corresponding to the SRSS distribution can be derived. These shape vectors are shown in Figure F-13 for the three building configurations and three drift levels.

For the near-fault motions, spectral amplitudes and SRSS combinations were determined for each near fault

record. For the 8-story wall building, the periods used for the SRSS combinations were based on the initial stiffness, after gravity loading was applied.

F.3.2 Multiple Mode Pushover Analysis

One approach to represent the influence of higher modes on response quantities combines peak response quantities determined in separate pushover analyses for the first several modes using an SRSS combination. The procedure proposed by Chopra and Goel (2001) considers the potential for nonlinear response in each

(a) 3-Story Regular Steel Frame

(b) 3-Story Weak-Story Steel Frame

(c) 8-Story Reinforced Concrete Wall

Figure F-13   Shape vectors of the SRSS load pattern.

Roof ● → 1.00
9th ● → 0.61
8th ● → 1.04
7th ● → 0.88
6th ● → 0.40
5th ● → 0.30
4th ● → 0.25
3rd ● → 0.25
2nd ● → 0.21
1st ● 0.00

0.5% Drift Level

Roof ● → 1.00
9th ● → 0.62
8th ● → 1.07
7th ● → 0.90
6th ● → 0.41
5th ● → 0.31
4th ● → 0.25
3rd ● → 0.25
2nd ● → 0.21
1st ● 0.00

2% Drift Level

Roof ● → 1.00
9th ● → 0.64
8th ● → 1.12
7th ● → 0.95
6th ● → 0.43
5th ● → 0.32
4th ● → 0.26
3rd ● → 0.25
2nd ● → 0.21
1st ● 0.00

4% Drift Level

(d) 9-Story Regular Steel Frame

Roof ● → 1.00
9th ● → 0.61
8th ● → 1.04
7th ● → 0.88
6th ● → 0.40
5th ● → 0.30
4th ● → 0.25
3rd ● → 0.25
2nd ● → 0.21
1st ● 0.00

0.5% Drift Level

Roof ● → 1.00
9th ● → 0.61
8th ● → 1.05
7th ● → 0.88
6th ● → 0.40
5th ● → 0.30
4th ● → 0.25
3rd ● → 0.25
2nd ● → 0.21
1st ● 0.00

2% Drift Level

Roof ● → 1.00
9th ● → 0.62
8th ● → 1.08
7th ● → 0.92
6th ● → 0.42
5th ● → 0.31
4th ● → 0.25
3rd ● → 0.25
2nd ● → 0.21
1st ● 0.00

4% Drift Level

(e) 9-Story Weak-Story Steel Frame

Figure F-13   Shape vectors of the SRSS load pattern (continued).

independent modal analysis. According to their procedure, known as Multimode Pushover Analysis (MPA), capacity curves are developed for each "modal" response by applying lateral forces proportional to the mode shape amplitude and mass at each floor.

In the MDOF studies, capacity curves were determined by pushover analysis for each of the first three modes for each building model. In some cases the higher mode capacity curves displayed softening behavior similar to that observed in first mode pushover analyses. However, in other cases, the higher mode force patterns caused the roof displacement to reverse as inelasticity developed in the structure. Such reversals were observed for the 3rd mode pushover of the regular 3-story building (Figure F-14) and for the 2nd mode
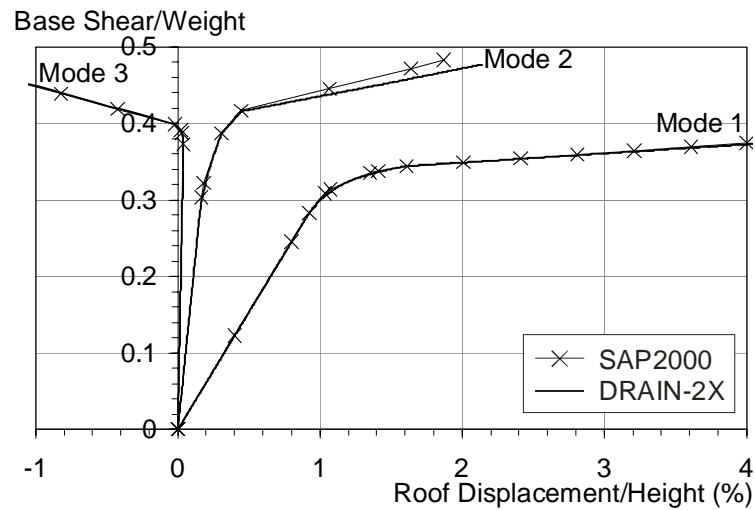
Figure F-14   First, second, and third mode pushover results for the 3-story regular steel frame.

pushover of the 3-story weak story building. Such reversals have also been observed by M. Aschheim and A. Chopra in previous analyses.

It is difficult to rationalize the use of a capacity-spectrum type procedure to identify a target displacement for capacity curves that do not display the usual softening behavior. Rather than making an *ad hoc* adjustment to the MPA method for just the 3-story buildings, a modified version of the MPA procedure capable of representing higher mode contributions was used for all five buildings. In the "modified MPA" procedure, elastic contributions associated with the 2nd and 3rd modes are combined with contributions from the 1st mode, which may be inelastic, using an SRSS combination.

For both the ordinary motions and the near-field motions, the target displacement used to determine the first mode contribution was the predetermined peak roof displacement, just as for the first mode pushover. In order to determine the higher mode contributions for the ordinary ground motions, mean spectra were computed for each building and drift level, using the ground motions as scaled to achieve the predetermined drifts. This allowed the contributions of the 2nd and 3rd modes to be determined directly from the mean spectra for the ordinary motions. For the near-field records, the elastic higher mode contributions were determined from the jagged elastic spectra associated with each unscaled near-field record. The higher-mode contributions were determined using spectra computed for viscous

damping ratios of 2% and 5% for the frame and wall buildings, respectively.

For the 8-story shear wall building, the first mode capacity curve was determined by applying lateral forces proportional to the initial mode shape; a bilinear approximation to the capacity curve was then determined, having an intersection at $0.6V_y$, where V_y is the yield strength of the fitted bilinear curve. The structure was pushed to the displacement corresponding to this point of intersection to determine the effective modal properties. The periods and modal participation factors associated with the tangent stiffness of the cracked wall at a base shear equal to $0.6V_y$ were used in the modified MPA procedure described above.

F.4   Accuracy of Estimates Made Using Simplified Procedures

This section compares the estimates of response quantities obtained using the simplified inelastic procedures with the values obtained by nonlinear dynamic analysis. Comparisons for the ordinary motions are presented in Section F.4.2 and those for near-field motions are presented in Section F.4.3, after a discussion of error evaluation in Section F.4.1.

F.4.1   Error Measurement

Two measures of error are used. For the ordinary motions, which were scaled to achieve predetermined target drifts, the error measure E_1 is defined as

$$E_1(i,j,k) = \left| \frac{Q_P(i,j,k) - \bar{Q}_D(i,j,k)}{\bar{Q}_D(i,j,k)} \right| \qquad (F-3)$$

where $Q_P(i,j,k)$ = pushover response quantity i at story/floor j for drift level k, and $\bar{Q}_D(i,j,k)$ = mean overall responses to the ordinary ground motions of the dynamic response quantity i at story/floor j at drift level k.

For the near-field motions, the peak roof drifts varied because the motions were used without scaling. For these motions, a second error measure, E_2, was defined as

$$E_2(i,j,k) = \left| \frac{\bar{Q}_P(i,j,k) - \bar{Q}_{D,l}(i,j,k)}{\bar{Q}_{D,l}(i,j,k)} \right| \qquad (F-4)$$

where $\bar{Q}_P(i,j,k)$ = mean overall near-fault responses of pushover response quantity i at story/floor j for drift level k, and $\bar{Q}_{D,l}(i,j,k)$ = mean overall near-fault responses of dynamic response quantity i at story/floor j at drift level k for record l.

F.4.2   Results for Ordinary Ground Motions

Complete results for the five example buildings are provided in Sections F.8.2 and F.8.3.

The minimum, maximum, mean, median, and mean plus and minus one standard deviation values of the dynamic response quantities to the ordinary ground motions are plotted for each floor or story in Section F.8.2 (Figure F-32 through F-46). These plots include the deterministic results obtained using the various pushover techniques, plotted using various line styles. Errors in the pushover estimates relative to mean dynamic response quantities, calculated using the error measure E_1, are plotted as a function of drift level and pushover technique for each of the buildings in Section F.8.3 (Figures F-47 through F-51). The mean error is the mean of the errors calculated over the height of the building, and the maximum error is the maximum of the errors over the height of the building.

A summary of the results relating to peak responses, their estimates, and the errors of these estimates, is presented in the following subsections.

F.4.2.1   Floor Displacements

The peak displacement response showed the smallest variance relative to that observed for the other response

quantities. Coefficients of variation are plotted in Section F.8.6 (Figures F-77 through F-81). The variance for the 8-story wall building was appreciably less than that of the frame buildings. The low variance in the displacement response of the five buildings is attributed to the relatively small contribution of higher modes to displacements, coupled with methodology of the study, in which the ordinary ground motions were scaled to obtain peak roof displacements equal to predetermined values.

The displacement response of the buildings generally followed an approximate first mode pattern. Exceptions to this pattern were noted as follows: (1) the response of the regular 9-story building to the CNP106 record appeared to be affected by higher modes at 4% drift; (2) substantial variability in the displacement pattern was observed for the 9-story weak story building at 2% drift, with a weak story developing for some motions but not others.

Peak displacement estimates were generally quite good for all load patterns. Differences occurred primarily with the rectangular load pattern, and for the 9-story frames, the code load pattern.

F.4.2.2   Interstory Drift Ratios

The peak interstory drifts of the 8-story shear wall building displayed little variance, in contrast to the larger variance evident in the interstory drifts of the frame buildings. All pushover techniques provided good estimates of the interstory drifts of the shear wall building at all drift levels, with slightly larger discrepancies occurring for the code and rectangular load patterns. This indicates that even the interstory drifts were dominated by response in a quasi-first mode for the shear-wall building.

The largest mean interstory drift ratios for the regular 3-story frame were about 20% greater than the average roof drift ratio at 0.5% drift, and decreased to about 10% greater than the average roof drift ratio at 4% drift. For the regular 9-story frame, the largest mean interstory drift ratios were about 35% greater than the average roof drift ratio at 0.5% drift, and increased to about 65% greater at roof drifts of 2% and 4%. Thus, while it appears that higher modes make larger relative contributions to the interstory drifts of frame structures, particularly longer period frame structures, the relative contribution may increase or decrease as drift levels increase and inelasticity develops.

Of the seven pushover methods considered, only the modified MPA procedure explicitly accounts for higher

modes. For the frame structures, this procedure often provided more accurate estimates of peak interstory drifts relative to the other pushover procedures. However, even the multiple mode estimates of frame interstory drifts were less than the mean dynamic values for the upper stories of the regular 9-story frame at the low and moderate drift levels and for several stories above the weak story of the 9-story weak-story frame at drifts of 2% and 4%.

The original MPA procedure and the modified MPA procedure used in the MDOF studies both use SRSS combinations and assume that there is no interaction of the modes, as is the case for elastic response. The SRSS combinations of response peaks, using the first three modes, nearly always underestimated the peak interstory drifts of the 3- and 9-story frames at 0.5% drift, suggesting that the SRSS estimates are not necessarily an upper bound to the mean dynamic peaks,[1] and that, in the case of the 9-story frames, consideration of additional modes may be required for improved estimates of interstory drift. Randomness in the timing of "modal" peaks generates variability in interstory drifts, limiting the potential accuracy of prospective estimates of interstory drift for individual events.

Interestingly, for each of the single mode load vectors except the rectangular load vector, the maximum of the interstory drifts determined over the height of the five buildings was a good estimate of the interstory drift that occurred in the nonlinear dynamic analyses at that story in the building. Furthermore, this maximum interstory drift provided a reasonable estimate of the largest interstory drifts that developed over the height of each structure. The weak story frames provide one illustration of this finding—each of these pushover methods provided good estimates of the interstory drifts that occurred at the weak stories of the 3- and 9-story weak story frames at drift levels of 2% and 4%. Of interest, this observation held even though the story at which the maximum interstory drift is calculated may vary with the choice of pushover load vectors.

F.4.2.3   Story Shears

The peak dynamic story shears begin with disproportionately large values at the uppermost story of all five buildings and increase monotonically towards the base. For the regular frames, peak dynamic story shears often exceeded pushover estimates, at all stories. For the regular 3-story frame, the modified MPA procedure underestimated story shears at 0.5% drift and significantly overestimated story shears at 4% drift. For the regular 9-story frame, the modified MPA procedure underestimated story shears over most of the building height at 0.5% drift, and overestimated story shears and 2% and 4% drift. The other pushover techniques generally had larger error.

For the weak story frames, all pushover techniques except for the modified MPA procedure provided good estimates of the lowest story shear at 2% and 4% drift. The dynamic shears in the remaining stories greatly exceeded the single-mode estimates at these drift levels. Estimates for these stories using the modified MPA procedure could be substantially more or less than the dynamic values, with the tendency to overestimate story shears becoming more pronounced with increasing drift levels. A possible improvement may be to include more modes, with each modal contribution reduced in some way as drift levels increase.

For the shear-wall building, the pattern of peak story shears changed with increasing drift. Response at 0.2% drift was marked by a quasi-first mode pattern, with a disproportionately large shear at the uppermost story. With increasing drift, the shears at the uppermost two stories and lowest three stories increased disproportionately, particularly for the lowest two stories. At 0.2% drift, the pattern of the story shears was offset from the code pattern by a more or less constant amount that resembles the F_t force used in the Equivalent Lateral Force procedure of earlier codes[2]. At 1% drift, the modified MPA procedure typically underestimated the story shears for the lowest stories, although the estimates improved at 2% drift. Estimates with the other procedures were not as good at the 1% and 2% drift levels. The rectangular load pattern, often used to bound wall shears for design, underestimated the shears over the entire height of the wall at the 1% and 2% drift levels, and underestimated the shears over the upper four stories at the 0.2% drift level.

F.4.2.4   Overturning Moments

The peak dynamic overturning moments displayed less variance than the story shears. The overall pattern of overturning moments was captured with the single-load

---

1. This may be because the modal peaks were estimated with a 2% damped spectrum, but the damping present in the nonlinear dynamic analyses may have been lower for some modes, thus leading to underestimates of higher mode contributions to drift.

2. Perhaps a better correlation would have been observed if the exponent k had been determined based on the effective period of the structure rather than the initial period.

Table F-8	Peak Roof Drift Ratios for the Five Building Models (%)			
Building Model	Near-Fault Record			
	ERZMV1	RRSMV1	LUCMV1	SCHMV1
3-story frame (regular)	4.07	4.96	1.79	2.62
3-story frame (weak story)	2.95	3.62	2.13	2.12
8-story wall	1.24	2.06	0.64	0.73
9-story frame (regular)	1.91	1.84	1.69	1.82
9-story frame (weak story)	1.88	1.85	1.71	2.13

vector techniques except for the 9-story weak story building, and the single-load vector techniques gave similar estimates, with the exception of the rectangular and code load vectors. Although the overall pattern was captured, the dynamic values were substantially underestimated in some cases, particularly at the upper stories and for the higher drift levels. The modified MPA procedure was inconsistent, sometimes providing accurate estimates and sometimes severely overestimating or underestimating the peak overturning moments.

F.4.3   Results for Near Field Motions

Sections F.8.4 and F.8.5 (Figures F-52 through F-71, and Figures F-72 through F-76) provide complete results of the analyses of the response of the examples to the near-field ground motions. Peak roof drift ratios obtained with the unscaled near-field motions were generally within or close to the ranges of predetermined drifts used with the ordinary ground motions (Table F-8), ranging between 1.79% and 4.96% for the 3-story frames, 1.69% and 1.88% for the 9-story frames, and 0.64% and 2.06% for the 8-story wall building.

For the near field motions, peak interstory drifts for the regular frames were at most about 25% higher than the average roof drift for the 3-story frame and were at most about 110% higher than the average roof drift for the 9-story frame. While these values are larger than the mean values reported in Section F.3.1 for the ordinary motions, they are not inconsistent with the peak values of interstory drift observed for the ordinary motions.

Errors in the estimates of the response quantities for both the ordinary and near fault ground motions are presented in Figures F-72 through F-76 for all buildings and pushover load vectors. The mean of the values of the error measure E_2 over the height of the buildings is plotted according to the drift level for the ordinary motions and is also plotted for the near-fault motions.[1] Maximum values of this error measure over the height of each building are also plotted. Note that the error measure E_2, when applied to the ordinary motions, is equivalent to the error measure E_1, because the mean of the pushover estimates is simply the single estimate obtained at a predetermined drift level.

A review of Figures F-72 through F-76 shows that the quality of the estimates is, in general, as good or better than the estimates made for the ordinary ground motions, with the exception of displacement estimates of the 9-story weak-story building. In some cases the weak-story frame showed a clear weak story response (RRSMV1 and LUCMV1 ground motions), while in other cases, peak interstory drifts in the weak story were only moderately elevated over those occurring in the regular frames for the same motion (ERZMV1 and SCHMV1 ground motions). These differences occurred even though the peak roof drifts of the 9-story weak-story frame (1.71% to 2.13%) were similar to those of the regular 9-story frame (1.69% to 1.91%). For those cases in which weak story responses occurred, the pushover methods provided good estimates of displacement response. Only for the two near-fault motions that did not generate a weak-story response were the estimates poor.

F.5   Equivalent SDOF Estimates of Peak Roof Displacement Response

The preceding analyses of the example buildings for MDOF effects focused on the accuracy of estimates made using various load vectors for building models subjected to prescribed peak drift levels. Underlying this approach was the assumption that accurate estimates of the peak roof displacement can be obtained using the simplified inelastic procedures. Work by many researchers, including Chopra et al. (2003), Miranda (1991), Collins et al. (1995), Seneviratna and Krawinkler (1997), and Cuesta and Aschheim (2001), indicates a tendency for the equivalent SDOF models to overestimate peak roof displacements of inelastic structures, by up to 20% or more, depending on the level of nonlinearity in the system. To illustrate this

---

1. The E_2 error measure is defined in Section F.4.1.

tendency, estimates were made for the five example buildings based on their first mode capacity curves. The estimates were made using the ATC-40 and FEMA 356 relationships for establishing the yield-strength coefficient of the equivalent SDOF system.

F.5.1   Analysis Details

Peak roof displacement estimates were made for the five example buildings subjected to the 11 ordinary ground motion records scaled to achieve the predetermined drift levels and for the unscaled near-field ground motions. Estimates were made for cases in which P-Delta effects were included as well as for cases in which P-Delta effects were excluded. Results are reported in detail for cases in which the bilinear curve, fitted to the capacity curve obtained from a first mode pushover analysis, displayed a positive post-yield stiffness. P-Delta effects were included for the 3-story frames and the 8-story wall (Figure F-8). However, to avoid a negative post-yield stiffness for the 9-story frames, P-Delta effects had to be excluded for the analyses of these frames.

In cases in which P-Delta effects were considered, the mode shape and the nonlinear static analysis were determined with P-Delta effects included, and the applied lateral force is plotted rather than the base shear (which is amplified due to P-Delta). In cases in which P-Delta effects were not considered, the mode shape and nonlinear static analysis were determined without considering P-Delta effects. For each case considered, ground motions were scaled to obtain the predetermined target drift levels for the MDOF models. If P-Delta effects were included, they were included in the nonlinear MDOF dynamic analyses and were represented using bilinear hysteretic models for the steel frame buildings and a stiffness degrading model for the concrete shear-wall building, with initial- and post-yield stiffnesses adjusted to reflect the effects of P-Delta on the MDOF capacity curves. Similarly, if P-Delta effects were not considered, they were excluded from both the MDOF and SDOF analyses.

"Equivalent" SDOF (ESDOF) systems were determined according to the methods of ATC-40 and FEMA 356. For both methods, the yield displacement Δ_y of the ESDOF system is determined as

$$\Delta_y = \frac{\Delta_{y,roof}}{\Gamma_1} \tag{F-5}$$

where $\Delta_{y,\,roof}$ = the roof displacement at yield, and Γ_1 = the first mode participation factor (given by $\phi^T M1 / \phi^T M \phi$)[1].

In the ATC-40 method, the yield strength coefficient of the ESDOF system is given by

$$C_y = \frac{S_a}{g} = \frac{V_{y,mdof}/W}{\alpha_1} \tag{F-6}$$

where S_a = the pseudo-acceleration associated with yield of the ESDOF system, g = the acceleration of gravity, $V_{y,\,mdof}$ = the yield strength of the MDOF system, W = the weight of the MDOF system, and α_1 = the modal mass coefficient (given by $\Gamma_1(\phi^T M1/1^T M1)$).

In the FEMA 356 method, the yield strength coefficient of the ESDOF system is approximated as

$$C_y = \frac{S_a}{g} = \frac{V_{y,mdof}}{W}\Gamma_1 \tag{F-7}$$

which relies on the approximation $\Gamma_1 \approx 1/\alpha_1$.

If ϕ is set equal to an elastic mode shape, the ATC-40 method produces an ESDOF system that has a period of vibration equal to the period associated with the mode shape. However, the approximation in Equation F-7 causes the period of vibration and the yield strength coefficient of the FEMA 356 ESDOF system to deviate slightly from the corresponding period of the MDOF system.[2]

The ESDOF systems resulting from the ATC-40 and FEMA 356 methods were subjected to the scaled ground motion records, determined for each building model and drift level. A bilinear hysteretic model was used for the frames, and a simple stiffness degrading model was used for the ESDOF system representing the 8-story wall building. The resulting peak displacement was scaled by Γ_1 to obtain the estimated peak roof displacement.

---

1. For simplicity in presentation, this document presumes that ϕ has been normalized to unit amplitude at the roof.

2. Note that if higher modes are to be considered, Γ_i is a poor approximation to $1/\alpha_i$, for $i > 1$.

F.5.2 Analysis Results

The ratio of the roof displacement estimated with the ESDOF system and the peak roof displacement that developed in the nonlinear dynamic analysis of the MDOF system was determined for each building model and each ground motion record. Statistics of this ratio, termed the "displacement ratio," were determined for each building model at each drift level and for the set of near fault motions. The minimum, maximum, mean, median, and standard deviation of this ratio were computed. Detailed results for the ordinary motions are summarized for the ATC-40 formulation (Equation F-6) in Figure F-15.

Mean displacement ratios for the ordinary motions were between approximately 0.95 and 1.25 for the five buildings (Figure F-15), with a tendency to increase with increasing roof drift. Similar means were obtained with the FEMA 356 formulation (Equation F-7), although dispersions were larger for this formulation. Accuracy was similar for the near-field motions. The ATC-40 formulation is preferred because it resulted in smaller dispersions, accurately reflects the frequency content of the excitation for elastic response, and is consistent with common derivations of "equivalent" SDOF systems.

Accuracy was compromised in cases in which the post-yield stiffness of the ESDOF system was negative. In such cases, there was a tendency for the displacements of the equivalent SDOF systems to be exaggerated, with some SDOF systems collapsing, although the MDOF systems simply reached their predetermined drifts. For such cases, nonlinear dynamic analyses may be preferred, given the potential for ESDOF systems to significantly overestimate the roof displacement.

F.6 Scaled NDP Analysis Method

F.6.1 Background

The ATC-55 MDOF studies were conducted to illustrate the accuracy of several available pushover methods for estimating peak response quantities, by comparison with results obtained from nonlinear dynamic analyses. The pushover techniques were not consistently able to provide accurate estimates of response quantities (interstory drifts, story shears, and overturning moments) for many of the example buildings. The difference between the pushover estimates and the results from nonlinear dynamic analyses is attributed primarily to the presence of higher modes or MDOF effects. Although scatter is to be expected in the results from nonlinear dynamic analyses, the dispersion in the

peak dynamic values of interstory drifts, story shears, and overturning moments was relatively small, and the values of these quantities could differ significantly from the estimates obtained using the various pushover methods.

The Scaled NDP is based on the idea that a relatively small number of nonlinear dynamic analyses can be used to estimate the response quantities of interest. In the Scaled NDP (described in Section 9.5.2), the ground motion records are scaled so that the peak roof displacement matches the target displacement determined from nonlinear static analysis. Each dynamic analysis contributes positively to the estimate of the central tendency and range of dynamic response values. In contrast, none of the pushover methods was able to consistently provide reliable estimates of the peak interstory drifts, story shears, and overturning moments, for the example buildings considered.

F.6.2 Elaboration of Step 3 and Examples

Step 3 of the basic procedure described in Section 9.5.2 suggests that estimates of a response quantity at the mean plus κ standard deviation level can be determined by multiplying the mean of the response quantity observed in the n dynamic analyses by a coefficient. Let the sample mean of the response quantity of interest be designated by $\bar{x}_n$. As shown in Section F.6.3, if the response quantities are normally distributed, the quantity $c(1+\kappa COV)\bar{x}_n$ exceeds the true mean plus κ standard deviations with confidence level α. In the preceding, c is given by

$$c = \frac{1}{1-\left(\Phi^{-1}(\alpha)\right)\dfrac{COV}{\sqrt{n}}} \qquad (F-8)$$

where $\Phi^{-1}_{t,n-1}(\alpha)$ represents the value of the variate of the Student's t-distribution with n-1 degrees of freedom at a confidence level of α, and COV represents the coefficient of variation determined for the sample of n observations of the response quantity x.

Equation F-8 simplifies to $c = 1$ for a confidence level, α, of 50%. For a confidence level of 90%, Equation Equation F-8 can be solved to obtain the values of c given in Table F-9.

Thus, the quantity $c(1+\kappa COV)\bar{x}_n$ is said to exceed the true mean plus κ standard deviation value with confidence level α. The quantity κ assumes a value of zero where estimates of the true mean are sought.

(a) 3-Story Regular Steel Frame

(b) 3-Story Weak-Story Steel Frame

(c) 8-Story Shear Wall

(d) 9-Story Regular Steel Frame

(e) 9-Story Weak-Story Steel Frame
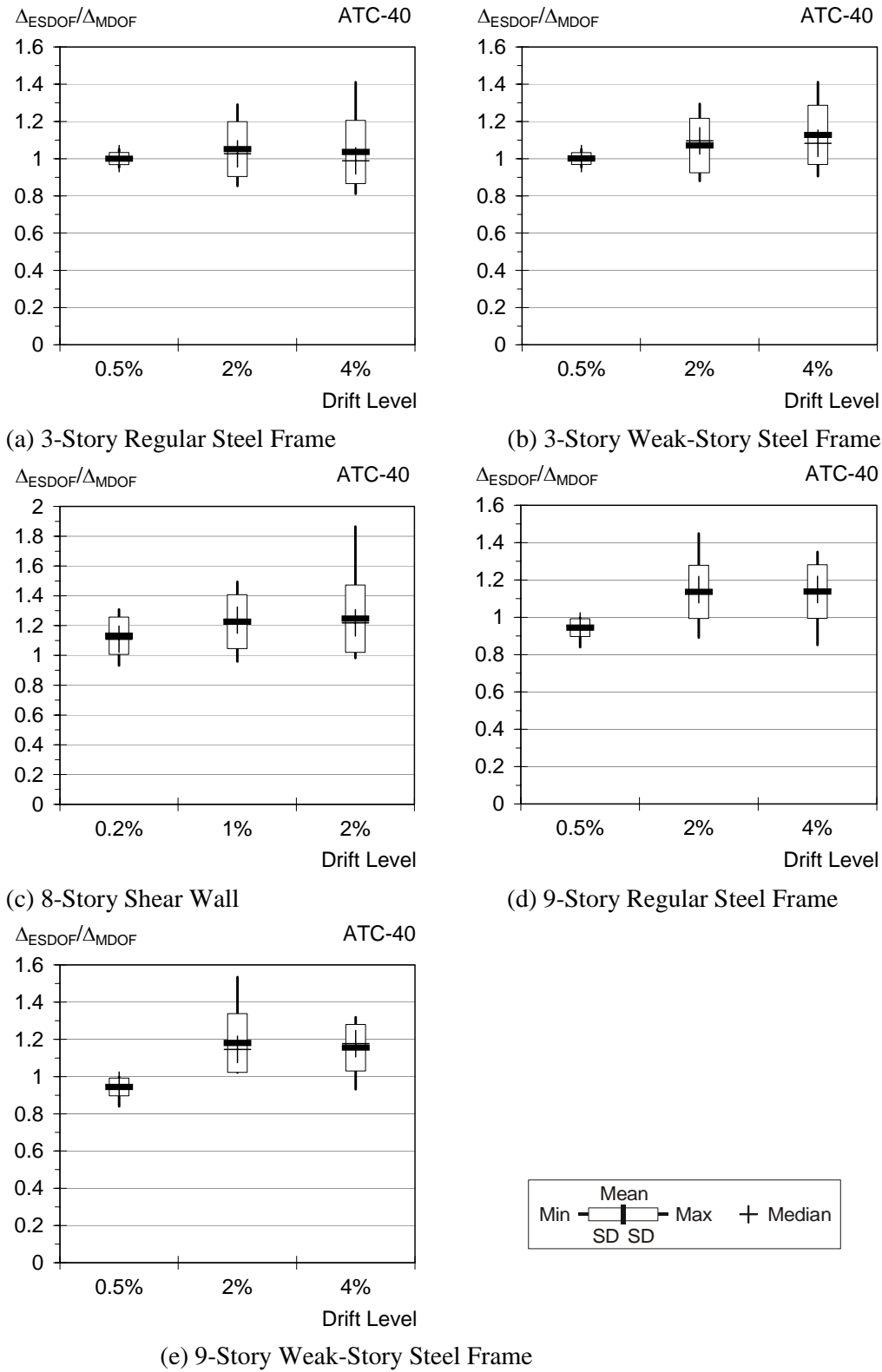
Figure F-15   Example statistical distributions of displacement ratios for the ordinary ground motions.

Table F-9   Values of *c* at the 90% Confidence Level

n	$\Phi_{t,n-1}^{-1}(\alpha)$	Coefficient of Variation									
		0.05	0.10	0.15	0.20	0.25	0.30	0.35	0.40	0.45	0.50
3	1.886	1.06	1.12	1.20	1.28	1.37	1.48	1.62	1.77	1.96	2.19
5	1.533	1.04	1.07	1.11	1.16	1.21	1.26	1.32	1.38	1.45	1.52
7	1.440	1.03	1.06	1.09	1.12	1.16	1.20	1.24	1.28	1.32	1.37
10	1.372	1.02	1.05	1.07	1.10	1.12	1.15	1.18	1.21	1.24	1.28
20	1.328	1.02	1.03	1.05	1.06	1.08	1.10	1.12	1.13	1.15	1.17
50	1.299	1.01	1.02	1.03	1.04	1.05	1.06	1.07	1.08	1.09	1.10
100	1.290	1.01	1.01	1.02	1.03	1.03	1.04	1.05	1.05	1.06	1.07

Table F-9 also can be used to indicate the number of analyses to run—that is, the point at which additional analytical data are of negligible benefit. The derivation of Equation F-8 is provided in Section F.6.3 below.

F.6.2.1   Example Illustrations

Interstory Drift Estimate: The sample mean of the peak values of interstory drift at the lowest story of the 9-story frame at a predetermined roof drift of 4% is $\bar{x}_n = 6.5\%$. The true COV is estimated from the 11 peak dynamic responses to be 0.16. For this COV, Equation F-8 results in $c = 1.05$. The true mean value of peak interstory drift is estimated to not exceed $c\bar{x}_n = 1.05(6.5\%) = 6.8\%$ at the 90% confidence level. That is, there is a 90% probability that the true mean peak interstory drift at the lowest story is less than 6.8% at the hazard level that produces a roof drift of 4%.

Story Shear Estimate: The sample mean of the peak story shears at the lowest story of the 8-story wall at a predetermined roof drift of 2% is $\bar{x}_n = 1070$ kips. To guard against the potential for shear failure, an "upper bound" limit on shear demands is desired. Based on the 11 analyses, the true COV of the peak story shears is estimated to be 0.22. Using Equation F-8, $c = 1.10$. Therefore, there is a 90% probability that the true mean plus one standard deviation peak story shear is less than $(1 + \kappa \text{COV}) c\bar{x}_n = 1.10(1 + 0.22)(1070 \text{ kips}) = 1440$ kips, for the hazard that produces a roof drift of 2%.

Note that the numerical values determined by this approach should be considered estimates rather than

exact values. The estimates are considered to be more reliable, in general, than those determined using only static analysis techniques.

F.6.3   Statistical Basis

Equation F-8 was derived assuming that the response quantities are normally distributed, an assumption that is approximately applicable even for log-normally distributed data if the dispersion in the data is not large.

Problem Statement: A response quantity *X* has peak values x_1, x_2, …x_n in *n* dynamic analyses of a structure. The mean of the *n* responses is $\bar{x}_n$. The responses are assumed to be normally distributed, with mean μ and standard deviation σ. What is the scale factor *c'* such that $c'\bar{x}_n$ exceeds $\mu + \kappa\sigma$ with a specified level of confidence α?

Answer:

1. *X* is normally distributed with true mean μ and standard deviation σ_x. That is, X ~ N(μ, σ).

2. The sample mean of *X* is given by $\bar{x}_n$ where

$$\bar{x}_n \sim N\left(\mu, \frac{\sigma}{\sqrt{n}}\right) \tag{F-9}$$

3. If the standard deviation σ is estimated by the sample standard deviation *s*, then the sample mean has the Student's *t*-distribution with *n*-1 degrees of freedom:

$$\bar{x}_n \sim t_{n-1}\left(\mu, \frac{s}{\sqrt{n}}\right) \qquad \text{(F-10)}$$

This can be expressed as

$$\frac{\bar{x}_n - \mu}{s/\sqrt{n}} \sim t_{n-1}(0,1) \qquad \text{(F-11)}$$

4. We seek to establish c' such that

$$P(c'\bar{x}_n > \mu + \kappa\sigma) = \alpha \qquad \text{(F-12)}$$

which can be restated as

$$P\left(\bar{x}_n < \frac{\mu + \kappa\sigma}{c'}\right) = 1 - \alpha \qquad \text{(F-13)}$$

5. Given Equation F-10, this probability can be re-expressed as

$$\Phi_{t,n-1}\left(\frac{\frac{\mu + \kappa\sigma}{c'} - \mu}{s/\sqrt{n}}\right) = 1 - \alpha \qquad \text{(F-14)}$$

where $\Phi_{t,n-1}$ is the cumulative distribution function for the Student's t-distribution with n-1 degrees of freedom. Thus,

$$\Phi_{t,n-1}^{-1}(1-\alpha) = \left(\frac{\frac{\mu + \kappa\sigma}{c'} - \mu}{s/\sqrt{n}}\right) \qquad \text{(F-15)}$$

6. Algebraic manipulation allows c' to be expressed as

$$c' = \frac{1 + \kappa\sigma/\mu}{1 + \Phi_{t,n-1}^{-1}(1-\alpha)\frac{s/\mu}{\sqrt{n}}} \qquad \text{(F-16)}$$

or equivalently as

$$c' = \frac{1 + \kappa COV}{1 - \Phi_{t,n-1}^{-1}(\alpha)\frac{COV}{\sqrt{n}}} \qquad \text{(F-17)}$$

where σ/μ is approximated by the sample coefficient of variation, COV. For convenience, we may express $c' = c(1 + \kappa COV)$ where

$$c = \frac{1}{1 - \Phi_{t,n-1}^{-1}(\alpha)\frac{COV}{\sqrt{n}}} \qquad \text{(F-18)}$$

where $\Phi_{t,n-1}^{-1}(\alpha)$ is the value of the variate of the Student's t-distribution with n-1 degrees of freedom at a confidence level of α.

F.6.4 Observed Coefficients of Variation

The coefficients of variation (*COV*) of the response quantities determined in the MDOF studies are plotted in Section F.8.6 (Figures F-77 through F-81). The COVs are plotted for each response quantity at each floor or story for each of the five building models, at each of the three drift levels. In general, the COVs are highest at the upper stories and near the base of each model, and differ for each response quantity. The COVs for floor displacements diminish to zero at the top, due to the methodology employed in the study.

Approximate upper bounds to the COVs are tabulated in Table F-10, where "approximate" indicates that the limit was exceeded by a small amount at a limited number of locations. The COVs appear to increase with the number of stories (or period) and appear to be larger

Table F-10   Approximate Upper Bounds to the COVs over the Height of each Building Model

Building Model	Interstory Drift	Story Shear	Overturning Moment
3-story frame	0.15	0.15	0.15
3-story frame (weak story)	0.20	0.15	0.15
8-story wall	0.10	0.20	0.15
9-story frame	0.20	0.20	0.20
9-story frame (weak story)	0.30	0.25	0.25

for buildings with weak story behavior. It is suggested that a COV of 0.25 to 0.30 may be appropriate for all quantities in cases where a sufficient number of analyses are not available for establishing an accurate estimate of the COV.

F.7 Energy-based Approaches for Pushover Analysis

Motivated by the difficulties associated with reversals of the higher mode capacity curves (see Figure F-14), Hernández Montes et al. (2003) formulated an energy-based pushover analysis approach, in which a displacement is derived that represents the work done by the lateral forces acting through the floor displacements during the pushover analysis. The energy-based displacement is derived to coincide with the spectral displacement of conventional pushover approaches in the elastic portion of the response. However, the resulting capacity curves do not display the reversals observed in some conventional higher mode pushover analyses. The energy-based pushover approach was applied to the five example buildings to estimate (1) roof displacements based on response in the first mode and (2) other response quantities using a multiple mode procedure. Results are reported in the following.

F.7.1 Peak Displacement Response

As described in Section F.5, many research studies have reported a tendency for conventional procedures to overestimate peak roof displacement of structures responding inelastically by up to 20% or more. This tendency is illustrated for the five example buildings in Figure F-15. These results are compared with estimates made using the energy-based first mode capacity curve in Table F-11.

The data in Table F-11 suggest that the energy-based approach provides an improvement in roof displacement estimates for the four frames. Note that the same hysteretic model was used for the frame elements and for the corresponding equivalent SDOF systems. Results for the wall building are more difficult to interpret because SDOF responses were computed using a simple stiffness-degrading model, while the MDOF responses were computed using a fiber element. Nevertheless, the energy-based displacement may be capable of providing improved estimates of roof displacement response.

Table F-11   **Means of the Ratio of Roof Displacements: SDOF Estimate / Actual MDOF**

Building	Roof Drift Level	Conventional First Mode	Energy-Based First Mode
3-story frame (with *P*-Delta)	0.5%	1.00	1.00
	2%	1.05	1.03
	4%	1.04	1.02
3-story weak story frame (with *P*-Delta)	0.5%	1.00	1.00
	2%	1.07	0.94
	4%	1.13	0.98
8-story wall (with *P*-Delta)	0.2%	1.13	1.16
	1%	1.23	1.20
	2%	1.25	NA[1]
9-story frame (without *P*-Delta)	0.5%	0.94	0.95
	2%	1.14	1.03
	4%	1.14	1.02
9-story weak-story frame (without *P*-Delta)	0.5%	0.94	0.95
	2%	1.18	1.05
	4%	1.16	1.03

[1]. NA: the nonlinear static analysis failed to converge.

F.7.2 Multiple Mode Estimates of Response Quantities

As described in Section F.3.2, the contributions of higher modes to response quantities were evaluated using a modified MPA procedure in which only elastic contributions of the higher modes were used, because the conventional multimode pushover procedure could not be used due to reversals of some higher mode capacity curves. The development of the energy-based pushover method provides a way to account for the potentially inelastic response associated with each of the modes, because the pushover curves obtained with the energy-based approach display the usual softening behavior. One concern with such a procedure is that responses in each mode are determined independently, and hence, estimates of response quantities computed by SRSS combinations can exceed capacity limits on force and moment. Results obtained with the modified

MPA procedure, used in the first portion of the MDOF studies, are compared in this section with the results obtained using a modified MPA procedure in which potentially inelastic responses are considered using the energy-based pushover curves.

In the energy-based modification to the multimode pushover analysis procedure, independent pushover analyses are done in each of the first three modes. For consistency, the target displacement for the first mode was set equal to the predetermined roof drift. The target displacements of the second and third modes were determined by application of an R-C_1-T relationship to the mean spectrum, which was determined for the scaled ground motions used for each building and drift

level. The R-C_1-T relationship that was applied is given by Equation 5-1. Response quantities were determined for each of these modal pushover analyses at the corresponding target displacements. SRSS combinations of these quantities were then taken.

Figure F-16 compares results obtained with the modified MPA and energy-based multiple mode procedures against the backdrop of results obtained in the dynamic responses. A sampling of results are plotted that correspond to those presented in Section F.8.2. In some cases the results obtained with the energy-based multiple mode procedure are improvements, but the estimates still are not consistently reliable.
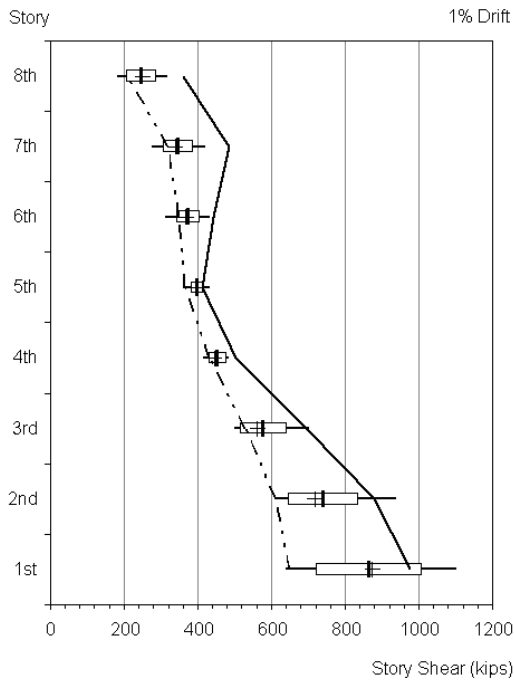
(a) **Story shears for 8-story wall at 1% drift**
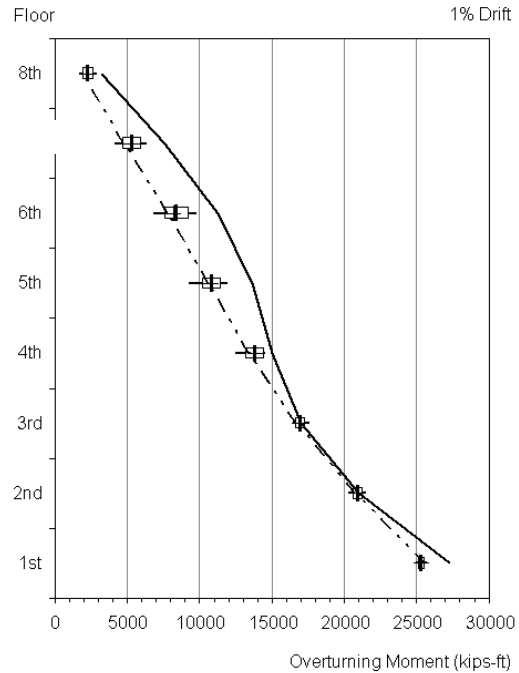
(b) **Overturning moments for 8-story wall at 1% drift**
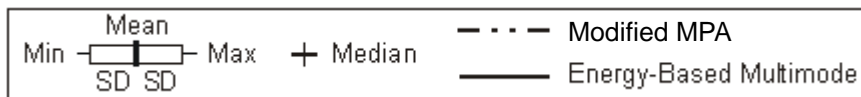
Figure F-16   Example comparisons of energy-based and conventional multiple mode calculations.
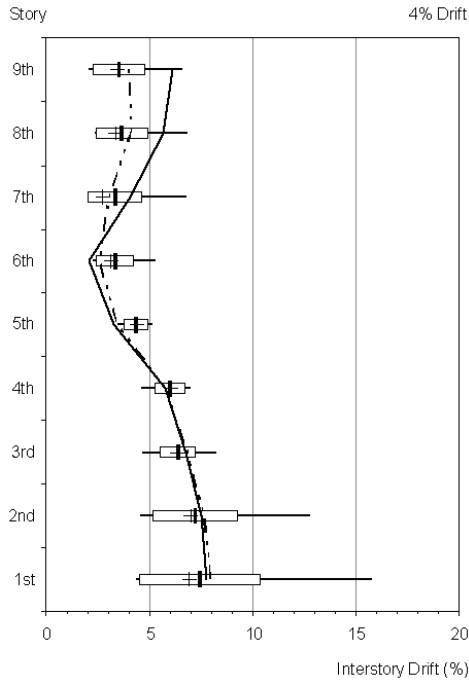
(c) Interstory drifts for 9-story frame at 4% drift
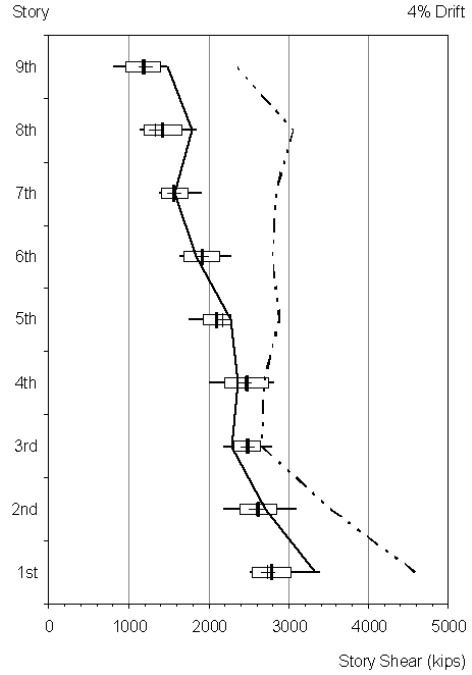
(d) Story shears for 9-story frame at 4% drift
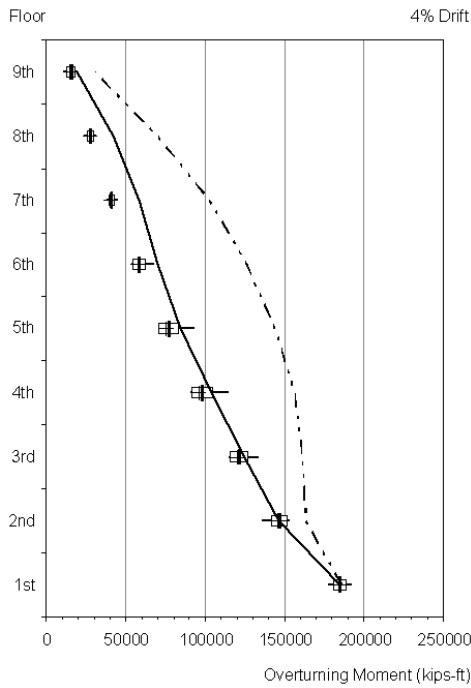
(e) Overturning moments for 9-story frame at 4% drift
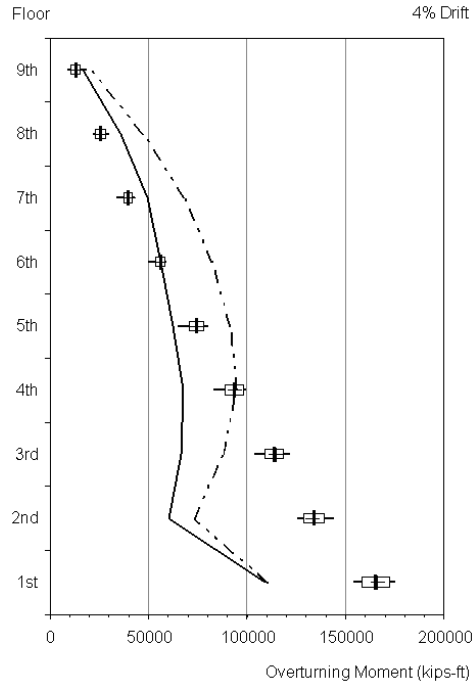
(f) Overturning moments for 9-story weak story frame at 4% drift
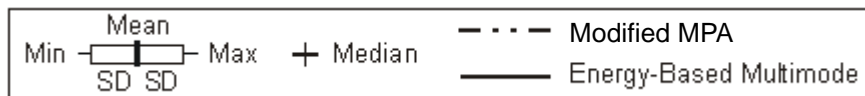
Figure F-16   Example comparisons of energy-based and conventional multiple mode calculations (continued).

F.8 Detailed Figure Sets for the MDOF Examples

This section contains detailed figure sets resulting from the analyses described earlier in this Appendix. Section F.8.1 provides details of the ground motions, and includes plots of spectral acceleration and spectral displacement in addition to acceleration, velocity, and displacement time histories for the unscaled ground motions.

Section F.8.2 presents plots that compare the deterministic response quantities obtained in the static pushover analyses with the statistical distributions obtained in the dynamic analyses for the 11 ground motions. Results are presented for the peak values of each response quantity over the height of each building model, for the five building models, each at three predetermined values of roof drift.

Section F.8.3 presents an evaluation of mean and maximum errors in the static analysis estimates of the mean dynamic results presented in Section F.8.2. Mean and maximum errors in these estimates over the height

of each building model are plotted, for each static analysis method, for each response quantity, and for each building model at each of three predetermined drift levels. See Section F.4.1 for further information.

Section F.8.4 presents plots that compare the deterministic response quantities obtained in the static pushover analyses with the peak values obtained in the dynamic analyses, for each building model subjected to each near-field ground motion. The peak roof drift obtained in the dynamic analysis and used in the static pushover analysis is shown.

Section F.8.5 presents an evaluation of mean and maximum errors in the static analysis estimates of the near-field response values, as described in Section F.4.1 These errors are plotted together with those obtained for the ordinary ground motions for comparison purposes.

Section F.8.6 presents observed coefficients of variation of the response quantities determined for the ordinary (Site Class C) motions.

F.8.1   Ground Motion Details
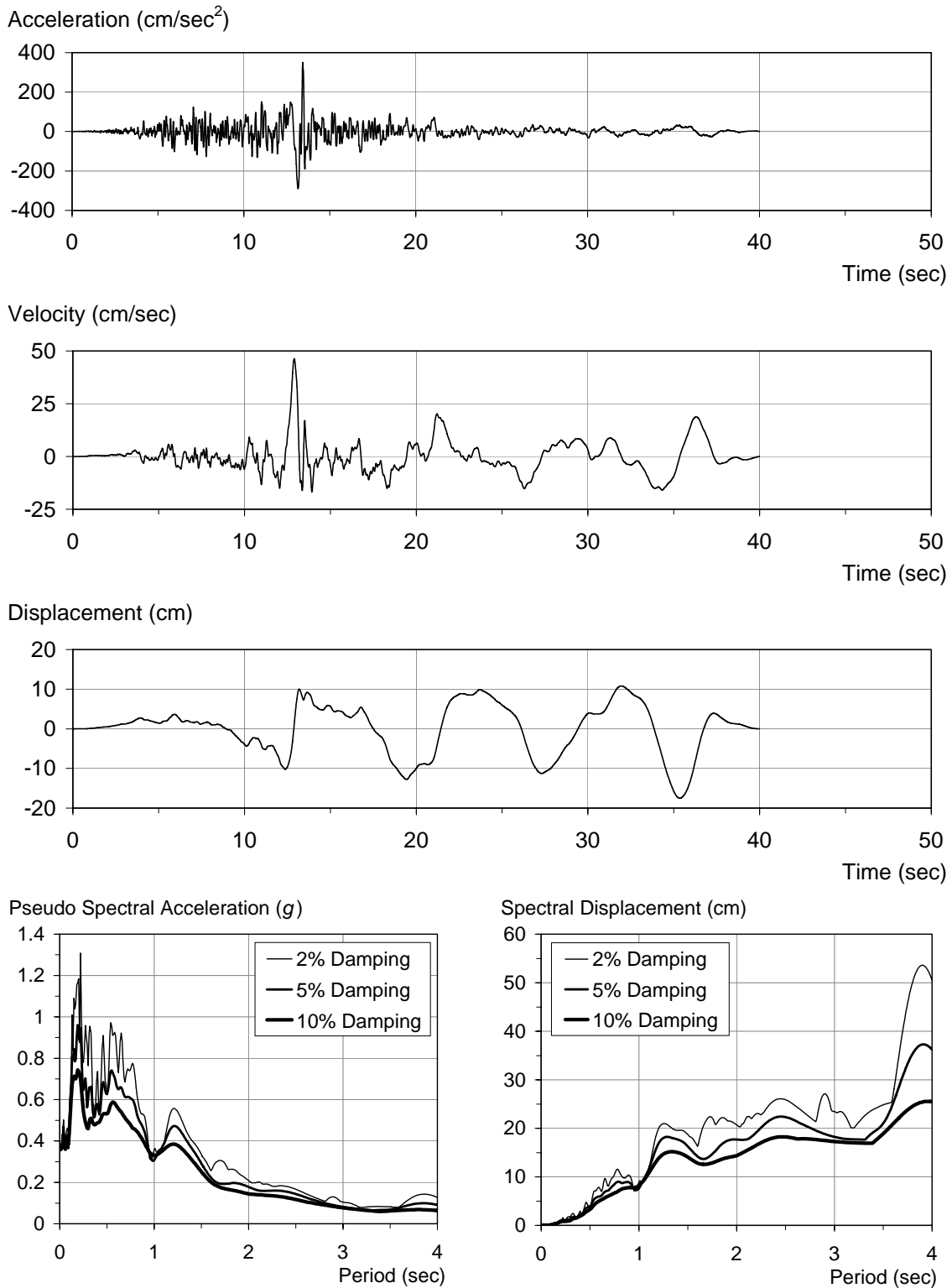
Figure F-17   Characteristics of the ICC000 ground motion
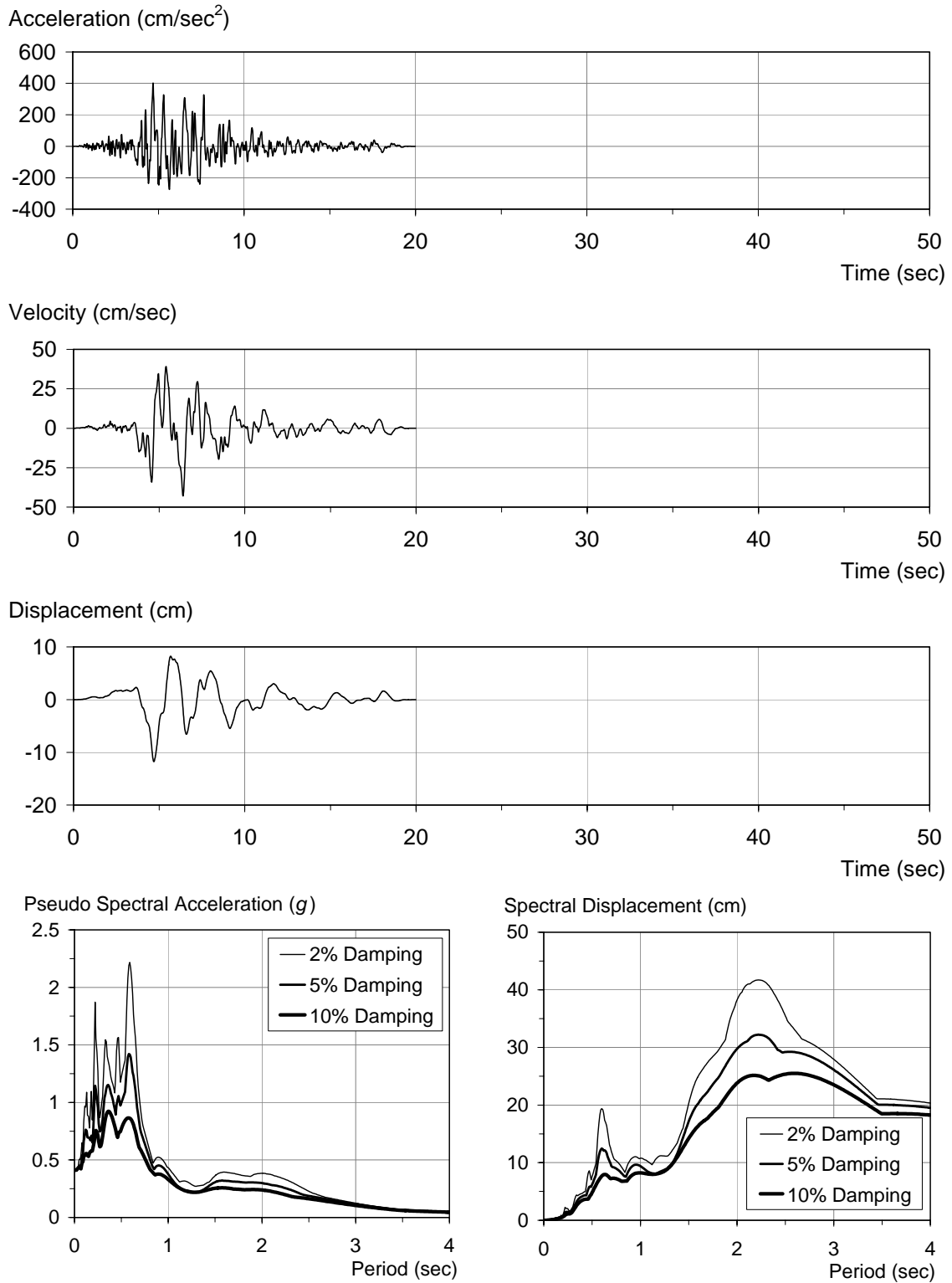
Figure F-18   Characteristics of the LOS000 ground motion
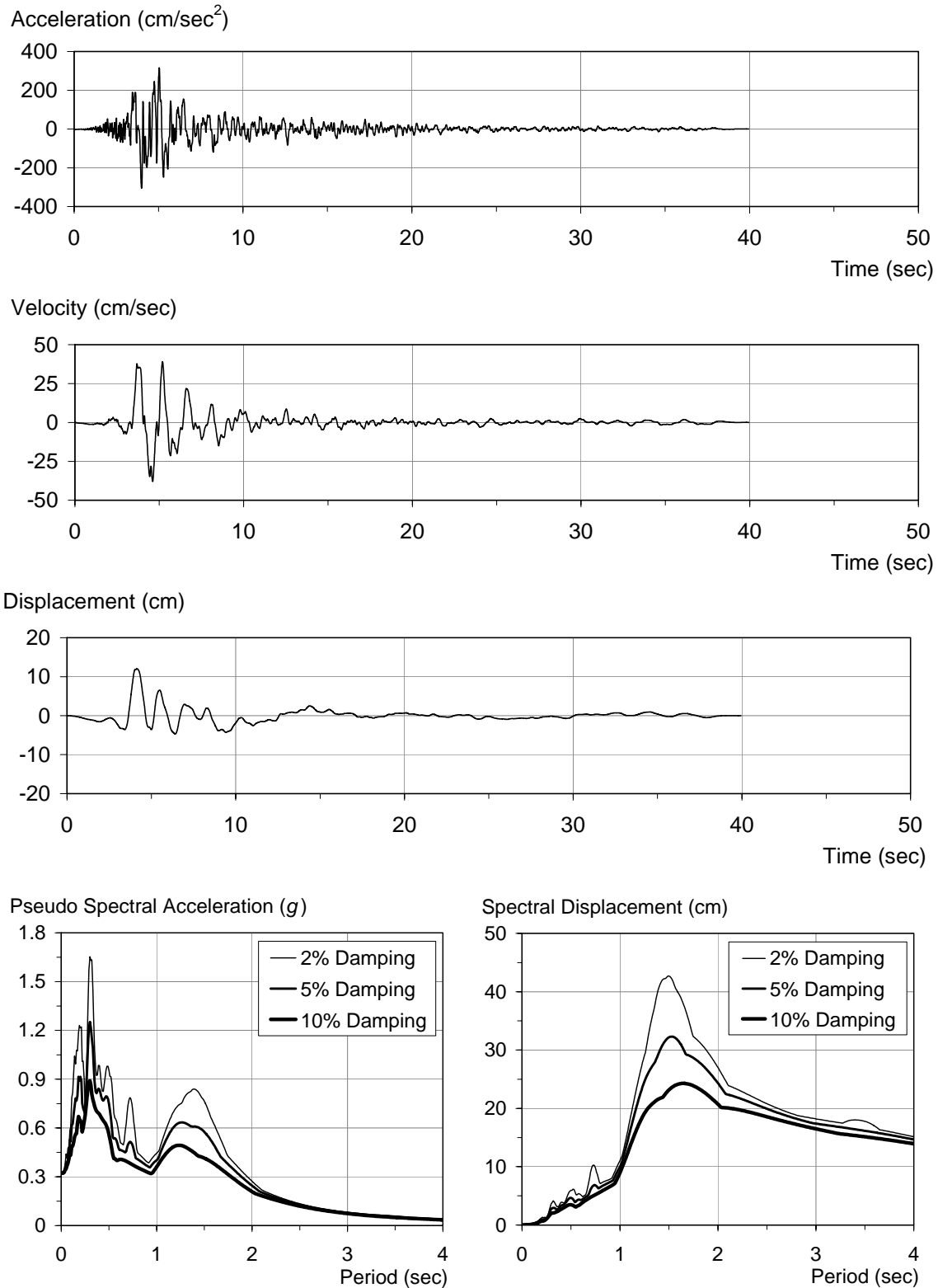
Figure F-19   Characteristics of the G02090 ground motion
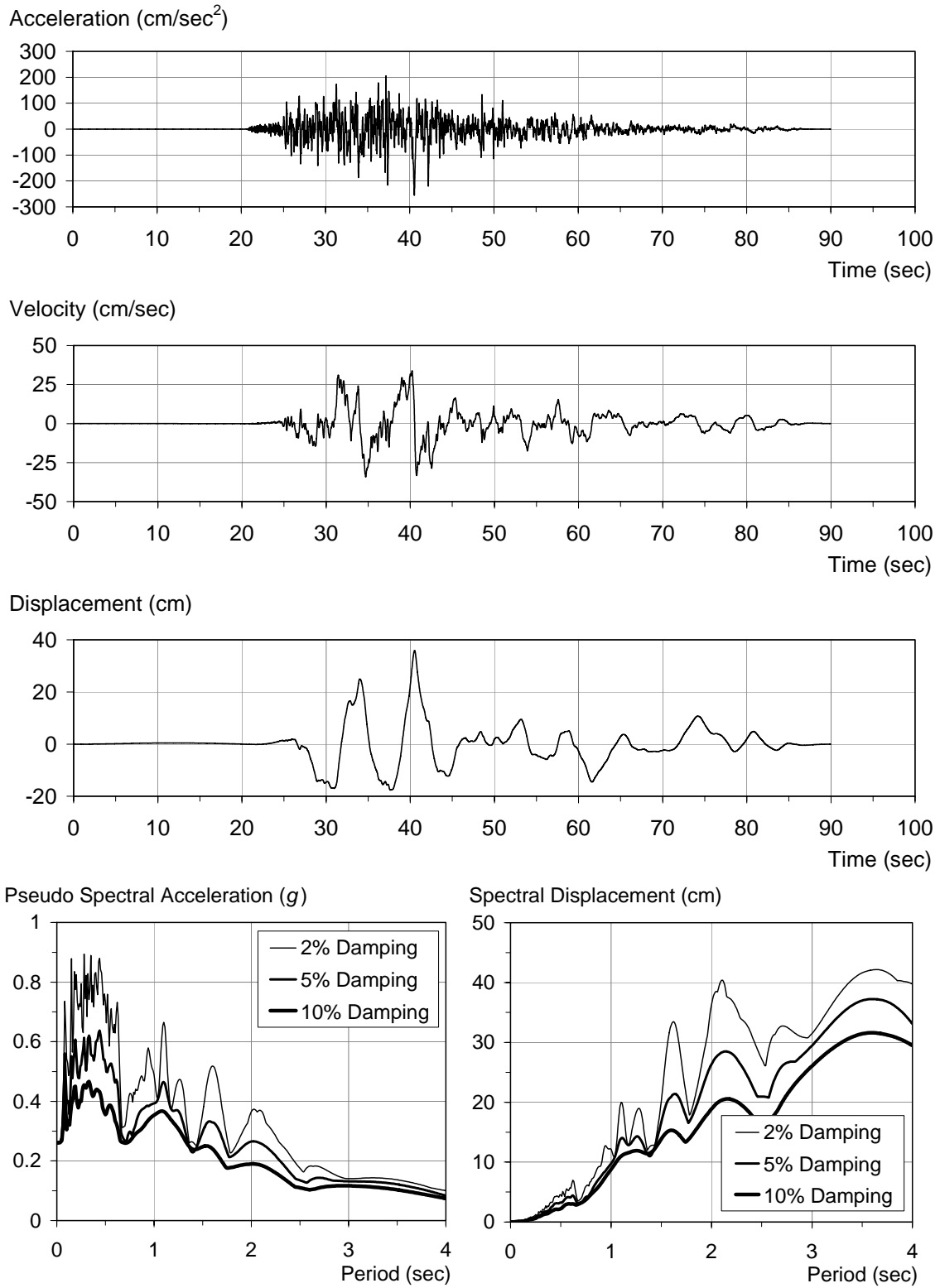
Figure F-20   Characteristics of the TCU122N ground motion
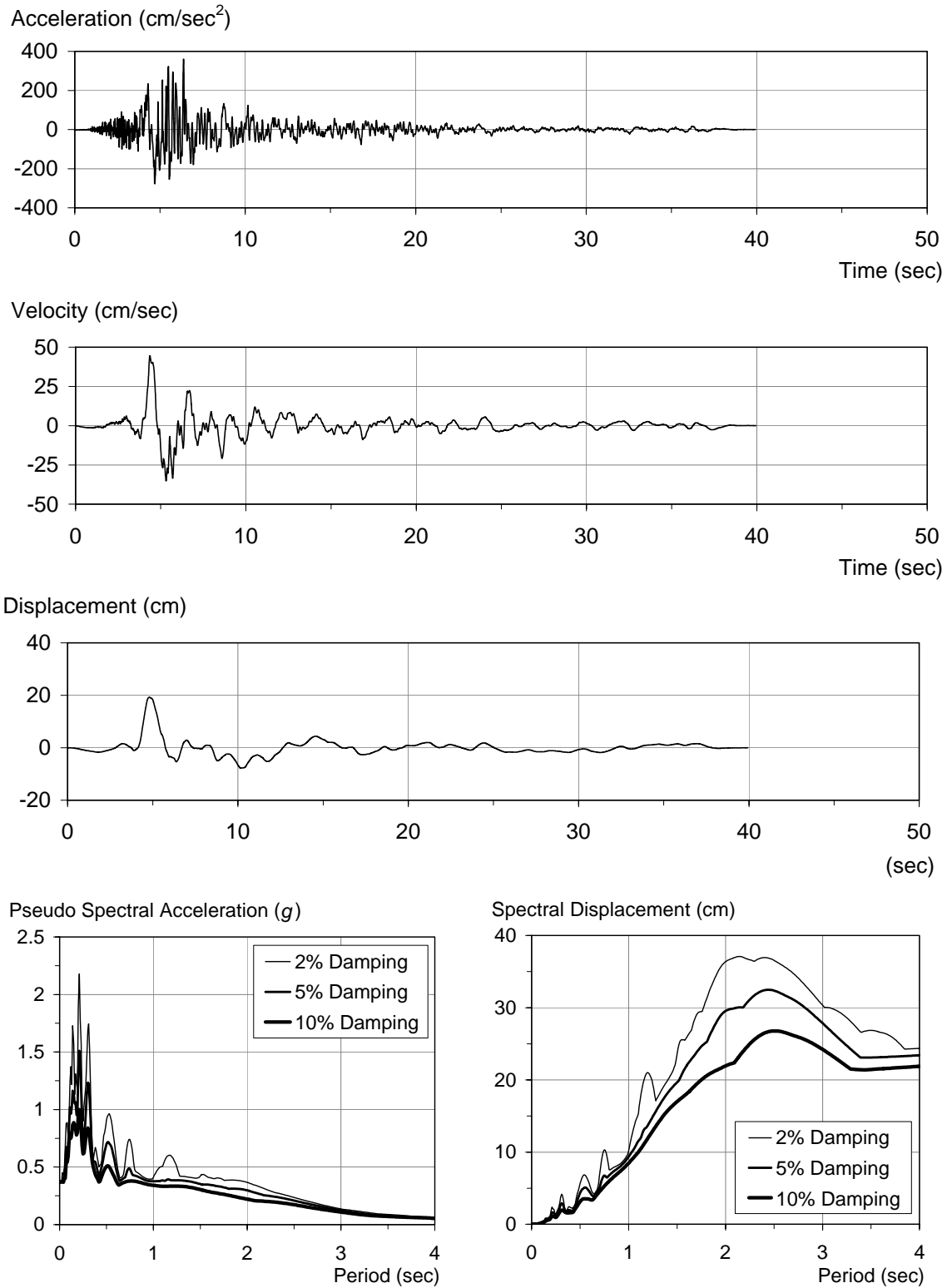
Figure F-21   Characteristics of the G03090 ground motion
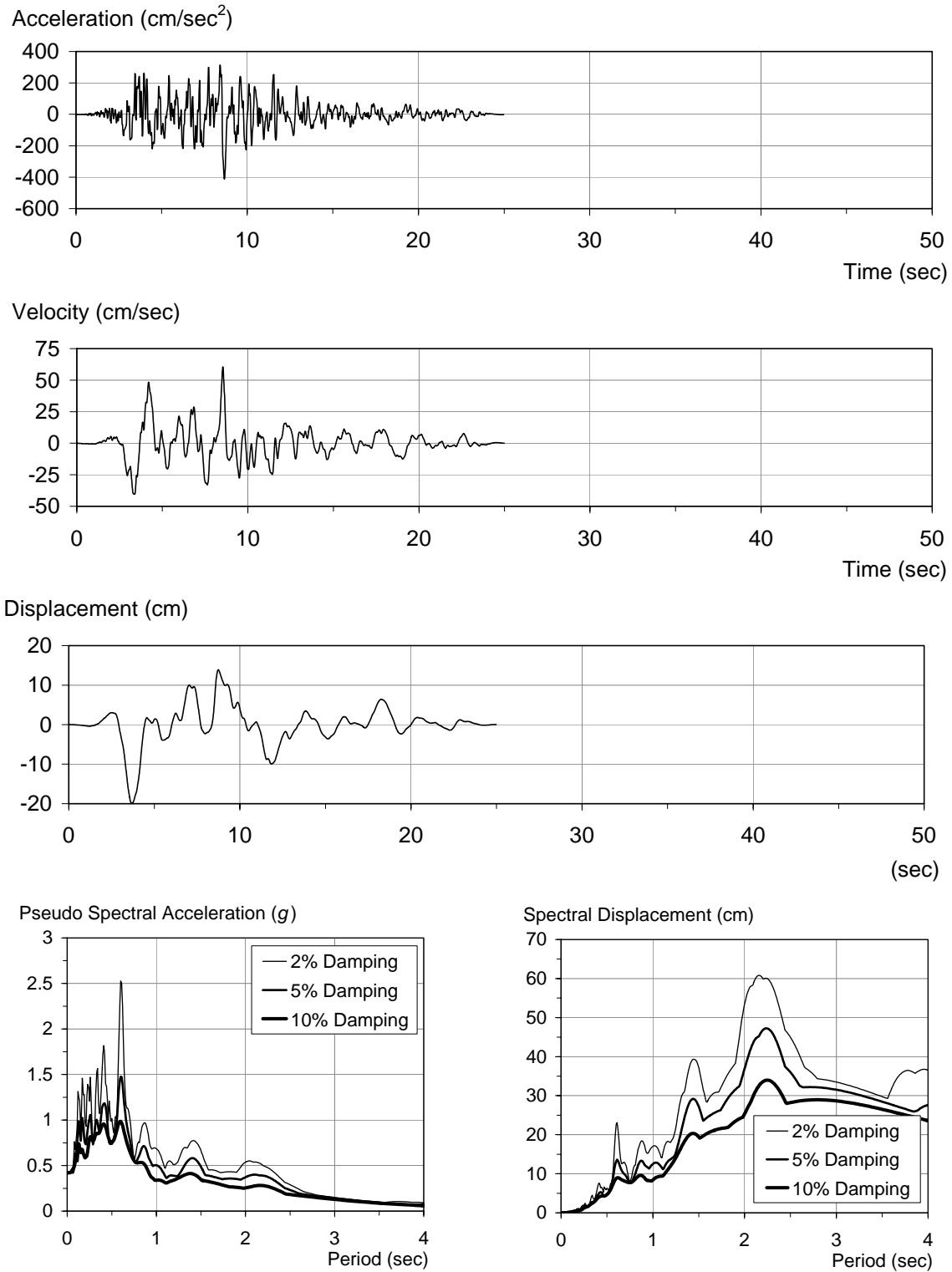
Figure F-22   Characteristics of the CNP196 ground motion

Acceleration (cm/sec^2)

Time (sec)

Velocity (cm/sec)

Time (sec)

Displacement (cm)

Time (sec)

Pseudo Spectral Acceleration (*g*)

Period (sec)

Spectral Displacement (cm)

Period (sec)
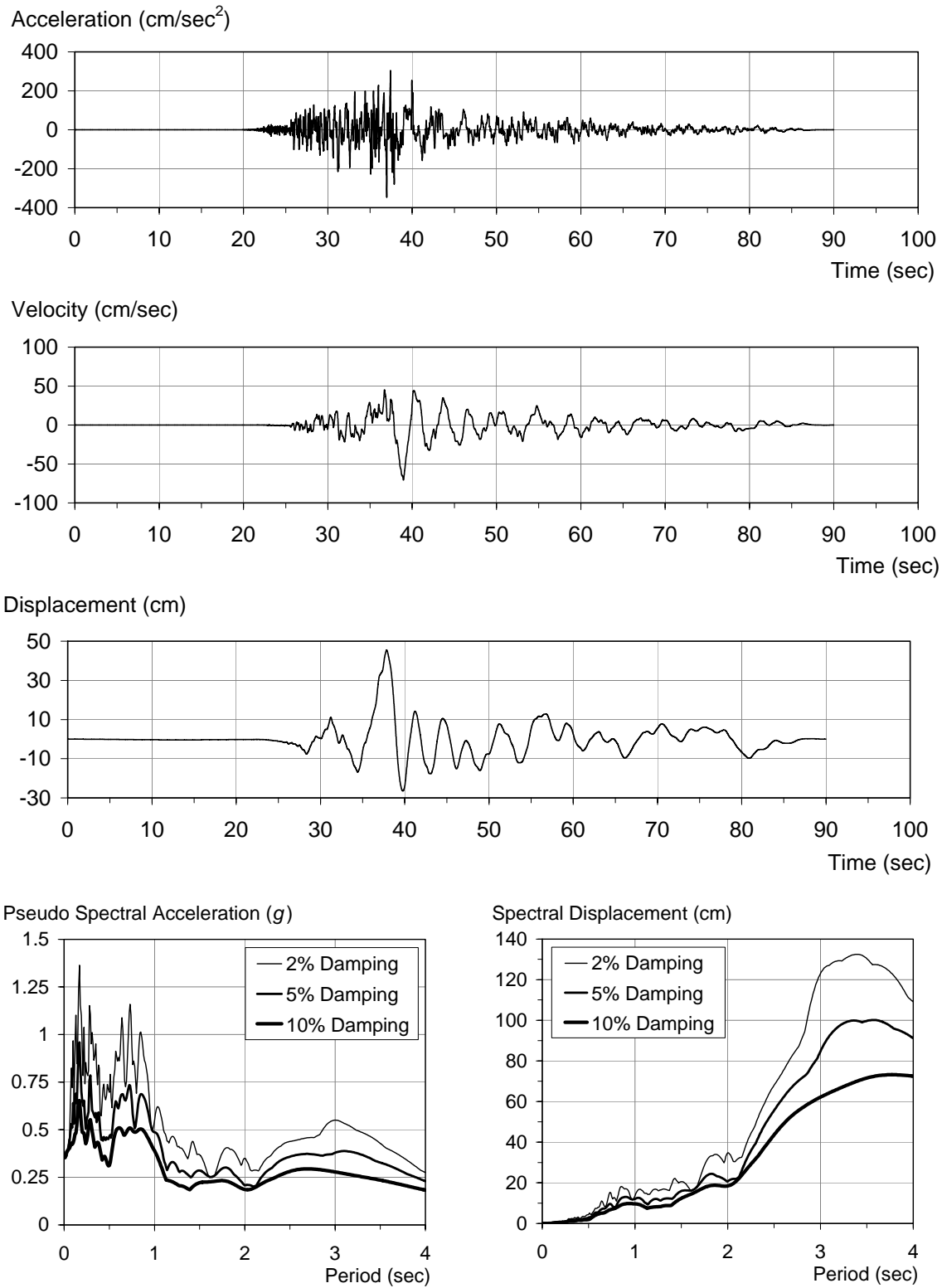
Figure F-23   Characteristics of the CHY101W ground motion

Acceleration (cm/sec²)

Velocity (cm/sec)

Displacement (cm)

Pseudo Spectral Acceleration (*g*)

Spectral Displacement (cm)
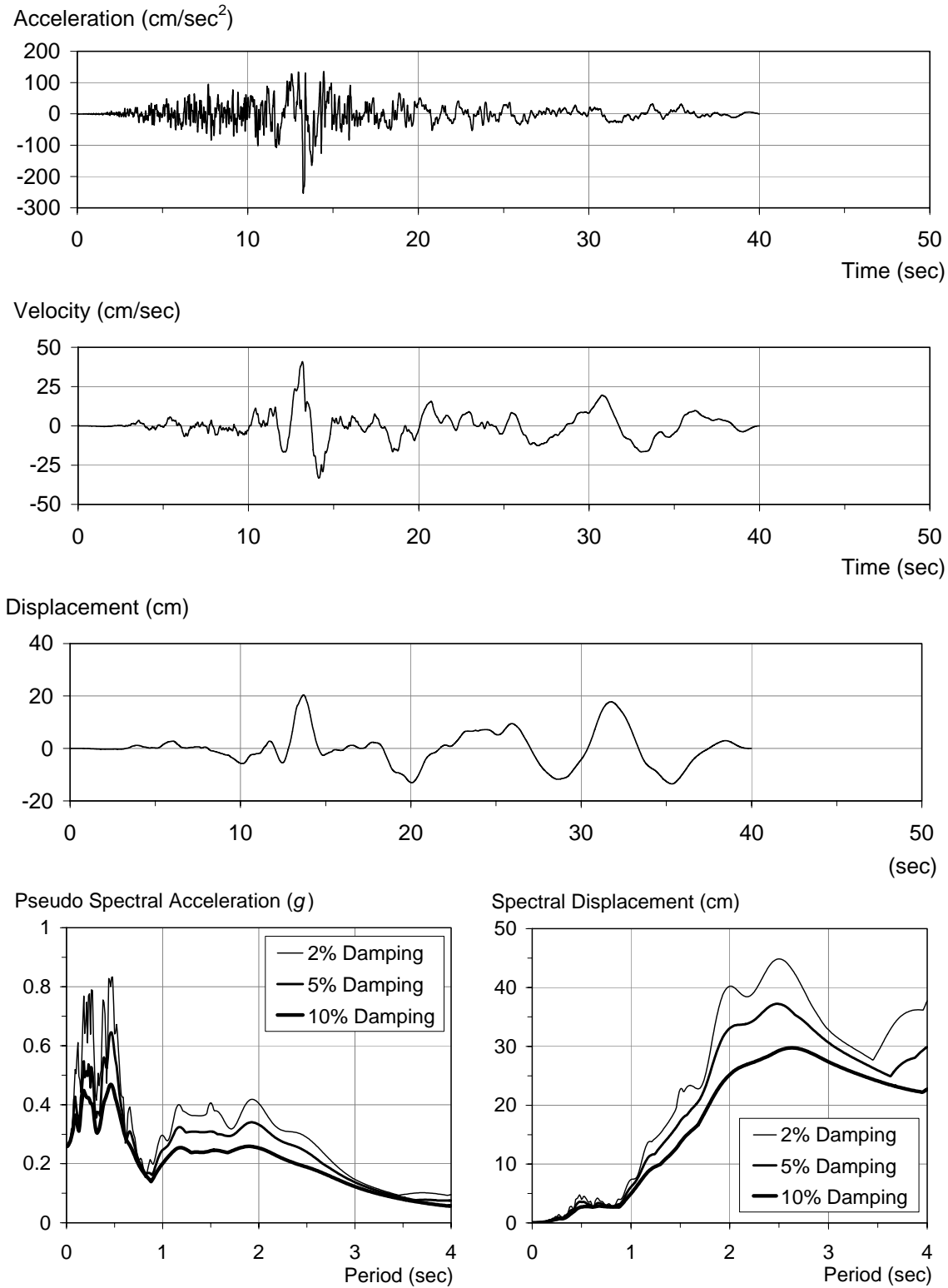
Figure F-24   Characteristics of the ICC090 ground motion
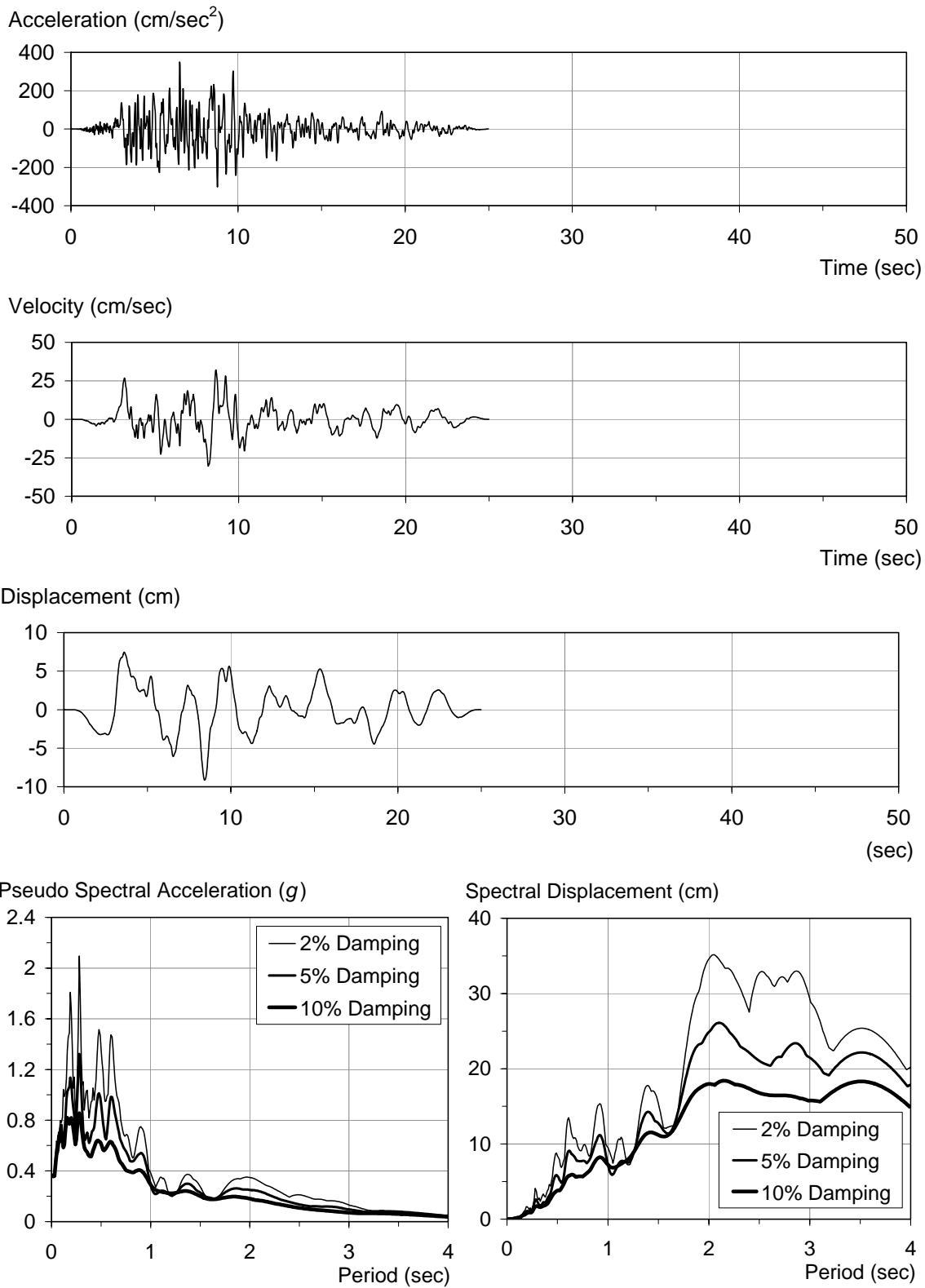
Figure F-25   Characteristics of the CNP106 ground motion

Acceleration (cm/sec^2)

Velocity (cm/sec)

Displacement (cm)

Pseudo Spectral Acceleration (*g*)

— 2% Damping
— 5% Damping
— 10% Damping

Spectral Displacement (cm)

— 2% Damping
— 5% Damping
— 10% Damping
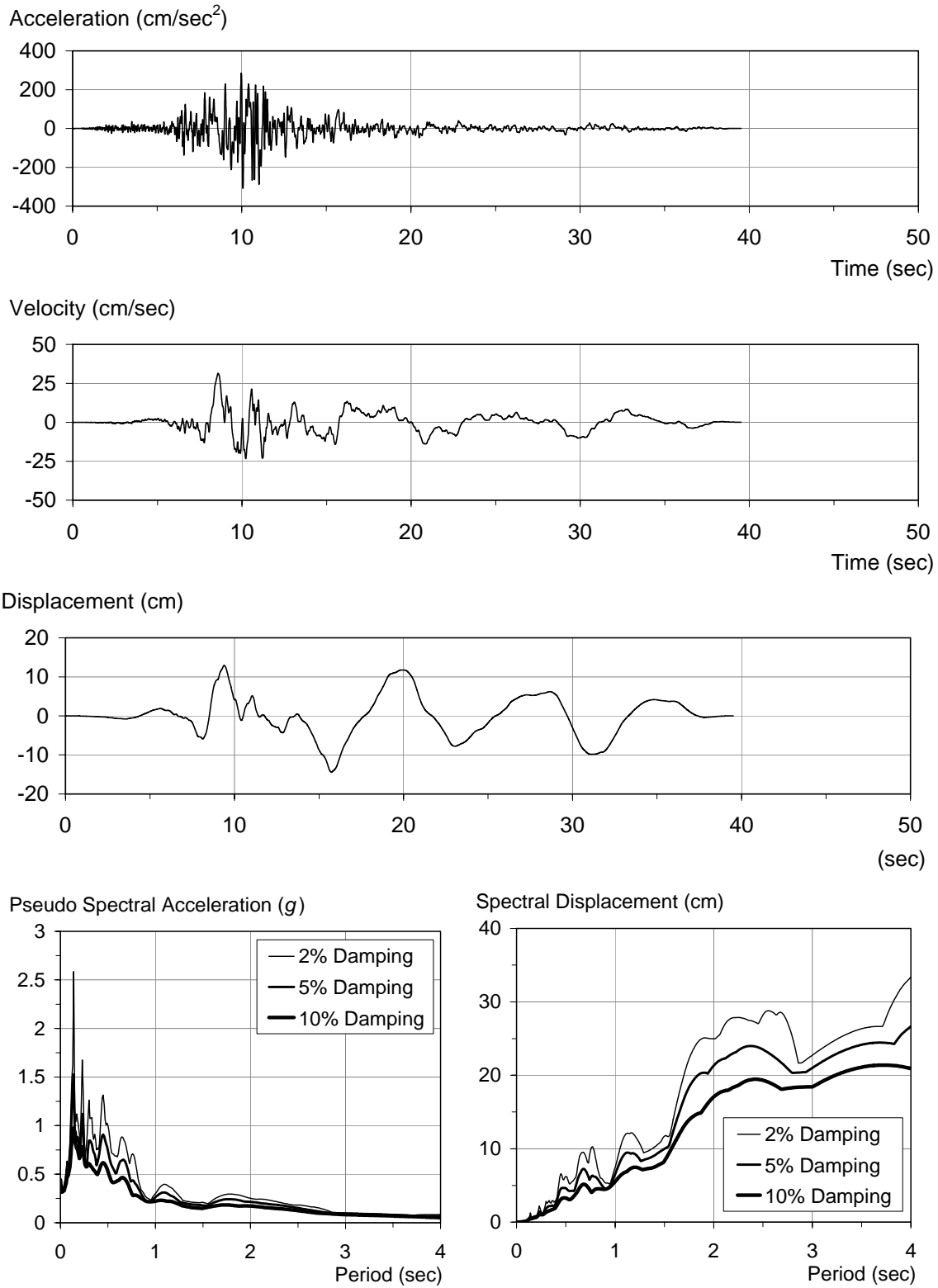
Figure F-26   Characteristics of the E02140 ground motion

Acceleration (cm/sec^2)

Velocity (cm/sec)

Displacement (cm)

Pseudo Spectral Acceleration (*g*)

Spectral Displacement (cm)
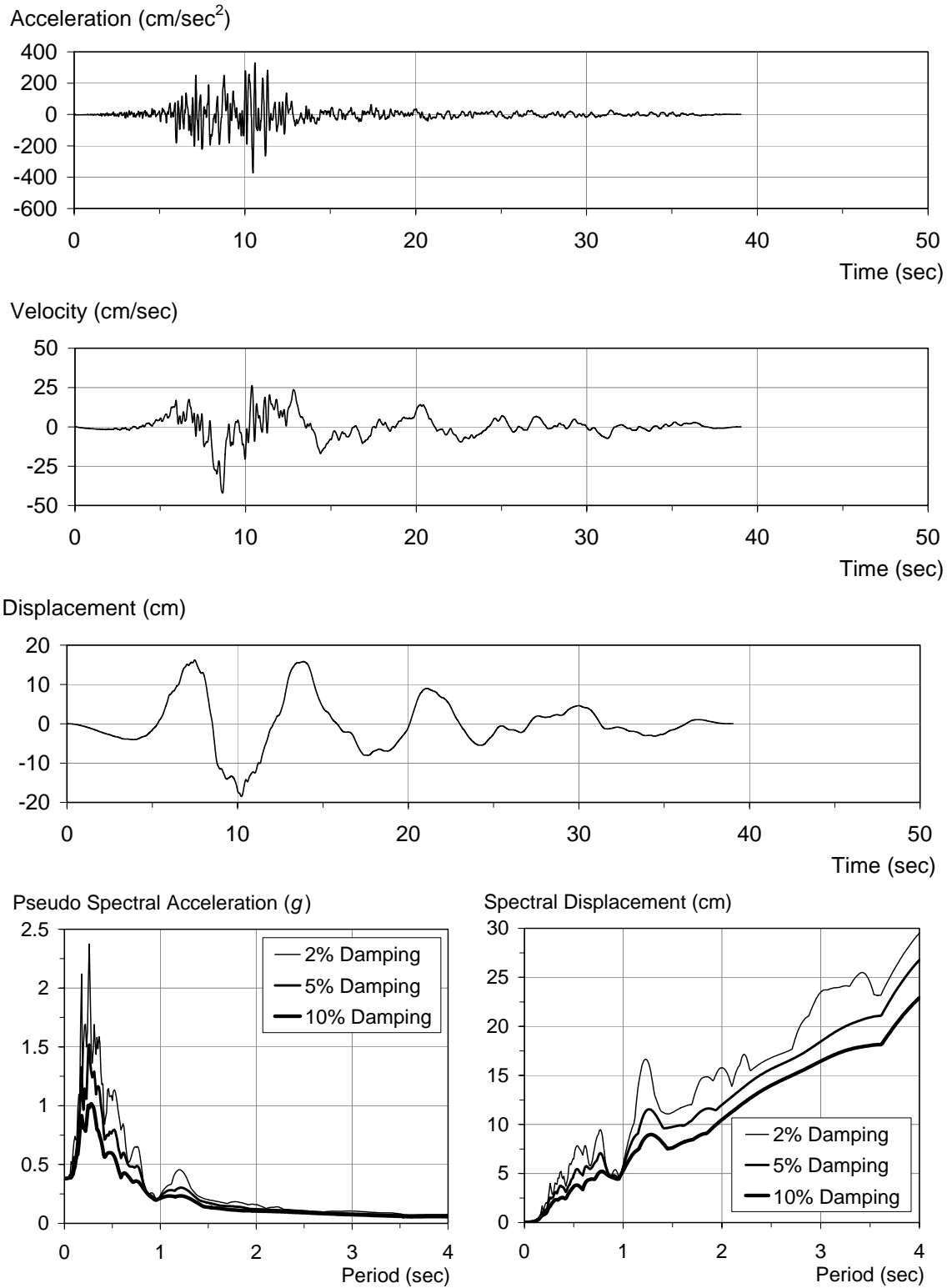
Figure F-27   Characteristics of the E11230 ground motion

Acceleration (cm/sec^2)

Velocity (cm/sec)

Displacement (cm)

Pseudo Spectral Acceleration (*g*)

— 2% Damping
— 5% Damping
— 10% Damping

Spectral Displacement (cm)

— 2% Damping
— 5% Damping
— 10% Damping
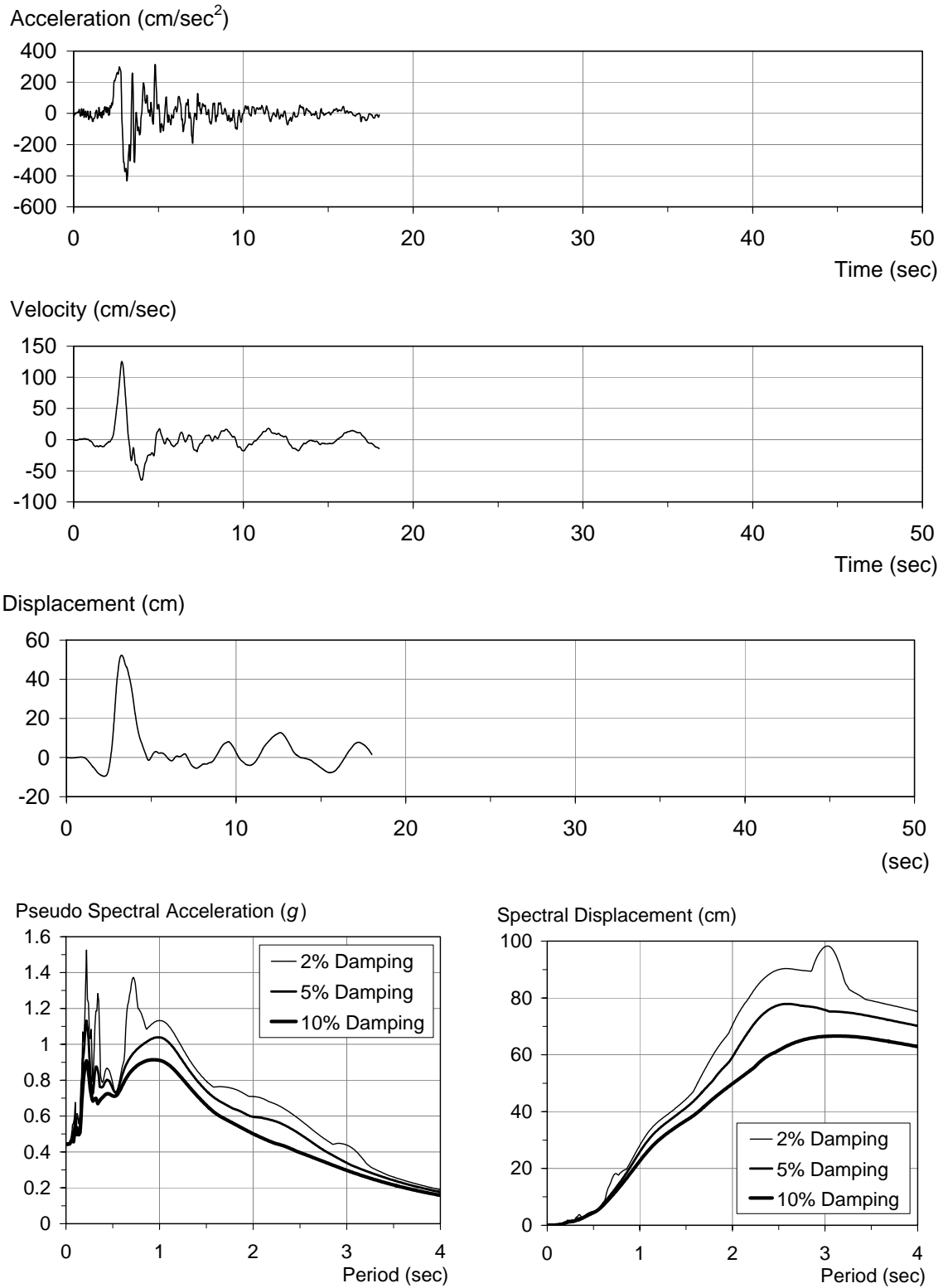
Figure F-28   Characteristics of the ERZMV1 ground motion

Acceleration (cm/sec^2)

Velocity (cm/sec)

Displacement (cm)

Pseudo Spectral Acceleration (*g*)

Spectral Displacement (cm)
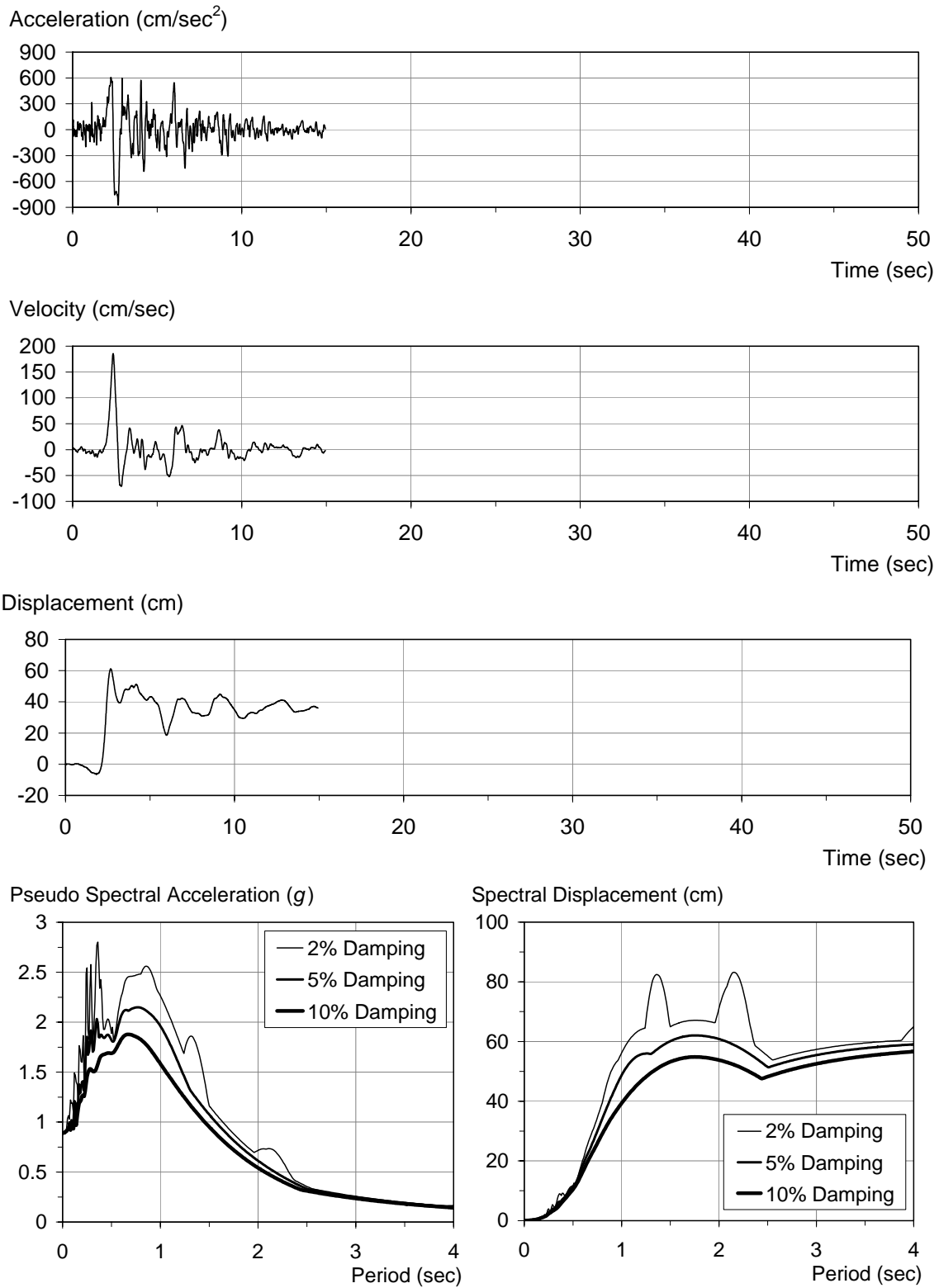
Figure F-29   Characteristics of the RRSMV1 ground motion
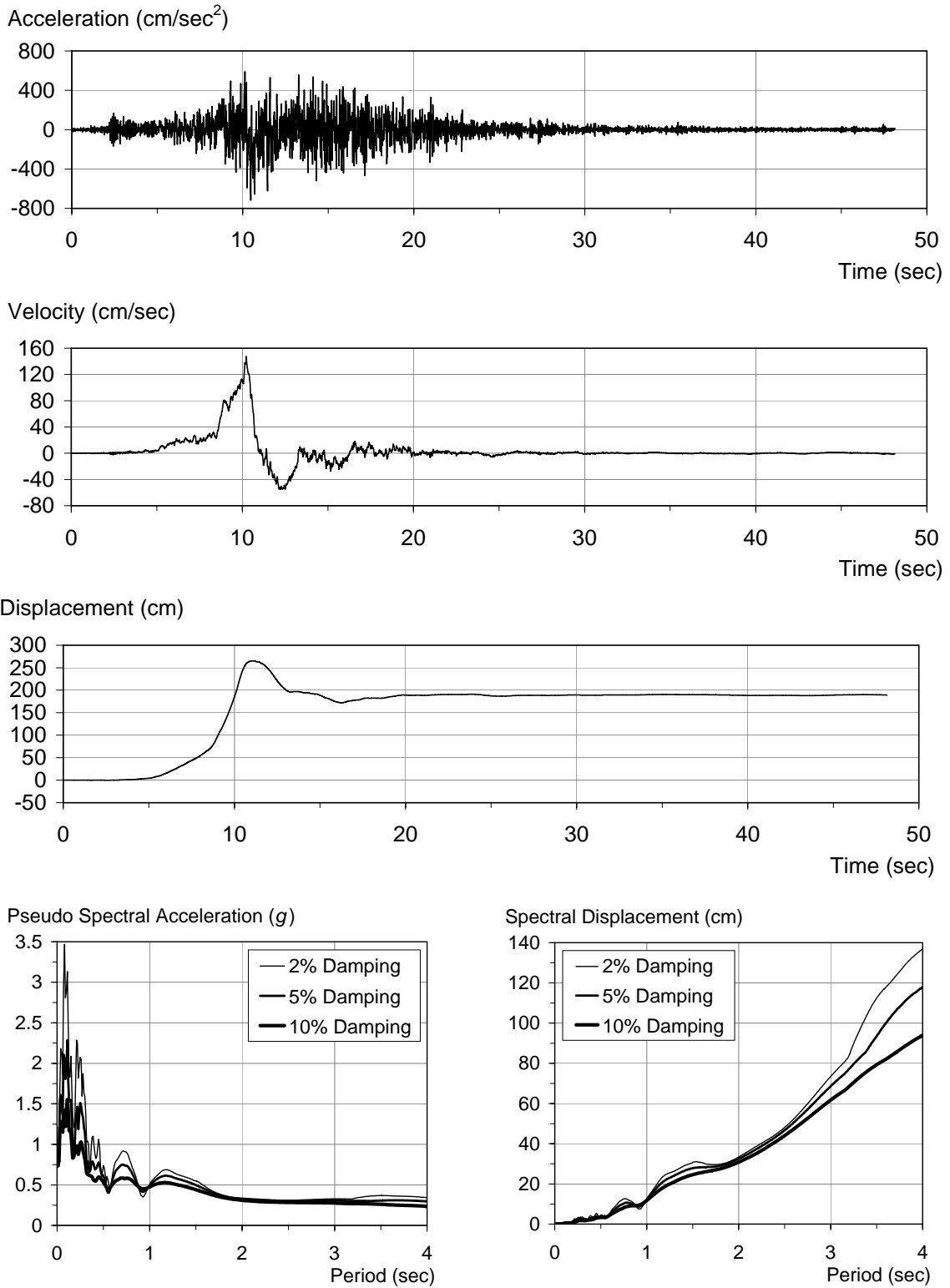
Figure F-30   Characteristics of the LUCMV1 ground motion
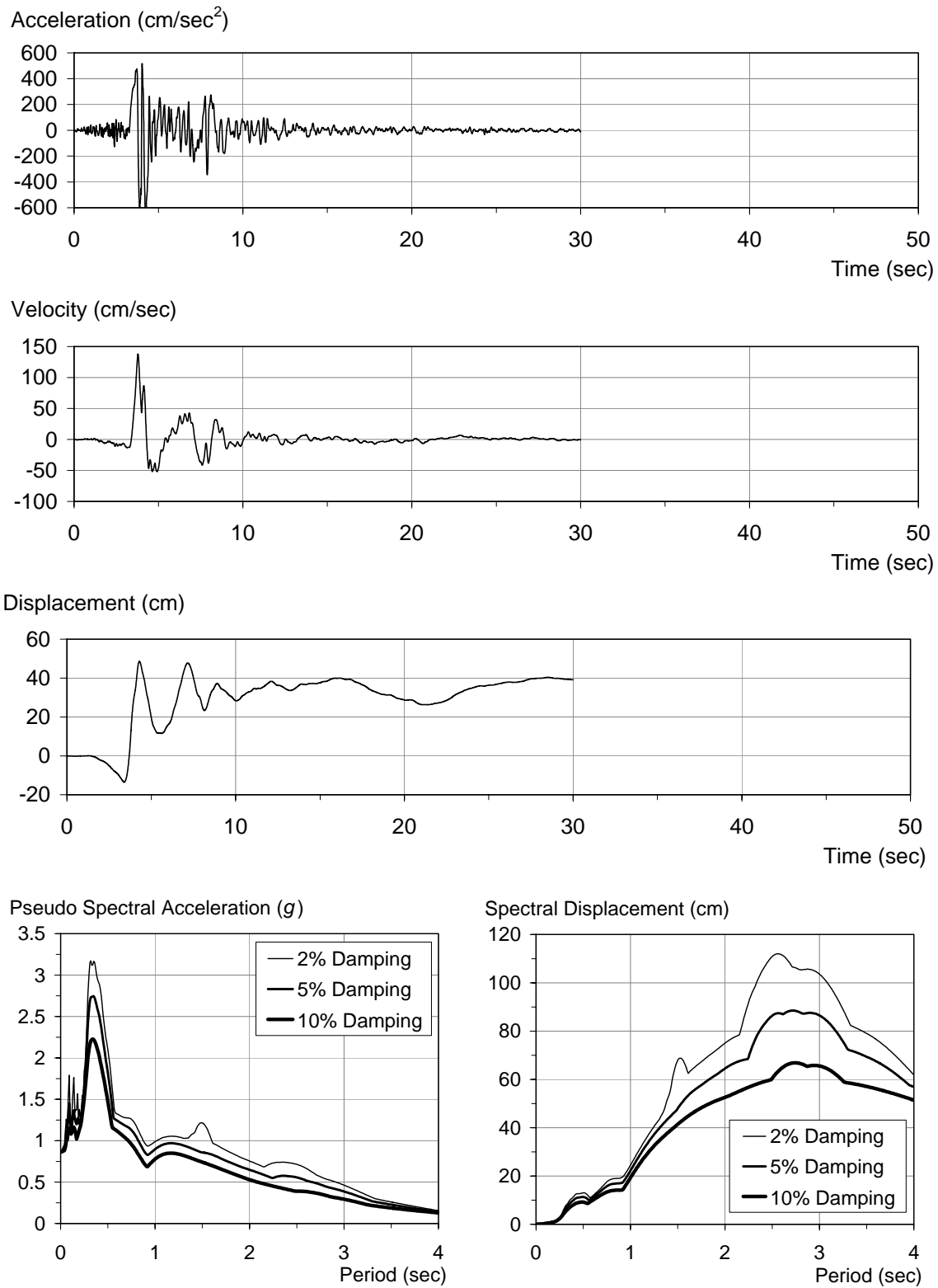
Figure F-31   Characteristics of the SCHMV1 ground motion

F.8.2 Responses to Ordinary (Site Class C) Motions
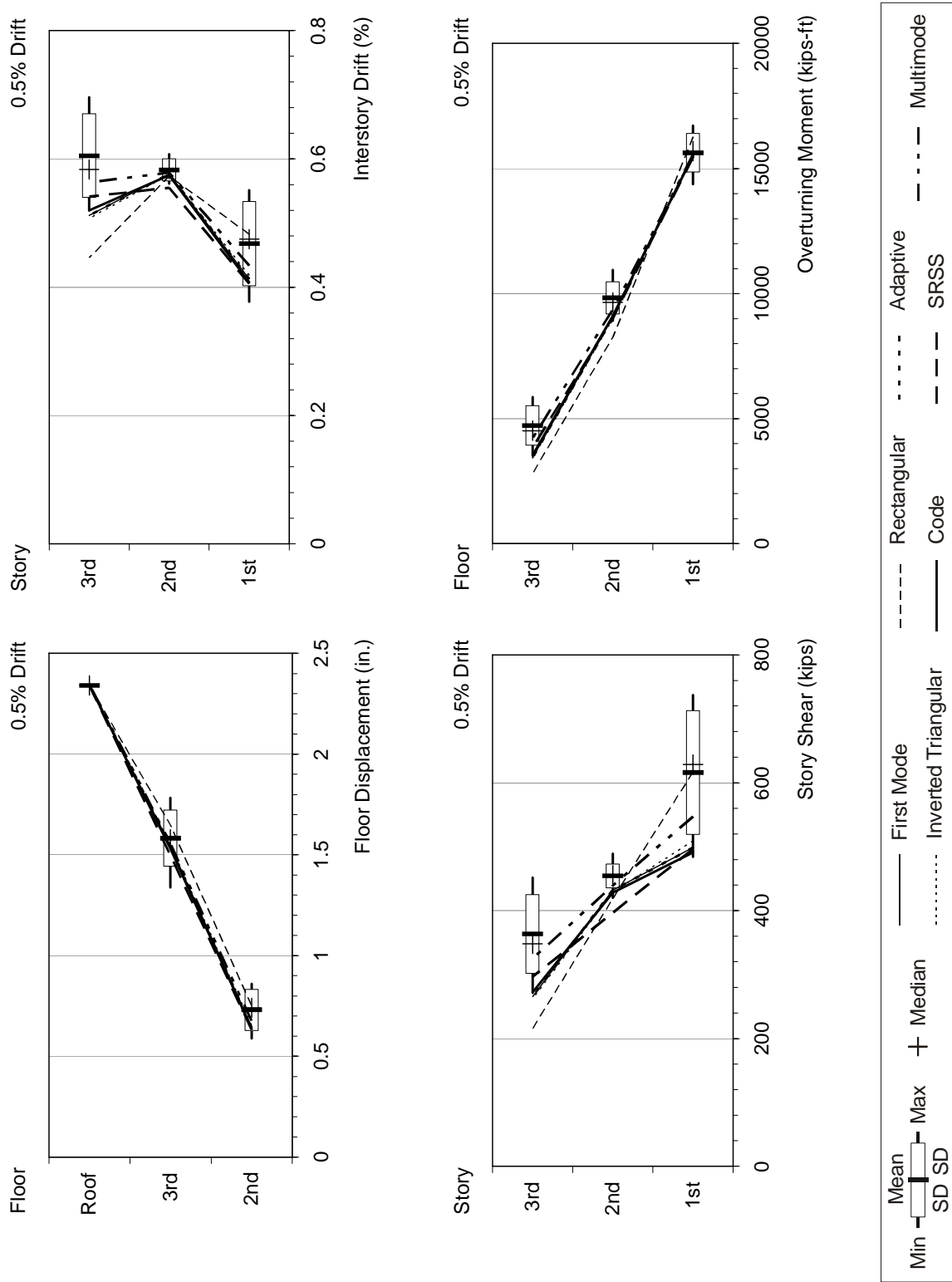
Figure F-32   Response quantities of the 3-story building for 0.5% drift level
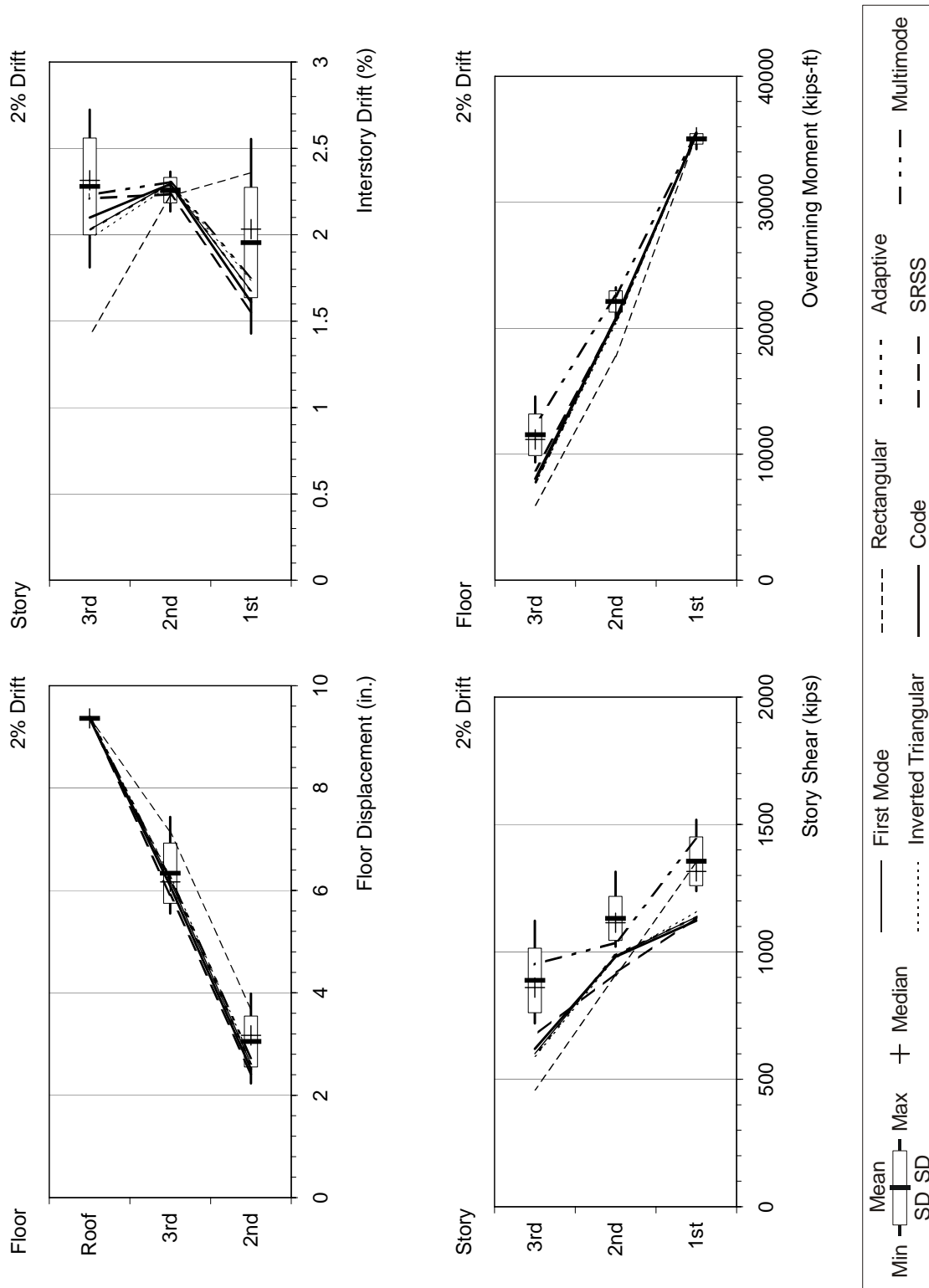
Figure F-33   Response quantities of the 3-story building for 2% drift level
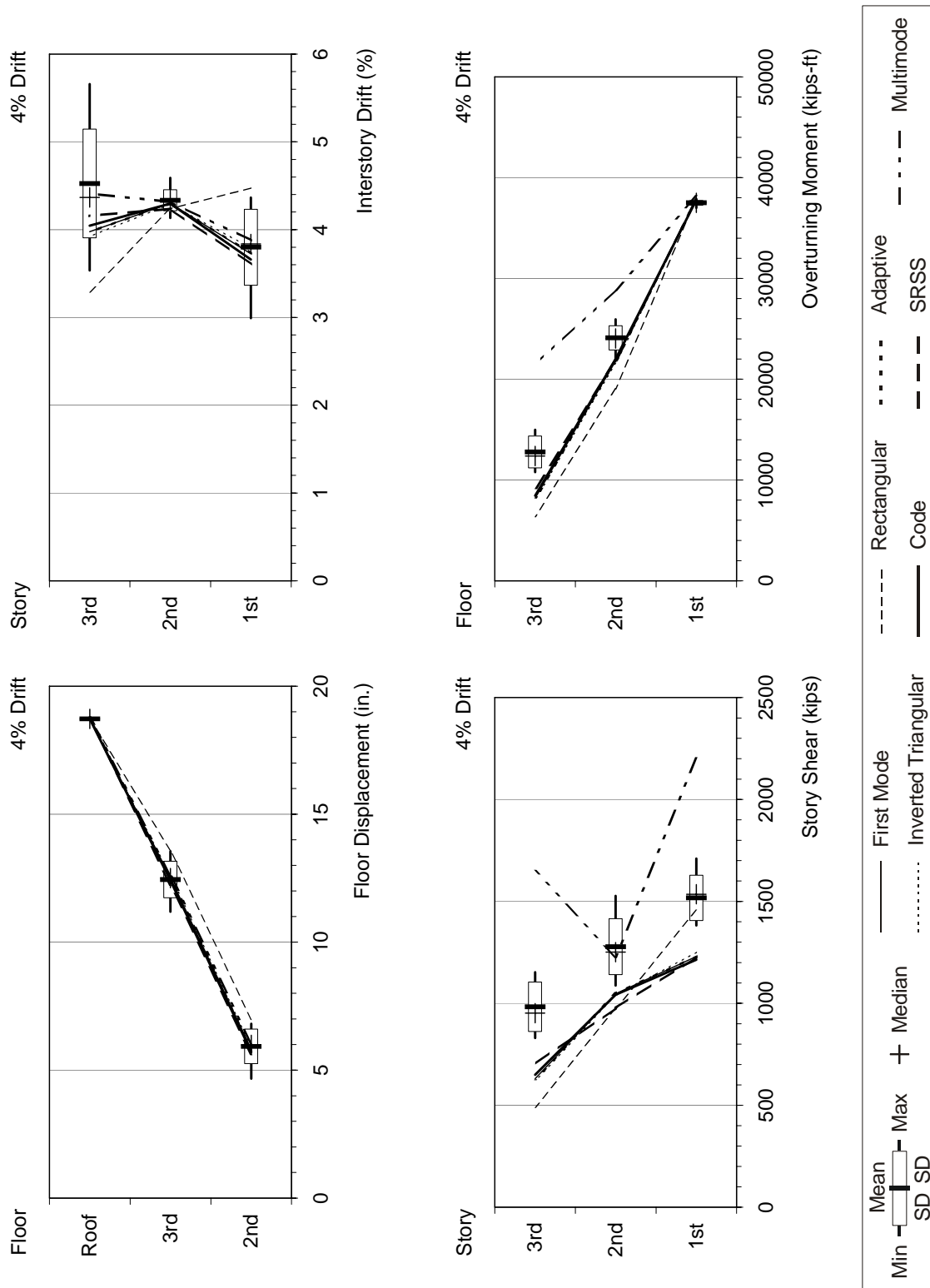
Figure F-34   Response quantities of the 3-story building for 4% drift level
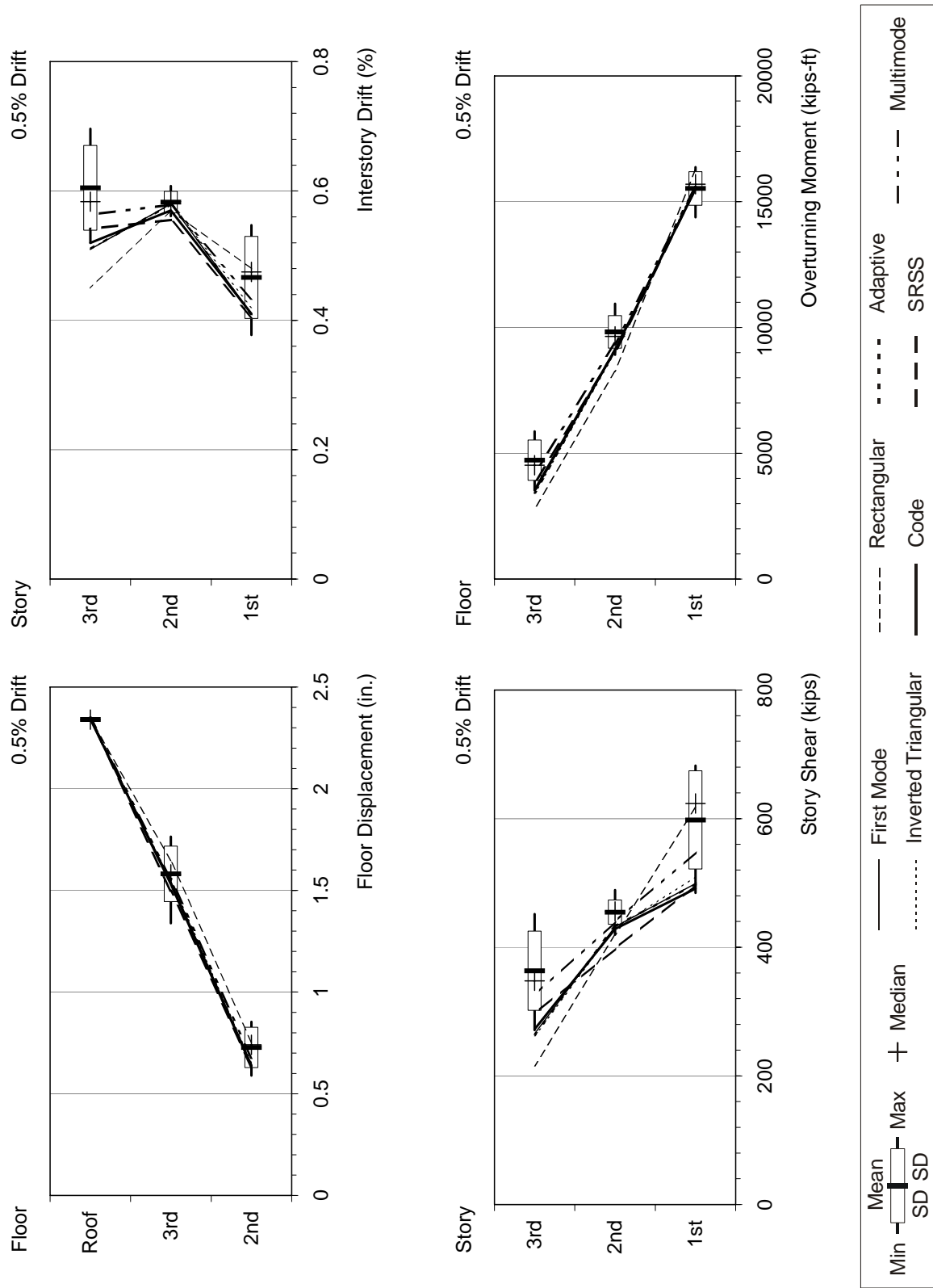
Figure F-35   Response quantities of the 3-story weak-story building for 0.5% drift level
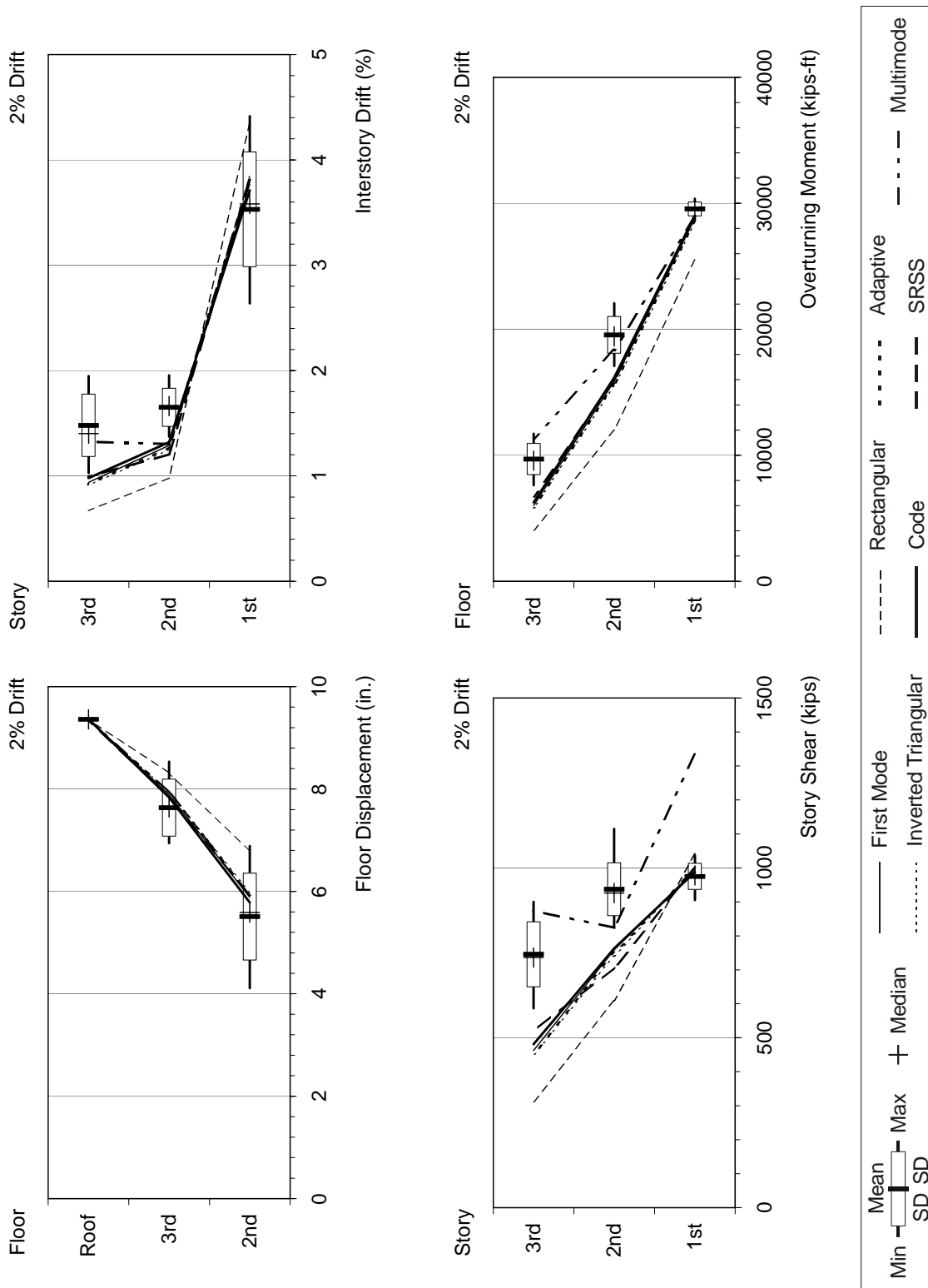
Figure F-36   Response quantities of the 3-story weak-story building for 2% drift level
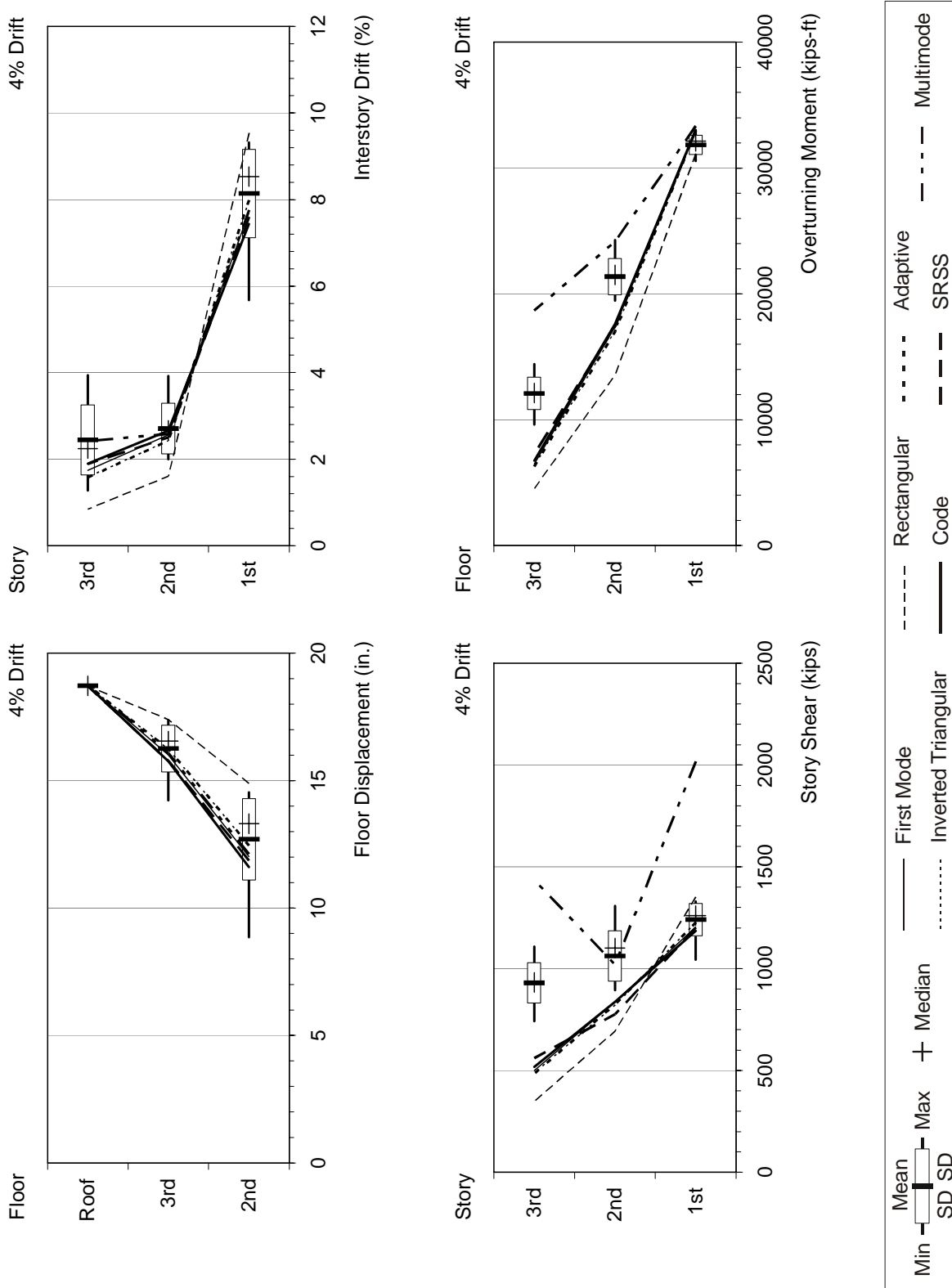
Figure F-37   Response quantities of the 3-story weak-story building for 4% drift level
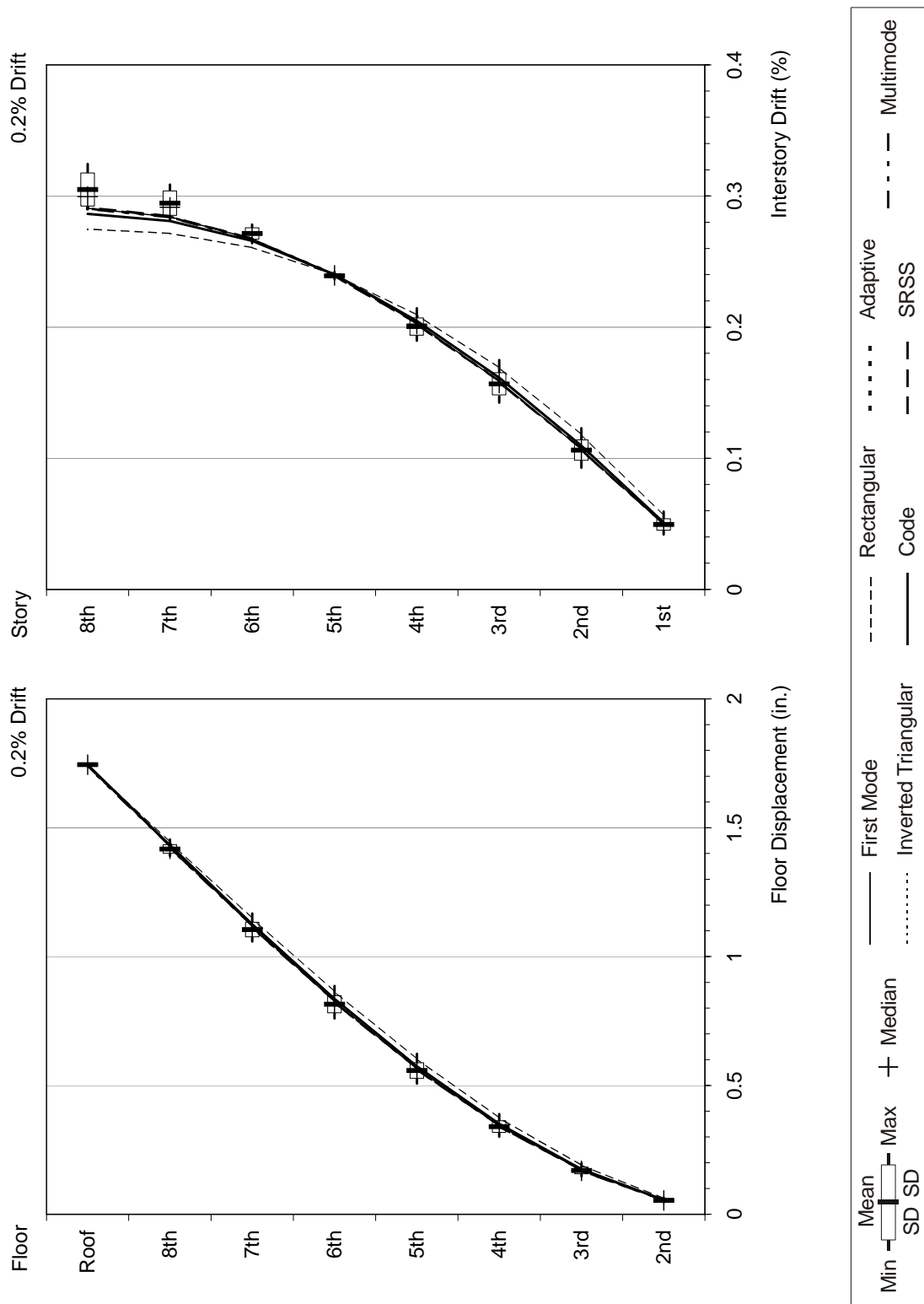
Figure F-38   Response quantities of the 8-story building for 0.2% drift level
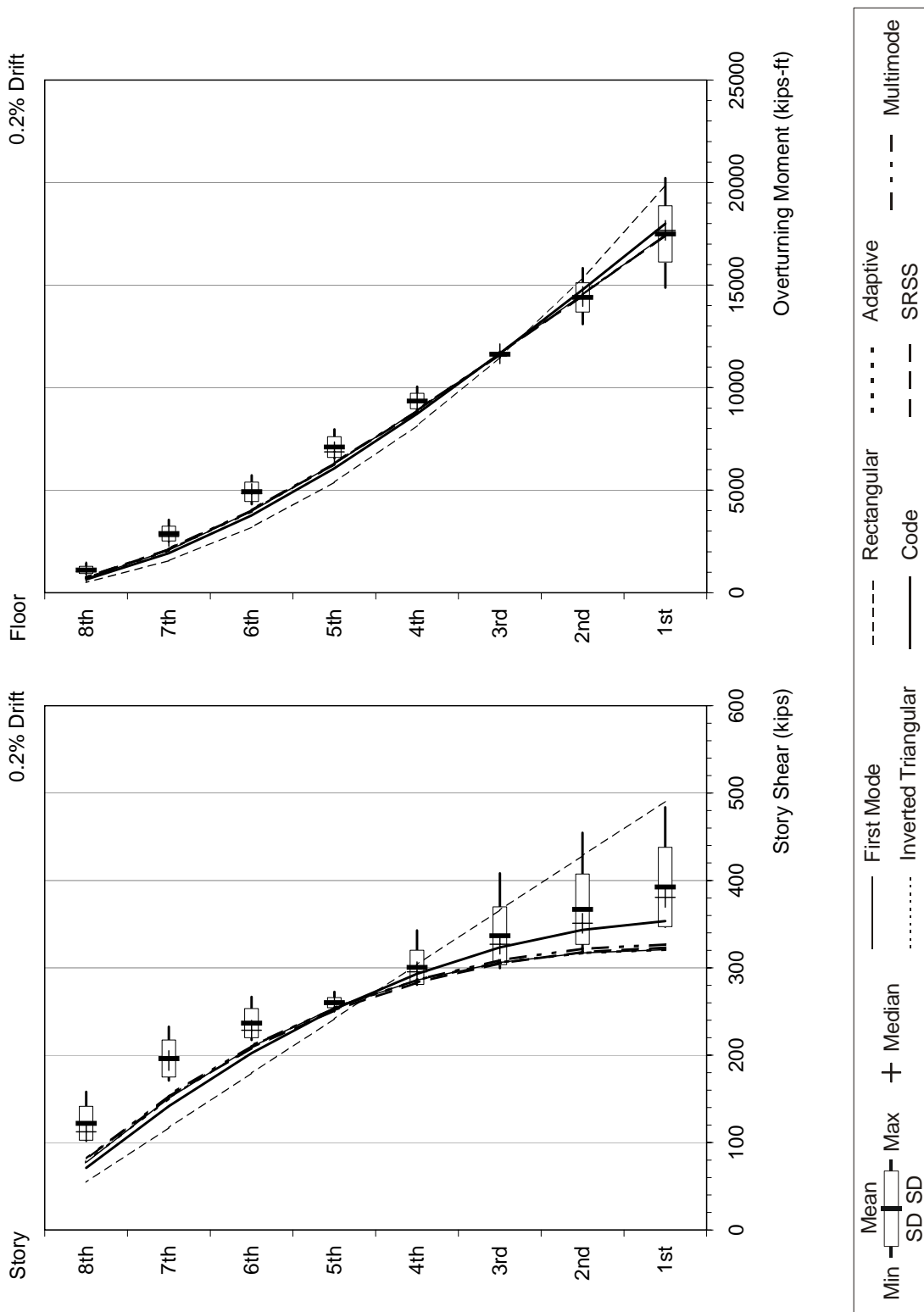
Figure F-38   Response quantities of the 8-story building for 0.2% drift level (continued)
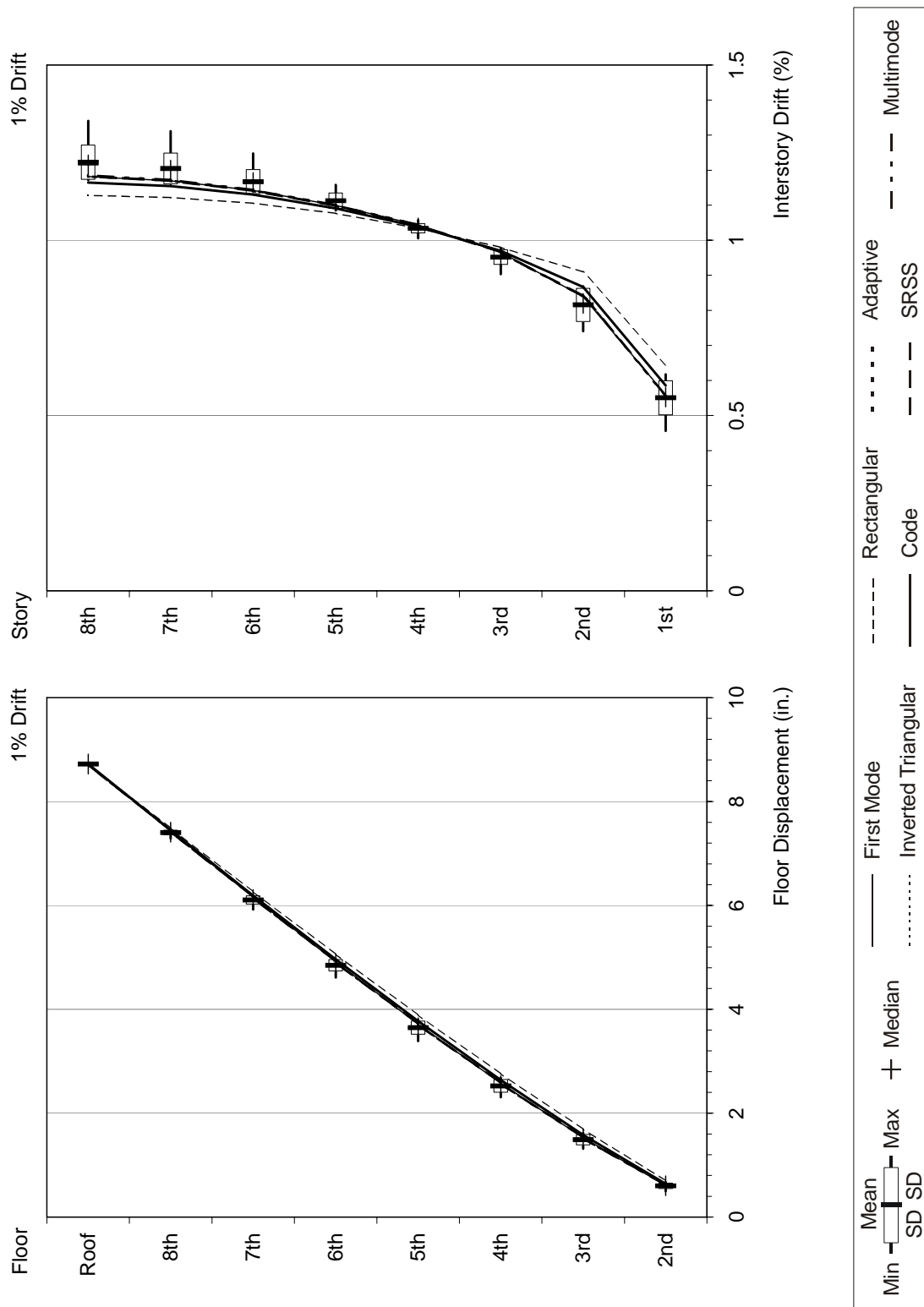
Figure F-39   Response quantities of the 8-story building for 1% drift level
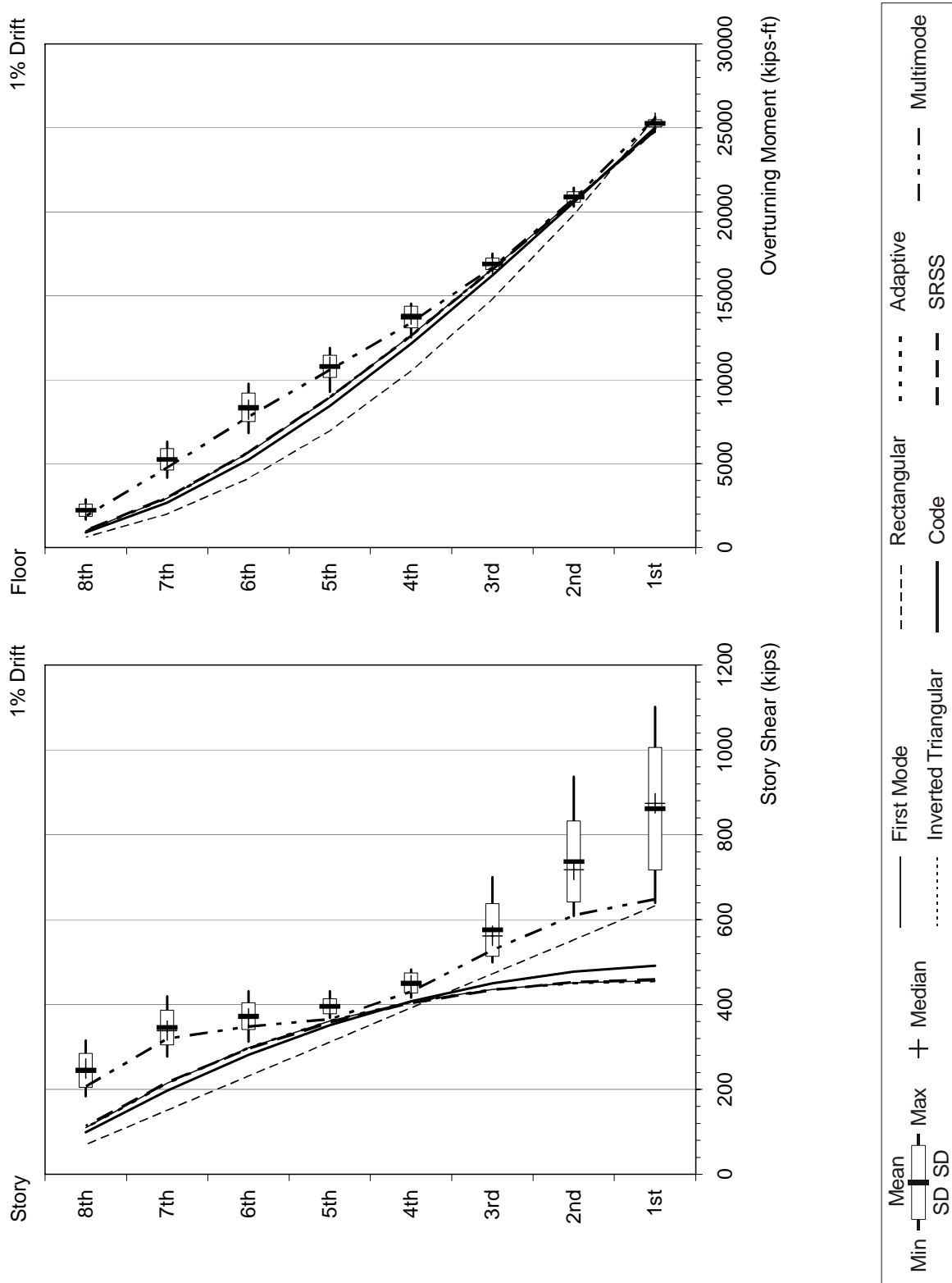
Figure F-39   Response quantities of the 8-story building for 1% drift level (continued)
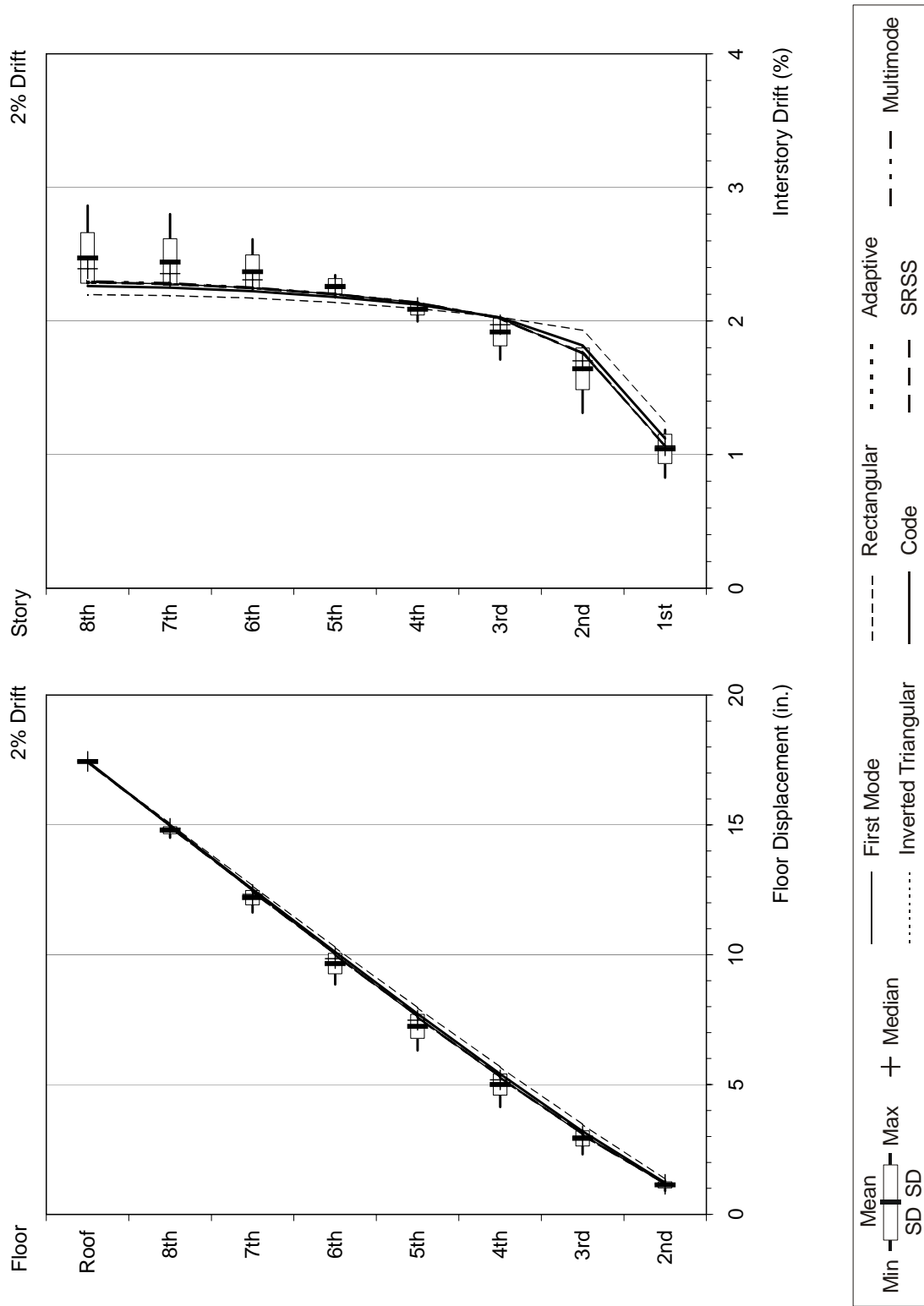
Figure F-40   Response quantities of the 8-story building for 2% drift level
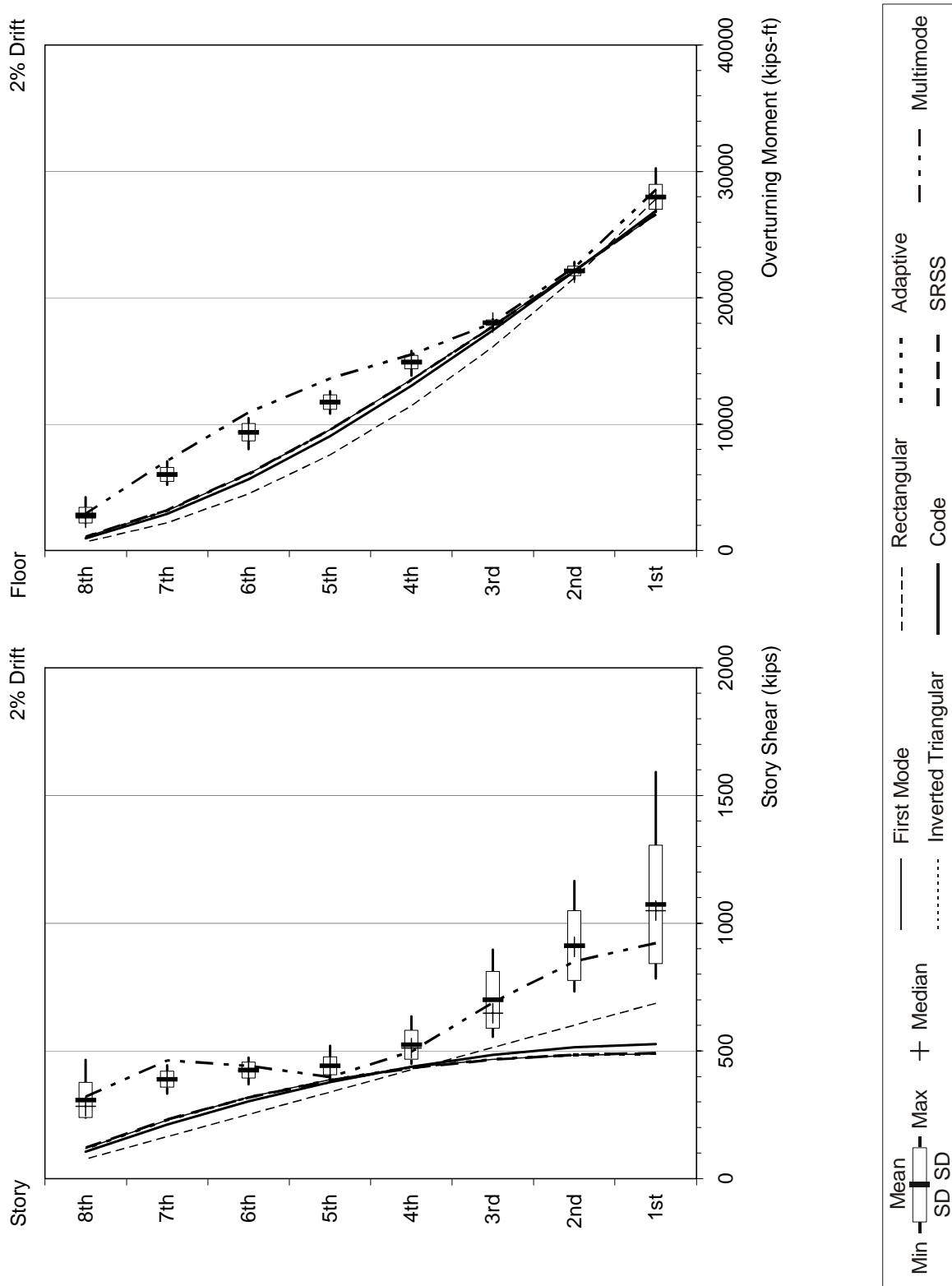
Figure F-40   Response quantities of the 8-story building for 2% drift level (continued)
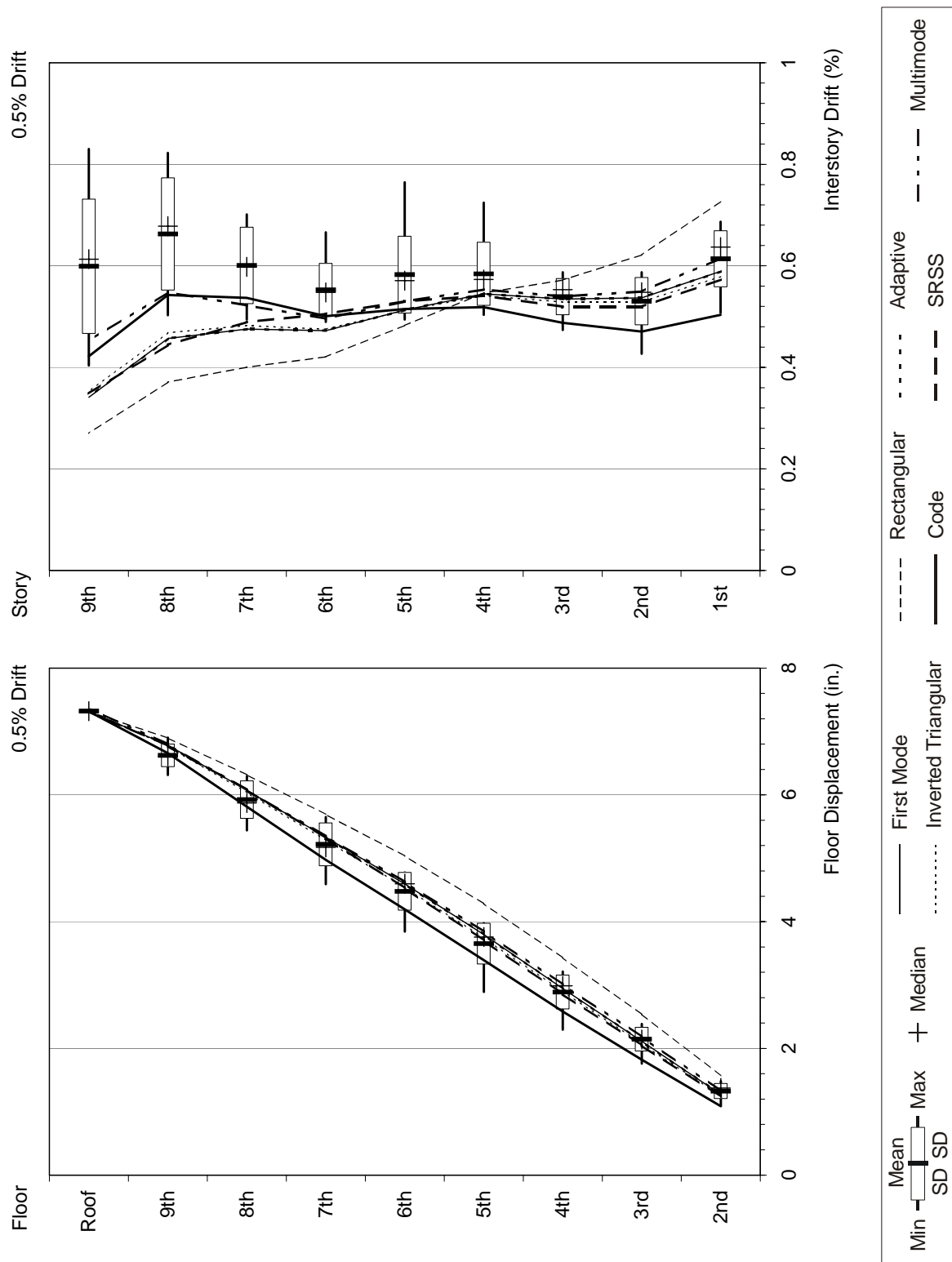
Figure F-41   Response quantities of the 9-story building for 0.5% drift level
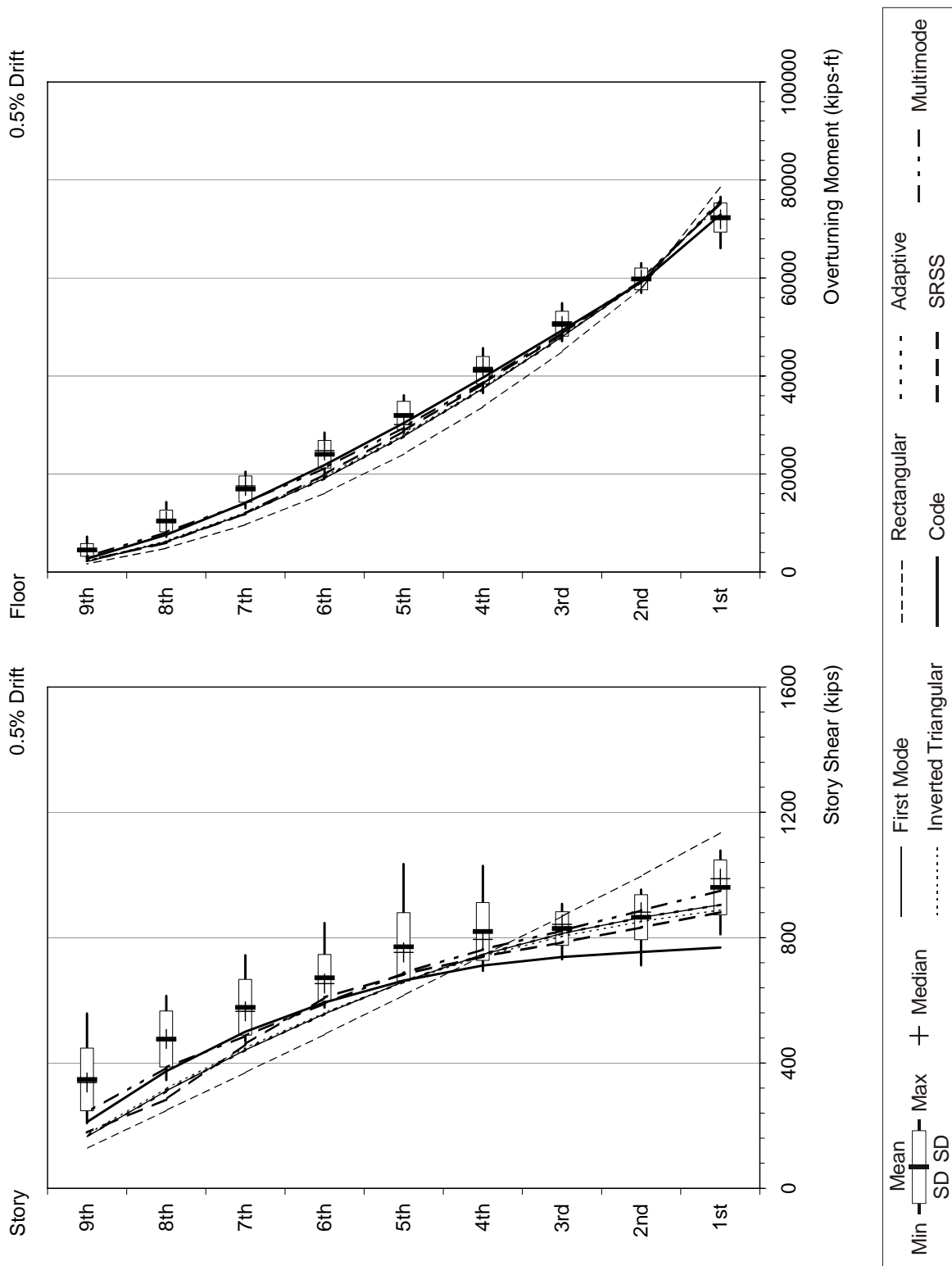
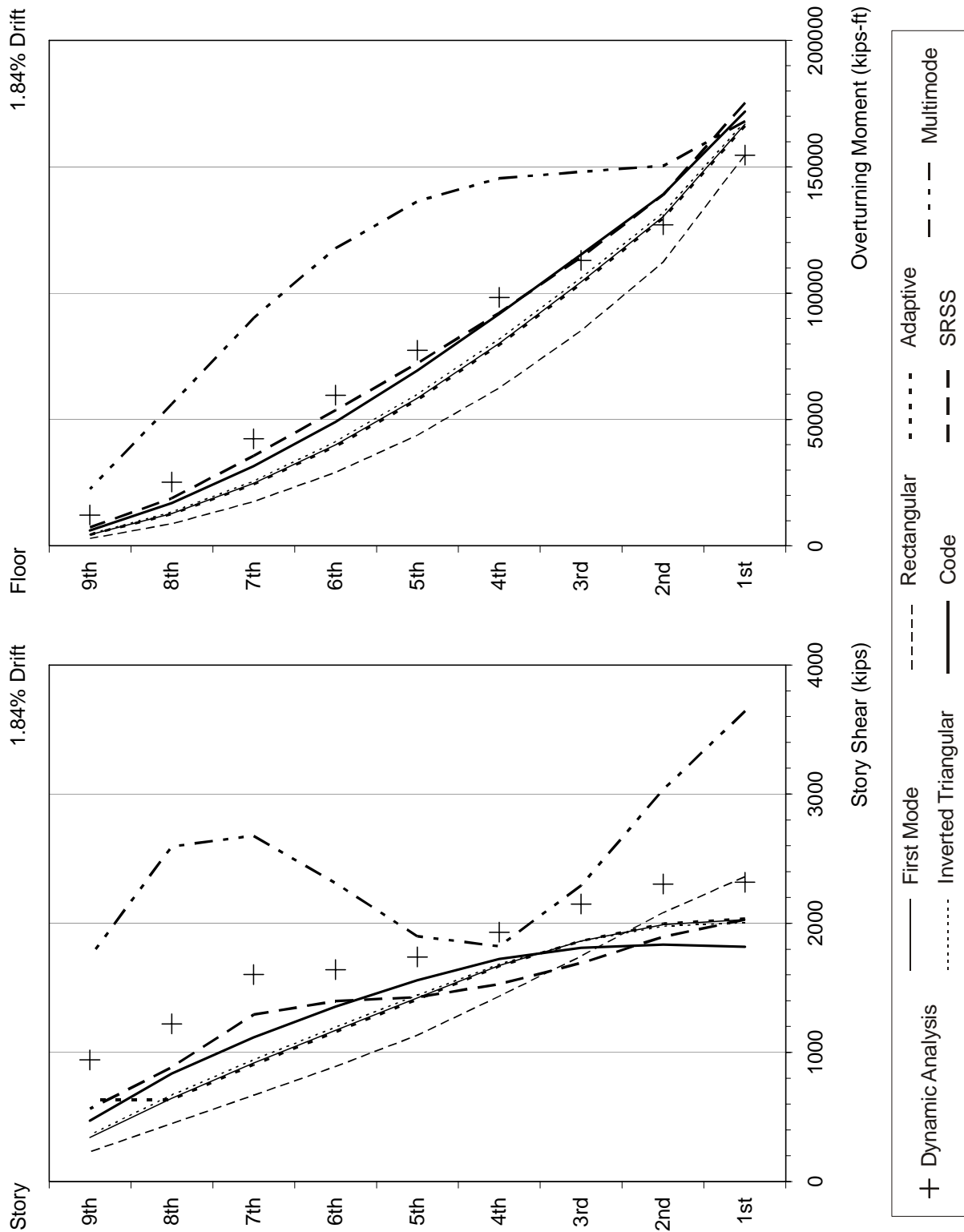Figure F-41   Response quantities of the 9-story building for 0.5% drift level (continued)
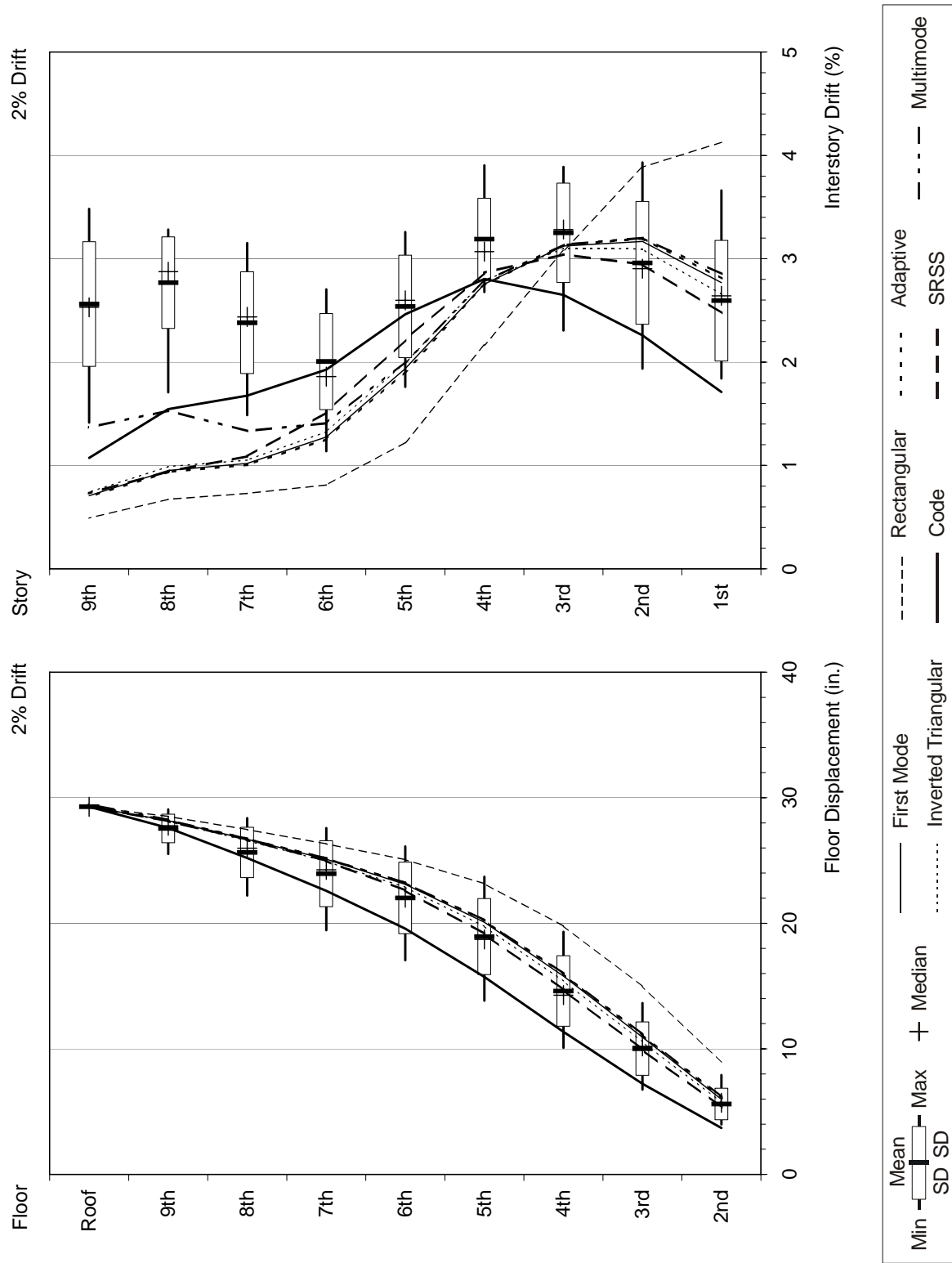
Figure F-42   Response quantities of the 9-story building for 2% drift level
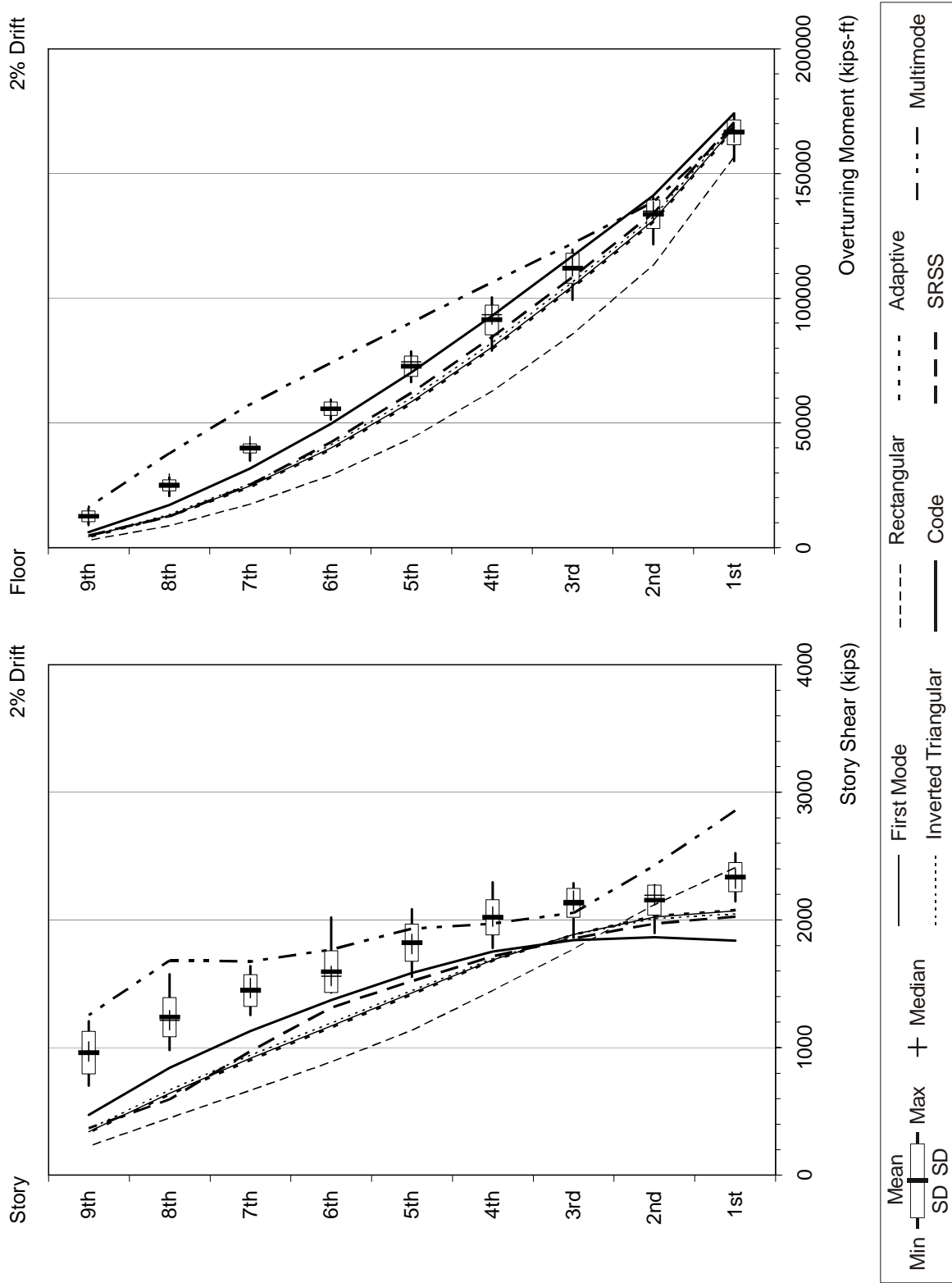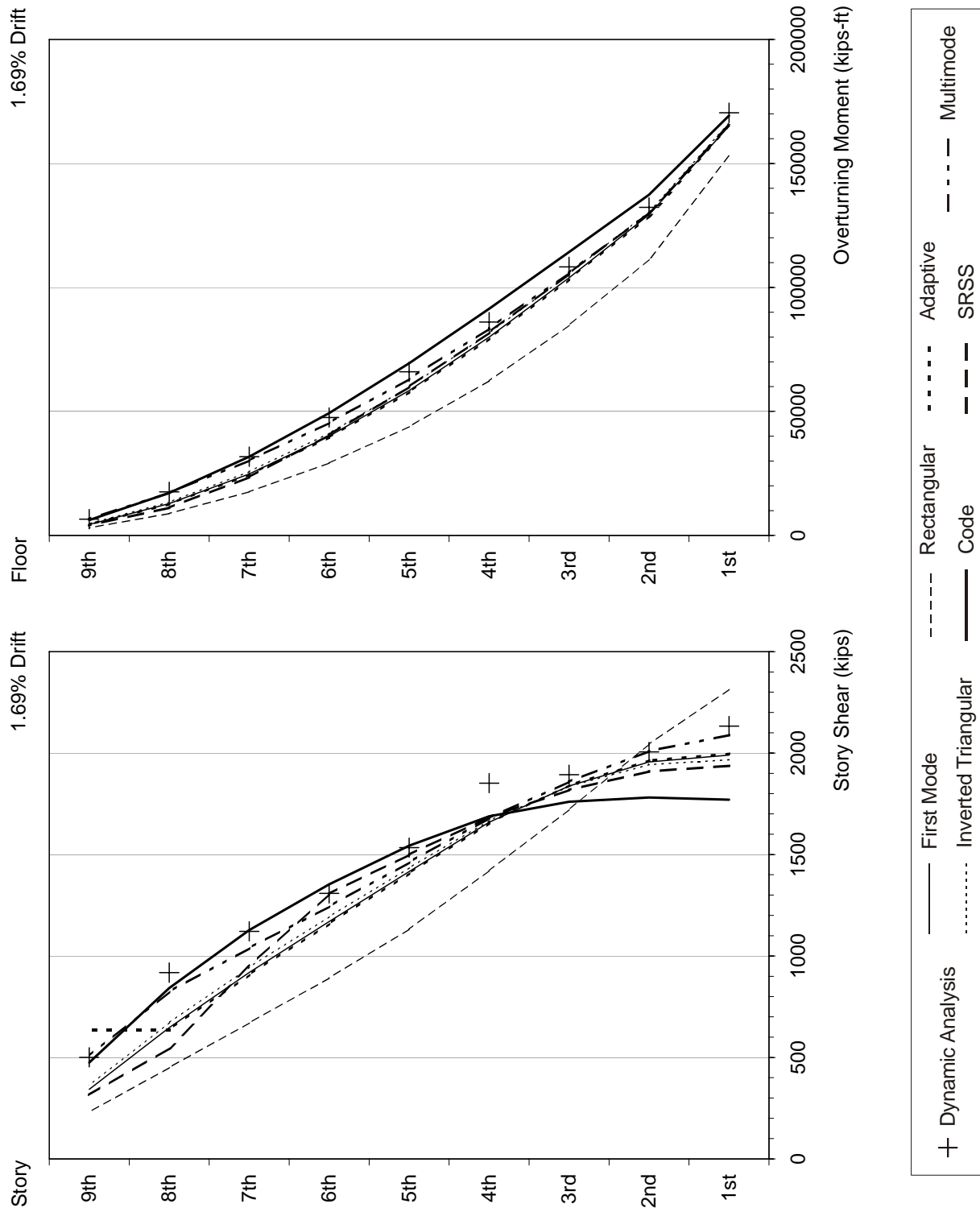
Figure F-42   Response quantities of the 9-story building for 2% drift level (continued)
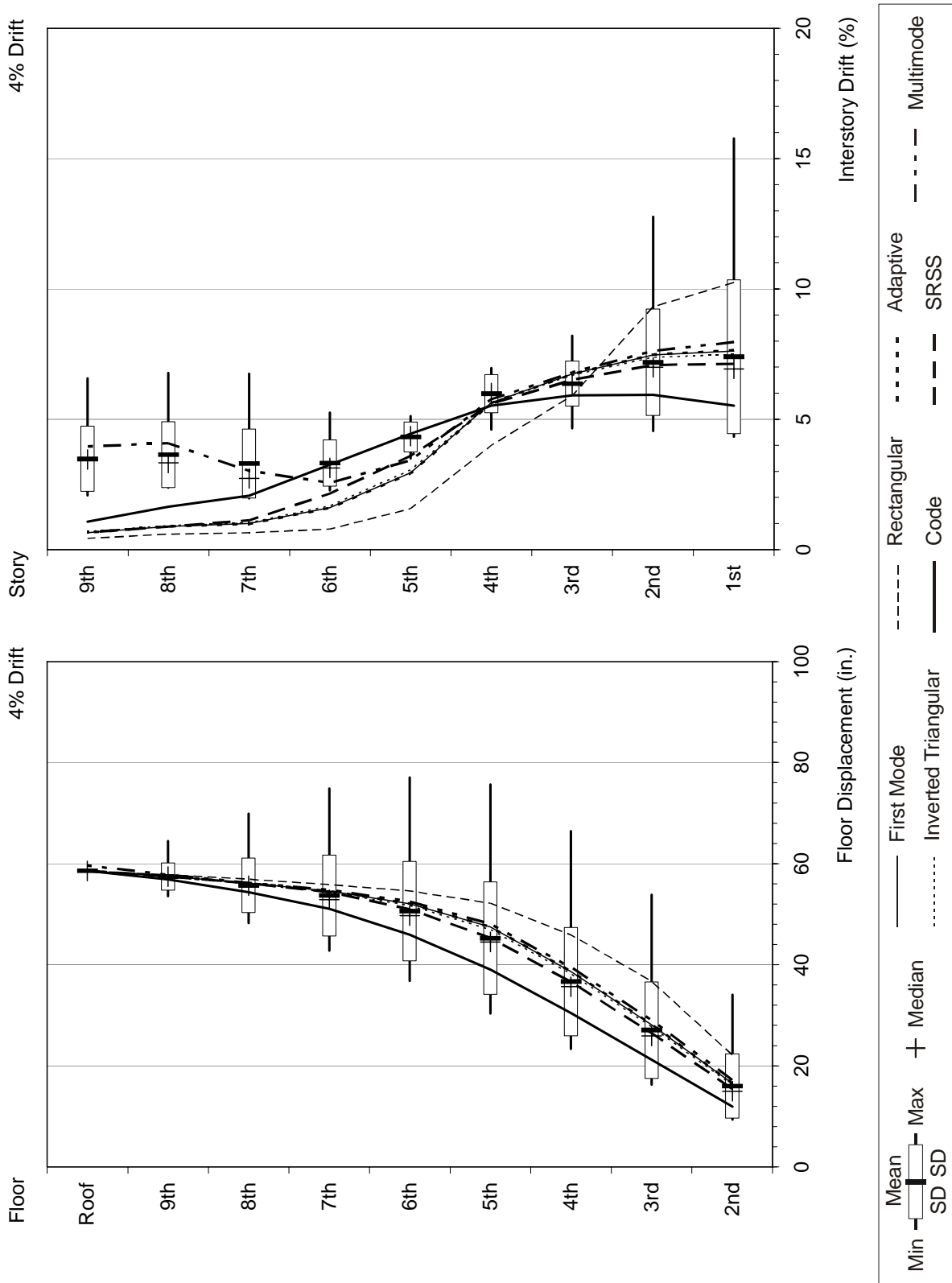
Figure F-43   Response quantities of the 9-story building for 4% drift level
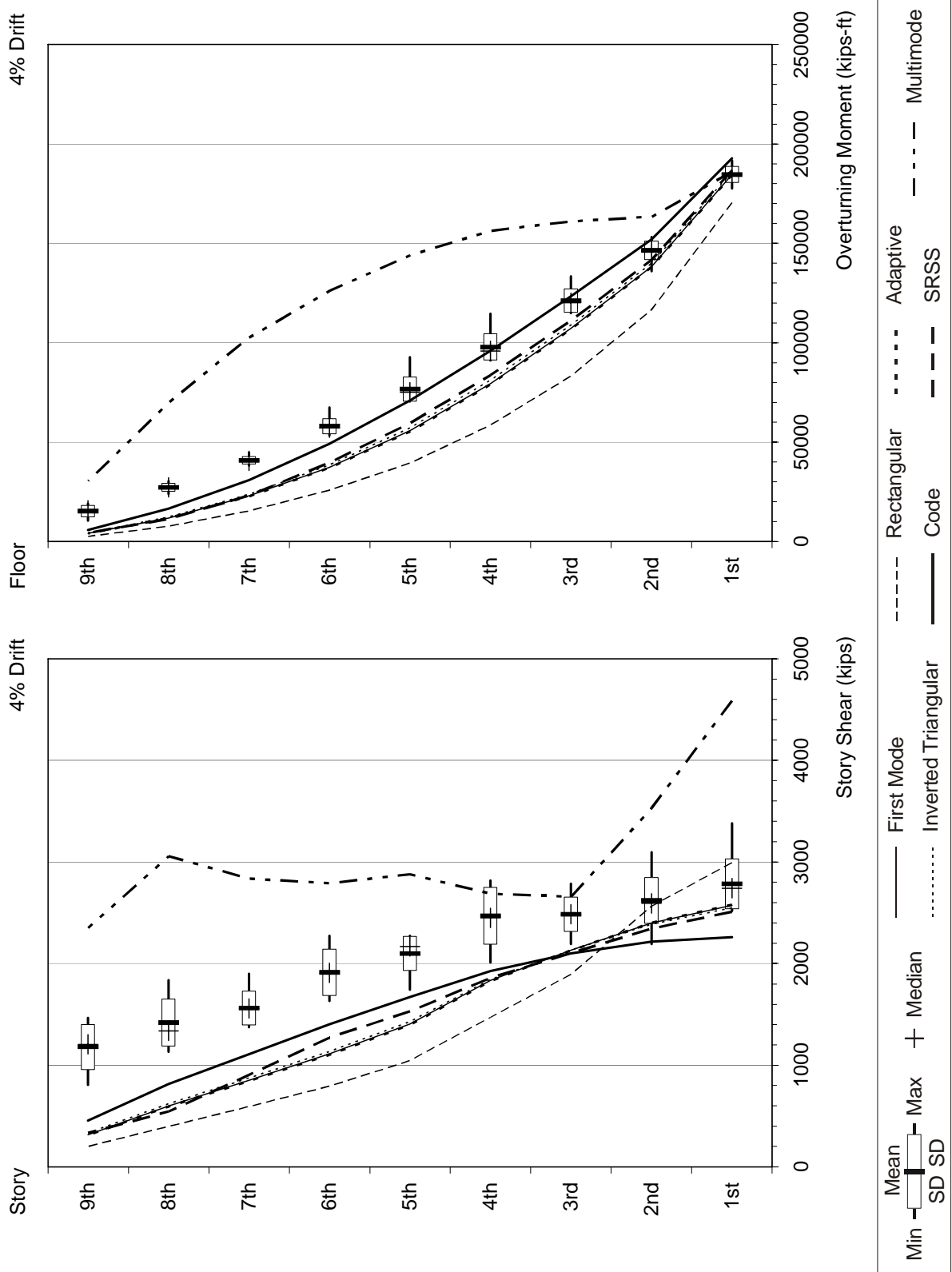
Figure F-43   Response quantities of the 9-story building for 4% drift level (continued)
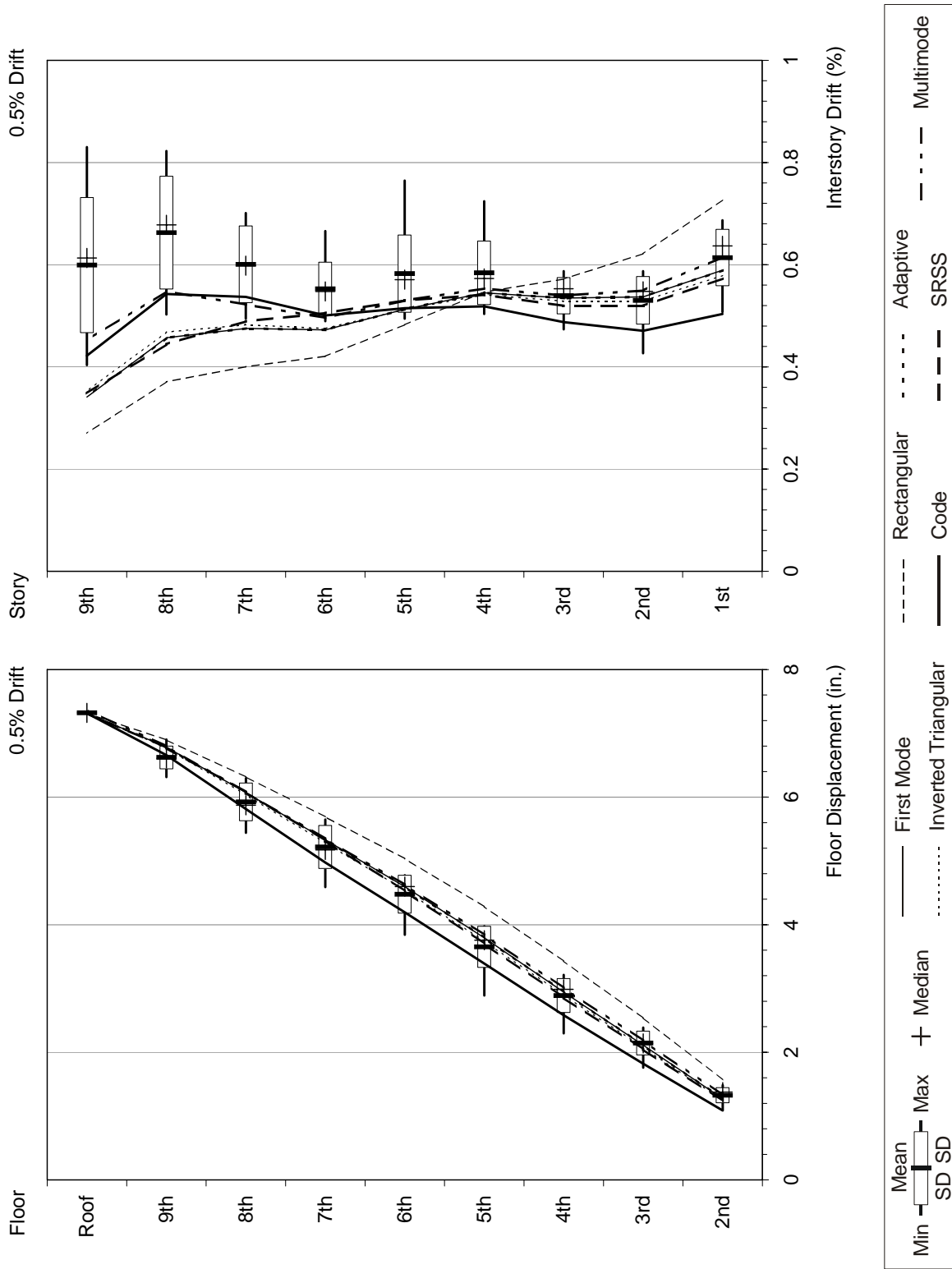
Figure F-44   Response quantities of the 9-story weak-story building for 0.5% drift level
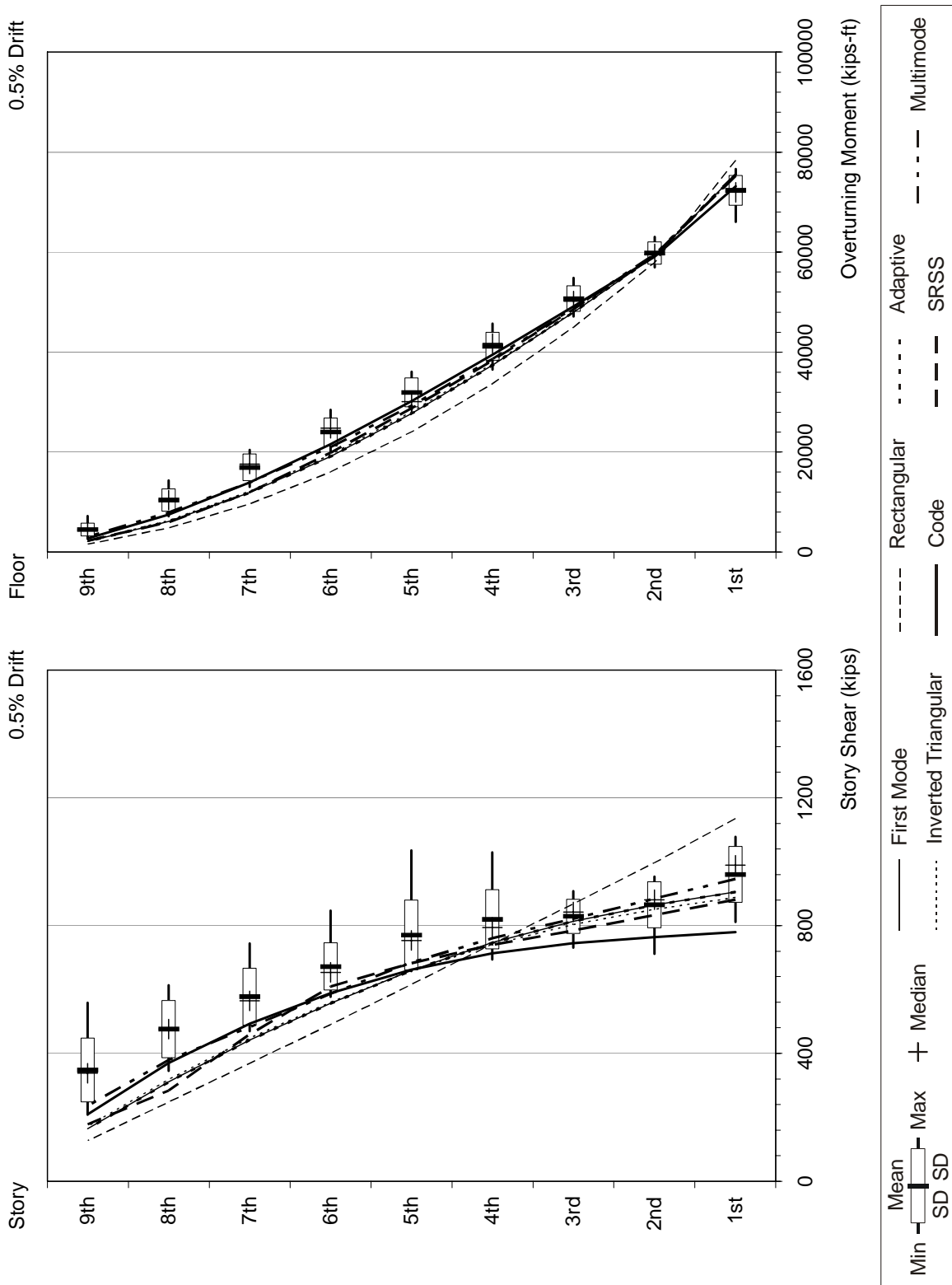
Figure F-44   Response quantities of the 9-story weak-story building for 0.5% drift level (continued)
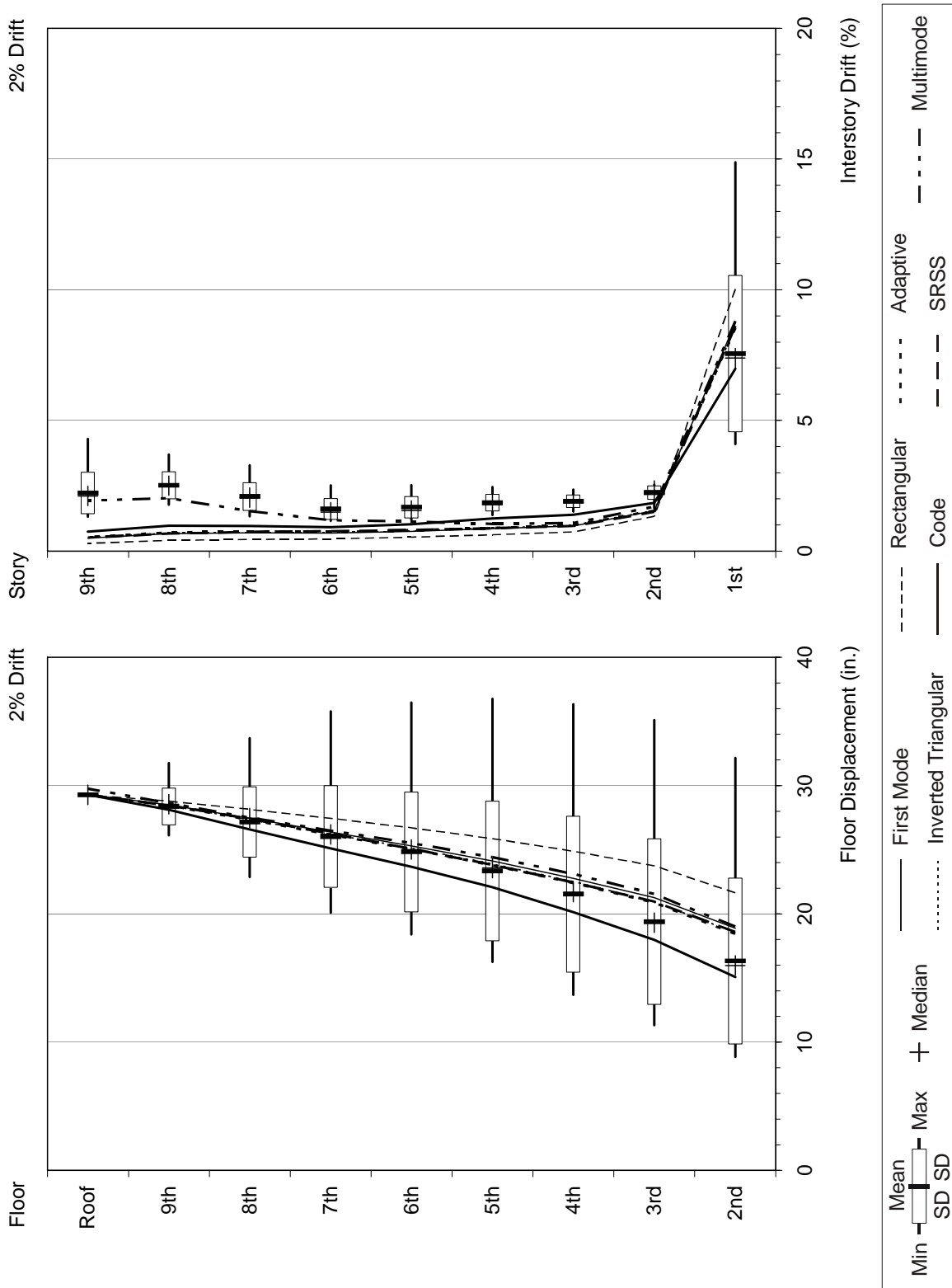
Figure F-45   Response quantities of the 9-story weak-story building for 2% drift level
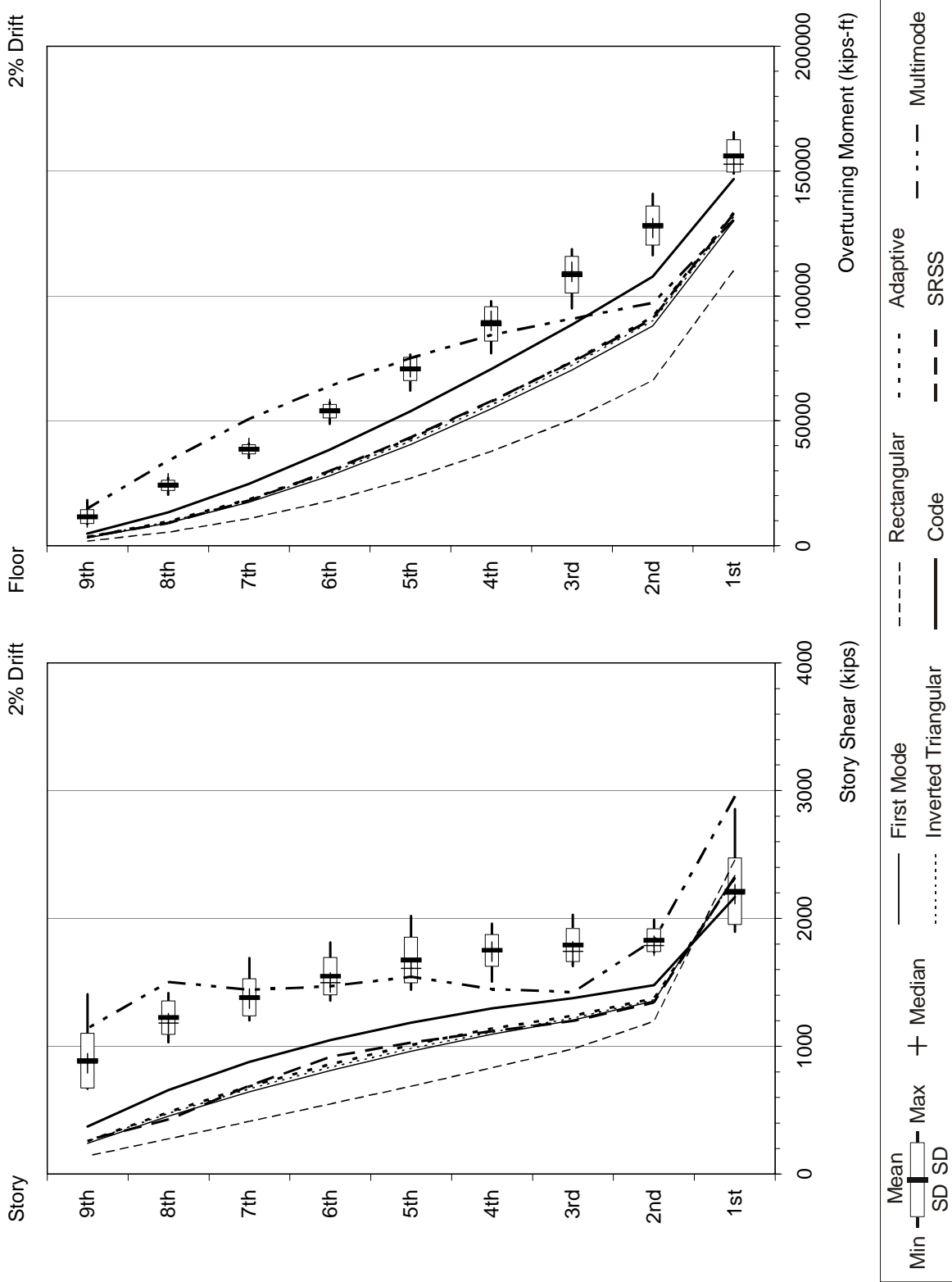
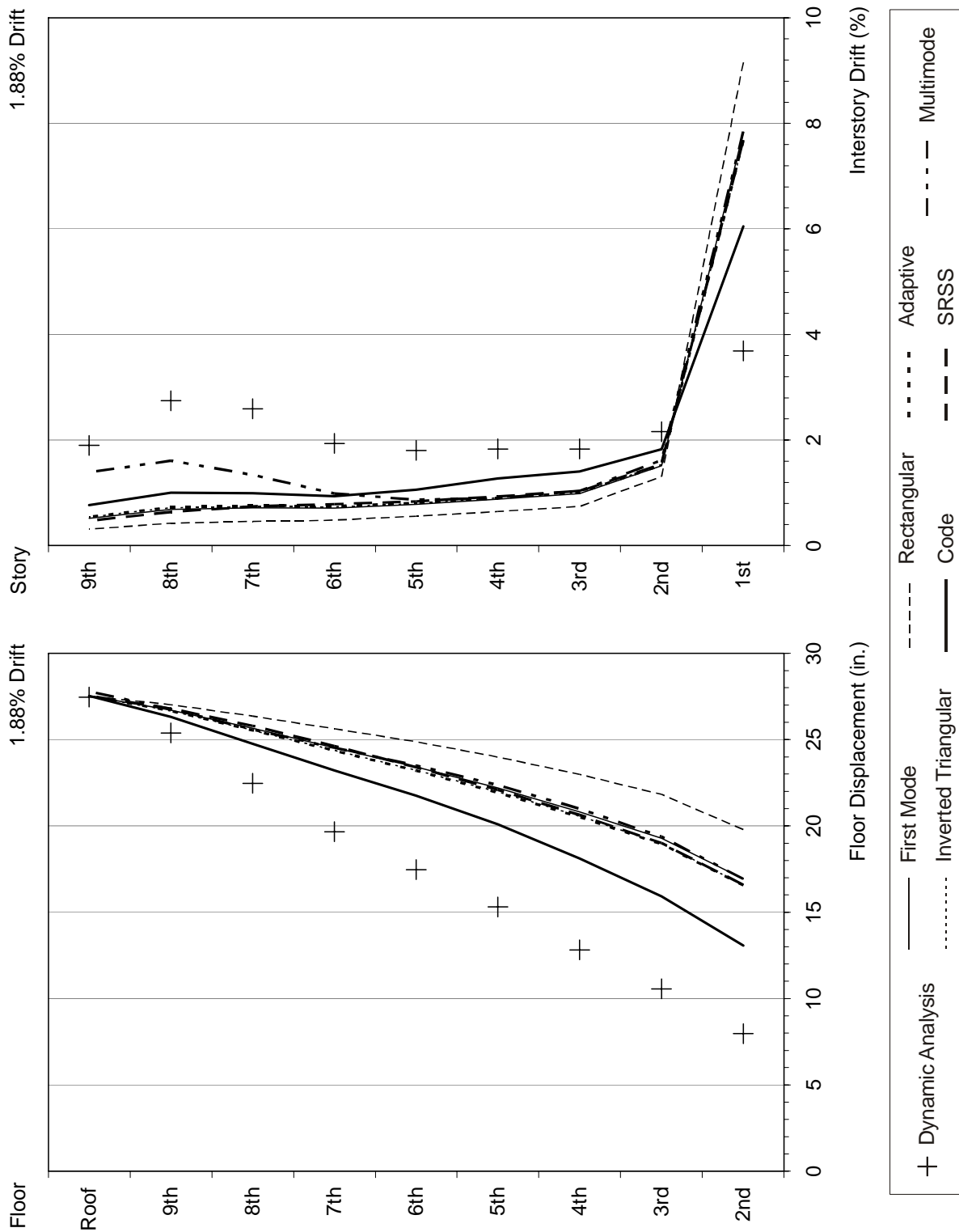Figure F-45   Response quantities of the 9-story weak-story building for 2% drift level (continued)
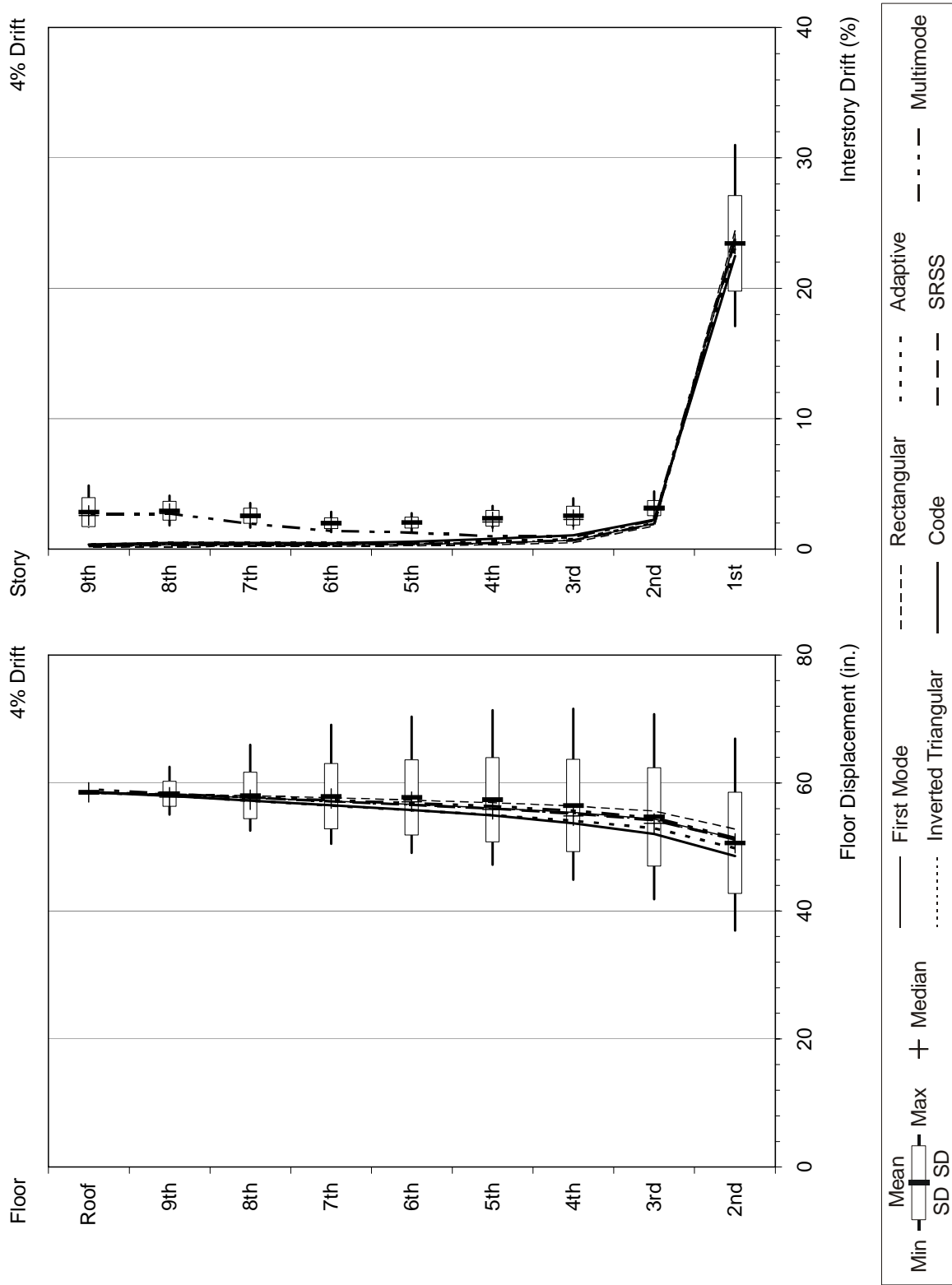
Figure F-46   Response quantities of the 9-story weak-story building for 4% drift level
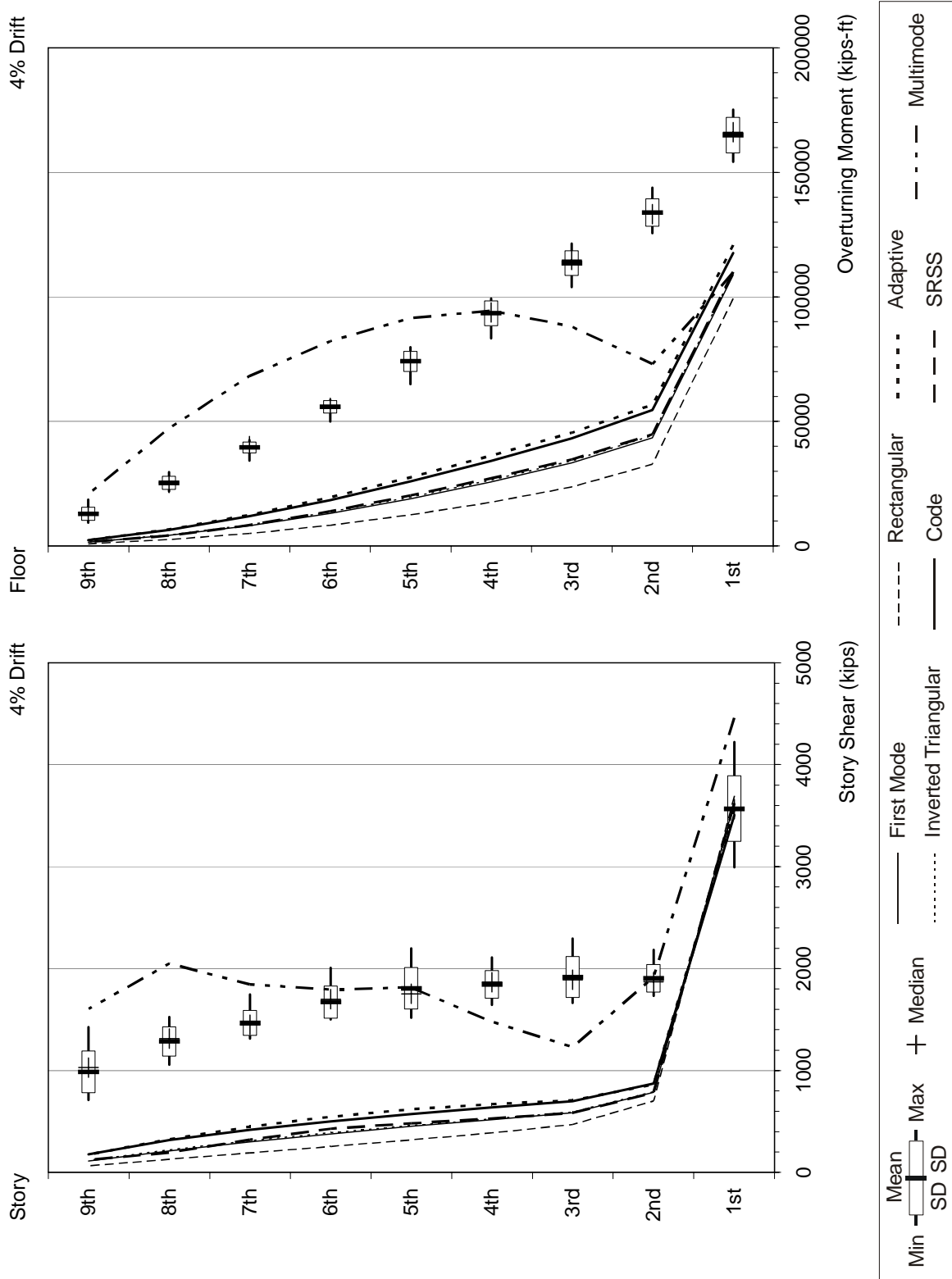
Figure F-46   Response quantities of the 9-story weak-story building for 4% drift level (continued)

F.8.3   Errors Associated with Ordinary (Site Class C) Motions
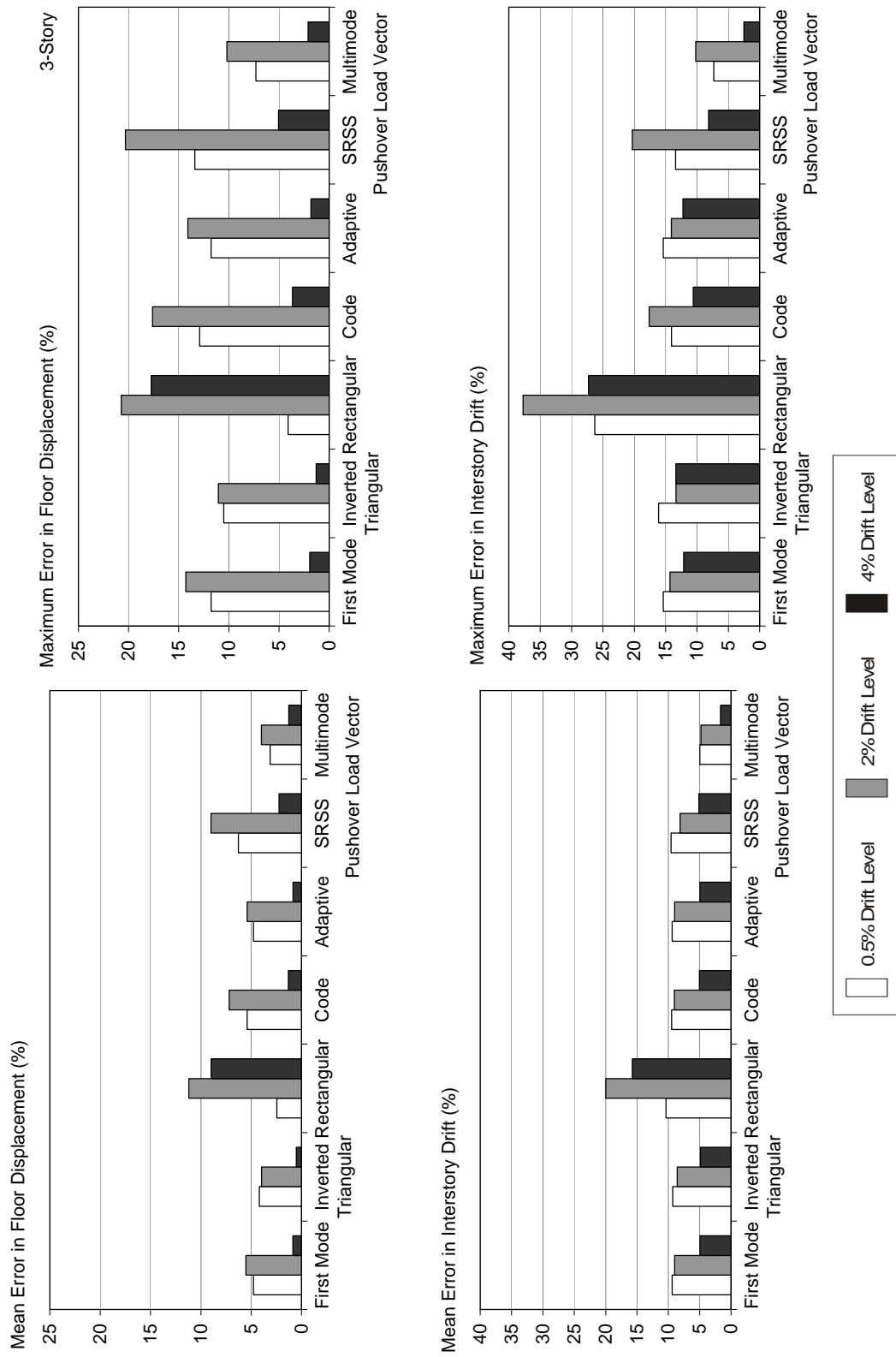
Figure F-47   Mean and maximum errors for the 3-story building
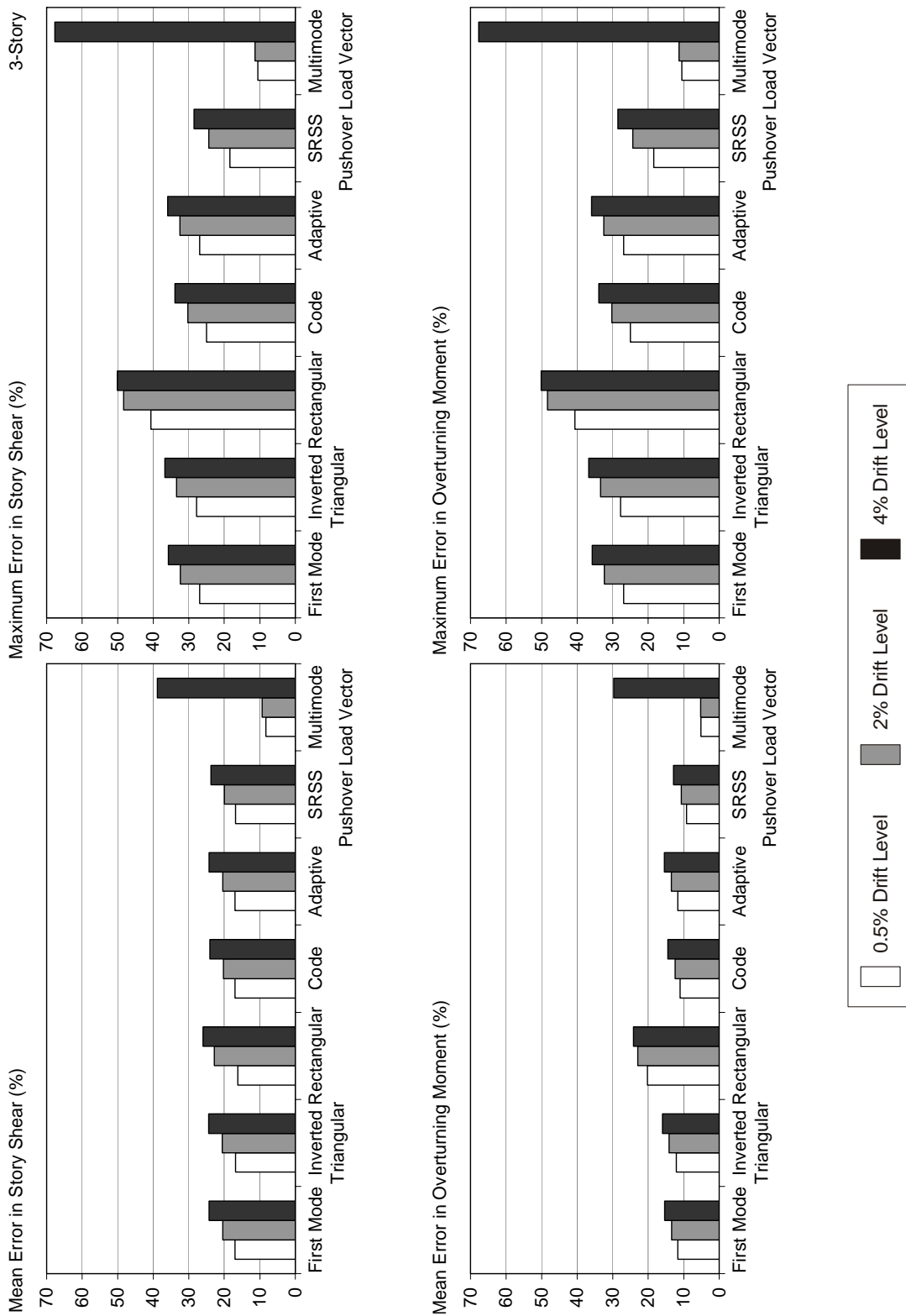
Figure F-47　　Mean and maximum errors for the 3-story building (continued)
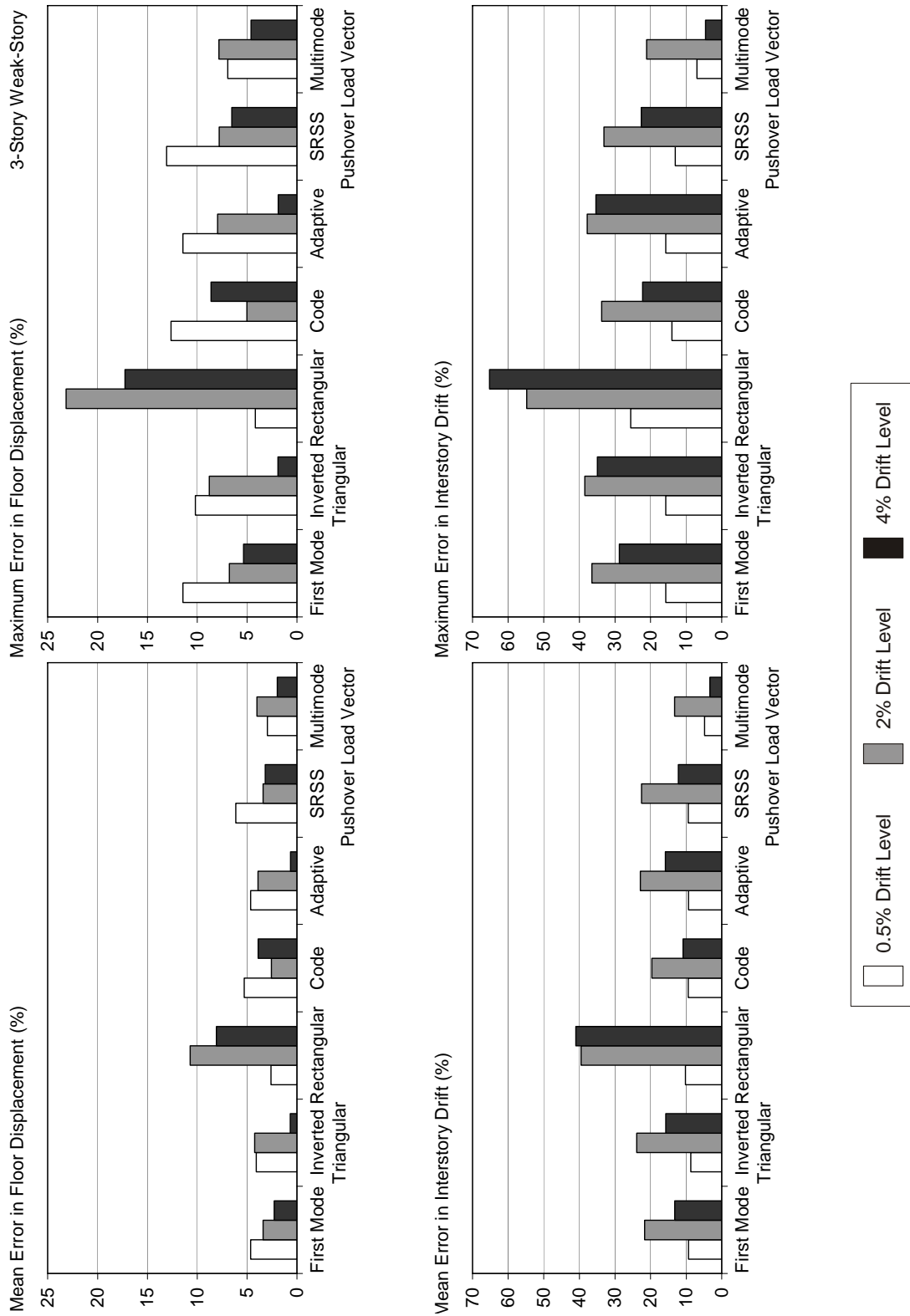
Figure F-48   Mean and maximum errors for the 3-story weak-story building
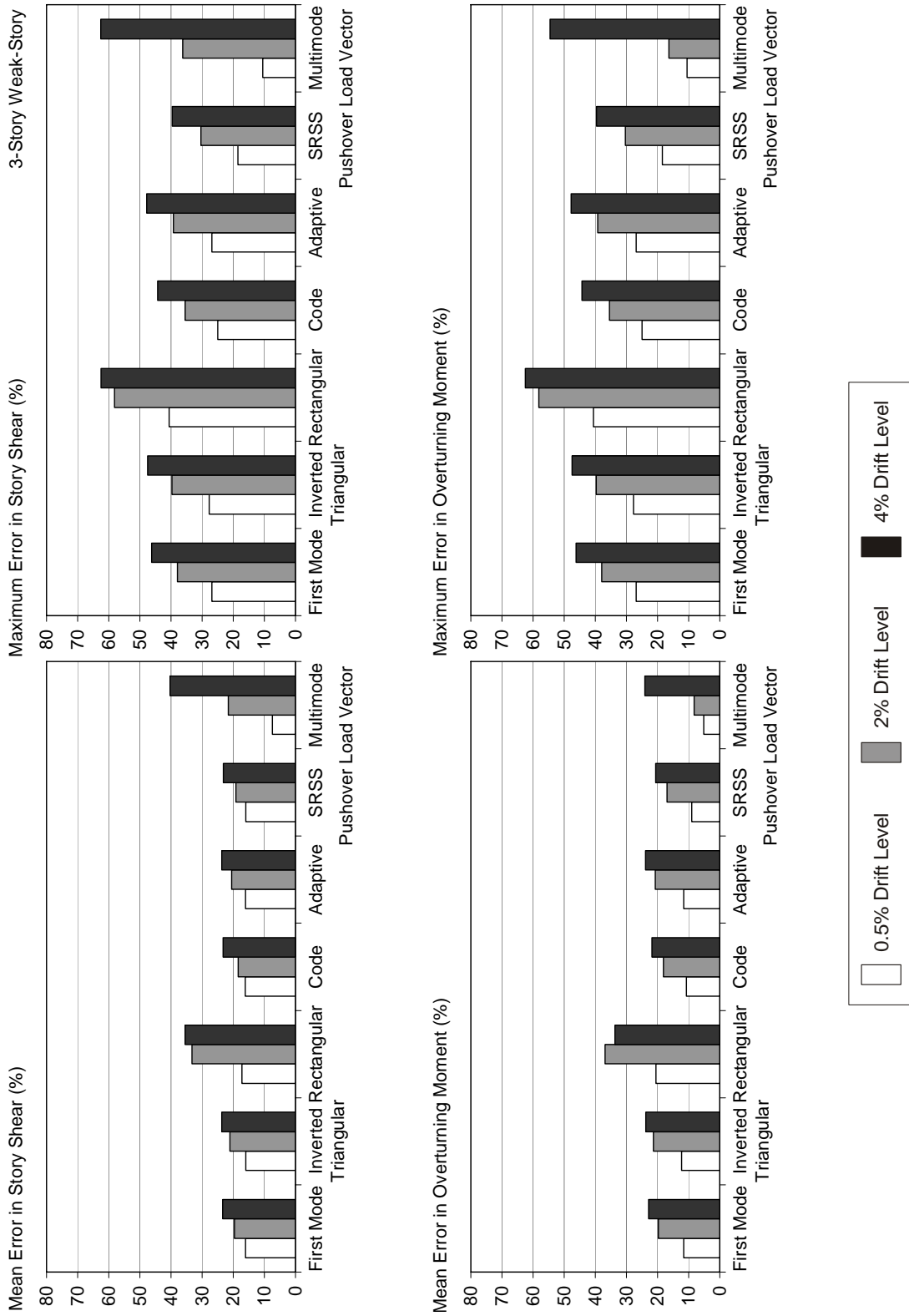
Figure F-48   Mean and maximum errors for the 3-story weak-story building (continued)
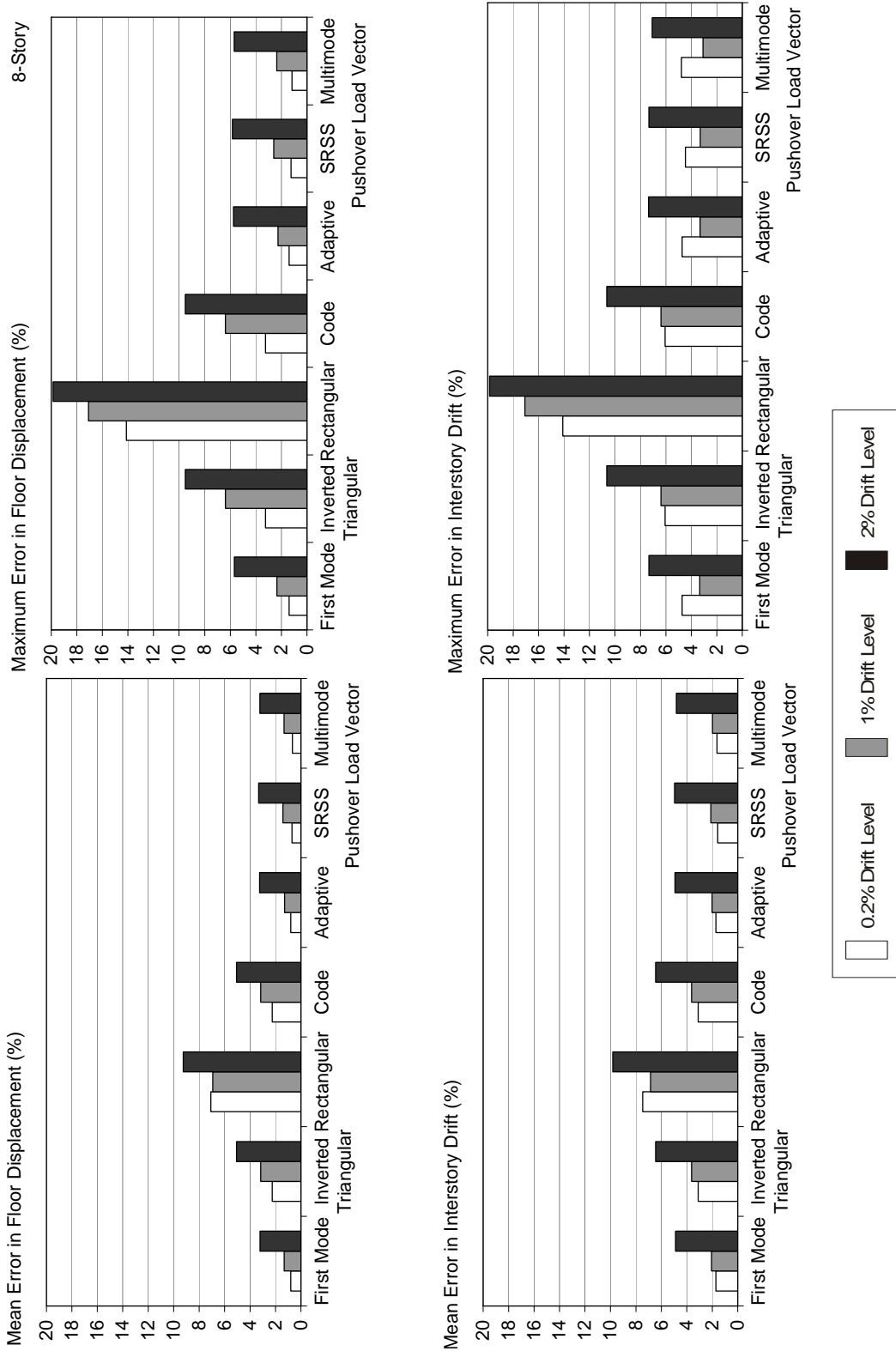
Figure F-49   Mean and maximum errors for the 8-story building
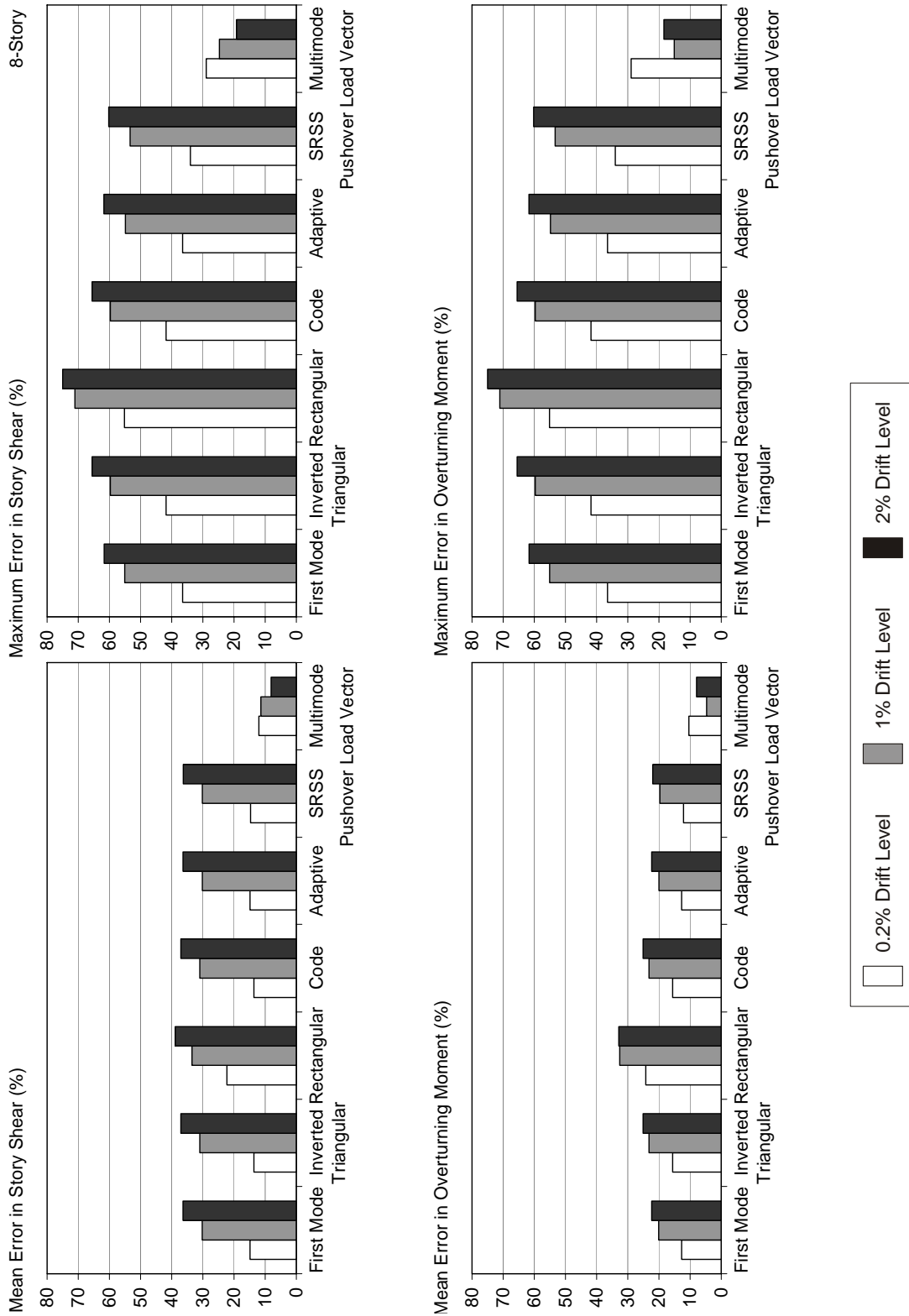
Figure F-49   Mean and maximum errors for the 8-story building (continued)
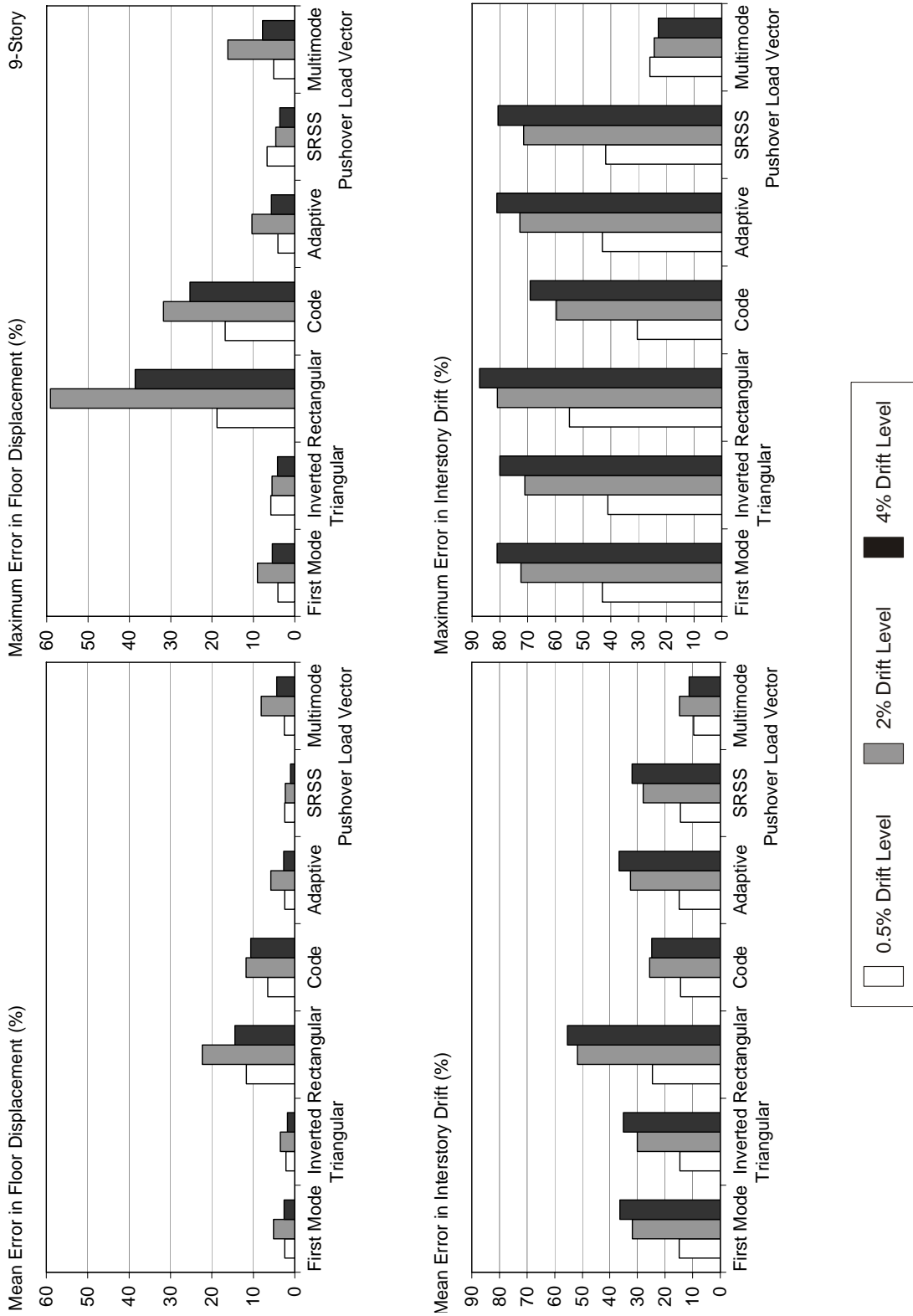
Figure F-50   Mean and maximum errors for the 9-story building
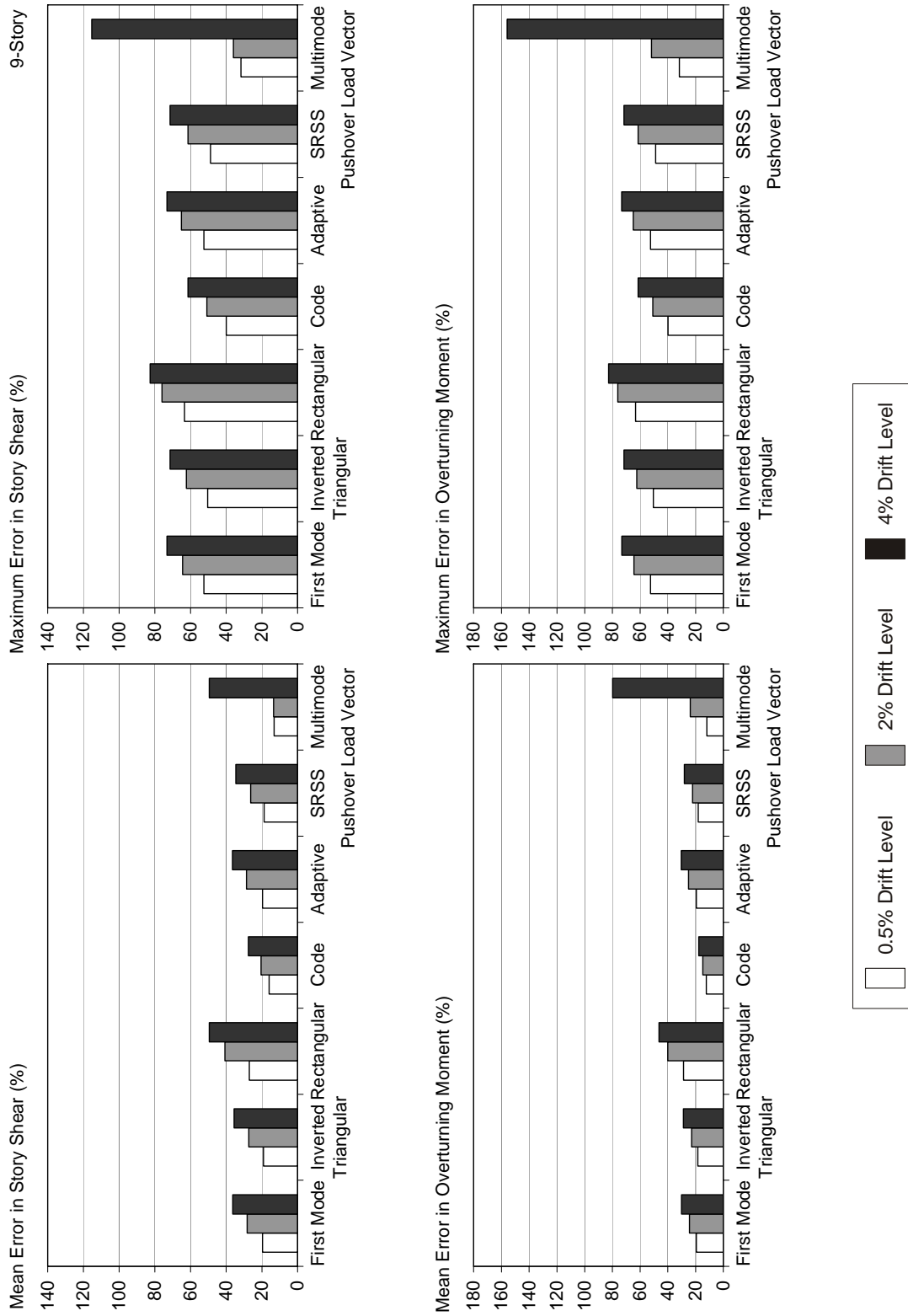
Figure F-50   Mean and maximum errors for the 9-story building (continued)
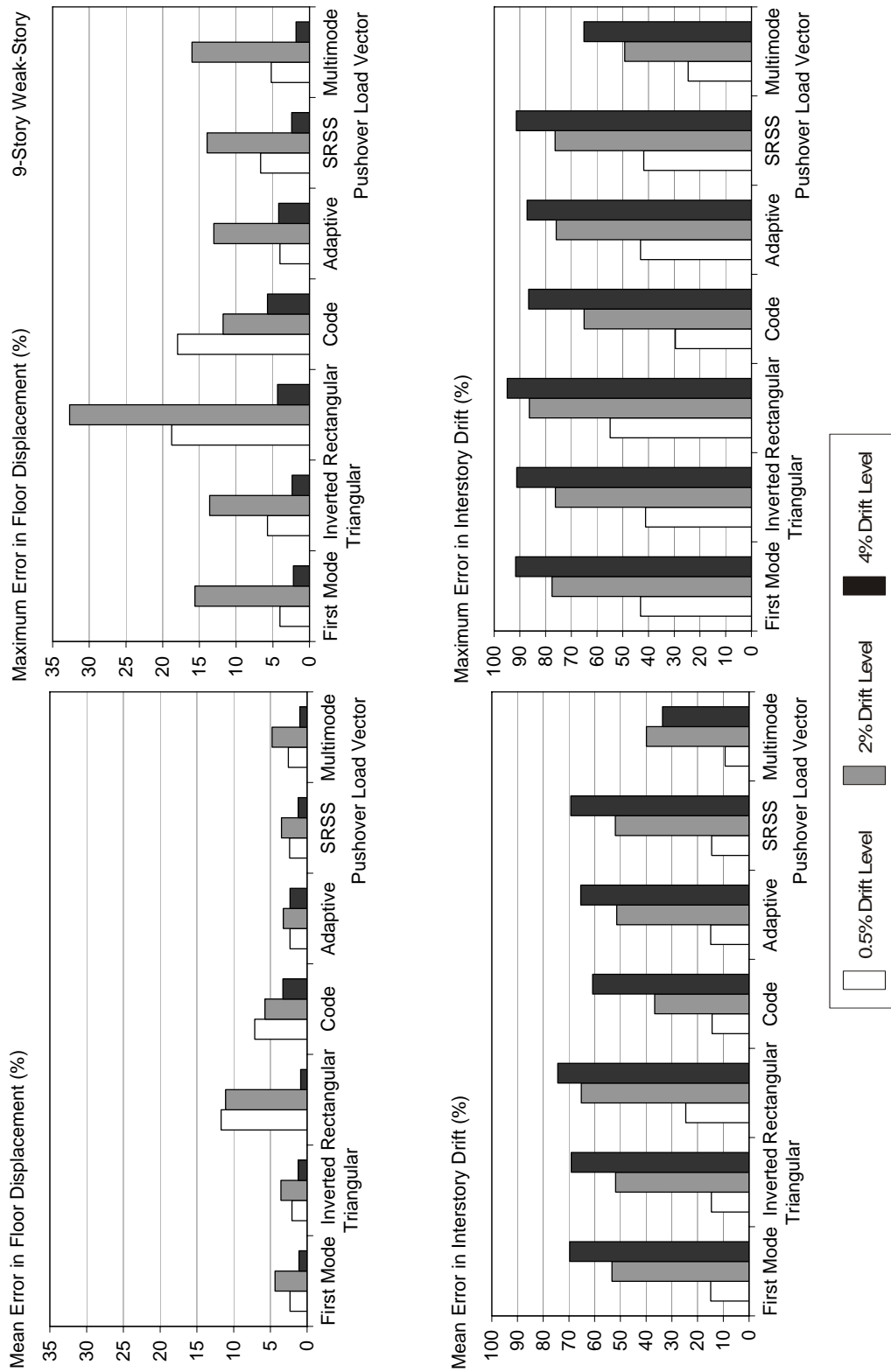
Figure F-51   Mean and maximum errors for the 9-story weak-story building
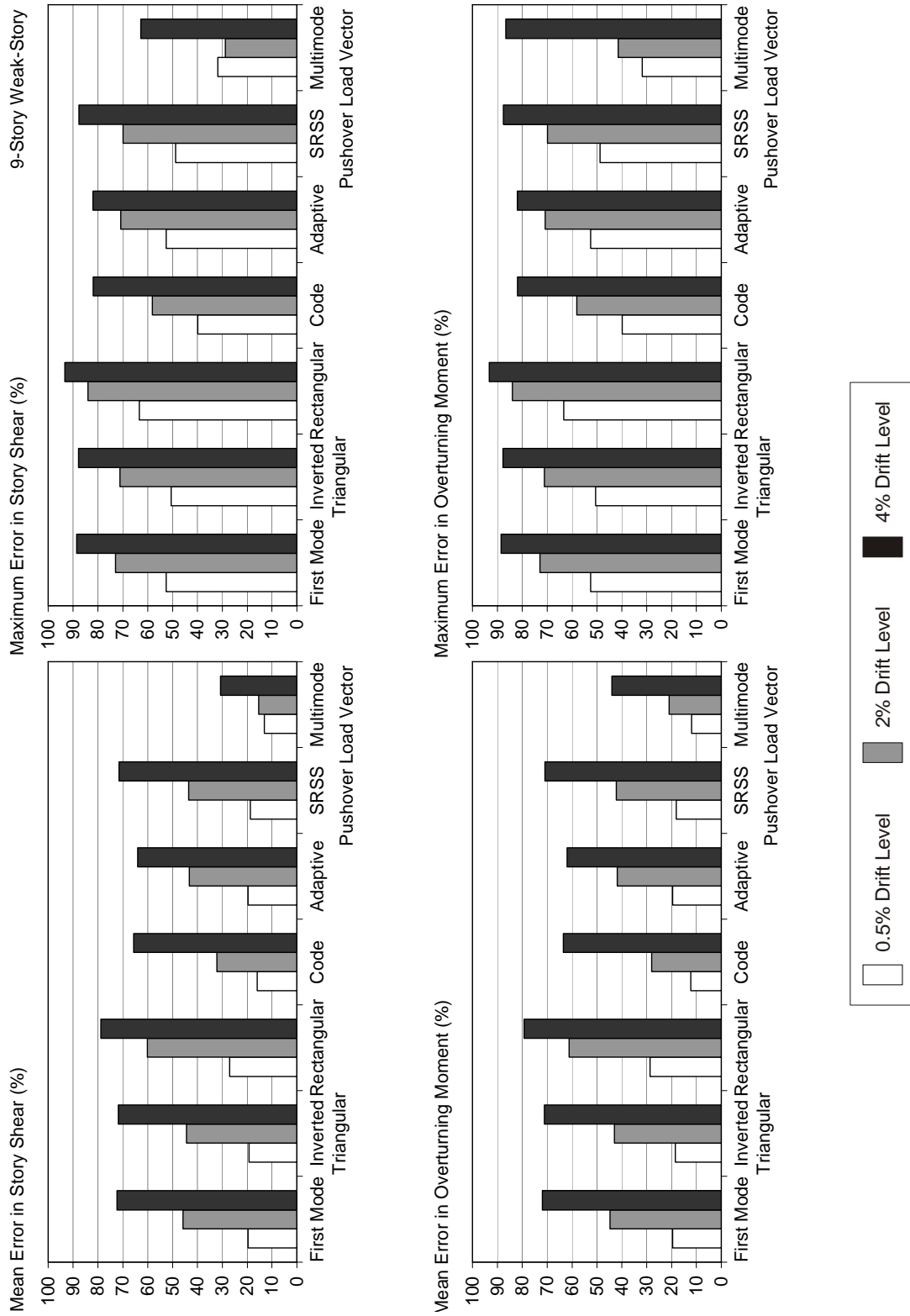
Figure F-51   Mean and maximum errors for the 9-story weak-story building (continued)

F.8.4 Responses to Near Fault Motions
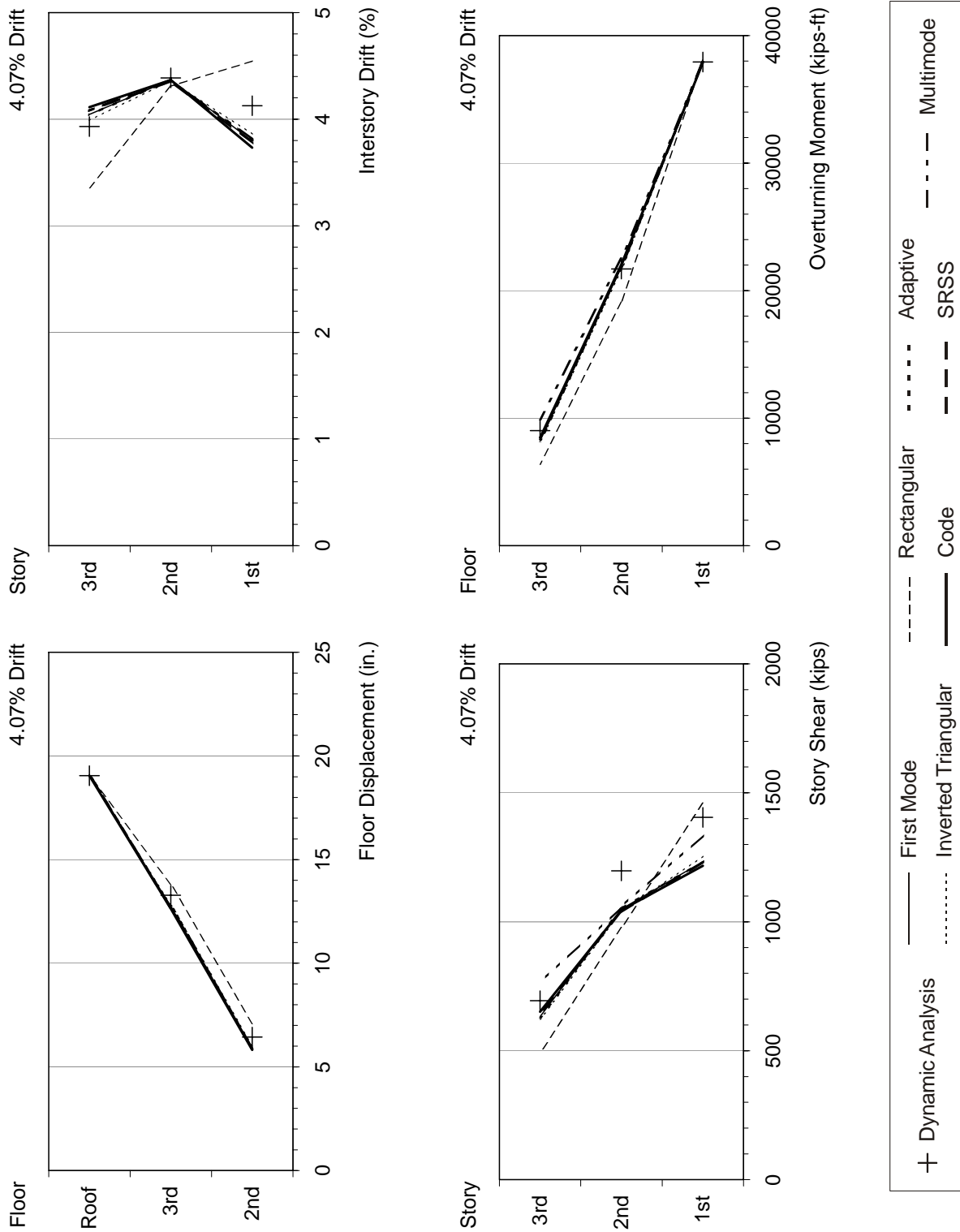
Figure F-52   Response quantities of the 3-story building under ERZMV1 ground motion
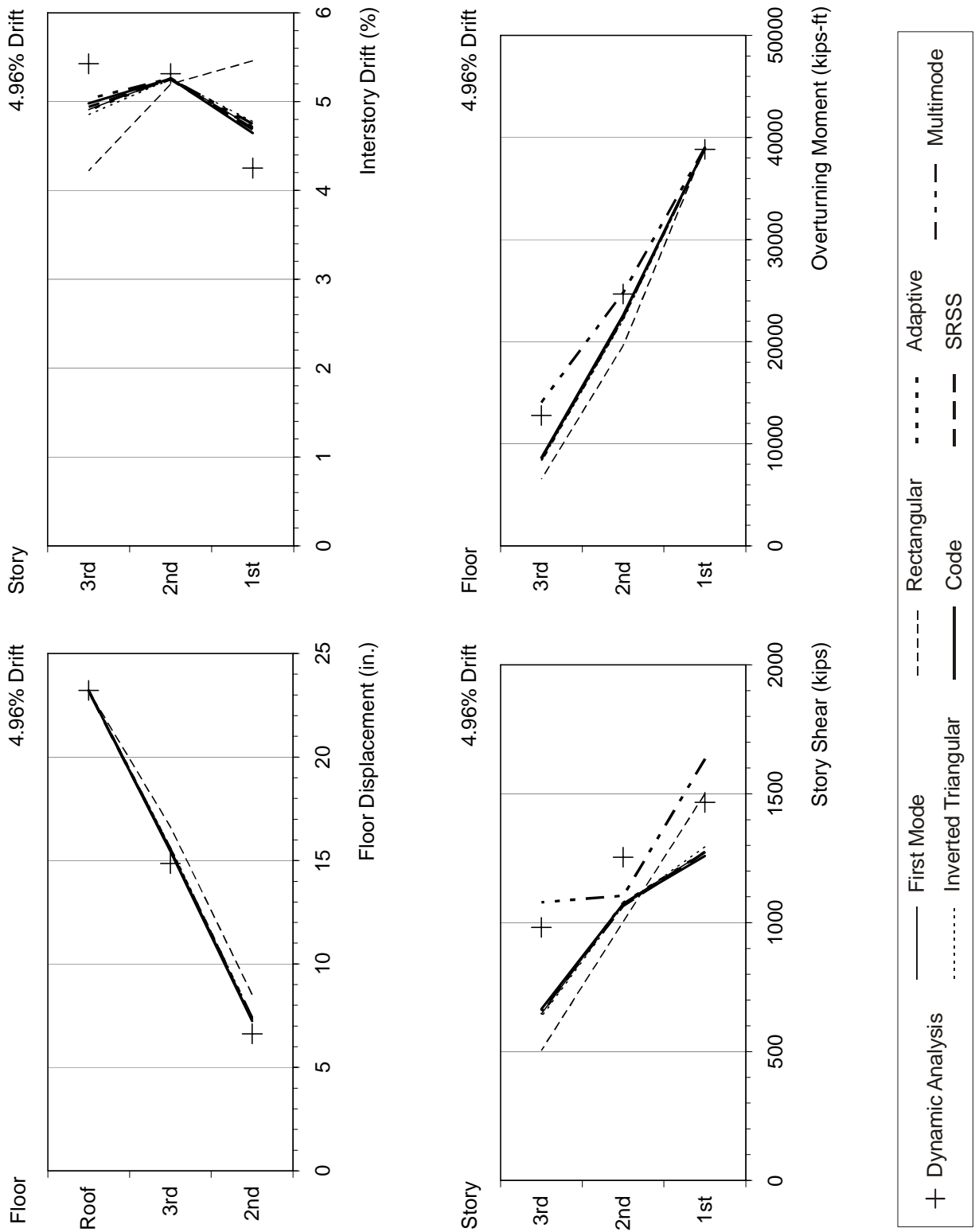
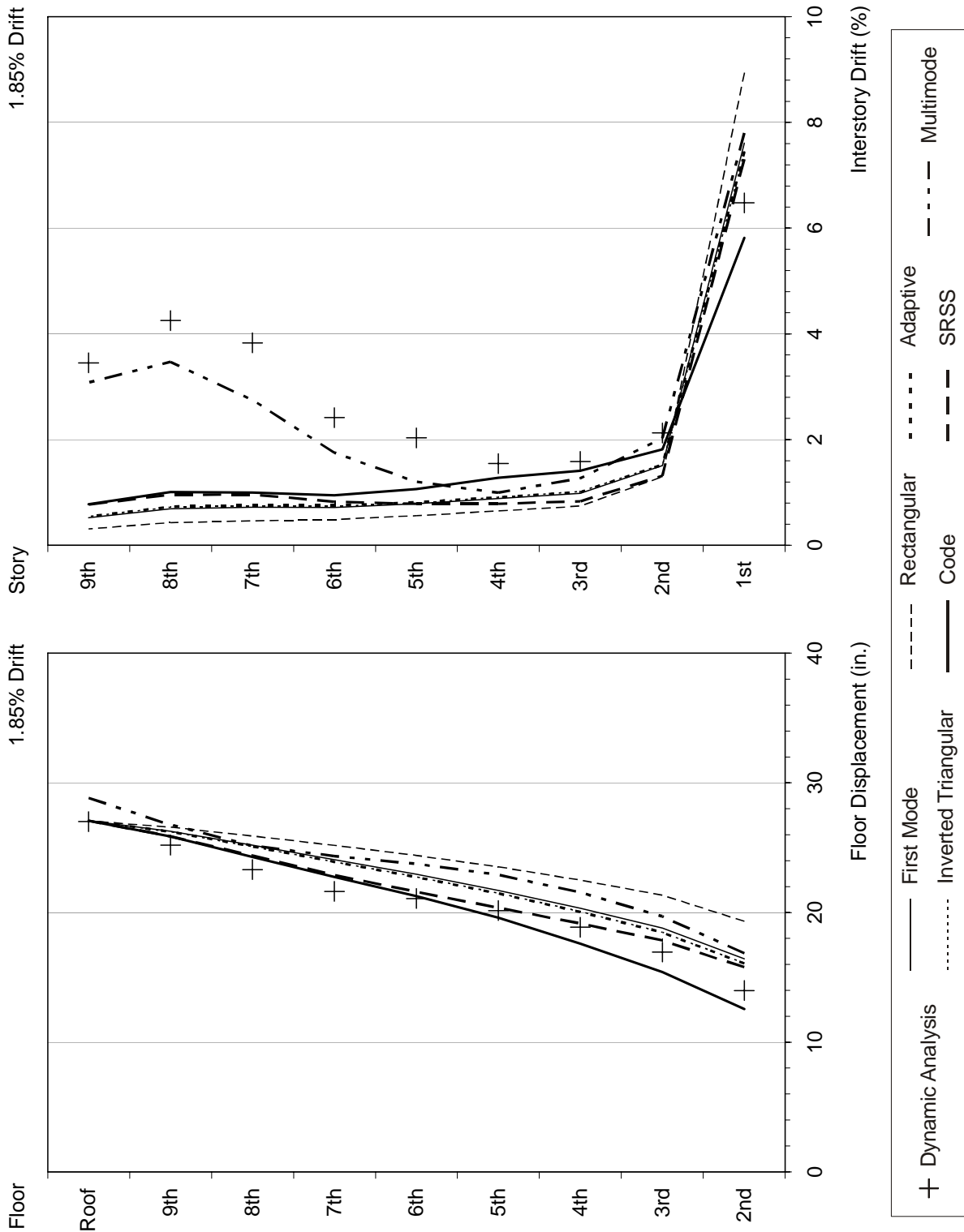Figure F-53   Response quantities of the 3-story building under RRSMV1 ground motion
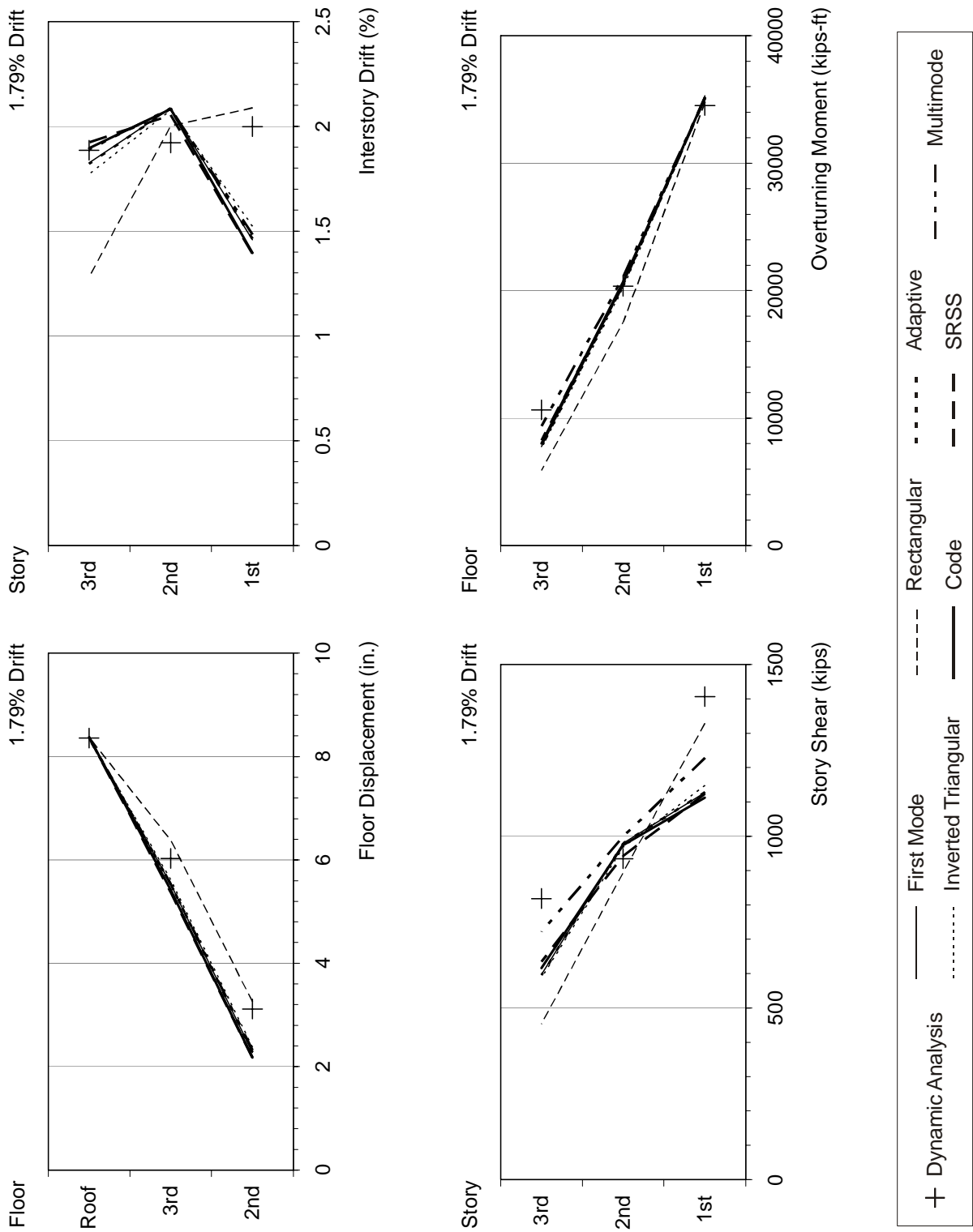
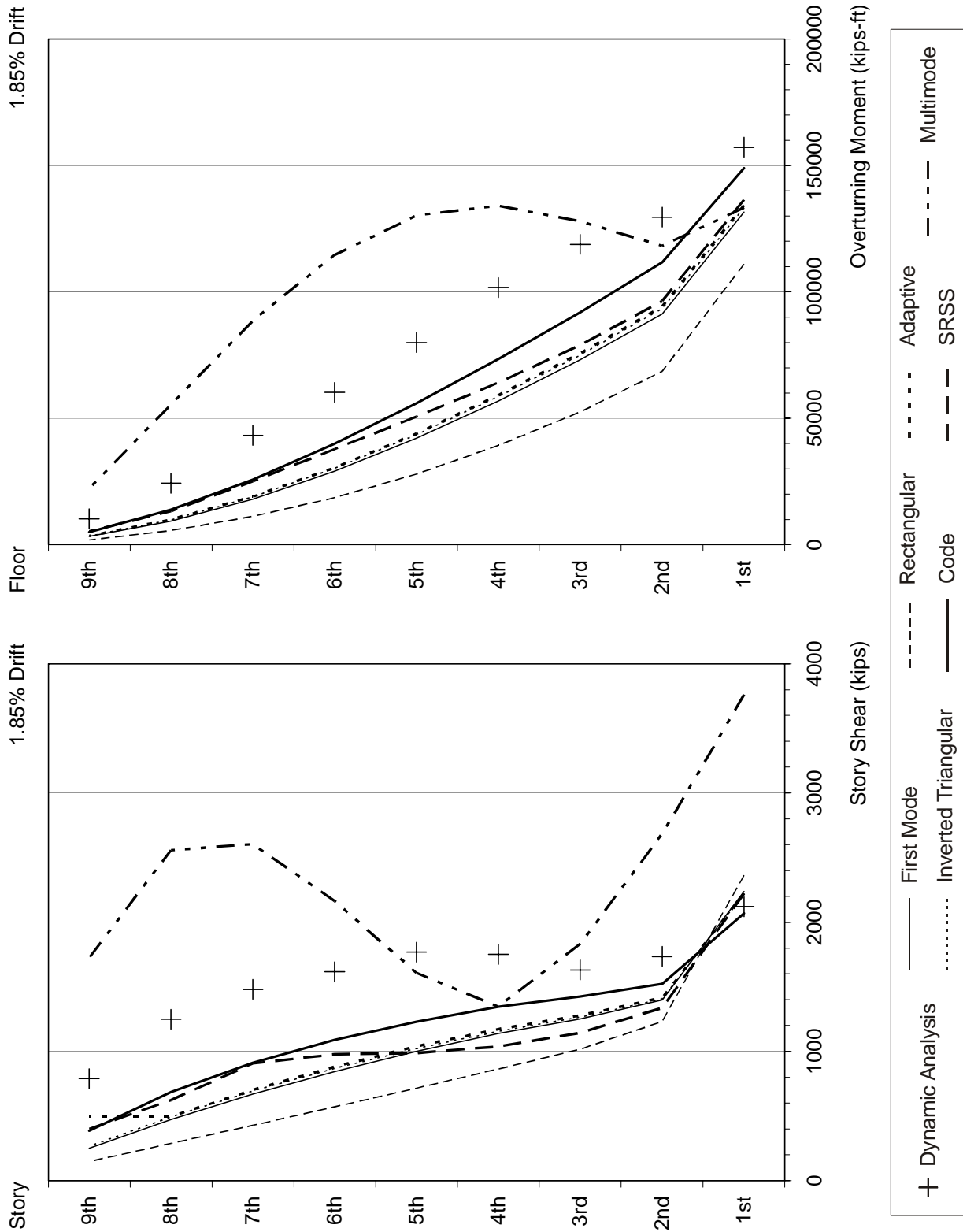Figure F-54   Response quantities of the 3-story building under LUCMV1 ground motion
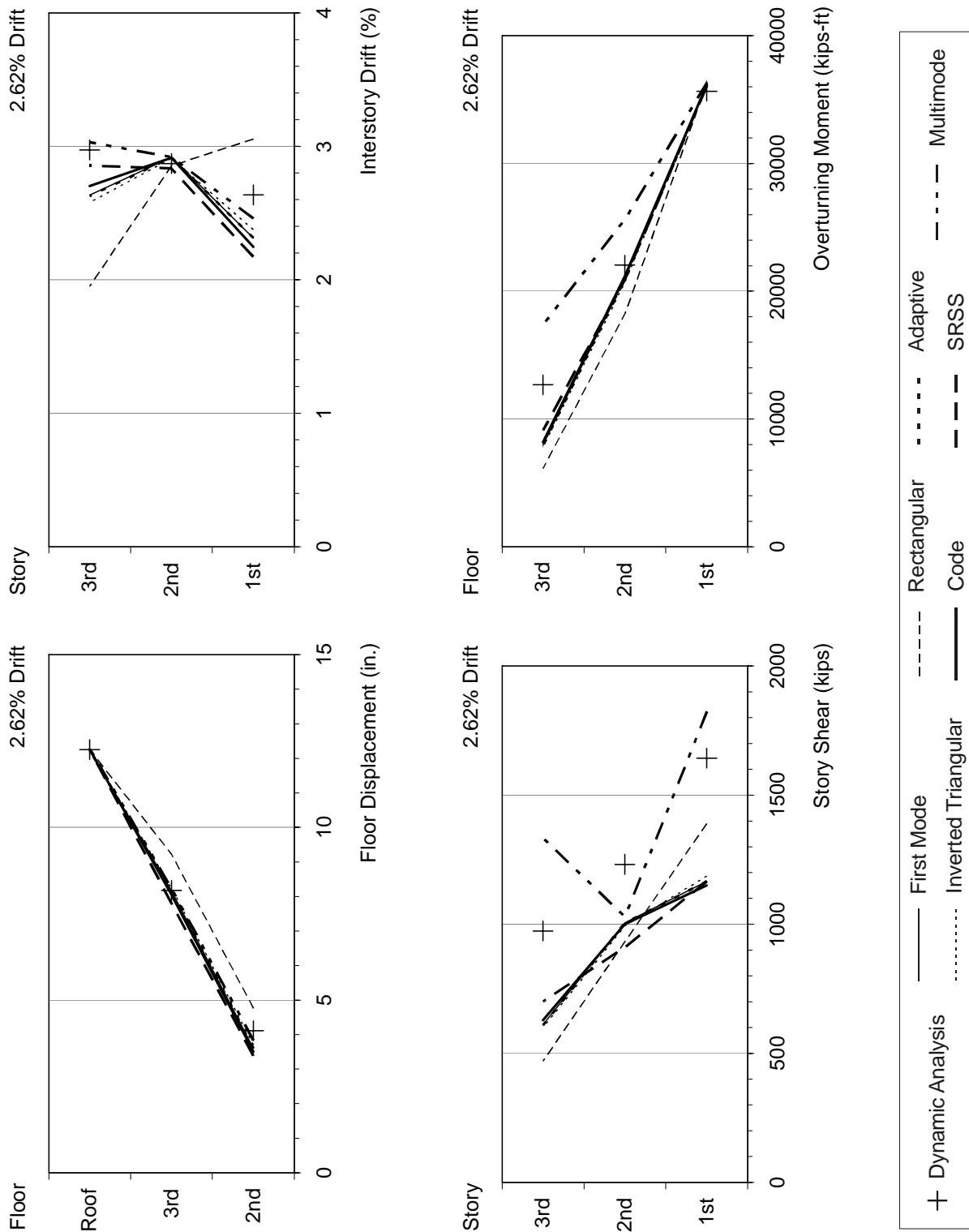
Figure F-55   Response quantities of the 3-story building under SCHMV1 ground motion
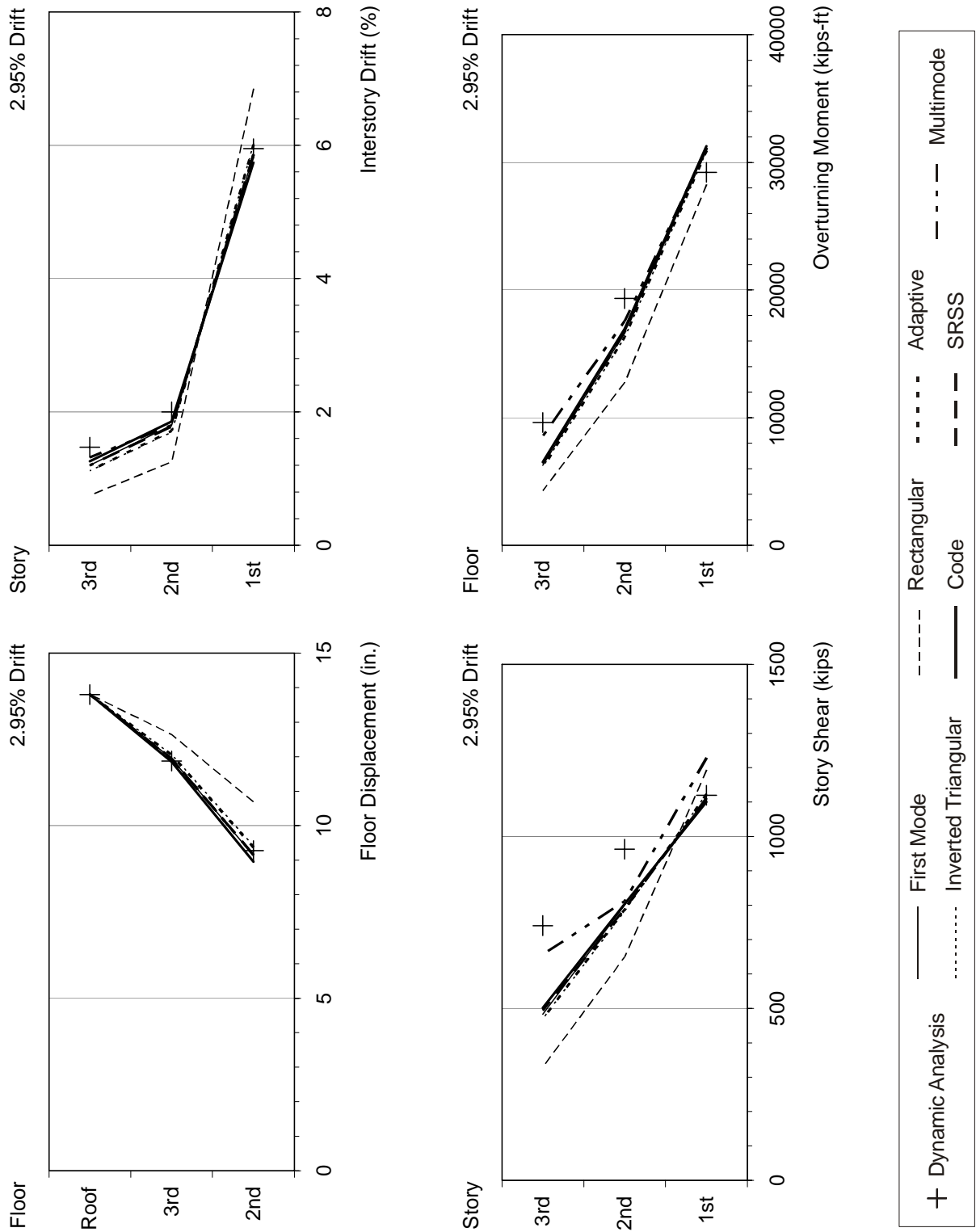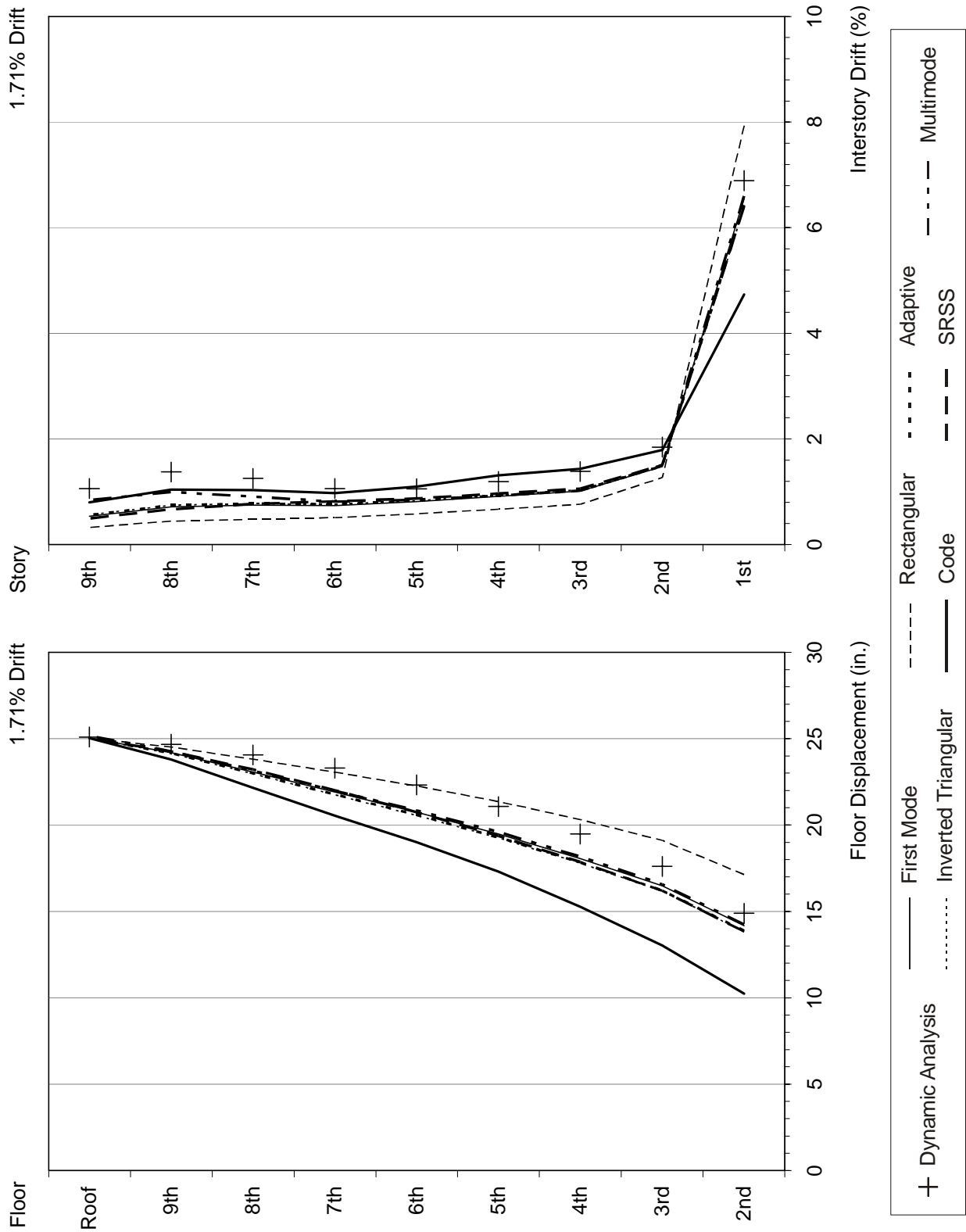
Figure F-56   Response quantities of the 3-story weak-story building under ERZMV1 ground motion
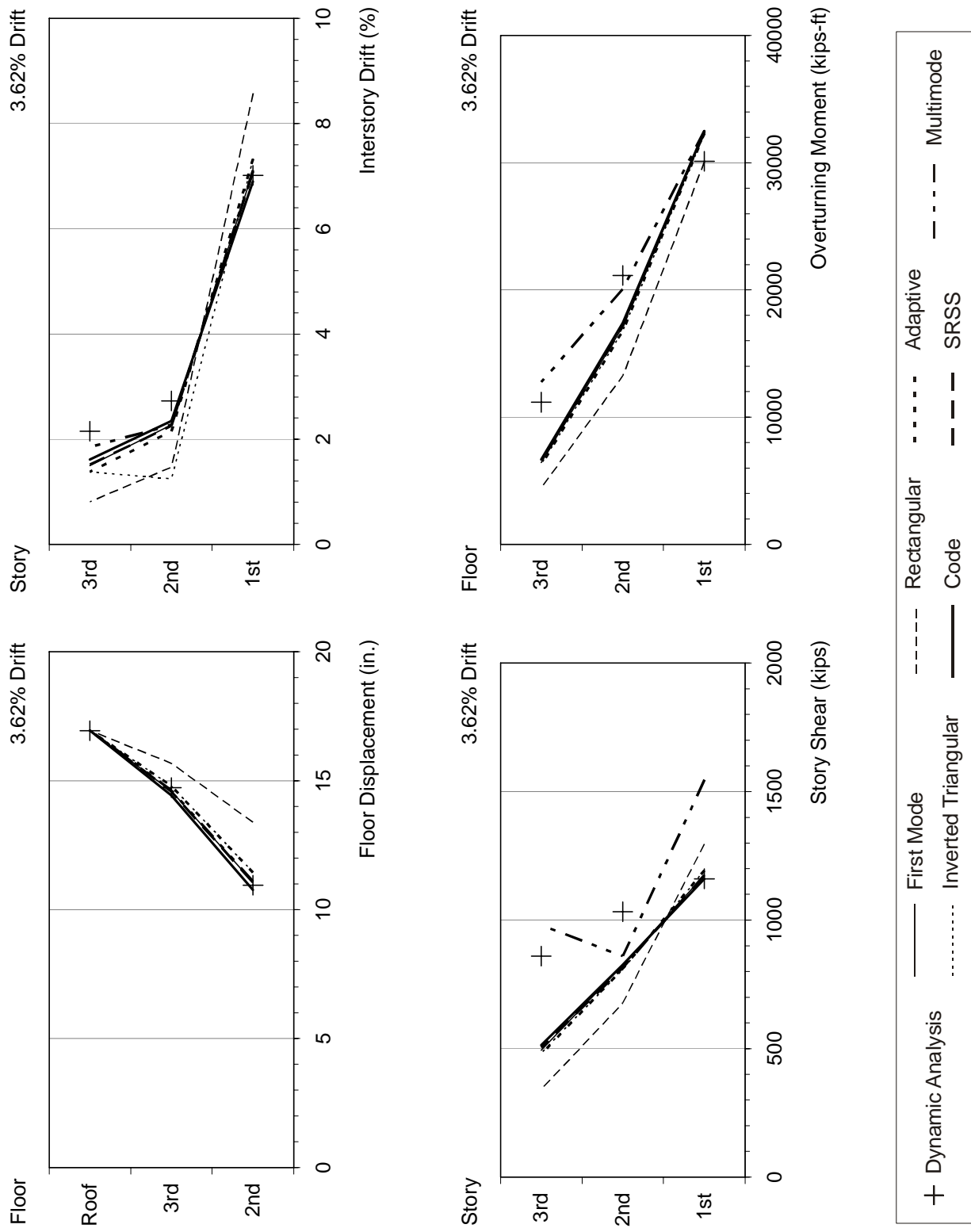
Figure F-57   Response quantities of the 3-story weak-story building under RRSMV1 ground motion
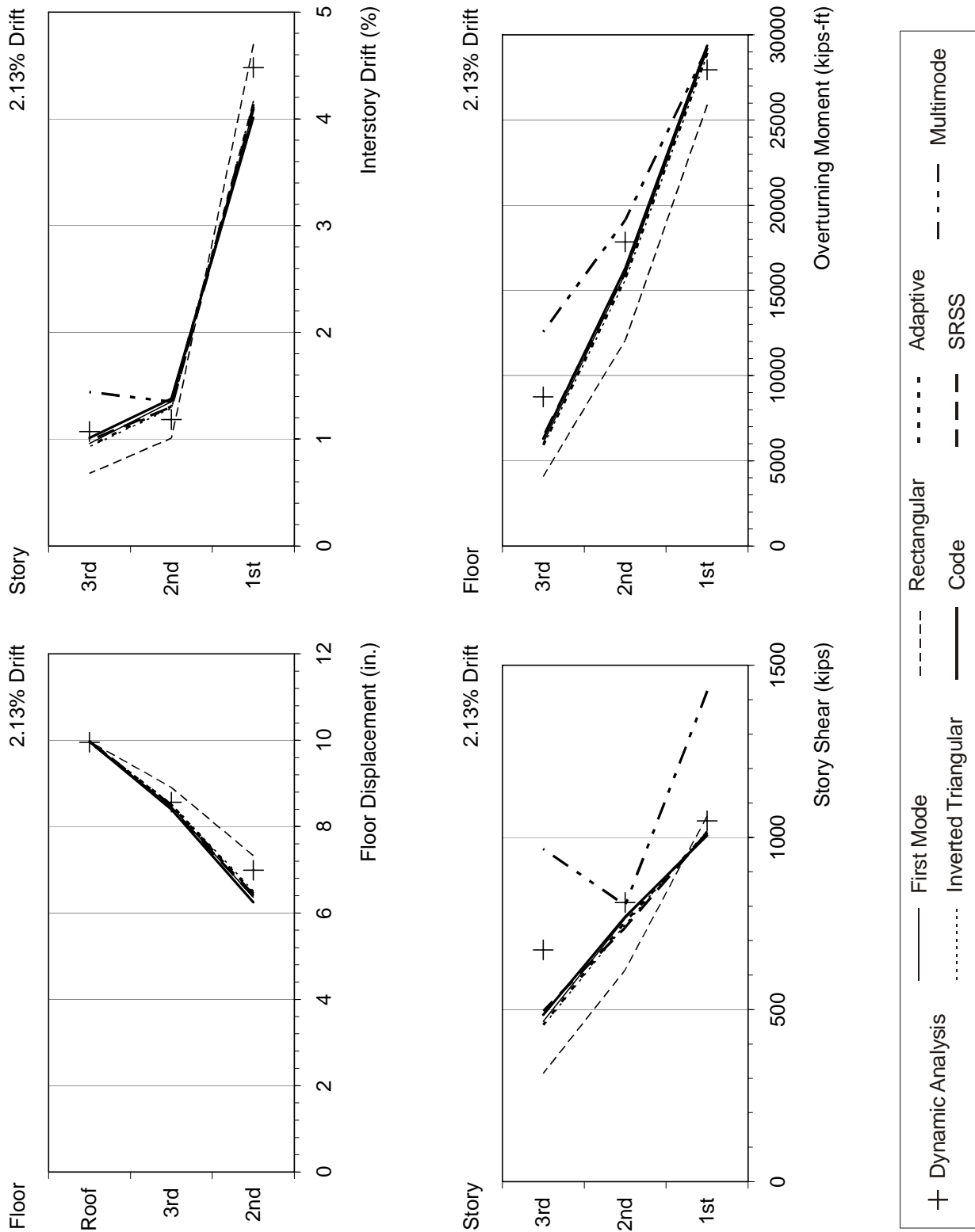
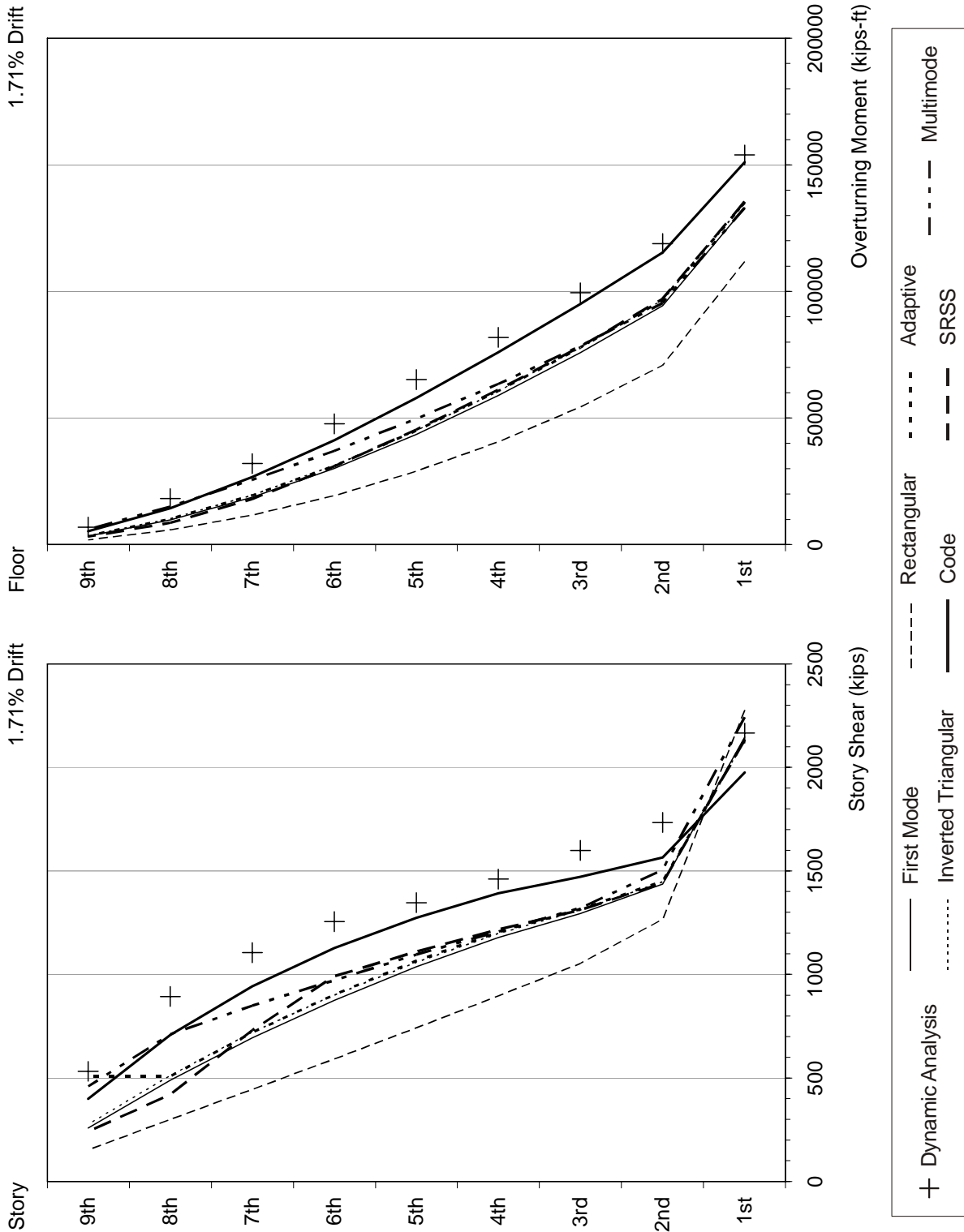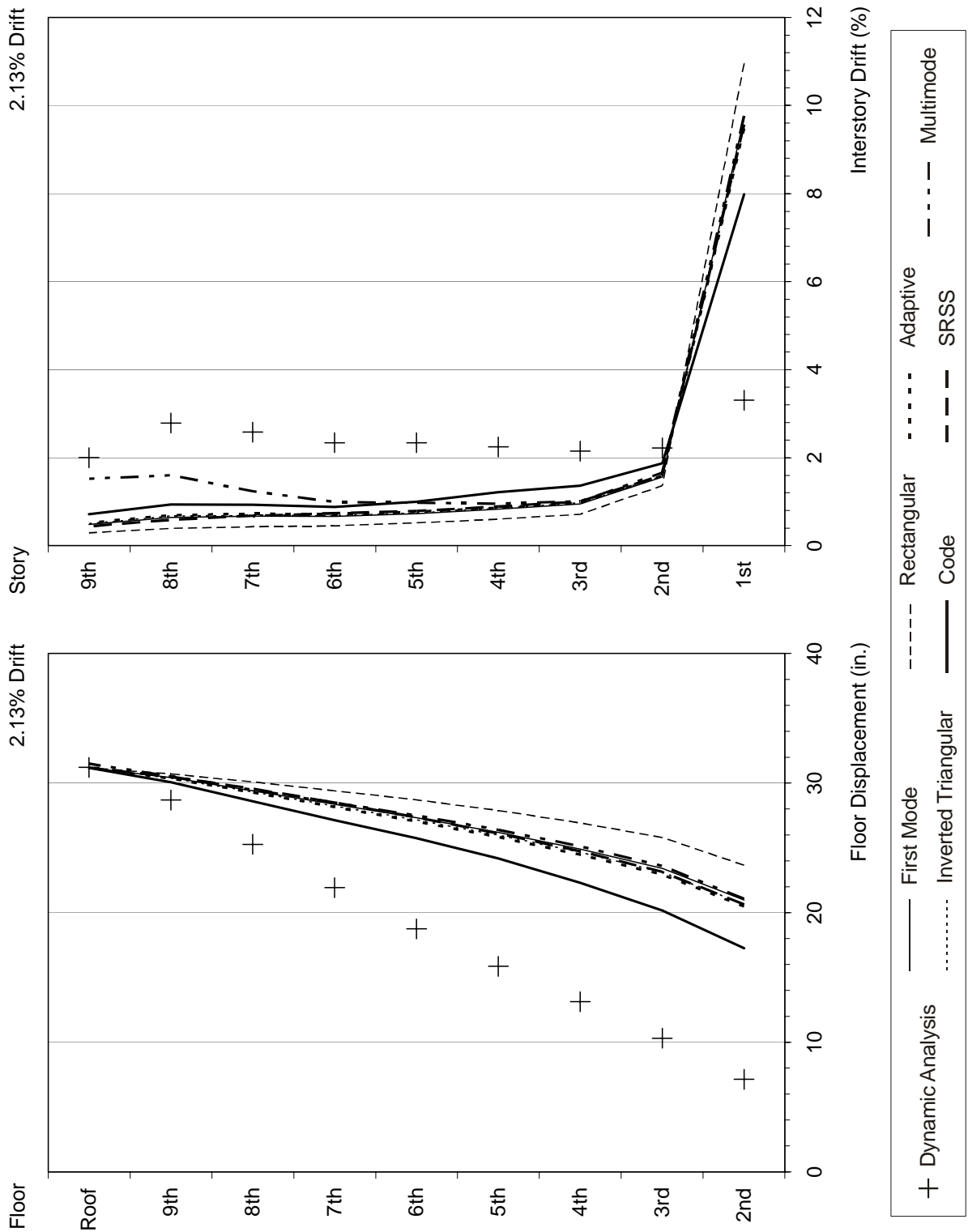Figure F-58   Response quantities of the 3-story weak-story building under LUCMV1 ground motion
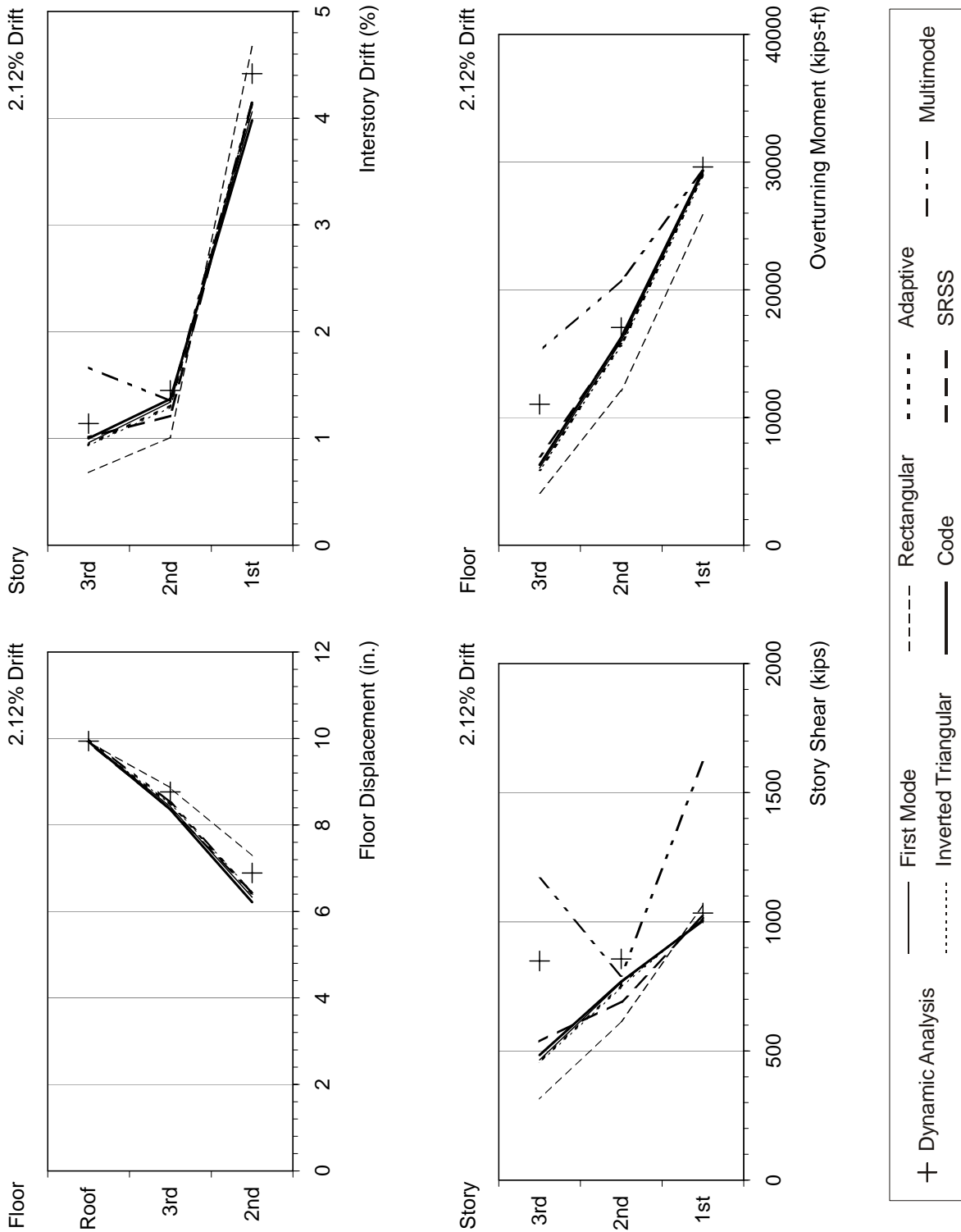
Figure F-59   Response quantities of the 3-story weak-story building under SCHMV1 ground motion
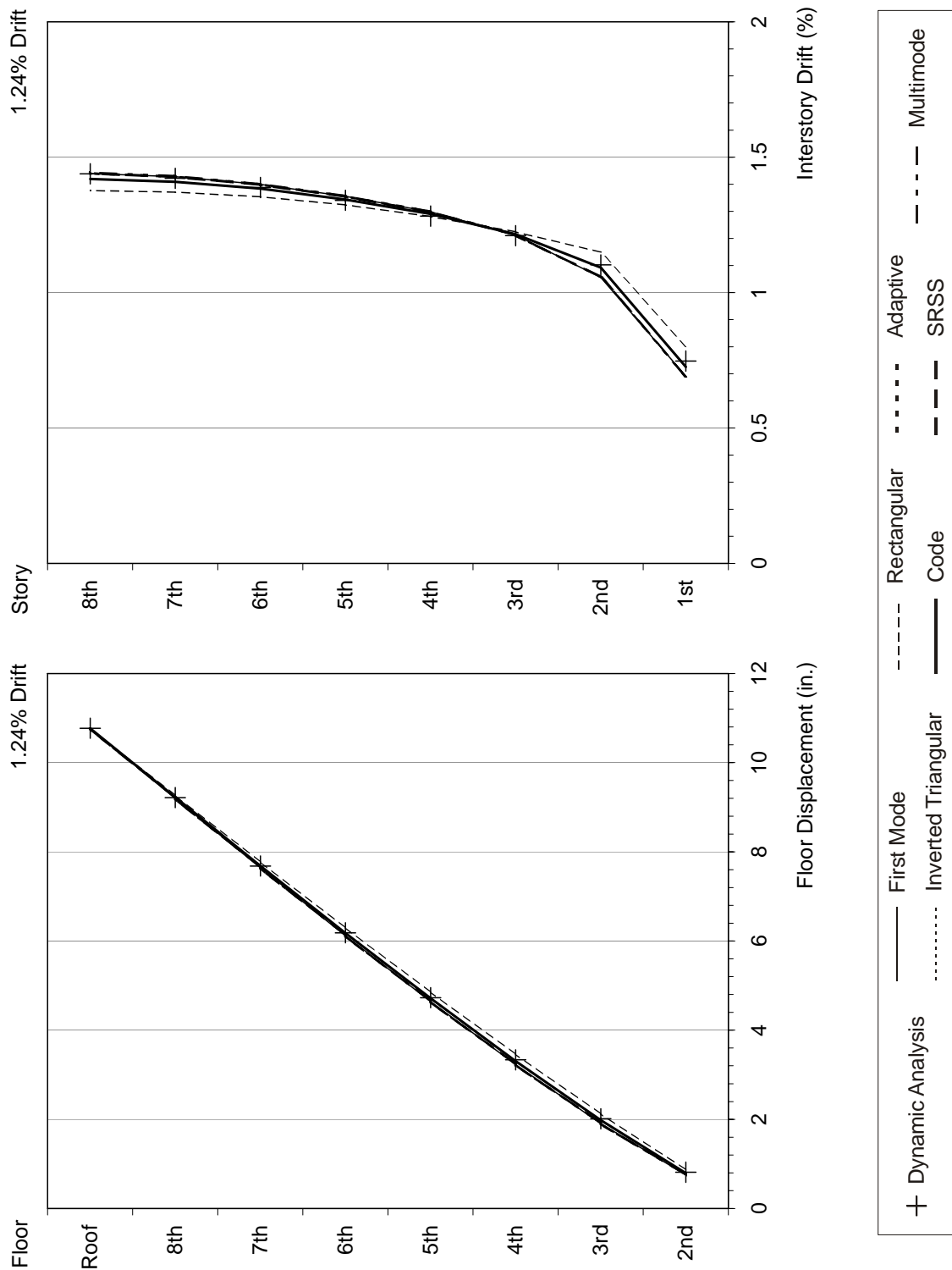
Figure F-60   Response quantities of the 8-story building under ERZMV1 ground motion
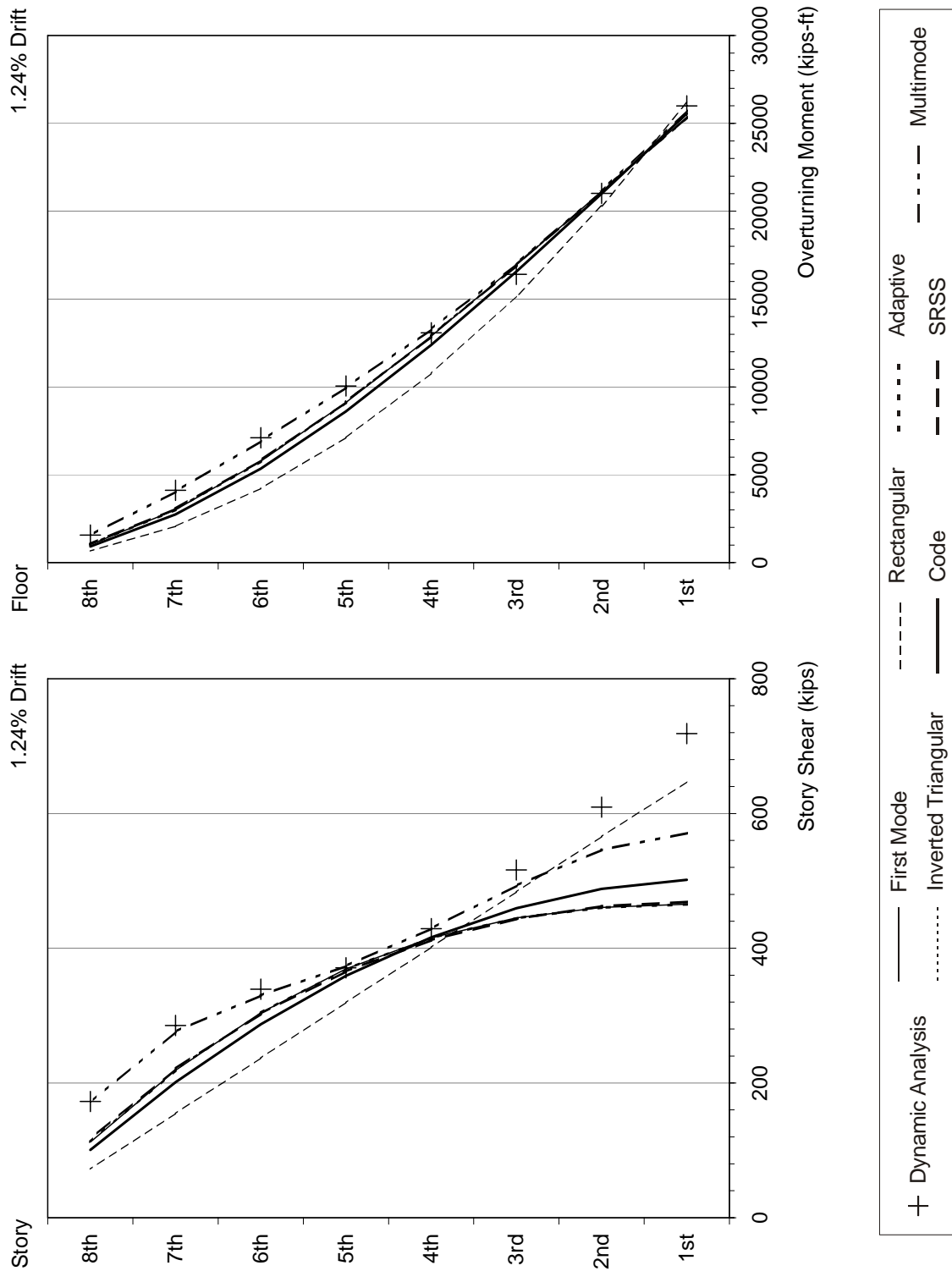
Figure F-60   Response quantities of the 8-story building under ERZMV1 ground motion (continued)
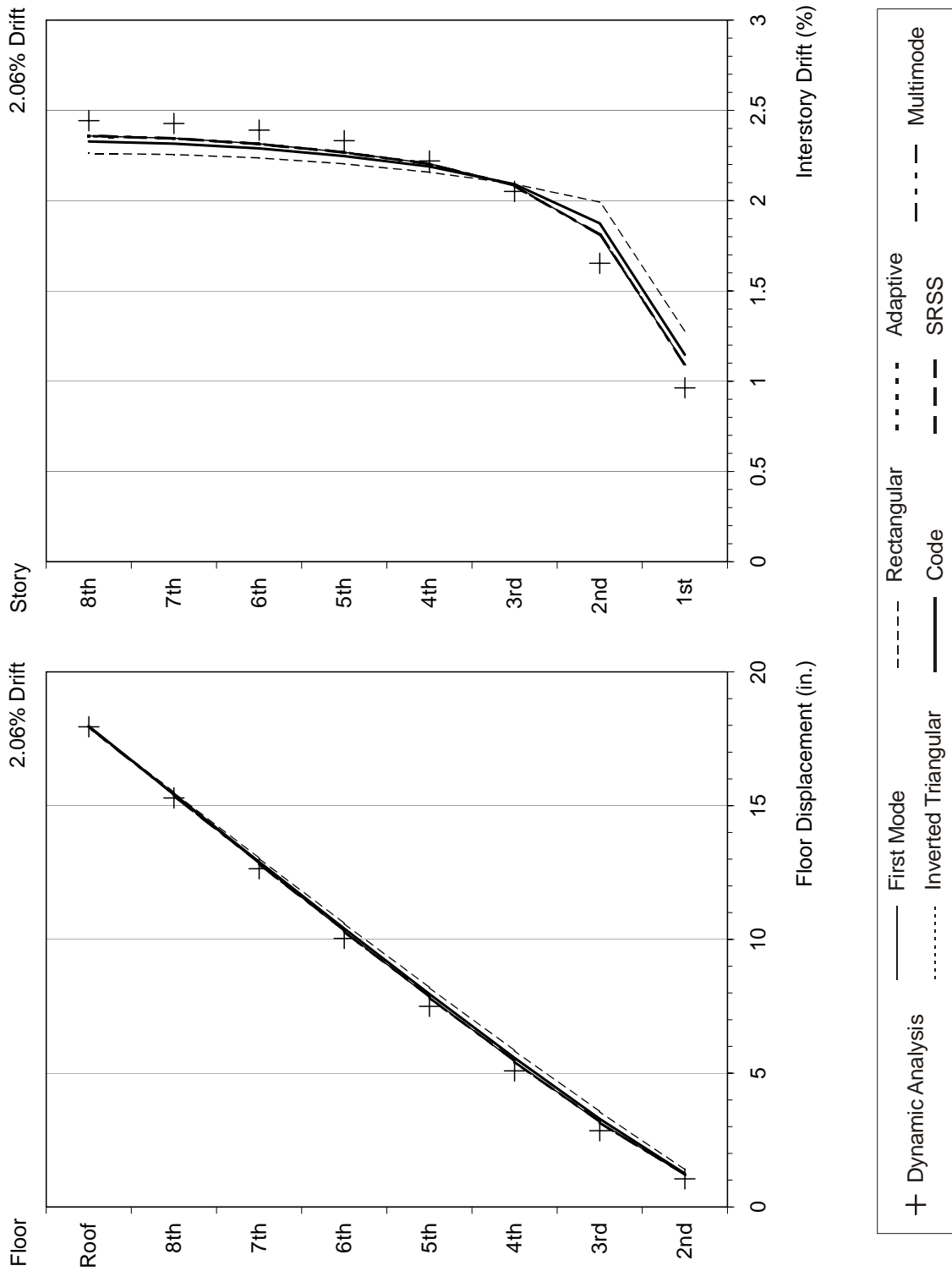
Figure F-61   Response quantities of the 8-story building under RRSMV1 ground motion
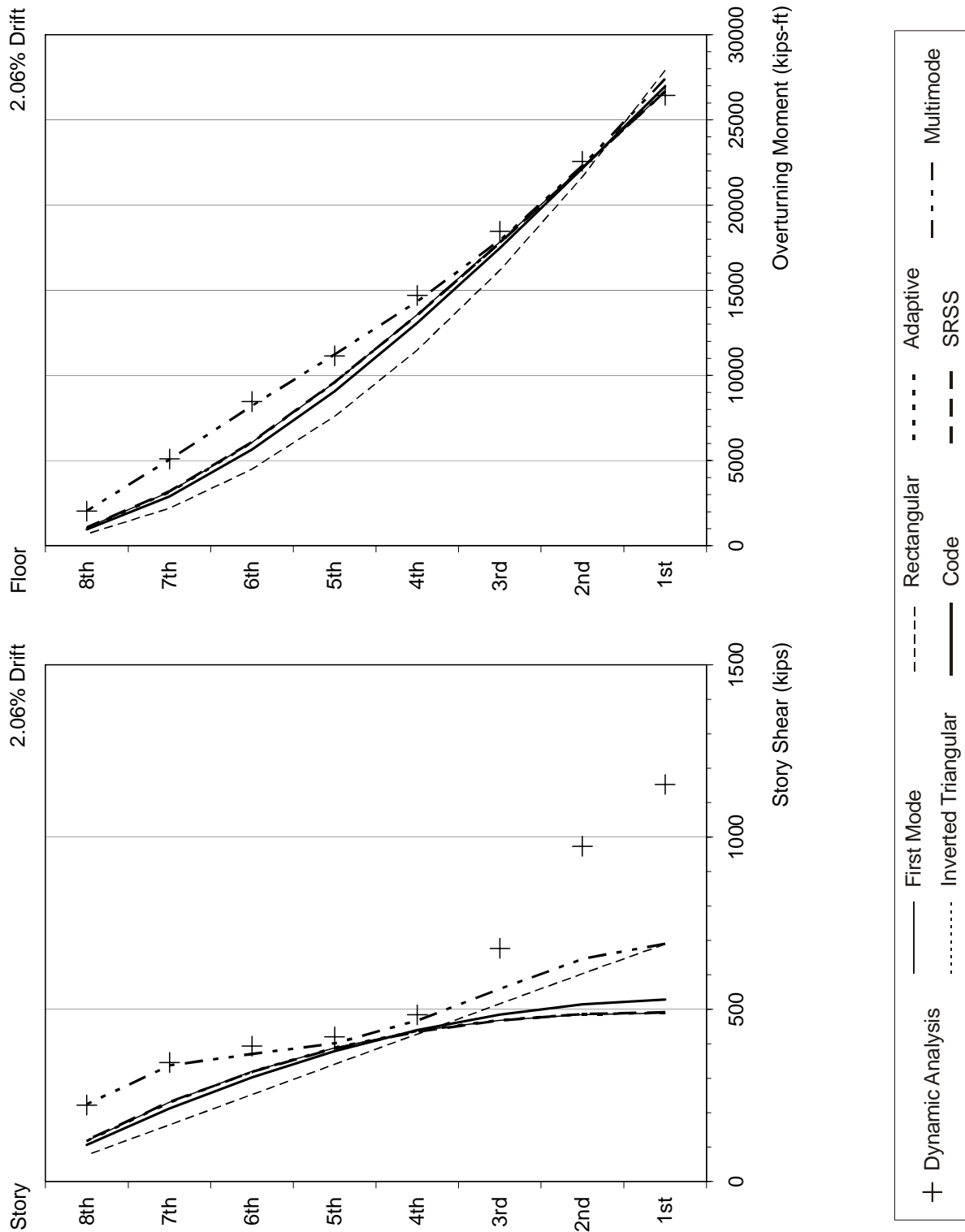
Figure F-61   Response quantities of the 8-story building under RRSMV1 ground motion (continued)
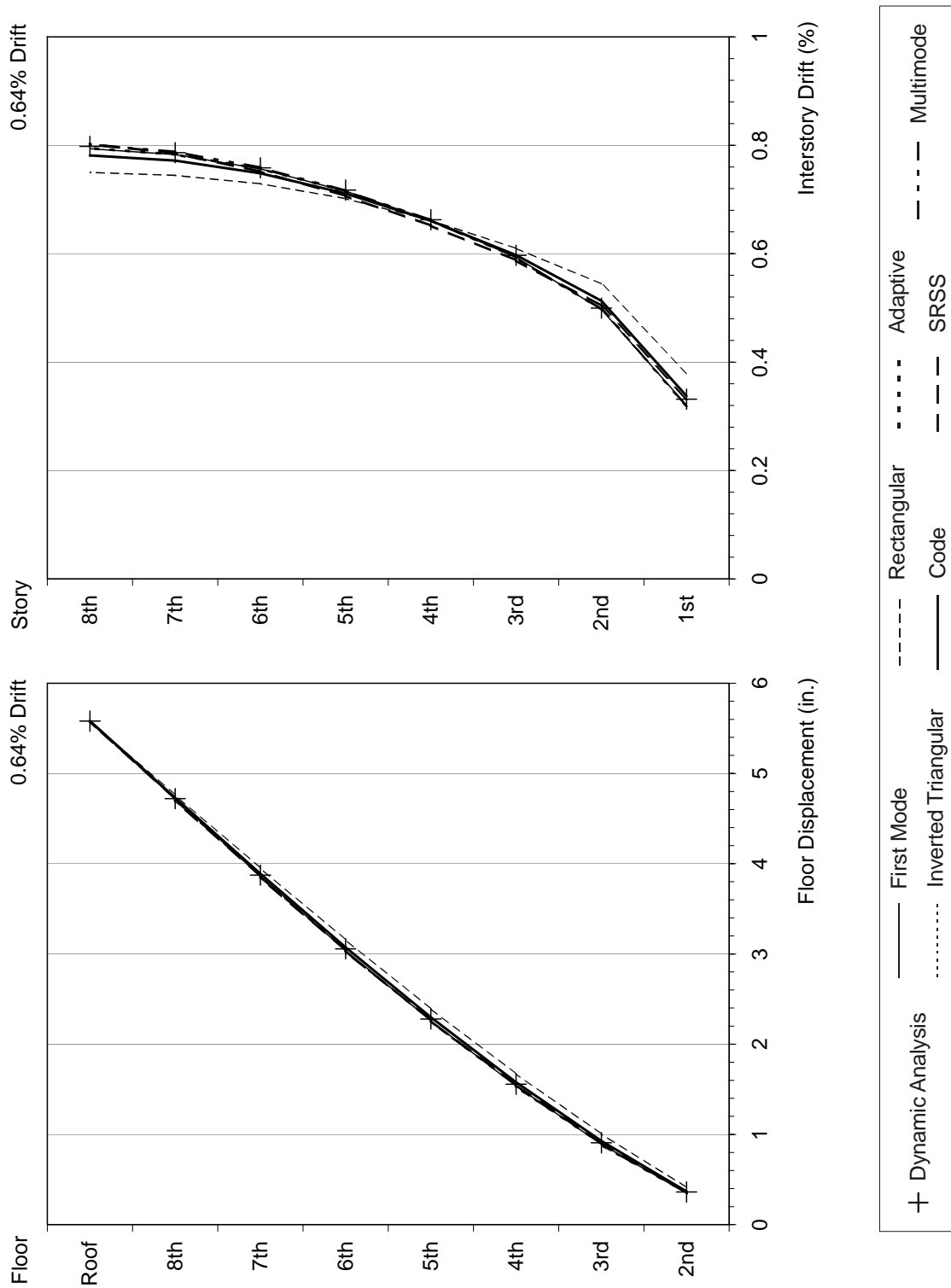
Figure F-62   Response quantities of the 8-story building under LUCMV1 ground motion
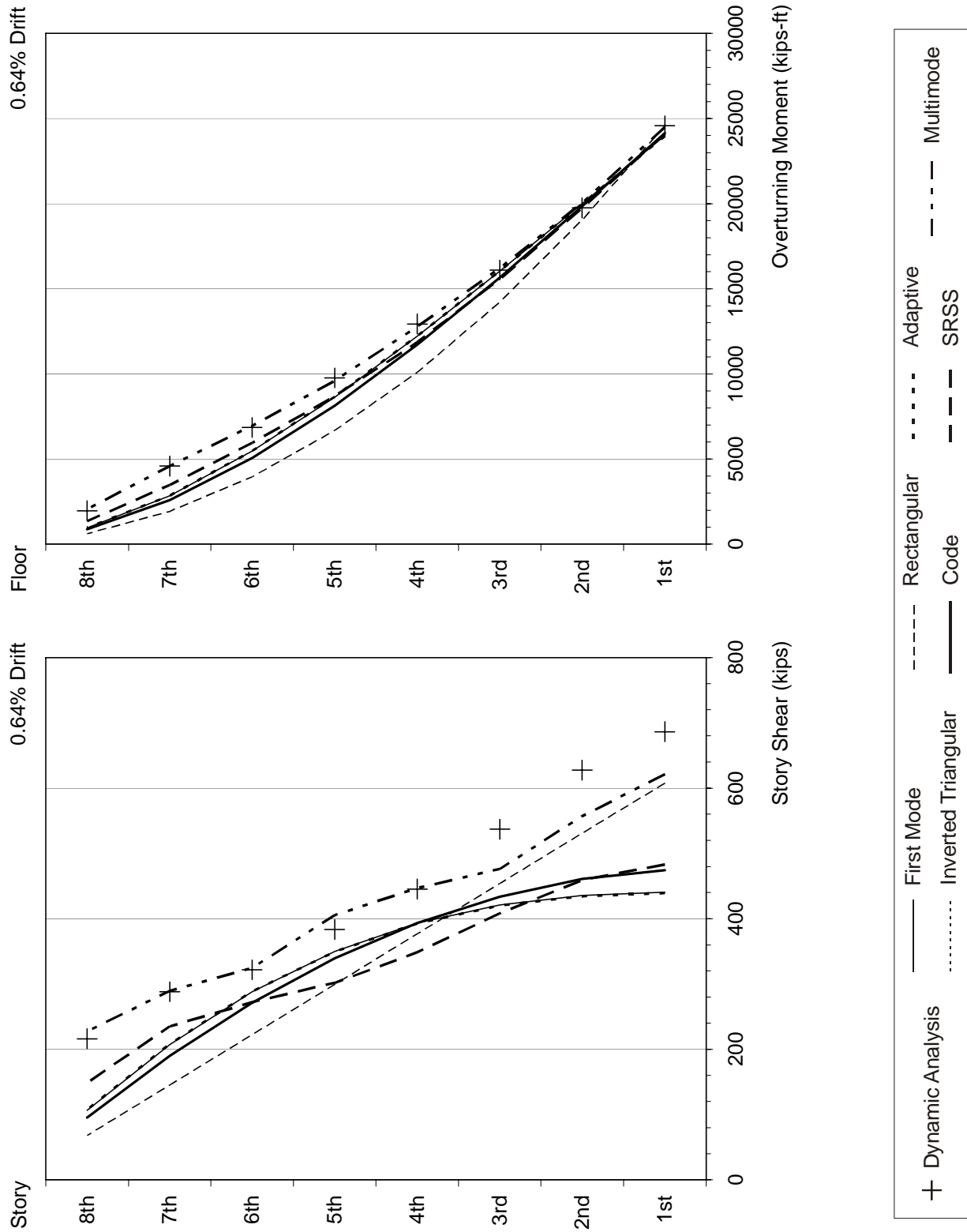
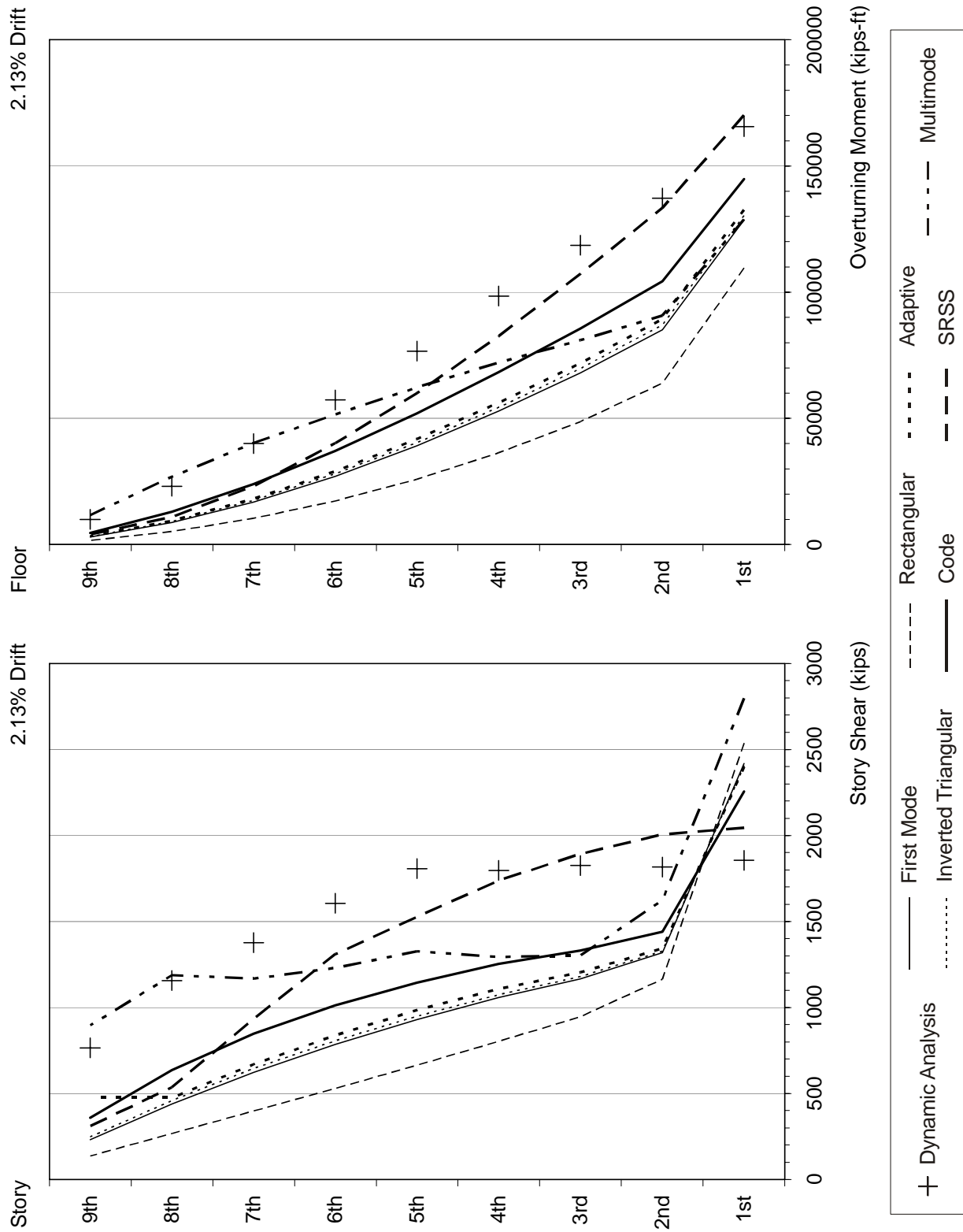Figure F-62   Response quantities of the 8-story building under LUCMV1 ground motion (continued)
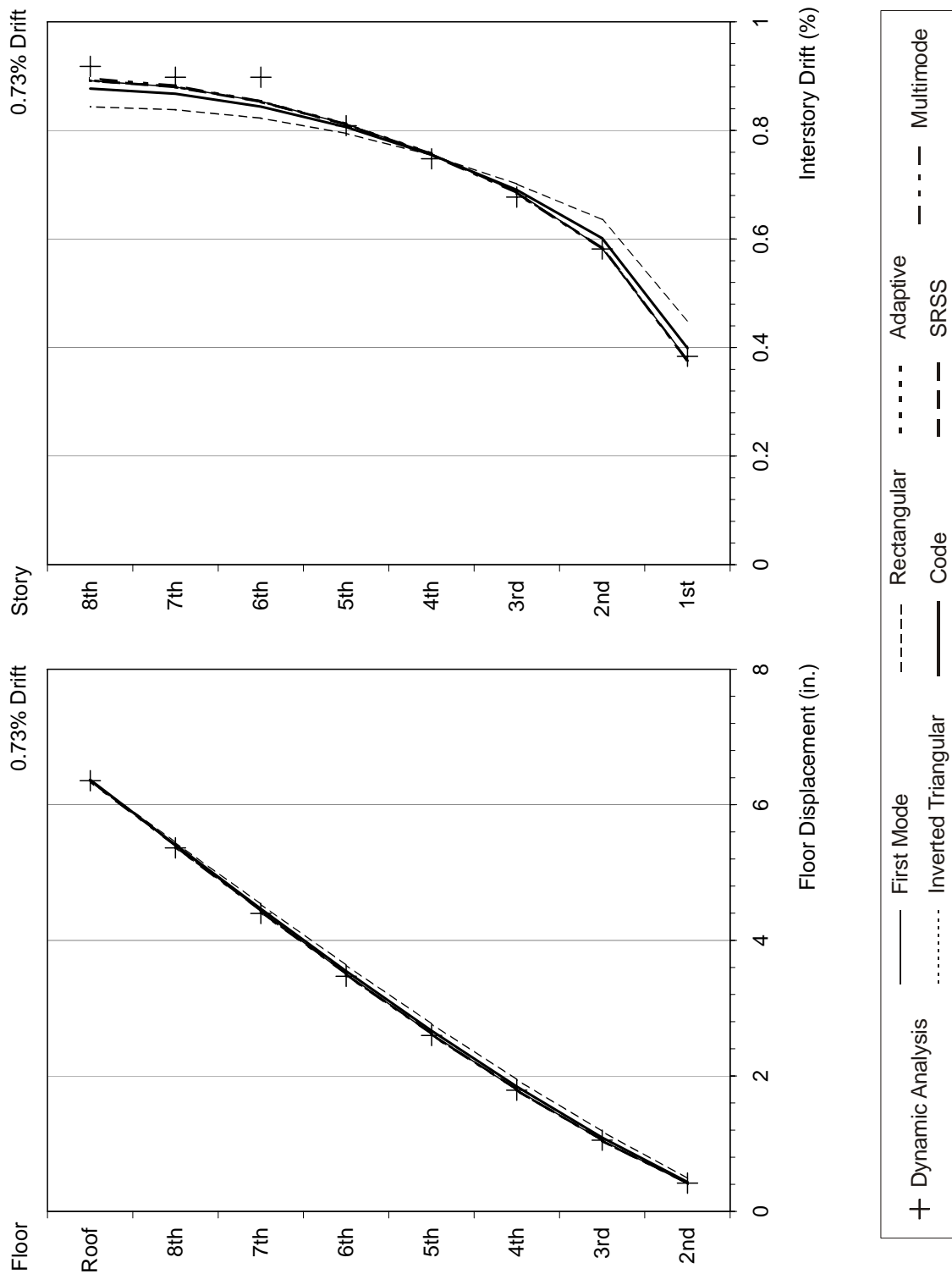
Figure F-63   Response quantities of the 8-story building under SCHMV1 ground motion
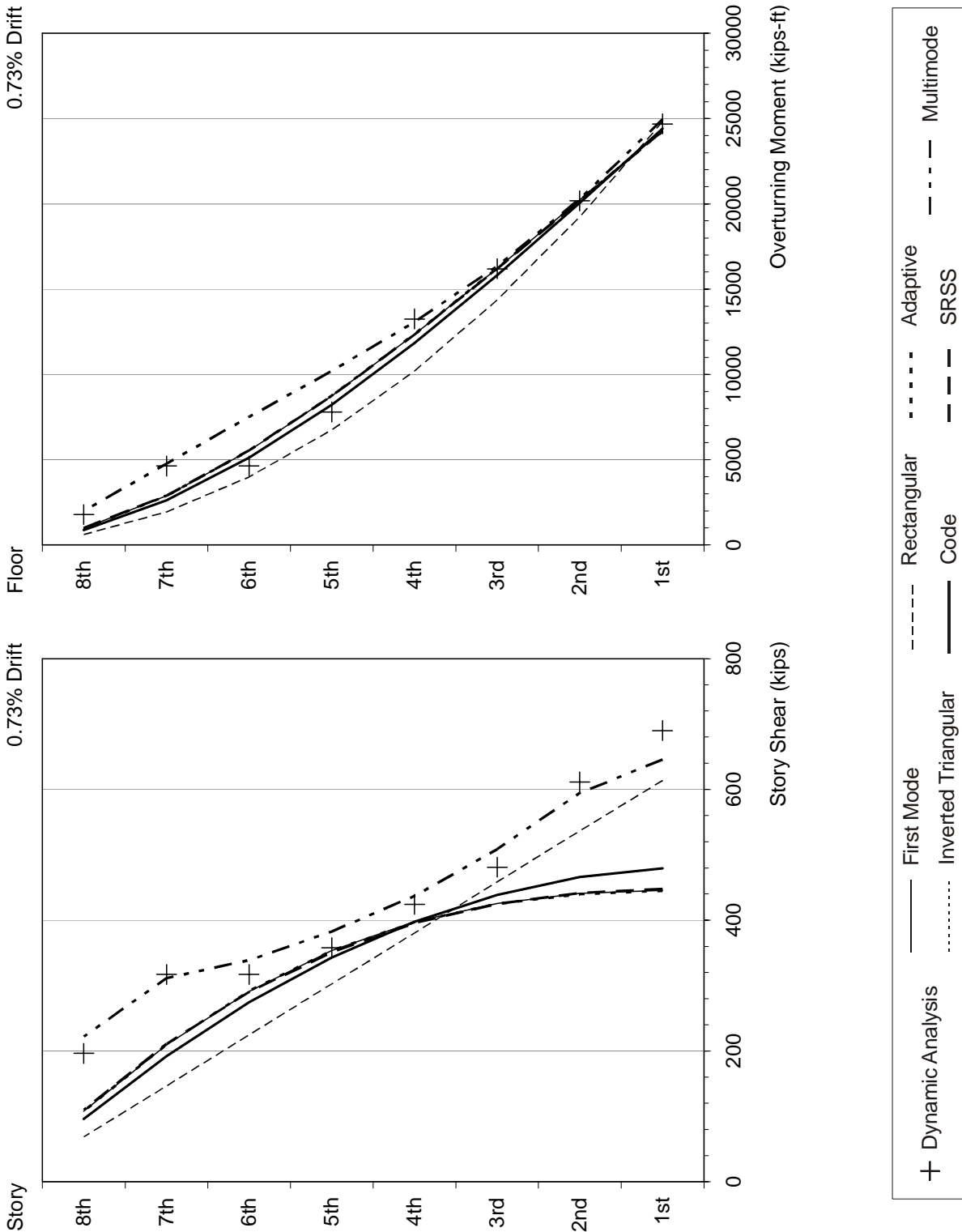
Figure F-63   Response quantities of the 8-story building under SCHMV1 ground motion (continued)
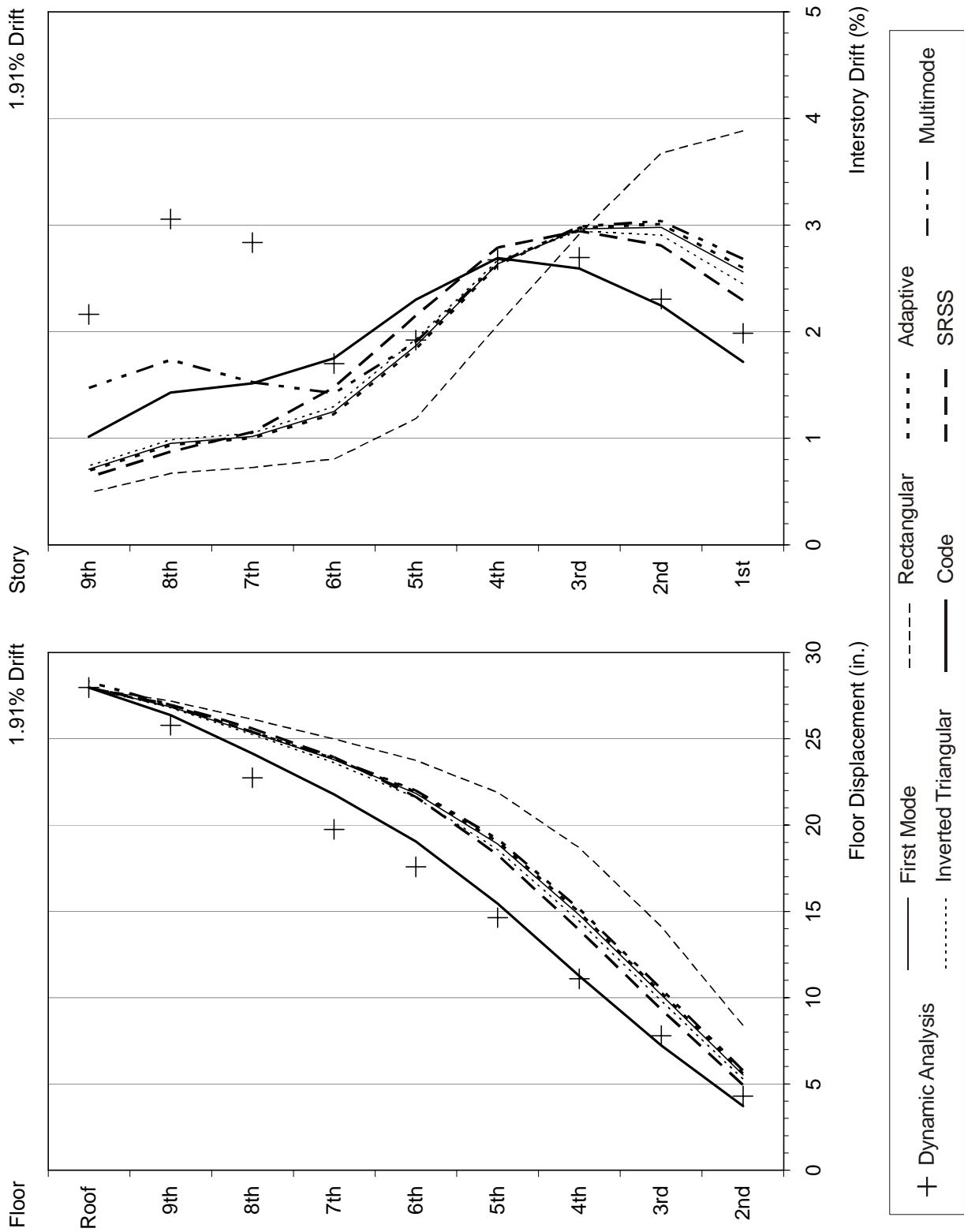
Figure F-64   Response quantities of the 9-story building under ERZMV1 ground motion
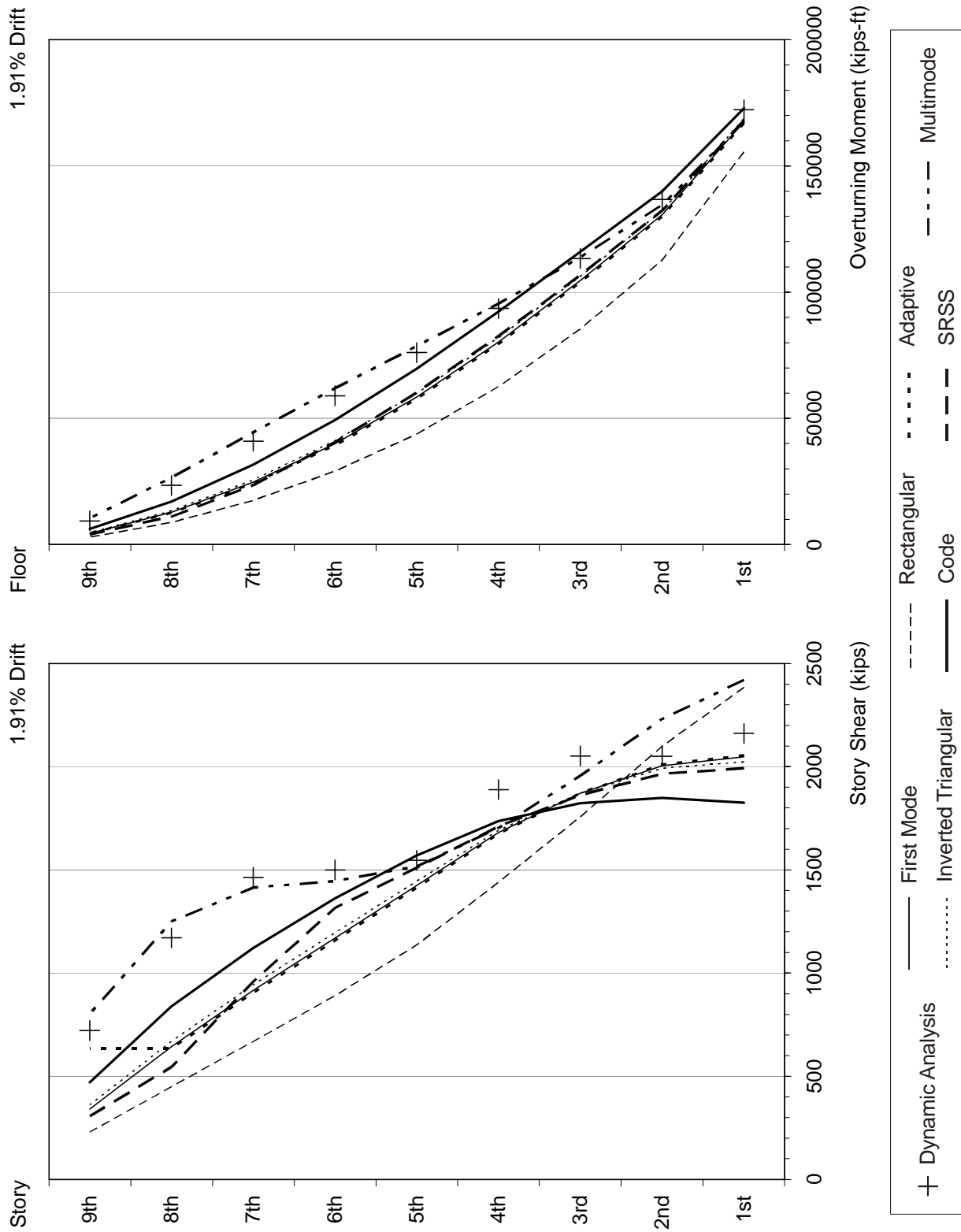
Figure F-64   Response quantities of the 9-story building under ERZMV1 ground motion (continued)
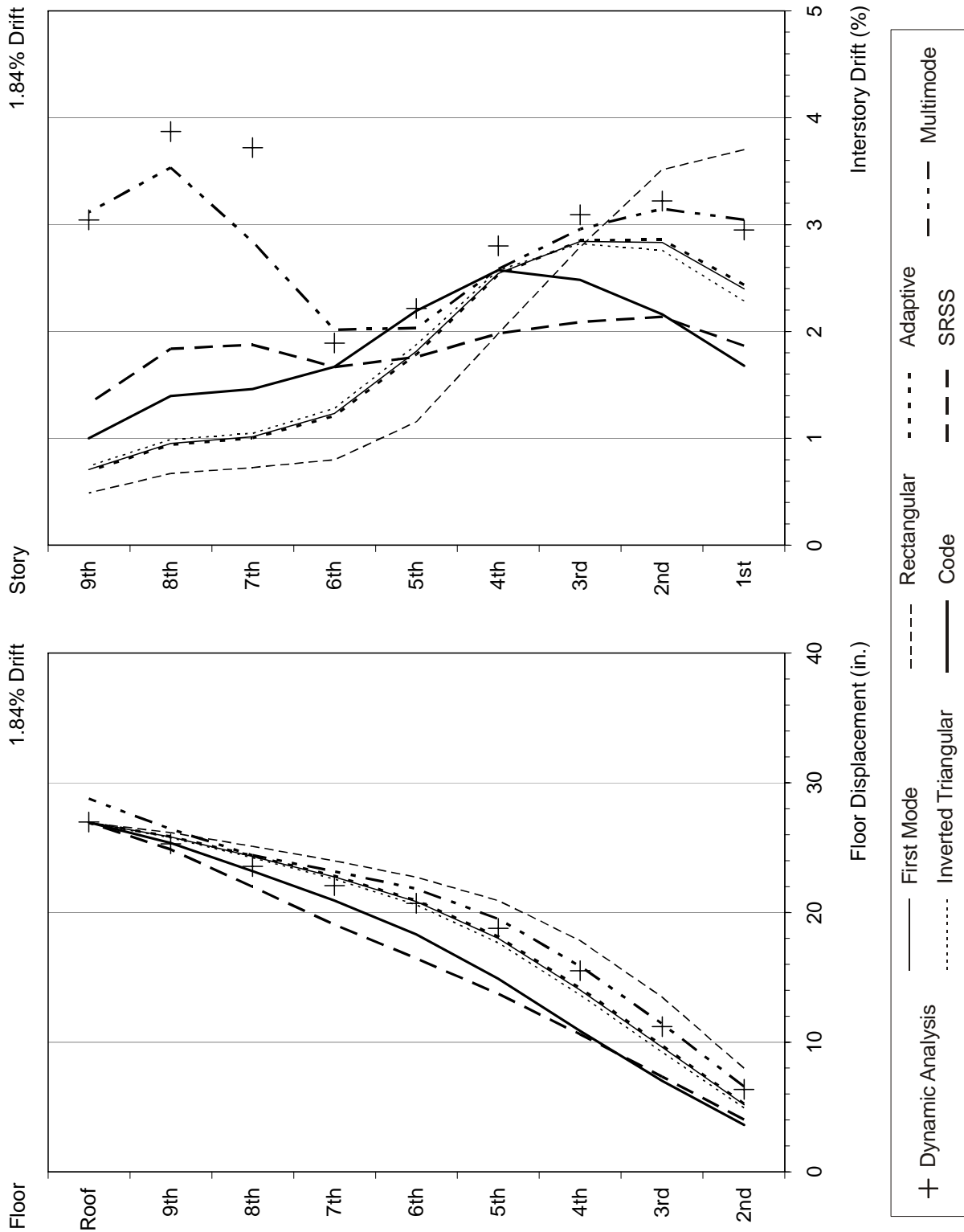
Figure F-65   Response quantities of the 9-story building under RRSMV1 ground motion

Figure F-65   Response quantities of the 9-story building under RRSMV1 ground motion (continued)
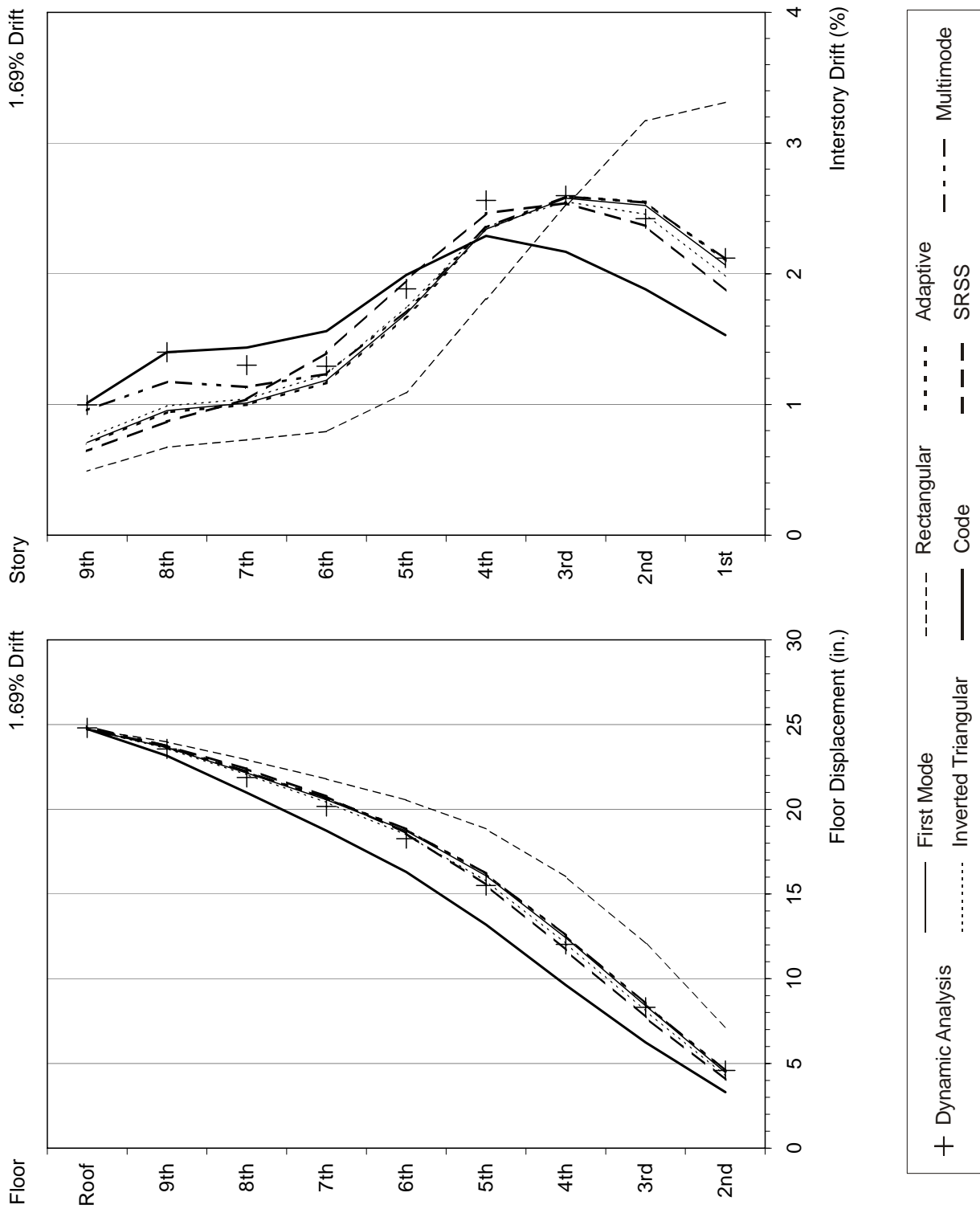
Figure F-66   Response quantities of the 9-story building under LUCMV1 ground motion

Figure F-66   Response quantities of the 9-story building under LUCMV1 ground motion (continued)
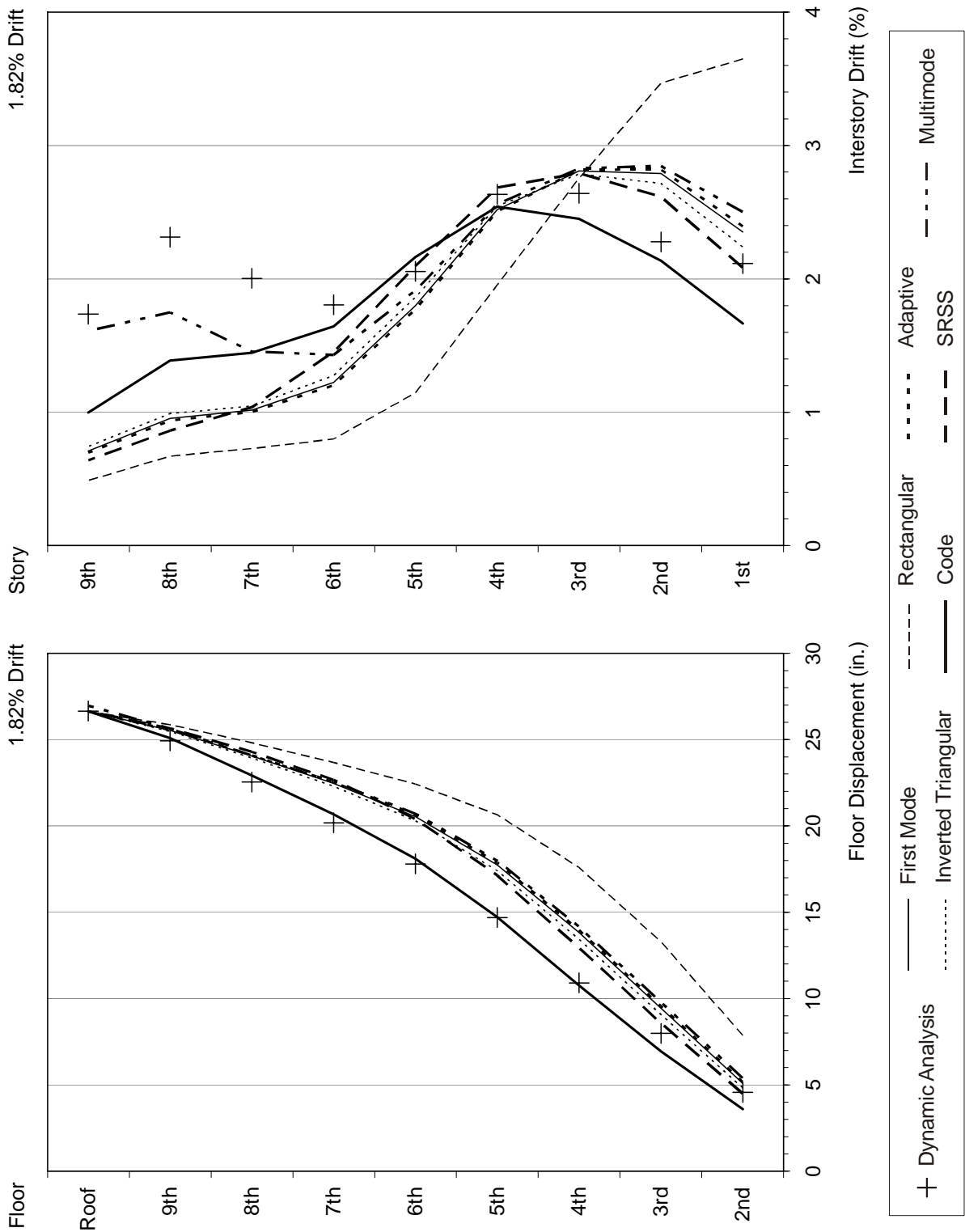
Figure F-67   Response quantities of the 9-story building under SCHMV1 ground motion
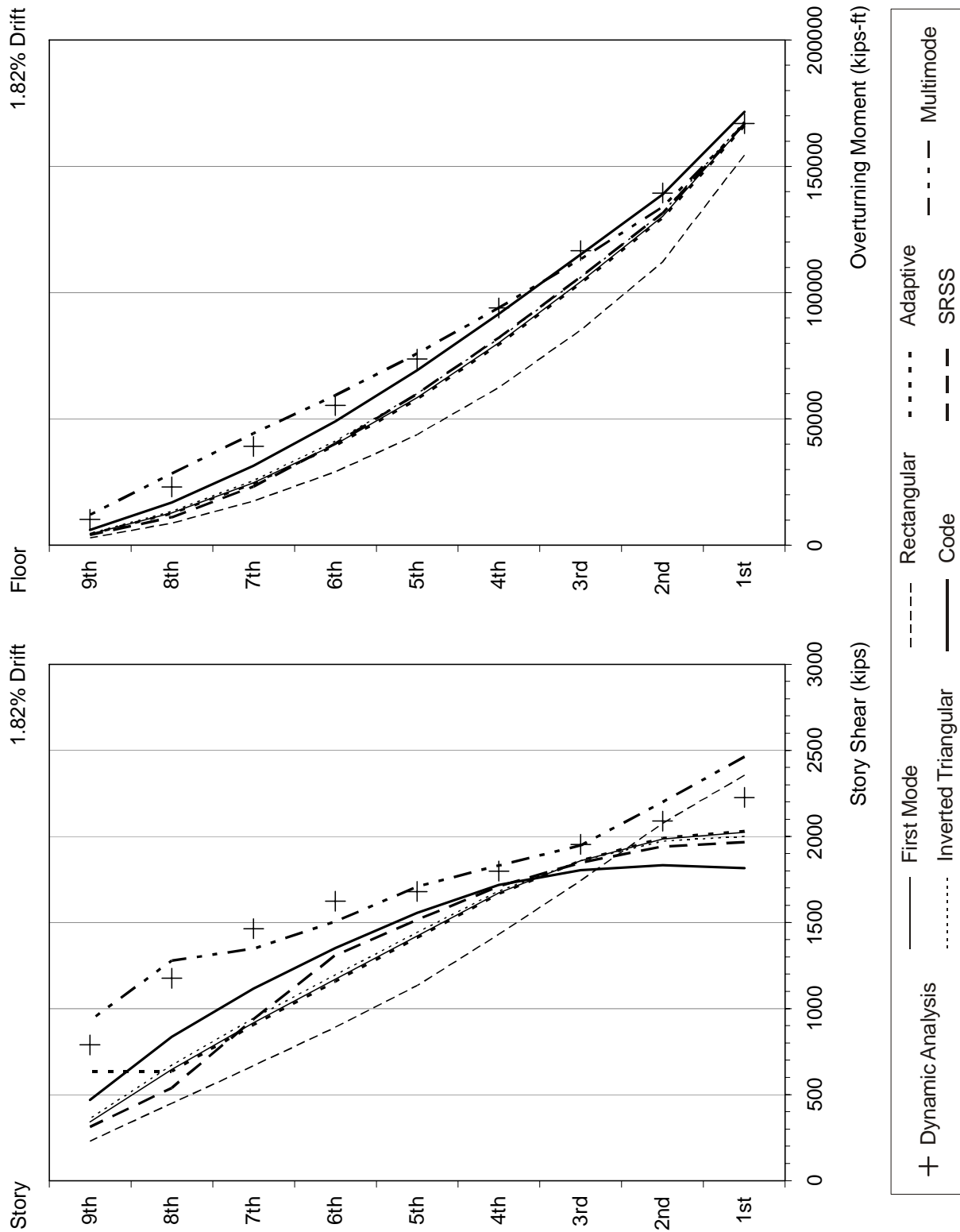
Figure F-67   Response quantities of the 9-story building under SCHMV1 ground motion (continued)

Figure F-68   Response quantities of the 9-story weak-story building under ERZMV1 ground motion
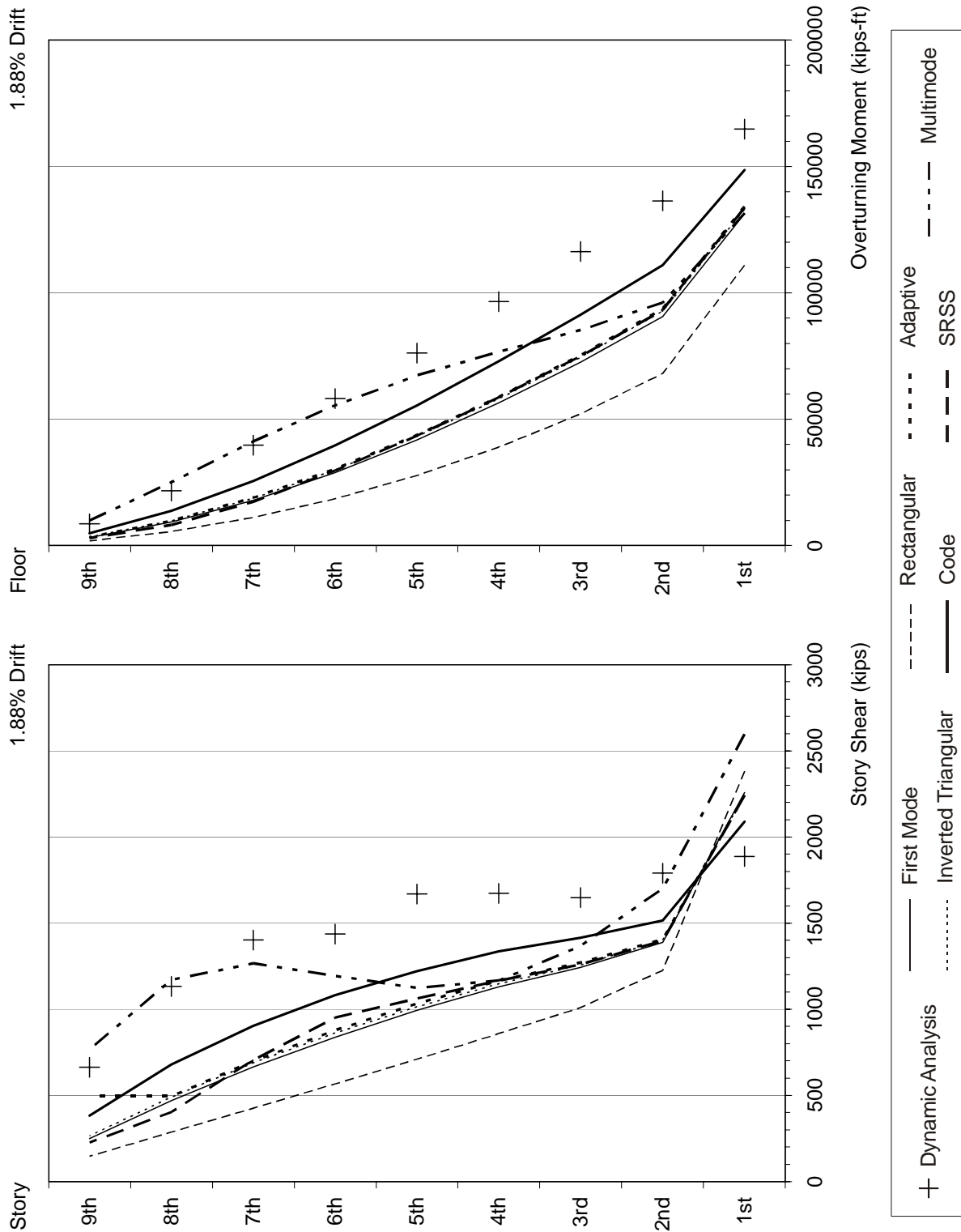
Figure F-68   Response quantities of the 9-story weak-story building under ERZMV1 ground motion (continued)

Figure F-69   Response quantities of the 9-story weak-story building under RRSMV1 ground motion

Figure F-69   Response quantities of the 9-story weak-story building under RRSMV1 ground motion (Continued)

Figure F-70   Response quantities of the 9-story weak-story building under LUCMV1 ground motion

Figure F-70   Response quantities of the 9-story weak-story building under LUCMV1 ground motion (continued)

Figure F-71   Response quantities of the 9-story weak-story building under SCHMV1 ground motion

Figure F-71   Response quantities of the 9-story weak-story building under SCHMV1 ground motion (continued)

F.8.5   Errors Associated with Near Fault Motions
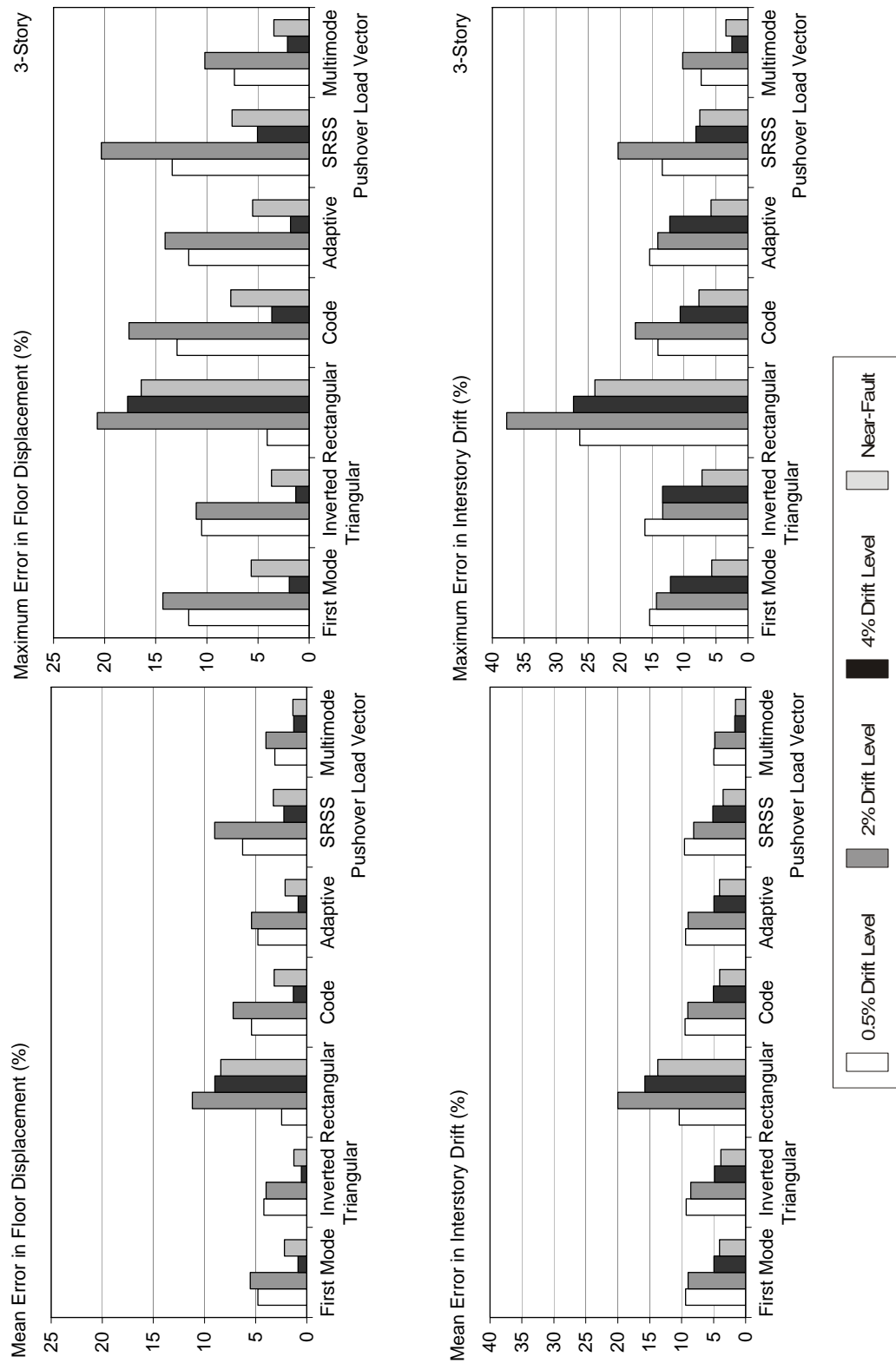
Figure F-72   Mean and maximum errors for the 3-story building
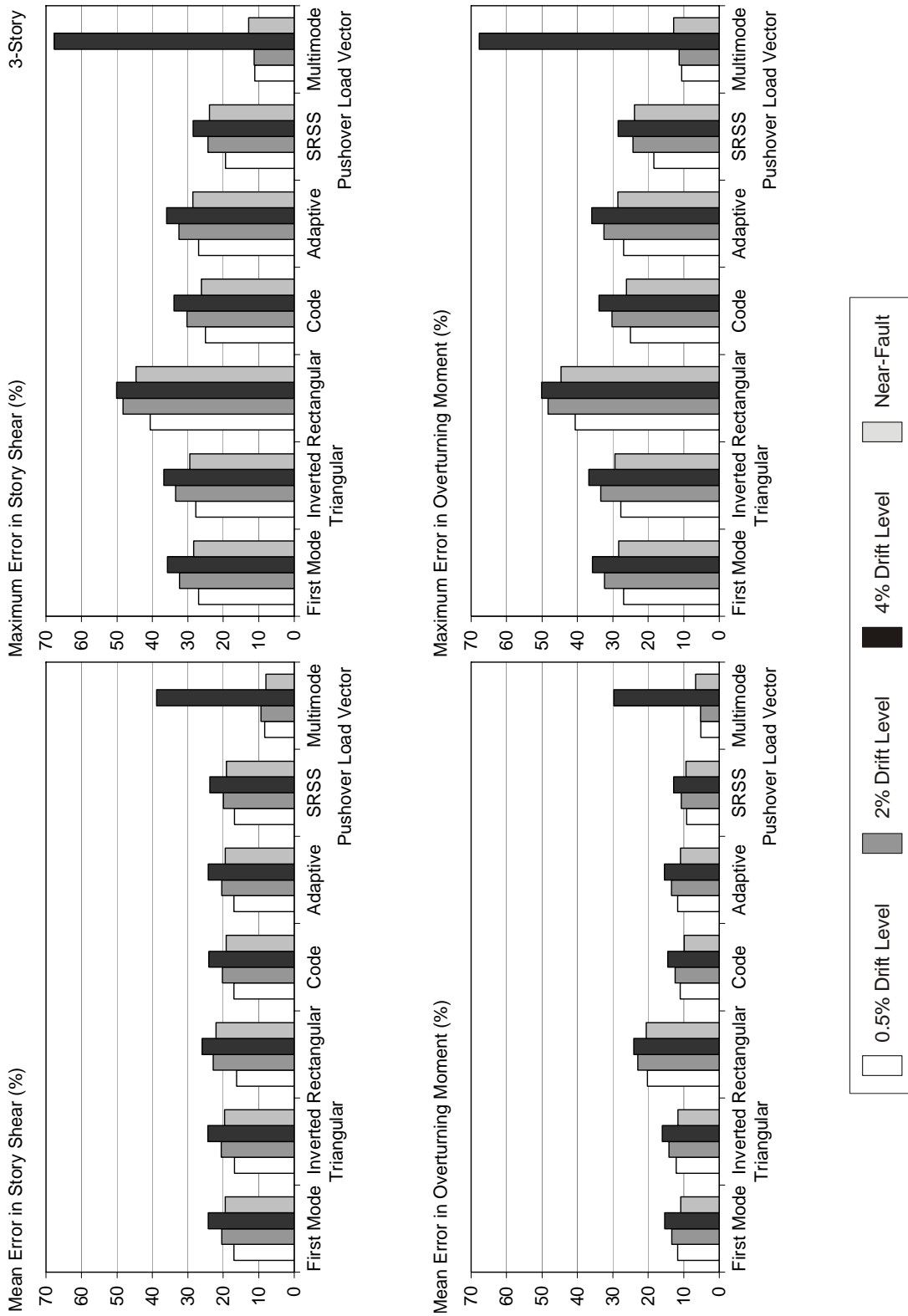
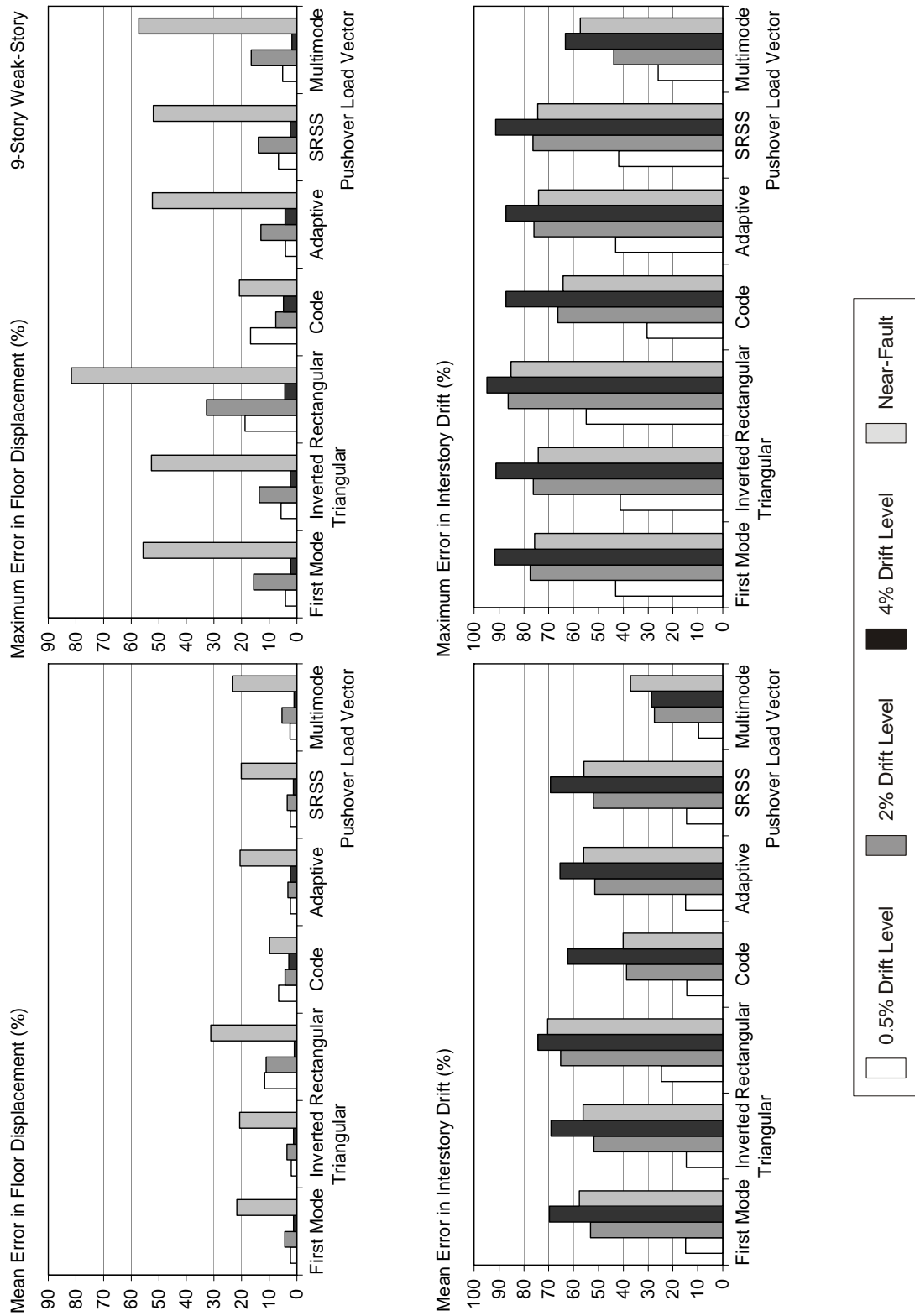Figure F-72   Mean and maximum errors for the 3-story building (continued)
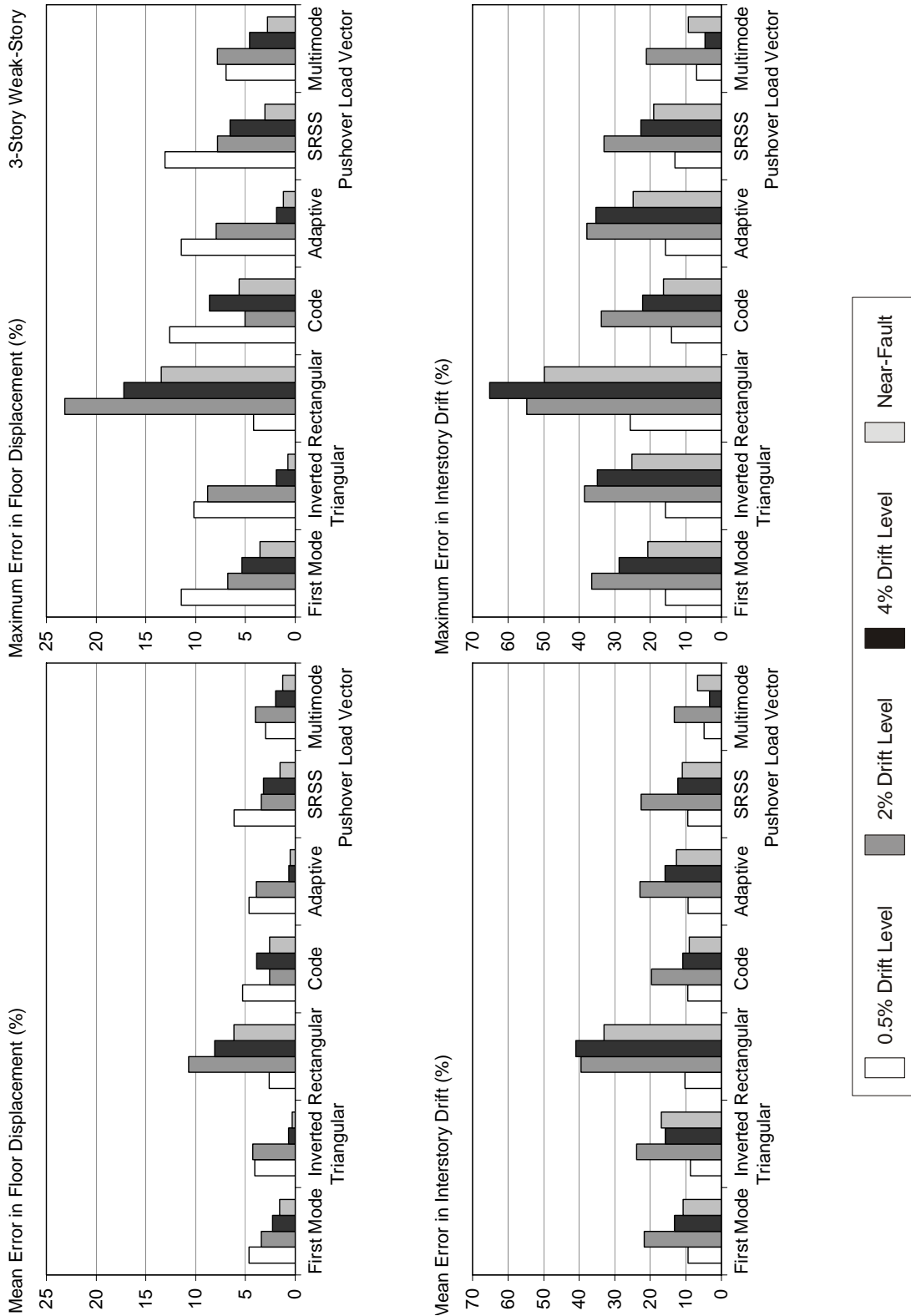
Figure F-73   Mean and maximum errors for the 3-story weak-story building
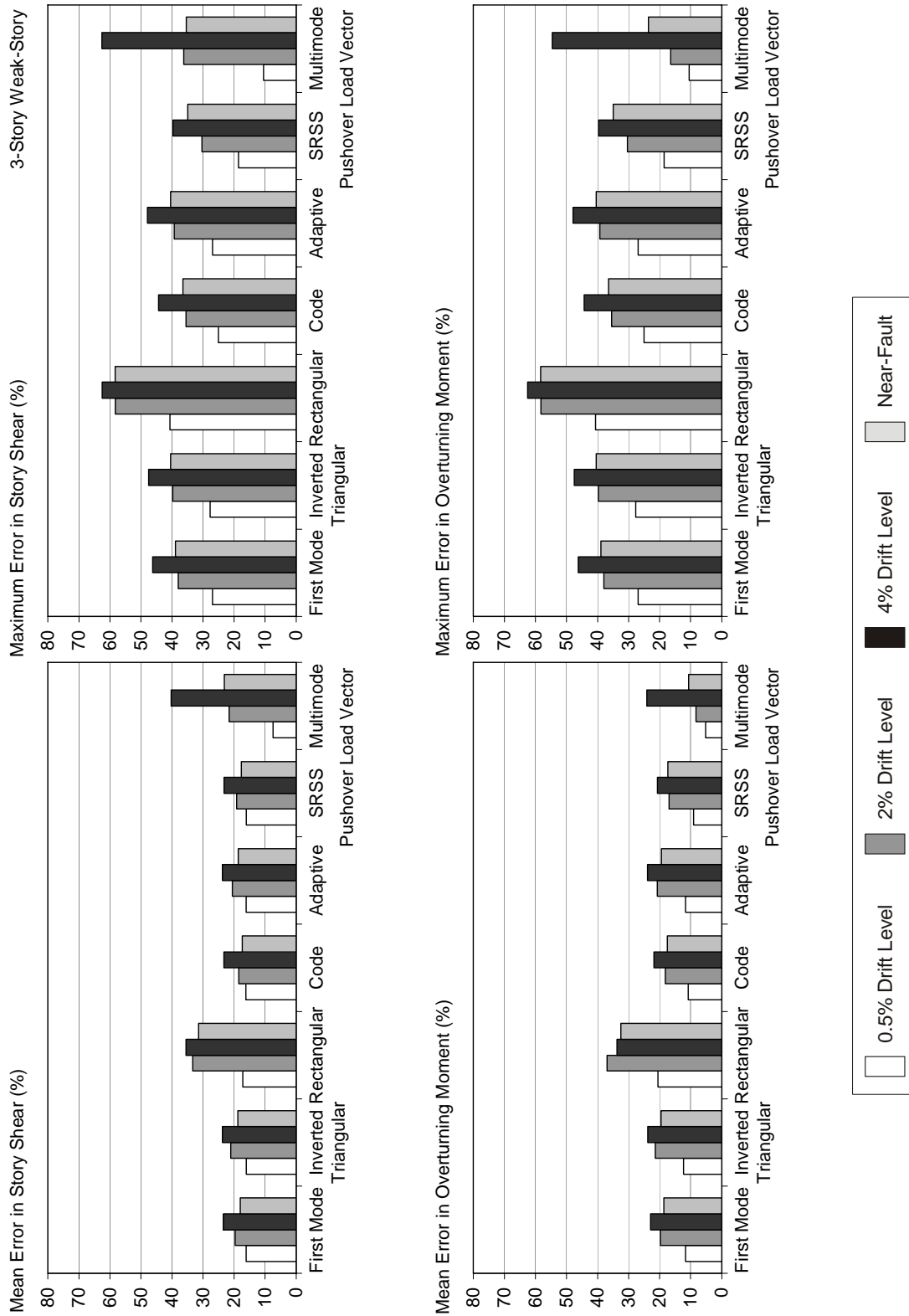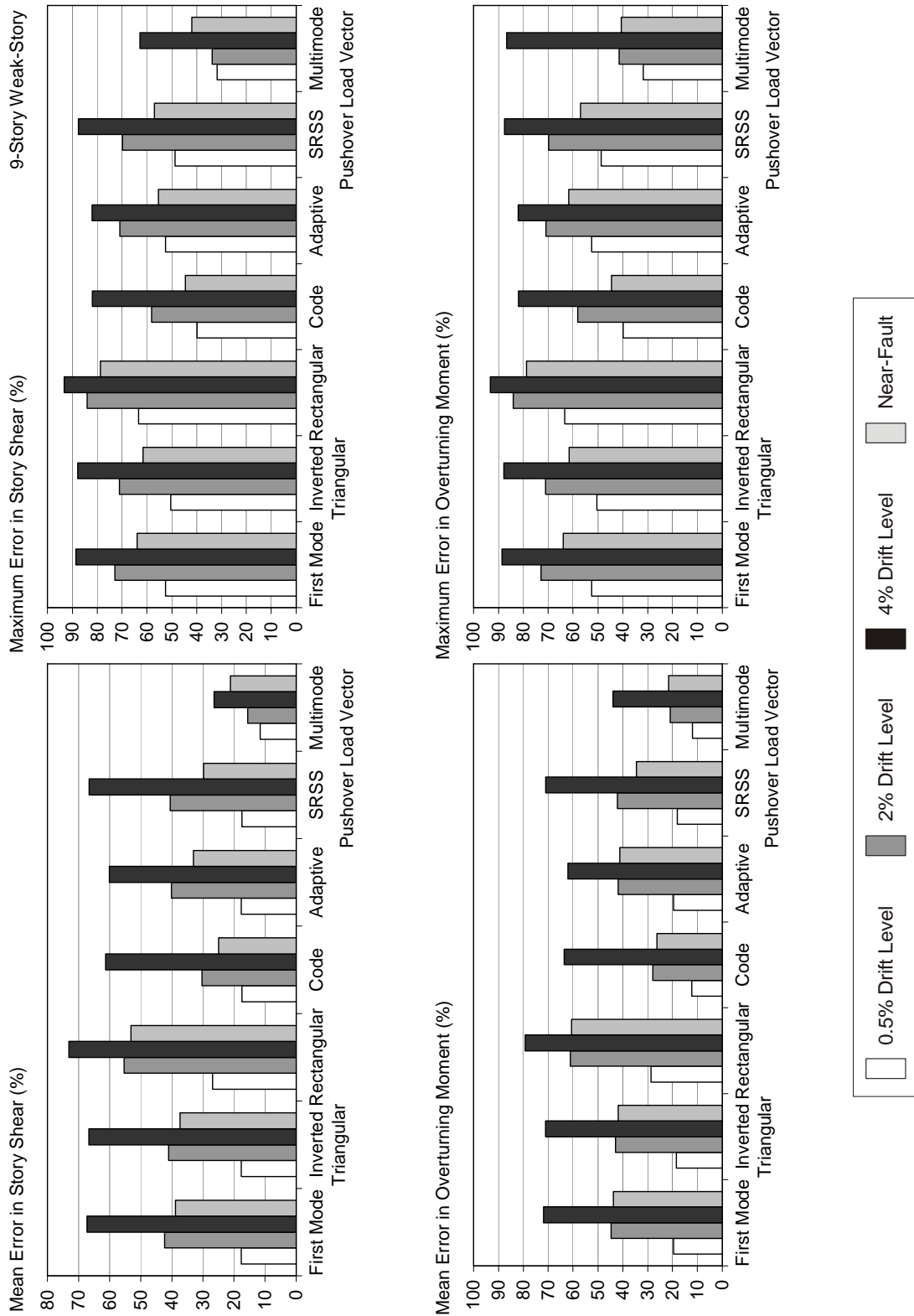
Figure F-73   Mean and maximum errors for the 3-story weak-story building (continued)
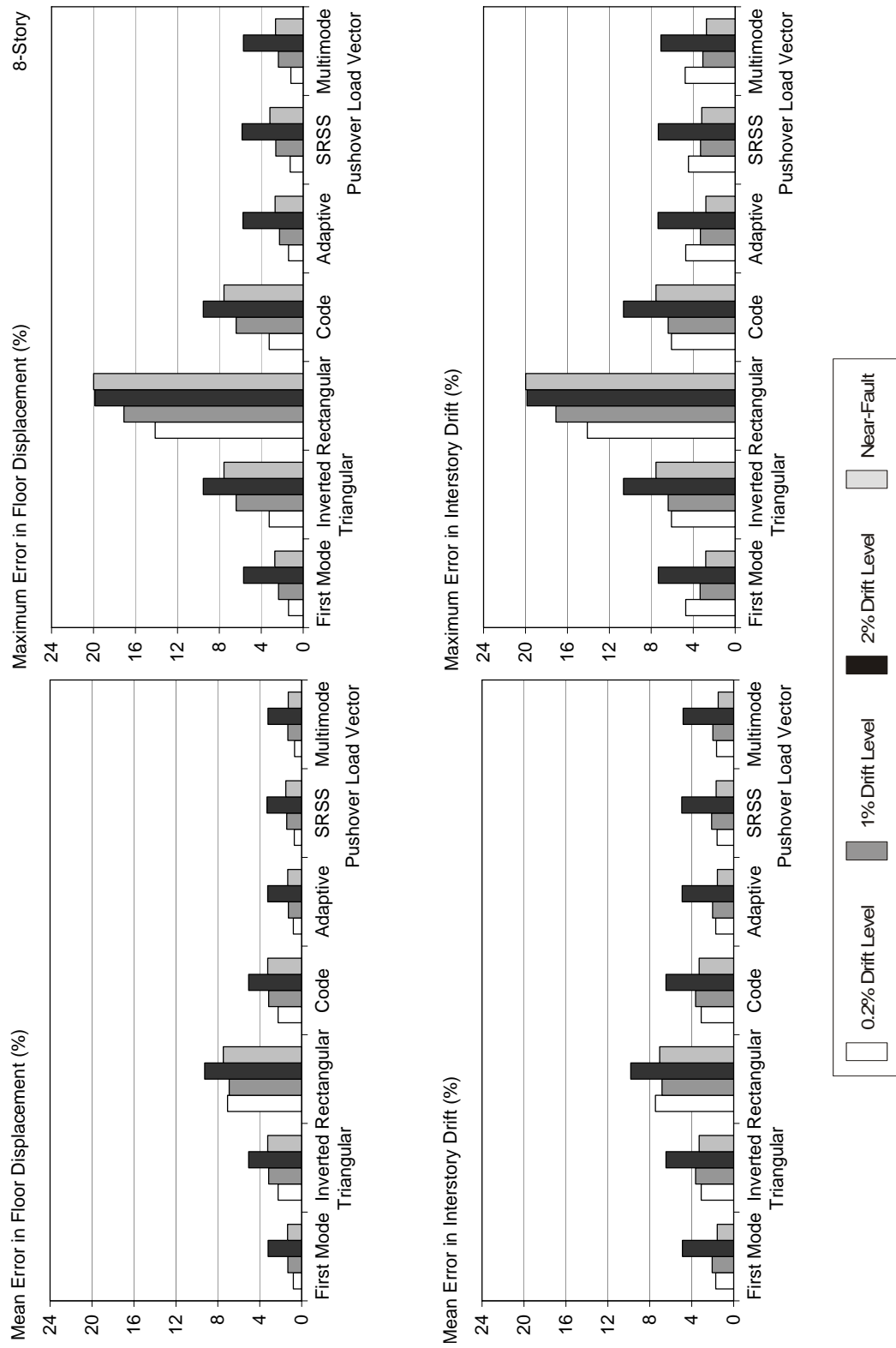
Figure F-74   Mean and maximum errors for the 8-story building
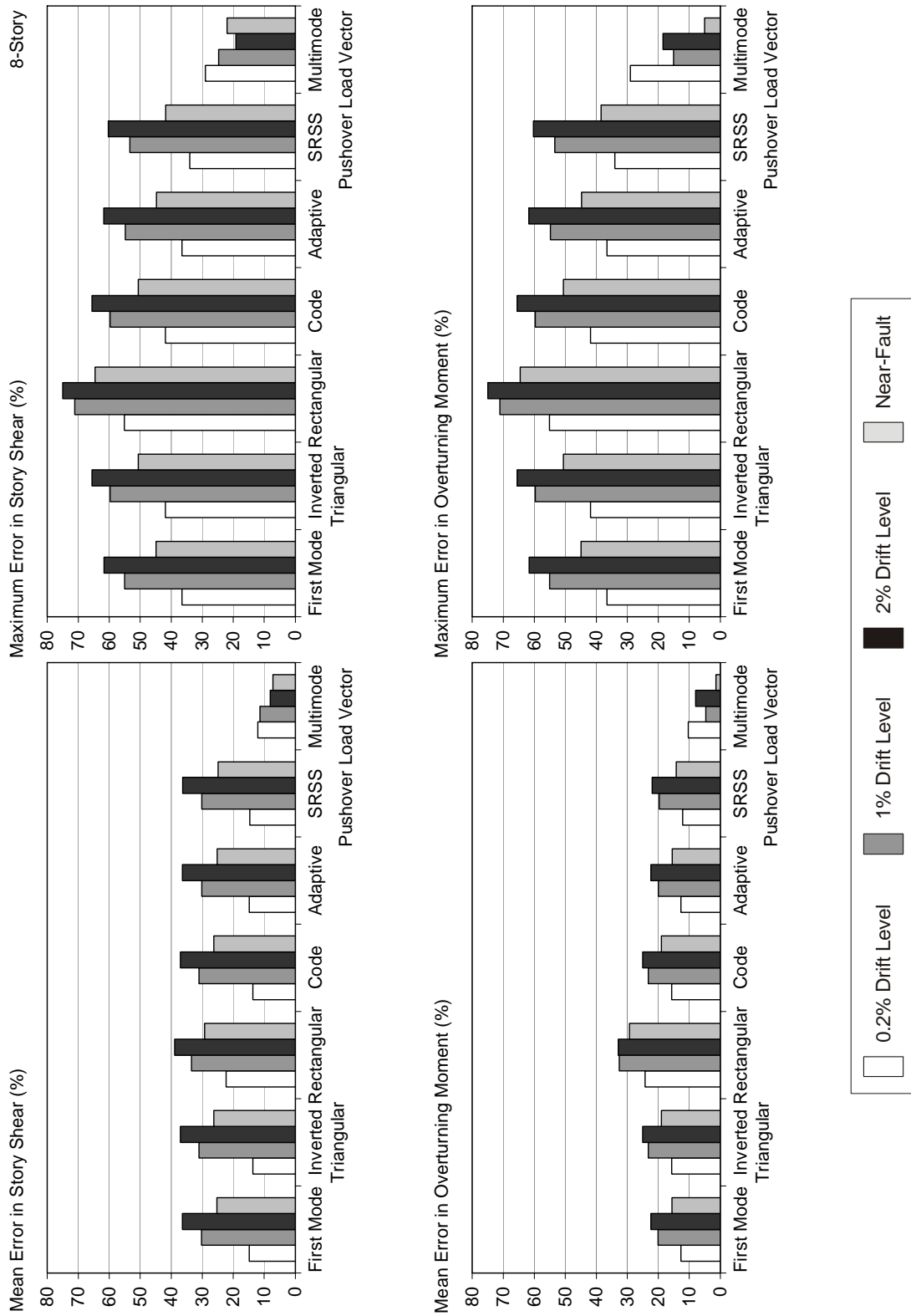
Figure F-74   Mean and maximum errors for the 8-story building (continued)
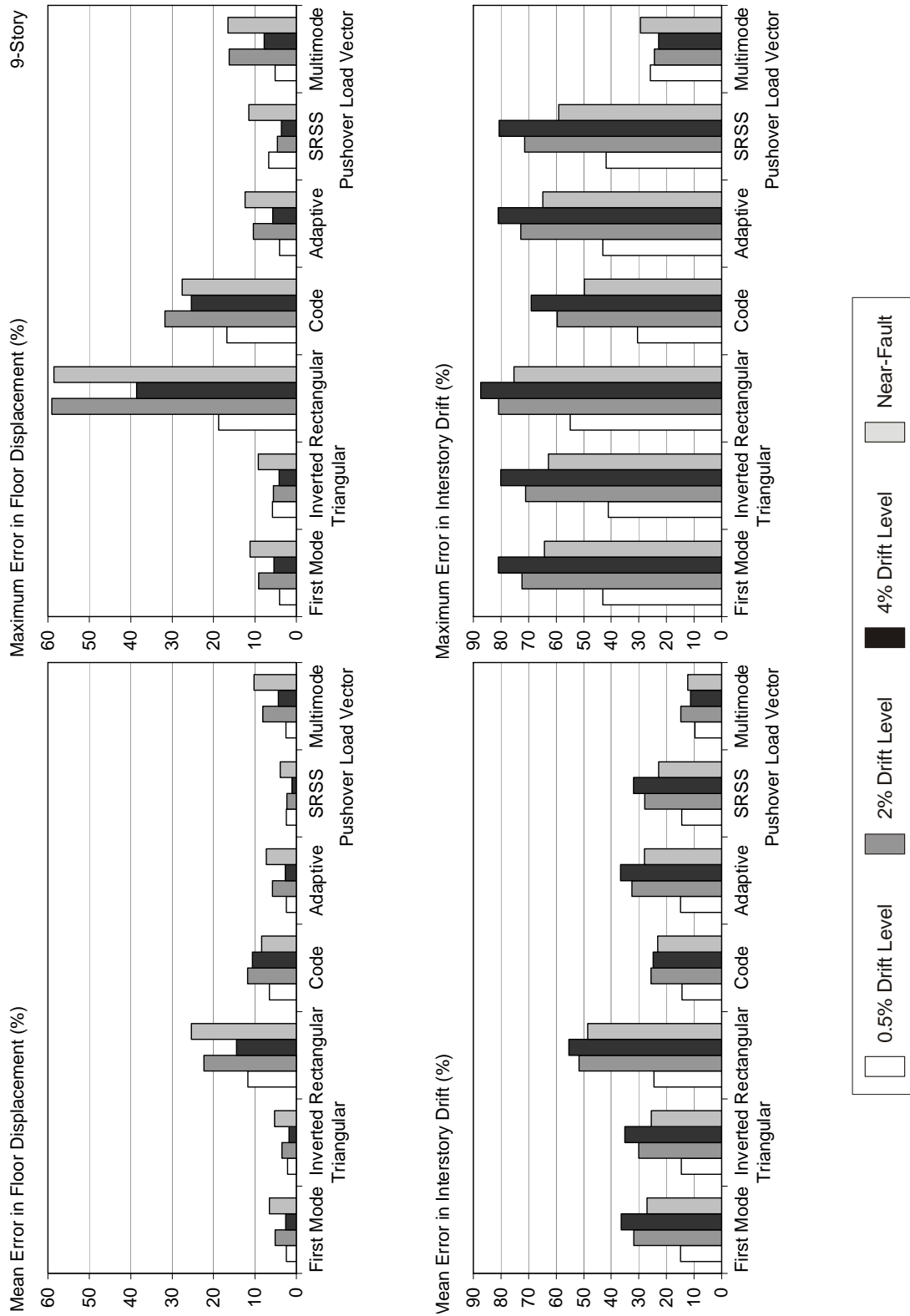
Figure F-75   Mean and maximum errors for the 9-story building
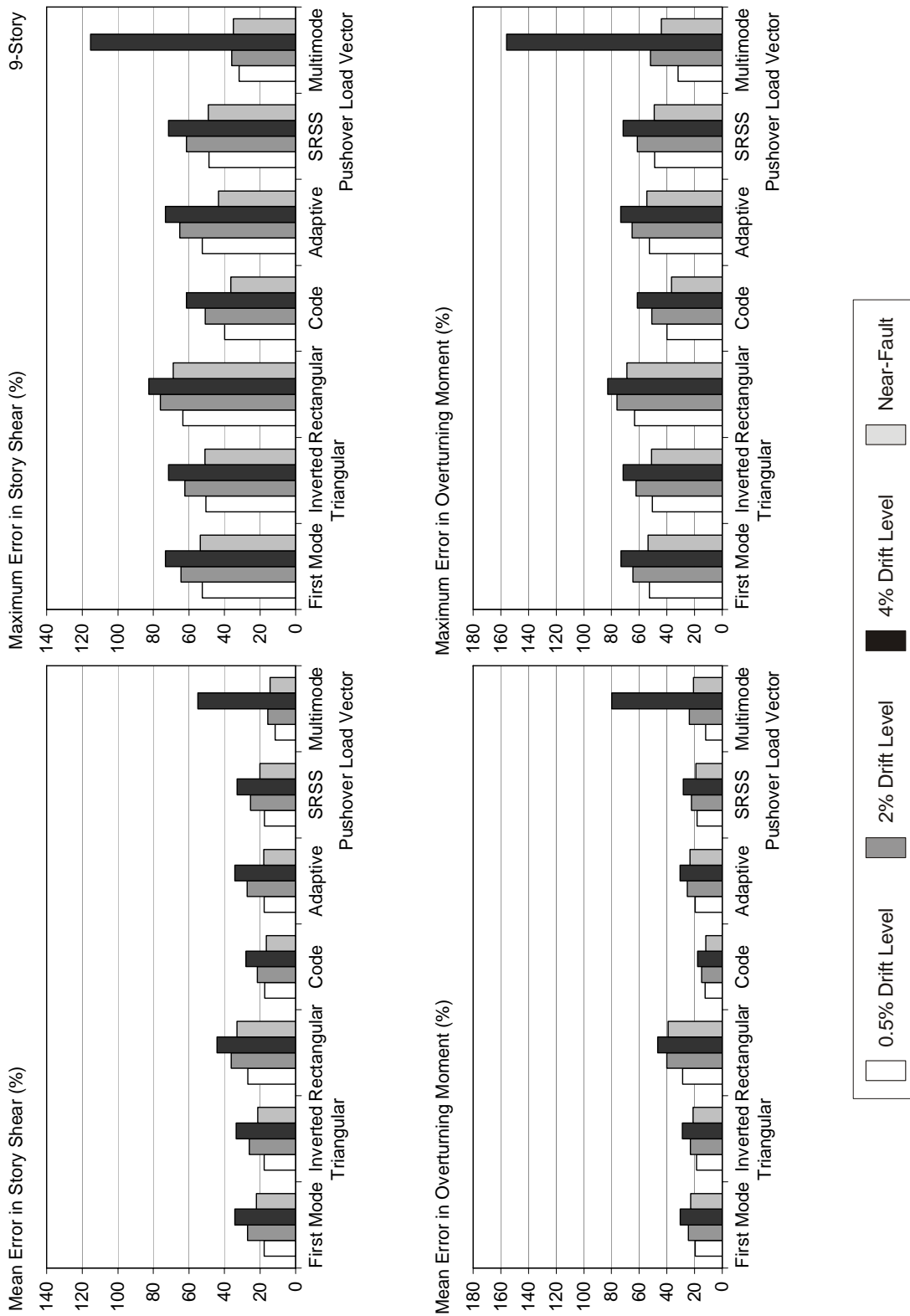
Figure F-75   Mean and maximum errors for the 9-story building (continued)

Figure F-76   Mean and maximum errors for the 9-story weak-story building

Figure F-76   Mean and maximum errors for the 9-story weak-story building (continued)

F.8.6 Observed Coefficients of Variation of the Response Quantities Determined for the Ordinary (Site Class C) Motions
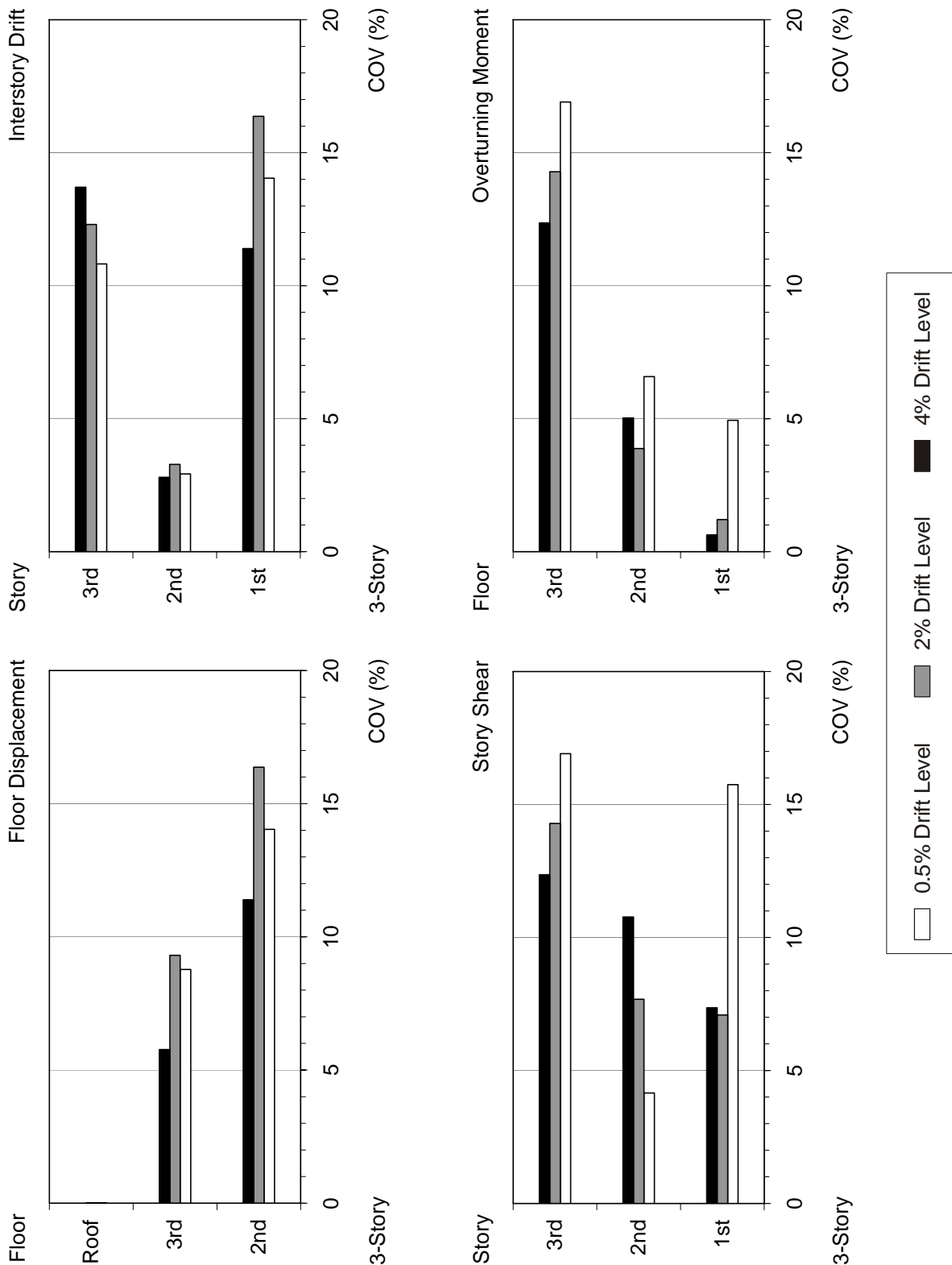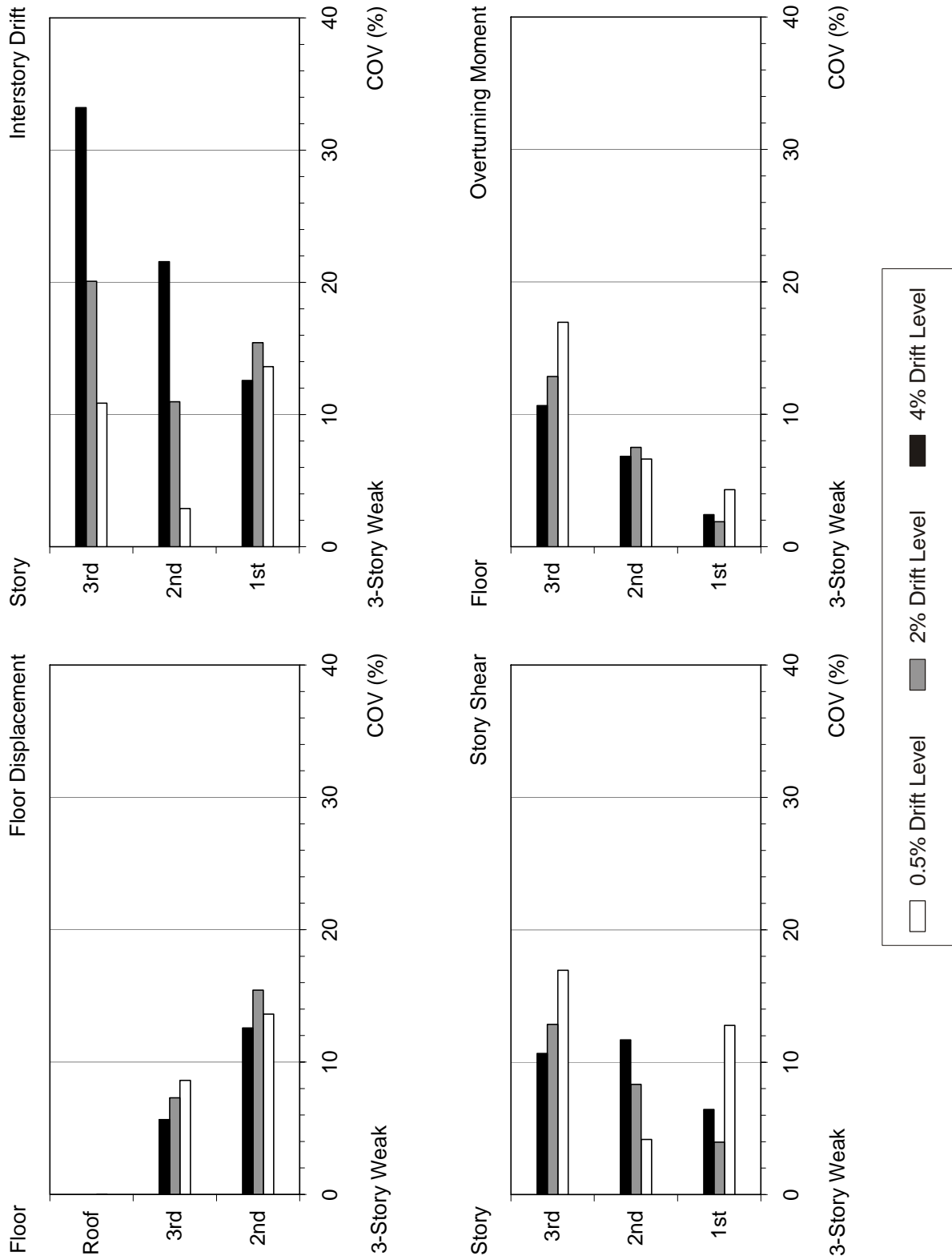

Figure F-77   Observed COVs for the 3-story frame building.

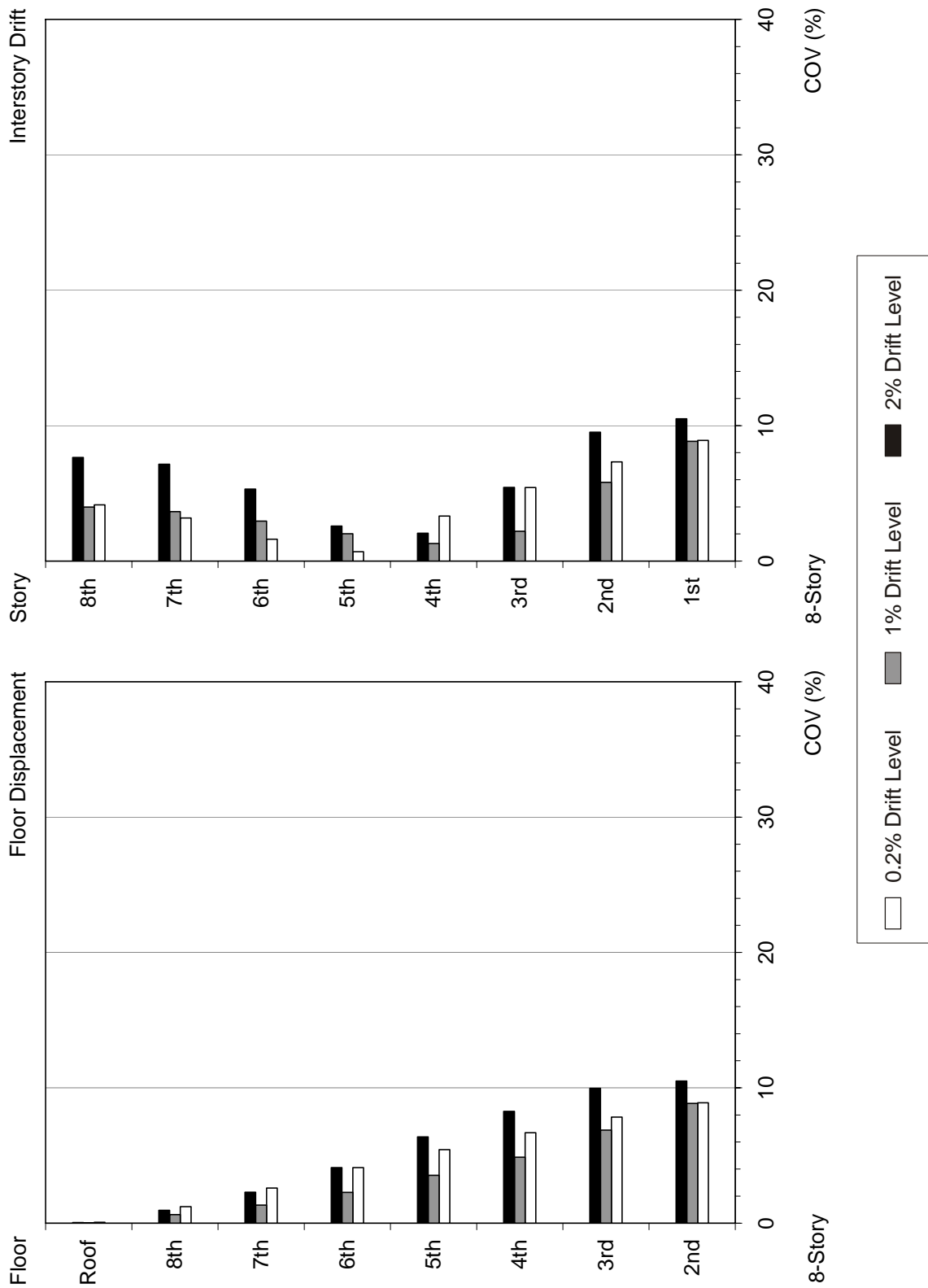Figure F-78   Observed COVs for the 3-story weak story frame building

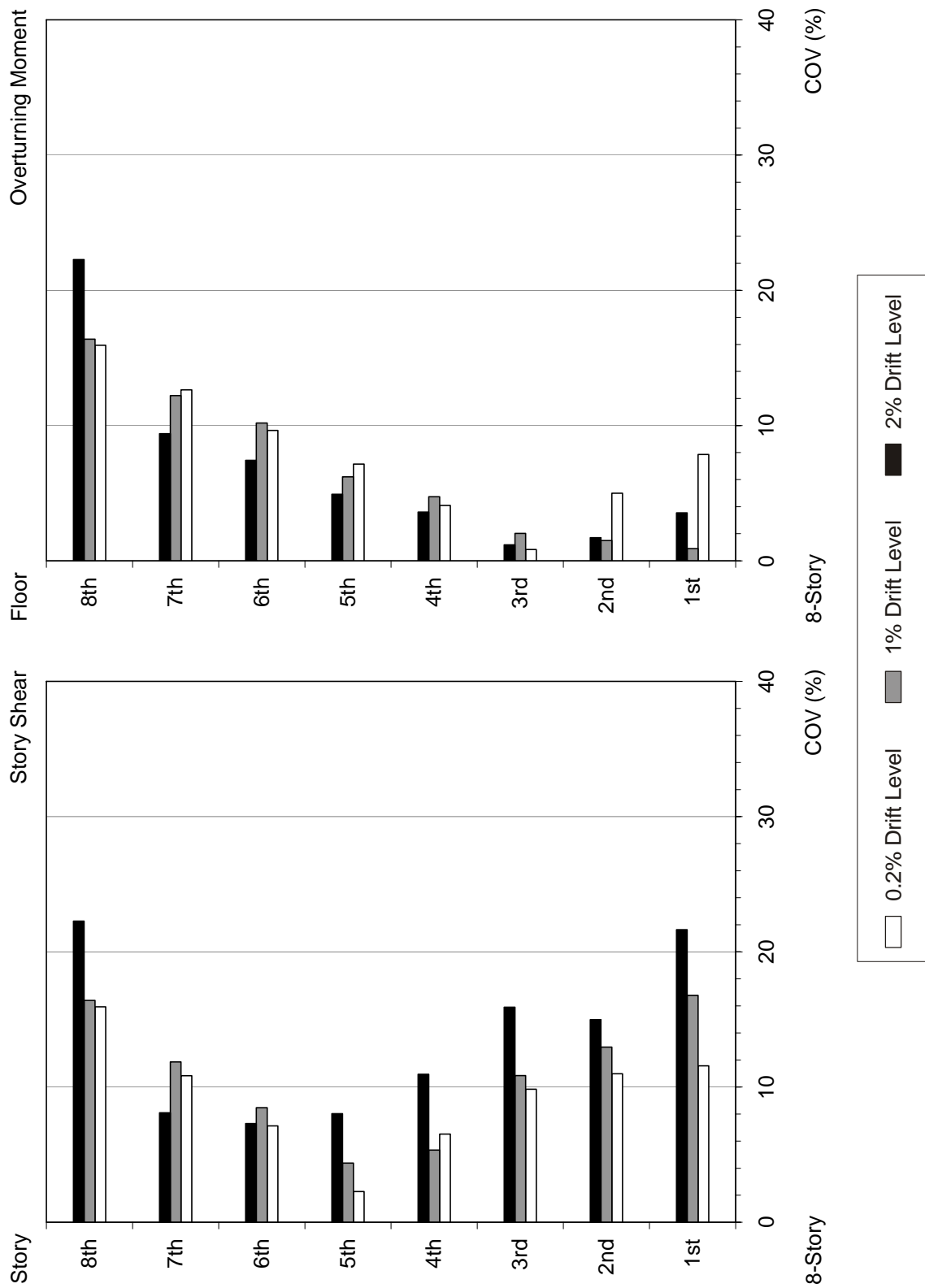Figure F-79   Observed COVs for the 8-story wall building

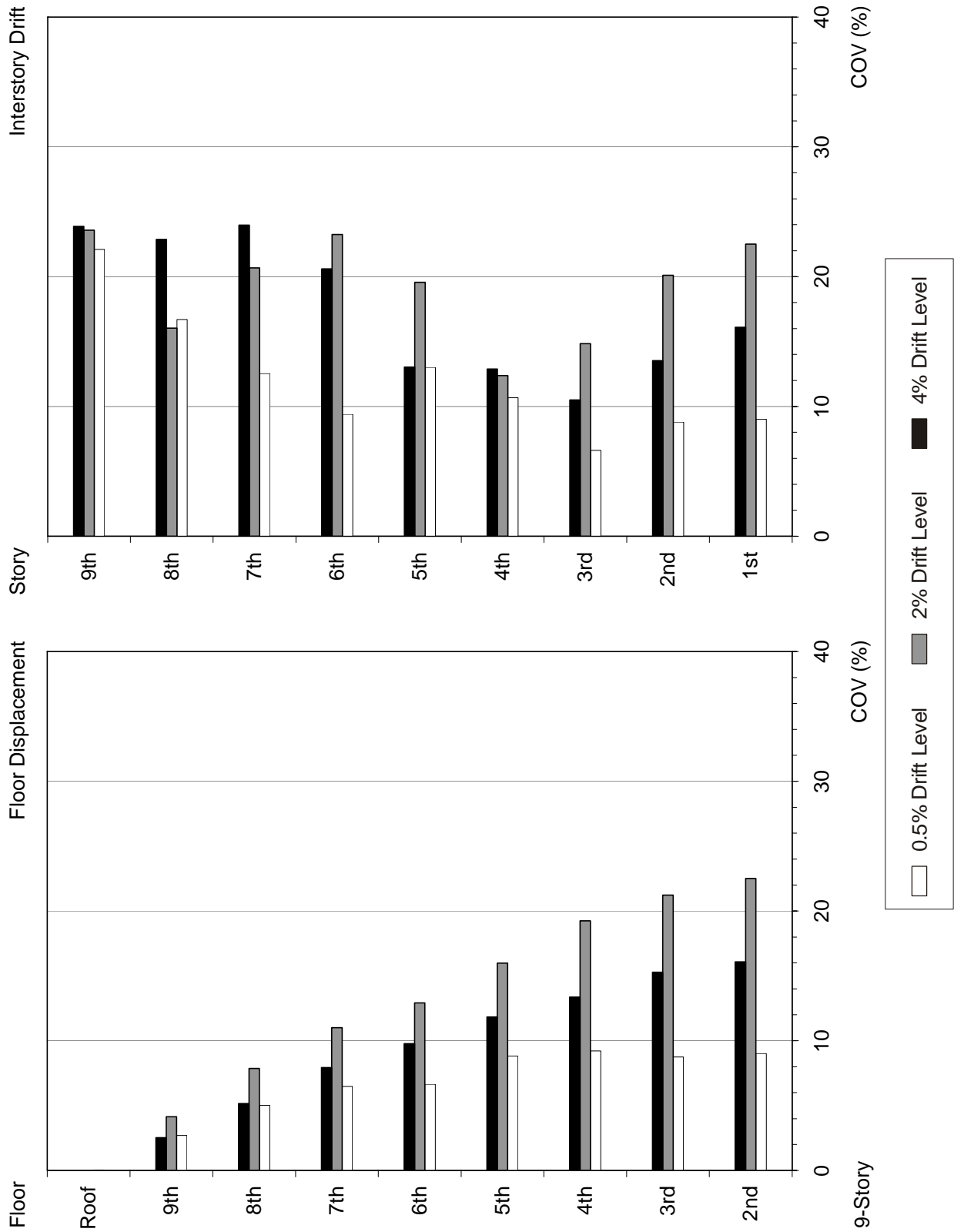Figure F-79   Observed COVs for the 8-story wall building (continued)

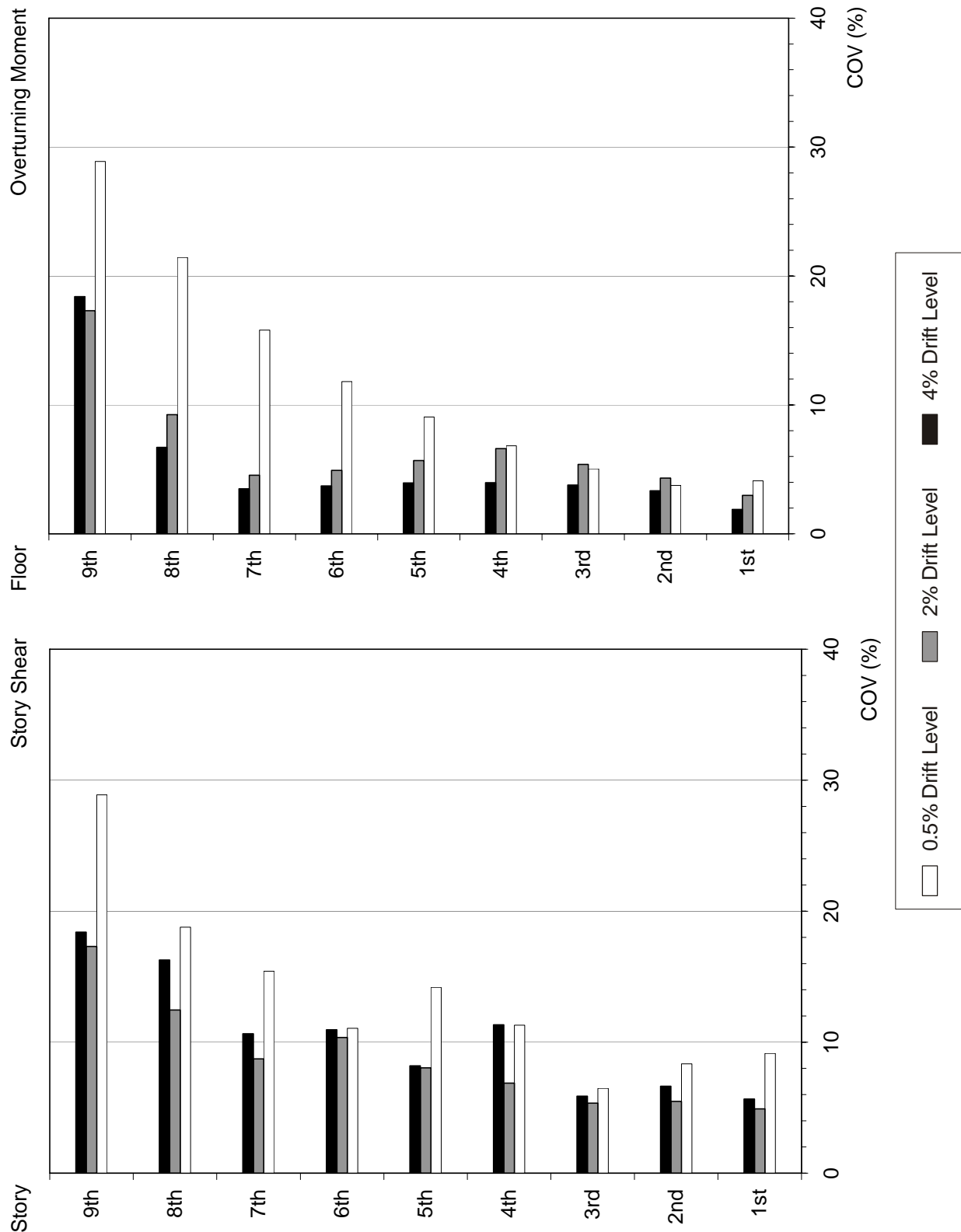Figure F-80　　Observed COVs for the 9-story frame building

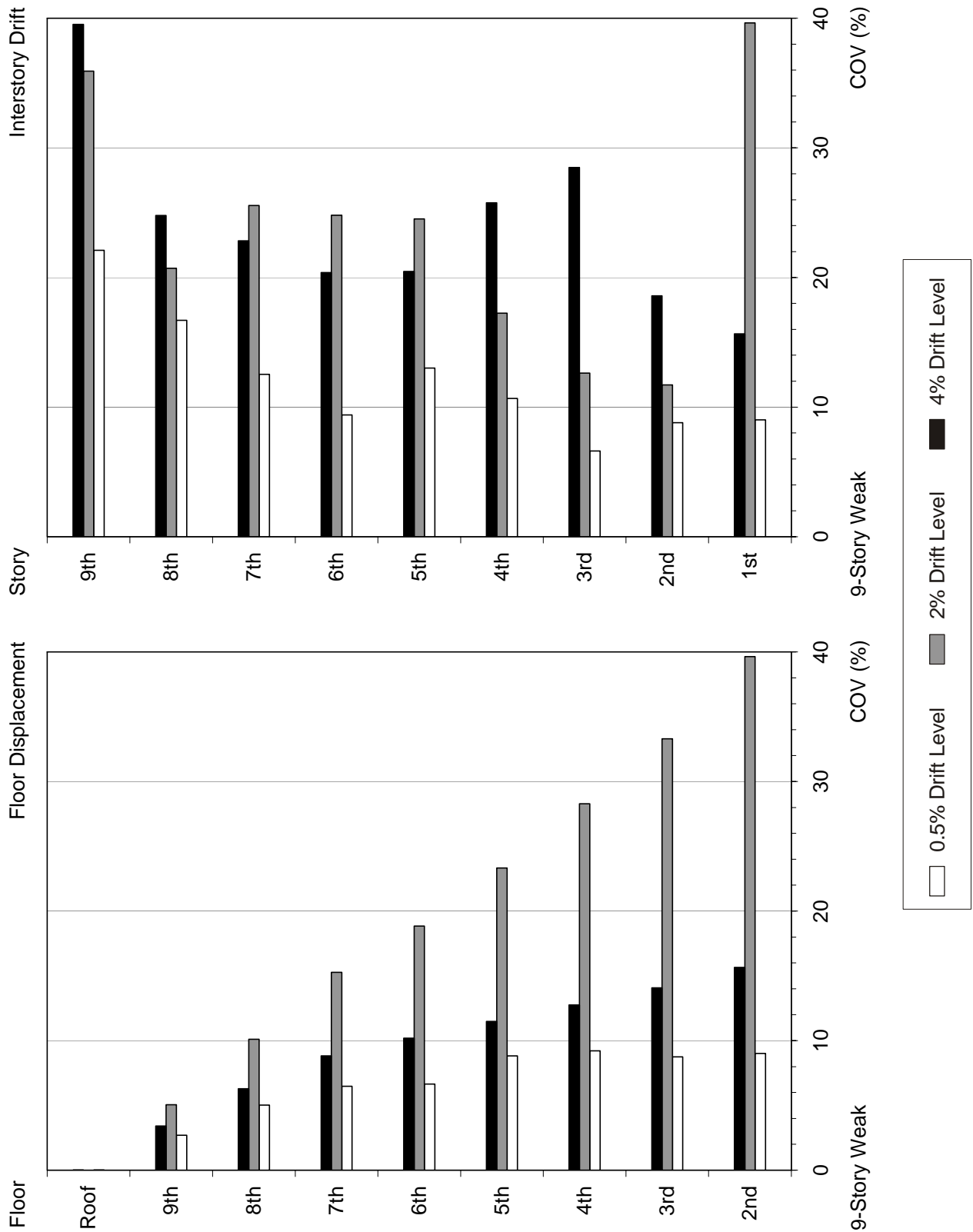Figure F-80   Observed COVs for the 9-story frame building (continued)

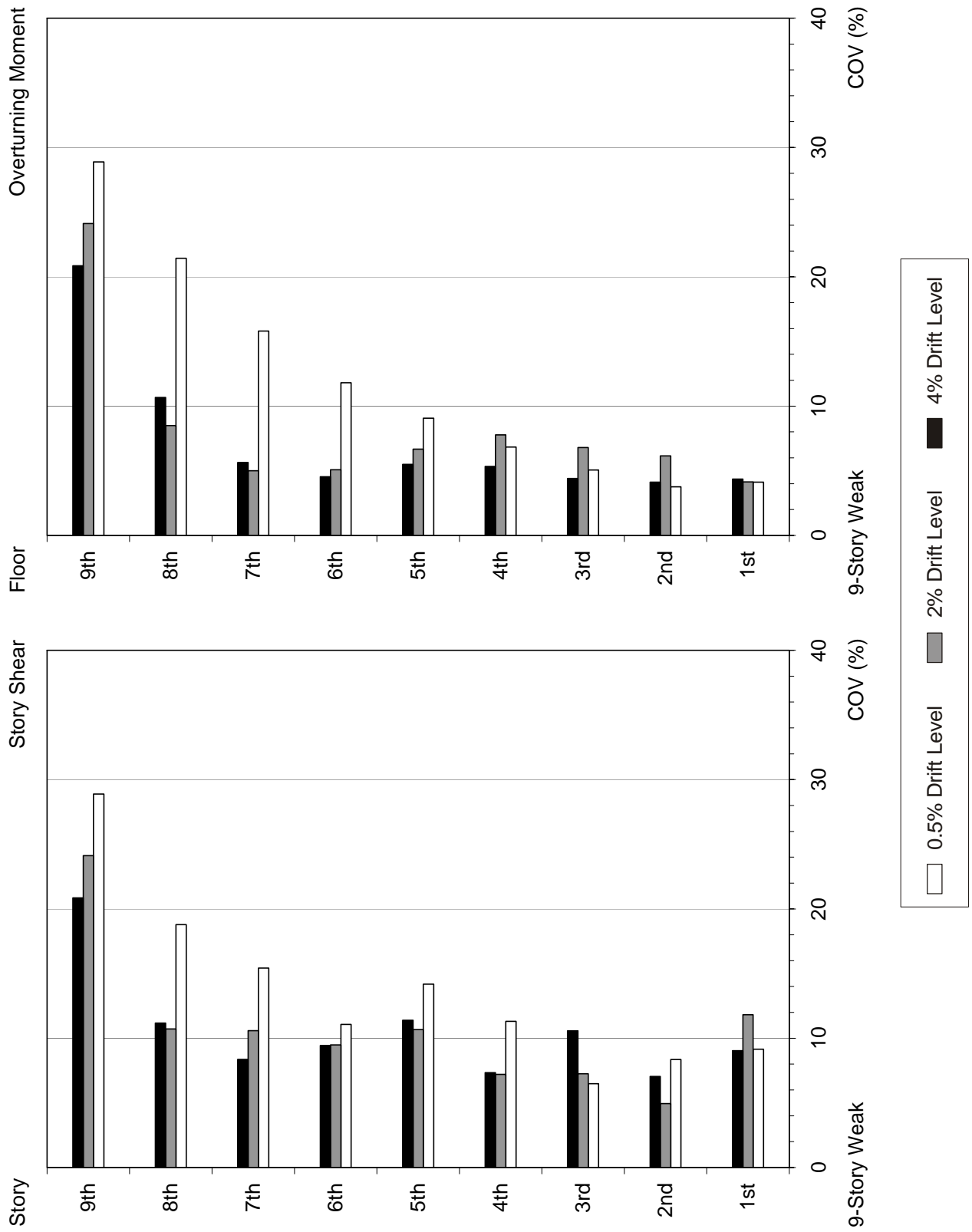Figure F-81   Observed COVs for the 9-story weak story frame building

Figure F-81   Observed COVs for the 9-story weak story frame building (continued)

F.9 References

Chopra, A., and Goel, R., 2001, *A Modal Pushover Analysis Procedure to Estimate Seismic Demands for Buildings: Theory and Preliminary Evaluation* PEER Report No. 2001/03, Pacific Earthquake Engineering Research Center, University of California, Berkeley.

Chopra, A.K., and Goel, R.K., 2002, "A modal pushover analysis procedure for estimating seismic demands for buildings," E*arthquake Engineering and Structural Dynamics*, Vol. 31, pp. 561-582.

Chopra, A.K., Goel, R.K., and Chintanapakdee, C., 2003, "Statistics of single-degree-of-freedom estimate of displacement for pushover analysis of buildings," *Journal of Structural Engineering*, Vol. 129, No. 4, pp. 459-469.

Collins, K.R., Wen, Y.K., and Foutch, D.A., 1995, *Investigation of Alternative Seismic Design Procedures for Standard Buildings*, UILU-ENG-95-2003 Report, Civil Engineering Studies, Structural Research Series No. 600, Dept. of Civil Engineering, University of Illinois at Urbana-Champaign, 187 pages.

Cuesta, I., and Aschheim, M.A., 2001, *Using Pulse R-Factors to Estimate Structural Response to Earthquake Ground Motions*, CD release 01-03, Mid-America Earthquake Center, Urbana, Illinois.

Hernández Montes, E., Kwon, O-S, and Aschheim, M., 2004, "An energy-based formulation for first- and multiple-mode nonlinear static (pushover) analy-ses," *Journal of Earthquake Engineering,* Vol. 8, No. 1, pp. 69-88.

Iwan, W.D., and Chen, X.D., 1995, "Important near-field ground motion data from the Landers earthquake," *Proceedings 10th European Conference on Earthquake Engineering*, Vol. 1, A.A. Balkema, Rotterdam, pp. 229-234.

Miranda, E., 1991, *Seismic Evaluation and Upgrading of Existing Buildings*, Ph.D. thesis, University of California at Berkeley.

SAC, 2000, *State of the Art Report on Systems Performance of Steel Moment Frames Subject to Earthquake Ground Shaking*, FEMA 355C Report, prepared by the SAC Joint Venture (a partnership of the Structural Engineers Association of California, the Applied Technology Council, and California Universities for Research in Earthquake Engineering) for the Federal Emergency Management Agency, Washington, D.C.

Seneviratna, G. D.P.K., and Krawinkler, H., 1997, *Evaluation of Inelastic MDOF Effects for Seismic Design*, BLUME-120 Report, John A. Blume Earthquake Engineering Center, Stanford, California, 177 pages.

FEMA Reports

FEMA 368, 2000, *NEHRP Recommended Provisions for Seismic Regulations for New Buildings and Other Structures, Part 1 - Provisions*, prepared by the Building Seismic Safety Council for the Federal Emergency Management Agency, Washington, D.C.